The Dissertation Committee for Darshan Jitendra Sachde Certifies that this is the approved version of the following dissertation:

Absorber Performance and Configurations for CO_2 Capture using Aqueous Piperazine

Committee:

Gary Rochelle, Supervisor

Michael Baldea

Abhoyjit Bhown

Eric Chen

Gyeong Hwang

Absorber Performance and Configurations for CO_2 Capture using Aqueous Piperazine

by

Darshan Jitendra Sachde, B.S. CH.E; M.P.Aff.; M.S.E

Dissertation

Presented to the Faculty of the Graduate School of

The University of Texas at Austin

in Partial Fulfillment

of the Requirements

for the Degree of

Doctor of Philosophy

The University of Texas at Austin

May 2016

Dedication

To my family

Acknowledgements

The past five years at the University of Texas at Austin have been the most challenging and rewarding period of my professional and educational life. This is in no small part due to the amazing group of intelligent, kind, and supportive people I have worked with in many ways at UT.

First and foremost, I'd like to thank Dr. Rochelle for everything he has done for me over the years. His role in my personal and professional development is far greater than the title of advisor would convey. He encouraged and sparked my interest in research as an undergraduate, continued to expand my view as we worked on public policy issues, and ultimately led me along every step of my development as an engineer. He has constantly challenged me to think about problems in new and different ways and I have never walked out of a meeting with him without learning something new. The seemingly simple task of keeping up with him in our discussions has led me to a much deeper understanding of chemical engineering. The time, passion, and energy he invests in his students, graduate and undergraduate, is the model of what it means to be an educator. More importantly, Dr. Rochelle is a better person than he is researcher, educator, and engineer – he has taught me that dedication to your work does not come at the expense of family and faith, but that each is an important part of defining a person.

I would also like to thank my committee members. I was fortunate to take a graduate course from Dr. Michael Baldea, which was one of the most challenging and interesting courses during my time at UT. He was always available to talk and I know he will be a great asset to the department for years to come. Dr. Abhoyjit Bhown of EPRI was a true pleasure to interact with at our research meetings and conferences – he always

asked insightful, thought-provoking questions of me and provided feedback at many stages of this work – he is someone I look up to in our field. Dr. Eric Chen spent many hours with me as I developed pilot plant analyses and is someone I consider a friend and mentor. His efforts at the Separations Research Program are invaluable to our research group. I have known Dr. Gyeong Hwang since he taught me undergraduate Transport Phenomena many years ago. He is one of the kindest and most approachable people I have interacted with in my years at UT and his fundamental questions about my work always sparked interesting discussions.

I have been fortunate to interact with many of Dr. Rochelle's research group members over the years, and I am indebted to a long list of his previous students. I want to acknowledge a few who I have worked with closely over the past five years. First, I'd like to thank Dr. Jorge Plaza for mentoring me as he finished his dissertation – I now have full appreciation for the time he took for me during a stressful period. I'd like to thank my officemates Peter Frailie, Steven Fulk, Brent Sherman, and Yue Zhang for sharing coffee runs, discussions about sports, politics, and research, and for generally creating an enjoyable work environment. Yue has been a huge help to me over the last couple of years and I am excited to see the great work she does in her time at UT. In addition, I would like to thank Yong Kim, my undergraduate research assistant, who made many contributions to this work and was a pleasure to work with. I'd also like to thank the many other research group members I collaborated and commiserated with: Tarun Madan, Yu-Jeng Lin, Chao Wang, Di Song, Lynn Li, Omkar Namjoshi, Kent Fischer, Paul Nielsen, Stuart Cohen, Alex Voice, Ye Yuan, Yang Du, Junyuan Ding, Matt Beaudry, Matt Walters, Humera Rafique, and Nathan Fine. I was lucky to share my time at UT with such an exceptional group of people. Finally, as everyone in our research group knows, Maeve Cooney is the real reason everything functions on a daily basis. I

have really enjoyed our random chats about everything from dogs to politics in her office – even if it started with an excuse about an overdue progress report.

Our work at UT would not be possible without the contributions and support of our sponsors in the Texas Carbon Management Program, many of whom I have met at our research meetings where they have provided technical and professional advice – it is truly an invaluable experience to interact with so many academic, industrial, and public sector leaders as a student. I hope the program stays strong for years to come as it has value beyond the research it has produced.

Finally, all of my accomplishments have come from the sacrifices of my family. My parents, who left everything in India to come to the U.S. to provide us with opportunities they never had, have always been an inspiration to me. My father did not get to see where my sister and I ended up in life, but I hope we have made him proud. My mother is a reminder to me that strong women rarely get credit for all that they endure and overcome. My sister has always been there when I've needed it and I have never done enough in return as the older brother. Last, but not least, to my beautiful wife Sara – you and our daughter Annika are the best things in my life. You have supported me at every step of my academic journey, even when it seemed like it might never end. I don't tell you enough how much you mean to me and how lucky I am to have you – I can't imagine doing any of this without you. Our best years as a family are only beginning.

Absorber Performance and Configurations for CO_2 Capture using Aqueous Piperazine

Darshan Jitendra Sachde, Ph.D.

The University of Texas at Austin, 2016

Supervisor: Gary Rochelle

Absorber design for CO_2 capture with amine solvents is complicated by the presence of temperature gradients and multiple rate controlling mechanisms (chemical reaction and convective mass transfer). The development of rigorous rate-based models has created the opportunity to study the performance limiting mechanisms in detail. A structured approach was developed to validate absorber models, identify limiting phenomena, and develop configurations that specifically address limiting mechanisms. A rate-based model utilizing concentrated aqueous piperazine (PZ) was the focus of model validation and process development.

The model was validated using pilot plant data, matching the number of transfer units (NTU) within $\pm$ 1% while identifying a systematic bias (loading measurement) between the model and pilot plant data. The validated model was used to define limiting cases (isothermal and adiabatic absorbers) to study the effects of operating conditions on the formation of temperature-induced mass transfer pinches. The method allowed for screening of intercooling benefits – high CO_2 applications (15% - 27% CO_2) require intercooling over the entire practical loading range for PZ and benefit significantly from simple in-and-out intercooling with limited additional benefit expected from advanced design. Low CO_2 (4% CO_2) applications are expected to benefit the most from improved

intercooling, but also have the largest operating window without the need for intercooling (< 0.22 mol CO_2/mol alkalinity for 8 m PZ).

An analogous approach was developed to study rate mechanisms. A mass transfer parameter sensitivity analysis approach was developed to identify the relative contribution to overall mass transfer resistance of each mechanism as a function of operating conditions and position in the absorber column. The pseudo-first order and instantaneous reaction asymptotic solutions to the reaction-diffusion problem were used to define a dimensionless parameter that quantifies the approach of the modeling results to the limiting conditions and was found to be predictive of the relative liquid film resistance (diffusion vs. reaction) at all conditions. The results of the analysis indicated that the absorber is strongly diffusion controlled, has limited gas-film resistance, and that equilibrium constraints at the rich end of the absorber (depletion of free amine) significantly increase diffusion limitations.

Finally, the validation and mechanistic studies provided the basis for four new absorber configurations: 1) integration of a spray nozzle in the intercooling loop, 2) solvent recycle intercooling, 3) integrated flue gas and solvent cooling functions, 4) hybrid intercooling (high intensity contacting with intercooling). Each approach coupled mass transfer enhancement with intercooling and provided new degrees of freedom for operation and design of absorbers for CO_2 capture.

Table of Contents

List of Tables

List of Figures

Chapter 1: Introduction and Background

1.1 Status of CO_2 Capture

The Kyoto Protocol, adopted in 1997, signaled a potential consensus for international policy action to address climate change and initiated extensive research into greenhouse gas management (GHG) management and mitigation strategies. Early research on climate stabilization scenarios proposed the application of carbon capture and storage (CCS) to fossil fuel electricity generation as a critical component (or "wedge") required to achieve near term emissions reductions. In particular, the need to scale-up well-developed existing technologies was emphasized as a necessary part of any GHG mitigation strategy (Pacala & Socolow, 2004).

In response to this emphasis on near-term emissions reductions, capture applications focused on flue gas from coal-fired power plants due to the dominant position of coal in electricity generation markets. As Figure 1-1 depicts, coal accounted for over 50% of electricity generation in the United States (U.S.) in 2000 with the electricity generation sector accounting for 35% of all CO_2 emissions in the U.S (U.S. Energy Information Administration, 2014).

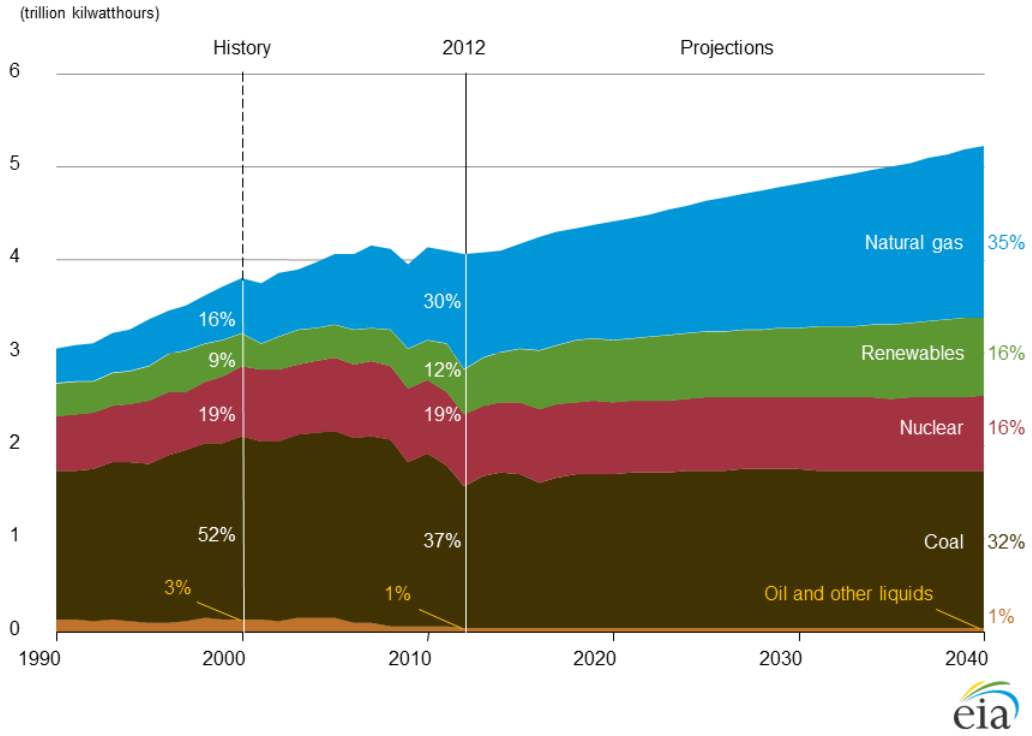

Figure 1-1: Electricity generation by fuel source in the United States, 1990 – 2040 (U.S. Energy Information Administration, 2014)

Furthermore, coal was expected to remain the dominant fuel in the electricity generation sector due to the large existing stock of coal-fired power plants and the abundance of relatively cheap domestic coal in the U.S. In response, capture technology was developed targeting flue gas concentrations representative of coal-fired boilers (12-15 mole % CO_2). The technology options for capture can be broadly classified into post-combustion, pre-combustion, and oxy-combustion technologies. Post-combustion technology was recognized as the most realistic option to retrofit existing coal-fired power plants since pre-combustion and oxy-combustion require major rebuild/modification of the combustion portion of the process and are better suited for long-term new build plants (Deutch & Moniz, 2009). Additionally, absorption-stripping

with amine solvents was identified as the most established technology in post-combustion capture based on extensive development in industrial processes (Rochelle, 2009). A technical review of 95 post-combustion capture research projects confirmed the prominence of absorption-stripping (60% of all projects) at all levels of development, but particularly for technologies approaching commercial deployment (Bhown & Freeman, 2011). The focused research efforts with amine scrubbing have reached demonstration scale on power plant flue gas with the operation of capture from a 110 MW slipstream from the SaskPower Boundary Dam coal-fired power plant (Massachussetts Institute of Technology, 2015).

However, recent developments in climate change policy, prevailing economic conditions, and the electricity generation sector in the United States have led to re-evaluation of mitigation strategies. First, the absence of comprehensive climate change legislation or associated market incentives for carbon capture has led to a focus on CO_2 capture for utilization (e.g. enhanced oil recovery (EOR), sale to secondary use markets) to offset costs associated with capture and transport of CO_2. The aforementioned Boundary Dam project includes EOR and sale of CO_2 to secondary markets, and sale of by-products to address project costs. While power plants such as Boundary Dam represent ideal application of capture process, large scale projects will generally lack sufficient access to economic incentives without government regulations or markets. However, smaller scale projects have introduced a wide variety of CO_2 sources as potential capture targets with potentially favorable economics. For example, the M.I.T. Carbon Capture and Sequestration Technologies Program cites projects for capture from steel, cement, refineries, ethanol/methanol production, and natural gas processing among others (Massachussetts Institute of Technology, 2015). These sources include a wide range of CO_2 flue gas concentrations, approaching 30 % CO_2 in some cases.

More significantly, the electricity generation sector in the United States has undergone a drastic shift due to large-scale extraction of natural gas from shale formations. Figure 1-1 also illustrates the increasing role of natural gas combustion in the electricity generating sector from 2009 forward. Despite lower CO_2 emissions from natural gas combined cycle (NGCC) facilities compared to coal-fired boilers (higher plant efficiencies, lower C:H ratio in the fuel), large-scale deployment of NGCC power plants is inadequate as a mitigation strategy. Methane leakage during natural gas production and displacement of renewable energy technology would further reduce limited GHG emissions benefits realized via fuel switching (Shearer, et al., 2014). Meaningful emissions reductions from continued expansion of NGCC would therefore require CCS for NGCC plants as well. NGCC plants present a unique set of design challenges with large flue gas volumes and dilute CO_2 concentrations (3–5 mol% CO_2), when compared to coal-fired boilers.

The post-combustion capture technology that has been developed to target coal-fired boilers can be readily adapted to alternate flue gas sources as a tail-end technology. Thus, while coal-fired boilers will remain an important target of capture technology, amine scrubbing technology should be customized for a variety of flue gas sources to account for the range of projects that may be dictated by local economic incentives or policy requirements. The wide range of CO_2 concentrations and sources as potential targets for CO_2 capture have generated a need for systematic evaluation of capture process development as a function of flue gas conditions and validation of model predictions and processes over a wide-range of operating conditions. The broad design and development of technology also promises to yield insights regarding general design procedures, the fundamental phenomena governing capture process performance, and the

effect of operating conditions on the cost of capture when a process is optimally designed for its application.

1.2 Amine Scrubbing Process Design and Modeling

Even as capture technology approaches commercial scale for power generation systems, active research continues in the development of new solvents, process configurations, process control, optimization, system modeling, and economics. Development and use of rigorous process models underlies many of these research areas. Figure 1-2 depicts a simple absorption-stripping process configuration to illustrate the primary unit operations that must be modeled.

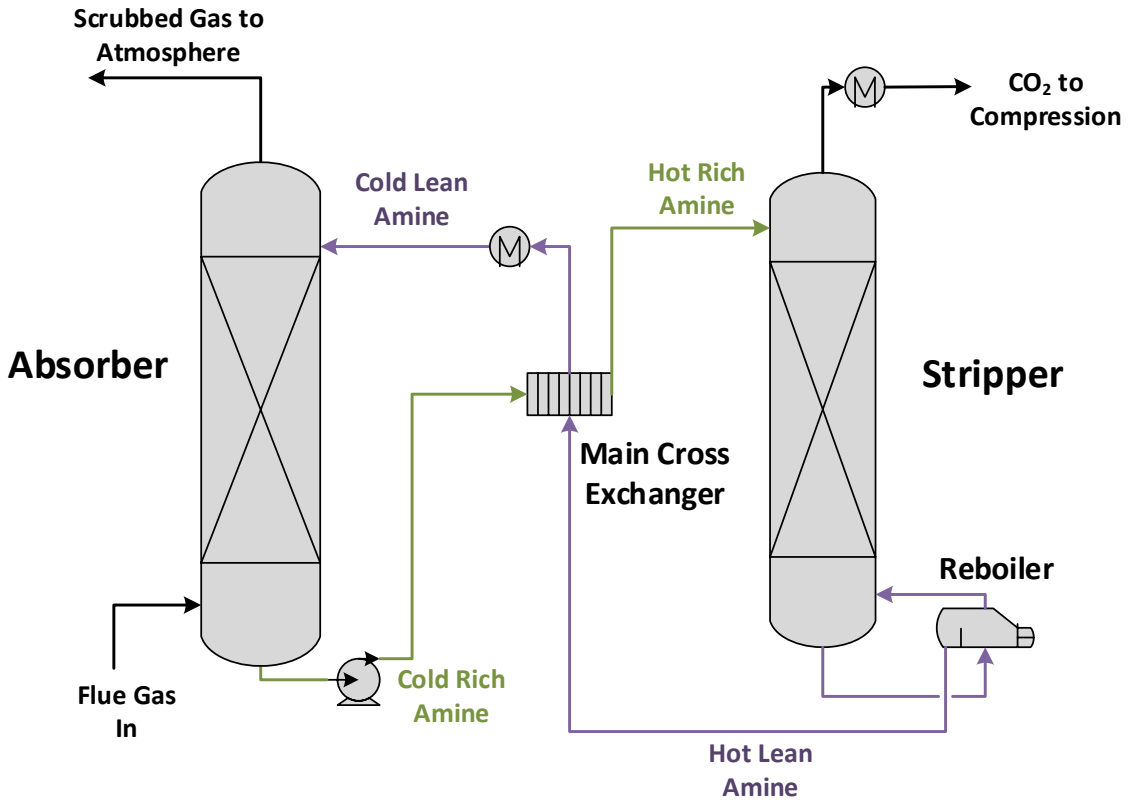

Figure 1-2: Simple Absorption-Stripping Process Flow Diagram

In the basic absorption-stripping process, flue gas enters the bottom of the packed absorber column after passing through pre-treatment processes (flue gas desulfurization, direct contact cooling, etc.). The flue gas counter-currently contacts a lean solvent that is fed at the top of the absorber and absorbs CO_2 as it moves down the column. The scrubbed gas passes through a water wash (not pictured, nominally located in the top of the absorber) to recover amine in the gas phase and is vented to the atmosphere. The rich solvent leaves the bottom of the absorber where it is pumped through a cross-exchanger where it is heated by the hot lean solvent returning from the stripping process. The rich amine is fed at the top of the stripper, where it counter-currently contacts hot vapor moving up the stripper column from the reboiler. The vapor strips CO_2 from the solvent, passes through a condenser to remove water, and is sent to the compression system for transport and storage. The stripped, or lean, solvent leaves the reboiler and is re-circulated to the absorber after being cooled in the cross-exchanger and trim cooler.

1.2.1 Absorber Development for CO_2 Capture

The design and development of the absorber unit operation will be the primary focus of this work. The process description in the preceding discussion highlights the role of the absorber in overall process design. Absorber design is a balance between mass transfer requirements (e.g., packing or other internals) and energy costs of system (lean loading and solvent circulation). There are two aspects of absorber design for CO_2 capture with amine solvents that add significant complexity to the modeling and design process. First, the CO_2 absorption process is rate-based where physical mass transfer and chemical reaction are both significant (reaction-diffusion problem) in determining overall mass transfer resistance. Therefore, equilibrium design procedures are inadequate and the

data requirements (quantity and quality) and modeling complexity increase significantly as each underlying mechanism must be represented accurately to model the coupled absorption problem.

Secondly, the reaction between amines and CO_2 generates heat in the solvent, coupling heat and mass transfer, and invalidates the significant simplification of an isothermal absorber. The heat generated in the solvent is transferred between the phases by water – this process leads to a temperature maximum (or bulge) in the absorber. The temperature bulge in the absorber can limit overall absorption capacity and rates by introducing a temperature-induced equilibrium constraint on the process. Properly modeling and understanding the effects of the temperature gradients in the absorber is essential to design and optimization of the absorption process.

Prior research in absorber modeling has focused extensively on model development to provide tools to adequately represent the aforementioned phenomena in the absorber. However, rigorous model development built on high quality experimental data does not ensure that the absorption process is accurately represented. In addition, a rigorous model does not imply that optimal absorption process design is obvious or trivial; in fact, the rigorous representation ensures that many additional variables are represented that ultimately influence process design and development. Therefore, this work will shift to a focus on absorber process design by validating and applying an existing modeling framework. Specifically, the work will focus on concentrated piperazine (PZ) due to extensive prior development of the solvent. Previous researchers developed the thermodynamic and kinetic framework (Cullinane, 2005), (Hilliard, 2008), (Plaza, 2011), (Frailie, 2014) required to model PZ processes and began the effort of evaluating process configurations and costs (Plaza, 2011), (Frailie, 2014). The "Independence" solvent model was developed in Aspen Plus® which allows

implementation of a rate-based absorber model to account for the effects of mass transfer with chemical reaction, heat transfer, column internals, and hydraulics (Frailie, 2014). The use of a rigorous modeling framework will facilitate a systematic study of absorber performance to guide process development as a function of operating conditions and equipment specifications.

1.3 RESEARCH OBJECTIVES

The following research objectives will detail the approach used to validate a rigorous model, use the model to develop insights regarding mechanisms controlling process performance, and developing novel absorber designs driven by the newly developed mechanistic understanding. The over-arching goals of the research are to use a rigorous rate-based model of a packed absorber column utilizing amine-based solvents to accomplish the following:

1) Connect absorber performance results to the fundamental mass transfer, thermodynamic, and kinetic properties that form the basis of the model. Identify limiting phenomena for absorber performance.
2) Generalize absorber performance as a function of operating conditions and solvent characteristics.
3) Develop new process designs over the entire range of relevant applications and conditions based on findings of the previous two steps.

An important extension of these goals is to yield insights beyond the model and solvent system studied by defining approaches to evaluate rate-based models, identifying mechanisms that are generally important to amine scrubbing absorption processes, and providing performance generalizations as a function of operating conditions and

equipment specifications that extend to other amine/solvent systems. Several research activities have been outlined to achieve these broad objectives.

Absorber Model Validation: Pilot Plant Data Reconciliation

The rate-based absorber model is built from the bottom-up using experimental data to regress the mass transfer, kinetic, and thermodynamic parameters used in the final absorber model. The model in this state only represents the experimental data and may be connected semi-empirically to expected performance in an operating column. Data from a pilot scale column can provide a means to validate or correct the model to improve prediction of large-scale performance results (packing required, CO_2 absorbed, etc.). Validation of the absorber model with pilot plant data will require the following:

1) Pilot plant data from a range of operating conditions and equipment configurations that cover relevant design conditions for the field.
2) Error quantification for the pilot plant data itself (random error in the pilot measurements).
3) Minimization of error between model predicted and pilot plant measured results by allowing model adjustments.

Process Development: Parameter Sensitivity Analysis

Mass transfer performance in the absorber is dictated by coupled differential equations for mass transfer with chemical reaction and heat transfer subject to constraints imposed by phase and thermal equilibria. The parameters defining the transport, kinetic and thermodynamic models are not explicitly varied in process optimization, but understanding the relative importance of each of the fundamental contributions to mass transfer rates can guide design and development of absorbers. Furthermore, sensitivity analysis of parameters in the underlying models allows comparison of model behavior to

theoretical understanding of the process and can identify limitations or shortcomings of the overall absorber model. The following tasks are proposed to achieve the stated goals of parameter sensitivity:

1) **Parameter selection** will include identification of parameters with large inherent uncertainty in measurement (e.g., mass transfer coefficients), parameters identified through pilot plant analysis, and parameters expected to be significant from theoretical understanding of the process and literature review.
2) **Sensitivity analyses** will include systematic evaluation of selected parameters over a range of relevant operating conditions and applications to identify important parameters as a function of the design choices and constraints. This includes evaluation of parameter sensitivity as a function of position within the column itself as process conditions (e.g., loading, temperature, driving forces) can vary widely in the absorber. The results will guide development and optimization of novel process design as a function of the specific conditions for operation.

Process Development: Maximizing Solvent Capacity and Process Screening

Absorber design can be viewed as a trade-off between capital costs (packing requirement) and energy performance (measured as solvent circulation rate for the absorber). The development of new absorber configurations is driven by maximizing solvent capacity with the minimum packing requirement. To develop new absorber designs to achieve this goal, a screening method is proposed to identify operating conditions where new designs may provide large benefits and to rank designs relative to a

common baseline. An adiabatic absorber and isothermal absorber (bounding cases) will be used to develop a screening method for new designs.

1) **Minimum solvent rate analysis** will be used to evaluate the base case absorber designs in the limit of "infinite packing" to determine the maximum solvent capacity or best energy performance for each design at a given operating condition.
2) **Evaluation of the packing requirement** as a function of solvent rate (moving away from the limiting minimum solvent rate case) will identify mass transfer limitations in the base case designs.

Process Development: Novel Configuration Development

Flow sheets will be developed for a series of representative capture application cases (e.g. NGCC, coal-fired boiler, steel blast furnace) using results from preceding activities. The focus of flow sheet development will be intercooling configurations and hybrid contacting (i.e., use of different mass transfer contacting methods based on the operating conditions of the column or in a portion of the column). The goal will be to develop absorber design targeted for specific process conditions and limiting phenomena for the equipment and solvent system. The tasks required for this activity include:

1) Identification of potential flow sheets including discrete design choices (e.g., intercooling vs. no intercooling) based on the preceding screening work.
2) Development of incremental economic analysis to narrow the window of operating conditions and equipment specifications.
3) Systematic comparison of novel designs to baseline flowsheets to quantify performance improvement and provide fundamental explanations for the predicted benefits.

Chapter 2: Model Validation – Pilot Plant Analysis[1]

An important aspect of process model development is validation of the model with pilot scale data. Rate-based absorber models are developed from the bottom-up based on experimental scale data representing the underlying thermodynamic, kinetic, and transport properties that govern mass transfer with chemical reaction. The accuracy and validity of the experimental data and the ability of the model to properly represent the data do not constitute validation of the model for purposes of process design and development. Pilot scale (or larger) data tests the ability of the model to represent process performance as predicted by the interaction of all of the underlying phenomena the model was designed to represent. In addition, the model may not adequately capture all phenomena relevant for true process conditions and scale, and the pilot plant data provides an opportunity to "tune" and adjust the model to represent process performance.

2.1 Overview of Pilot Plant Data Reconciliation and Model Validation

In general, data reconciliation can be described as a constrained optimization problem where measured values from a plant or experiment are adjusted to satisfy physical constraints (e.g., mass or energy balance). Data reconciliation can be coupled with model validation by using a model to represent the mass and energy balance and associated constitutive relationships describing the rate processes underlying the balance equations. This work proposes combined reconciliation and validation by using pilot plant data from the Separations Research Program (SRP) at the University of Texas at Austin and a rigorous rate-based absorber model built in Aspen Plus®.

[1] This chapter includes a summary of two manuscripts and will reproduce significant portions of the documents with permission of the authors. See (Sachde, et al., 2013) (included in Appendix C) and (Zhang, et al., 2016).

Within the literature, approaches to quantify model and pilot plant differences, define acceptable model predictions, identify sources of error in the model and pilot plant data, and correct models varies widely. The majority of model validation activities related to CO_2 capture in literature perform a simple calculation of deviation between model predictions and pilot data for select material and energy balance results. A qualitative assessment usually determines the adequacy of the model prediction. While the use of this approach can be justified for general screening of multiple models/simulation packages or by a lack of data regarding measurement error, the method has several shortcomings when attempting to rigorously validate and improve models. Select examples from literature are highlighted here to demonstrate more rigorous methods of evaluating model performance with pilot plant data.

Researchers at the Laboratory of Engineering Thermodynamics (LTD) at the University of Kaiserslautern in Germany evaluated a rate-based absorber model using data from several MEA campaigns at multiple pilot scales (von Harbou, et al., 2014). The authors found that specific conditions were very sensitive to changes in the input parameters and could not be adequately modeled with the exact reported values. In general, treating pilot plant model inputs (e.g., feed flows, temperatures, etc.) as deterministic values does not adequately account for the range of valid model results based on uncertainty in the inputs. Further, authors found that measurement error increased at larger scale facilities and reconciliation was not possible without explicit accounting of error at the larger scale plants.

Additionally, the lack of error quantification in the pilot plant data eliminates the possibility of making a quantitative assessment about the adequacy of the model prediction (i.e., are the model predictions within the uncertainty in the measured data?). Work on reactive distillation at LTD incorporated a more rigorous approach to data

reconciliation and error analysis (von Harbou, et al., 2013). The authors used measurement error to identify variables with gross error (required a statistically significant change in the parameter value compared to the measured error to satisfy basic constraints of the pilot plant data i.e., mass and energy balance closure). The authors then used numerical perturbation of their model to propagate error to model predictions to make a quantitative assessment of model results.

2.1.1 Proposed Reconciliation Method

The current work proposes a data reconciliation and model validation procedure developed around the "Data-Fit" tool in Aspen Plus® which allows for simultaneous data reconciliation, gross error detection, and parameter estimation (i.e., model parameter corrections to fit pilot plant data). The objective function defined for the reconciliation tool is presented in Equation 2.1.

$$\min_{v,input} \frac{1}{2} \sum_{i=1}^{N} \left(\frac{\text{Measured}_i - \text{Reconciled}_i}{\sigma_{Measured,i}} \right)^2 \qquad 2.1$$

where,

Measured, i = Measured value input or result parameter,

Reconciled, i = Reconciled value of input or result parameter,

σi = Variance of measured values from plant or experiment,

v = Vector of adjustable or varied parameters,

Input = Reconciled input parameters.

The proposed method is a modification and extension on the approach used by Plaza for model reconciliation of pilot plant data from the Pickle Research Center (PRC)

plant operated by the Separations Research Program (SRP) facility at the University of Texas at Austin (Plaza, 2011). The approach can be summarized in the following steps:

1) Error Quantification and Data Consistency Check: This step includes quantification of random error in all pilot measurements and inputs using the available replicate measurements. Basic material balance checks for the measured components (CO_2 and PZ) will be performed to ensure internal consistency for data from the plant.
2) Gross Error Detection: Prior to any adjustment of model parameters, the Aspen Plus® model will be used to reconcile the measured pilot plant data with model predictions based on the quantified uncertainty in step 1. Variables that require changes that are statistically different from the measured values will be identified as variables with gross error or bias.
3) Data Reconciliation with Parameter Adjustment: If the model cannot be reconciled with pilot data within the measured uncertainty, adjustable parameters from the model will be added to the reconciliation process. However, only a single adjustment parameter will be added at once to prevent over-specification or interaction between adjustment parameters. Several cases will be run to generate a list of potential model adjustments required to reconcile the model with the pilot data.

The goal of this systematic approach is to identify potentially problematic error inherent to the pilot plant data itself followed by identification of potential model adjustments that may illuminate physical explanations for any differences between the model and pilot plant.

2.2 Pilot Plant and Model Overview

2.2.1 Pilot Plant Description

The pilot plant at PRC consists of a full absorption-stripping process which has been operated with various amine solvents to capture CO_2 from a synthetic flue gas. The basic absorber configuration at PRC is depicted in Figure 2-1.

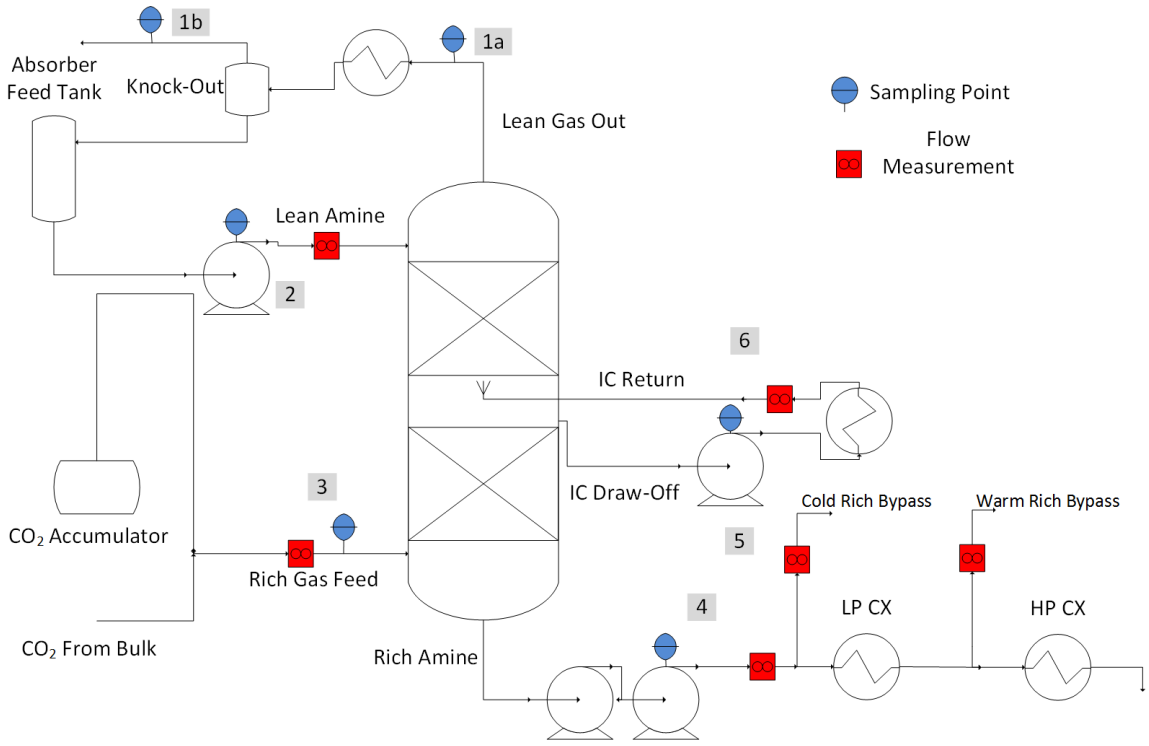

Figure 2-1: Absorber PFD for the pilot plant absorber column operated by the Separations Research Program at the University of Texas at Austin. Configuration based on the October 2011 campaign. The column has an inner diameter of 0.43 m and a total of 6.1 m of packing evenly split in two beds and includes intercooling (with or without spray return) between the beds. Points 1 through 6 correspond to liquid/gas sampling or flow measurement points used in the material balance evaluation.

The absorber at PRC includes two beds of packing (6.1 m total) with solvent intercooling capabilities. The intercooling function can be a simple "in-and-out" where

the solvent is cooled between the beds and returned to the bottom section liquid distributor or it can be returned via a spray nozzle into the underside of the top bed of packing (sprayed upwards). “Spray’ intercooling generates additional mass transfer area as part of the intercooling loop and acts a solvent recycle. The performance of the spray nozzle will be isolated after model validation.

The rate-based model will be used to predict absorber performance (CO_2 removal) based on the material balance measurements in Figure 2-1. Validation of material balance closure and quantification of the uncertainty associated with raw pilot plant data is discussed in Appendix C. Campaigns utilizing piperazine (PZ) as the solvent are summarized in Table 2-1.

Table 2-1: History of Piperazine Pilot Plant Campaigns at SRP – Operating Conditions and Absorber Specifications

Pilot Plant Campaigns		Nov. 2008[1]	Sept. 2010[1]	Dec. 2010[1]	Oct. 2011	Nov. 2013	Mar. 2015
Operating Conditions	Solvent	5 – 9 m PZ	8 m PZ	8 m PZ	3.6 – 3.8 m PZ	8 m PZ	5 – 8 m PZ
	Lean Loading (mol CO_2 /mol alk.)	0.25 - 0.33	0.21 - 0.30	0.25 - 0.30	0.24 - 0.26	0.22	0.18 - 0.26
	Liquid Rate (m3/hr)	2.7 - 4.1	1.8 - 5.9	1.8 - 5.9	2.7	2.5 - 5	1.6 - 3.2
	Gas Rate[2] (actual m3/min)	10	7 - 21	10 - 19	10	10 - 19	10 - 14
	CO_2 Gas Inlet (mol%)	12%	12%	12%	12%	12%	6 - 12%
	CO_2 Removal Spec	60 - 90%	80 - 93%	70 - 93%	70 - 90%	80 - 90%	70 - 97%
Absorber Specifications	Column Inner Diameter (m)	0.43					
	Packed Height (m)	6.1 (2 x 3.05)					
	Packing Type & Specific Area(m2/m3)	Structured 205X	Hybrid 250	Hybrid 250	Structured 350Z	Hybrid 250	Hybrid 250
	Intercooling	No	Yes/No	Yes	Yes (with Spray)/No	Yes (with Spray)	Yes (with Spray)/No
Proposed Model Adjustments	Interfacial Area Factor	1.17 ± 0.15	1.02 ± 0.16	0.72 ± 0.13	See Results		N/A
	CO_2 Multiplier	1.05 + 0.03	1.05 + 0.03	1.06 ± 0.04			N/A
	# of Runs Evaluated	14	12	9	11	4	21

1: Campaigns evaluated by Plaza (Plaza, 2011)
2: Feed Gas at ambient conditions (temperature and water content)

The focus of this work will be the final 3 campaigns which span the full range of operating conditions and include the spray intercooling feature for the first time.

2.2.2 Rate-Based Absorber Model Description

The full details of the rate-based absorber model will not be repeated here and can be reviewed in Appendix C and subsequent chapters. The model consists of three major components:

1) Solvent model ("Independence"): Developed by Frailie to represent concentrated PZ. Includes thermodynamics, kinetics and transport properties of the solvent (Frailie, 2014);
2) Packing/Mass Transfer models: Liquid-film, gas-film, and effective area models developed as a function of packing type and operating conditions (Tsai, 2010) (Wang, 2015);
3) Numerical integration scheme for rate-based absorber: Described in Appendix B.

Parameters from the solvent and packing models will be considered when adjustment is required to match the pilot scale data.

2.3 Key Results from Data Reconciliation and Model Validation

2.3.1 Identification of Systematic Bias via Data Reconciliation

The data reconciliation process was used for two campaigns in Table 2-1: October 2011 (see Appendix C) and November 2013. The process for previous campaigns allowed multiple model parameters to be adjusted simultaneously to fit the pilot plant data (area correction and CO_2 multiplier in Table 2-1) (Plaza, 2011). The method was developed to correct the most probable sources of offset between the model and pilot data

beyond the uncertainty in the model inputs and results. However, as the table shows, the model corrections are not consistent between campaigns, and the area factor even changes the direction of model correction (increase and decrease of interfacial area required). This makes it difficult to identify trends in model corrections that might indicate a source of bias. The approach in the current work proposes using each adjustable parameter independently (only one adjustable parameter per reconciliation process). This produced a series of proposed model corrections that each provides a unique mechanistic or analytical explanation for the offset between the pilot plant and model (Sachde, et al., 2013). The major finding of this process for the two campaigns (October 2011 and November 2013) was an apparent systematic bias between the model predictions and the pilot plant. Table 2-2 summarizes the independent interfacial area and CO_2 corrections (adjustment to the lean solvent loading) required to fully reconcile the model with the pilot plant data (primarily CO_2 removal).

Table 2-2: Model Parameter Adjustments Required for November 2013 and October 2011 PZ Pilot Plant Campaigns

Parameter	Correction Factor: November 2013	Correction Factor: October 2011
CO_2 Correction (Lean Solvent Loading)	1.073 ± 0.013	1.075 ± 0.011
Interfacial Area	0.61 ± 0.01	0.74 ± 0.03
Interfacial Area (Adjusted)**	0.74 ± 0.01	$0.74 + 0.03$

** The adjustment to the area correction is required because the different packing types used in each campaign have different fractional or wetted areas available for mass transfer as predicted by interfacial area model. The adjustment normalizes the packing types to operate with the same fractional wetted area when operated at the same conditions. The result of the normalization is that both campaigns require an identical reduction (percentage or relative basis) in packing area to match the CO_2 transfer rates measured in the pilot plant.

As indicated in Table 2-1, the two campaigns covered a wide range of operating conditions (solvent concentration, gas flow rates, CO_2 removal) and different packing types. Therefore, the finding of identical corrections (albeit for a limited set of data) strongly suggest the presence of a systematic bias between the model and pilot plant data.

There are several items supporting the CO_2 correction predicted by the reconciliation process. First, two researchers working independently on the stripping portion of the process for the October 2011 campaign arrived at a very similar correction for the model (5% correction to CO_2 in the lean solvent) (Madan, et al., 2013) (Walters, et al., 2013). Subsequently, a density correlation developed by Freeman (based on the same data used to develop the PZ solvent model) was modified for the presence of an inhibitor used in the pilot plant solvent (Freeman, 2011). The modified density model is presented in Equation 2.2 (Walters & Rochelle, 2012) (Song & Rochelle, 2015) .

$$\frac{\rho_{SOLN}}{\rho_{H_2O}} = 0.0407 * c_{CO_2} + 0.008 * c_{PZ} + 0.991$$
$$\frac{\rho_{ADJ}}{\rho_{SOLN}} = 0.00741 * \omega_{Inhibitor} + 1.0018 \qquad 2.2$$

where:

ρ_{SOLN} = Liquid mass density of loaded solution (kg/ m^3);

ρ_{H2O} = Reference density of water at temperature of loaded solution (kg/ m^3);

ρ_{ADJ} = Loaded solution density adjusted for presence of inhibitor (kg/ m^3);

c_i = Concentration of component i (mol/kg);

$\omega_{Inhibitor}$ = Weight fraction of inhibitor in solution.

The updated model was used to provide predictions of CO_2 loading at the pilot plant from inline density measurements. The result of this process yielded a systematic offset of 7% between the density predicted loadings (Equation 2.2) and the titration measured loadings at the pilot plant (Zhang, et al., 2016). Based on the consistent correction of CO_2 required across different sources, the CO_2 adjustment was selected as the primary method to correct for the bias between the model and pilot plant performance. The adjusted model can then be used to identify the impact of process modifications (e.g., spray nozzle return for the intercooling loop). The detailed results of the reconciled and adjusted model can be found in Appendix C (Sachde, et al., 2013).

2.3.2 Quantifying the impact of spray intercooling

A spray nozzle was added to the intercooling loop in the pilot plant to generate additional mass transfer area in the column. The solvent is pumped off of a chimney tray between the packed beds, through a heat exchanger to be cooled to approximately 40°C, and returned to the column via a spray nozzle. The nozzle generates mass transfer area by converting the kinetic energy of the solvent into "new" liquid surface (droplets of liquid) via pressure drop across the nozzle. In addition, the nozzle is oriented to spray upwards into the underside of the top bed of packing, generating additional mass transfer area through the process of impaction and drop break-up. This modification can be viewed as a "retrofit" option for processes where additional packing cannot be easily added to a column and additional mass transfer area is required to meet a performance specification.

To model the effect of the spray nozzle, the following approach was implemented:

1) Correct the baseline model (without a spray nozzle) for systematic bias via the lean solvent CO_2 correction. The model should now represent the general material and energy balance of the pilot plant without a spray nozzle.
2) For pilot plant experiments with the spray nozzle, add an additional section of well-mixed packing with a pump-around (or recycle) to represent the spray nozzle section of the column. Create a new adjustable model parameter to represent the mass transfer area of the "spray" section in the model.
3) Perform a full data reconciliation (to account for uncertainty in model inputs and measured results from the pilot plant) with the adjustable area of the spray nozzle accounting for performance differences not covered by the data reconciliation and the bias correction.

This process yields an equivalent area of packing that represents the mass transfer performance of the spray nozzle. This area prediction was correlated (Figure 2-2) to the solvent mass flow rate through the spray nozzle (proxy for kinetic energy of the solvent)

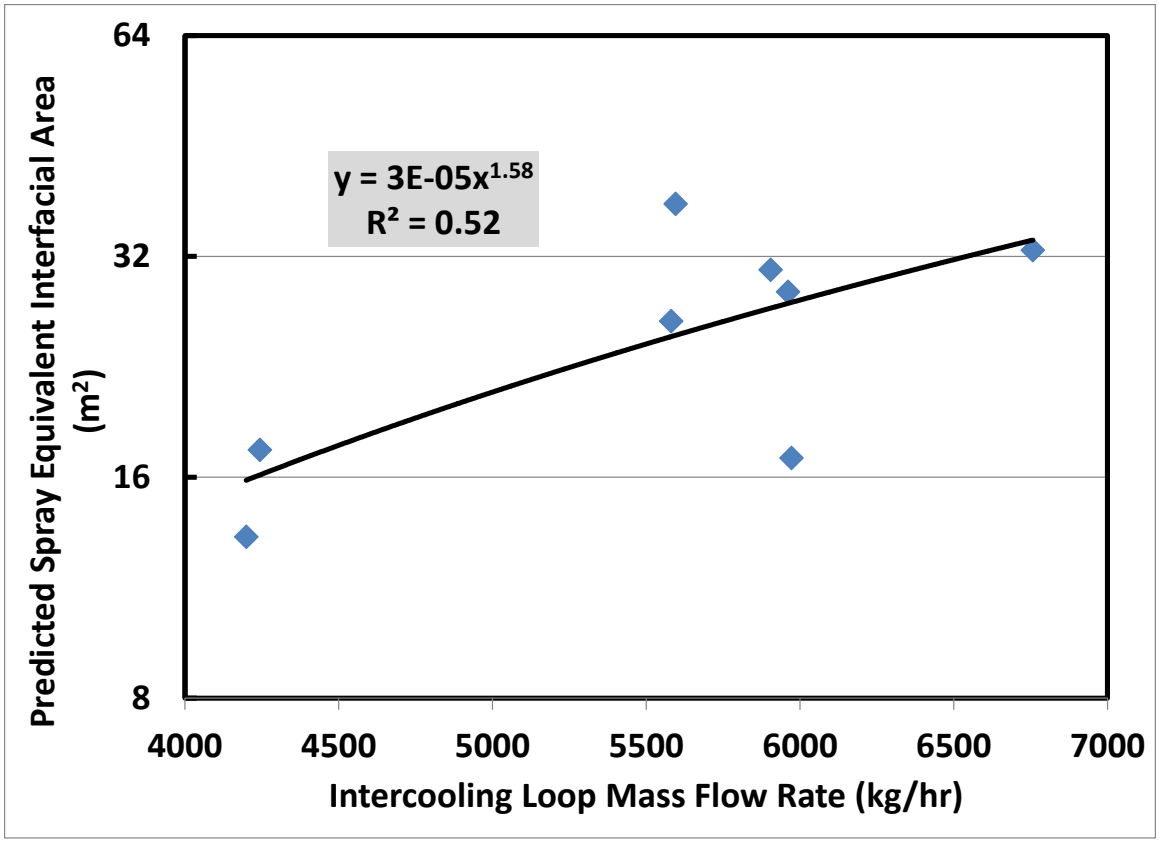

Figure 2-2: Spray nozzle mass transfer area as a function of solvent mass flow rate through the spray nozzle. The spray nozzle area is quantified and modeled as an equivalent wetted area of packing. Reproduced with authors' permission (Sachde, et al., 2013).

The area added by the spray nozzle corresponded to an addition of approximately 5 – 20% additional packing to the pilot plant for October 2011 campaign (Sachde, et al., 2013). The simple model connecting the kinetic energy of the solvent to the mass transfer area of the spray explains a majority of the variability in a limited data set. To further improve characterization of spray nozzle performance, a larger set of pilot data and a larger set of variables (surface tension of solvent, distance from nozzle to droplet impact site, etc.) could be used to develop a more detailed and robust spray nozzle model. However, the primary purpose of the current work is not to characterize the spray, but

rather to provide a method to estimate the contribution of the spray to the overall performance of the pilot plant.

2.3.2.1 Screening Economic Evaluation of Spray Nozzle Benefits

The mass transfer area generated by the spray (Figure 2-2) can be assigned a value by calculating the cost of purchasing an equivalent amount of packing. This approach neglects the detailed cost implications of installing packing vs. a spray nozzle, which may be a determining factor in the case of a retrofit application where significant modification of the column would be required to add packing. Nonetheless, the packing cost savings generated by the spray (or spray benefit) can be compared to the primary cost associated with generating the mass transfer area – the pumping costs associated with the pressure drop of the spray. If the incremental costs of the pressure drop outweigh the cost of purchasing an equivalent amount of packing, it provides an indication that spray nozzles are not an efficient way to generate mass transfer area in amine capture systems when compared to structured packing. Table 2-3 presents the data used to perform the incremental economic analysis.

Table 2-3: Assumptions for Incremental Economic Evaluation of Spray Nozzle

Capital Cost Assumptions		Operating Cost Assumptions	
Interest Rate Of Capital	12.50%	Annual Operating Hours[2]	7446
Amortized Lifetime (years)	15	Cost of Electricity ($/MWh)[3]	56.6
Amortization Factor[1]	15%	Overall Pump Efficiency[4]	55%
		Spray Nozzle Type[5]	Full Cone, ¾"

1: Amortization factor calculated from interest rate and loan term. Provides (equal) annual payments when multiplied by principal.

2: Capacity Factor = 85% **(National Energy Technology Laboratory, 2010)**

3: 2012 Texas Industrial Average Cost of Electricity **(U.S. Energy Information Administration, 2013)**

4: Pump efficiency is average value over range of flow rates considered in this analysis based on the pilot plant pump curve.

5: Nozzle from Spraying Systems Co.®, Spiral Jet® - 3/4HHSJX-SS120210

The annualized capital (packing cost) and operating (pumping) costs were calculated by Equations 2.3 and 2.4.

$$Annualized\ Packing\ Benefit = UC_{Packing} * Spray\ Eq.Vol.* AF \qquad 2.3$$

$$AF = i + \left(\frac{i}{(1+i)^n - 1} \right)$$

where:

$UC_{Packing}$ = Unit cost of packing ($/m^3) – see Figure 2-3;

Spray Eq. Vol. = Equivalent volume of packing required to replicate spray performance (m^3) – see Figure 2-2.

AF = Amortization factor (or annuity calculation);

i = Annual interest rate (as % or fraction) – See Table 2-3;

n = Term of loan or project (years) – See Table 2-3;

$$Annual\ Pumping\ \mathrm{Cos}t = UC_{Electricity} * \left[\frac{\dot{m}_{spray} * \left(\frac{\Delta P_{NOZZLE} + \Delta P_{Height}}{\rho_{solvent}} \right)}{1000 * \eta_{Pump}} \right] \qquad 2.4$$

where:

$UC_{Electricity}$ = Unit cost of electricity ($/kWh) – see Table 2-3;

$\dot{m}_{spray}$ = Mass flow rate through spray nozzle (kg/s);

ΔP_{Nozzle} = Pressure drop across the spray nozzle (Pa);

ΔP_{Height} = Pressure drop for pumping head from liquid draw to nozzle (Pa);

$\rho_{solvent}$ = Mass density of solvent (kg/m^3);

η_{Pump} = Pump efficiency – See Table 2-3;

The packing costs were calculated using data and a simple linear correlation from previous work by Tsai corrected to 2012 U.S. dollars (Tsai, 2010). The original data and correlation from Tsai are shown in Figure 2-3.

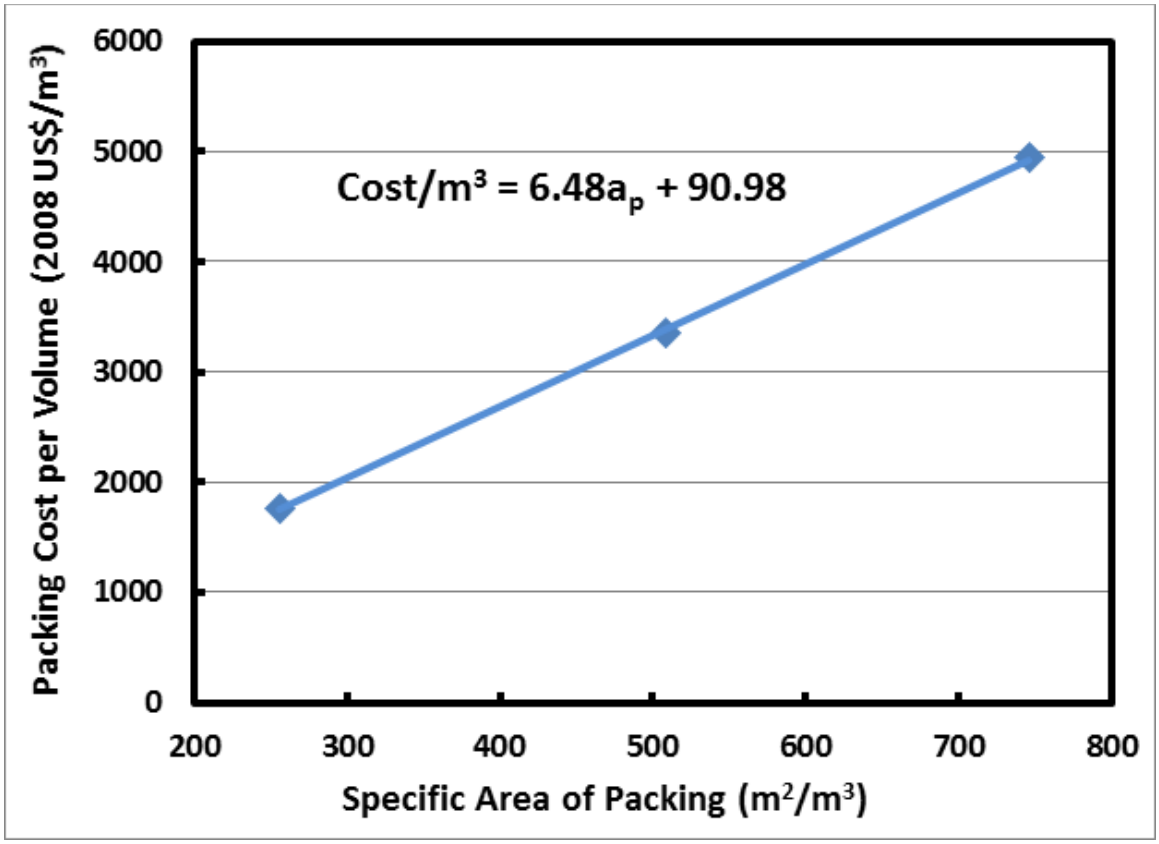

Figure 2-3: Prediction of packing cost per unit volume from the packing specific area based on data collected by Tsai for 3 packing sizes (250, 500, 750 m^2/m^3) (Tsai, 2010)

The packing cost data by Tsai will represent a generic cost of packing used to assign value to the spray mass transfer area in this analysis. Ideally, a broader set of data would be used, but the data from Tsai provide relatively recent representative costs for the type of structured packing commonly used in CO_2 capture applications.

Finally, the pressure drop for the spray nozzle was calculated from the following correlation developed from vendor data (Spraying Systems Co., 2012):

$$\Delta P_{Nozzle} = 0.0307 * Q^2 \qquad 2.5$$

where:

ΔP_{Nozzle} = Pressure drop across the spray nozzle, bar;

Q = Volumetric flow rate (m^3/s).

The results of the analysis are presented in Figure 2-4.

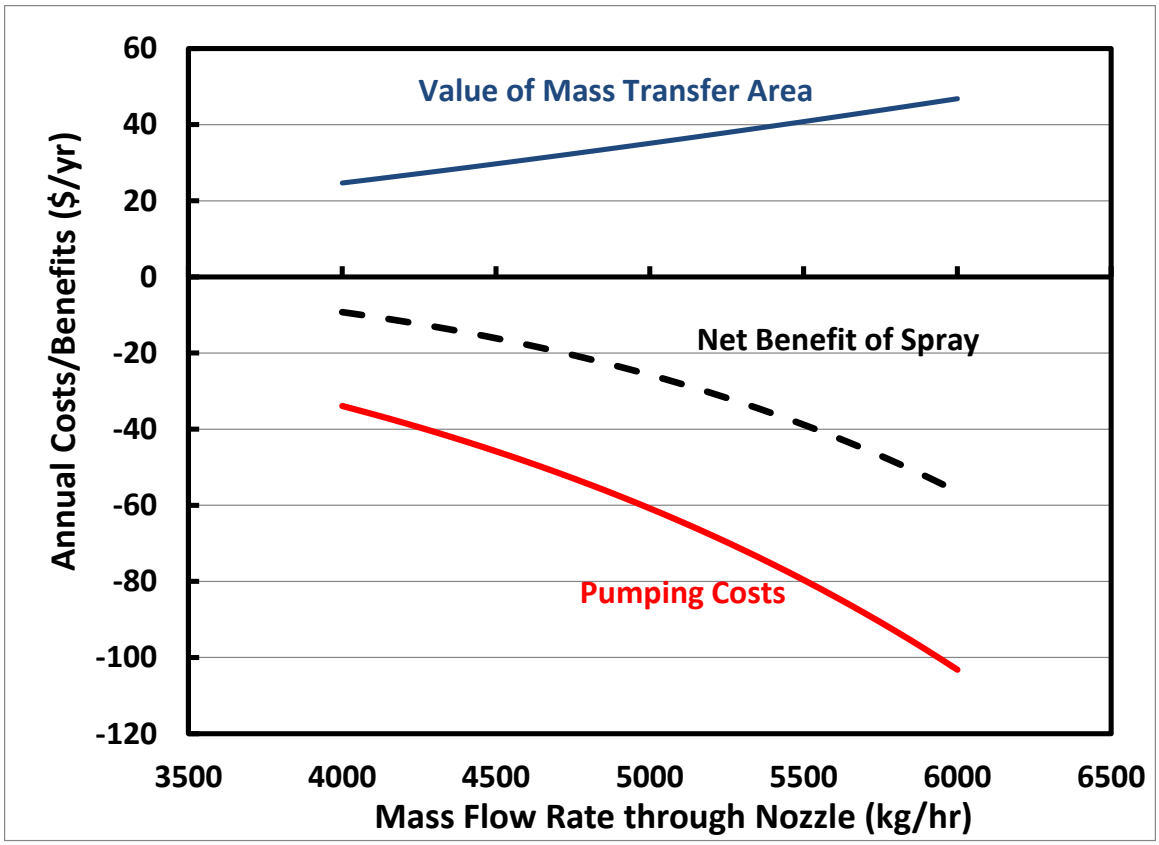

Figure 2-4: Net benefit of the mass transfer area generated by a spray

As the results show, across the entire range of operating conditions at the pilot plant, the cost of pumping the solvent to generate the necessary pressure drop for the spray nozzle is consistently higher than the value of an equivalent amount of packing. The unit cost of packing (Figure 2-3) would need to increase by approximately 50% before the spray nozzle would become competitive in the operating range in Figure 2-4.

Therefore, the results indicate that generating mass transfer area via the spray is not as efficient purchasing packing. However, the analysis does not preclude the use of sprays as a retrofit option for constructed columns or as an option to provide design and operating flexibility in new columns (turn on and off as needed, limit need to "over-design" packing). The analysis also does not consider the peripheral costs (packing support structures, liquid distributors, etc.) which might make a spray more attractive compared to packing in certain cases.

2.4 USING THE CORRECTED MODEL TO PREDICT PILOT PLANT PERFORMANCE

The final step of the validation process was to use the updated model to predict the performance of the March 2015 pilot plant campaign. This campaign included spray intercooling to validate the regressed spray nozzle model and a wide range of operating conditions (low lean loading, low flue gas CO_2, high CO_2 removal – see Table 2-1) not included in the original reconciliation and model adjustment process. This method of validation tests the robustness of the proposed model correction.

2.4.1 Summary of Model Prediction Results

A full discussion of the model prediction results for the March 2015 campaign can be found in the work by Zhang (Zhang, et al., 2016). Results for model predictions of pilot plant performance, as quantified by the number of transfer units (NTU), are presented in Figure 2-5 and Figure 2-6 (NTU defined in Equation 2.6).

$$NTU = -ln(1 - f_{CO_2}) \tag{2.6}$$

where:

NTU = Number of transfer units;

f_{CO2} = Fraction of CO_2 removed.

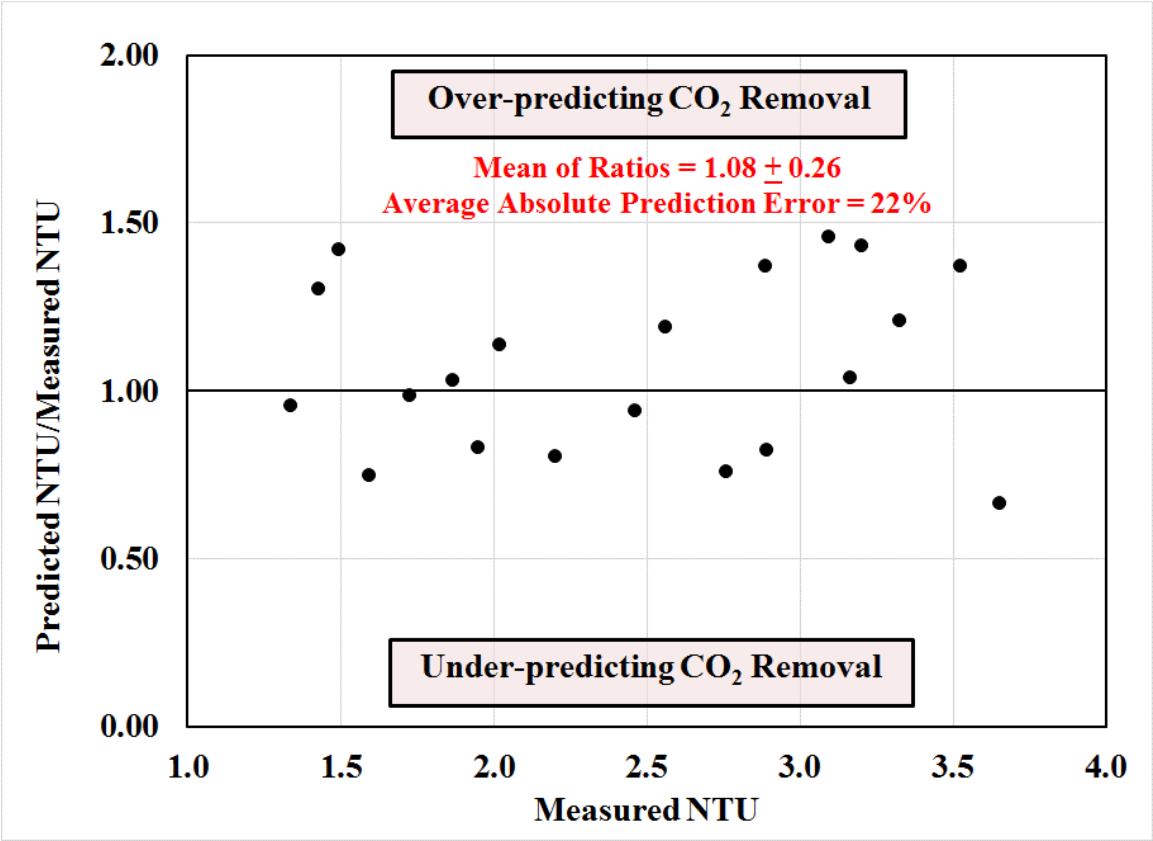

Figure 2-5: Ratio of model-predicted NTU to pilot plant measured NTU (Equation 2.6) as a function of measured NTU. Data based on absorber gas-side CO_2 material balance. Model predictions apply CO_2 multiplier (1.07) to lean solvent to correct for model bias (Table 2-2). No data for run 4. Data from (Zhang, et al., 2016).

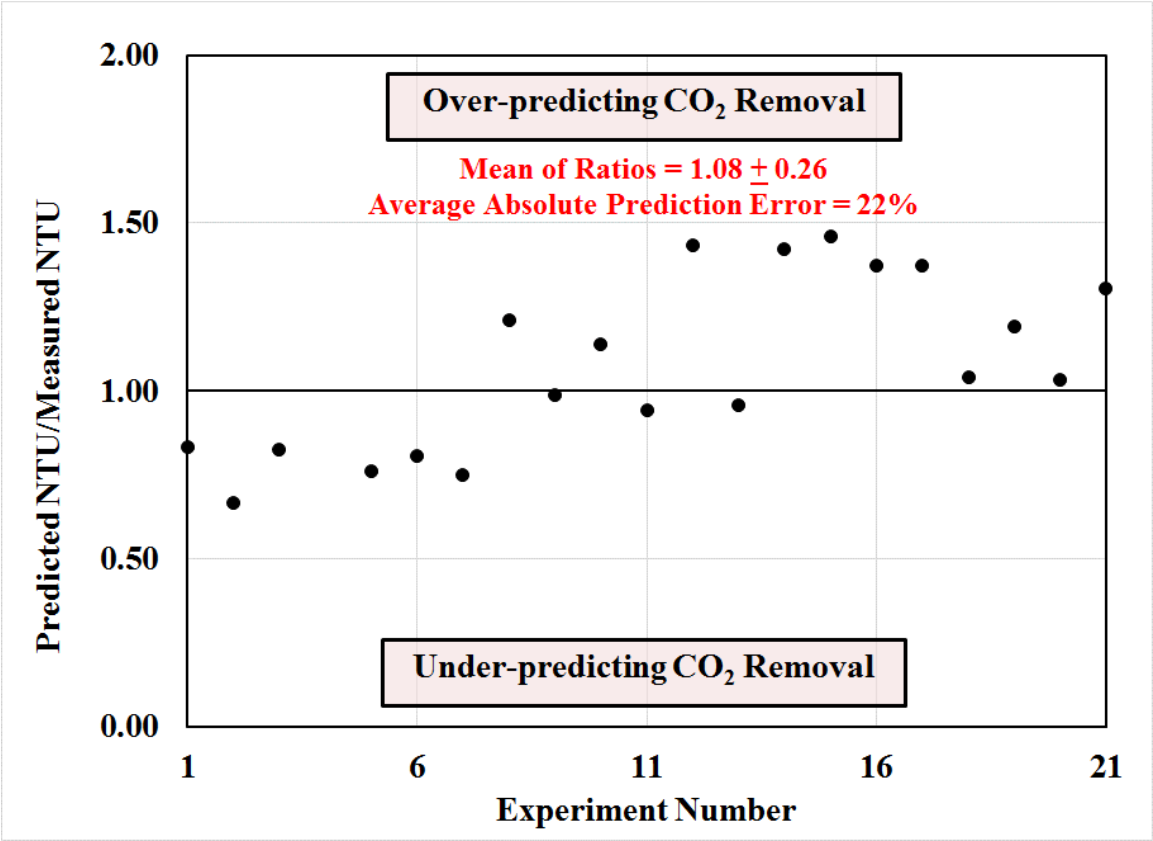

Figure 2-6: Ratio of model-predicted NTU to pilot plant measured NTU (Equation 2.6) as a function of experiment number (or time). Data based on absorber gas-side CO_2 material balance. Model predictions apply CO_2 multiplier (1.07) to lean solvent to correct for model bias (Table 2-2). No data for run 4. Data from (Zhang, et al., 2016).

Figure 2-5 indicates the model does not have a clear systematic bias or trend as a function of the NTU, but tends to generally over-predict CO_2 removal (mean ratio of predicted to measured NTU = 1.08).

However, Figure 2-6 suggests that a time dependence or correlation exists within the data. The model exhibits a trend from slight under-prediction to over-prediction of CO_2 removal. If the transition from run 11 to 12 is designated the midpoint of the campaign (no data for run 4), 8 of 10 runs are under-predicted in the first-half of the

campaign and 9 of 10 runs are over-predicted for the second half of the campaign. The most severe over-predictions also occur in a group from run 12 to 17. An investigation of operating conditions did not provide an additional correlation beyond the progression of time through the campaign. The campaign does contain several high CO_2 removal cases (>93% CO_2 removal, >2.66 NTU) that are outside of the range from which the model corrections were developed or any previous campaigns have operated (Table 2-1). Therefore, the potential for model error that was imperceptible at lower CO_2 removal or issues with analytical measurements operating near detection limits can lead to issues that were not identified in prior campaigns. The high removal runs (2, 3, 5, 8, 12, 15-18) account for much of the scatter in the preceding figures. However, as noted for Figure 2-5, there is not a clear trend with the measured NTU, so the high removal cases alone do not explain the trend in time. The high removal cases do provide an opportunity to investigate model performance at near pinched (small driving forces) conditions, where the vapor-liquid equilibrium aspects of the model become controlling.

In general, the average error in the campaign is high compared to the error in the reconciled dataset from which the model adjustment was developed (October 2011 and November 2013 campaigns). In those original cases, the error in predicted vs. measured NTU was approximately 1%. While the error when using the model in a predictive fashion might be expected to be higher than when fitting the data to minimize the model error, the hypotheses of a single systematic bias as the main source of error is not strictly supported by the results of this final campaign unless the time-dependent trends can be explained.

2.4.2 General Absorber Performance Results from the Pilot Plant

The March 2015 campaign also yielded an important insight for absorber performance as a function of piperazine concentration.

Table 2-4: Parametric testing of solvent concentration (5 m vs. 8 m PZ) at the SRP pilot plant. All cases operated with spray intercooling. Reproduced with permission from authors (Zhang, et al., 2016).

Test	PZ (molal)	Solvent Rate (m^3/hr)	Gas Rate (actual m^3/min)	Lean Loading (mol CO_2/mol alk.)	Lean P*CO_2 @ 40°C	Rich Loading (mol CO_2/mol alk.)	CO_2 Removal
1	5	3.2	14.2	0.235	107	0.347	80%
	8			0.236	85	0.329	75%
2	5	3.2	9.9	0.238	114	0.340	96%
	8			0.239	91	0.320	93%
3	5	2.3	9.9	0.221	83	0.374	94%
	8			0.225	68	0.333	91%

The volumetric solvent flow rates are equivalent in Table 2-4, which indicates a larger mass flow rate for 8 m PZ (higher density) compared to 5 m PZ. In addition, the inherently larger solvent capacity of 8 m PZ (more amine circulating per mass of solvent) and the larger lean end driving forces for 8 m PZ in every test (as indicated by the lean equilibrium partial pressure in Table 2-4) indicate favorable conditions for 8 m PZ in terms of driving forces for CO_2 absorption. However, in every case in the table, 5 m PZ outperforms 8 m PZ in terms of CO_2 captured. The results indicate that the reduced viscosity of 5 m PZ has a strong impact on absorber performance. This provides preliminary evidence of the significance of the liquid-film physical mass transfer coefficient (k_L) for absorber performance – results in Chapter 5 indicate that the model used in this work predicts significant resistance from k_L. In addition, modeling results predicted significant performance benefits in the absorber with 5 m PZ (Sachde &

Rochelle, 2014). The pilot plant data provides the strongest evidence of the performance enhancement provided by reduced viscosity for amine solvents operating in the fast reaction regime.

2.5 Validating Rate Parameters with Pilot Plant Data

The focus in the preceding sections has been to use the model to match the performance of the absorber primarily in terms of the overall CO_2 material balance (or CO_2 removal). This was the motivation for only adjusting a single parameter to match pilot plant data. However, the pilot plant data includes a liquid-side CO_2 (mid-loading) measurement at Point 6 in Figure 2-1. By adding this data, an additional degree of freedom is created via the second, separate material balance that can be performed around either half of the absorber column. However, there is no gas-side measurement in the pilot plant at this location to confirm the material balance closure as in the full absorber column balance, and liquid-side measurements have inherently larger uncertainty as part of the analytical methods to measure the CO_2 content. Therefore, the reliability of this second material balance is questionable.

Nonetheless, the additional degree of freedom allows an adjustment to fit the overall CO_2 material balance (e.g., CO_2 correction or area correction) and a separate adjustment to fit the independent material balance (or relative rates of CO_2 removal in the top and bottom beds) around half of the absorber. The relative rates of CO_2 transfer are most strongly impacted by the rate-parameters of the model – kinetics and physical mass transfer coefficients (see Chapter 5 for an extended discussion). Therefore, using the mid-loading data, the rate parameters of the model can be validated (or adjusted). The mid-loading data for the October 2011 campaign suggest that the removal on the lean-end

(top) of the absorber is over-predicted relative to the rich end of the column. This is consistent with liquid-film mass transfer coefficients that are too low (diffusion-limited system in the rich end - see Chapter 5 for sensitivity of model to k_L and Appendix A for a possible explanation of under-reported k_L measurements). As a result, the liquid-film mass transfer coefficients were increased by a factor of 3 (see Appendix A), while the mass transfer area was used to maintain the removal specification. The expectation of this approach was that the overall volumetric mass transfer coefficient (k_L*a) would remain roughly constant. The resulting area modification was a factor of 0.40 (or decrease by a factor of 2.5). Therefore, the new overall k_La (3*0.4 = 1.2) increased by 20% over the original values. The resulting mid-loading predictions are presented in Table 2-5

Table 2-5: Comparison of mid-loading predictions for the October 2011 campaign – original reconciled values (via lean CO_2 correction only) vs. updated values with new k_L (3*base) and area (0.4*base) values.

	Delta Loading (Mid - Lean) (mol CO_2/mol alkalinity)			Predicted/Measured	
Run	Measured	Original Prediction	Updated Prediction	Original Ratio	Updated Ratio
1	0.041	0.055	0.046	1.35	1.14
2	0.046	0.099	0.048	2.17	1.04
3	0.049	0.097	0.058	1.99	1.18
4	0.046	0.097	0.053	2.10	1.14
5	0.046	0.098	0.049	2.13	1.06
6	0.040	0.103	0.058	2.55	1.44
7	0.036	0.094	0.052	2.64	1.45
8	0.038	0.057	0.048	1.49	1.27
9	0.035	0.103	0.060	2.90	1.68
10	N/A	N/A	N/A	N/A	N/A
11	0.035	0.089	0.048	2.57	1.37

The method improves mid-loading predictions significantly over the base case, but the model still systematically over-predicts the removal in the top portion of the

column. This method merits further consideration in future reconciliation as it represents an alternate source of bias that may be impacting model predictions and may provide a route to develop new mass transfer coefficient values for the amine scrubbing process.

2.6 CONCLUSIONS

The rigorous rate-based absorber model using aqueous piperazine as the solvent was validated and adjusted using pilot plant data from the Separations Research Program pilot plant at the University of Texas at Austin. A data reconciliation procedure was implemented to simultaneously account for the measurement uncertainty for the pilot plant measured inputs and to the model (flows, temperatures, etc.) and the uncertainty in the output metrics of the model (CO_2 removal, outlet temperatures, etc.). In addition, an adjustable parameter was defined to allow fitting of the model to pilot data for any unexplained offset in the reconciliation process. The key findings of this reconciliation process can be summarized as follows:

- A systematic bias between the model and pilot plant data was identified by a consistent model adjustment across two pilot plant campaigns covering a wide range of operating conditions and different types of packing.
    - The model bias could be corrected by an increase in the lean solvent loading of ~7% or by a 25% reduction in packing mass transfer area.
    - The CO_2 correction had independent corroboration from separate stripper model validation and via a modified density-predicted loading.
- The adjusted model was used in a second stage of data reconciliation to isolate the performance of a spray nozzle added to the intercooling loop in the pilot plant.

- The mass transfer area of the spray nozzle was regressed during the reconciliation process and correlated to the kinetic energy (via mass flow rate) of the solvent.
- The spray nozzle added between 5 and 20% additional mass transfer area to the column measured as an equivalent packing area.
- A screening economic analysis to compare the cost of the pressure drop through the spray nozzle to the value of the mass transfer area added (quantified via the cost of an equivalent area of structured packing) revealed that the spray nozzle pumping costs always outweigh the value of area generated and that the spray nozzle is only beneficial where a packing cannot be added (retrofit).

The final approach to model validation consisted of using the adjusted model to predict the performance of a new pilot plant campaign.

- The model predicted NTU with an average error of 22% and over-predicted NTU on average (mean ratio of predicted/measured = 1.08).
- The data showed a correlation with time (i.e., experiment number) exhibiting a distinct shift from consistent under-prediction to over-prediction of CO_2 removal half way through the campaign. The worst fit of individual experiments occurred together in a cluster of runs in the second half of the campaign.
- A pilot plant parametric study of absorber performance as a function of PZ concentration revealed that 5 m PZ significantly outperformed 8 m PZ in terms of mass transfer rates, indicating a strong impact of viscosity on absorber performance and the potential importance of liquid-film physical mass transfer in amine absorbers.

2.6.1 Open Research Issues

- The operation of the absorber at high CO_2 removal conditions provides an opportunity to validate different absorber performance mechanisms related to operating near a pinch (small driving forces). Specifically, equilibrium constraints become controlling at pinched conditions and provide an opportunity to validate model VLE. Further validation of the model is need at these conditions.
- The spray nozzle model developed in this work is largely empirical and is coupled to the packing mass transfer models used in the regression process (spray represented as a packed bed). If the spray nozzle continues to be used as a component of the pilot plant (or other modeling activities), the spray model should be de-coupled from packing models by regressing a combined k_La to represent the true performance of the spray as a function of operating conditions.
- Mid-loading measurements (or similarly, mid-column gas measurements) create a new degree of freedom for model validation of the absorber via a secondary material balance around half of the absorber. This new degree of freedom can be used to validate rate mechanisms in the absorber by considering the relative rates of CO_2 absorption in each half of the column and identifying the controlling mechanism in the model which can be used to fit the new pilot plant data point. This is particularly relevant for the validation or measurement of physical-liquid film mass transfer coefficients, which are difficult to measure and extrapolate from experimental conditions to conditions in an actual amine absorber. Initial attempts with the approach of varying the overall volumetric mass transfer coefficient (k_La) indicates significant improvement in model prediction of mid-

loading compared to the base case, but still exhibits a consistent trend of over-predication.

Chapter 3: Adiabatic Absorbers – Minimum Solvent Rates and Pinch Behavior

CO_2 capture with amine solvents results in the generation of a temperature maximum (or bulge) within the column due to heat released by absorption and reaction of CO_2 and simultaneous transfer of water. The higher solvent temperature limits the maximum capacity of the solvent (as measured by the change in solvent loading for a given CO_2 removal) and reduces average driving forces through the column. The reduced solvent capacity results in deterioration of the energy performance of the stripping system while the reduced driving forces can result in increased packing (capital cost) requirements in the absorber.

Cooling the solvent at intermediate locations in the column (intercooling) to remove heat generated by CO_2 absorption can mitigate the capacity and driving force limitations, but the conditions of absorber operation (CO_2 concentration in flue gas, lean loading, L/G, etc.) dictate the potential benefit that may be extracted from the intercooling operation. Quantifying the potential benefits of intercooling and generalizing the trends in these benefits with operating conditions can allow absorber and intercooling design optimized for the specific operating conditions.

This chapter will present a systematic evaluation of the potential solvent capacity benefits of intercooling benefits by considering the two important relevant limiting designs – adiabatic and isothermal absorbers. The analysis will be performed across a range of CO_2 flue gas sources and operating conditions with the goal of providing fundamental explanations for deviation from isothermal (or ideal) solvent capacity and generalizing the results based on these underlying mechanisms. The results will allow recommendations regarding the conditions for the application of intercooling and for development of improved intercooling design.

3.1 Evaluation of Existing Literature

3.1.1 Temperature Maxima and "Critical" L/G

While the phenomena of temperature maxima in gas absorbers has been studied extensively for a variety of gas-liquid systems (e.g., physical absorption of ammonia in water (Bourne & von Stockar, 1974)), the results have not been generalized as a function of operating conditions, specifically in the context of amine-based absorbers for CO_2 capture applications. In addition, the basic phenomena of temperature-related mass transfer pinches (and associated increase in solvent circulation rates) is well-understood. However, linking process and operating conditions to the fundamental mechanisms and explaining process performance from this first-principles level has not been possible prior to the development of rigorous rate-based models such as the one utilized in this work.

Kohl and Nielsen provide an extensive, but qualitative and general, discussion of thermal effects for amine-based systems used in gas treating (hydrocarbon) applications (Kohl & Nielsen, 1997). The authors describe the nature of the temperature bulge in columns as a function of amine type (rate of reaction with amines), operating conditions such as liquid-to-gas ratio (L/G), and discuss impacts on operation of amine absorbers. In addition, an empirical method is proposed to determine the distribution of reaction heat between the vapor and liquid phases. The goal of the work is not to develop detailed mechanistic explanations for the temperature effects on absorber performance, but rather to provide simplified design procedures and general operating guidelines to account for the temperature effects.

Kvamsdal and Rochelle performed a detailed analysis of the effects of the temperature bulge on mass transfer performance of absorber columns using amine solvents for CO_2 capture (Kvamsdal & Rochelle, 2008). The study introduced the concept of a "critical" liquid-to-gas ratio (L/G) where the temperature maximum occurs in the

middle of the column and the enthalpy leaving with the gas and liquid, respectively, are balanced. The authors systematically evaluated the effect of L/G on the magnitude and location of the temperature bulge in the column. Key observations included the shift of the temperature bulge from the lean end of the column, where enthalpy was primarily carried by the gas, to rich end of the column, where the enthalpy was primarily carried by the liquid, with a sharp transition in bulge location at the critical L/G. However, the authors evaluated the effect of L/G at a fixed lean loading and packing height, limiting generalization of results.

Plaza extended the concept of a critical L/G by evaluating rich loading and solvent capacity as a function of lean loading for multiple solvents (monoethanolamine, potassium carbonate/piperazine, and piperazine) with a coal-fired boiler flue gas (12 mol% CO_2) (Plaza, 2011). The analysis identified a range of lean loadings where the temperature bulge limits solvent capacity and the critical L/G corresponding to a lean loading where the temperature bulge reaches a maximum and solvent capacity is expected to be the most severely limited. Plaza was also able to use column temperature and mass transfer profiles to qualitatively describe the phenomena underlying the trends in solvent capacity. Finally, the work included an empirical approach to predict the critical L/G based on the detailed modeling results.

The current work will build on the concepts of the previous authors with a focus on systematically evaluating the process performance impacts (solvent capacity) of temperature effects in adiabatic absorbers as a function of operating conditions and flue gas CO_2 concentration. The analysis will also generalize results as a function of the operating conditions, providing fundamental explanations for the link between process conditions and temperature limitations of absorber performance, and identify opportunities for intercooling implementation and development.

3.2 MODELING FRAMEWORK

The absorber model used for the intercooling evaluation was implemented in Aspen Plus® in the RateSep^{TM} module. The key components of the model are rigorous representations of solvent thermodynamics and kinetics, mass transfer and fluid mechanics in packing, and the physical properties of the system over the range of expected operating conditions.

All of the subsequent analysis will utilize concentrated aqueous piperazine (PZ) as the solvent. The thermodynamic model for the PZ-H_2O-CO_2 system was developed from experimental amine pK_a, CO_2 solubility, heat capacity, speciation, and amine volatility data by regression of Gibbs free energy, enthalpy, heat capacity, and activity coefficient parameters within the electrolyte non-random two liquid (e-NRTL) framework (Frailie, 2014).

The kinetics for the PZ model are described by the following reaction set:

$$PZCOO^- + PZH^+ \leftrightarrow H^+PZCOO^- + PZ \quad 3.1$$

$$PZCOO^- + H_2O + CO_2 \rightarrow H^+PZCOO^- + HCO_3^- \quad 3.2$$

$$2PZ + CO_2 \rightarrow PZH^+ + PZCOO^- \quad 3.3$$

$$2PZCOO^- + CO_2 \rightarrow H^+PZCOO^- + PZ(COO)_2^{2-} \quad 3.4$$

The first reaction is an equilibrium (proton transfer) reaction while reactions 2 through 4 are reversible finite rate reactions where the corresponding reverse reactions complete the reaction set for PZ. Arrhenius rate expressions represent the rate constants for the kinetic reactions (including forward and reverse rates) where the pre-exponential and activation energy parameters were regressed from wetted wall column data collected over a range of temperatures, solvent concentrations, and loadings relevant for capture applications

considered in this work. Finally, physical property models for binary diffusion coefficients, viscosity, and density were regressed as a function of amine concentration, loading, and temperature. For a detailed description of the "Independence" PZ model, see Frailie (Frailie, 2014).

Mass transfer and area models were developed by Wang via regression of experimental data from a pilot scale column with a variety of random and structured packings (Wang, 2015). The area model developed by Wang is a modification of a model developed by Tsai (see Tsai for full theoretical and experimental details of the area model) (Tsai, 2010).

3.3 Analysis Overview and Methodology

Table 3-1 summarizes the conditions used for the evaluation of temperature-related performance restrictions. The analysis was conducted for 50 - 95% removal of CO_2 utilizing concentrated (5, 8 molal) piperazine (PZ) as the solvent. The lower end of the proposed lean loading ranges in Table 3-1 would lead to precipitation in practice with the PZ solvent (Freeman, 2011). However, the wide range is included as an extrapolation of the PZ model in an attempt to allow generalization of the results.

Table 3-1: Summary of Intercooling Analysis Operating Conditions

Flue Gas Source	**Inlet CO_2** (mol%)	**Lean Loading Range** mols CO_2/mols alkalinity	**Flue Gas Flow** (kmol/s)
Natural Gas Combined Cycle (NGCC)	4.1	0.10 - 0.30	31.2
Coal-Fired Boiler	14.7	0.10 - 0.36	18.9
Steel Blast Furnace	27	0.10 - 0.39	10.4
Lean solvent and flue gas feed at 40°C for all cases. Flue gas saturated to water.			

One of the major results developed from the analysis will be solvent capacity or the minimum solvent rate, which will be used interchangeably to describe the maximum liquid-phase loading (or total concentration of CO_2 in all forms – see Equations 3.1- 3.4) that can be achieved before the solvent is saturated. Thus, for a given CO_2 transfer rate from the gas, a lower solvent rate corresponds to higher solvent capacity by simple material balance on the absorber.

For the range of conditions identified in the table, the solvent capacity for an adiabatic (no intercooling) absorber and an isothermal ("perfect" intercooling) absorber operated at 40 °C will be quantified. These designs represent limiting cases of absorber performance. The adiabatic absorber (limited by temperature-induced equilibrium constraints) represents minimum solvent capacity and the isothermal absorber represents the maximum solvent capacity for a given operating condition. Figure 3-1 illustrates the approach used in this analysis.

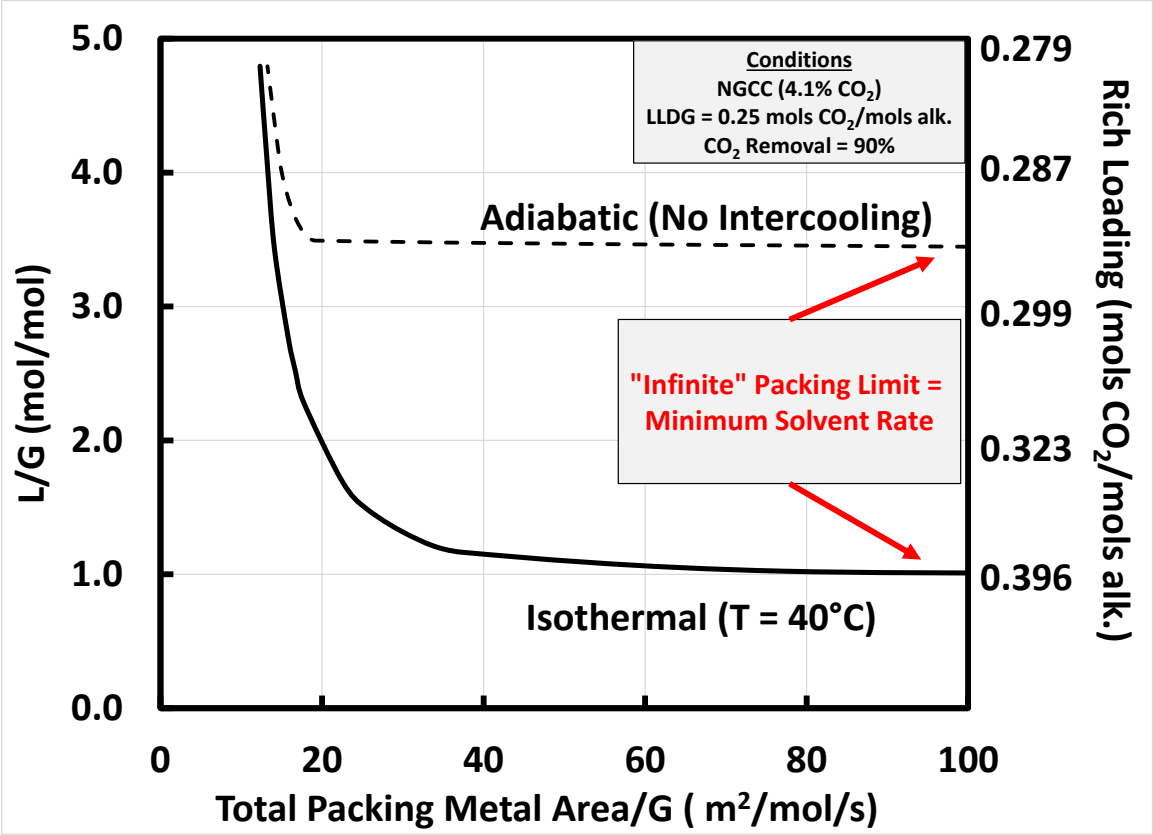

Figure 3-1: Example of design curves for packing-solvent rate trade-off. Each curve (dashed = adiabatic, solid = isothermal) represents the packing requirement to achieve 90% CO_2 removal for a fixed lean loading and given liquid to gas ratio (L/G). At each point, the lean loading, removal, and solvent rates are fixed, so a unique rich loading exists (secondary y-axis). The horizontal asymptote is the minimum solvent rate (L_{MIN}) or best energy performance achievable for a given absorber design.

Each curve represents the packing required for a given liquid to gas ratio (L/G) for each absorber design moving from one asymptotic limit (vertical asymptote of infinite solvent rate and minimum packing) to another (horizontal asymptote of infinite packing and minimum solvent rate). In practice, the infinite solvent rate asymptote does not provide a physically meaningful or quantifiable limit as the packing will approach zero for all designs in this limit. The minimum solvent rate (L_{MIN}) asymptote will be used to

evaluate solvent capacity in this work. The L_{MIN} for any absorption process can be defined as the solvent rate required to achieve a specific solute removal (or specific gas inlet and outlet compositions) for a given inlet solvent composition (loading) with infinite mass transfer area available. In practice, "infinite mas transfer area" is defined by adding a finite amount of packing to the absorber until the asymptote in Figure 3-1 is evident (cannot reduce the solvent rate further while achieving the removal specification). In addition, a mass transfer pinch (zero driving force) can be confirmed with operating and equilibrium curves for the absorber (discussed in subsequent sections).

Lower values of L_{MIN} are associated with better overall energy performance of the system (reduced sensible heat requirements in stripping system, enhanced rich loading to improve CO_2/H_2O selectivity in the stripping system, and reduced pumping costs across the entire system). The ratio of the adiabatic L_{MIN} to the isothermal L_{MIN} at each condition can serve as a screening tool for the conditions where cooling the solvent (intercooling) will be beneficial for energy performance. A high ratio indicates potentially significant benefits of intercooling. A ratio equal to (or approaching) unity indicates that the capacity benefits of intercooling are negligible or non-existent.

The next chapter will consider mass transfer constraints or packing requirements to approach maximum solvent capacity. The "infinite" packing limit is not a practical operating condition due to potentially prohibitive packing costs and operational instability near pinched conditions. Therefore, to fully evaluate absorber designs, the trade-off between solvent rate and packing requirement must be explicitly quantified.

3.4 Minimum Solvent Rate Analysis

Figure 3-2, Figure 3-3, and Figure 3-4 include the L_{MIN} ratios for an adiabatic (no intercooling) absorber for all three flue gas sources in Table 3-1.

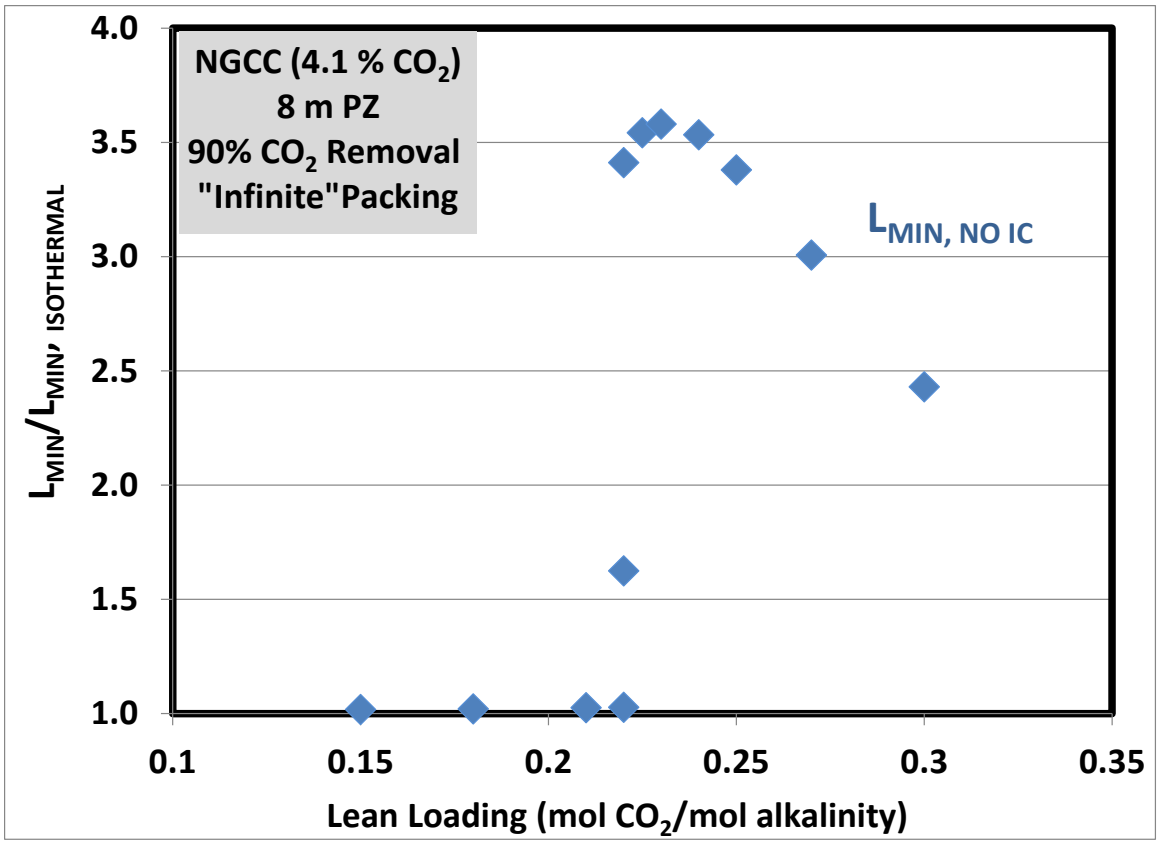

Figure 3-2: NGCC power plant flue gas (4.1% CO_2). Ratio of the minimum solvent rate ("infinite" packing) achieved for an adiabatic absorber (no intercooling) to an isothermal absorber (40 °C) for 90% CO_2 capture with 8 m PZ.

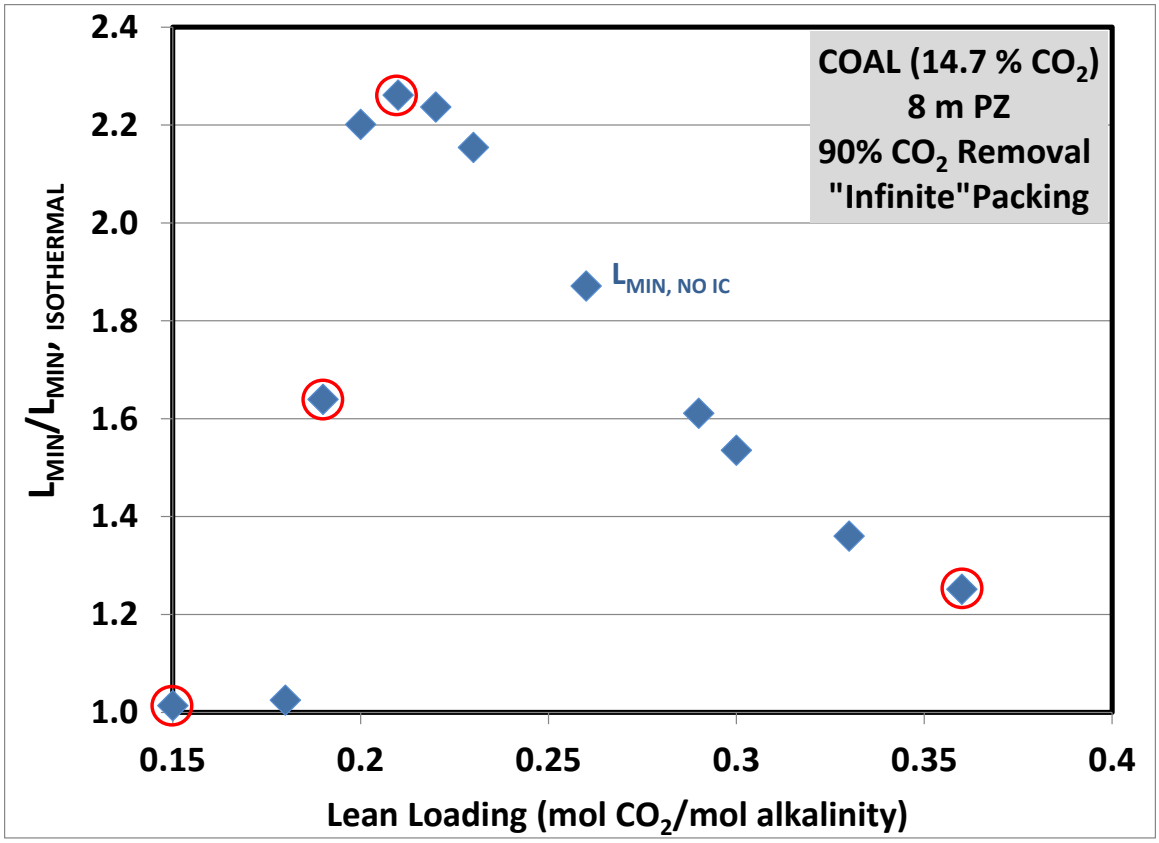

Figure 3-3: Coal-fired boiler flue gas (14.7% CO_2). Ratio of the minimum solvent rate ("infinite" packing) achieved for an adiabatic absorber (no intercooling) to an isothermal absorber (40 °C) for 90% CO_2 capture utilizing 8 m PZ. Points denoted by a red circle have corresponding equilibrium-operating line charts in Figure 3-5 to Figure 3-8.

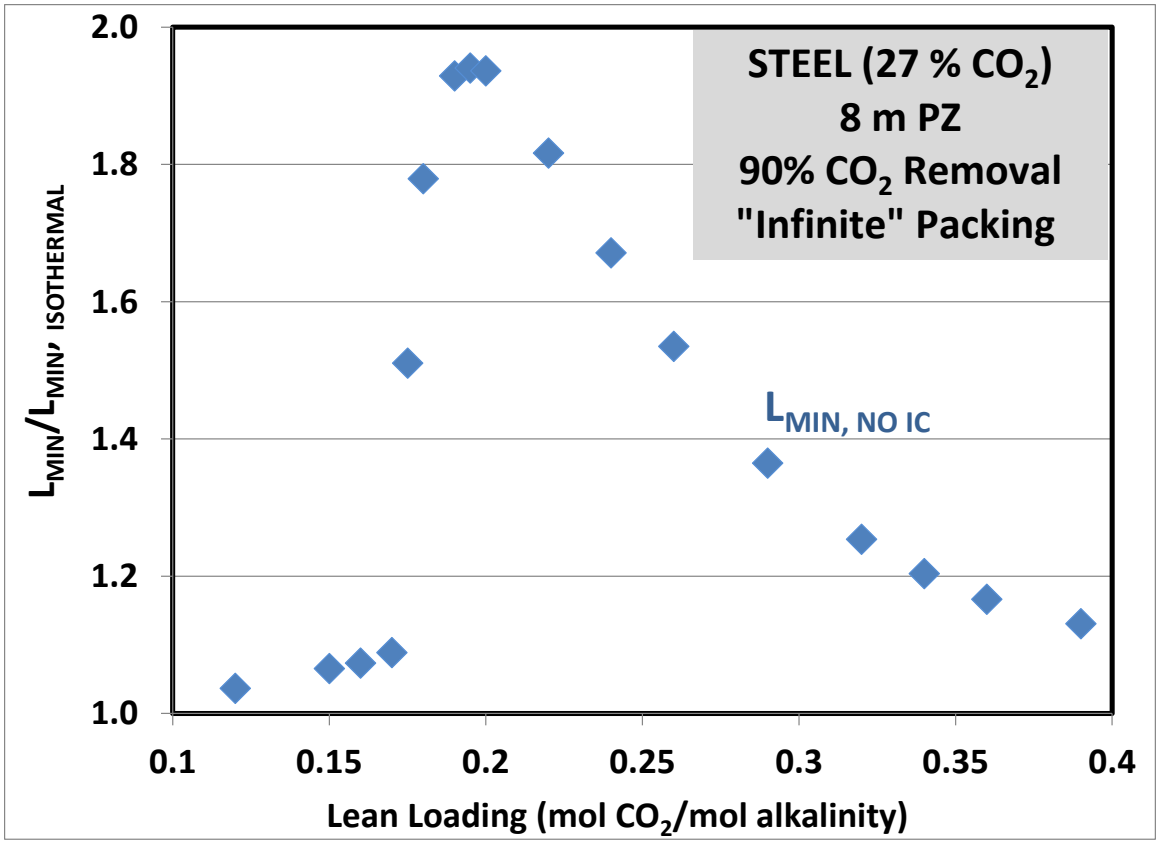

Figure 3-4: Steel blast furnace flue gas (27% CO_2). Ratio of the minimum solvent rate ("infinite" packing) achieved for an adiabatic absorber (no intercooling) to an isothermal absorber (40 °C) for 90% CO_2 capture utilizing 8 m PZ.

In all three cases, an intermediate range of loadings results in the largest ratios (largest deviation from an ideal isothermal absorber) and identifies conditions where the greatest energy benefits may be attained via intercooling. At extreme loadings (low and high) the ratios approach unity, indicating intercooling will provide limited benefits.

The data for each of the preceding figures along with relevant temperatures are included in Table 3-2 through Table 3-4 for reference throughout the following discussion.

Table 3-2: Summary of Minimum Solvent Analysis Results: NGCC (4.1% CO_2), G_{INLET} = 31.2 kmol/s, $T_{GAS,IN}$ = $T_{LIQUID,IN}$ = 40°C, 90% CO_2 Removal, 8 m PZ.

Lean Loading	Lean End Driving Force (P^*_{CO2}/P_{CO2})	Minimum Solvent Rate (L_{MIN}/G)			Rich Loading		Temperatures		
		Isothermal	Adiabatic	$L_{MIN,\ ADIABATIC}$ / $L_{MIN,\ ISOTHERMAL}$	Isothermal	Adiabatic	Max Liquid	Liquid Outlet	Vapor Outlet
mol CO_2/mol alk.		mol/mol	mol/mol		mol CO_2/mol alk.		°C		
0.15	21.89	0.60	0.61	1.02	0.395	0.391	55.9	42.7	53.3
0.18	13.92	0.68	0.70	1.02	0.395	0.391	56.2	42.7	53.0
0.21	8.24	0.79	0.81	1.03	0.395	0.390	56.6	42.6	52.6
0.22	6.78	0.84	0.86	1.03	0.395	0.390	56.8	42.6	52.4
0.22	6.78	0.84	1.36	1.62	0.395	0.328	59.5	44.0	52.0
0.22	6.78	0.84	2.86	3.41	0.395	0.271	63.5	49.0	45.3
0.225	6.10	0.86	3.06	3.54	0.395	0.273	63.8	49.4	43.6
0.23	**5.53**	**0.89**	**3.19**	**3.58**	**0.395**	**0.276**	**63.9**	**49.6**	**42.7**
0.24	4.47	0.95	3.35	3.53	0.395	0.284	63.7	49.7	41.3
0.25	3.59	1.01	3.42	3.38	0.395	0.293	63.1	49.5	40.8
0.27	2.29	1.18	3.54	3.01	0.395	0.311	61.5	49.0	40.3
0.3	1.16	1.55	3.76	2.43	0.395	0.339	56.9	48.0	40.1

Table 3-3: Summary of Minimum Solvent Analysis Results: COAL (14.7% CO_2), G_{INLET} = 18.9 kmol/s, $T_{GAS,IN}$ = $T_{LIQUID,IN}$ = 40°C, 90% CO_2 Removal, 8 m PZ.

Lean Loading	Lean End Driving Force (P^*_{CO2}/P_{CO2})	Minimum Solvent Rate (L_{MIN}/G)			Rich Loading		Temperatures		
		Isothermal	Adiabatic	$L_{MIN,\ ADIABATIC}$ / $L_{MIN,\ ISOTHERMAL}$	Isothermal	Adiabatic	Max Liquid	Liquid Outlet	Vapor Outlet
mol CO_2/mol alk.		mol/mol	mol/mol		mol CO_2/mol alk.		°C		
0.15	78.76	1.94	1.96	1.01	0.422	0.420	76.0	42.7	68.3
0.18	50.09	2.18	2.23	1.02	0.422	0.412	77.0	43.0	67.7
0.19	42.45	2.27	3.73	1.64	0.422	0.332	79.8	52.2	62.9
0.2	35.65	2.37	5.23	2.20	0.422	0.301	80.7	57.4	52.1
0.21	**29.64**	**2.49**	**5.62**	**2.26**	**0.422**	**0.304**	**80.5**	**58.1**	**45.3**
0.22	24.41	2.61	5.84	2.24	0.422	0.311	80.0	58.1	42.2
0.23	19.91	2.75	5.91	2.15	0.422	0.319	79.1	57.7	41.3
0.26	10.33	3.25	6.09	1.87	0.422	0.347	73.3	56.2	40.8
0.29	5.24	3.99	6.43	1.61	0.422	0.372	65.1	54.4	40.5
0.3	4.18	4.32	6.64	1.54	0.422	0.379	62.5	53.7	40.4
0.33	2.13	5.73	7.79	1.36	0.422	0.398	55.2	51.0	40.2
0.36	1.04	8.50	10.64	1.25	0.422	0.410	49.0	47.6	40.0

Table 3-4: Summary of Minimum Solvent Analysis Results: STEEL (27% CO_2), G_{INLET} = 10.4 kmol/s, $T_{GAS,IN}$ = $T_{LIQUID,IN}$ = 40°C, 90% CO_2 Removal, 8 m PZ

Lean Loading	Lean End Driving Force (P^*_{CO2}/P_{CO2})	Minimum Solvent Rate (L_{MIN}/G)			Rich Loading		Temperatures		
		Isothermal	Adiabatic	$L_{MIN,\ ADIABATIC}$ / $L_{MIN,\ ISOTHERMAL}$	Isothermal	Adiabatic	Max Liquid	Liquid Outlet	Vapor Outlet
mol CO_2/mol alk.		mol/mol	mol/mol		mol CO_2/mol alk.		°C		
0.12	217.97	3.09	3.21	1.04	0.431	0.421	86.5	45.0	78.5
0.15	143.91	3.42	3.65	1.07	0.431	0.416	87.1	46.5	77.6
0.16	124.49	3.55	3.81	1.07	0.431	0.413	87.4	47.2	77.2
0.17	107.11	3.69	4.01	1.09	0.431	0.411	87.6	48.0	76.7
0.175	99.32	3.76	5.67	1.51	0.431	0.345	88.6	57.5	70.2
0.18	91.52	3.83	6.82	1.78	0.431	0.321	88.9	61.3	61.9
0.19	77.56	3.99	7.70	1.93	0.431	0.315	88.8	63.1	51.4
0.195	**70.81**	**4.08**	**7.91**	**1.94**	**0.431**	**0.317**	**88.6**	**63.3**	**47.7**
0.2	65.13	4.16	8.06	1.94	0.431	0.318	88.4	63.3	44.8
0.22	44.60	4.56	8.28	1.82	0.431	0.336	86.5	62.4	41.5
0.24	29.41	5.03	8.41	1.67	0.431	0.354	81.0	61.2	41.2
0.26	18.88	5.62	8.63	1.53	0.431	0.372	74.0	59.8	41.0
0.29	9.57	6.81	9.30	1.36	0.431	0.394	65.3	57.3	40.7
0.32	4.88	8.65	10.85	1.25	0.431	0.409	58.0	54.0	40.4
0.34	3.09	10.54	12.69	1.20	0.431	0.416	53.8	51.5	40.3
0.36	1.89	13.50	15.75	1.17	0.431	0.421	50.0	48.9	40.1
0.39	0.78	23.74	26.84	1.13	0.431	0.426	45.1	44.8	40.0

3.4.1 Fundamental Explanations

3.4.1.1 Equilibrium and Operating Line Constructions

To understand the trends with loading, equilibrium-operating line constructions can provide insight into the effect of a temperature bulge in the column on the maximum capacity attainable (L_{MIN} achieved). Figure 3-5 through Figure 3-8 include representative equilibrium-operating line charts in the three loading ranges (low, mid, and high) for the coal-fired boiler application. The loadings selected for detailed analysis are highlighted in Figure 3-4 (red circles) for reference.

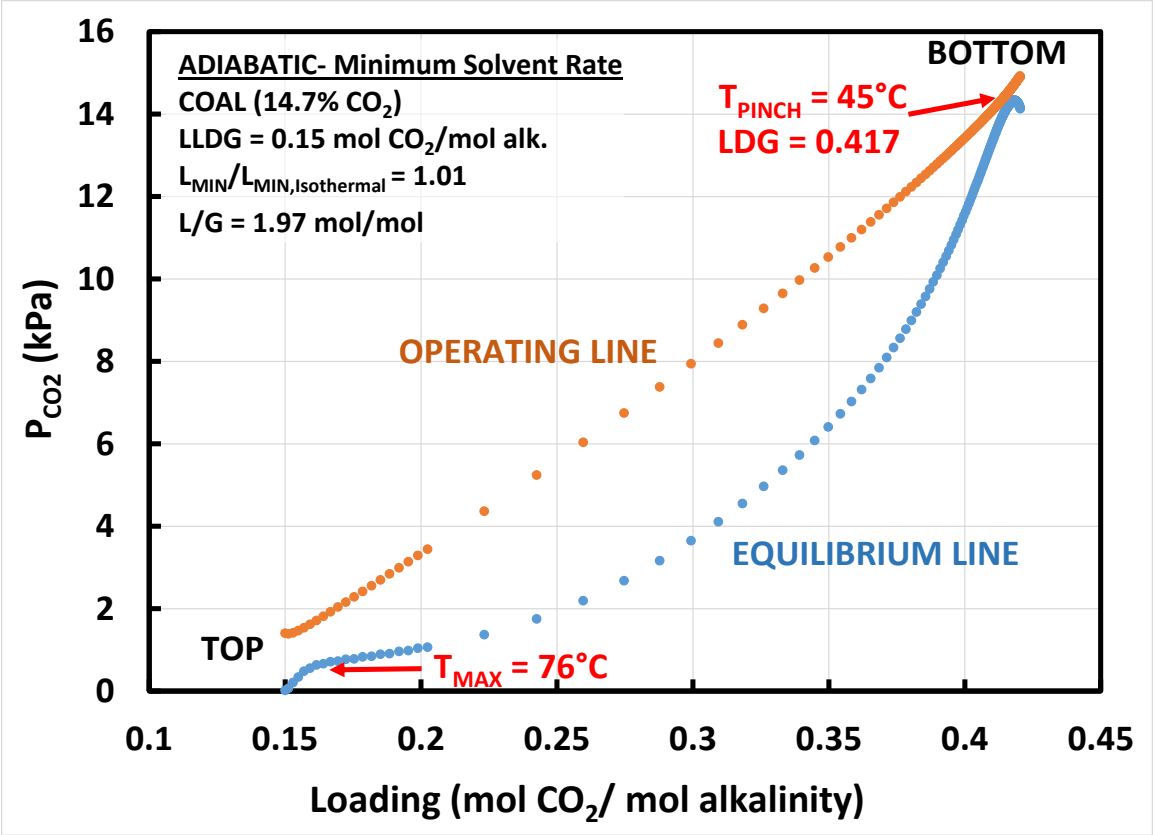

Figure 3-5: Operating and equilibrium curves @ LLDG = 0.15 mol CO_2/mol alk. Adiabatic absorber operated at L_{MIN} ("infinite" packing) for 90% CO_2 removal from coal-fired boiler flue gas (14.7% CO_2). The mass transfer pinch (contact of equilibrium and operating lines) occurs at the rich end of the column (bottom, 45°C), unrelated to the max temperature (76 °C) near the lean end (top).

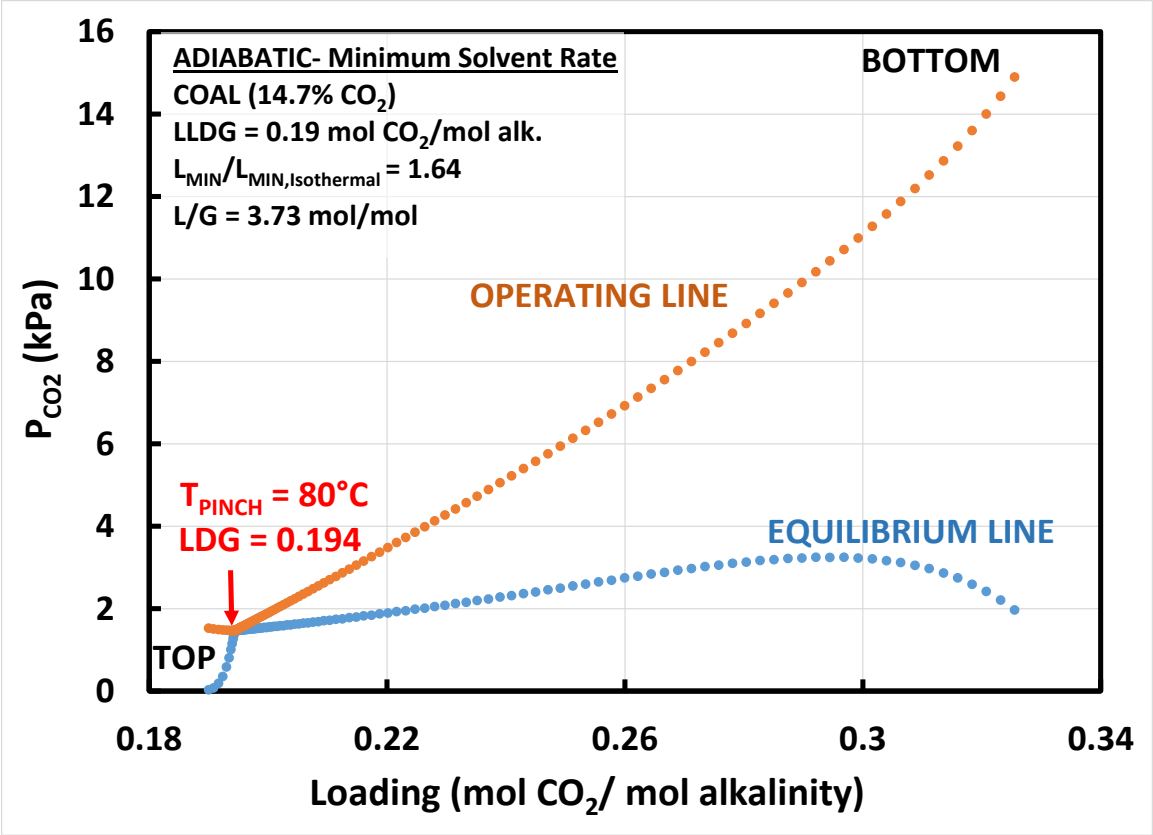

Figure 3-6: Operating and equilibrium curves @ LLDG = 0.19 mol CO_2/mol alk. Adiabatic absorber operated at L_{MIN} ("infinite" packing) for 90% CO_2 removal from coal-fired boiler flue gas (14.7% CO_2). The mass transfer pinch (contact of the equilibrium and operating lines) occurs near the lean end of the column and coincides with the maximum temperature (80 °C).

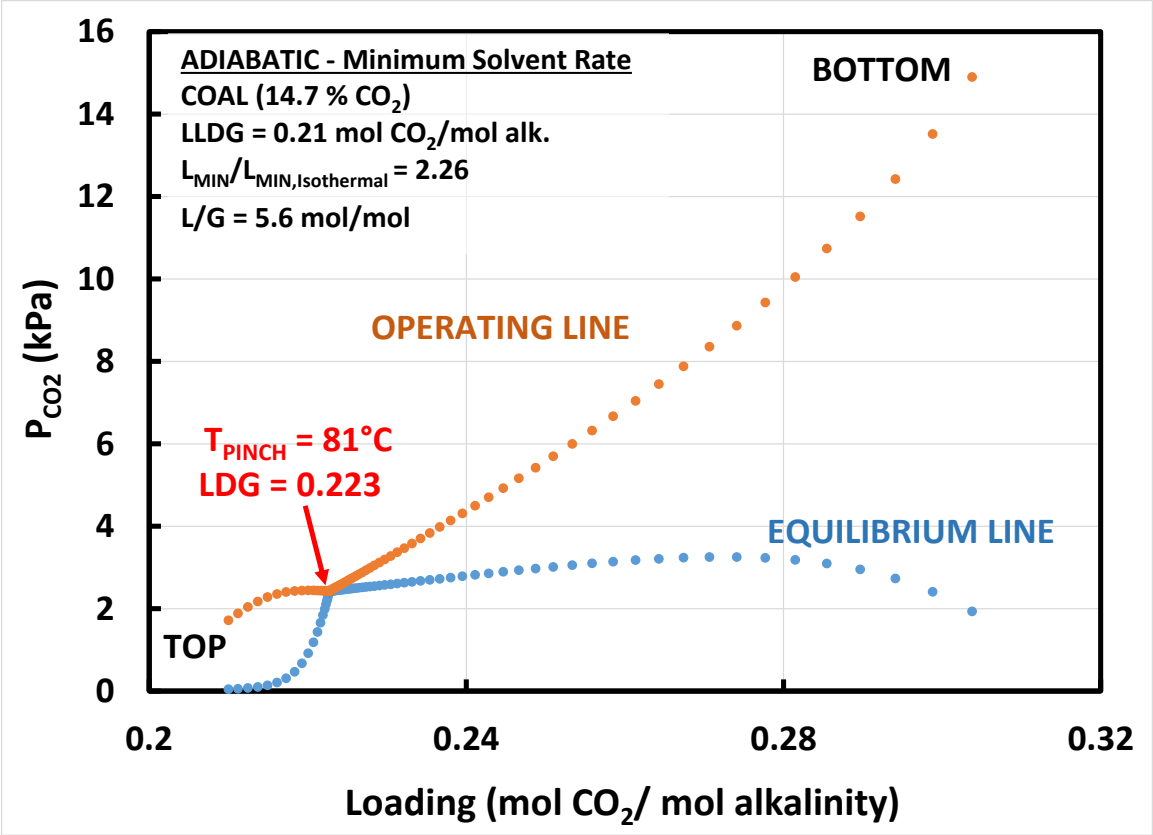

Figure 3-7: Operating and equilibrium curves @ LLDG = 0.21 mol CO_2/mol alk. Adiabatic absorber operated at L_{MIN} ("infinite" packing) for 90% CO_2 removal from coal-fired boiler flue gas (14.7% CO_2). This condition represents the largest deviation from isothermal performance ($L_{MIN}/L_{MIN,Isothermal}$ = 2.26). The mass transfer pinch (contact of the equilibrium and operating lines) occurs near the lean end of the column and coincides with the maximum temperature (81 °C).

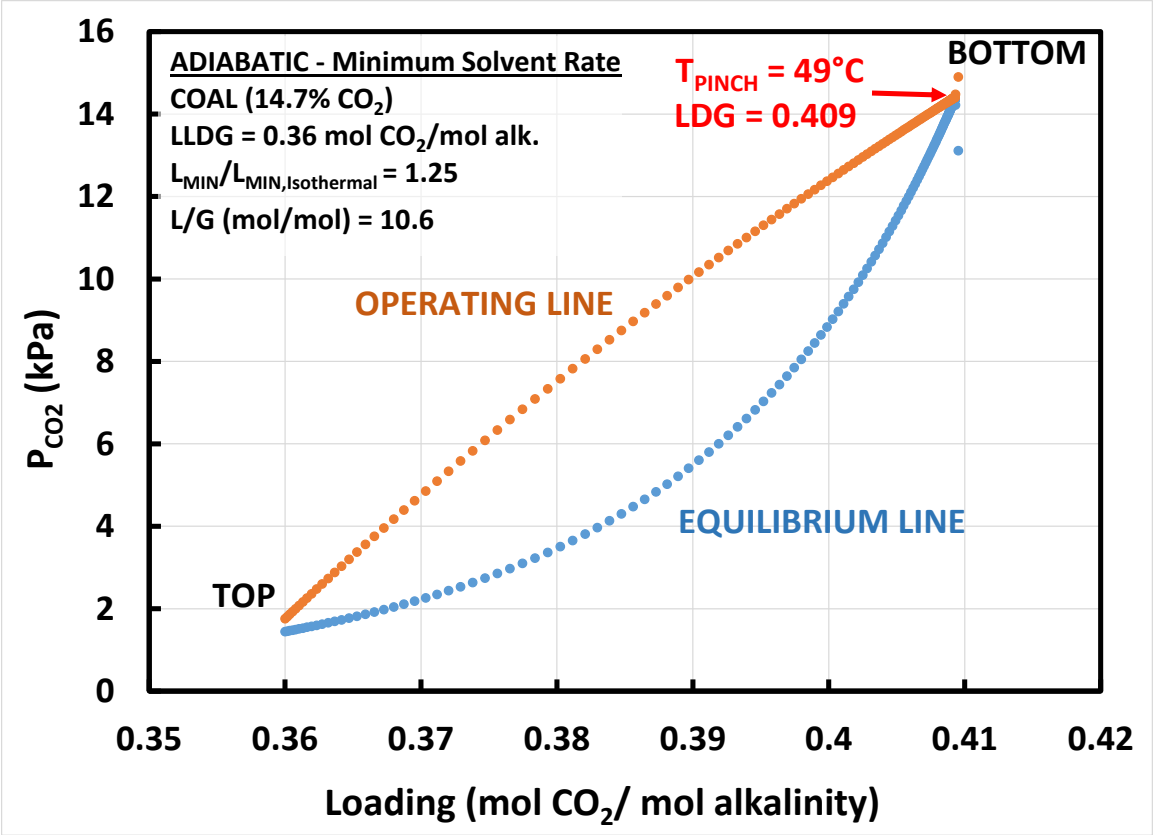

Figure 3-8: Operating and equilibrium curves @ LLDG = 0.36 mol CO_2/mol alk. Adiabatic absorber operated at L_{MIN} ("infinite" packing) for 90% CO_2 removal from coal-fired boiler flue gas (14.7% CO_2). The mass transfer pinch (contact of the equilibrium and operating lines) occurs near the rich end of the column and coincides with the maximum temperature (49 °C).

The slope of the operating line (upper line in orange) in the preceding figures represents the liquid to gas ratio (L/G). The curvature present in the operating lines is due to the concurrent transfer of water and an L/G that may vary significantly in different parts of the column. This differs from the typical binary diagram with only a single transferring component. As the liquid rate is reduced, the slope of the operating line is reduced until it comes in contact with the equilibrium line; at this point in the column, there is no driving force for mass transfer (the column is "pinched"), and the solvent rate cannot be reduced any further while meeting the 90% removal specification. Therefore,

the slope of the operating line when the pinch occurs represents the minimum solvent rate to achieve 90% removal for the given operating conditions and column configuration. The best performance (in terms of solvent circulation or L_{MIN}) achievable for a given operating condition corresponds to a mass transfer pinch at the rich end (bottom) of the column at the column feed temperature (an isothermal pinch or complete saturation of the solvent). Equilibrium-operating line constructions provide insight into the effect of a temperature bulge in the column on the approach to this best case performance.

In Figure 3-5, the maximum solvent temperature occurs near the top of the column due to the relatively low L/G at the lean operating conditions. At the low L/G condition, the gas heat capacity dominates and carries heat generated by CO_2 absorption to the top of the column. The low lean loading (0.15 mol CO_2/mol alk.) also imposes large driving forces at the top of the column, so the temperature bulge in this region does not result in a mass transfer pinch. The pinch occurs near the rich end of the column at a temperature of 45°C. Therefore, while some benefit can be derived by reducing the temperature at the rich end of the column, the temperature maximum in the column does not limit the solvent capacity - this is reflected in the close approach to isothermal performance ($L_{MIN}/L_{MIN,Isothermal}$ = 1.01). The benefit of intercooling in this low lean loading region is negligible from a solvent capacity perspective.

In Figure 3-6 and Figure 3-7, a mass transfer pinch coincides with the temperature bulge at the lean end of the column. In this loading range, the solvent carries an increasing portion of the heat generated by CO_2 absorption and the heat is “trapped” in the column. The temperature bulge is limiting the solvent capacity (as noted by the reduced rich loading values in Figure 3-6 and Figure 3-7). This condition corresponds to the largest potential benefit from intercooling via removal of the temperature-induced mass transfer pinch.

Figure 3-7 corresponds to the largest deviation from isothermal capacity across the entire range of lean loadings evaluated for the coal-fired boiler ($L_{MIN}/L_{MIN,\ ISOTHERMAL}$ = 2.26). The temperature-related pinch is still at the lean end of the column (most of the removal occurs below the pinch). This seems to contradict the hypotheses of previous researchers that the critical L/G condition (where intercooling benefits are maximized) corresponds to a pinch in the middle of the column. This condition will be investigated further in the subsequent section.

Finally, in Figure 3-8, the high lean loading results in a temperature bulge at the rich end of the column. The high L/G (liquid heat capacity dominates) required in this loading region drives the temperature bulge to the bottom of the column and results in a comparatively low maximum column temperature (49°C). The mass transfer pinch occurs at this bulge, but the low temperature and proximity to the rich end of the column results in a performance very close to an isothermal column. Therefore, intercooling will provide limited benefits in this loading region.

The trends for the NGCC case (Figure 3-2) and the steel-blast furnace case (Figure 3-4) can also be explained by the same phenomena in the column:

1) Lean end temperature bulge at low loadings *does not* form a mass transfer pinch due to large driving forces near temperature maxima;
2) As lean loading is increased, a lean end pinch forms at the temperature bulge and severely limits absorption capacity of the solvent;
3) At high lean loadings, the solvent rate has increased sufficiently to push the temperature bulge (i.e., large heat capacity) to the rich end of the column and simultaneously moderate the temperature, limiting the effect of the mass transfer pinch on solvent capacity.

3.4.1.2 Lean Pinch Formation and Multiple Steady States

As noted in the preceding discussion, the formation of a lean end pinch at the temperature bulge is the precipitating phenomena that leads to an operating region where intercooling is essential for the energy performance of amine-based solvent systems. In Figure 3-2 to Figure 3-4, the transition to this region appears to be discontinuous as a function of loading. The NGCC case (Figure 3-2) exhibits multiple steady states at the loading where the transition occurs (0.22 mol CO_2/mol alkalinity), and will be investigated to understand the nature of this important transition in process performance.

Figure 3-9 summarizes the pinch behavior at the transition loading.

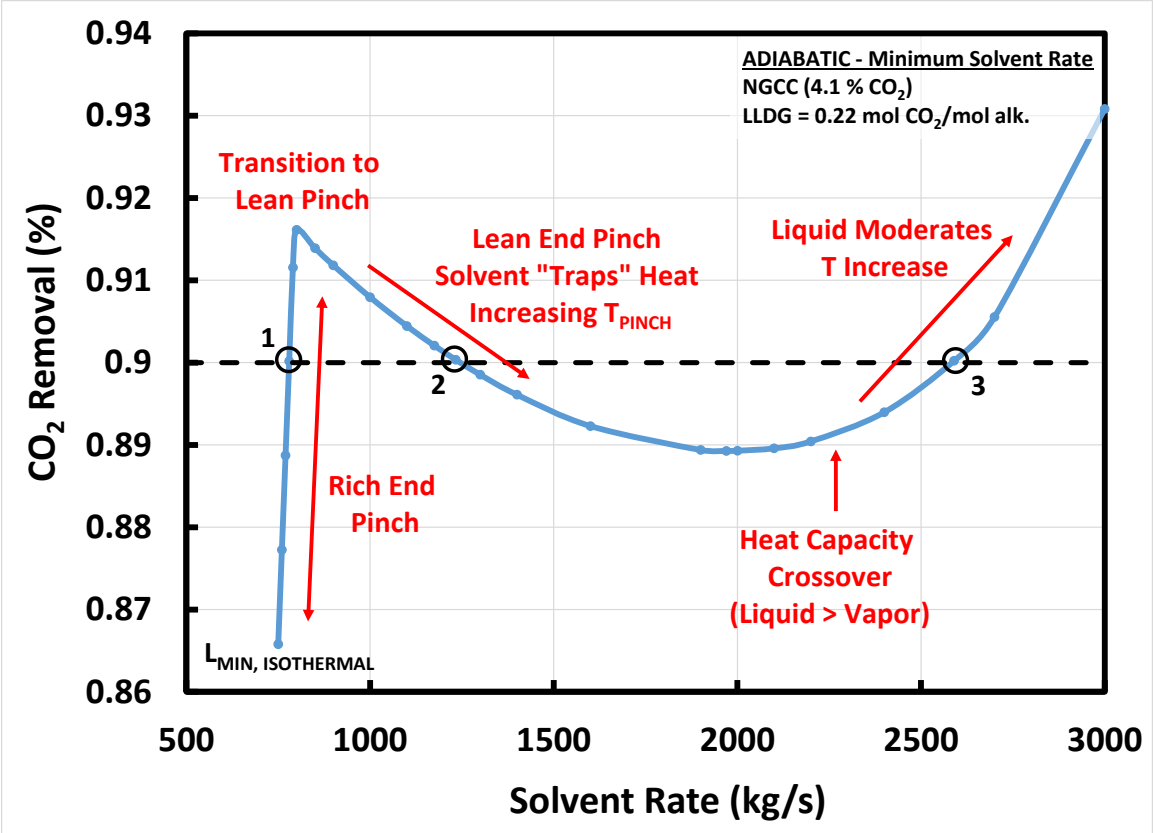

Figure 3-9: Lean end pinch formation at the transition loading (0.22 mol CO_2/mol alk.) for an adiabatic absorber, NGCC power plant flue gas (4.1% CO_2), 8 m PZ. Three steady state solvent rates achieve 90% CO_2 removal (identified in the figure) as the solvent rate increases from the isothermal minimum ($L_{MIN, ISOTHERMAL}$).

CO_2 absorption is expected to increase monotonically with solvent rate at a given lean loading due to the relaxing of equilibrium constraints in the column. However, Figure 3-9 exhibits two distinct extrema (minimum and maximum) where the trends with solvent rate change. This behavior can be explained by the physical phenomena governing each range of solvent rate. As the solvent rate is initially increased from the isothermal minimal solvent rate (lowest solvent rate possible), a rich end pinch exists which is preventing the adiabatic absorber from achieving 90% removal of CO_2. As the solvent rate is increased to overcome the rich end equilibrium constraint, the CO_2 removal

initially rises rapidly as expected. However, the solvent simultaneously "traps" heat in the column exacerbating the impact of the lean end temperature bulge until a lean end pinch is formed. This transition from rich to lean pinch was illustrated as a function of lean loading in the preceding section (Figure 3-5 to Figure 3-6). In this transition to a lean end pinch, the first steady-state is realized for the NGCC application (L_{MIN} = 780 kg/s).

The formation of the pinch coincides with a sharp change in the trend with solvent rate. Increasing the solvent rate carries heat to the lean end pinch and outweighs any general equilibrium benefits of increasing the solvent rate. Therefore, the CO_2 removal drops over a range of solvent rates. In this lean-end pinch controlled region, a second steady state occurs (L_{MIN} = 1234 kg/s).

As the solvent rate is continually increased, the CO_2 removal reaches a minimum before there is sufficient solvent to overcome both the temperature and equilibrium constraints. As the solvent rate is increased from this local minima, the CO_2 removal rises once again as expected. The total liquid and vapor heat capacities[2] crossover in this region. The liquid heat capacity becomes dominant, carrying heat out of the column while moderating temperatures and the CO_2 removal rises rapidly with solvent rate again. The third steady state (L_{MIN} = 2590 kg/s) is achieved in this region where the solvent moderates liquid temperatures. The relationship between the solvent and vapor heat capacities will be investigated in detail in the subsequent sections as this becomes the dominant phenomena after the lean pinch formation.

Figure 3-9 also has several important practical implications. First, two of the three steady state solvent rates which meet the 90% removal specification present operational and process control challenges. The first steady state exists in a region where CO_2

[2] The total heat capacity refers to the mass flow rate*specific heat capacity of each phase and includes the latent heat of vaporization of water for the vapor phase.

removal is very sensitive to solvent rate (steep slope) and can easily reach an unstable condition (lean end pinch) if the solvent rate is not controlled carefully. This region clearly offers benefits of enhanced energy performance with the lower solvent rates, and allowing some operational flexibility on CO_2 removal targets (i.e., lower removal) might make this a feasible operating region.

The second steady state exists after lean end pinch formation where the solvent rate exhibits and inverse relationship with CO_2 removal. Operating in this region means control systems must account for this change in the relationship between a control variable and specification. If the control system is designed for general operation (solvent rate increase is followed by removal increase), the control scheme can drive the system away from the desired steady state and process specifications.

In addition, identification of the three steady state operating conditions is important for design calculations. The wide range of solvent rates (varies by a factor of ~4) will lead to drastically different equipment sizes, solvent inventories, and capital and operating cost splits. Therefore, careful selection of the operating condition with an associated control scheme to maintain operation in the desired region is required for robust design calculations near these lean-pinch forming regions.

3.4.1.3 Critical L/G Concept and Temperature Effects

The trends in Figure 3-9 are not limited to the transition loading discussed in the preceding section – they reflect general behavior at all loadings and all CO_2 flue gas concentrations in this study (this will be explored in section 3.4.2). That is, at every lean loading in Figure 3-2 to Figure 3-4, a solvent rate increase from the isothermal minimum will result in lean end pinch formation, a transition phase where the solvent "traps" heat

at the bulge, and ultimately a region where dominant liquid phase heat capacity allows moderation of temperature effects and improved equilibrium performance of the solvent.

At lean loadings below the transition loading (larger driving forces), the pinch formation and transitions will all occur at CO_2 removal rates above the 90% constraint, and thus the only feasible steady state solution that achieves 90% removal will occur before a lean end pinch is formed (rich end pinch region). Conversely, as the lean loading increases above the transition (driving force drops), the pinch formation and solvent rate transitions will occur at CO_2 removal rates below the 90% constraint, and therefore only one feasible steady state will be realized (the final high solvent rate steady state). Eventually, as the lean loading is further increased, the solvent rate will increase sufficiently that the lean end equilibrium constraint is readily overcome and the high solvent rate steady state condition is not far removed from the isothermal minimum solvent rate (all transitions in Figure 3-9 would occur over a narrow range of solvent rates).

The discrete solvent rates that achieve 90% removal at each lean loading form the continuous trends as a function of lean loading in Figure 3-2 to Figure 3-4. Similarly, the individual temperature maxima and total heat capacities of each phase at each unique solvent rate-lean loading combination can be used to develop continuous trends as well. Figure 3-10 adds absorber outlet (vapor and solvent) and maximum (solvent) temperatures to the L_{MIN} analysis to expand on the observations at each individual lean loading. Figure 3-11 provides the corresponding total vapor and liquid heat capacities to explain the temperature trends. The vapor heat capacity includes the capacity of the vapor to carry water (latent heat of vaporization).

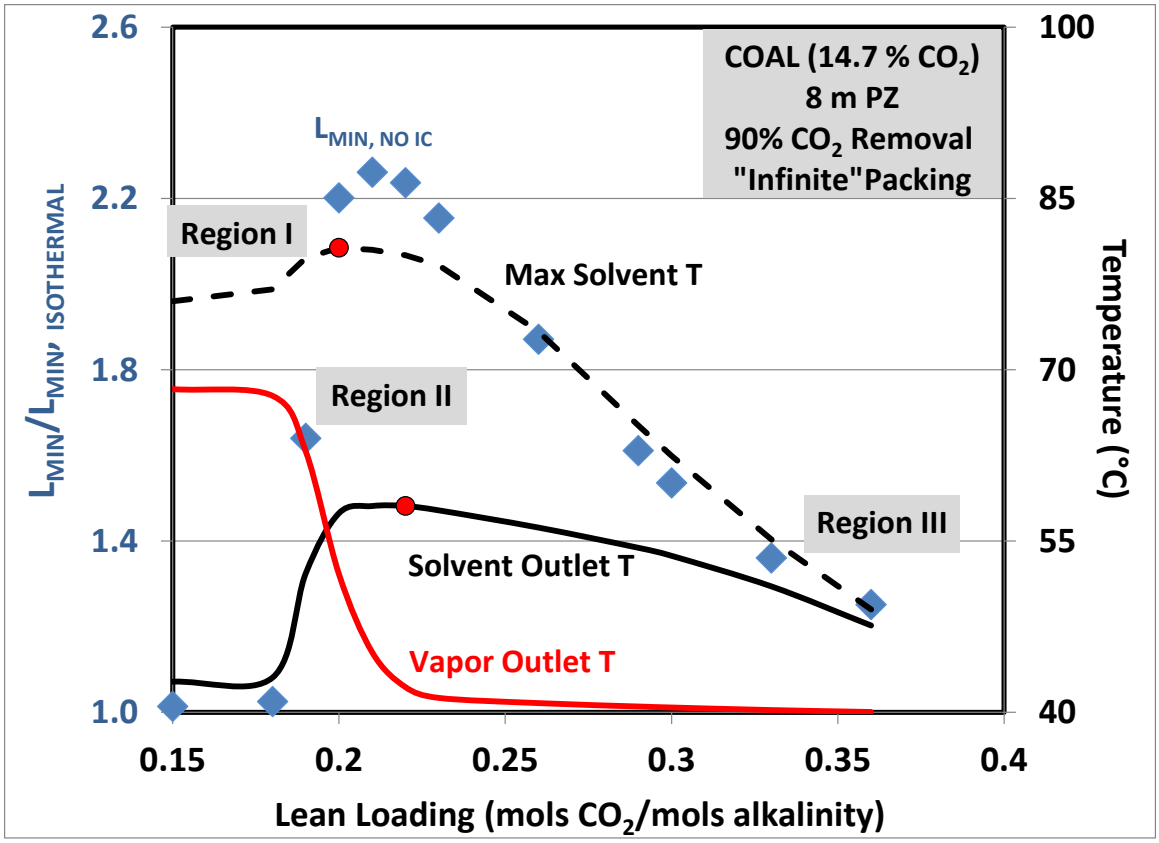

Figure 3-10: Ratio of L_{MIN} ("infinite" packing) for an adiabatic absorber to an isothermal absorber (40 °C) for 90% CO_2 capture from a coal-fired boiler (14.7% CO_2) utilizing 8 m PZ (primary y-axis). Solvent outlet and maximum temperatures and vapor outlet temperatures for each lean loading (secondary y-axis). The three regions identify vapor heat capacity control (I), balanced vapor and liquid heat capacities (II), and liquid heat capacity control (III). Red points = maximum values.

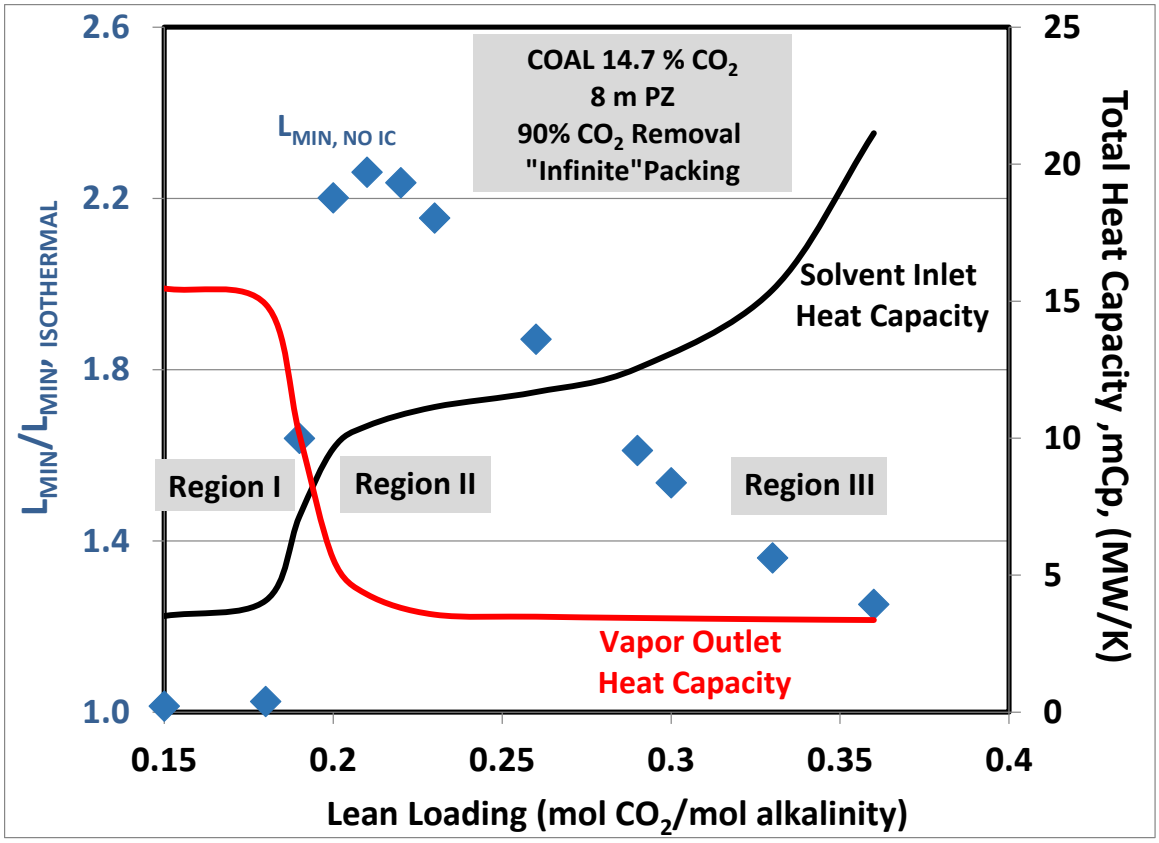

Figure 3-11: Ratio of L_{MIN} ("infinite" packing) for an adiabatic absorber to an isothermal absorber (T = 40 °C) for 90% CO_2 capture from a coal-fired boiler (14.7% CO_2) utilizing 8 m PZ (primary y-axis). Total solvent inlet heat capacity (mass flow rate * specific heat capacity) and total vapor outlet heat capacity (mass flow rate * specific heat capacity + latent heat of water) for each lean loading (secondary y-axis). The three regions identify vapor heat capacity control (I), balanced vapor and liquid heat capacities (II), and liquid heat capacity control (III).

The two preceding figures taken together with the mass transfer pinch behavior at each lean loading (e.g., Figure 3-9) can fully describe the governing phenomena for trends in solvent capacity with lean loading. In Figure 3-10 and Figure 3-11, 3 regions represent distinct phenomena in the column:

- Region I: In this region, the liquid to gas ratio (L/G) is low corresponding to a low lean loading and the absence of a temperature bulge related pinch. The maximum

solvent temperature (Figure 3-10) is near the maximum value achieved across the entire loading range, but large driving forces prevent a lean end pinch that violates the CO_2 removal constraint (90%) and prevents the associated increase in solvent rate required to overcome the constraint. The vapor carries a majority of the heat from the bulge out of the column. The vapor outlet temperature and, correspondingly, total vapor heat capacity are at a maximum in this region.

- Region II: As the lean loading increases, the reduced driving forces lead to a lean end pinch at the temperature bulge that limits the ability to reach 90% CO_2 removal. The solvent rate increases significantly after the pinch is formed to overcome the equilibrium constraint associated with the temperature bulge. The total liquid heat capacity increases while the vapor heat capacity drops until the total heat capacities (or heat carrying ability) of the two phases are approximately equivalent. This condition represents the maximum retention of heat in the column (the capacity of the solvent to carry heat down the column is matched by the ability of the vapor to carry the heat to the top of the column). The "heat trapping" effect is further validated by the fact that the maximum temperature observed in the absorber across the entire loading range occurs at (or near) the heat capacity cross-over. This cross-over (equal heat capacities) has been proposed as a definition of the critical L/G (Kvamsdal & Rochelle, 2008). In this transition region, the liquid heat capacity becomes dominant, and the maximum temperature at the bulge is followed closely by the maximum solvent temperature at the absorber outlet as the heat is carried by the liquid down the absorber column. The maximum deviation from isothermal capacity occurs in this transition region as the bulge temperature is at its highest values and are

associated with a lean end pinch. This point of maximum deviation from isothermal capacity has also been defined as a critical L/G (Plaza, 2011).

- Region III: In this final region, the vapor heat capacity reaches a minimum as the vapor outlet temperature approaches 40°C (the inlet temperature). The solvent heat capacity is dominant, and increases significantly as the lean loading increases (reflecting inherent solvent capacity limitations in this region). The solvent circulation rate (and corresponding heat capacity) is sufficient to moderate the magnitude and rate of temperature rise generated in the solvent and results in a temperature bulge towards the rich end of the column. These effects significantly reduce the solvent capacity penalty of the temperature-related mass transfer pinch.

As the discussion of the 3 regions illustrates, several distinct phenomena occur sequentially to explain the effects of the temperature bulge on solvent capacity. These phenomena arise from the behavior exhibited at a single lean loading as the solvent rate is increased (c.f., Figure 3-9). Thus, a description is proposed to expand on the concept of a single critical L/G that previous researchers defined for the varying phenomena:

1) The initiating phenomena is the formation of a limiting lean end pinch at the temperature bulge, which is a function of the maximum temperature achieved in the column (dictated by CO_2 concentration in the flue gas, heat of absorption of the solvent, and relative transfer rates of water and CO_2) and the operating loading/driving forces for mass transfer. The effect of transfer rates will be considered in section 3.4.3 – the rate phenomena are important in this region of pinch formation and differentiate it from the mechanisms after pinch formation, which are dominated by heat capacity effects and solvent rate effects. The solvent rate does increase with lean loading and contributes to "trapping" heat, but is not

the primary phenomena in the formation of a pinch – as noted, the increasing L/G in region I has minimal impact on the maximum temperature realized in the column and therefore is not the primary explanation for the formation of the pinch.

2) The "heat trapping effect" that occurs with increasing solvent rate (and exacerbates the solvent capacity penalty) reaches a maximum near the point where the total liquid and vapor heat capacities are equal. As will be discussed in subsequent sections, the difference in the solvent and vapor heat capacities when the lean pinch forms will determine how much the solvent rate must increase to reach this cross-over point to overcome the equilibrium restrictions imposed by the lean pinch.
3) The subsequent buffering of solvent temperature by the high L/G follows as a result of the increasing solvent rate required to overcome the mass transfer pinch and the heat capacity difference of the two phases.

3.4.2 Generalizing Solvent Capacity Trends for Adiabatic Absorbers

The preceding discussion provides fundamental explanations for the observed trends in the deviation from isothermal capacity for adiabatic absorbers. While the mechanisms are the same as the process conditions are changed (e.g., flue gas concentration), the effect of process variables cannot be generalized from the preceding physical explanations alone. Therefore, the minimum solvent rate analysis was systematically repeated for various operating conditions to generalize the trends in solvent capacity for adiabatic absorbers.

3.4.2.1 Flue Gas CO_2 Concentration

The mechanisms discussed in the previous section (mass transfer pinch formation and subsequent solvent rate effects) for a coal-fired boiler and NGCC application are generally applicable for any flue gas CO_2 concentration. However, the impact of the phenomena on process performance shows some notable differences as a function of CO_2 concentration. Figure 3-12 re-plots the deviation from the isothermal solvent rate for each of the 3 flue gas sources as a function of lean loading for direct comparison.

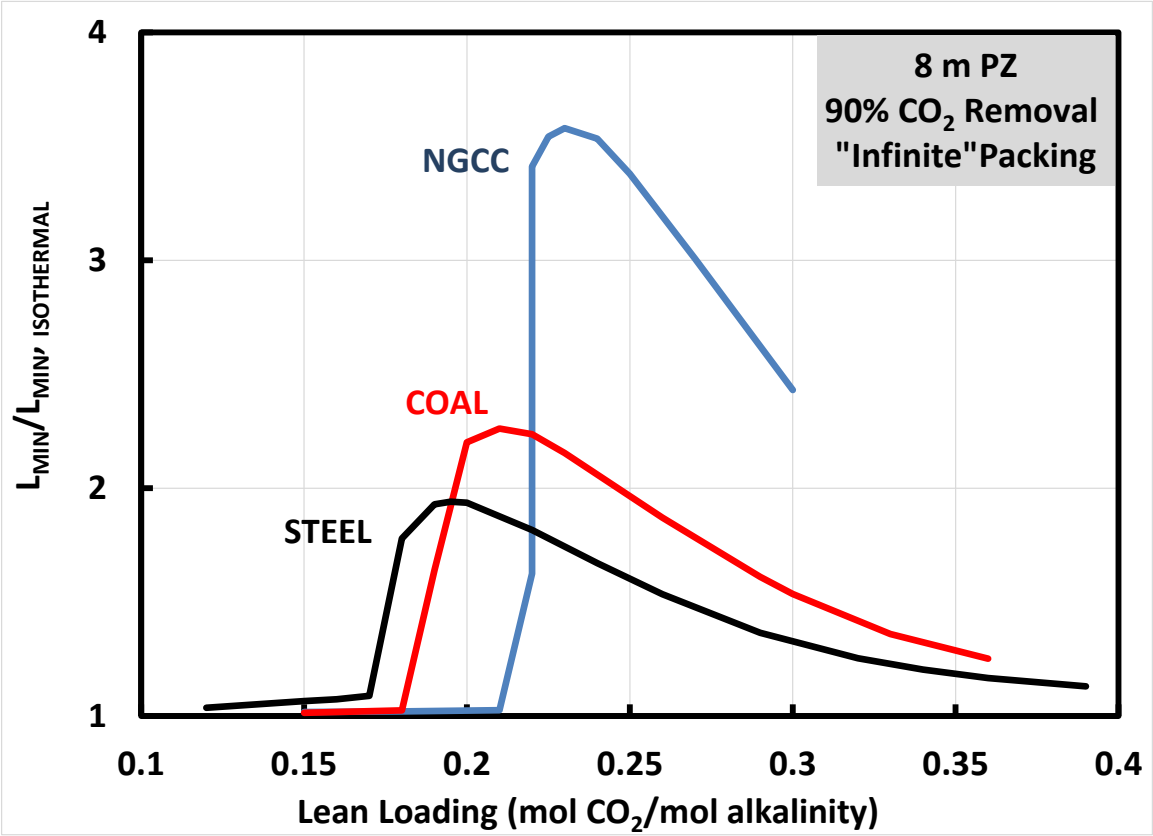

Figure 3-12: L_{MIN} analysis summary for an adiabatic absorber for NGCC (4.1% CO_2), coal-fired boiler (14.7% CO_2), and steel blast furnace (27% CO_2), 8 m PZ, 90% CO_2 capture.

Figure 3-12 highlights two important differences. First, the lean loading (transition loading) where each application exhibits a lean end pinch and deviates from the isothermal baseline *increases with decreasing CO_2 flue gas concentration*. This result has an important practical implication – as the CO_2 concentration in the flue gas drops, the lean loading window where the absorber can be operated without intercooling expands (or, equivalently, without a significant energy penalty associated with large solvent circulation rates). The stripper energy performance is an optimization, in part, between the sensible heat associated with the mass of circulating solvent and the steam requirements to strip the CO_2 from the solvent to achieve leaner loadings. By expanding the window of lean loadings where a lower solvent circulation rate can be applied without modification of the absorber, the stripper energy performance is more likely to be at or near an optimum operating condition. Therefore, the lower CO_2 flue gas concentration provides more operational and design flexibility for the capture system.

The fundamental explanation for this trend with loading can be developed from Figure 3-13, which presents the same curves for deviation from isothermal capacity as a function of the driving force at the lean end (top) of the absorber column.

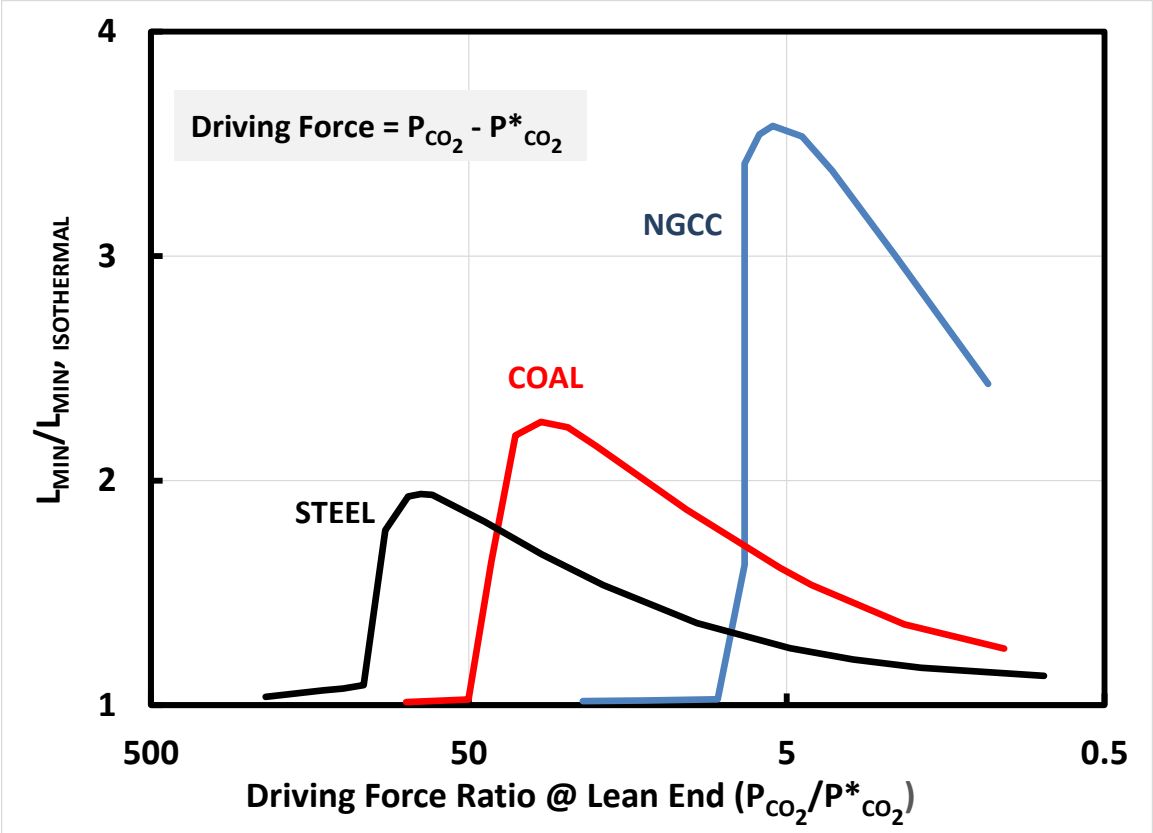

Figure 3-13: L_{MIN} analysis summary as a function of lean end driving force (equilibrium partial pressure of CO_2 – gas-side partial pressure of CO_2) for an adiabatic absorber for NGCC (4.1% CO_2), coal-fired boiler (14.7% CO_2), and steel blast furnace (27% CO_2), 8 m PZ, 90% CO_2 capture.

The figure indicates that the driving force where the lean end pinch forms (sharp rise in each curve) drops with CO_2 concentration. This follows directly from the lean loading result - as the gas side partial pressure drops with CO_2 concentration in the flue gas, the equilibrium partial pressure of the lean solvent increases with the transition loading for each application. The driving force indicates how close each application is to a lean pinch – as noted in the preceding discussion, the formation of a mass transfer pinch near the lean end of the column is the initiating phenomena for the deteriorating performance of the adiabatic absorber. Lower CO_2 flue gas concentrations result in lower temperatures at

the temperature bulge where the lean end pinch forms (compare temperatures in Table 3-2 through Table 3-4). This results in reduced equilibrium partial pressures at a given loading, and allows for operation at higher loadings before a lean end pinch becomes limiting.

The second major observation from Figure 3-12 is that the maximum deviation from isothermal behavior *decreases with increasing CO_2 concentration*. The NGCC case reaches a maximum ratio of approximately 3.5, coal reaches a maximum of 2.2, and steel reaches a maximum of 2. This trend appears counter-intuitive since the higher CO_2 cases yield the highest absolute temperatures in the column (Table 3-2 through Table 3-4) and might be expected to exhibit the greatest temperature limitations on solvent capacity. However, the explanation can be developed by evaluating the lean pinch formation behavior for each flue gas source at the loading where the maximum deviation from isothermal solvent capacity occurs. Figure 3-14 through Figure 3-16 examine the transition from the isothermal to adiabatic minimum solvent rate for each case.

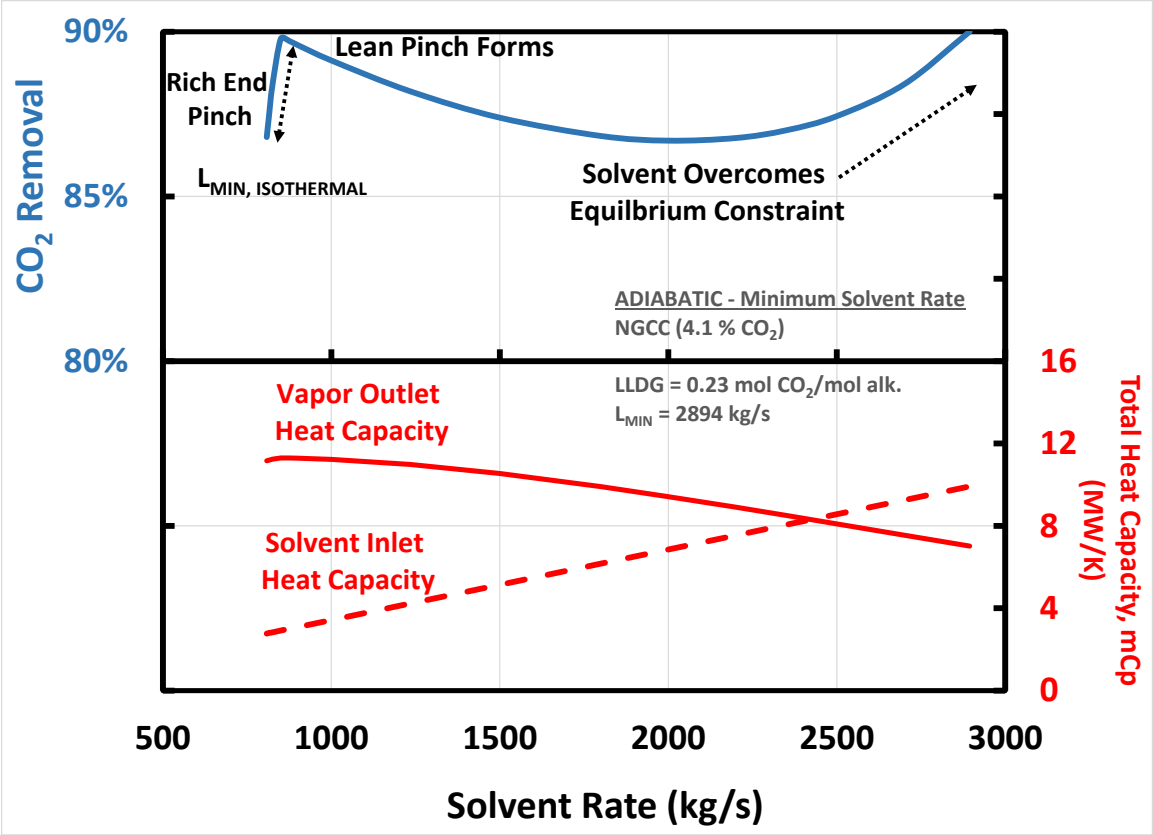

Figure 3-14: NGCC (4.1% CO_2) Lean pinch formation and total heat capacity (mC_P) for the vapor outlet and solvent inlet (lean end of the absorber) @ LLDG = 0.23 mol CO_2/mol alk. (8 m PZ). Solvent rate is increased from $L_{MIN, ISOTHERMAL}$ to $L_{MIN, ADIABATIC}$. The total heat capacity of the vapor includes the ability of the vapor to carry water (i.e., includes enthalpy of vaporization of water). Lean loading corresponds to maximum deviation from $L_{MIN, ISOTHERMAL}$ for an adiabatic absorber (see Figure 3-2).

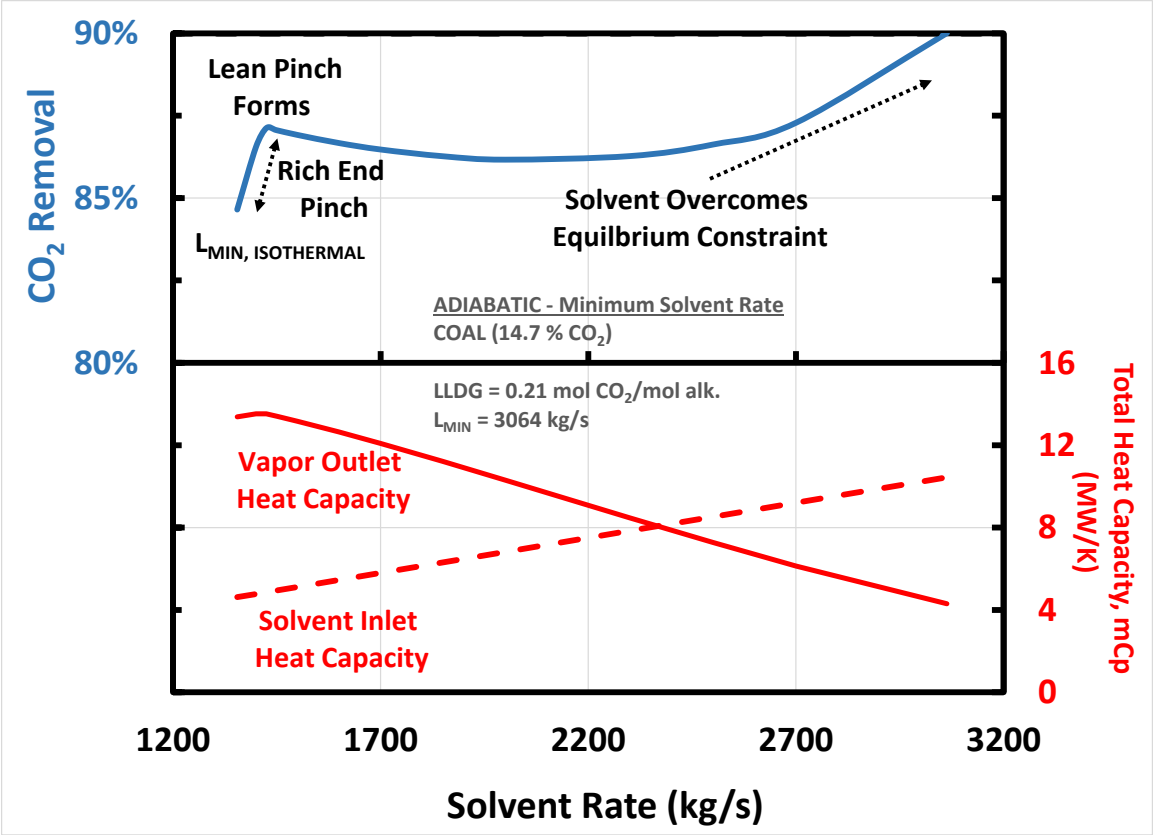

Figure 3-15: Coal-fired boiler (14.7% CO_2) Lean pinch formation and total heat capacity (mC_P) for the vapor outlet and solvent inlet (lean end of the absorber) @ LLDG = 0.21 mol CO_2/mol alk. (8 m PZ). Solvent rate is increased from $L_{MIN, ISOTHERMAL}$ to $L_{MIN, ADIABATIC}$. The total heat capacity of the vapor includes the ability of the vapor to carry water (i.e., includes enthalpy of vaporization of water). Lean loading corresponds to maximum deviation from $L_{MIN, ISOTHERMAL}$ for an adiabatic absorber (see Figure 3-3).

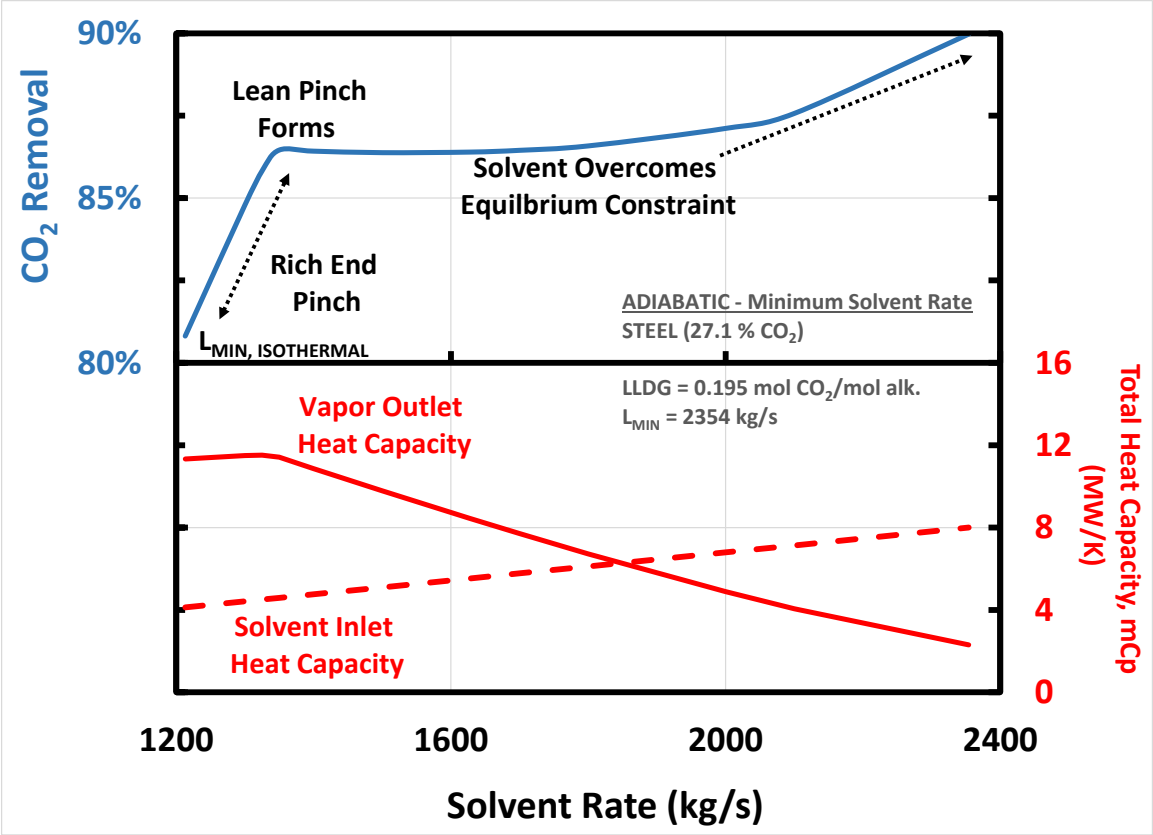

Figure 3-16: Steel blast furnace (27% CO_2) Lean pinch formation and total heat capacity (mC_P) for the vapor outlet and solvent inlet (lean end of the absorber) @ LLDG = 0.195 mol CO_2/mol alk. (8 m PZ). Solvent rate is increased from $L_{MIN, ISOTHERMAL}$ to $L_{MIN, ADIABATIC}$. The total heat capacity of the vapor includes the ability of the vapor to carry water (i.e., enthalpy of vaporization of water). Lean loading corresponds to maximum deviation from $L_{MIN, ISOTHERMAL}$ for an adiabatic absorber (see Figure 3-4).

As in the discussion of the multiple steady state solutions at the transition lean loading (Figure 3-9), the three figures above exhibit the same sequence of mechanisms as the solvent rate is increased from the isothermal minimum to the adiabatic minimum: lean pinch formation, heat "trapping" at the pinch, and dominant liquid heat capacity to overcome equilibrium constraints. The major difference from the transition loading region is that the lean pinch and subsequent transition to equal heat capacity occurs at

CO_2 removal rates below 90%. The higher lean loadings (smaller driving forces) in the maximum deviation region ensure the lean end pinch occurs before the system can reach 90% removal. The three figures also include the total vapor and liquid heat capacities. In each case, the crossover of the heat capacities is followed by a significant improvement in CO_2 removal as a function of solvent rate. The solvent circulation is sufficient to remove heat from the temperature bulge and relax the associated lean end pinch. To facilitate comparison of the trends, the CO_2 removal and heat capacity curves are re-plotted for all flue gas sources in Figure 3-17.

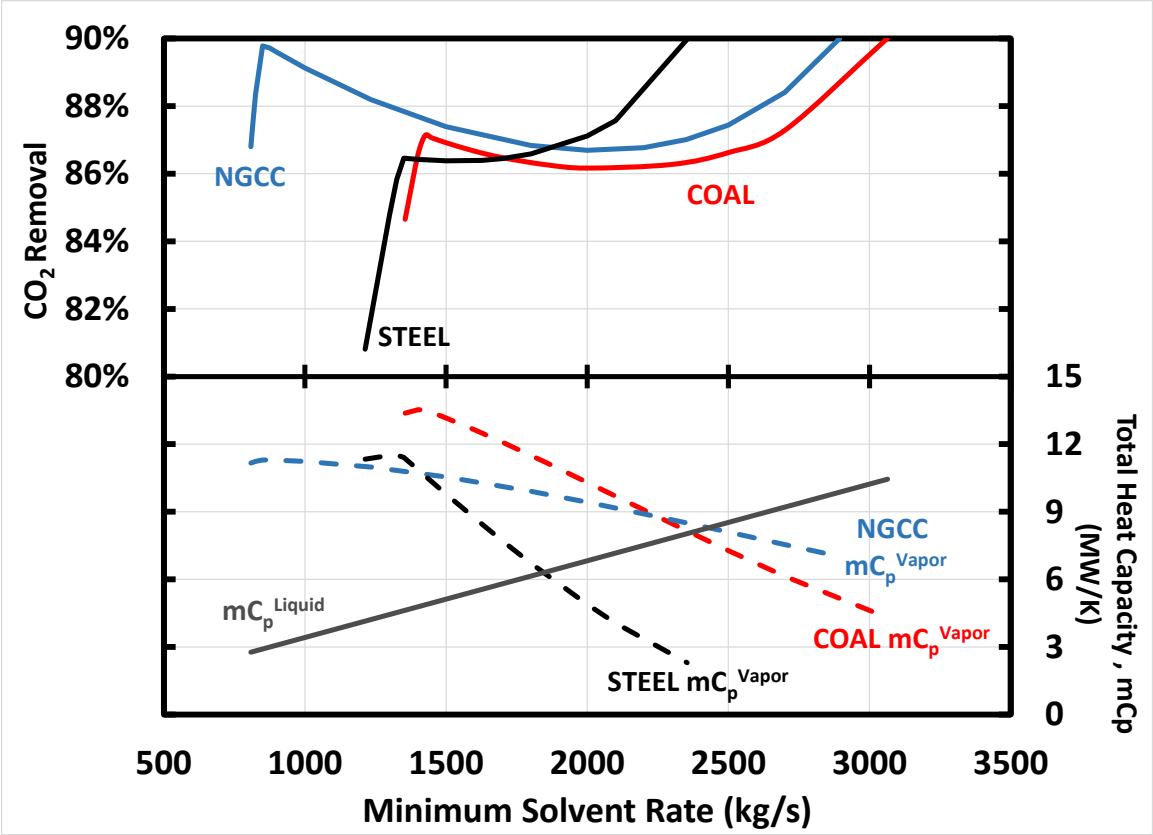

Figure 3-17: Summary of lean pinch and heat capacity curves - NGCC (4.1% CO_2, LLDG = 0.23 mol CO_2/mol alk.) coal-fired boiler (14.7% CO_2, LLDG = 0.21 mol CO_2/mol alk.), and steel blast furnace (27% CO_2, LLDG = 0.195 mol CO_2/mol alk.). Solvent rate is increased from $L_{MIN, ISOTHERMAL}$ to $L_{MIN, ADIABATIC}$. The total heat capacity of the vapor includes the ability of the vapor to carry water (i.e., enthalpy of vaporization of water). A single curve represents the total heat capacity of the liquid for all three flue gas applications since the total heat capacity is dominated by solvent flow rate.

The figure includes several important features to differentiate the performance with CO_2 flue gas concentration. First, the difference in isothermal flow rates for the 3 cases represent differences in the inherent solvent capacity at the given lean loading and the total CO_2 removed in each case. Once the lean end pinch forms (forms with relatively small change in the solvent rate for each case), the differences for trends in CO_2 removal with solvent rate (and ultimately the solvent rate required for 90% removal) are driven by

the heat capacity of each phase. Two aspects of the heat capacity curves explain the differences in the solvent rate increase required to overcome the lean end pinch for the 3 flue gas applications. First, the difference between the total liquid and total vapor heat capacity at the point where the lean end pinch forms indicates the "barrier" the solvent rate must overcome to begin moderating temperatures at the bulge to address the equilibrium constraint of the mass transfer pinch. The larger this difference in vapor and liquid heat capacity, the more the solvent rate will need to be increased to become the dominant heat carrying phase (after the heat capacity crossover). Table 3-5 summarizes this parameter for each of the flue gas sources.

Table 3-5: Vapor and liquid total heat capacity summary at maximum $L_{MIN}/L_{MIN,ISOTHERMAL}$

Flue Gas Source	Lean Loading @ Max $L_{MIN}/L_{MIN,ISOTHERMAL}$	Max $L_{MIN}/L_{MIN,ISOTHERMAL}$	Δ Total Heat Capacity @ Lean Pinch Formation ($mC_p^V - mC_p^L$)	Slope of Vapor Total Heat Capacity Curve
	mol CO_2/mol alk.		MW/K	J/kg-K
NGCC (Figure 3-14)	0.23	3.58	8.38	2000
COAL (Figure 3-15)	0.21	2.26	8.66	5600
STEEL (Figure 3-16)	0.195	1.94	6.83	8900

The steel case has the smallest heat capacity "barrier" (6.83 MW/K) and should require the smallest proportional increase in solvent rate. However, the coal and NGCC cases exhibit similar "barriers" yet the NGCC case requires a much larger relative solvent increase. The second item in Table 3-5 above, the slope of the total vapor heat capacity curves, provides an explanation for this difference. The slope of the total vapor heat

capacity curves in Figure 3-17 indicates how effectively an incremental increase in solvent rate reduces vapor temperature and heat carried by the vapor. The slope of the curve increases with CO_2 flue gas concentration. This can be explained by the components of the total vapor heat capacity. First, the mass of the flue gas is highest in the NGCC case and drops with increasing CO_2 in the flue gas (see Table 3-1), and thus an incremental change in solvent rate will have the least impact of the NGCC flue gas – this is the dominant effect seen in the slopes of the 3 curves.

Secondly, the role of the enthalpy of vaporization of water varies strongly between the 3 cases. The temperature of the gas rises with flue gas CO_2 concentration, and correspondingly, the enthalpy of vaporization of water contributes more significantly to the total heat capacity. While the total heat capacity of the vapor at the lean pinch formation point in Figure 3-17 for each of the 3 applications does not differ significantly, the coal and steel cases are increasingly dependent on the contribution of water to the overall vapor heat capacity. For a given incremental increase in the solvent rate, the higher CO_2 applications (with higher temperatures) see a larger net condensation of water (larger driving force for water transfer) and the corresponding drop in the vapor temperature is larger. Therefore, the drop in the total heat capacity of the vapor is amplified as CO_2 concentration increases – larger water transfer rates remove more heat from a proportionally smaller amount of gas, reducing temperatures more rapidly, and ultimately reducing the dominant contribution of the latent heat of water to the overall heat capacity. This explains the progression of the slopes in Table 3-5 with flue gas concentration.

The result of the heat capacity effects is that the natural gas combined cycle application requires the largest increase in solvent rate to overcome the lean end pinch. The difference in total vapor and liquid heat capacities at pinch formation is similar to

that of coal, but the NGCC heat capacity is dominated by the mass of the gas compared to the coal and steel cases. Therefore, incremental increases in solvent rate have a more limited impact in reducing the heat carrying capacity of the vapor. In contrast, the steel case has a smaller difference in vapor and liquid heat capacities at pinch formation due to an inherently larger solvent circulation rate to treat a concentrated flue gas. In addition, the vapor heat capacity is dominated by the water content compared to the lower CO_2 cases, so the incremental increases in solvent readily reduces the total heat capacity (and temperature) of the vapor and the solvent becomes the dominant heat carrying phase.

3.4.2.2 Solvent Capacity Effects: 5 m PZ vs. 8 m PZ

The following figure compares the trend in deviation from isothermal capacity for 5 and 8 m PZ.

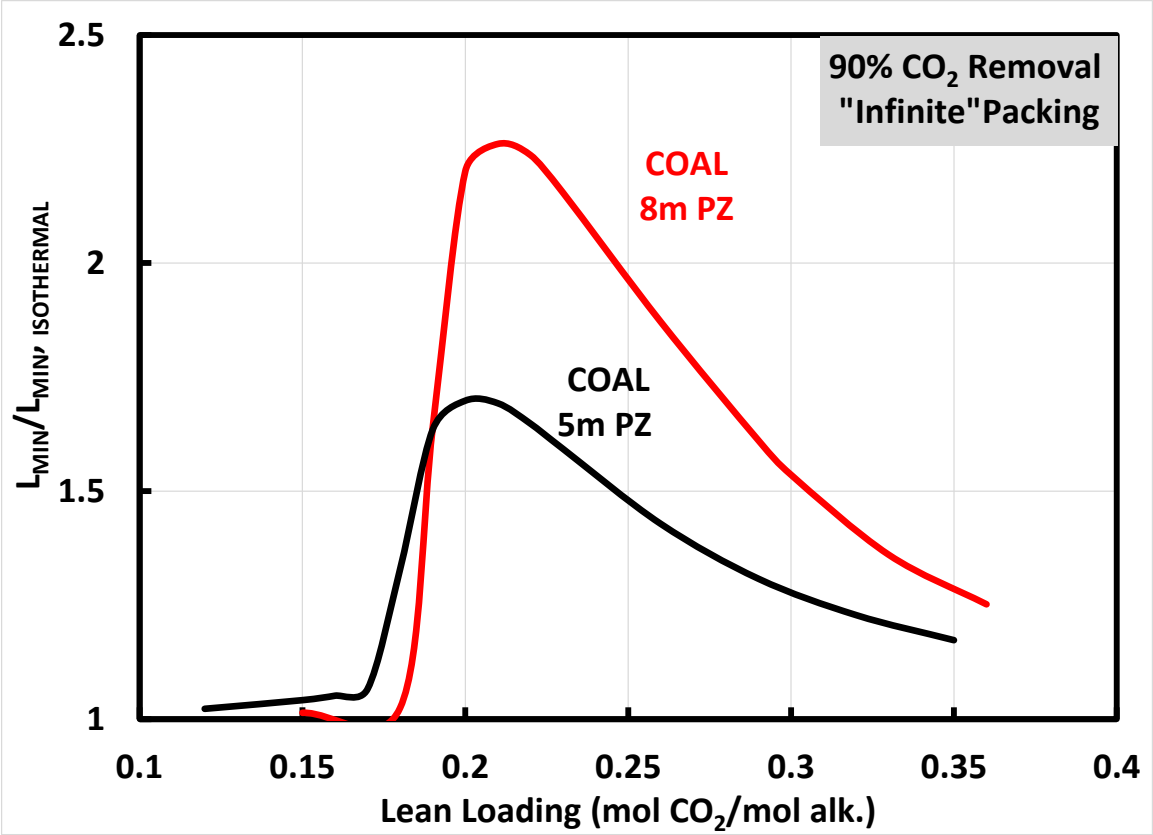

Figure 3-18: Ratio of L_{MIN} ("infinite" packing) for an adiabatic absorber to an isothermal absorber (40 °C), 5 vs. 8 m PZ, 90% CO_2 capture from a coal-fired boiler (14.7% CO_2).

As indicated by the figure, the transition loading is similar for 5 and 8 m PZ (dictated by similar VLE behavior as a function of loading and equivalent CO_2 removal leading to similar maximum temperatures in each case). However, the maximum deviation from isothermal capacity is much larger for 8 m PZ. This can be explained by the fact that the same absolute amount of solvent is required to overcome the nearly identical lean end temperature bulge and pinch that forms in both cases. Figure 3-19 compares the removal achieved for 5 and 8 m PZ as the solvent rate is increased from the isothermal minimum to the adiabatic minimum (at the loading where this deviation is the

largest for each solvent). The figure also includes the total vapor and liquid heat capacities for each case.

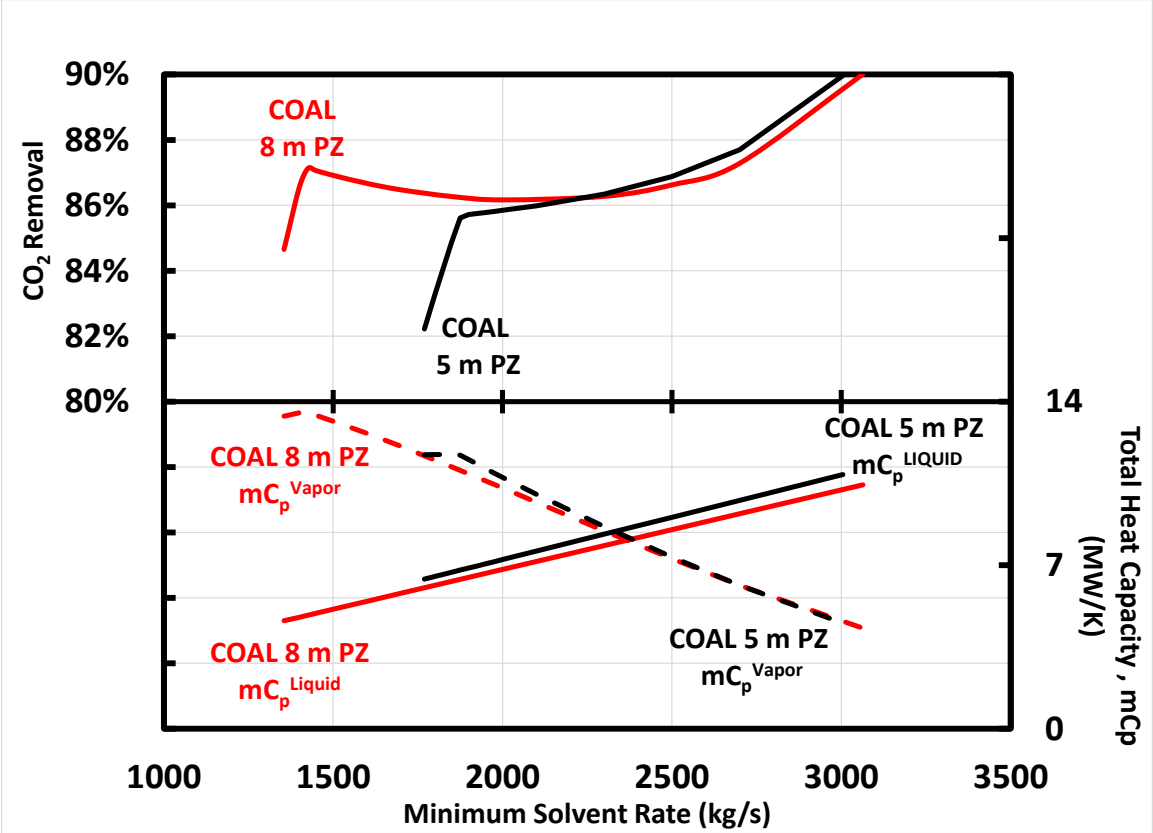

Figure 3-19: Lean pinch formation and total heat capacity (mC_P) for the vapor outlet and solvent inlet (lean end of the absorber) for capture from a coal-fired boiler (14.7% CO_2) utilizing 5 m PZ (LLDG = 0.20 mol CO_2/mol alk.) and 8 m PZ (LLDG = 0.21 mol CO_2/mol alk.). The solvent rate is increased from $L_{MIN, ISOTHERMAL}$ to $L_{MIN, ADIABATIC}$. The total heat capacity of the vapor includes the ability of the vapor to carry water (i.e., enthalpy of vaporization of water).

As the figure shows, the isothermal minimum solvent rate is higher for 5 m PZ due to the inherently lower solvent capacity. However, once the lean end pinch is formed for 5 m PZ, the 5 and 8 m PZ cases are essentially identical, confirming the hypotheses that the similar lean end pinch conditions require the same amount of solvent to

overcome the vapor heat capacity and equilibrium restriction. The heat capacity curves confirm the expected mechanism as the difference between the solvent and vapor heat capacities at the lean pinch are larger for 8 m PZ due to the lower solvent rate operating range. Table 3-6 normalizes the $L_{MIN}/L_{MIN,\ Isothermal}$ for the difference in isothermal capacity for 5 m and 8 m PZ. As expected, the values are essentially identical after this correction.

Table 3-6: Normalized $L_{MIN}/L_{MIN,\ ISOTHERMAL}$ for 5 and 8 m PZ using isothermal solvent capacity. Coal-fired boiler (14.7% CO_2).

	Lean Loading @ Max $L_{MIN}/L_{MIN,ISOTHERMAL}$	Max $L_{MIN}/L_{MIN,ISOTHERMAL}$	Isothermal Solvent Capacity	Normalized $L_{MIN}/L_{MIN,ISOTHERMAL}$ (8 m PZ baseline)
	mol CO_2/mol alk.		mol CO_2/kg(PZ+H_2O)	
8 m PZ	0.21	**2.26**	2.01	2.26
5 m PZ	0.20	**1.70**	1.50	2.27

3.4.2.3 CO_2 Removal Effect

The preceding analysis has focused on a CO_2 removal constraint of 90%. However, as was apparent in the discussion of multiple steady states, the CO_2 removal specification can shift the region of pinch behavior in which an absorber is operating. In addition, as the amount of CO_2 absorbed increases, the maximum temperature achieved in the absorber increases, shifting the conditions where a lean end pinch is developed. Figure 3-20 summarizes the effect of CO_2 removal on deviation from isothermal capacity as a function of lean loading.

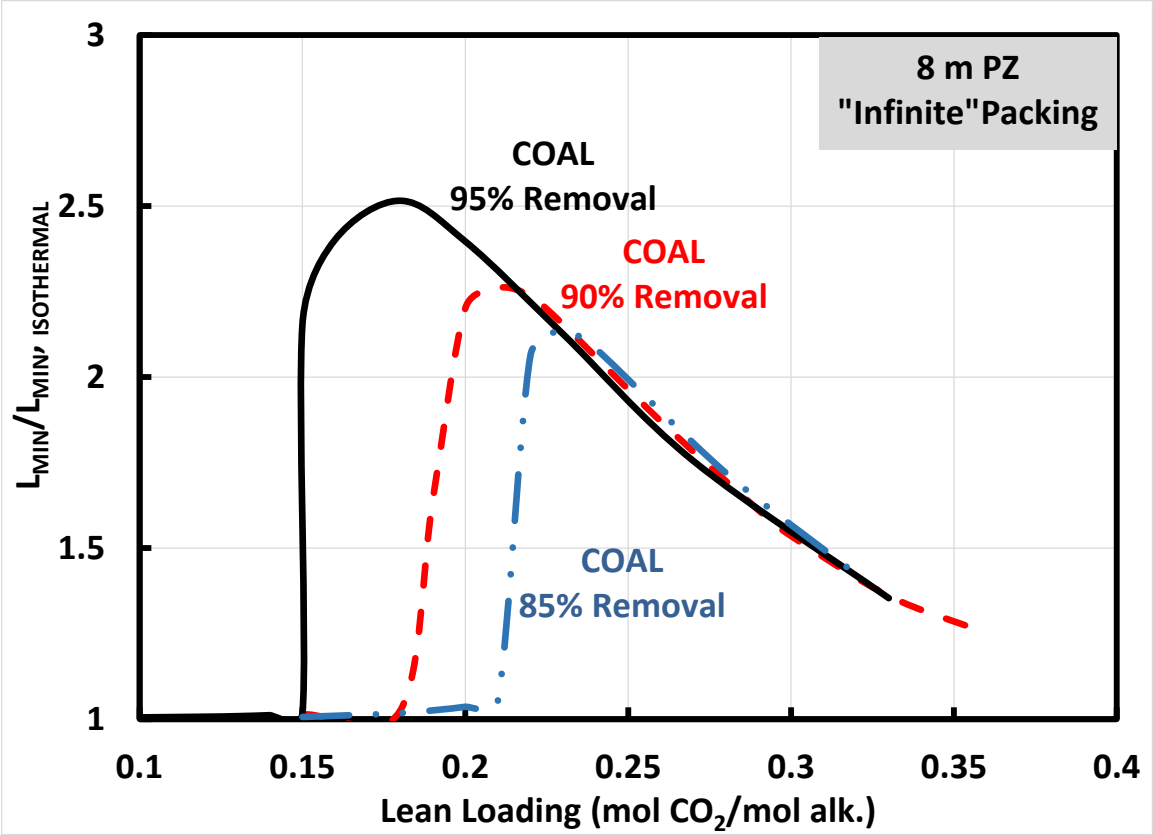

Figure 3-20: Ratio of L_{MIN} ("infinite" packing) for an adiabatic absorber to an isothermal absorber (40 °C) for 85 - 95% CO_2 capture from a coal-fired boiler (14.7% CO_2) utilizing 8 m PZ.

As expected, the higher temperatures in the higher CO_2 removal cases result in the development of a pinch at leaner conditions. The maximum deviation from isothermal minimum solvent rate ($L_{MIN}/L_{MIN, ISOTHERMAL}$) increases with CO_2 removal: 2.14 for 85% removal, 2.26 for 90% removal, and 2.52 for 95% removal. There are two reasons for this trend:

1) the higher removal cases have a lower baseline isothermal solvent rate (better isothermal capacity at leaner loadings – this is the dominant effect) ;
2) the higher temperatures for higher CO_2 removal require a larger absolute solvent rate to overcome the lean end temperature bulge.

As discussed previously, relaxing the CO_2 removal constraint can provide important design and operational flexibility. The loading window where the absorber can be operated without intercooling (minimal solvent circulation increase over isothermal) is larger with lower CO_2 removal specifications.

3.4.3 Mass Transfer Rate Effects

The discussion of minimum solvent rates and mass transfer pinches has largely focused on equilibrium considerations and overall energy balance considerations. However, the formation of a temperature bulge, magnitude of the bulge, and associated conditions at the lean end pinch are also a function of the relative amounts of CO_2 and water transferred above and below the pinch (and the different enthalpy changes associated with the transfer of each species).

Water is vaporized below the mass transfer pinch, leading to the drop in solvent temperature below the bulge; this water is then returned to the solvent above the pinch. Therefore, the rate at which water is transferred to and from the gas relative to rate at which CO_2 is absorbed will dictate how rapidly the temperature rises, and ultimately determine the loading where a pinch will form.

To test the effect of rates on the minimum solvent rate, a simple sensitivity study was performed at a single operating condition from the preceding analysis (Coal-fired boiler, lean loading = 0.20 mol CO_2/ mol alkalinity). The gas film mass transfer coefficient (k_g), which is expected to be important for water transfer, and the kinetic constants (CO_2 transfer – see Equations 3.1 to 3.4) were independently increased to observe a change in the CO_2 removal above and below the pinch and the change in minimum solvent rate to achieve 90% removal. The results for the study are summarized in Table 3-7.

Table 3-7: Effect of rate parameters (reaction rates and gas-film mass transfer coefficient) on mass transfer and L_{MIN} associated with temperature-induced lean end pinch.

COAL, 8m PZ, LLDG = 0.20 mol CO_2/mol alk.		BASE CASE	5 x Reaction Rates	5 x kg
CO_2 Transfer Rate[1] (kmol/s)	Above Pinch	0.22	0.30	0.11
	Below Pinch	2.28	2.27	2.28
	TOTAL	2.50	2.57	2.40
CO_2 Removal[1]		90%	92.5%	86.2%
Max Solvent Temperature (°C)		80.7	80.3	81.4
L_{MIN} to achieve 90% removal		2829	2354	3320
% Change from BASE		---	-17%	17%
1: CO_2 in Inlet Gas = 2.78 kmol/s				

The reaction rate and k_g have opposite effects, as expected. The increase in reaction rates increases the amount of CO_2 absorbed above the lean pinch and allows for a ~17% reduction in the minimum solvent rate compared to the base case. In contrast, the increase in k_g yields reduced removal above the pinch due to an increase in the relative transfer rate of water to CO_2 requires a ~17% increase in the minimum solvent rate to achieve 90% removal. The results for the increased k_G can be explained as follows:

1) The transition from a rich end pinch (temperature bulge is not limiting) to a limiting lean end pinch occurs at a comparatively lower solvent rate and higher bulge temperature.
2) The reduced liquid heat capacity and enhanced vapor heat capacity (higher temperatures) when the pinch forms indicates (as in the previous discussion for varying CO_2 flue gas concentration) that a proportionally larger increase in

solvent rate will be required to overcome the pinch at the enhanced k_G conditions.

Similar logic can be applied for the enhanced reaction case to describe the reduced solvent rate requirement for 90% removal. Further analysis is needed to generalize the rate effects, but the initial results indicate that the minimum solvent rate for adiabatic absorbers is not simply a thermodynamic phenomenon as in the typical isothermal rich end pinch case.

3.5 CONCLUSIONS

The key findings of the evaluation of adiabatic absorbers and pinch phenomena associated with minimum solvent rates can be summarized as follows:

- Operation of adiabatic absorbers in specific lean loading ranges can lead to severe penalty in solvent circulation requirements compared to an isothermal baseline. The governing phenomena for these solvent capacity penalties can be summarized as follows:
    - Lean end pinch formation at the temperature bulge occurs at all lean loadings. CO_2 removal constraint determines if lean pinch is limiting at given operating conditions.
    - Solvent rate increases to overcome lean end pinches initially "trap" heat in the column as the liquid rate is insufficient to moderate temperatures or carry heat away from the bulge. This leads to a drop in removal with increasing solvent rate.
    - As the solvent rate is increased further, the total liquid and vapor heat capacities (mC_P) as calculated at the top of the absorber will crossover

(The vapor heat capacity includes the enthalpy of vaporization of water for the vapor saturated at outlet conditions). This condition identifies the point where the liquid can effectively moderate bulge temperatures and address the equilibrium constraint.

- The non-monotonic behavior of CO_2 removal as a function of solvent rate through each of the preceding transitions can lead to multiple steady state solvent rates that meet the CO_2 removal specification. The first two steady states (prior to and immediately after lean pinch formation) may be unstable or present process control challenges.

- Flue gas CO_2 concentration has two critical effects on pinch formation and the associated solvent capacity penalty:
  - Lower CO_2 flue gas concentrations (and associated lower temperatures) allow operation with wider range of lean loading without a limiting lean end pinch. This provides flexibility in the design and operation of these systems (operation without intercooling).
  - The solvent capacity penalty (measured as the ratio of the adiabatic minimum solvent rate (L_{MIN}) to the isothermal minimum solvent rate ($L_{MIN, ISOTHERMAL}$)) decreases as the flue gas CO_2 concentration increases:
    i. NGCC (4.1% CO_2): Maximum $L_{MIN}/L_{MIN, ISOTHERMAL} = 3.58$
    ii. COAL (14.7% CO_2): Maximum $L_{MIN}/L_{MIN, ISOTHERMAL} = 2.26$
    iii. STEEL (27.1% CO_2): Maximum $L_{MIN}/L_{MIN, ISOTHERMAL} = 1.94$
    iv. The trend is associated with the solvent rate increase required to overcome the difference in total heat capacities (vapor vs. liquid) to allow the solvent to moderate temperatures and address equilibrium constraints. NGCC, with inherently low L/G, has the

largest “heat capacity deficit” to overcome. In coal and steel cases, a relatively larger portion of the heat capacity of the gas is carried in water (due to higher temperatures), which provides large incremental benefits as the solvent rate is increased and allows efficient cooling of the gas and approach to the heat capacity crossover point.

- Operating 5 and 8 m PZ for the same flue gas (composition and gas rate) and CO_2 removal rate requires the same absolute amount of solvent to overcome the temperature-related pinch. The inherently lower capacity of 5 m PZ means the increase in solvent rate over the isothermal baseline is relatively smaller for 5 m PZ and limits the benefits of intercooling.
- Operating with lower CO_2 removal targets limits the impact of temperature restrictions in the absorber:
    - Lower removal specifications allow operation over a wider range of lean loading without generating a performance limiting lean end pinch.
    - The solvent capacity penalty increases with CO_2 removal since the leaner operating region yields a lower baseline solvent rate (better solvent capacity) and requires a larger increase to overcome a pinch at higher temperatures.
- Temperature-related pinches are a rate-dependent phenomena, unlike isothermal saturation of the solvent (strictly thermodynamic phenomena):
    - Lean end pinches are affected by relative rates of water and CO_2 transfer and thus are impacted by the mass transfer and kinetic properties in an absorber system. In addition, the minimum solvent rate used in design

calculations or for the identification of a pinched condition in a model will be affected by the rate parameters of the specific model.

- **Open Research Questions**:
    - How do the rates of CO_2 absorption and water transfer effect pinch formation? Is the lean end pinch observed in this work unique to "fast" amine solvents? Development of a dimensionless relationship to predict the effect of CO_2 and water transfer rates on pinch formation would be a useful generalization for absorber design.
    - A shortcut method to predict the transition loading for a given solvent and operating condition (CO_2 removal, flue gas concentration) was developed as part of this work but was very sensitive to assumptions about CO_2 removal above the pinch. A better approximation of removal at the mass transfer pinch is needed to improve the prediction of lean loading where adiabatic absorbers become limited by a temperature bulge induced mass transfer pinch.

Chapter 4: Benefits and Limitations of Simple Intercooling

The preceding chapter provided a detailed discussion of the effects of temperature maxima on absorber performance in CO_2 capture as a function of operating conditions with a description of the fundamental phenomena underlying the performance trends. The work in this chapter will be an extension of the analysis of the previous chapter to consider the effect of cooling the solvent at intermediate locations in the column (intercooling) to remove heat generated by CO_2 absorption. Intercooling can mitigate the solvent capacity and driving force limitations, but the conditions of absorber operation (CO_2 concentration in flue gas, lean loading, L/G, etc.) dictate the potential benefit that may be extracted from the intercooling operation. Quantifying the potential benefits of intercooling and generalizing the trends in these benefits with operating conditions can allow absorber and intercooling design optimized for the specific operating conditions.

This chapter will evaluate the benefit of intercooling in comparison to the two limiting designs developed in Chapter 3 – adiabatic and isothermal absorbers. Minimum solvent rate analysis will repeated for an intercooled absorber to quantify the approach to the isothermal solvent capacity and the benefit over the adiabatic design as a function of CO_2 flue gas concentration and operating conditions. As with the adiabatic design, the trends in the approach to isothermal capacity will be evaluated at a fundamental level (analysis of equilibrium pinch formation) to explain the limitations of the simple intercooling design. A new set of operating conditions (lean loading range) will be identified for opportunity to improve solvent capacity with advanced intercooling design.

Finally, the L_{MIN} analysis only describes the solvent capacity benefits and neglects the mass transfer requirements in a practical absorber design. This work will add design curves which reflect the trade-off between solvent circulation rates and packing

mass transfer area as absorber design moves away from the minimum solvent rate. This method will allow comparison of intercooled and adiabatic absorbers to an isothermal baseline across a realistic range of operating conditions. Operating conditions will be identified where intercooling provides the largest benefit in terms of solvent capacity and mass transfer performance and conditions where significant improvement can be achieved with improved intercooling design.

4.1 Evaluation of Existing Literature

Intercooling the solvent in gas absorption systems is a well-established process modification in industrial applications (e.g., (Jackson & Sherwood, 1941)). In addition, the concept has been extended to commercial scale for CO_2 capture with amines in industrial gas treating applications (Reddy, et al., 2008) and at the pilot scale in CO_2 capture from power plant flue gas (Plaza, et al., 2010). Most recently, the first commercial scale facility (139 MW) for CO_2 capture from power plant flue gas was started-up at the SaskPower Boundary Dam Power Station. The commercial solvent and process design by Shell Cansolv included the application of intercooling in the absorber (Stephenne, 2014).

4.1.1 Intercooling Benefits and Design for Amine-Based Capture Systems

Evaluation of temperature profiles in commercially available amine-based absorber systems led to a recommendation of intercooling for higher CO_2 concentrations (coal-fired boiler vs. natural gas combined cycle) and designated the optimum location for intercooling near the rich end of the column where equilibrium limitations were expected to be most significant (Reddy, et al., 2008). Following the recommendations of the commercial process analysis, a modeling study found no benefit of intercooling for an

NGCC application and limited benefit for a coal-fired boiler application with intercooling located near the bottom of an absorber (Ystad Marchioro, et al., 2012).

Other studies found varying results with flue gas CO_2 concentration, solvent concentration, and intercooling method (e.g., flue gas cooling vs. solvent intercooling) (Kvamsdal, et al., 2011); (Karimi, et al., 2011). The location of intercooling was not always optimized in these studies and the general purpose of the studies was not to systematically evaluate the effect of operating conditions on intercooling, but rather to study the entire capture system performance at specific discrete operating conditions of practical interest. In general, the studies concluded intercooling was beneficial for the coal application but not for the NGCC case.

In a similar study for a blast furnace application with high CO_2 partial pressure in the flue gas (100 kPa), the authors studied simple intercooling and flue gas cooling as part of capture system optimization (Tobiesen, et al., 2007). The intercooling location was fixed (near the bottom of the column) and the packed height of the column was fixed for various cases. The authors found significant energy benefits with the implementation of intercooling for the high CO_2 application and concluded performance enhancement was due to enhanced solvent capacity at the bottom of the column. Flue gas cooling was found to have limited benefit.

A screening study of flowsheet modifications for capture with monoethanolamine included the evaluation of intercooling as a process modification (Le Moullec & Kanniche, 2011). The authors found that the intercooler was best placed in the middle to bottom of the column and reasoned that the driving force benefits in this portion of the column outweighed potential mass transfer limitations imposed by lower temperatures.

Finally, Plaza found that optimizing the location of intercooling had limited benefit, but the analysis was limited to minimum solvent rate, or pinched, conditions (Plaza, 2011).

In general, it is difficult to make broad recommendations or conclusions about intercooling for amine based capture systems from the existing literature because the studies either fix equipment configurations (e.g., amount of packing, location of intercooler, etc.) or operating conditions (e.g., lean loading, solvent rate, etc.). Furthermore, the underlying mechanisms governing intercooling benefits are not discussed in detail, making it difficult to explain why intercooling performance and benefits appear to vary over the conditions used in literature studies. These areas will be the focus of the current work with the goal of providing a general understanding of the performance benefits and limitations of intercooling.

4.2 MODELING FRAMEWORK

The absorber model used for the intercooling evaluation was implemented in Aspen Plus® in the RateSep^{TM} module. The key components of the model are rigorous representations of solvent thermodynamics and kinetics, mass transfer and fluid mechanics in packing, and the physical properties of the system over the range of expected operating conditions.

All of the subsequent analysis will utilize 8 m aqueous piperazine (PZ) as the solvent. The thermodynamic model for the PZ-H_2O-CO_2 system was developed from experimental amine pK_a, CO_2 solubility, heat capacity, speciation, and amine volatility data by regression of Gibbs free energy, enthalpy, heat capacity, and activity coefficient parameters within the electrolyte non-random two liquid (e-NRTL) framework.

The kinetics for the PZ model are described by the following reaction set:

$$PZCOO^- + PZH^+ \leftrightarrow H^+PZCOO^- + PZ \quad 4.1$$

$$PZCOO^- + H_2O + CO_2 \rightarrow H^+PZCOO^- + HCO_3^- \quad 4.2$$

$$2PZ + CO_2 \rightarrow PZH^+ + PZCOO^- \quad 4.3$$

$$2PZCOO^- + CO_2 \rightarrow H^+PZCOO^- + PZ(COO)_2^{2-} \quad 4.4$$

The first reaction is an equilibrium (proton transfer) reaction while reactions 2 through 4 are reversible finite rate reactions where the corresponding reverse reactions complete the reaction set for PZ. Arrhenius rate expressions represent the rate constants for the kinetic reactions (including forward and reverse rates) where the pre-exponential and activation energy parameters were regressed from wetted wall column data collected over a range of temperatures, solvent concentrations, and loadings relevant for capture applications considered in this work. Finally, physical property models for binary diffusion coefficients, viscosity, and density were regressed as a function of amine concentration, loading, and temperature. For a detailed description of this "Independence" PZ model, see Frailie (Frailie, 2014).

Mass transfer and area models were developed by Wang via regression of experimental data from a pilot scale column with a variety of random and structured packings (Wang, 2015). The area model developed by Wang is a modification of a model developed by Tsai (see Tsai for full theoretical and experimental details of the area model) (Tsai, 2010).

4.3 Analysis Overview and Methodology

The analysis in this chapter will focus on the simple intercooling configuration depicted in Figure 4-1.

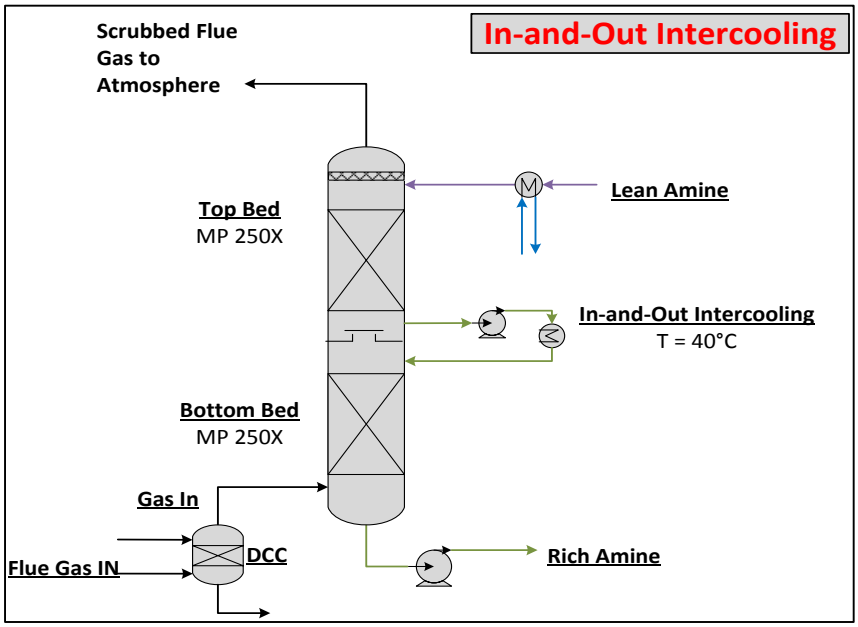

Figure 4-1: Absorber PFD for In-and-Out Intercooling. Two sections of packing (MP 250X) are used with liquid draw-off, cooling, and return between the packed sections. The solvent is cooled to 40 °C before returning to the column.

In-and-out intercooling will be compared to the limiting cases of an adiabatic and isothermal absorber that were discussed extensively in the previous chapter. The major objectives of the current analysis are:

1) Evaluate effectiveness of simple intercooling in terms of solvent capacity (minimum solvent rate analysis) and mass transfer performance;
2) Provide fundamental explanations for the performance trends of the simple intercooling design;

3) Define and identify optimal location of intercooling as a function of operating conditions;
4) Identify conditions where simple intercooling is ineffective or provides potential for significant performance improvement with enhanced design.

Table 4-1 summarizes the conditions used for the evaluation. The analysis was conducted for 90% removal of CO_2 utilizing concentrated (8 molal) piperazine (PZ) as the solvent. The lower end of the proposed lean loading ranges in Table 4-1 would lead to precipitation in practice with the PZ solvent (Freeman, 2011). However, the wide range is included as an extrapolation of the PZ model in an attempt to allow generalization of the results.

Table 4-1: Summary of Intercooling Analysis Operating Conditions

Flue Gas Source	**Inlet CO_2** (mol%)	**Lean Loading Range** (mols CO_2/mols alkalinity)	**Flue Gas Flow** (kmol/s)
Natural Gas Combined Cycle	4.1	0.10 - 0.30	31.2
Coal-Fired Boiler	14.7	0.10 - 0.36	18.9
Steel Blast Furnace	27	0.10 - 0.39	10.4
Lean solvent and flue gas feed at 40°C, MP-250X packing for all cases, Max approach to flooding = 70%. Flue gas saturated to water.			

The approach used in Chapter 3 will be extended to the simple intercooling configuration in Figure 4-1. For the range of conditions identified in the table, the solvent capacity for the intercooled absorber will be compared to the limiting cases of an adiabatic (no intercooling) absorber and an isothermal ("perfect" intercooling) absorber operated at 40°C. The adiabatic absorber (limited by temperature-induced equilibrium constraints)

represents minimum solvent capacity and the isothermal absorber represents the maximum solvent capacity for a given operating condition. Figure 4-2 illustrates the approach used in this analysis.

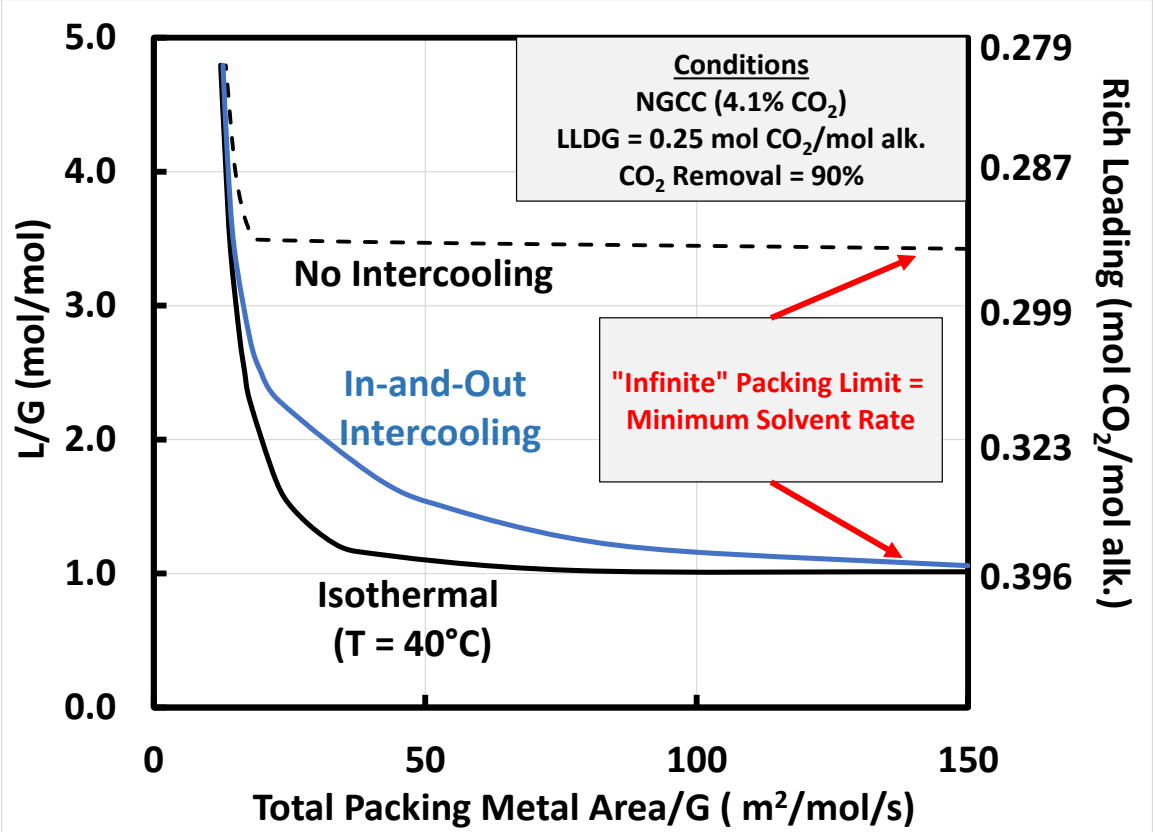

Figure 4-2: Example of design curves for packing-solvent rate trade-off. Each curve (dashed = adiabatic, solid = isothermal, blue = intercooled) represents the packing requirement to achieve 90% CO_2 removal for a fixed lean loading and given liquid to gas ratio (L/G). At each point, the lean loading, removal, and solvent rates are fixed, so a unique rich loading exists (secondary y-axis). The horizontal asymptote is the minimum solvent rate (L_{MIN}) or best energy performance achievable for a given absorber design.

Each curve represents the packing required for a given liquid to gas ratio (L/G) for each absorber design moving from one asymptotic limit (vertical asymptote of infinite solvent rate and minimum packing) to another (horizontal asymptote of infinite packing and minimum solvent rate). In practice, the infinite solvent rate asymptote does not provide a physically meaningful or quantifiable limit as the packing will approach zero for all designs in this limit. The minimum solvent rate (L_{MIN}) asymptote will be used to evaluate solvent capacity in this work. The L_{MIN} for any absorption process can be defined as the solvent rate required to achieve a specific solute removal (or specific gas inlet and outlet compositions) for a given inlet solvent composition (loading) with infinite mass transfer area available. Lower values of L_{MIN} are indicative of larger solvent capacity and are associated with better overall energy performance of the system (reduced sensible heat requirements in stripping system, enhanced rich loading to improve CO_2/H_2O selectivity in the stripping system, and reduced pumping costs across the entire system). The ratio of the L_{MIN} for a given absorber design to the isothermal L_{MIN} at each condition can serve as a screening tool for the effectiveness of the design in achieving maximum solvent capacity. A high ratio indicates a temperature-induced limitation and an opportunity for improved absorber design. A ratio equal to (or approaching) unity indicates that the absorber design under consideration is effective at mitigating temperature-related constraints and the capacity benefits of an improved absorber design are negligible or non-existent.

The minimum solvent rate analysis only addresses one aspect of absorber design. In practice, absorber design is a trade-off between maximizing the solvent capacity (operating close to L_{MIN}) and minimizing the mass transfer area (capital cost associated with packing or other contacting internals). The optimal absorber design (defined in terms of solvent capacity) identified for a given operating condition via the minimum

solvent rate analysis will be further evaluated in this work for mass transfer constraints or packing requirements to approach maximum solvent capacity. The curves in Figure 4-2 are representative of the packing-solvent circulation rate trade-off, and will be developed over the range of conditions in Table 4-1.

4.4 Minimum Solvent Rate Analysis

Figure 4-3, Figure 4-4, and Figure 4-5 include the L_{MIN} ratios for an adiabatic (no intercooling) and intercooled (in-and-out intercooling) absorber for all three flue gas sources in Table 4-1.

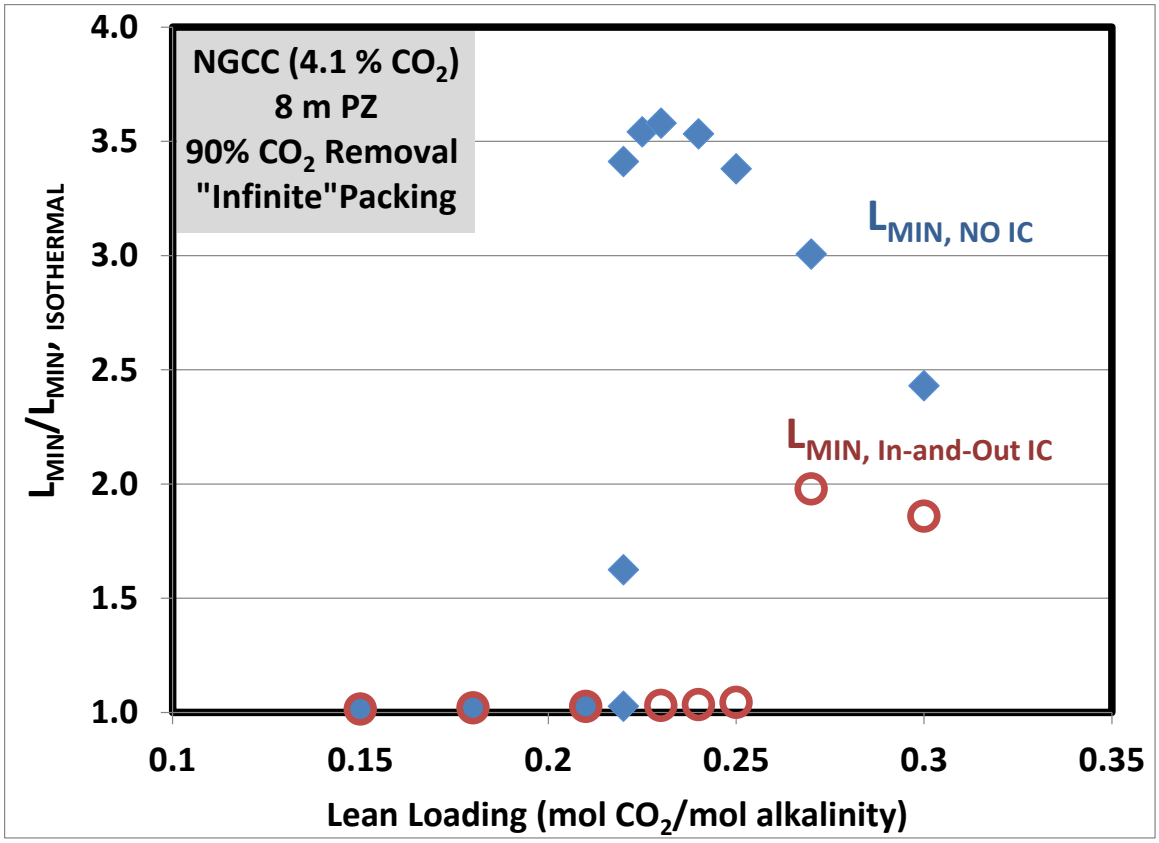

Figure 4-3: NGCC power plant flue gas (4.1% CO_2). Ratio of the minimum solvent rate ("infinite" packing) for an adiabatic absorber (no intercooling) and intercooled absorber (in-and-out intercooling) to an isothermal absorber (40 °C) for 90% CO_2 capture with 8 m PZ.

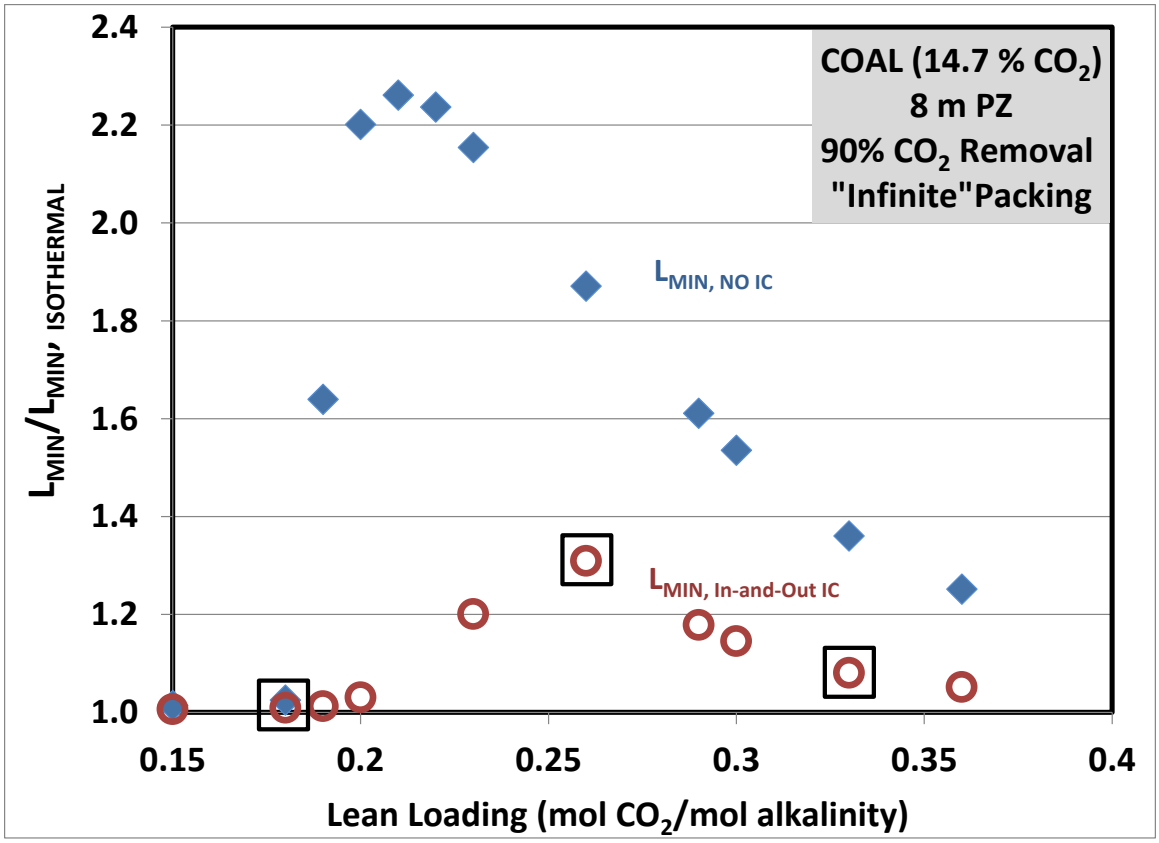

Figure 4-4: Coal-fired boiler flue gas (14.7% CO_2). Ratio of the minimum solvent rate ("infinite" packing) for an adiabatic absorber (no intercooling) and intercooled absorber (in-and-out intercooling) to an isothermal absorber (40 °C) for 90% CO_2 capture with 8 m PZ. Points denoted with a black square have corresponding equilibrium-operating line charts in Figure 4-6 to Figure 4-8.

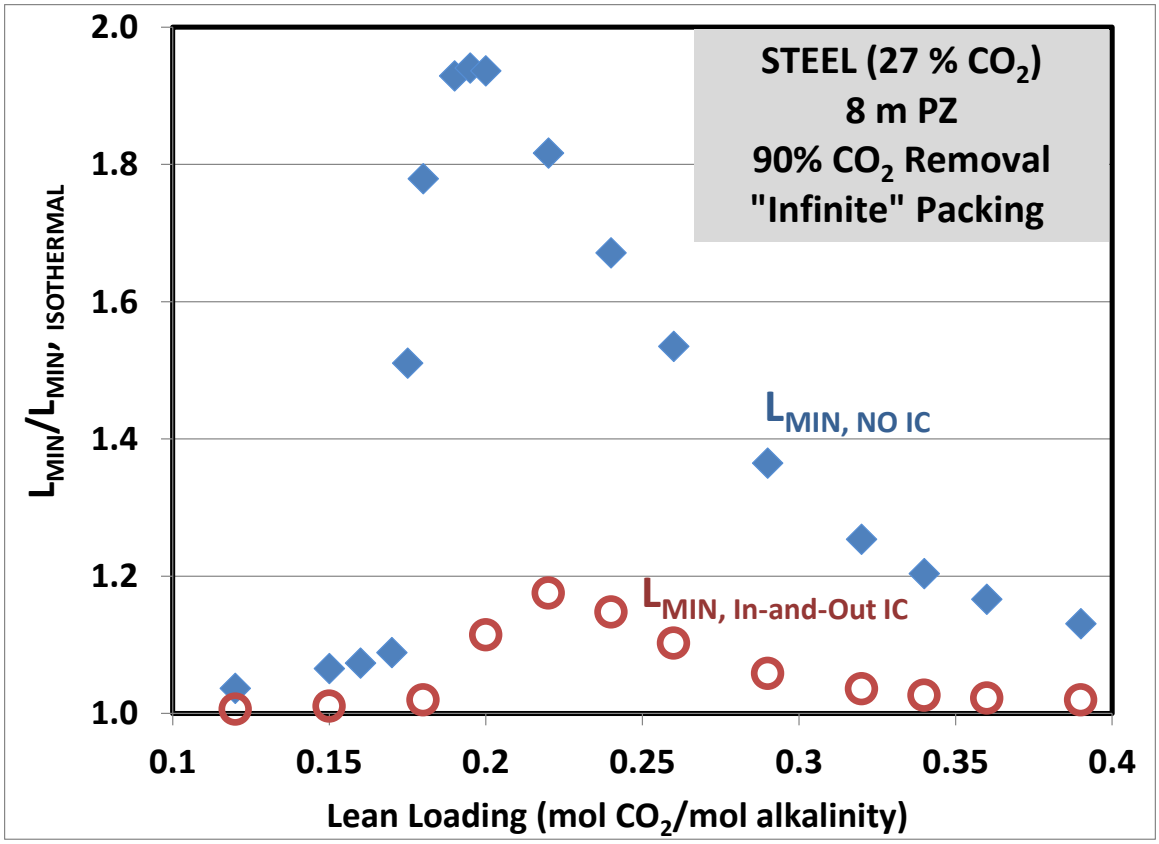

Figure 4-5: Steel blast furnace flue gas (27% CO_2). Ratio of the minimum solvent rate ("infinite" packing) for an adiabatic absorber (no intercooling) and intercooled absorber (in-and-out intercooling) to an isothermal absorber (T = 40 °C) for 90% CO_2 capture utilizing 8 m PZ.

The figures clearly demonstrate the benefit of intercooling – across the entire range of conditions for each flue gas source, intercooling has significantly improved the approach to isothermal (or ideal) solvent capacity over the adiabatic absorbers evaluated in Chapter 3. In all three cases, the simple intercooling method mirrors the trend of the adiabatic absorbers - an intermediate range of lean loadings results in the largest ratios (largest deviation from an ideal isothermal absorber) and identifies conditions where additional solvent capacity benefits could be attained with an improved intercooling method. However, the solvent capacity penalty in this region is much lower than with an

adiabatic absorber and the intercooled absorber has expanded the range of loadings (at the low and high end) where the system operates near isothermal performance.

The data for the intercooled absorber in each of the preceding figures along with relevant temperatures are included in Table 4-2 through Table 4-4 for reference throughout the following discussion. See Chapter 3 for the data on adiabatic absorbers.

Table 4-2: NGCC (4.1% CO_2), Summary of Minimum Solvent Analysis Results for an intercooled absorber (in-and-out intercooling): 90% CO_2 Removal, 8 m PZ

Lean Loading	Lean End Driving Force (P^*_{CO2}/P_{CO2})	Minimum Solvent Rate			Rich Loading		Intercooled Absorber Temperatures		
		Isothermal	Intercool	$L_{MIN, ICOOL} / L_{MIN, ISOTHERMAL}$	Isothermal	Intercool	Max Liquid	Liquid Outlet	Vapor Outlet
mol CO_2/mol alk.		kg/s	kg/s		mol CO_2/mol alk.		°C		
0.15	21.89	527	535	1.01	0.395	0.391	55.6	42.7	53.0
0.18	13.92	608	620	1.02	0.395	0.391	55.6	42.7	52.5
0.21	8.24	715	734	1.03	0.395	0.390	55.8	42.6	51.9
0.23	5.53	808	833	1.03	0.395	0.390	55.9	42.6	51.2
0.24	4.47	864	893	1.03	0.395	0.390	55.1	42.6	50.1
0.25	3.59	927	968	1.04	0.395	0.389	55.4	42.6	48.1
0.27	2.29	1084	2145	**1.98**	0.395	0.333	58.8	45.6	41.3
0.3	1.16	1444	2684	1.86	0.395	0.351	54.6	45.8	40.1

Table 4-3: COAL (14.7% CO_2), Summary of Minimum Solvent Analysis Results for an intercooled absorber (in-and-out intercooling): 90% CO_2 Removal, 8 m PZ

Lean Loading	Lean End Driving Force (P^*_{CO2}/P_{CO2})	Minimum Solvent Rate			Rich Loading		Intercooled Absorber Temperatures		
		Isothermal	Intercool	$L_{MIN, ICOOL} / L_{MIN, ISOTHERMAL}$	Isothermal	Intercool	Max Liquid	Liquid Outlet	Vapor Outlet
mol CO_2/mol alk.		kg/s	kg/s		mol CO_2/mol alk.		°C		
0.15	78.76	1032	1038	1.01	0.422	0.421	75.8	42.6	68.1
0.18	50.09	1173	1184	1.01	0.422	0.420	76.7	42.7	67.4
0.19	42.45	1229	1244	1.01	0.422	0.419	77.0	42.7	67.0
0.2	35.65	1289	1328	1.03	0.422	0.416	77.3	43.3	66.1
0.23	19.91	1507	1810	1.20	0.422	0.390	73.2	47.3	52.3
0.26	10.33	1807	2366	**1.31**	0.422	0.384	70.9	49.8	41.4
0.29	5.24	2243	2643	1.18	0.422	0.402	64.6	47.9	40.7
0.3	4.18	2436	2790	1.15	0.422	0.407	62.1	47.0	40.6
0.33	2.13	3266	3530	1.08	0.422	0.415	54.8	44.4	40.2
0.36	1.04	4900	5154	1.05	0.422	0.419	48.7	42.6	40.0

Table 4-4: STEEL (27% CO_2), Summary of Minimum Solvent Analysis Results for an intercooled absorber (in-and-out intercooling): 90% CO_2 Removal, 8 m PZ

Lean Loading	Lean End Driving Force (P^*_{CO2}/P_{CO2})	Minimum Solvent Rate			Rich Loading		Intercooled Absorber Temperatures		
		Isothermal	Intercool	$L_{MIN, ICOOL}/L_{MIN, ISOTHERMAL}$	Isothermal	Intercool	Max Liquid	Liquid Outlet	Vapor Outlet
mol CO_2/mol alk.		kg/s	kg/s		mol CO_2/mol alk.		°C		
0.12	217.97	894	900	1.01	0.431	0.430	85.7	43.0	77.8
0.15	143.91	1001	1012	1.01	0.431	0.429	86.2	43.4	76.7
0.18	91.52	1134	1156	1.02	0.431	0.427	86.7	44.2	74.8
0.2	65.13	1242	1384	1.11	0.431	0.408	85.2	49.7	65.5
0.22	44.60	1370	1610	**1.18**	0.431	0.400	83.3	52.1	50.7
0.24	29.41	1524	1750	1.15	0.431	0.407	80.8	51.5	42.1
0.26	18.88	1715	1891	1.10	0.431	0.415	75.2	49.6	41.3
0.29	9.57	2102	2225	1.06	0.431	0.424	65.7	46.3	40.9
0.32	4.88	2699	2796	1.04	0.431	0.427	58.0	43.9	40.5
0.34	3.09	3314	3402	1.03	0.431	0.429	53.7	42.8	40.3
0.36	1.89	4275	4370	1.02	0.431	0.430	49.9	41.9	40.2
0.39	0.78	7458	7604	1.02	0.431	0.430	45.0	40.0	40.0

4.4.1 Fundamental Explanations

4.4.1.1 Equilibrium and Operating Line Constructions

Operating and equilibrium line constructions can be used to study the effect of mass transfer pinches on the solvent capacity for an intercooled absorber. Figure 4-6 to Figure 4-8 include representative equilibrium-operating line charts in the three loading ranges (low, mid, and high) for the coal-fired boiler application. The loadings selected for detailed analysis are highlighted in Figure 4-4 (black squares) for reference.

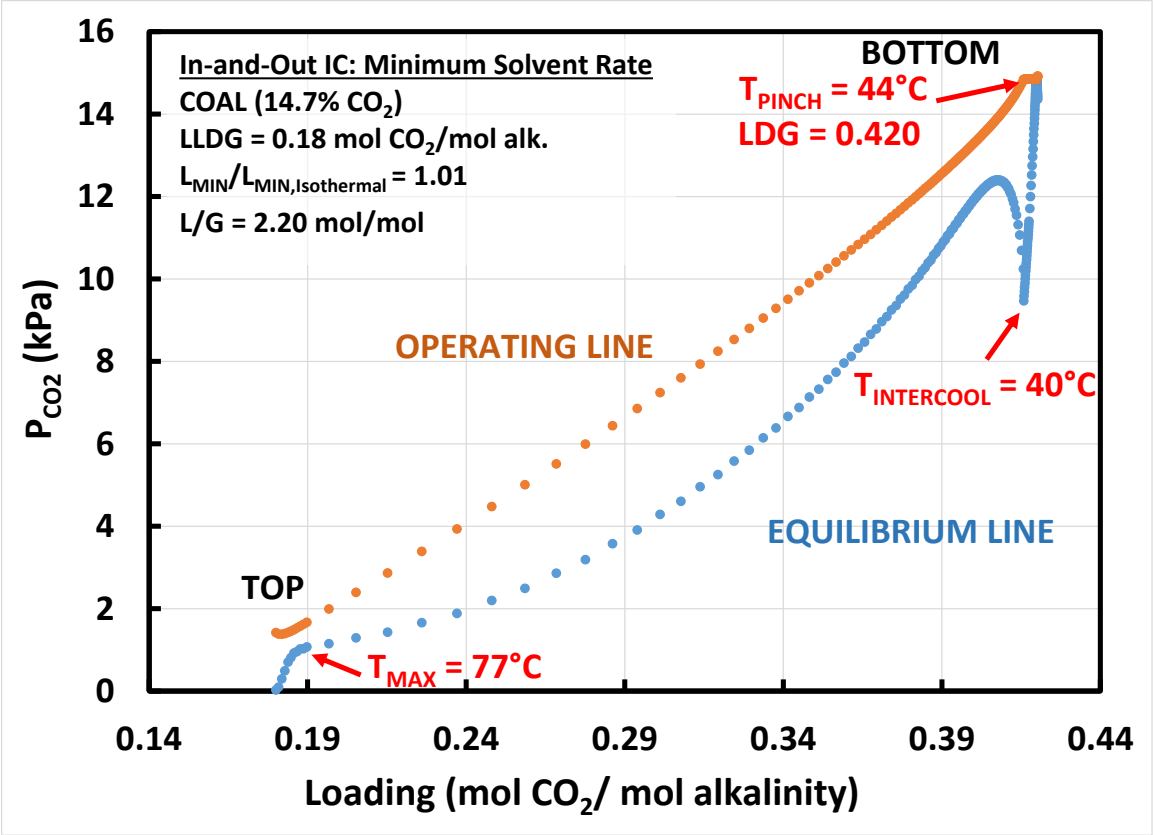

Figure 4-6: Operating and equilibrium curves @ LLDG = 0.18 mol CO_2/mol alk. for an intercooled absorber (in-and-out intercooling) operated at L_{MIN} ("infinite" packing) to achieve 90% CO_2 removal from a coal-fired boiler (14.7% CO_2). The mass transfer pinch (contact of the equilibrium and operating lines) occurs at the rich end of the column (bottom, 44°C), unrelated to the maximum temperature (77 °C) near the lean end (top).

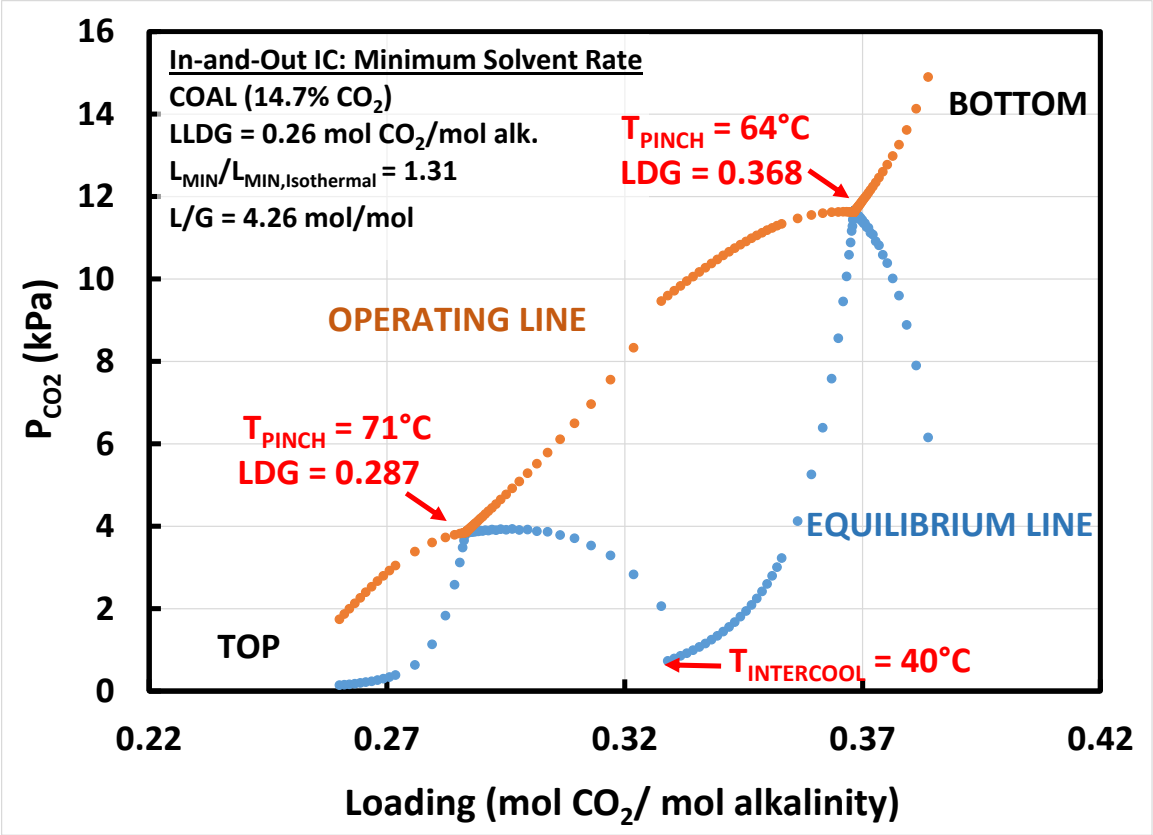

Figure 4-7: Operating and equilibrium curves @ LLDG = 0.26 mol CO_2/mol alk. for an intercooled absorber (in-and-out intercooling) operated at L_{MIN} ("infinite" packing) to achieve 90% CO_2 removal from a coal-fired boiler (14.7% CO_2). This condition represents the largest deviation from isothermal performance ($L_{MIN}/L_{MIN, Isothermal}$ = 1.31). Two mass transfer pinches (contact of the equilibrium and operating lines) occur, one on either side of the intercooler. The pinch above the intercooler occurs near the lean end of the column and coincides with the maximum temperature (71 °C). The pinch below the intercooler occurs near the rich end of the column with a secondary temperature maximum (64°C).

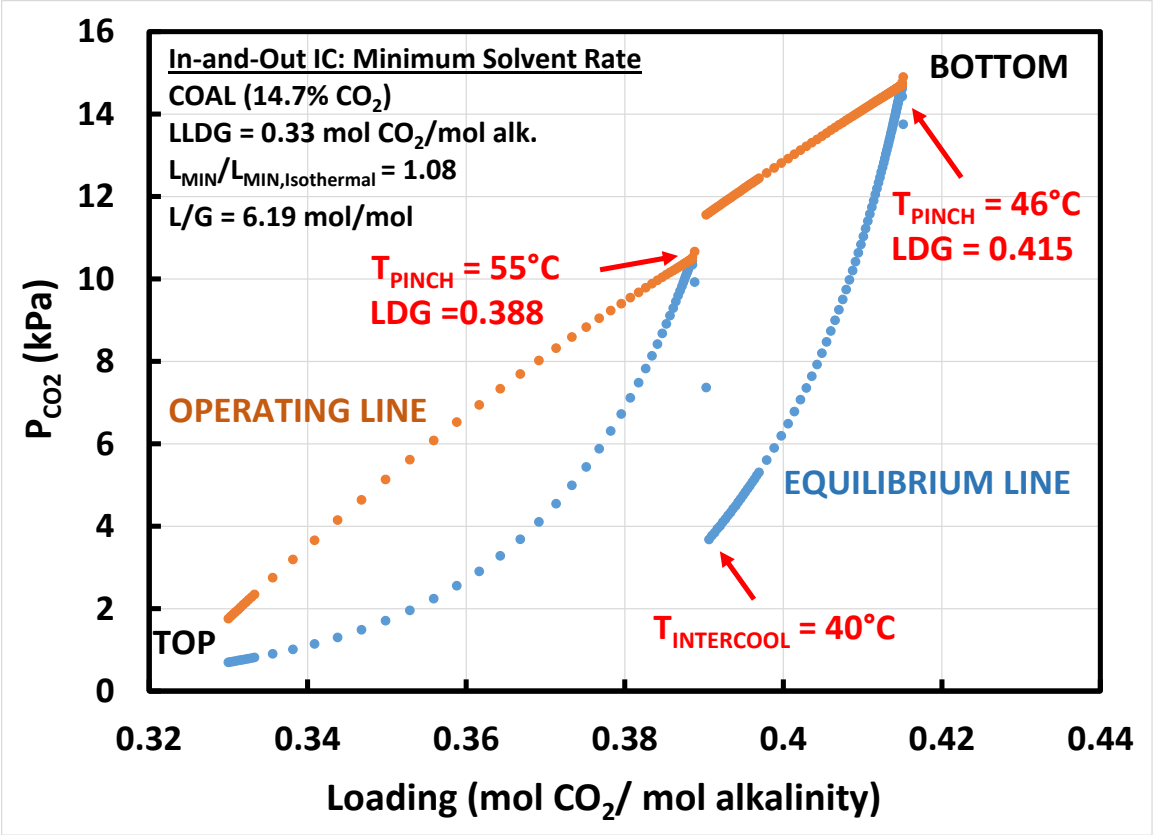

Figure 4-8: Operating and equilibrium curves @ LLDG = 0.33 mol CO_2/mol alk. for an intercooled absorber (in-and-out intercooling) operated at L_{MIN} ("infinite" packing) to achieve 90% CO_2 removal from a coal-fired boiler (14.7% CO_2). Two mass transfer pinches (contact of the equilibrium and operating lines) occur, one on either side of the intercooler. The top pinch occurs immediately above the intercooler and coincides with the maximum temperature (55 °C) in the absorber. The pinch below the intercooler occurs near the rich end of the column with a secondary temperature maximum (46°C).

The slope of the operating line (upper line in orange) in the preceding figures represents the liquid to gas ratio (L/G). The curvature present in the operating lines is due to the concurrent transfer of water and an L/G that may vary significantly in different parts of the column. This differs from the typical binary diagram with only a single transferring component. As the liquid rate is reduced, the slope of the operating line is reduced until it comes in contact with the equilibrium line; at this point in the column,

there is no driving force for mass transfer (the column is "pinched"), and the solvent rate cannot be reduced any further while meeting the 90% removal specification. Therefore, the slope of the operating line when the pinch occurs represents the minimum solvent rate to achieve 90% removal for the given operating conditions and column configuration. The best performance (in terms of solvent circulation or L_{MIN}) achievable for a given operating condition corresponds to a mass transfer pinch at the rich end (bottom) of the column at the column feed temperature (and isothermal pinch). Equilibrium-operating line constructions provide insight into the effect of a temperature bulge in the column on the approach to this best case performance.

The apparent discontinuity in the equilibrium curves in each of the figures represents the intercooler, which reduces the temperature to 40°C and reduces the corresponding equilibrium partial pressure of CO_2. An important aspect of modeling the minimum solvent rate for an intercooled absorber (and a key difference from the adiabatic absorbers in the previous chapter) is the location of the intercooler. Since the limiting pinch behavior of the absorber can occur above or below the intercooler (lean or rich end pinch), and it is impossible to know *a priori* where the pinch will occur, a single position for intercooling cannot be defined when modeling a minimum solvent rate case. Fixing the intercooler in a location (or equivalently, the packing distribution around the intercooler) will lead to a false pinch in one of the two sections based on the CO_2 - removed in each of the sections based on the arbitrary constraint on the packing distribution – this will provide an inaccurate value for the minimum solvent rate. Instead, the intercooling must be modeled at an arbitrary location and packing must be added to both sides of the intercooler independently until a limiting pinch is achieved (adding packing on either side will not change the CO_2 removal).

In Figure 4-6, a rich end pinch is developed below the intercooler and nearly all of the CO_2 removal occurs above the intercooler (quantified by the change in loading on the x-axis in each section of the column). In this region of low lean loading, the liquid-to-gas ratio (L/G) is small with the gas carrying the heat generated by CO_2 absorption towards the top of the column, where the maximum solvent temperature (77°C) occurs. However, the driving forces are large at these lean operating conditions (low equilibrium partial pressure of CO_2 for the solvent) and a mass transfer pinch does not occur at the bulge. The rich end pinch occurs at 44°C, closely approximating an isothermal pinch, as evidenced by the approach to the isothermal solvent rate ($L_{MIN}/L_{MIN,\ ISOTHERMAL} = 1.01$). The solvent mass flow rate at these conditions is inadequate to provide much intercooling capacity (low total heat capacity of the solvent). Therefore, the function of intercooling at this condition is to provide enough CO_2 removal at the bottom of the absorber to prevent a limiting lean end pinch without resulting in a severe rich end restriction (high temperatures below the intercooler).

Figure 4-7 represents the intermediate range of lean loading operating conditions, where the simple intercooling approach experiences the largest deviations from isothermal performance. Two distinct mass transfer pinches exist on either side of the intercooler. The mass transfer pinch above the intercooler coincides with a temperature bulge at the lean end of the column (71°C). In this loading range, the solvent carries an increasing portion of the heat generated by CO_2 absorption and the heat is "trapped" in the column and a limiting lean end pinch forms at as the solvent rate is increased from the isothermal minimum to achieve 90% removal. The cooled solvent leaving the intercooler similarly traps heat in the rich end of the absorber until a second pinch is formed below the intercooler. This pinch corresponds to second temperature maximum (64°C) below the intercooler. At conditions where a limiting lean end pinch forms, the two sections of

the absorber are effectively behaving as two adiabatic absorbers to balance the temperature limiting restriction on the column. If insufficient CO_2 is removed below the intercooler, the lean end pinch will become more restrictive (increase the solvent rate required to achieve 90% removal). Similarly, if insufficient CO_2 is absorbed above the intercooler, the pinch below the intercooler will become more severe (higher temperatures, occur closer to the intercooler/leaner loading) and require an increase in solvent rate to meet the removal requirement. Therefore, the "double pinch" seen in this case is a defining characteristic of intercooled absorbers which are operating at conditions (lean loading, maximum temperatures, etc.) which form a limiting lean end pinch. An alternate interpretation of this phenomena is that an intercooled absorber "splits" the temperature bulge that is formed in adiabatic absorber. The intercooled absorber is not truly equilibrium limited by temperature effects until a pinch is formed at both temperature maxima – this is where the deviation from isothermal capacity begins to occur (Figure 4-4). The NGCC case provides a clear illustration of this transition behavior from a rich end pinch away from the temperature bulge, to a lean end pinch at the temperature bulge above the intercooler (not restricting), and finally to the double pinch that restricts column performance. The next section will explore this transition behavior.

Finally, in Figure 4-8, the high lean loading is associated with a high L/G (liquid heat capacity dominates) and pushes each mass transfer pinch and temperature bulge towards the bottom of their respective column sections while moderating the maximum temperatures (55°C and 46°C). The intercooler removes the heat associated with the lean limiting bulge and has sufficient capacity to push the secondary bulge and pinch to the rich end of the column. The result is a column approximating an isothermal rich end pinch ($L_{MIN}/L_{MIN,\ ISOTHERMAL} = 1.01$)

The trends for the NGCC case (Figure 4-3) and the steel-blast furnace case (Figure 4-5) can also be explained by the same phenomena in the column:

4) Lean end temperature bulge at low loadings does not form a mass transfer pinch due to large driving forces near temperature maxima and the loading range for operating without a lean pinch is expanded (compared to an adiabatic column) by CO_2 removal below the intercooler;
5) Lean end pinch forms at the temperature bulge and secondary pinch is formed below the intercooler as CO_2 removal is balanced around the intercooler to minimize the restriction of the lean end pinch – the double pinch indicates the intercooled system fully equilibrium constrained by temperature effects (neither section can operate without temperature restriction).
6) The solvent rate is increased until liquid phase heat capacity carries each temperature bulge to the bottom of the packed bed – the intercooler removes the lean end temperature restriction and the high solvent rate moderates the temperature at the rich end, limiting the effect of the mass transfer pinch on solvent capacity.

4.4.1.2 Pinch Transitions: NGCC Case

The coal case (and similarly, the steel application) exhibit a sharp transition from a rich end pinch away from the lean end temperature bulge (Figure 4-6) to a double pinch that indicates the column is limited by temperature effects. The NGCC case, however, exhibits three steps in this transition illustrated in the following figures:

1) Rich end pinch away from both temperature maxima: No temperature restrictions on equilibrium (Figure 4-9, LLDG = 0.23 mol CO_2/mol alkalinity).

2) Lean end pinch @ top bulge/ Rich end pinch away from bottom bulge: No restriction on equilibrium despite a lean pinch because bottom section can form a true rich end pinch away from bottom bulge (Figure 4-10, LLDG = 0.24 mol CO_2/mol alkalinity).
3) Double Pinch (at each temperature bulge): System is equilibrium limited by temperature and true rich end pinch cannot be achieved (Figure 4-11, LLDG = 0.27 mol CO_2/mol alkalinity).

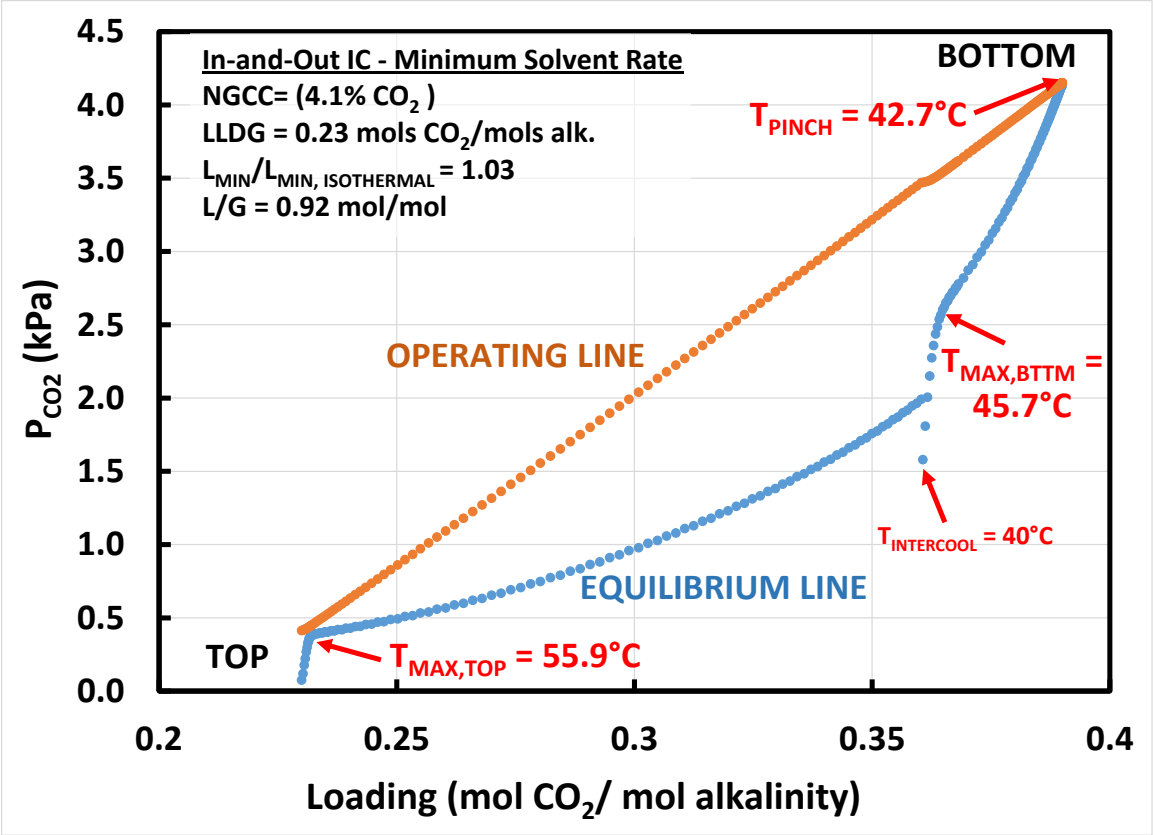

Figure 4-9: Operating and equilibrium curves @ LLDG = 0.23 mol CO_2/mol alk. for an intercooled absorber (in-and-out intercooling) operated at L_{MIN} ("infinite" packing) to achieve 90% CO_2 removal from a NGCC power plant (4.1% CO_2). The mass transfer pinch (contact of the equilibrium and operating lines) occurs at the rich end of the column (bottom, 43°C), unrelated to the maximum temperature in the top section (56°C) or bottom section (46°C).

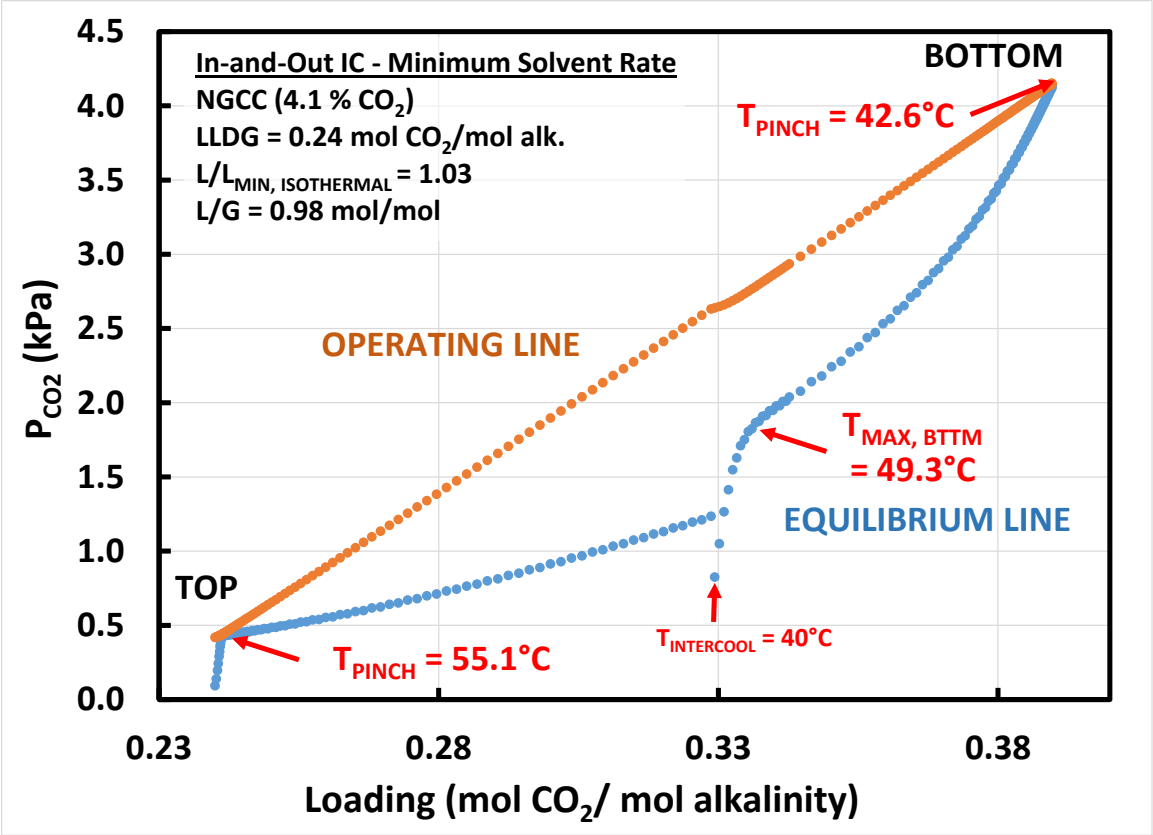

Figure 4-10: Operating and equilibrium curves @ LLDG = 0.24 mol CO_2/mol alk. for an intercooled absorber (in-and-out intercooling) operated at L_{MIN} ("infinite" packing) to achieve 90% CO_2 removal from a NGCC power plant (4.1% CO_2). Two mass transfer pinches occur (contact of the equilibrium and operating lines): 1) Rich end pinch (bottom, 43°C), unrelated to the maximum temperature in the bottom section (49°C); 2) Lean end pinch (top) at the maximum temperature (55°C).

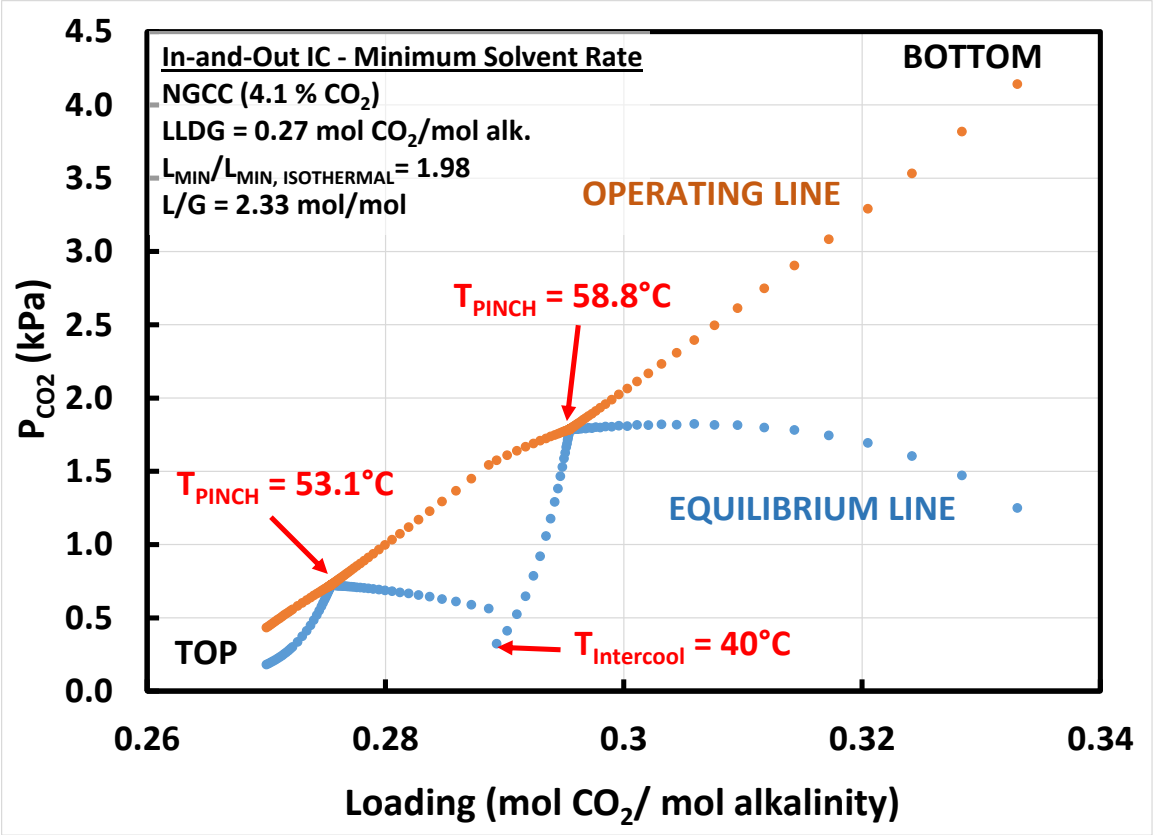

Figure 4-11: Operating and equilibrium curves @ LLDG = 0.27 mol CO_2/mol alk. for an intercooled absorber (in-and-out intercooling) operated at L_{MIN} ("infinite" packing) to achieve 90% CO_2 removal from a NGCC power plant (4.1% CO_2). This condition represents the largest deviation from isothermal performance ($L_{MIN}/L_{MIN, Isothermal}$ = 1.98). Two mass transfer pinches (contact of the equilibrium and operating lines) occur: 1) The pinch above the intercooler occurs near the lean end of the column and coincides with the maximum temperature (53°C) in the top section; 2) The pinch below the intercooler occurs at the maximum temperature in the column (59°C).

As the figures illustrate, the NGCC case exhibits a gradual transition to the formation of a true temperature restriction (double pinch). The lower temperatures and lower L/G in the NGCC case expand the window where a pinched system will form. This behavior will also be relevant as the system moves away from L_{MIN} as the limiting pinches will also be the limiting driving force for mass transfer.

4.4.1.3 Pinch Formation: Comparison to an Adiabatic Absorber

As discussed in the preceding chapter, the formation of a lean end pinch at the temperature bulge is the precipitating phenomena that limits adiabatic absorber performance and requires a significant increase in the solvent rate from the isothermal minimum. The discussion in the previous section indicates that the formation of temperature bulge related pinches are also the initiating phenomena for intercooled absorbers. However, the equilibrium constraint is much less restrictive for the intercooled absorbers in two ways:

1) The lean loading range to achieve 90% removal without limiting temperature-related pinches is larger;
2) The increase in solvent rate required to overcome the pinches after formation is much smaller (reduced deviation from the isothermal baseline in Figure 4-3 through Figure 4-5).

The first benefit of intercooling is explained by the preceding discussion – intercooling reduces the maximum solvent temperature at the bulge (compared to an adiabatic absorber at the same conditions) by removing CO_2 below the intercooler to delay the onset of the lean pinch. The second phenomena requires further investigation of the pinch formation behavior.

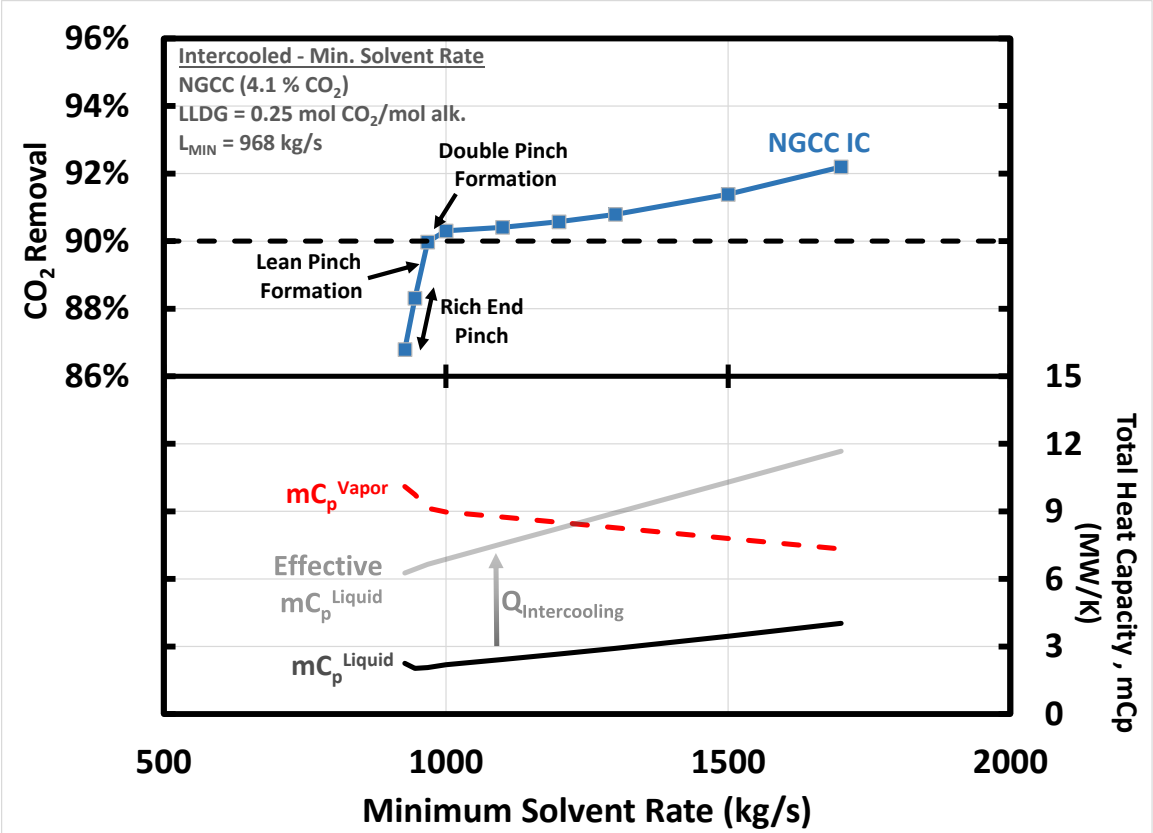

Figure 4-12: Lean end pinch formation @ LLDG = 0.25 mol CO_2/mol alk. for an intercooled absorber (in-and-out intercooling) for capture from a NGCC power plant (4.1% CO_2) utilizing 8 m PZ. The solvent rate increases from the isothermal minimum solvent rate ($L_{MIN, ISOTHERMAL}$ = 927 kg/s) to the final L_{MIN} required to achieve 90% removal ($L_{MIN, INTERCOOL}$ = 968 kg/s). The restricting double pinch forms after 90% removal is achieved in this case (one benefit of intercooling).

Several features of the pinch formation and transition to higher solvent rates are notable for the intercooled absorber. First, for the case in Figure 4-12, the lower temperatures in the intercooled absorber at the lean end bulge allow 90% CO_2 removal to be achieved before the double pinch is formed (i.e., before the column is equilibrium-limited by temperature) – the solvent rate therefore remains close to the isothermal minimum. After the formation of a pinch on both sides of the intercooler, the absorber exhibits a monotonic trend in CO_2 removal as a function of solvent rate. The slope of the curve has

changed (an incremental increase in solvent rate is less effective at providing additional driving force benefits), but the behavior is different from an adiabatic absorber which exhibits a non-monotonic trend which requires a significant solvent increase to overcome the lean end pinch (c.f., Chapter 3, Figure 3-9).

The solvent is more effective at addressing the equilibrium constraint associated with the temperature related pinches in the intercooled absorber case. As Figure 4-12 shows, this is due to the heat removed at the intercooler. In an adiabatic absorber, this heat would be returned to the solvent in the form of water vapor which is condensed above the bulge to generate the temperature rise (along with CO_2 absorption) at the lean end of the absorber. Therefore, the intercooler is effectively doubling the heat carrying capacity of the solvent since the heat absorbed in the top of the column is removed from the system instead of returned to the lean end pinch. As depicted in Figure 4-12, when the heat removed at the intercooler is considered, the liquid and vapor heat capacities are much more closely matched and exhibit a crossover point as in an adiabatic absorber. The intercooled absorber is essentially two adiabatic absorbers operating in series – the top section, which operates with double the effective total heat capacity due to the intercooler, and the bottom section, which operates as a normal adiabatic absorber. A new degree of freedom is introduced – the amount of CO_2 removed in each absorber – that delays the onset and minimizes the impact of a temperature pinch. This explains why the solvent is less constrained by carrying heat away from the bulge and can address the equilibrium constraint more effectively than in an adiabatic absorber.

As noted, the adiabatic absorber exhibits non-monotonic trends in CO_2 removal as a function of solvent rate that can lead to multiple steady states (c.f., Chapter 3, Figure 3-9). This is another important advantage of an intercooled absorber and the trend in Figure 4-12 (which is consistently monotonic for intercooled absorbers across the

conditions evaluated in this work). The unstable steady states described for the adiabatic absorber do not exist and the operations and control of the system, even with a lean end pinch, is more straightforward.

4.5 Design Curves and Mass Transfer Performance

The benefit of simple intercooling over an adiabatic absorber is significant when considering solvent capacity effects. However, absorbers are not operated at the minimum solvent rate due to the prohibitive packing costs. The number of transfer units required for a given separation rises exponentially as an inverse function of the driving force, making operating with a "pinch" infeasible. To provide a practical assessment of the benefits of intercooling, design curves (as in Figure 4-2) were developed for each of the three flue gas sources at a lean loading in each of 4 unique regions identified from the minimum solvent rate plots (Figure 4-3 to Figure 4-5):

1) "Over-stripped" region: This is the low loading region in each of the L_{MIN} figures where the adiabatic absorber approximates the isothermal minimum solvent rate ($L_{MIN,\ ADIABATIC}/L_{MIN,\ ISOTHERMAL} \approx 1$, no lean end pinch restriction). "Over-stripping" corresponds to the idea that the low loadings in this region typically drive the stripping system away from an energy optimum due to a significant increase in stripping steam requirements, though a specific stripper analysis would be needed to verify the energy performance as a function of loading (e.g., (Lin & Rochelle, 2014) and (Frailie, 2014)) .
2) Simple Intercooling region: This is the region where the adiabatic absorber performance deteriorates due to a lean pinch ($L_{MIN,\ ADIABATIC}$ rises rapidly) but in-and-out intercooling prevents a lean pinch and approaches the isothermal

minimum ($L_{MIN,\ ADIABATIC}/L_{MIN,\ ISOTHERMAL} >> 1$, $L_{MIN,\ INTERCOOL}/L_{MIN,\ ISOTHERMAL} \approx 1$).

3) Advanced Intercooling region: This region is characterized by deviation from isothermal minimum solvent rates for both the adiabatic and in-and-out intercooled absorbers indicating limiting lean end pinches for both designs ($L_{MIN,\ ADIABATIC}/L_{MIN,\ ISOTHERMAL} >> 1$, $L_{MIN,\ INTERCOOL}/L_{MIN,\ ISOTHERMAL} > 1$).. An improved intercooling design is expected to provide solvent capacity benefits in this region.

4) Large solvent rate region: This high loading region corresponds to inherently large liquid-to-gas ratios which moderate temperature effects and push temperature maxima to the ends of packed sections for adiabatic and intercooled absorbers. This region is of limited practical interest due to the extreme solvent circulation rates required.

Table 4-5 defines the loading values for each region and flue gas source. Figure 4-13 identifies the 4 regions for the coal case on the L_{MIN} figure.

Table 4-5: Summary of Lean Loading Ranges Defined for Design Curve Analysis

Operating Regions	Loading Range (mol CO_2/mol alkalinity)		
	Natural Gas Combined Cycle (NGCC)	**Coal-Fired Boiler**	**Steel Blast Furnace**
"Over-Stripped"	0.15–0.21	0.15–0.18	0.12-0.17
Simple Intercooling	0.22–0.26	0.19–0.21	0.18 – 0.19
Advanced Intercooling	> 0.26	0.22–0.30	0.20 – 0.29
Large Solvent Rate	N/A	> 0.30	> 0.30

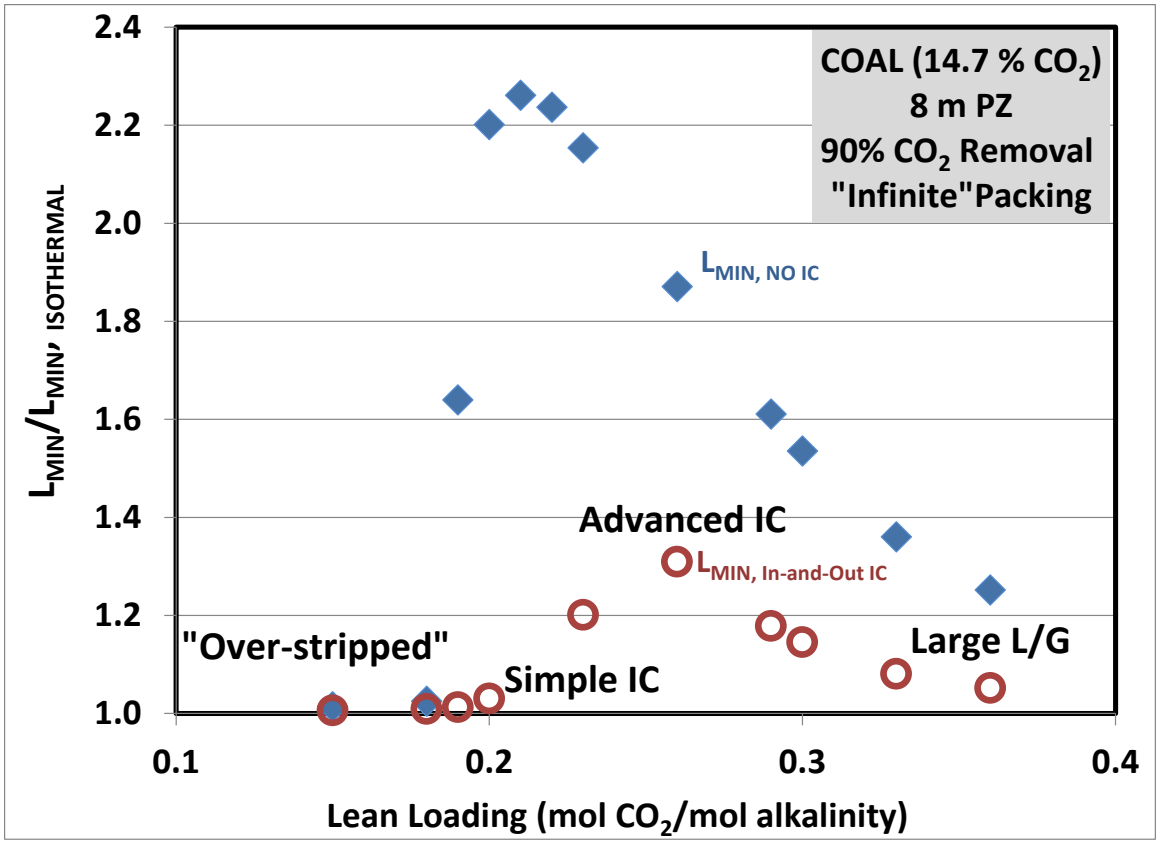

Figure 4-13: Four regions corresponding to different L_{MIN} limitations are identified for design curve analysis, coal-fired boiler flue gas (14.7% CO_2). Ratio of L_{MIN} ("infinite" packing) for an adiabatic absorber (no intercooling) and intercooled absorber (in-and-out intercooling) to an isothermal absorber (40 °C) for 90% CO_2 capture with 8 m PZ.

A total of 11 cases are defined by Table 4-5. The design curves for the three NGCC cases are presented here – the analogous curves for coal and steel are included in Appendix E.

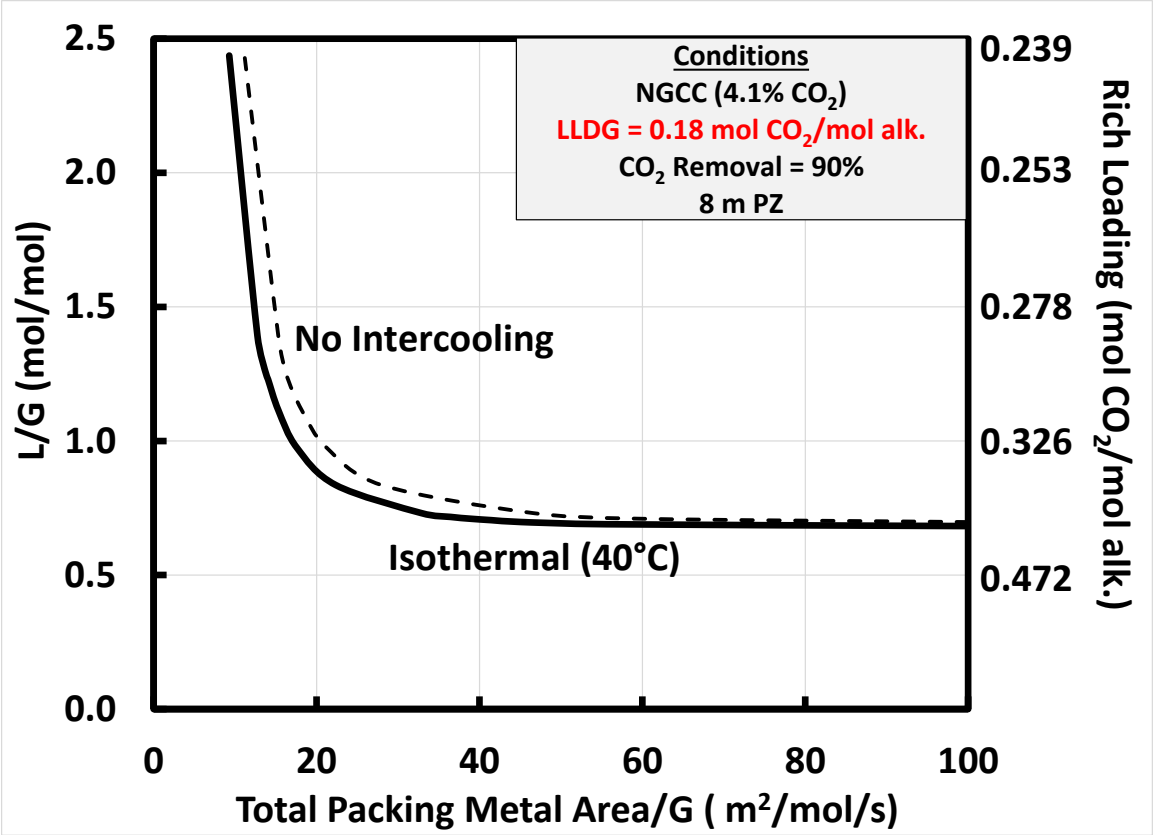

Figure 4-14: Packing-solvent rate trade-off, NGCC flue gas (4.1 mol% CO_2), "over-stripped" loading region (LLDG = 0.18 mol CO_2/mol alk.). Each curve (dashed = adiabatic, solid = isothermal) represents constant 90% CO_2 removal. Unique rich loading for each L/G is on secondary y-axis. The asymptote each curve reaches with increasing packing area is the minimum solvent rate (L_{MIN}).

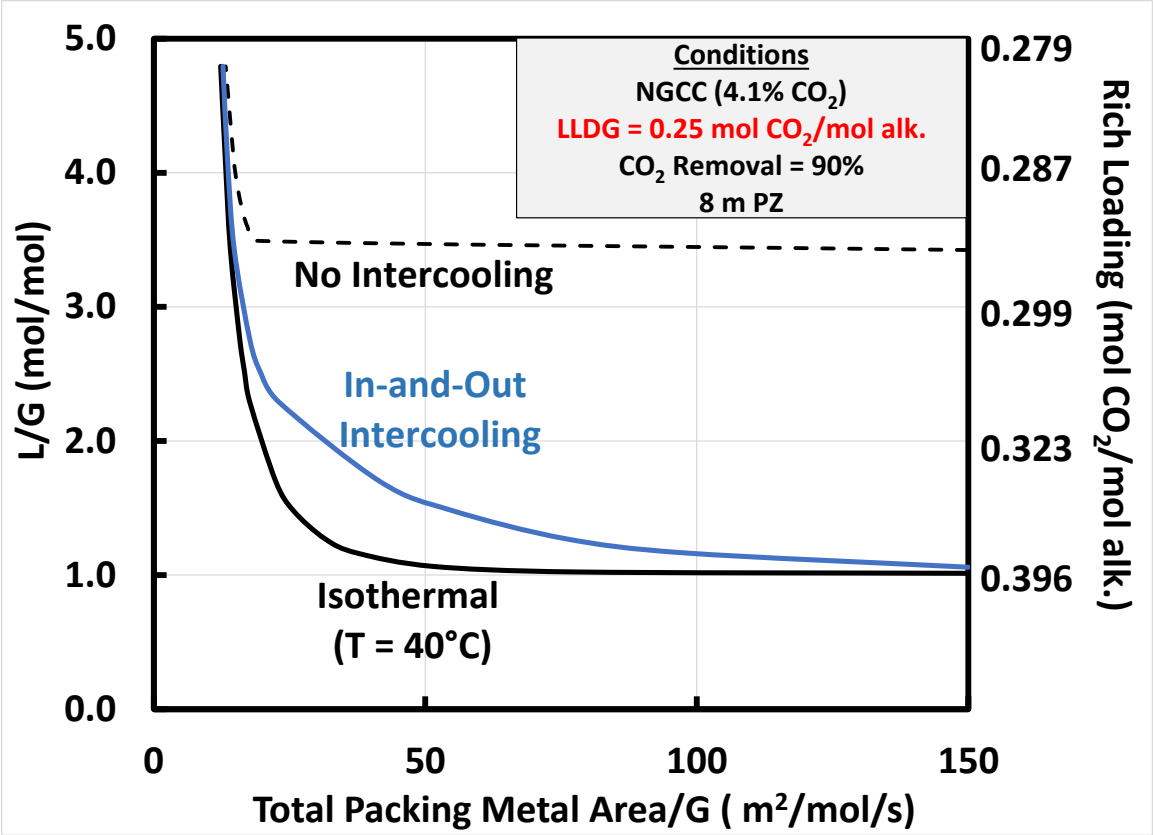

Figure 4-15: Packing-solvent rate trade-off, NGCC flue gas (4.1 mol% CO_2), simple intercooling loading region (LLDG = 0.25 mol CO_2/mol alk.). Each curve (dashed = adiabatic, solid = isothermal, blue = intercooled) represents constant 90% CO_2 removal. Unique rich loading for each L/G is on secondary y-axis. The asymptote each curve reaches with increasing packing area is the minimum solvent rate (L_{MIN}).

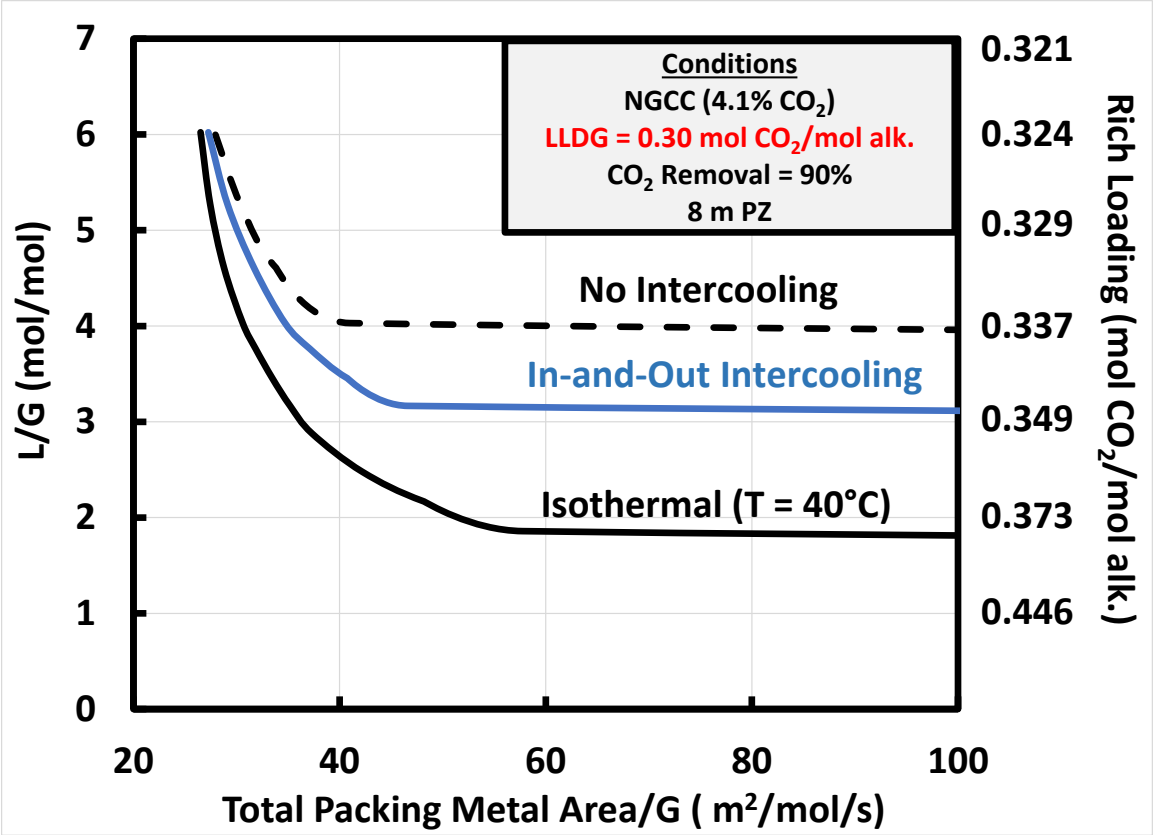

Figure 4-16: Packing-solvent rate trade-off, NGCC flue gas (4.1 mol% CO_2), advanced intercooling loading region (LLDG = 0.30 mol CO_2/mol alk.). Each curve (dashed = adiabatic, solid = isothermal, blue = intercooled) represents constant 90% CO_2 removal. Unique rich loading for each L/G is on secondary y-axis. The asymptote each curve reaches with increasing packing area is the minimum solvent rate (L_{MIN}).

In each figure, the slope of the design curves depict the packing-energy cost (solvent rate) trade-off in the approach to the minimum solvent rate. When comparing two designs, a steeper slope indicates better mass transfer performance (enhanced driving forces or mass transfer efficiency as defined by the controlling resistance) – less packing is required to approach the minimum solvent rate. Therefore, an absorber design or solvent system with enhanced mass transfer (improved packing or contacting equipment, enhanced gas/liquid turbulence, reduced viscosity) can result in a design curve *outside* of

the isothermal curve (a simple packed absorber in this analysis). The isothermal curve is strictly limiting in the minimum solvent rate asymptote and only represents the best case driving forces for an absorber at all other conditions. Mass transfer performance of absorbers with PZ will be discussed extensively in Chapters 5 and 6 as part of developing novel absorber configurations.

The design curves can also be used to define an optimum (or near optimum) operating condition (specific solvent rate) which balances the packing and solvent rate trade-off. This solvent rate can be defined as a multiple of the minimum solvent rate (e.g., L/L_{MIN} =1.2) and provides an approach to absorber design – define the minimum solvent rate for the design and specified operating conditions, and evaluate packing requirements as the solvent rate is moved away from the minimum. As the discussion in the preceding sections in this chapter (and the previous chapter) indicate, quantifying the minimum solvent rate can be non-trivial (multiple steady states, intercooling location, etc.) so the isothermal minimum solvent rate serves as a useful baseline as it strictly depends on the solvent VLE and inlet flue gas composition (solvent is saturated to the inlet CO_2 concentration at the absorber temperature).

The design curves above and in the appendix are useful for visualizing the relationship between packing requirements and solvent rates for different absorber designs, but a quick screening method for the performance of the absorber design will be developed in section 4.5.2 to summarize the results of this analysis.

4.5.1 Optimal Intercooling Location

Each point on the design curve for in-and-out intercooling represents an absorber design with an "optimal" location for intercooling, where the optimum design is defined by the intercooling location which minimizes the total packing requirement. The

optimization was performed using the flowsheet optimization tool in Aspen Plus®. However, the packing optimization problem has a single equality constraint (90% removal) with two optimization variables (two packed bed heights) which means the problem only has one true degree of freedom (one of the two bed heights can be varied freely while the second must satisfy the removal constraint). Therefore, the problem is easily tractable by a trail-and-error or "brute force" method or an offline Newton's method if an approximate function is defined from discrete modeling cases. The resulting optimal location of intercooling for individual cases that define the design curves in the preceding analysis was evaluated as a function of operating conditions (solvent rate, CO_2 concentration in flue gas, lean loading).

4.5.1.1 Optimal Intercooling Location for NGCC Application

The optimal intercooling results for the NGCC application are described in Figure 4-17.

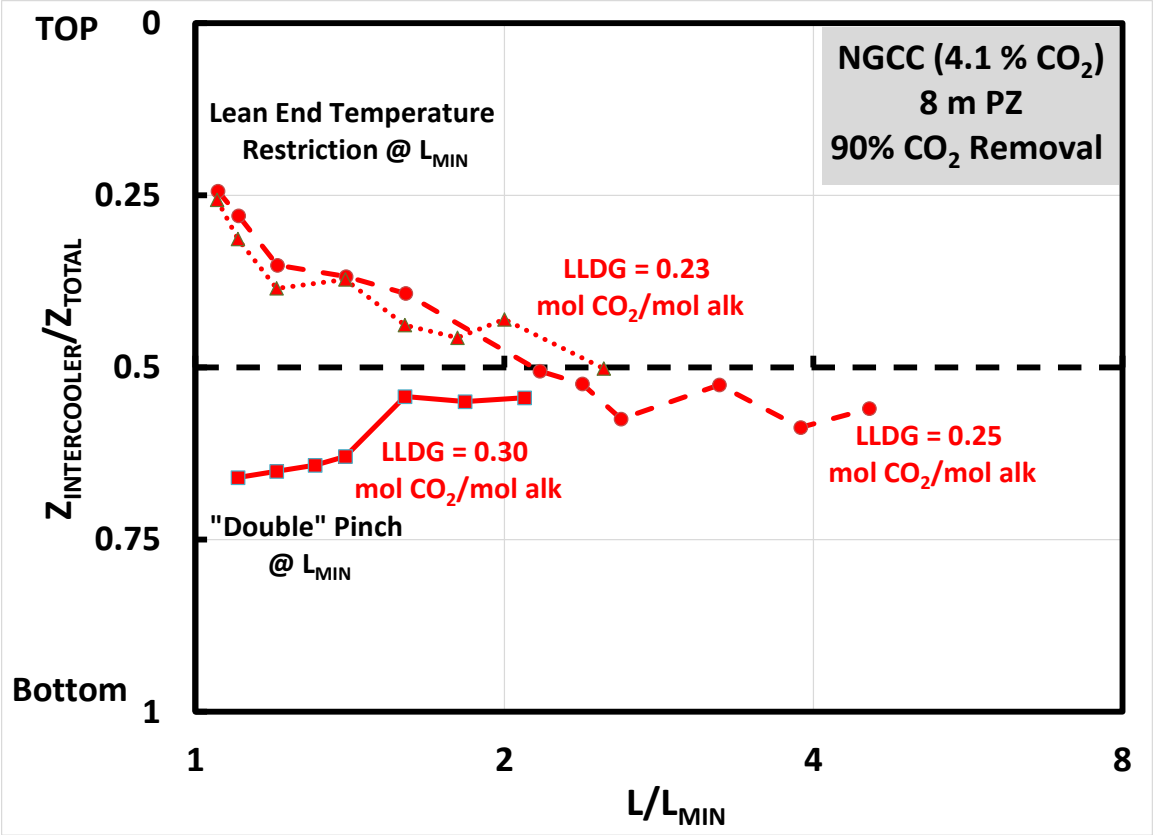

Figure 4-17: Location of the intercooler for in-and-out intercooling method (Figure 4-1) as a function of solvent rate for 90% capture from a NGCC power plant (4.1 mol% CO_2) at three lean loadings (8 m PZ): 0.23 (dotted line), 0.25 (dashed line), 0.30 (solid line) mol CO_2/mol alk. Intercooling location is defined as a normalized, or relative, position in the overall packed height of the column. The solvent rate is defined as a multiple of the L_{MIN} (L/L_{MIN}) for the intercooled absorber at the given lean loading. The intercooling position is determined by the packing distribution around the intercooler that will minimize the total packing area in the column – each point in the chart represents an independent optimization at the given conditions. Pinch conditions at L_{MIN} are described for each case.

The NGCC case exhibits two distinct trends in the optimal location of intercooling. At the lower loadings (0.23 and 0.25 mol CO_2/mol alkalinity), the intercooler position starts near the top of the column when the absorber is operated near L_{MIN}. As solvent rate is increased ("relax" equilibrium pinch conditions, larger driving forces), the intercooler moves down the column to approximately the middle of the

column ($Z_{INTERCOOLER}/Z_{TOTAL} \approx 0.5$). The higher loading region shows the opposite trend – the intercooler starts near the bottom of the absorber and moves up towards the middle of the column as a function of solvent rate. The two trends as a function of loading can be explained by the underlying pinch behavior at the minimum solvent rate.

Figure 4-9 described the pinch phenomena at a lean loading of 0.23 mol CO_2/mol alkalinity (analogous to the 0.25 loading case). The temperature-related pinch occurs at the lean end of the column, while the overall column is able to achieve a true rich end pinch (not related to a temperature bulge). Therefore, the restricting pinch is at the lean end of the column and the initial optimum position of the intercooler is located towards the top of the column in Figure 4-17 ($Z_{INTERCOOLER}/Z_{TOTAL} \approx 0.25$) to limit the packing in this equilibrium constrained section. As the solvent rate increases, the pinch is relaxed in the lean end of the column, and more packing (proportionally) is allocated above the intercooler (i.e., intercooler moves down the column). Eventually, when the solvent rate is $L/L_{MIN} \approx 2$, the temperatures have been moderated and the driving forces are generally large throughout the column, so intercooling has limited effect. The intercooler stays in a "neutral" position ($Z_{INTERCOOLER}/Z_{TOTAL} \approx 0.5$) as the solvent rate increases further.

At higher loadings (0.30 mol CO_2/mol alkalinity in Figure 4-17), a "double" pinch occurs at L_{MIN} (e.g., Figure 4-11) and the rich end pinch associated with a temperature bulge is limiting – this will be discussed further in the next section. As the solvent rate is increased, the restricting pinch in the bottom section benefits and the intercooler moves up the column (relatively more packing in the bottom section). As with the lower loading region, when the solvent rate is $L/L_{MIN} \approx 2$, the intercooler has limited impact and approaches a "neutral" location at $Z_{INTERCOOLER}/Z_{TOTAL} \approx 0.5$.

4.5.1.2 Optimal Intercooling Location for Coal and Steel Applications

The coal-fired boiler and steel blast furnace results are described in Figure 4-18 and Figure 4-19.

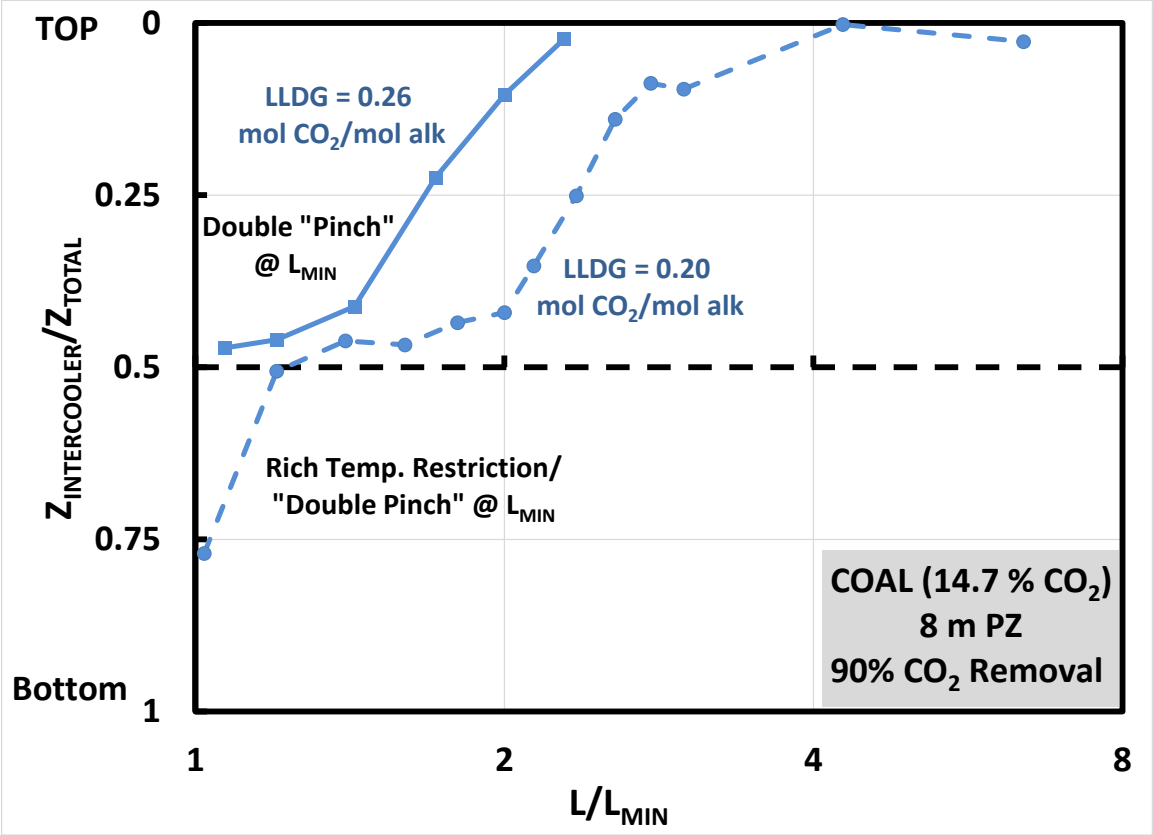

Figure 4-18: Location of the intercooler for in-and-out intercooling method (Figure 4-1) as a function of solvent rate for 90% capture from a coal-fired boiler (14.7 mol% CO_2) at two lean loadings (8 m PZ): 0.20 (dashed line) and 0.26 (solid line) mol CO_2/mol alk. Intercooling location is defined as a normalized, or relative, position in the overall packed height of the column. The solvent rate is defined as a multiple of the minimum solvent rate (L/L_{MIN}) for the intercooled absorber at the given lean loading. The intercooling position is determined by the packing distribution around the intercooler that will minimize the total packing area in the column – each point in the chart represents an independent optimization at the given conditions. Pinch conditions at L_{MIN} are described for each case.

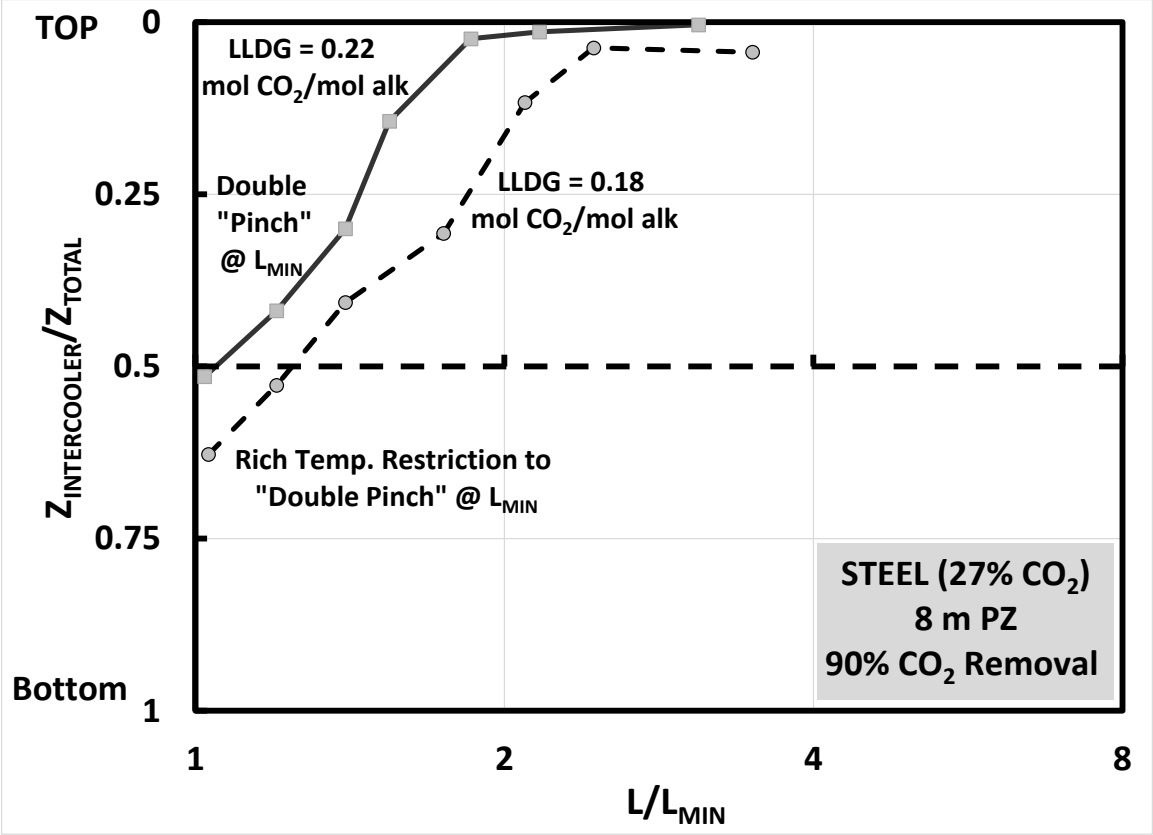

Figure 4-19: Location of the intercooler for in-and-out intercooling method (Figure 4-1) as a function of solvent rate for 90% capture from a steel blast furnace (27 mol% CO_2) at two lean loadings (8 m PZ): 0.18 (dashed line) and 0.22 (solid line) mol CO_2/mol alk. Intercooling location is defined as a normalized, or relative, position in the overall packed height of the column. The solvent rate is defined as a multiple of the minimum solvent rate (L/L_{MIN}) for the intercooled absorber at the given lean loading. Two lean loadings are presented: The intercooling position is determined by the packing distribution around the intercooler that will minimize the total packing area in the column – each point in the chart represents an independent optimization at the given conditions. Pinch conditions at L_{MIN} are described for each case.

All of the coal and steel cases depicted exhibit the same general trend – as the solvent rate is increased, the intercooler moves up the column until it eventually reaches the top of the column ($Z_{INTERCOOLER}/Z_{TOTAL} \approx 0$). The limiting pinch in each case is a rich end temperature-related pinch – either as part of the "double" pinch or independently - Figure 4-7 illustrates the "double" pinch for the 0.26 mol CO_2/mol alkalinity case.

In each case, as the solvent rate is increased, the restricting rich pinch is relaxed and the intercooler moves to a relatively higher position in the column (larger portion of packing below the intercooler. As in the gas case, continued increase of the solvent rate beyond $L/L_{MIN} \approx 2$ reduces the impact of intercooling (moderated temperatures, large driving forces throughout) and the intercooler moves to a "neutral" position, in this case, $Z_{INTERCOOLER}/Z_{TOTAL} \approx 0$.

As the lean loading increases for each flue gas application, the corresponding intercooling location is higher in the column for a given L/L_{MIN}. For a given L/L_{MIN}, the absolute solvent rate and L/G is higher for the higher loading (baseline L_{MIN}) is higher, so the solvent is able to address the temperature restriction at the rich end of the column more effectively.

4.5.1.3 Generalizations about optimized intercooling location

As the cases in the previous discussion illustrate, the starting position and trend in intercooling location are dependent on the underlying mass transfer pinch phenomena which are most clearly illustrated at L_{MIN}. The cases with a lean-end limiting pinch (generally the NGCC application) start with an intercooler towards the top of the column and the position drops as the solvent rate is increased. For the rich end temperature-limited cases, the intercooler generally starts towards the bottom or middle of the column and moves up with increasing solvent rate. In all cases, as the solvent rate exceeds L/L_{MIN}

≈ 2, intercooling has limited impact, and the optimization will simply drive the intercooler to the nearest "neutral" or equilibrium position – in this analysis, that is the middle or top of the column, although presumably the bottom of the column would be a similar limiting position.

A rich-end temperature limited case is plotted for each flue gas concentration in Figure 4-20 to provide general conclusions about the effect of CO_2 concentration.

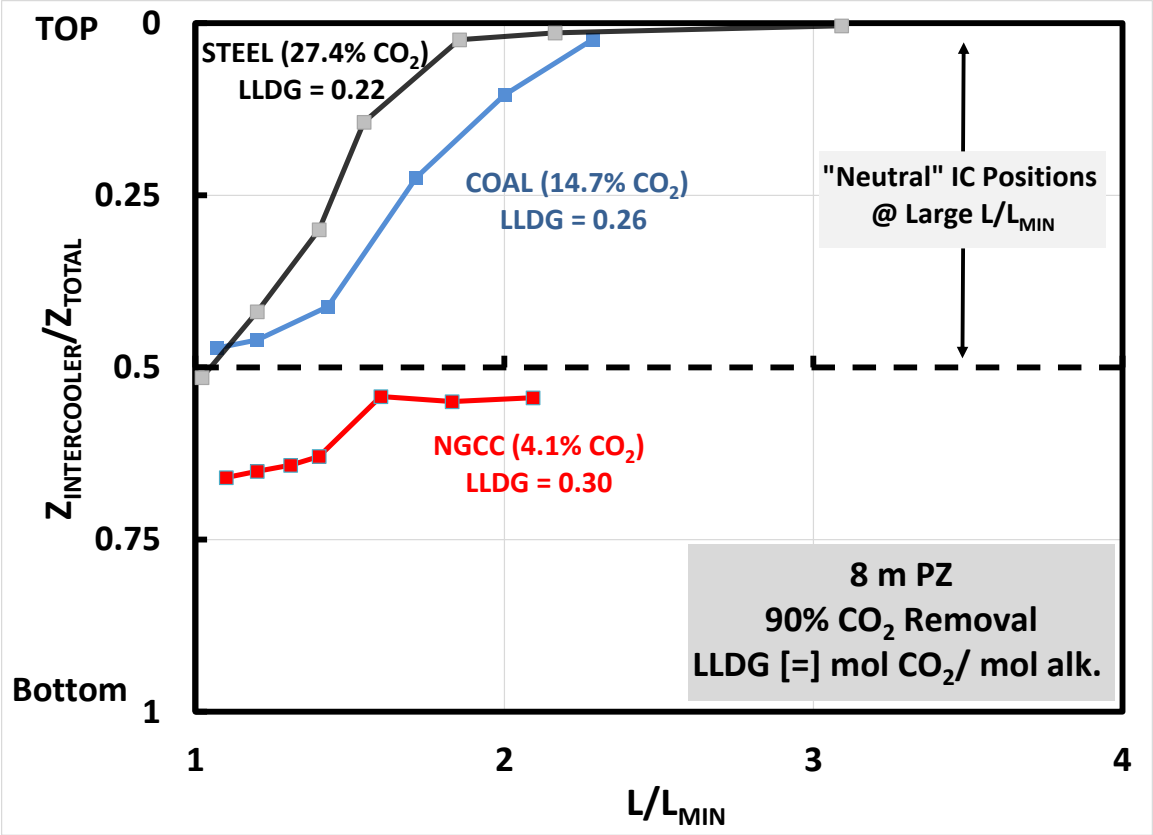

Figure 4-20: Location of the intercooler for in-and-out intercooling method (Figure 4-1) as a function of solvent rate for rich end temperature limited cases for NGCC (red, 4.1% CO2), coal (blue, 14.7% CO2), and steel (black, 27% CO2). Intercooling location is defined as a normalized, or relative, position in the overall packed height of the column. The solvent rate is defined as a multiple of L_{MIN} (L/L_{MIN}) for the intercooled absorber at the given lean loading. The intercooling position is determined by the packing distribution around the intercooler that will minimize the total packing area in the column – each point in the chart represents an independent optimization at the given conditions.

The figure shows that the coal and steel cases start with the intercooler around the mid-point of the column while the NGCC case starts lower in the column, and the rise in the column as a function of L/L_{MIN} is fastest for steel and slowest for NGCC. These trends are consistent with the increasing L/G with CO_2 concentration – for a given

L/L_{MIN}, the corresponding L/G is larger for higher CO_2 concentrations. The inherently larger total solvent heat capacity overcomes the temperature restrictions in the column more readily for the high CO_2 applications.

Finally, if the analysis is considered in a reasonable operating range of solvent rates (~ 1.1 to 1.8*L_{MIN}), the optimal intercooling position generally falls in the middle 50% of the column for all cases ($Z_{INTERCOOLER}/Z_{TOTAL}$= 0.25 to 0.75). Therefore, an extreme position of intercooling may indicate an unrealistic operating solvent rate for the design (e.g., operating too close to L_{MIN}).

4.5.1.4 Intercooling Optimization and Relative Pinch Concept

The discussion of trends in optimal intercooling position has focused on the underlying pinch behavior (managing the restricting pinch above or below the intercooler). Therefore, the optimal packing distribution in an absorber should correspond to a "balanced" or equivalent approach to a mass transfer pinch on either side of the intercooler, to a first approximation. However, the lean end of the absorber will inherently have smaller absolute driving forces (lower CO_2 partial pressure in the gas) after CO_2 has been removed from the gas, and appear closer to a pinch. To properly assess the equilibrium constraint imposed by the solvent, a normalized driving force or definition is proposed:

$$\text{Normalized Driving Force} = \frac{P_{CO_2} - P^*_{CO_2}}{P_{CO_2}} = 1 - \frac{P^*_{CO_2}}{P_{CO_2}} \qquad 4.5$$

where:

P_{CO_2} = Bulk partial pressure of CO_2 in the gas phase (Pa);

$P^*_{CO_2}$ = Partial pressure of CO_2 in equilibrium with the bulk solvent (Pa).

As the parameter approaches 1, the relative driving force is large (unloaded solvent) and as it approaches zero the column is pinched due to equilibrium limitation in the solvent (saturated solvent). When the two sections of an intercooled absorber have the same minimum normalized driving force or "relative pinch", the absorber packing distribution around the intercooler is expected to be at an optimum value. The theoretical support for this concept comes from the definition of transfer units in defining overall absorber packing height. Equation 4.6 presents the height of packing in the two absorber sections in a general expression in terms of the number of transfer units (NTU) and (HTU).

$$Z_{TOTAL} = Z_{TOP} + Z_{BOTTOM}$$

$$= HTU_{TOP} NTU_{TOP} + HTU_{BTTM} NTU_{BTTM}$$

$$= \left(\frac{V}{K_G a_e S}\right)_{TOP} \left(\int_{y_{OUT}}^{y_{MID}} \frac{dy_{CO_2}}{y_{CO_2} - y^*_{CO_2}}\right) + \left(\frac{V}{K_G a_e S}\right)_{BTTM} \left(\int_{y_{MID}}^{y_{IN}} \frac{dy_{CO_2}}{y_{CO_2} - y^*_{CO_2}}\right) \quad 4.6$$

where:

Z_{TOTAL} = Total packing height of column;

Z_{TOP} = Packing height of top bed or section of column;

Z_{BOTTOM} = Packing height of bottom bed or section of column;

y_{CO_2} = Bulk mole fraction of CO_2 in the gas phase;

$y^*_{CO_2}$ = Vapor mole fraction of CO_2 in equilibrium with the bulk solvent;

y_{MID} = Bulk mole fraction of CO_2 leaving bottom/entering top bed;

y_{IN} = Bulk mole fraction of CO_2 in the gas phase entering the column;

y_{OUT} = Bulk mole fraction of CO_2 in the gas phase leaving the column;

V = Total gas phase molar flow rate;

K_G = Overall mass transfer coefficient for gas-phase driving force;

a_e = Effective area of packing per unit column volume (m^2/m^3);

S = Column cross-sectional area (m^2);

As written, the HTU is assumed constant over the absorber, but in practice is part of the rigorous numerical integration over the column. However, the theoretical expression for packing height provides insight into assigning an optimal distribution of packing between the two beds. If the HTU, or mass transfer efficiency, of the packing does not vary greatly from top to bottom of the column (not strictly valid – see Chapter 5 for detailed discussion), the minimization of packing is based on the NTU terms only. These terms represent the change in composition of the solute (or CO_2 removed) relative to the average driving force in the section of the column. Therefore, to minimize the total packing area, the CO_2 removed in each packed bed should be balanced based on the driving force available for mass transfer in the section. This is consistent with the normalized driving force concept, which compares the driving force to the gas phase composition at a discrete point in the column to determine the approach to a mass transfer pinch on a common basis through the column.

The following figures show the relative pinch profiles for the optimized packing distribution for coal-fired boiler cases that fall in a practical solvent operating range (1.1 to 1.8*L_{MIN}). At extreme solvent rates (high or low), the packing distribution will not have meaning as the column will either be pinched (close to L_{MIN}) or the driving forces will be large everywhere and intercooling position has no effect and the relative pinch concept is not meaningful.

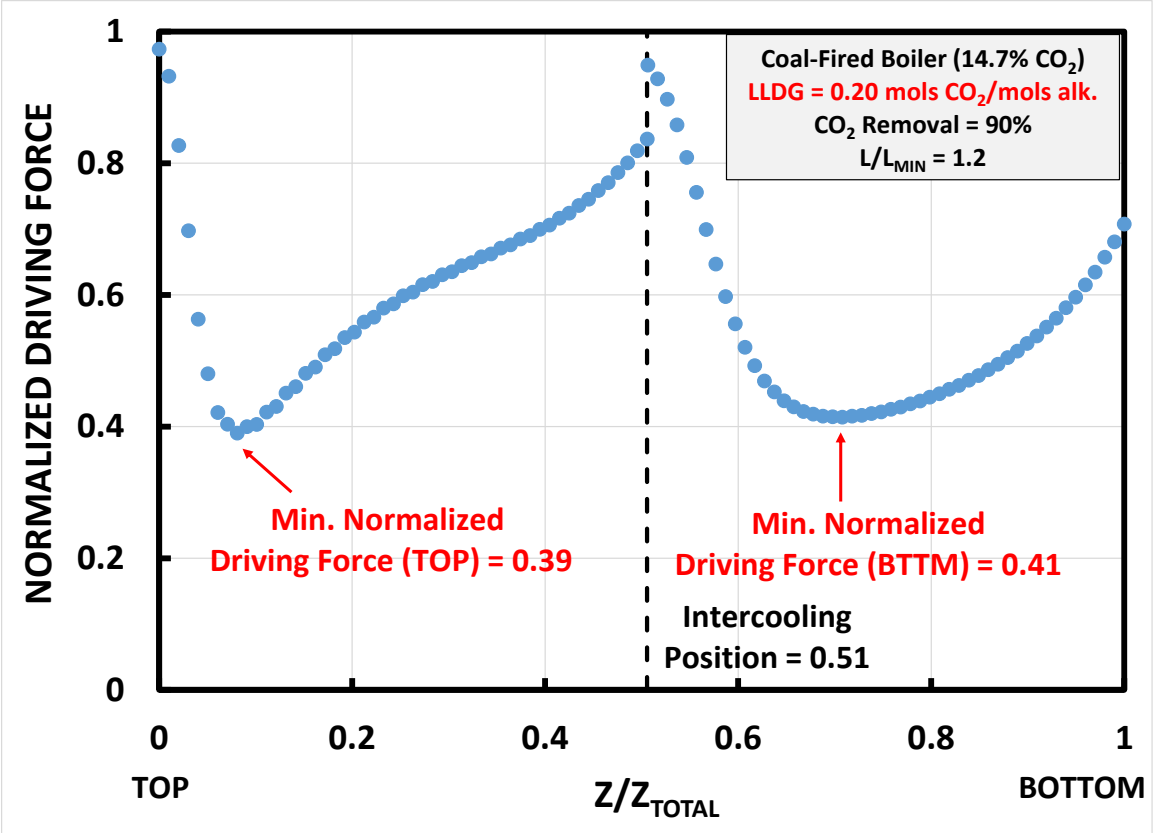

Figure 4-21: Normalized driving force profile @ LLDG = 0.20 mol CO_2/mol alk. and L/L_{MIN} = 1.2 (8 m PZ) for an in-and-out intercooled absorber with optimum packing split (minimize total packing area) for 90% CO_2 capture from a coal-fired boiler (14.7 mol% CO_2). Relative pinch (or minimum normalized driving force) identified for each packing section.

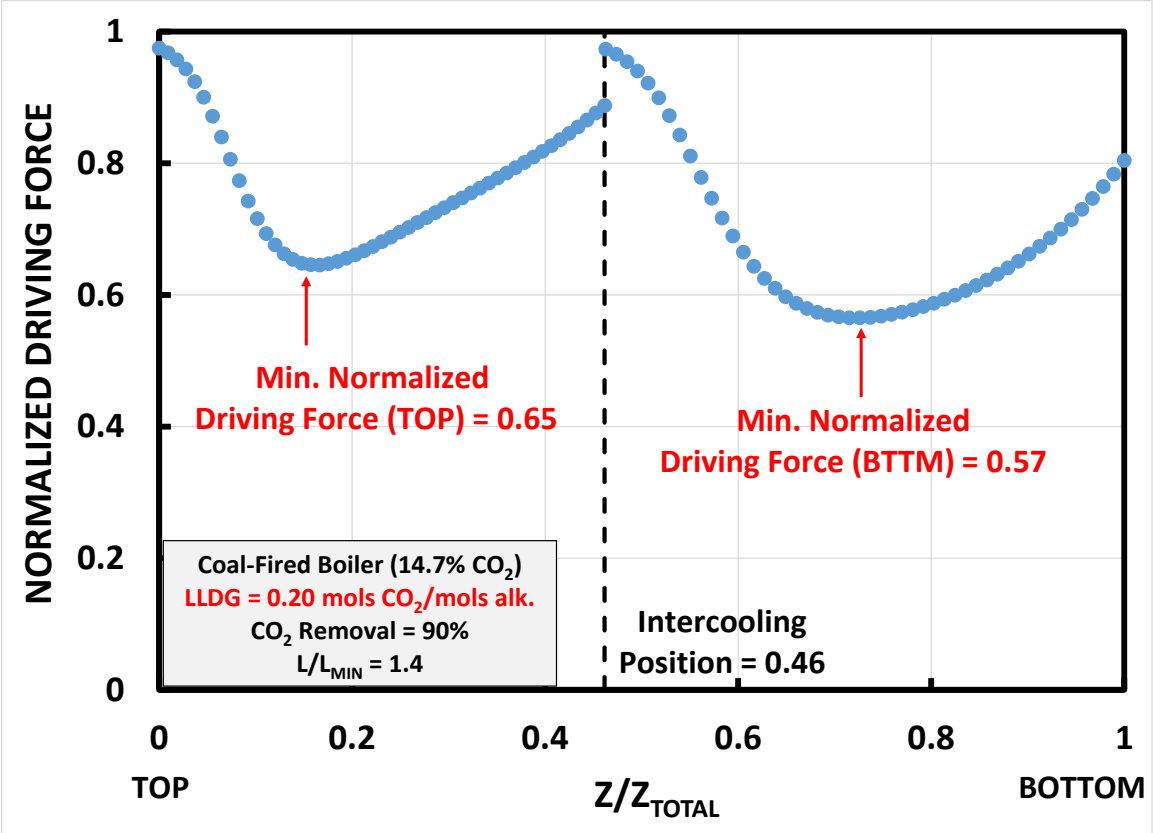

Figure 4-22: Normalized driving force profile @ LLDG = 0.20 mol CO_2/mol alk. and L/L_{MIN} = 1.4 (8 m PZ) for an in-and-out intercooled absorber with optimum packing split (minimize total packing area) for 90% CO_2 capture from a coal-fired boiler (14.7 mol% CO_2). Relative pinch (or minimum normalized driving force) identified for each packing section.

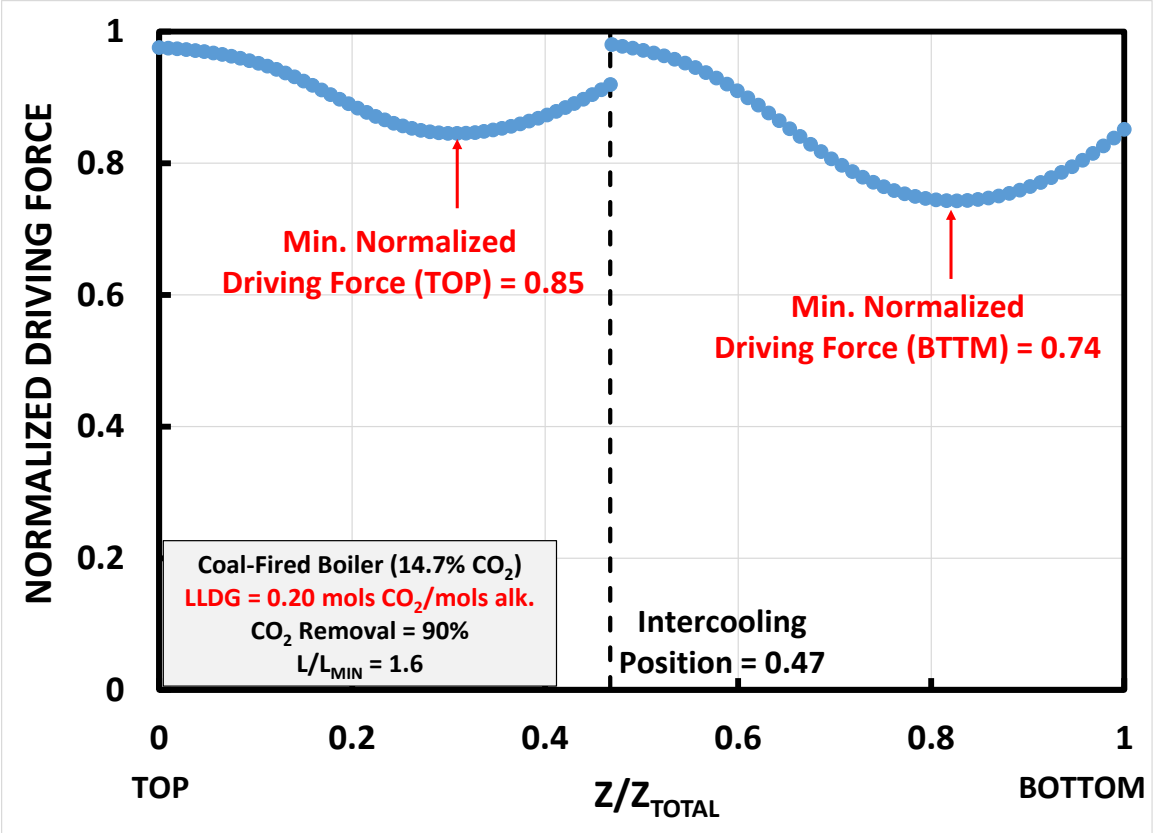

Figure 4-23: Normalized driving force profile @ LLDG = 0.20 mol CO_2/mol alk. and L/L_{MIN} = 1.6 (8 m PZ) for an in-and-out intercooled absorber with optimum packing split (minimize total packing area) for 90% CO_2 capture from a coal-fired boiler (14.7 mol% CO_2). Relative pinch (or minimum normalized driving force) identified for each packing section.

As the figures show, the relative pinch, and normalized driving force profile in general, is very closely matched in the two packing sections for all cases (minimum relative pinch values are within ~15% of one another). This trend is consistent for the NGCC and steel cases in a practical operating range as well. The deviation from balanced pinches can be explained by the HTU term in Equation 4.6, as the mass transfer efficiency may vary with position in the column. However, even with differences in mass transfer efficiency over the column, the relative pinch is a good predictor of optimal packing distribution in intercooled absorbers.

4.5.2 Quantifying Benefits of Intercooling and Potential for Development

For every point on a design curve for any absorber configuration, the solvent rate-packing area combination represents a unique design requirement to meet 90% CO_2 removal. In practice, this combination of solvent rate and packing requirement can be converted to a total cost, generating total cost curves for each design. The difference between any two cost curves would represent a total cost savings of the improved design. However, the goal of this analysis is not to develop a detailed economic optimum; rather, the goal is to screen for the conditions where a significant improvement can be made over an adiabatic or simple intercooled absorber (in-and-out intercooling) with an advanced design and to rank the operating conditions where the most benefit might be derived. Once this screening process is complete, unique novel absorber designs can be developed for specific operating conditions and detailed equipment design and economic evaluation are appropriate. Therefore, the method for evaluating the base case design (adiabatic or intercooled) will be to compare the integrated area between the base case design curve and the isothermal design curve. To perform the integration, limits on the area (x-axis) for the integration must be defined. A realistic operating window of solvent circulation rates based on the isothermal column was used to define the limits. The minimum and maximum area limits were defined by $1.8*L_{MIN,\ ISOTHERMAL}$ and $1.05*L_{MIN,\ ISOTHERMAL}$, respectively. Figure 4-24 depicts the aforementioned integration.

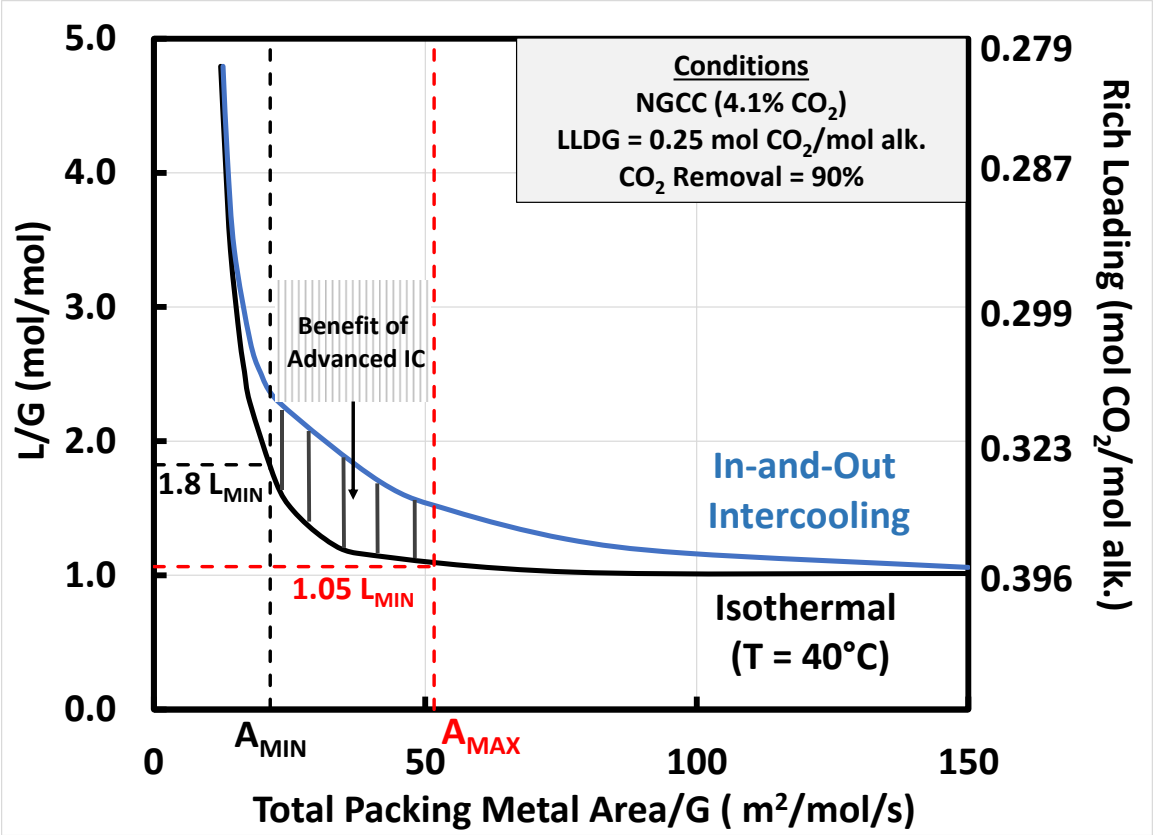

Figure 4-24: Integration method to quantify potential benefit of advanced intercooling. Each curve (solid = isothermal, blue = intercooled) represents the packing requirement to achieve 90% CO_2 removal for a fixed lean loading and given liquid to gas ratio (L/G). The maximum and minimum areas for integration are defined by the isothermal curve at 1.05 and 1.8 x L_{MIN}, respectively. The area between the two curves represents the maximum benefit achievable with an advanced IC design.

This method provides a proxy for the maximum benefit that can be derived by improvement over the base design. As mentioned, the isothermal design is the limiting design at the minimum solvent rate. At other conditions, the isothermal absorber only represents the best case for driving forces, and better designs could be developed by enhancing limiting mass transfer mechanisms. However, the isothermal case still serves as a well-defined common baseline for comparison. Detailed discussion of limiting mass

transfer phenomena in absorber systems with PZ will be discussed in Chapter 5 as part of discussing further improvement in absorber design.

In practice, the ratio of the area under the best case absorber design to the area under isothermal absorber design curve was used to quantify the "deviation" from isothermal performance – this provides a relative or normalized metric that allows comparison across the varying operating conditions in the 11 cases (different baselines in each case). Table 4-6 summarizes the results of the integration analysis. The large solvent rate region is excluded from the analysis due to the limited practical value of absorber development and operation at the extreme solvent flow rates in the region.

Table 4-6: Summary of Potential Benefits of Advanced Intercooling Design

NGCC (4.1 mol% CO_2)			
Intercooling Region	**LLDG (mol CO_2/mol alk.)**	**Intercooling Method**	Integrated "Intercooling Benefit"
Over-stripped	0.18	NONE	1.14
Simple Intercooling	0.25	In-and-Out IC	1.50
Advanced IC	0.30	In-and-Out IC	1.60
Coal (14.7 mol% CO_2)			
Intercooling Region	**LLDG (mol CO_2/mol alk.)**	**Intercooling Method**	Integrated "Intercooling Benefit"
Over-stripped	0.15	NONE	1.08
Simple Intercooling	0.20	In-and-Out IC	1.09
Advanced IC	0.26	In-and-Out IC	1.13
Steel (27 mol% CO_2)			
Intercooling Region	**LLDG (mol CO_2/mol alk.)**	**Intercooling Method**	Integrated "Intercooling Benefit"
Over-stripped	0.12	NONE	1.08
Simple Intercooling	0.18	In-and-Out IC	1.02
Advanced IC	0.22	In-and-Out IC	1.07

The table clearly highlights the importance of intercooling development for the NGCC application – in all three regions, the largest deviation between the best absorber design in the region and an isothermal absorber occur for the NGCC application. Specifically, in the simple intercooling and advanced intercooling regions, the NGCC application has a significantly larger potential benefit from improved intercooling design. In the simple intercooling region, despite achieving near isothermal capacity (Figure 4-3), in-and-out intercooling appears to suffer from driving force limitations when approaching the minimum solvent rate (Figure 4-15). Therefore, advanced intercooling concepts have potential in a region where L_{MIN} analysis would have suggested limited benefit.

The results for the coal-fired boiler and steel-blast furnace applications indicate that the base case design (adiabatic absorber in the over-stripped region, in-and-out intercooling in the other regions) performs well (ratios all under 1.15). Even in the advanced intercooling region, where the simple intercooling design is limited by a lean-end pinch at minimum solvent rate conditions, the benefits of a potential advanced design are modest in the operating range of the absorber. The coal-fired boiler in this advanced intercooling region may be the only condition outside of the NGCC application that merits consideration for novel design development.

4.6 CONCLUSIONS

Simple (in-and-out) intercooling was studied as a function of flue gas CO_2 concentration and operating conditions to quantify solvent capacity and mass transfer benefits, identify limitations of simple intercooling, and understand underlying phenomena to explain performance trends. The following major findings were developed:

4.6.1 Solvent Capacity Effects and Pinch Formation in Intercooled Absorbers

- Simple intercooling significantly improves solvent capacity over an adiabatic absorber (measured by minimum solvent rate analysis and approach to isothermal ideal, L_{MIN} /$L_{MIN,\ ISOTHERMAL}$) for all conditions in the analysis
    - Maximum Deviation from Isothermal (L_{MIN} /$L_{MIN,\ ISOTHERMAL}$):
        i. $NGCC_{INTERCOOLED}$ = 1.98

           $NGCC_{ADIABATIC}$ = 3.58
        ii. $COAL_{INTERCOOLED}$ = 1.31

            $COAL_{ADIABATIC}$ = 2.26
        iii. $STEEL_{INTERCOOLED}$ = 1.18

             $STEEL_{ADIABATIC}$ = 1.94
- Simple intercooling expands loading range where a limiting temperature pinch is avoided and isothermal capacity is approached (L_{MIN} /$L_{MIN,\ ISOTHERMAL}$ ≈ 1):
        i. $NGCC_{INTERCOOLED}$ = ≤ 0.25 mol CO_2/mol alkalinity

           $NGCC_{ADIABATIC}$ = ≤ 0.22 mol CO_2/mol alkalinity
        ii. $COAL_{INTERCOOLED}$ = ≤ 0.20 mol CO_2/mol alkalinity

            $COAL_{ADIABATIC}$ = ≤ 0.18 mol CO_2/mol alkalinity
        iii. $STEEL_{INTERCOOLED}$ = ≤ 0.18 mol CO_2/mol alkalinity

             $STEEL_{ADIABATIC}$ = ≤ 0.17 mol CO_2/mol alkalinity
- Pinch formation and performance limitation is different for an intercooled absorber:
    - True rich end pinch forms (not associated with temperature bulge at lean end).
    - Lean pinch forms at bulge above intercooler, but system is not equilibrium limited if bottom bed still achieves true rich pinch

- "Double pinch" forms associated with bulge in each section (above and below IC). System is equilibrium limited and requires solvent rate increase.

- Intercooling can effectively be viewed as two adiabatic absorbers operated in series:
  - First (top) absorber effectively operates with double the total heat capacity of the nominal inlet solvent – this is because all of the heat generated by CO_2 absorption in this bed is removed at the intercooler instead of returning to the lean end of the column as water condensing from the gas as in a normal adiabatic absorber.
  - Second (bottom) absorber operates as a normal adiabatic absorber.
  - New degree of freedom (CO_2 removed in each section) allows moderation of the effect of temperature bulges in column – bulge is split between two sections and removal in section prevents formation of pinch/minimizes effect of existing pinches.

4.6.2 Design Curves and Packing-Solvent Rate Trade-Offs

- Design curves were developed to evaluate the performance of intercooling in terms of packing (mass transfer) – solvent rate trade-off or the packing required to approach L_{MIN} for each absorber design. The difference between intercooled (or adiabatic) absorber and an isothermal absorber in normal solvent operating range (1.05 to 1.8 L_{MIN}) was quantified as the area between the design curves. The results for 3 relevant loading regions led to the following conclusions:

i. "Over-stripped" or low lean loading region: Adiabatic absorber provides good performance in terms of solvent capacity and mass transfer and should be the default design for this operating region.

ii. "Simple Intercooling" or mid-loading region: Simple Intercooling is effective for coal and steel (high CO_2 applications) and should be the default design. For NGCC, while in-and-out intercooling approximates isothermal behavior at L_{MIN}, the performance in the operating solvent range is poor due to driving force limitations. Novel intercooling development is warranted.

iii. "Advanced Intercooling" or mid-loading region: Simple Intercooling is effective for coal and steel (high CO_2 applications) and should be the default design despite the deviation in solvent capacity at the limiting case of L_{MIN}. NGCC performs poorly compared to an isothermal absorber and novel intercooling design development is needed

- Optimal Intercooling Location: The optimal intercooling location (minimize total packing area) was defined for all flue gas applications and select lean loadings as a function of L/L_{MIN}:
  - Underlying pinch at L_{MIN} determines the trend in optimal intercooling position as a function of solvent rate:
    i. Double pinch or temperature-induced rich pinch @ L_{MIN}: Optimal IC positions starts in bottom half of column (or near the middle) and moves up column as L/L_{MIN} increases
    ii. Only limiting lean pinch: Optimal IC positions starts in top half (above IC) of column and moves down column as L/L_{MIN} increases

iii. ALL CASES: As L/L_{MIN} reaches large values ($L/L_{MIN} > \approx 2$), IC is not needed and optimal location is the nearest "neutral" location in the column (mid-point or top).

iv. ALL CASES: In normal operating range for solvent rates ($L/L_{MIN} < 2$), optimal IC locations falls in the middle 50% of column ($Z_{INTERCOOLER}/Z_{TOTAL} = 0.25$ to 0.75)

- Normalized driving force concept was introduced to explain optimal intercooling location. The driving force through the column is normalized by the partial pressure of CO_2 in the bulk gas to provide a measure of solvent equilibrium constraint. The optimal location of IC occurs when the "relative pinch" (or minimum normalized driving force) is equivalent on both sides of the intercooler. This result is consistent for all flue gas concentrations within the normal solvent operating window ($L/L_{MIN} = 1.1$ to 1.8).

Chapter 5: Mass Transfer Parameter Sensitivity Analysis

Absorber design choices reflect a balance between operating costs imposed on the capture system (via solvent circulation rate and rich loading) and capital costs (packing for mass transfer and absorber column structure). Previous work by the authors has focused on the use of intercooling in absorber columns to address equilibrium (or driving force) limitations imposed on absorber performance by elevated temperatures associated with heat of absorption (Sachde & Rochelle, 2014). However, addressing these limitations primarily impacts the operating cost of the system by reducing the solvent circulation requirements. Intercooling should be coupled with enhanced mass transfer performance to minimize packing requirement and capital costs of the absorber required to achieve solvent capacity benefits (Sachde & Rochelle, 2014).

Rate-based absorber models represent coupled differential equations for mass transfer with chemical reaction and heat transfer subject to constraints imposed by phase and thermal equilibria. The parameters defining the transport, kinetic and thermodynamic models are not explicitly varied in process optimization, but understanding the relative importance of each of the fundamental contributions to mass transfer rates can guide design and development of absorbers. Furthermore, sensitivity analysis of parameters in the underlying models allows comparison of model behavior to theoretical understanding of the process and can identify limitations or shortcomings of the overall absorber model. The focus of the current work will be to identify the limiting or controlling phenomena for mass transfer in an absorber utilizing concentrated piperazine (PZ) as the solvent. The controlling components of mass transfer resistance will be identified via sensitivity analysis of CO_2 transfer rates to mass transfer parameters as a function of operating conditions and flue gas source. The sensitivity analysis is also repeated over a range of

parameter values to represent uncertainty in the models and to generalize results for alternate amine systems, equipment specifications, or operating conditions. Theoretically limiting, or asymptotic cases, will be used to validate the sensitivity results and to provide insight into the fundamental mechanisms controlling mass transfer resistance in the absorber.

5.1 RATE-BASED MODELING FRAMEWORK

All analysis in this work will utilize aqueous piperazine (PZ) as the solvent for CO_2 absorption. The rate-based model used to rigorously evaluate CO_2 absorption into PZ can be described by its three major components:

1) solvent thermodynamic and kinetic model,
2) packing mass transfer model, and
3) numerical integration scheme.

5.1.1 PZ Solvent Model – Thermodynamics and Kinetics

The solvent model for PZ ("Independence" model) was developed in Aspen Plus® and consists of a thermodynamic and kinetic framework with parameters regressed from experimental data (Frailie, 2014). The thermodynamic model for the PZ-H_2O-CO_2 system was developed from experimental data for amine pKa, CO_2 solubility, heat capacity, speciation, and amine volatility by regression of Gibbs free energy, enthalpy, heat capacity, Henry's constant and activity coefficient parameters within the electrolyte non-random two liquid (e-NRTL) framework.

The reaction set for the PZ model is as follows:

$$PZCOO^- + PZH^+ \leftrightarrow H^+PZCOO^- + PZ \quad 5.1$$

$$PZCOO^- + H_2O + CO_2 \rightarrow H^+PZCOO^- + HCO_3^- \quad 5.2$$

$$2PZ + CO_2 \rightarrow PZH^+ + PZCOO^- \quad 5.3$$

$$2PZCOO^- + CO_2 \rightarrow H^+PZCOO^- + PZ(COO)_2{}^{2-} \quad 5.4$$

Arrhenius rate expressions were used to define rates for the kinetic reactions where the pre-exponential and activation energy parameters were regressed from wetted wall column data collected over a range of temperatures, solvent concentrations, and loadings relevant for capture applications considered in this work (Frailie, 2014). Reactions 2 through 4 are reversible and have corresponding reverse rate expressions which were regressed with the constraint of the equilibrium constant to ensure consistency with the thermodynamic model.

Finally, physical property models for binary diffusion coefficients, viscosity, and density were regressed as a function of amine concentration, loading, and temperature. The diffusion coefficient representations are particularly important in the subsequent sensitivity analysis. Two effective diffusion coefficients are specified for the liquid phase in the mass transfer model. The binary diffusion coefficients of CO_2, N_2, and O_2 (small molecules with low critical temperatures/limited physical solubility) were treated identically. Equation 5.5 specifies the effective diffusion coefficient of CO_2 (and N_2/O_2) in amine solution.

$$D_{CO_2,Am} = D_{CO_2,H_2O}\left(\frac{\mu_{H_2O}}{\mu_{Am}}\right)^{0.8} \quad 5.5$$

where:

D_{AB} = Binary Fickian diffusion coefficients;

μ_{Am} = Viscosity of loaded amine solution.

The relationship between diffusion of CO_2 in amine solutions and in water was determined by the modified Stokes-Einstein relation (Versteeg & van Swaaij, 1988). All remaining binary diffusion coefficients in the system (amine, water, and reaction product binary pairs) are represented by the effective diffusion coefficient in Equation 5.6.

$$D_{Am/Prod} = D_O \left(\frac{T}{313.15} \right)^{\beta} \left(\frac{\mu_{Am}}{0.0155} \right)^{\alpha} \quad 5.6$$

where:

D_O = Regression constant = 2.26 x 10^{-10};

T = Operating temperature (K);

β = Regression Constant = -2.58;

α = Regression Constant = -1.45;

μ = Viscosity of loaded amine solution (Pa-s).

Equation 5.6 is strictly an empirical expression which was regressed via wetted wall column data that included a range of solvent concentration, loading, and temperature (and implicitly, viscosity) (Frailie, 2014). As the system moves from the pseudo first order (PFO) limit to the instantaneous reaction limit (i.e., diffusion of amine and amine products controlled), the effect of temperature and viscosity on mass transfer will change, in part, via the controlling diffusion coefficient.

5.1.2 Packing Mass Transfer Model

The specific effects of fluid mechanics on mass transfer are determined by incorporating models for mass transfer in packed beds. Experiments in a pilot scale air-water column were used to develop semi-empirical models for interfacial area (a^I) and

gas- and liquid-side physical mass transfer coefficients (k_G and k_L). The interfacial area model used in this was developed by Tsai and is represented in Equation 5.7 (Tsai, 2010):

$$\frac{a^I}{a_p} = 1.34 * \left[\left(\frac{\rho_L}{\sigma} \right) g^{1/3} \left(\frac{Q}{L_p} \right)^{4/3} \right]^{0.116} \quad 5.7$$

where:

a^I = Effective or interfacial area of packing (m^2/ m^3);

a_p = Specific (geometric) area of packing (m^2/ m^3);

ρ_L = Liquid mass density (kg/ m^3);

σ = Surface tension (N/m);

g = Gravitational acceleration (m^2/s);

Q = Liquid volumetric flow rate (m^3/s);

L_p = Wetted perimeter in cross-sectional slice of packing (m).

The mass transfer coefficient models (Equations 5.8 and 5.9) were developed from data collected by Wang (Wang, 2015). All parameters in the equations were normalized to reference values (not shown) during the regression. Raw data and details of the regression included in Appendix A.

$$\frac{k_{L,AB}}{D_{AB}^{0.5}} = A * \left(u_L / a_p \right)^{x1} * \left(M_i \right)^{x2} * \left(\mu_L \right)^{x3} \quad 5.8$$

$$\frac{k_{G,AB}}{D_{AB}^{0.67}} = A * \left(u_G / a_p \right)^{y1} * \left(M_i \right)^{y2} \quad 5.9$$

where:

$k_{\#, AB}$ = Binary physical mass transfer coefficients, # = L(liquid) or G (gas) (m/s);

$u_{\#}$ = Superficial velocity, # = L(liquid) or G (gas) (m/s);

M_i = Mixing number - dimensionless parameter describing the number of mixing points in a characteristic volume of packing;

μ_L = Liquid viscosity (Pa-s).

The viscosity dependence assigned in Equation 5.8 represents the effect of viscosity on fluid mechanics and was derived via literature review (Appendix A). An additional viscosity effect enters the mass transfer coefficient via the binary diffusion coefficient (Equations 5.5 and 5.6). The overall dependence of the liquid-side mass transfer coefficient on viscosity (function of loading, temperature, and amine concentration) will be important in evaluating the results of mass transfer parameter sensitivity.

5.1.3 Numerical Integration Method

The integration of a rate-based stage (as depicted in Figure 5-1) at steady state includes three sets of differential equations: 1) component bulk material balance, 2) component film material balance, 3) constitutive mass transfer relationships. The following equations are presented in difference form (algebraic system) for the liquid phase as implemented in the numerical integration in Aspen Plus®.

$$0 = L_{j-1}x_{ij-1} - L_j x_{ij} + N_{ij}^{L} + r_{ij}^{L} \qquad 5.10$$

$$0 = N_{ij}^{INTF} - N_{ij}^{L} + r_{ij}^{film,L} \qquad 5.11$$

$$0 = \left[\Gamma_j^L\right](\bar{x}_j^{Intf} - \bar{x}_j) + \Delta\phi_j^E(\bar{x}_j\,\bar{z}_j) + \left[R_j^L\right](\bar{N}_j^L - N_t^L\bar{x}_j) \qquad 5.12$$

Where brackets [ ] indicate C-1 x C-1 matrix, overbar indicates C-1 vector, and:

j = Stage;

$\Delta\Phi^E$ = Electric potential driving force in ionic solutions;

z = Electric charge number of species;

R = Inverse mass transfer coefficient matrix;

N_t = Total molar flux = $\sum_{i=1}^{C} N_i$;

Equations 5.11 and 5.12 are also written for each segment in the discretized liquid film (see (Frailie, 2014), (Plaza, 2011), or (Chen, 2011) for film discretization schemes). Analogous vapor phase equations are implemented without reaction terms or discretization in the vapor film.

Equation 5.12 represents the Maxwell-Stefan constitutive equations for multi-component mass transfer relating the individual flux for each species to the driving force of all other species (Taylor & Krishna, 1993). The components of the inverse mass transfer coefficient matrix, which introduces coupling of binary mass transfer coefficients, can be defined as follows:

$$R_{ii} = \frac{x_i}{\rho a^I \kappa_{iC}} + \sum_{\substack{k=1 \\ k\neq i}}^{C} \frac{x_k}{\rho a^I \kappa_{ik}} \quad for\ i = 1:C-1$$
$$R_{ik} = -x_i\left(\frac{1}{\rho a^I \kappa_{ik}} - \frac{1}{\rho a^I \kappa_{iC}}\right) \quad for\ i = 1:C-1, i \neq k \qquad 5.13$$

The Maxwell-Stefan relationships add coupling of mass transfer outside of chemical reactions, but as discussed in Appendix B, these effects are unimportant for the mass transfer of CO_2 as specified in the "Independence" model. Several other

simplifications can be made to the above equations to allow for analytical evaluation of CO_2 mass transfer in amines using film theory at the asymptotic conditions discussed previously. The results of this evaluation are also discussed in detail in Appendix B.

5.2 MASS TRANSFER WITH FAST CHEMICAL REACTION

The rigorous mathematical description of the reaction-diffusion problem in CO_2 absorption by amines can be described by the species continuity equations for each component in each phase.

$$\frac{\partial c_i^P}{\partial t} = -\left(\frac{\partial N_i^P}{\partial x} \right) + R_i, \; for \; i = 1:C \tag{5.14a}$$

$$N_i^L = N_i^V, \; f_i^L = f_i^V \; @ \; Interface \tag{5.14b}$$

where:

C = Total number of components;

c^P_i = Molar concentration of species i, phase p (vapor or liquid);

N^P_i = Molar flux of species i, phase p (vapor or liquid);

f^P_i = Fugacity of species i, phase p (vapor or liquid);

R_i = Rate of production of moles of i per unit volume produced by chemical reaction.

The molar flux in Equation 5.14 can be defined in terms of driving forces or gradients via a constitutive relationship such as Fick's Law or the Maxwell-Stefan relations (Taylor & Krishna, 1993) as illustrated in the numerical methods in the previous section. The solution to the system of coupled differential equations and associated boundary conditions yield concentration profiles and transfer rates for each of the components in the system.

While the differential equations provide a full description of the physical system, isolating the effect of the physical parameters embedded in the equations on mass transfer rates requires a description of the solution to the system of equations. The concentration profiles in Figure 5-1 provide a general representation of absorption and reaction of CO_2 in amine solvents.

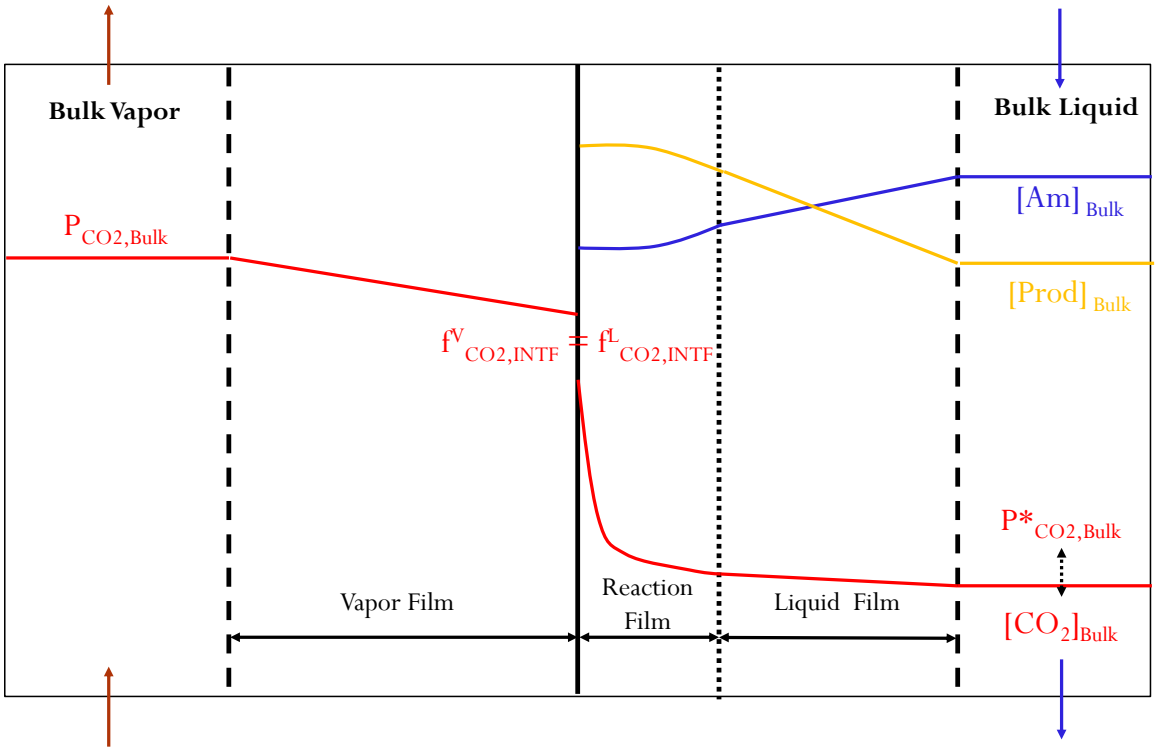

Figure 5-1: Concentration profiles for mass transfer with fast chemical reaction. In the case of CO_2 absorption by PZ, as many as 10 components may be present in the film due to reaction chemistry, but CO_2, amine (Am), and products (Prod) define the general categories relevant to mass transfer. Free CO_2 is at equilibrium at the vapor-liquid interface. P^{*}_{CO2} represents the partial pressure of CO_2 in equilibrium with the bulk liquid composition. The entire liquid film (liquid and reaction film) is discretized for numerical integration.

The distinctive feature of the film model for mass transfer with fast chemical reaction (e.g., CO_2 reaction with amines) is the presence of a "reaction film" where the

CO_2 concentration profile exhibits a steep gradient. A majority of the chemical reaction takes place in this portion of the film, with the remainder of the liquid film primarily representing diffusion of reactants and products. The representation as discrete stagnant films is a simplification of the actual physical phenomena in an absorber (i.e., counter-currently flowing bulk fluids with turbulent flow features present in each film and a non-uniform interface between phases). However, the film model identifies the key components of overall mass transfer resistance and can be used to develop a general mathematical description of mass transfer with chemical reaction for each of the components.

The mass transfer rates corresponding to the concentration profiles in Figure 5-1 can be represented in terms of gas-phase, liquid-phase, or overall driving forces:

$$N_{CO_2} = k_G(P_{CO_2}^{Bulk} - P_{CO_2}^{Intf}) \quad 5.15a$$

$$N_{CO_2} = Ek_{L,CO_2}([CO_2]^{Intf} - [CO_2]^{Bulk}) \quad 5.15b$$

$$N_{CO_2} = K_G(P_{CO_2}^{Bulk} - P_{CO_2}^{*Bulk}) \quad 5.15c$$

where:

N_{CO2} = CO_2 molar flux;

k_G = Gas-side physical mass transfer coefficient for CO_2;

P_{CO2}^{Bulk} = Partial pressure of CO_2 in bulk vapor;

P_{CO2}^{Intf} = Partial pressure of CO_2 at gas-liquid interface;

$k_{L,CO2}$ = Liquid-side physical mass transfer coefficient for CO_2;

$[CO_2]^{Bulk}$ = Concentration of free (unreacted) CO_2 in bulk liquid;

$[CO_2]^{Intf}$ = Concentration of free (unreacted) at gas-liquid interface;

E = Enhancement factor = $\left(N_{CO_2,REACTION} \Big/ N_{CO_2,NO\ REACTION} \right)$;

K_G = Overall gas-phase driving force based mass transfer coefficient;

P^{*Bulk}_{CO2} = Partial pressure of CO_2 in equilibrium with bulk liquid composition;

The CO_2 flux is equivalent for all expressions in Equation 5.15 if considered at the gas-liquid interface (via continuity) and can be used to define a series resistance model based on film theory:

$$\frac{1}{K_G} = \frac{1}{k_G} + \frac{H_{CO_2}}{Ek_{L,CO_2}} \qquad 5.16$$

where:

H_{CO2} = Henry's constant of CO_2 in amine solution.

The details of the rigorous solution to the system of differential equations are embedded in the concentration profiles and mass transfer coefficients used to define the CO_2 flux. The gas and liquid physical mass transfer coefficients (and associated physical and transport properties) in Equation 5.16 are described by semi-empirical models detailed in Equations 5.8 and 5.9. The enhancement factor describes the effect of chemical reaction on the flux of CO_2 and can be described in terms of asymptotic cases. The asymptotic solutions provide a clear relationship between flux and the individual mass transfer, kinetic, and physical properties that will guide the sensitivity analysis for the rigorous numerical model of the absorber.

5.2.1 Pseudo-First-Order Limit

The system of equations represented by Equation 5.14 can be solved analytically for CO_2 transfer in the liquid film at steady-state with several assumptions. The primary assumption made at the pseudo-first-order (PFO) asymptotic condition is that the amine

concentration is constant at the bulk value throughout the liquid film (not depleted by reaction/limited by diffusion). This condition and solution to the differential equation was considered in detail by Danckwerts and is reviewed in Appendix B (Danckwerts, 1970). The final expressions for flux are presented in Equations 5.17 and 5.18.

$$N_{CO_2} = k_{L,CO_2} \frac{Ha}{\tanh(Ha)} \left([CO_2]^{Intf} - \frac{[CO_2]^{Bulk}}{\cosh(Ha)} \right) \qquad 5.17$$

$$Ha = \sqrt{\frac{k_1 D_{CO_2}}{k_{L,CO_2}^{\ 2}}}$$

where:

k_1 = Pseudo-first-order rate constant = $k_2[Am]^{Bulk}$;

Ha = Hatta number;

When the Hatta number is greater than ~5, the hyperbolic tangent term in Equation 5.17 approaches 1 and the hyperbolic cosine term approaches infinity. This range for the Hatta number is consistent with the pseudo-first-order assumption (fast, but not instantaneous, reaction). Under this simplification, the flux of CO_2 can be expressed as:

$$N_{CO_2} = k_{L,CO_2} Ha [CO_2]^{Intf} \qquad 5.18a$$

$$N_{CO_2} = k_{L,CO_2} E^{PFO} [CO_2]^{Intf} \qquad 5.18b$$

$$N_{CO_2} = \sqrt{k_1 D_{CO_2}} [CO_2]^{Intf} \qquad 5.18c$$

where:

E^{PFO} = Pseudo-first-order enhancement factor = $Ha = \sqrt{\frac{k_1 D_{CO_2}}{k_{L,CO_2}^{\ 2}}}$.

The flux at PFO conditions is independent of the liquid-film physical mass transfer coefficient and has a half-order dependence on the diffusion coefficient of CO_2 and pseudo-first-order reaction constant. Equation 5.19 provides an alternate definition for the liquid-film mass transfer coefficient if the driving force is converted to a partial pressure driving force. This description is useful for experimental measurements of absorption at PFO conditions since the driving force is typically quantified in the gas phase.

$$N_{CO_2} = \frac{\sqrt{k_1 D_{CO_2}}}{H_{CO_2}} P^I_{CO_2} \tag{5.19a}$$

$$N_{CO_2} = k_g^{'} P^I_{CO_2} \tag{5.19b}$$

where:

$k_g^{'}$ = Liquid-film mass transfer coefficient in terms of gas phase driving force.

The pseudo-first-order solution provides one bounding condition for the sensitivity analysis.

The flux expressions in the preceding equations are presented for a single irreversible chemical reaction for simplicity since the general expression for the enhancement factor will be the same for reversible reactions – the reversibility is only relevant when considering the driving force at the PFO limit. Equation 5.20 is the Hatta number for the CO_2-PZ system represented by the Independence model.

$$Ha \approx \sqrt{\frac{(k_{PZ} a_{PZ} a_{PZCOO^-} \gamma_{CO_2} + k_{PZCOO^-} a^2_{PZCOO^-} \gamma_{CO_2}) D_{Am/\mathrm{Prod}}}{\overline{\rho} k_{L,CO_2} k_{L,Am/\mathrm{Prod}}}} \tag{5.20}$$

where:

k_{PZ} = Forward kinetic constant for reaction 5.3 (PZ acts as base);

k_{PZCOO-} = Forward kinetic constant for reaction 5.4 ($PZCOO^-$ acts as base);

a_i = Activity of component i (PZ or $PZCOO^-$);

γ_{CO2} = Activity coefficient of CO_2;

$\bar{\rho}$ = Molar density of loaded solution.

The modified Hatta number was derived by converting Equation 5.14 to dimensionless form when the reaction source term includes the forward rates of the two major reactions in the PZ-CO_2 system (reactions 5.3 and 5.4). Bicarbonate rates are not significant at conditions in this analysis allowing omission of reaction 5.2 in the Hatta number derivation. In addition, the Hatta number in Equation 5.20 is modified to account for activity based kinetics in the Independence model. The appearance of a mass transfer coefficient and diffusion coefficient representing amine and products in place of the expected CO_2 mass transfer dependence reflects an issue that arises from the implementation of film theory and calculation of film thickness as part of the numerical integration performed in Aspen Plus®. This issue is detailed in Appendix B.

5.2.2 Instantaneous Reaction Limit

Analytical solutions can also be developed for Equation 5.14 by considering the limit where chemical reaction occurs instantaneously when compared to diffusion. For reversible chemical reactions, chemical equilibrium is maintained at all points in the liquid film. Secor and Butler and Danckwerts used the method of Olander to illustrate that the differential equations (5.14) can be reduced to a balance between the diffusional flux of reactants and products by eliminating chemical reaction source terms via the chemical equilibrium constraint (Secor & Butler, 1967), (Danckwerts, 1970), (Olander,

1960). The flux and enhancement factor at the instantaneous reaction limit can then be described as follows after solving the new set of differential equations:

$$N_{CO_2} = E^{\infty} k_{L,CO_2} \left([CO_2]^{Intf} - [CO_2]^{*Bulk} \right)$$
$$E^{\infty} = 1 + \frac{k_{L,Am/\mathrm{Prod}} \left([\mathrm{Prod}]^{*Intf} - [\mathrm{Prod}]^{*Bulk} \right)}{k_{L,CO_2} \left([CO_2]^{Intf} - [CO_2]^{*Bulk} \right)} \qquad 5.21$$

where:

E^{∞} = Instantaneous reaction enhancement factor;

$[CO_2]^{*Bulk}$ = Equilibrium concentration of free (unreacted) CO_2 in bulk liquid;

$[CO_2]^{Intf}$ = Concentration of free (unreacted) CO_2 at gas-liquid interface;

$k_{L,Am/Prod}$ = Liquid-side physical mass transfer coefficient for amine and products;

$[Prod]^{*Bulk}$ = Equilibrium concentration of products in bulk liquid;

$[Prod]^{*Intf}$ = Equilibrium concentration of products at gas-liquid interface;

For the CO_2-PZ system used in this work, the concentration of products can be approximated as the total concentration of CO_2 in all forms (free and reacted)[3] since reaction products will be the dominant form of CO_2 present in the system at equilibrium. In addition, the leading term (unity) of the enhancement factor in Equation 5.21 is not significant for the range of values for the E^{∞} expected for this amine system. The enhancement factor for the CO_2-PZ system can be written as:

$$E^{\infty} \approx \frac{k_{L,Am/\mathrm{Prod}} \left([CO_2]^{*Intf}_{TOTAL} - [CO_2]^{*Bulk}_{TOTAL} \right)}{k_{L,CO_2} \left([CO_2]^{Intf} - [CO_2]^{*Bulk} \right)} \qquad 5.22$$

where:

[3] $[CO_2]^{TOTAL} = [CO_2]+[PZCOO^-]+[HCO_3^-]+[PZH^+]+[H^+PZCOO^-]+2*[PZ(COO)_2^{2-}]$

E^{∞} = Instantaneous reaction enhancement factor;

$[CO_2]^{*Bulk}$ = Equilibrium concentration of free (unreacted) CO_2 in bulk liquid;

$[CO_2]^{Intf}$ = Concentration of free (unreacted) CO_2 at gas-liquid interface;

$k_{L,Am/Prod}$ = Liquid-side physical mass transfer coefficient for amine and products;

$[CO_2]_{TOTAL}^{*Bulk}$ = Total concentration of all species containing CO_2 in bulk liquid at equilibrium;

$[CO_2]_{TOTAL}^{*Intf}$ = Total concentration of all species containing CO_2 at gas-liquid interface at equilibrium;

5.2.3 Dimensionless Group from Asymptotic Limits

The enhancement factors for the pseudo-first-order and instantaneous reaction limits represent the relevant bounding cases for the mass transfer with fast chemical reaction and the flux predicted by the absorber model should fall between these asymptotic limits. Previous researchers have used the limiting enhancement factors to qualitatively predict if a particular system is operating at or near one of the limiting conditions (Danckwerts, 1970):

$$\begin{aligned} &\text{PFO Limit}: 1 << Ha << E^{\infty} \\ &\text{Instantaneous Limit}: 1 << E^{\infty} << Ha \end{aligned} \qquad 5.23$$

The relationships defined in Equation 5.23 were developed considering single reversible reactions, but should be generally applicable. In the case of fast reactions with amines, the constraint that the enhancement factors must each be much larger than unity is generally satisfied as this is a definition of fast reaction. Equation 5.23 can be simplified and re-arranged into the following expressions:

$$\text{PFO Limit}: \phi = Ha/E^{\infty} << 1$$
$$\text{Instantaneous Limit}: \phi = Ha/E^{\infty} >> 1 \qquad 5.24$$

A new dimensionless ratio (referenced in this work as reaction enhancement ratio, Φ) is defined and compared to unity to determine approach to the limiting asymptotes. While Equation 5.24 is still qualitative since it is not an exact expression, this work will propose to define the limits quantitatively for the PZ system. In addition, it is hypothesized that a ratio near unity (Φ ≈ 1) indicates that the liquid film will be equally controlled by reaction and diffusion. Establishing consistency between results of the sensitivity analysis (described in the next section) and the predictions of Φ will provide theoretical validation of the absorber model and sensitivity analysis method. In addition, if Φ is well correlated with sensitivity analysis results, the ratio can provide fundamental explanations for trends in the controlling resistance in the absorber (e.g., function of position in the absorber, operating conditions, etc.).

Finally, the asymptotic enhancement factors can be used to expand the series resistance model proposed in Equation 5.16 to include the full range of conditions in the liquid film:

$$\frac{1}{K_G} = \frac{1}{k_G} + \frac{H_{CO_2}}{E^{PFO} k_{L,CO_2}} + \frac{H_{CO_2}}{E^{\infty} k_{L,CO_2}}$$
$$\frac{1}{K_G} = \frac{1}{k_G} + \frac{H_{CO_2}}{Ha\, k_{L,CO_2}} + \frac{m}{k_{L,Am/\mathrm{Prods}}}, m = \frac{\Delta P_{CO_2}}{\Delta [CO_2]^*_{TOTAL}} \qquad 5.25$$
$$\frac{1}{K_G} = \frac{1}{k_G} + \frac{1}{k_G^{'}} + \frac{m}{k_{L,Am/\mathrm{Prods}}}, m = \frac{\Delta P_{CO_2}}{\Delta [CO_2]^*_{TOTAL}}$$

where:

m = Slope of the vapor-liquid equilibrium curve.

The two equivalent expressions in Equation 5.25 represent the discrete sections of the liquid film in Figure 5-1 (reaction and diffusion) and reduce to the appropriate asymptotic limits based on the conditions defined in Equation 5.24. Note that the expressions in Equation 5.25 are not an exact solution for all condtions between the asymptotes as simple addition of asymptotic solutions is not a sufficiently general representation of the reaction-diffusion problem solution (see, for example (DeCoursey, 1982)).

Nonetheless, the series resistance model provides a good description of the various components of the overall mass transfer resistance. Therefore, the components of mass transfer resistance that must be considered in the sensitivity analysis can be defined from Equation 5.25 as gas-film diffusion resistance, chemical reaction resistance, and liquid-film diffusion resistance.

5.3 Mass Transfer Sensitivity Analysis Methods

The theoretical framework summarized in Equation 5.25 identifies the parameters that will be considered as part of the absorber sensitivity analysis. The sensitivity of CO_2 flux to gas-film diffusion resistance, chemical reaction resistance, and liquid-film diffusion resistance will be evaluated as described by Equation 5.26.

$$\left(\frac{\partial \ln N_{CO_2,i}}{\partial \ln \theta_n} \right)_{N_{CO_2,j\neq i},\theta_{m\neq n}} \quad \text{for Stages } i = 1 : N_{Stages} \quad \text{for Parameters } n = 1:3 \qquad 5.26$$

where:

Θ_n = Mass transfer parameter:

$\Theta_1 = k_G$, $\Theta_2 = k_L$, $\Theta_3 = \sqrt{k_{Rxn}}$;

k_{Rxn} = All forward and reverse rate constants ;

N_{Stages} = Total number of stages in absorber;

For each case evaluated in this study (see Table 5-1), mass transfer parameters were independently perturbed by +/- 1% for each stage of the absorber and the corresponding change in flux was recorded. The perturbation size for the parameters was selected to ensure local linearity of the flux as a function of all parameters to allow numerical approximation of the partial derivative while generating a computationally significant change in the flux. The partial derivatives in Equation 5.26 are calculated by averaging the flux over the range of perturbation in each parameter. The final result is a fractional resistance for each stage in the absorber that can be attributed to gas-side diffusion resistance, chemical reaction resistance, and liquid-film diffusion resistance. These 3 resistances should sum to approximately 1 if they account for all mass transfer resistance.

The sensitivity analysis was performed over a range of absorber operating conditions summarized by the cases in Table 5-1.

Table 5-1: Sensitivity Analysis Case and Operating Condition Summary. Conditions that differ from the base case (Case 1) are highlighted in the table.

Case	Flue Gas Source (mol % CO_2)	Solvent Concentration	Intercooling	LLDG	L/L_{MIN}	RLDG	k_L Value
		molal		mol CO2/mol alk.		mol CO2/mol alk.	
1	COAL (14.7%)	8	ISOTHERMAL	0.15	1.2	0.375	Base
2	COAL (14.7%)	8	***NONE***	0.15	1.2	0.375	Base
3	COAL (14.7%)	8	ISOTHERMAL	0.15	***1.8***	0.300	Base
4	COAL (14.7%)	8	ISOTHERMAL	***0.20***	1.2	0.380	Base
5	COAL (14.7%)	8	ISOTHERMAL	***0.26***	1.2	0.395	Base
6	COAL (14.7%)	***5***	ISOTHERMAL	0.15	1.2	0.371	Base
7	COAL (14.7%)	8	ISOTHERMAL	0.15	1.2	0.375	***5*Base***
8	COAL (14.7%)	8	ISOTHERMAL	0.15	1.2	0.375	***0.8*Base***
9	COAL (14.7%)	8	ISOTHERMAL	0.15	1.2	0.375	***0.5*Base***
10	***NGCC (4.1%)***	8	ISOTHERMAL	0.15	1.2	0.354	Base
11	***STEEL (27.1%)***	8	ISOTHERMAL	0.15	1.2	0.384	Base
12	COAL (14.7%)	8	***NONE***	0.15	1.2	0.375	***0.2 Base***
All Cases: **1) CO_2 Removal = 90%** **2) MP-250X Packing** **3) Max Approach to Flood = 70%**							

Case 1 will serve as the base case. The lean loading (0.15 mol CO_2/mol alkalinity) is outside of the normal operating window for 8 m PZ due to solubility concerns. However, the low value for lean loading ensures large variation in loading over the absorber to

provide insight into the effect of loading on mass transfer resistance. Furthermore, the base lean loading is in an operating region where intercooling is not necessary to achieve maximum solvent capacity (minimum solvent circulation rate) so the systematic effects of temperature can be studied without being conflated with solvent circulation effects (Sachde & Rochelle, 2014).

5.3.2 Mass Transfer Parameter Values

The base parameter values for all mass transfer parameters are those defined in the Independence model and discussed in section 5.1. Specifically, the base value for the liquid-side mass transfer coefficient is defined by Equation 5.8. Table 5-1 includes cases for high and low parameter values for k_L. These alternate values were selected to move the system towards asymptotic limits – high k_L values move the absorber closer to the PFO limit (reduces the Hatta number, c.f., Equation 5.20) and low k_L values move the absorber closer to the instantaneous limit (increases the Hatta number). Since all of the parameters in the liquid film are related by a dimensionless group, Φ (Equation 5.24), only one parameter needs to be modified to move the system towards a limiting condition. The value of k_L also has the largest degree of uncertainty among the mass transfer parameters evaluated in this work, and thus represents bounding cases for the model results in general. The k_L model details and range of values are discussed in Appendix A.

5.4 RESULTS

5.4.1 Validation of Dimensionless Group Method

The reaction enhancement ratio (Φ) defined from asymptotic enhancement factors can be compared to the parameter sensitivity results. Specifically, for each stage in a

column where the parameter sensitivity analysis was performed, the Hatta number and E^{∞} can be defined and used to calculate Φ. This ratio can be compared to the ratio of the fractional resistance of diffusion in the liquid film (via k_L sensitivity) to the fractional resistance of chemical reaction. The reaction enhancement ratio and parameter sensitivity ratio were calculated for all cases in Table 5-1 and compared in Figure 5-2.

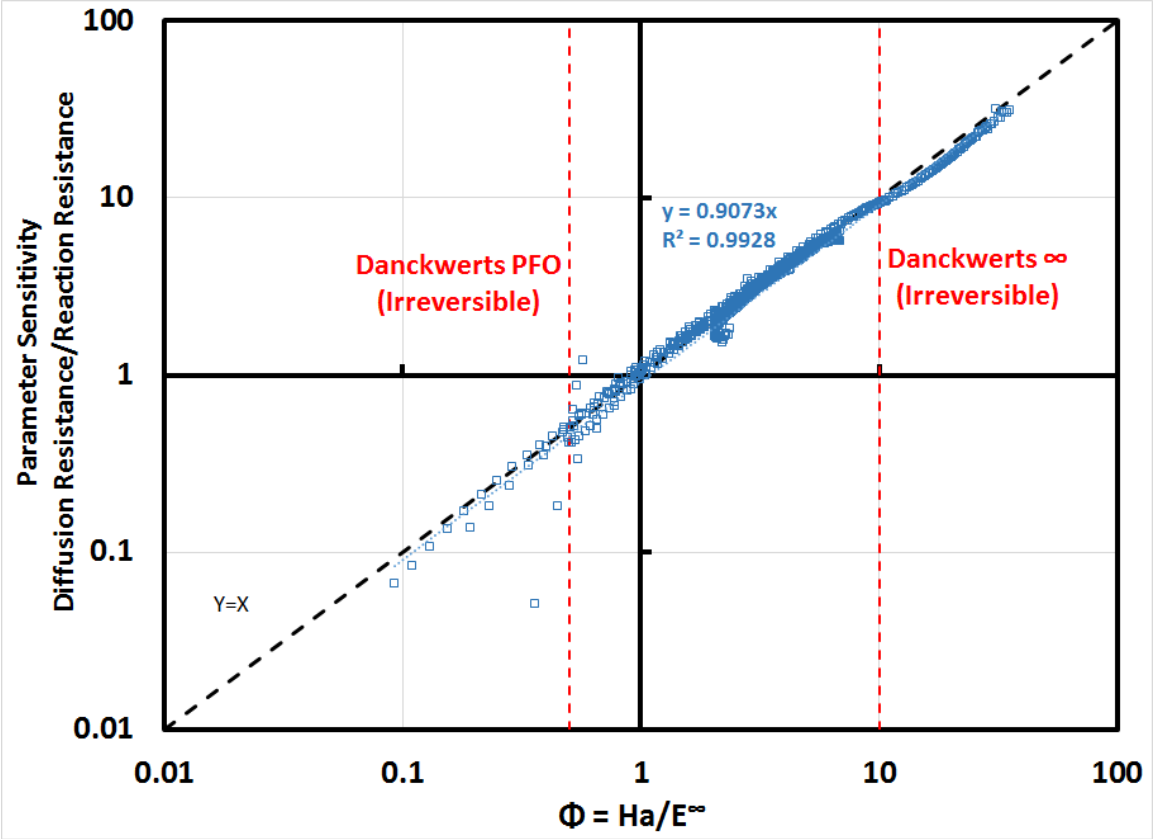

Figure 5-2: Parity plot of theoretical reaction enhancement ratio ($\Phi = Ha/E^{\infty}$) and the ratio of the components of liquid-film mass transfer resistance (diffusion and chemical reaction) as calculated by parameter sensitivity analysis. All cases included in the plot. Danckwerts' limits for pseudo-first order (PFO, $\Phi = 0.5$) and instantaneous (∞, $\Phi = 10$) reaction for irreversible chemical reaction provided as a reference (Danckwerts, 1970).

If the theoretical reaction enhancement ratio (Φ) is a perfect predictor of the liquid-film resistance distribution from sensitivity analysis, the points in the parity plot would fall on the diagonal of Figure 5-2 and yield a slope of 1. As seen in Figure 5-2, the two ratios are well-correlated, but not identical across the range of cases tested. The ratios appear to diverge beyond $\Phi \approx 10$. These points are almost exclusively from Case 12, which is

expected to be the most diffusion-controlled case (lowest k_L values). It is proposed that an absorber utilizing PZ is at the instantaneous reaction limit when $\Phi \approx 10$, and as Φ becomes larger than 10, the ratio of the computed fractional diffusion resistance to fractional reaction resistance will not change measurably (or in a computationally significant way). In addition, the PFO and instantaneous reaction limits identified by Danckwerts for irreversible chemical reaction are identified in the figure and appear to correspond fairly well to the conditions where the deviations occur in the parity plot (Danckwerts, 1970). The ratios are re-plotted in Figure 5-3 after omitting values outside of the Danckwerts limits.

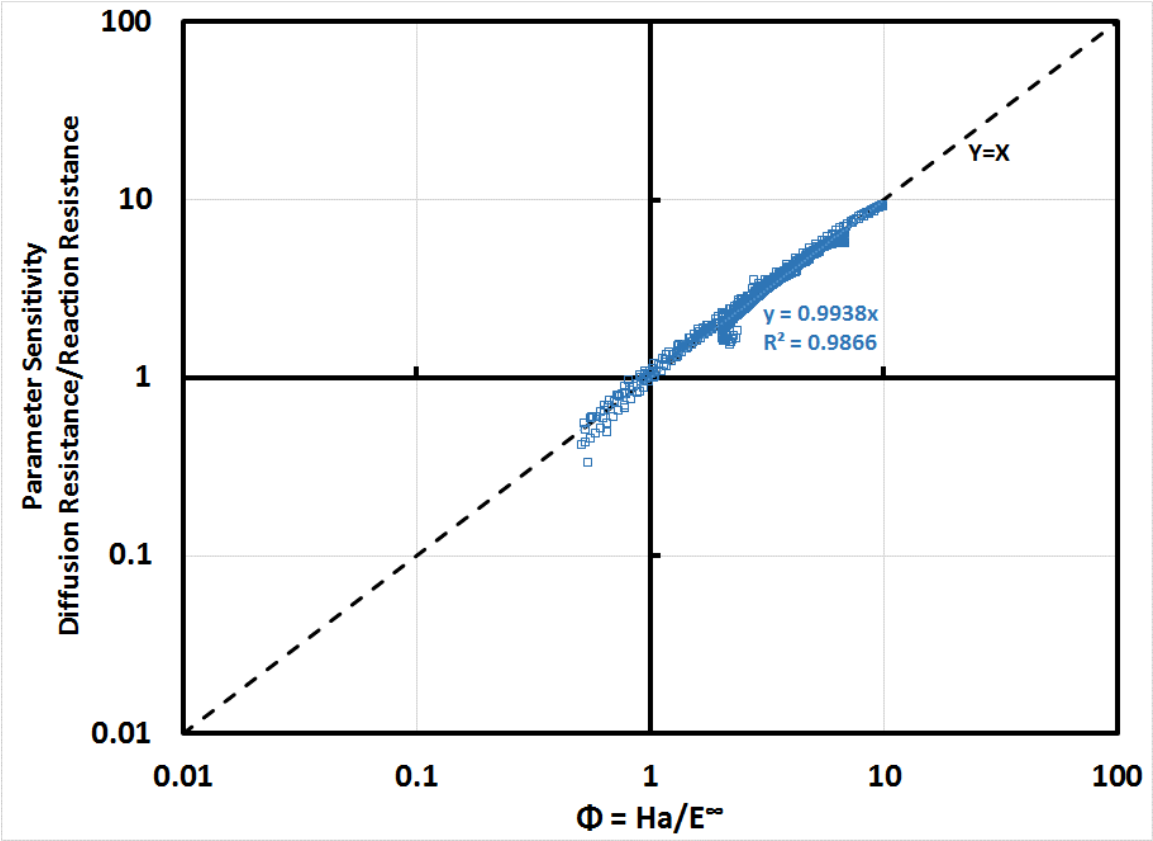

Figure 5-3: Parity plot of theoretical reaction enhancement ratio ($\Phi = Ha/E^{\infty}$) and the ratio of the components of liquid-film mass transfer resistance (diffusion and chemical reaction) as calculated by parameter sensitivity analysis. All cases included, points outside of Danckwerts' limits ($\Phi < 0.5$ & $\Phi > 10$) were omitted.

The results after omitting larger values of Φ indicate that the theoretical reaction enhancement ratio is a very good predictor of the distribution of liquid film resistance between diffusion and reaction. The boundary of $\Phi \approx 10$ can serve as a reasonable approximation for identifying the instantaneous reaction limit. However, a similar ratio was not clearly identified when $\Phi < 1$ to define the PFO limit though points as low as $\Phi \approx 0.1$ were included in the evaluation. Further investigation in this region may be required to quantify a limit. The correlation between the theoretical predictions and the parameter sensitivity results provide validation for the parameter sensitivity method.

The reaction enhancement ratio can also be used to provide fundamental explanations for the trends summarized by the parameter sensitivity results. To facilitate the analysis, Φ can be written in terms of the constituent parameters of Ha and E^{∞} and re-arranged to create a set of factors as detailed in Equation 5.27.

$$\phi = \left[\sqrt{\frac{(k_{Ha})}{\overline{\rho}}}\right]\left[\frac{1}{k_L^o}\right]\left[\left(\frac{D_{CO_2}}{D_{Am}}\right)^{0.25}\right]\left[\frac{\left([CO_2]^{Intf} - [CO_2]^{*Bulk}\right)}{\left([CO_2]^{*Intf}_{TOTAL} - [CO_2]^{*Bulk}_{TOTAL}\right)}\right] \qquad 5.27$$

$$\phi = [F_1][F_2][F_3][F_4]$$

where:

$k_{Ha} = k_{PZ} a_{PZ} a_{PZCOO^-} \gamma_{CO_2} + k_{PZCOO^-} a^2_{PZCOO^-} \gamma_{CO_2}$;

k_L^o = Diffusion coefficient independent portion of k_L (c.f., Equation 5.8).

The four factors reflect the important phenomena represented by the dimensionless groups - chemical reaction kinetics, physical mass transfer/fluid mechanics, diffusion, and driving force/equilibrium capacity of the solvent. The final term is also a representation of the slope of the vapor-liquid equilibrium curve of the solvent if the driving force is converted to the gas phase by accounting for the resistance due phase equilibria (Henry's constant in amine solution, c.f., Equation 5.25). The analysis can be used in a normalized form to compare relative changes in factors over a column or between different cases. Equation 5.28 illustrates the normalized form of the factor approach.

$$\frac{\phi^{NEW}}{\phi^{BASE}} = \left(\frac{[F_1]^{NEW}}{[F_1]^{BASE}}\right)\left(\frac{[F_2]^{NEW}}{[F_2]^{BASE}}\right)\left(\frac{[F_3]^{NEW}}{[F_3]^{BASE}}\right)\left(\frac{[F_4]^{NEW}}{[F_4]^{BASE}}\right) \qquad 5.28$$

where:

NEW = New or modified case or stage in a column;

BASE = Reference case or stage for comparison, (e.g., Case 1 in Table 5-1 or top stage in column);

5.4.2 Parameter Sensitivity Results

The sensitivity analysis results for Case 1 are summarized in Figure 5-4.

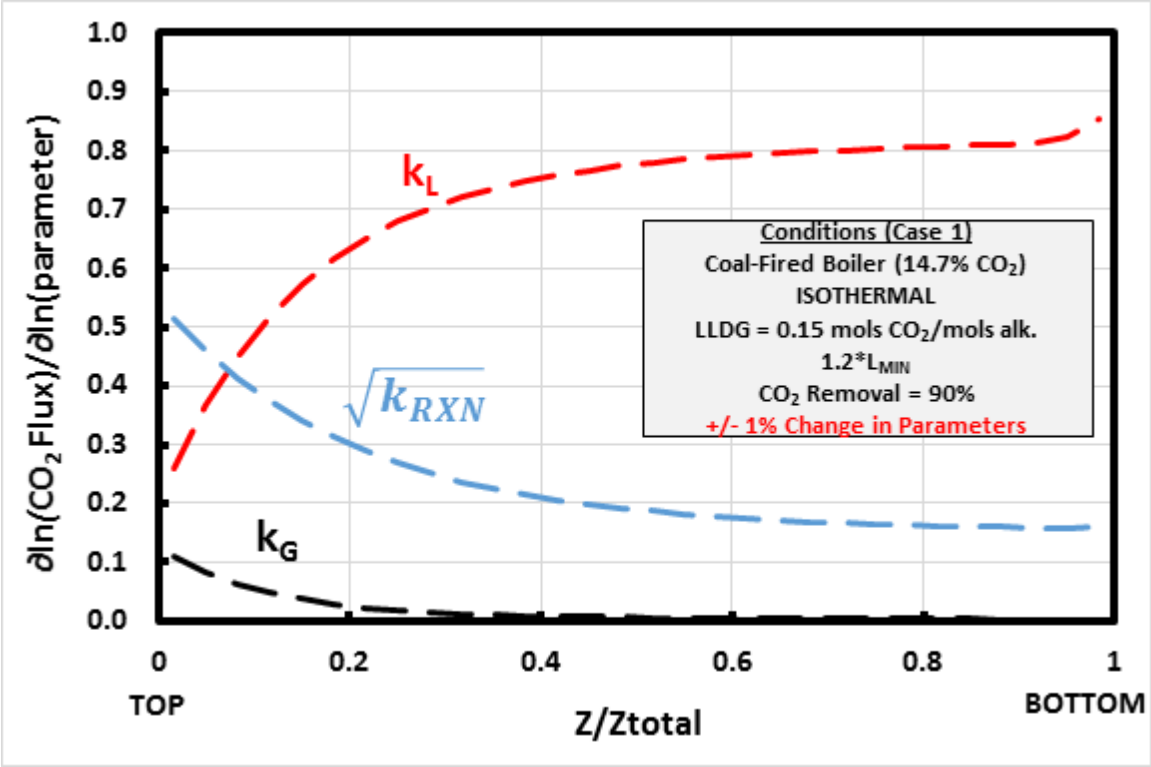

Figure 5-4: Case 1 Results. Sensitivity of CO_2 flux to mass transfer parameters: physical liquid-side (k_L) and gas-side (k_g) mass transfer coefficients and reaction rates (k_{rxn}) via kinetic constants in rate expressions. Parameters were independently perturbed +/- 1% from base value at each stage in the absorber. Analysis conducted for an isothermal absorber with 90% CO_2 capture from a coal-fired boiler (14.7% CO_2) using 8 m PZ.

Several observations can be developed from the base case results. First, the sum of the parameter sensitivity for all 3 parameters is approximately 1 at every point in the column. Therefore, overall mass transfer resistance is largely explained by the phenomena represented by the 3 parameters and the sensitivity results can be interpreted as fractional resistance or contribution to overall mass transfer resistance. With this interpretation of the results, the liquid-side diffusion resistance is dominant over a majority of the column, and increases monotonically from the top (lean end) of the column to the bottom (rich

end). Concurrently, the reaction resistance is controlling only near the lean end and reaches a minimum at the rich end of the column. The gas-side resistance is generally negligible with a small influence at the lean end of the column. These results indicate the absorption of CO_2 is liquid film controlled, but is not near the pseudo-first-order limit as the liquid-side physical mass transfer coefficient is important over the entire column. The system is closer to the instantaneous (diffusion limited) limit, particularly at the rich end of the column.

The trend from top (lean) to bottom (rich) in the column can be explained by considering the dimensionless group and factor analysis from Equations 5.27 and 5.28. The normalized reaction enhancement ratio (Φ) and component factors are plotted in Figure 5-5 for Case 1.

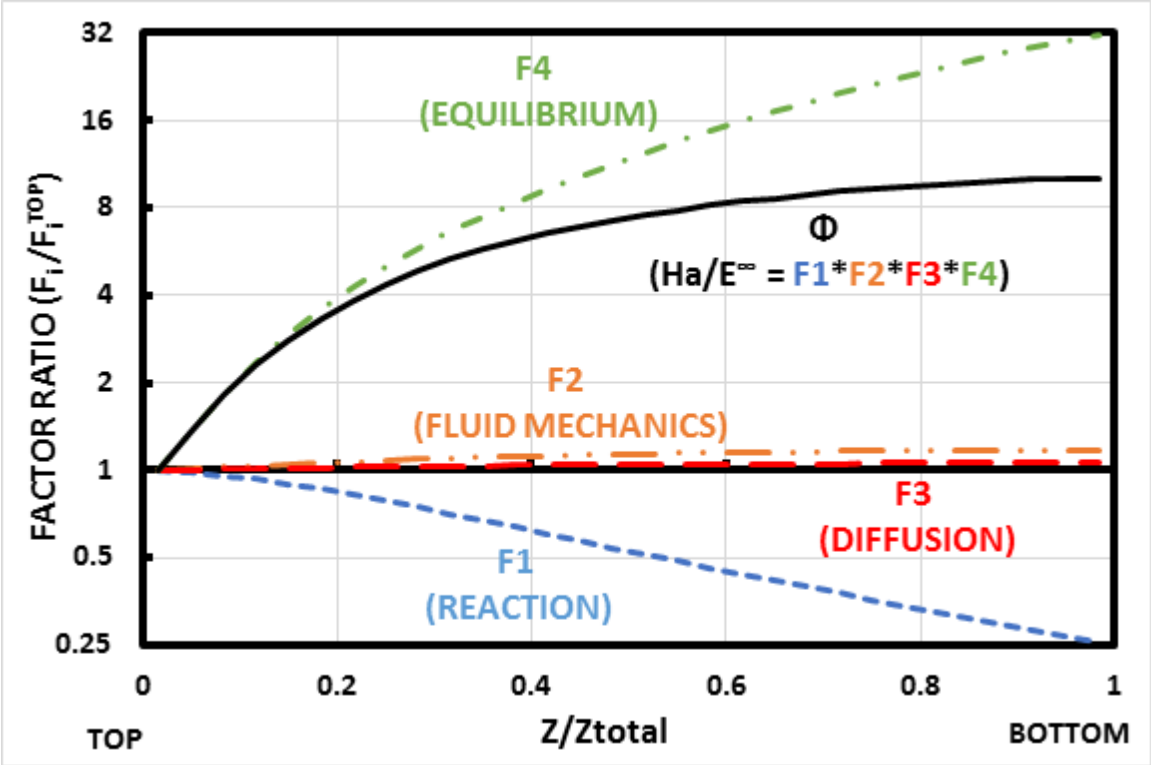

Figure 5-5: Dimensionless group analysis, Case 1. Each parameter in the plot is normalized to the value at the top (lean end) of the column to reflect changes in parameters over the column. Analysis conducted for an isothermal absorber with 90% CO_2 capture from a coal-fired boiler (14.7% CO_2) using 8 m PZ.

As the figure shows, the reaction enhancement ratio rises from the lean to rich end of the column, mirroring the rise in liquid-film diffusion control in Figure 5-4. Φ increases by a factor of 10 over the column and this rise is dominated by the equilibrium effects (F_4) or slope of the VLE curve, which changes by a factor of 30 over the column. As the loading increases from the lean to rich end of the column, the VLE curve becomes steeper and limits the equilibrium capacity of solvent (Figure 5-6). The VLE curve for 8 m PZ is provided in Figure 5-6 with the equilibrium (or maximum) rich loadings corresponding to CO_2 inlet concentrations for the three sources evaluated in this work.

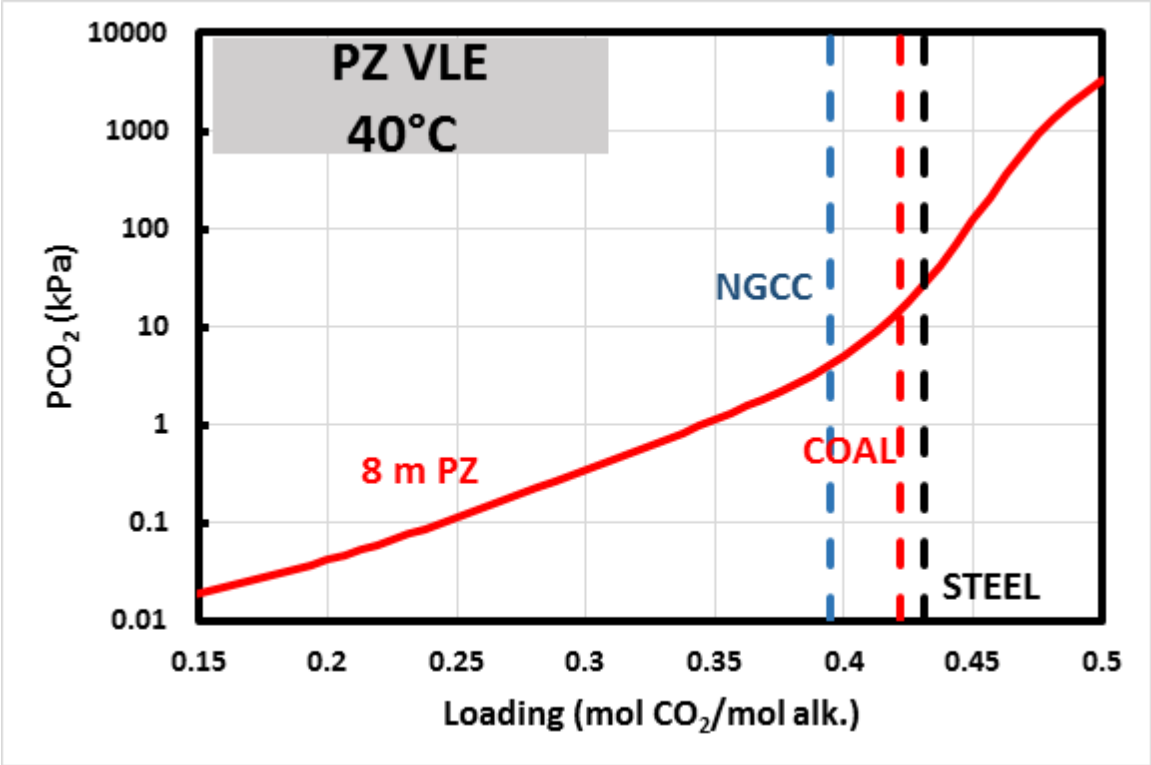

Figure 5-6: 8 m PZ VLE curve at 40°C. Maximum rich loadings are identified for NGCC (4.1% CO_2), Coal (14.7% CO_2), and Steel (27% CO_2) inlet flue gas compositions considered in this work.

The reaction rates are also limited with the change in loading (F_1) since free amine is depleted and slows the progression towards diffusion control in the liquid film. The remaining factors (fluid mechanics and diffusion) do not change significantly over the column compared to the equilibrium and reaction effects. The trends observed in Φ (and corresponding liquid-film control) over a column due to the loading effect for the base case is consistent for all cases in this analysis.

The results in Figure 5-4 can also be summarized by identifying several key features of the trends. The maximum fractional resistance values for each parameter can be used to identify limiting conditions in each case. In addition, the area under the curves in Figure 5-4 represent an average fractional resistance over the column since the curves

are plotted against a fractional height or area. The average resistance of each parameter can indicate the controlling phenomena for the column as a whole and can be used to compare different cases. These results are summarized in Table 5-2 for all cases in this study.

Table 5-2: Sensitivity Analysis Results Summary for All Cases. Average and maximum resistance for each mass transfer parameter with maximum values for each metric highlighted in the table.

Case	Flue Gas Source (mol % CO_2)	Solvent Concentration molal	Intercooling	LLDG mol CO2/ mol alk.	L/L_{MIN}	RLDG mol CO2/ mol alk.	k_L Value	Column Average Fractional Resistance			Max Fractional Resistance		
								k_L	k_G	Rxn	k_L	k_G	Rxn
1	COAL (14.7%)	8	ISOTHERMAL	0.15	1.2	0.375	Base	71%	2%	23%	86%	11%	51%
2	COAL (14.7%)	8	***NONE***	0.15	1.2	0.375	Base	62%	6%	28%	86%	15%	70%
3	COAL (14.7%)	8	ISOTHERMAL	0.15	***1.8***	0.300	Base	47%	***9%***	42%	82%	14%	58%
4	COAL (14.7%)	8	ISOTHERMAL	***0.20***	1.2	0.380	Base	69%	2%	24%	84%	9%	50%
5	COAL (14.7%)	8	ISOTHERMAL	***0.26***	1.2	0.395	Base	66%	1%	26%	82%	7%	49%
6	COAL (14.7%)	***5***	ISOTHERMAL	0.15	1.2	0.371	Base	47%	5%	43%	64%	17%	64%

Table 5-2: Continued.

Case	Flue Gas Source (mol % CO_2)	Solvent Concentration molal	Intercooling	LLDG mol CO2/ mol alk.	L/L_{MIN}	RLDG mol CO_2/ mol alk.	k_L Value	Column Average Fractional Resistance			Max Fractional Resistance		
								k_L	k_G	Rxn	k_L	k_G	Rxn
7	COAL (14.7%)	8	ISOTHERMAL	0.15	1.2	0.375	***5*Base***	32%	7%	**54%**	52%	**20%**	67%
8	COAL (14.7%)	8	ISOTHERMAL	0.15	1.2	0.375	***0.8*Base***	76%	1%	20%	90%	10%	52%
9	COAL (14.7%)	8	ISOTHERMAL	0.15	1.2	0.375	***0.5*Base***	83%	1%	14%	**95%**	6%	42%
10	***NGCC (4.1%)***	8	ISOTHERMAL	0.15	1.2	0.354	Base	55%	3%	36%	83%	14%	**77%**
11	***STEEL (27%)***	8	ISOTHERMAL	0.15	1.2	0.384	Base	77%	1%	18%	86%	11%	41%
12	COAL (14.7%)	8	***NONE***	0.15	1.2	0.375	***0.2 Base***	**87%**	1%	8%	**95%**	4%	30%

All Cases:
1) CO2 Removal = 90%
2) MP-250X
3) Max Approach to Flood = 70%

The results and trends in Table 5-2 will be discussed in detail in the subsequent sections.

5.4.2.1 Gas-Film Resistance

As in the base case (Case 1), the gas-film resistance does not contribute significantly across the range of conditions evaluated in this study. The average gas-side resistance in the absorber does not exceed 10% for any case, and the maximum resistance at any point in the column does not exceed 20% for any case. In the cases where gas-side resistance has the most influence (Cases 3 and 7), the liquid-film resistance has been reduced by extreme parameter values (high k_L) or operating conditions (high solvent circulation). Therefore, gas-film resistance will be neglected in further discussion and is unlikely to play an important role in absorber design with PZ.

5.4.2.2 Liquid-Film Resistance

The liquid-film resistance has been separated into diffusion and reaction resistance. Both are significant compared to gas-film resistance at all conditions in Table 5-2 In all but one case (Case 7), the average resistance across the column indicates that diffusion is the controlling mechanism in the liquid film. In case 7, the liquid-film physical mass transfer coefficient is 5 times the base value, moving the system towards the PFO limit or reaction control. In all cases, diffusion is the majority of the overall resistance at a point in the column (rich end) as indicated by the maximum fractional resistance values in Table 5-2. Therefore, the liquid-film resistance is generally controlled by diffusion for the PZ model across the range of operating conditions considered in this analysis.

5.4.2.3 Temperature Effects

Cases 1 and 2 compare parameter sensitivity results for isothermal and adiabatic absorbers at identical operating conditions to isolate of the effects of temperature on mass transfer resistance in an absorber. Figure 5-7 compares the parameter sensitivity results of the two cases.

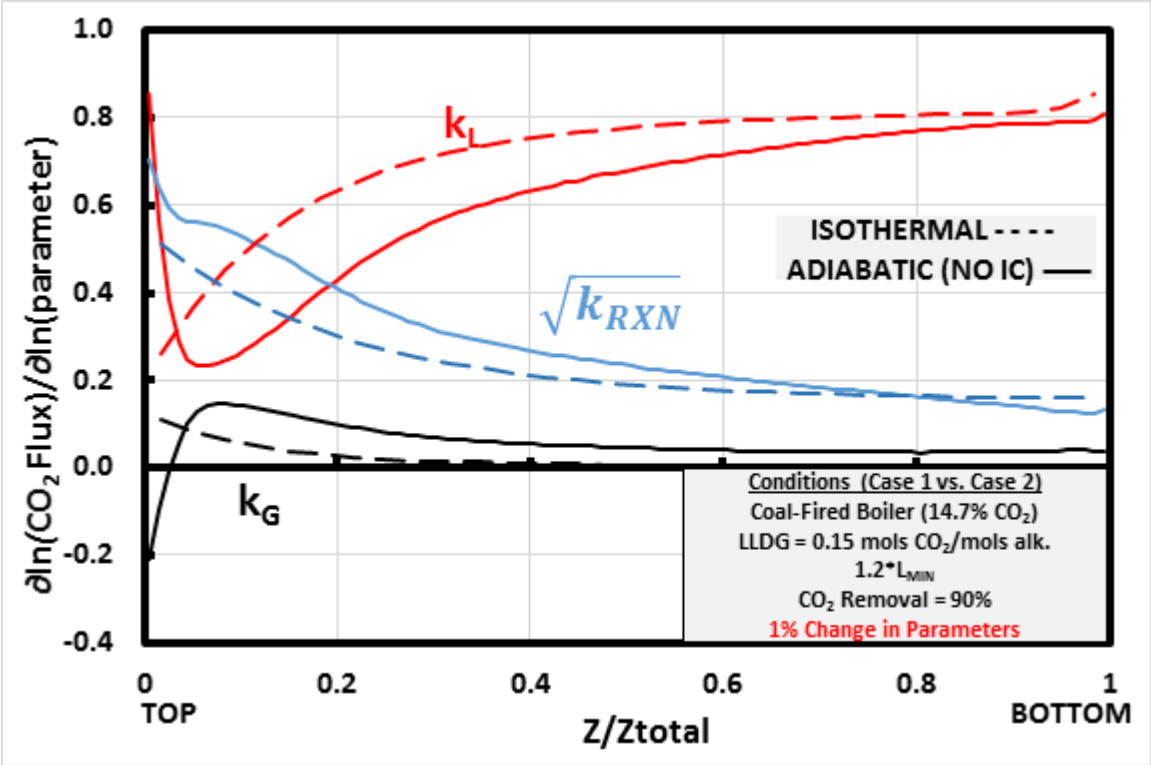

Figure 5-7: Case 1(Isothermal) and Case 2(Adiabatic) comparison. Sensitivity of CO_2 flux to mass transfer parameters: physical liquid-side (k_L) and gas-side (k_g) mass transfer coefficients and reaction rates (k_{rxn}) via kinetic constants in rate expressions. Parameters were independently perturbed +/- 1% from base value at each stage in the absorber. Analysis conducted with 90% CO_2 capture from a coal-fired boiler (14.7% CO_2) using 8 m PZ.

In general, the adiabatic absorber is less sensitive to liquid-film physical mass transfer (diffusion) than the isothermal absorber, and more sensitive to reaction and gas-film parameters. This is confirmed by the average resistance values reported in Table 5-2.

In addition, the adiabatic absorber exhibits non-monotonic trends over the absorber due to the presence of a temperature maxima in the column. This effect is most notable in the trend of the liquid-film mass transfer coefficient sensitivity which is isolated with column temperature in Figure 5-8.

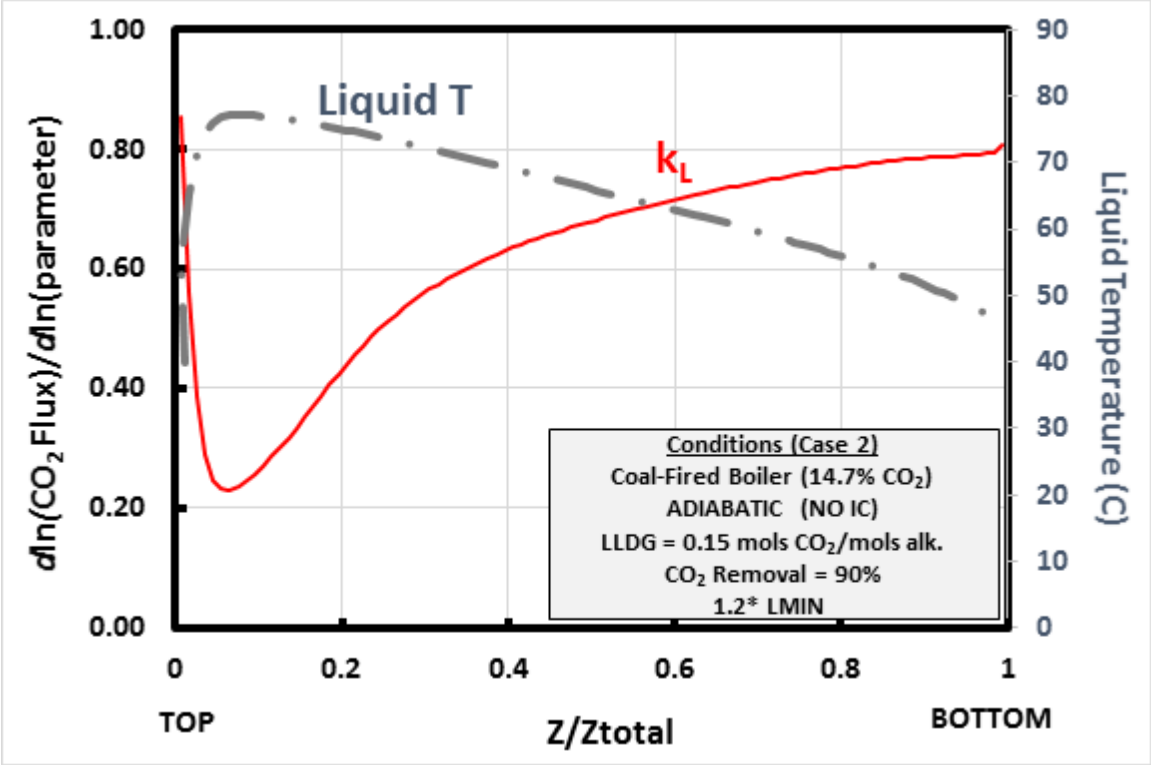

Figure 5-8: Case 2 physical liquid-side (k_L) sensitivity (primary y-axis) and column liquid temperature (secondary y-axis). Analysis conducted for an adiabatic absorber with 90% CO_2 capture from a coal-fired boiler (14.7% CO_2) using 8 m PZ.

The trend in liquid-film resistance can be evaluated with the dimensionless factor analysis over the column presented in Figure 5-9.

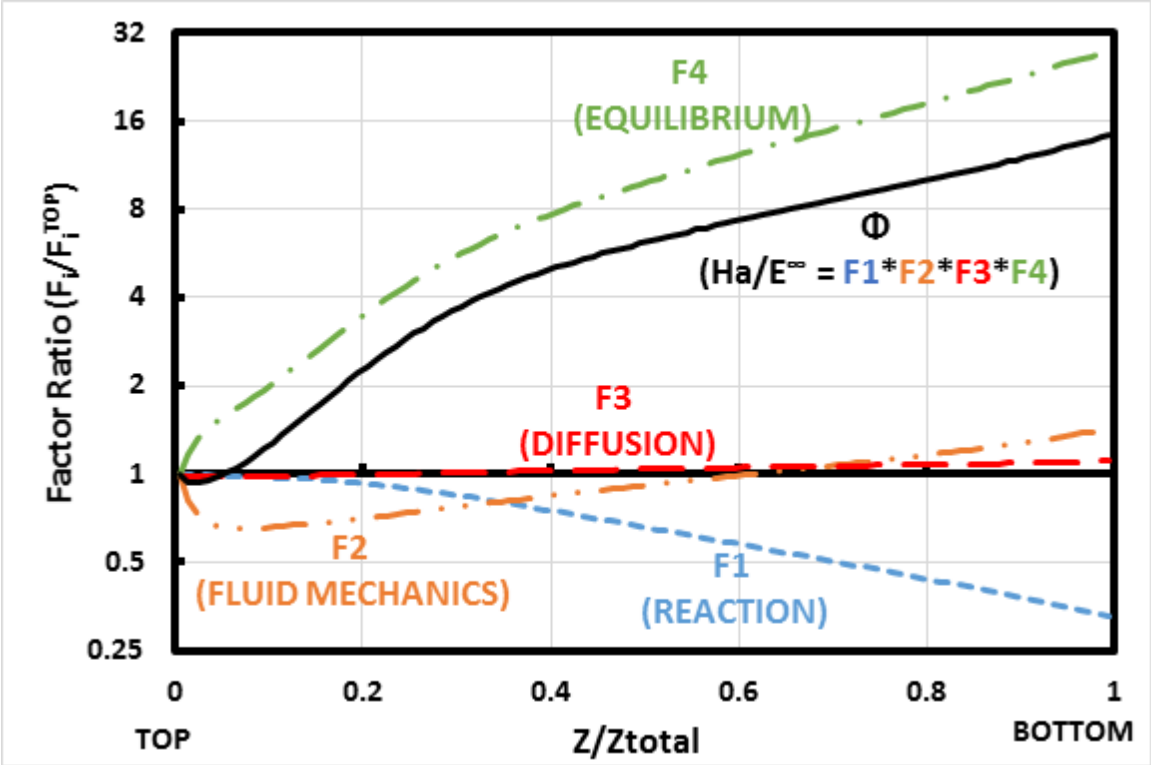

Figure 5-9: Dimensionless group analysis, Case 2. Each parameter in the plot is normalized to the value at the top (lean end) of the column to reflect changes in parameters over the column. Analysis conducted for an isothermal absorber with 90% CO_2 capture from a coal-fired boiler (14.7% CO_2) using 8 m PZ.

The figure details that the increase in liquid-film diffusion resistance over the column (change in Φ) is dominated by the equilibrium effect (F_4) as in the isothermal case. However, the initial drop in diffusion resistance at the lean end of the column can be attributed to a drop in the fluid mechanics (F_2) contribution to the mass transfer resistance. This phenomena can be explained by evaluating the mass transfer coefficient model in Equations 5.5 through 5.8. The primary effect of temperature is to reduce the viscosity of the amine solution and enhance diffusion and mass transfer coefficients in the system. The large changes in temperature near the lean end (top) of the column have a strong effect on the viscosity (reduced by approximately a third from the top of the

column to the temperature maxima). Beyond the temperature maxima, viscosity increases as expected with loading and temperature effects are minimal.

In general, the adiabatic and isothermal absorbers exhibit similar trends as a function of loading over the column. At most points in the column (omitting the region near the temperature maxima), the columns both exhibit similar levels of diffusion and reaction control and negligible gas-film resistance. Therefore, temperature effects are not considered to be a primary factor in evaluating mass transfer resistance and isothermal absorbers were used for a majority of the cases in this analysis (Table 5-1).

5.4.2.4 High and Low Parameter Values

As noted in section 5.3.2, several cases (7, 8, 9, and 12) were evaluated with significant modification of base k_L values to move the system towards asymptotic limits and reflect uncertainty in the mass transfer models. Cases 7 and 9 will be discussed here to represent high and low k_L values.

Case 7 considered liquid-film mass transfer coefficients at 5 times the base values to represent a case approaching PFO limit. Table 5-2 identifies Case 7 as the only case that is reaction limited in terms of average reaction control over the column (54%). However, even with this significant modification of model parameters, the liquid-film diffusion resistance is still significant over a large portion of the column and is controlling at the rich end. Figure 5-10 compares the parameter sensitivity for Case 7 to the base case.

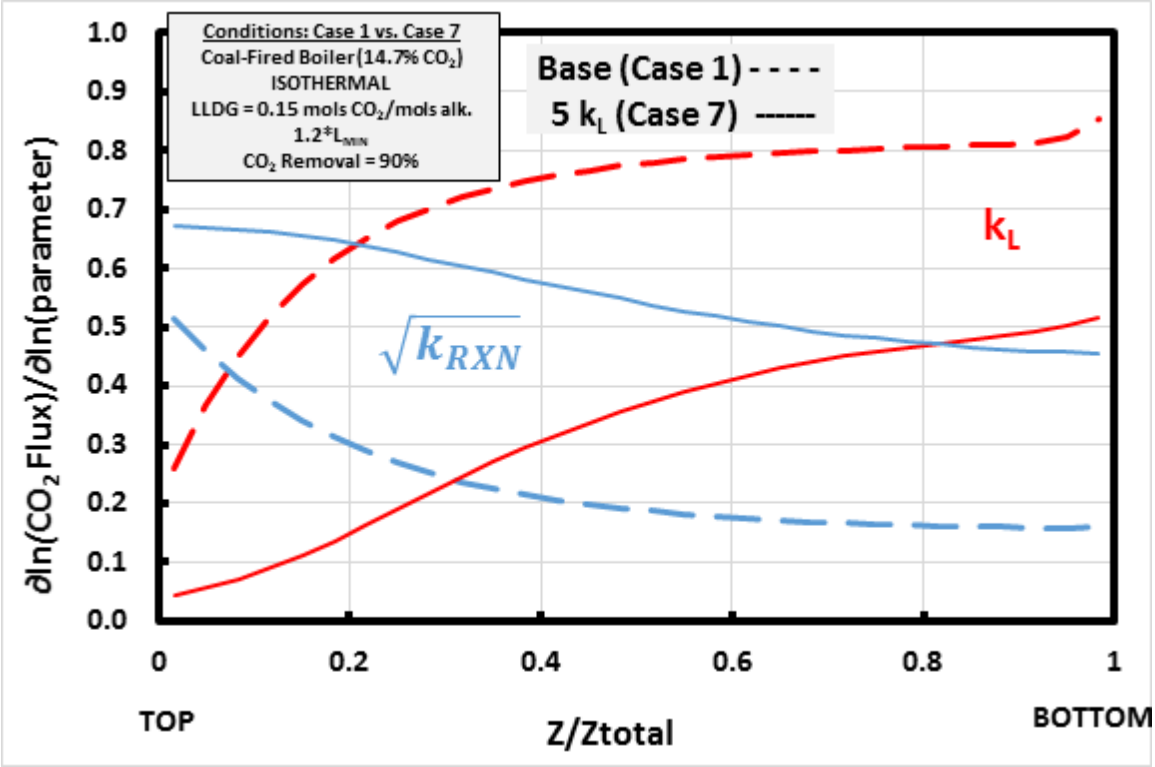

Figure 5-10: Case 1 (Base) and Case 7 (5*k_L) isothermal absorber comparison. Sensitivity of CO_2 flux to mass transfer parameters: physical liquid-side (k_L) mass transfer coefficient and reaction rates (k_{rxn}) via kinetic constants in rate expressions. Parameters were independently perturbed +/- 1% from base value at each stage in the absorber. Analysis conducted with 90% CO_2 capture from a coal-fired boiler (14.7% CO_2) using 8 m PZ.

Case 9 evaluated parameter sensitivity with k_L values at half of the base values. This case was expected to move the model closer to the instantaneous reaction limit, and Table 5-2 verifies that the average diffusion control over the column is significantly larger (>80% diffusion control) than the base case and reaches the highest recorded value for diffusion control in all of the cases tested (95%). Figure 5-11 summarizes the comparison of the low k_L case and base case parameter sensitivity.

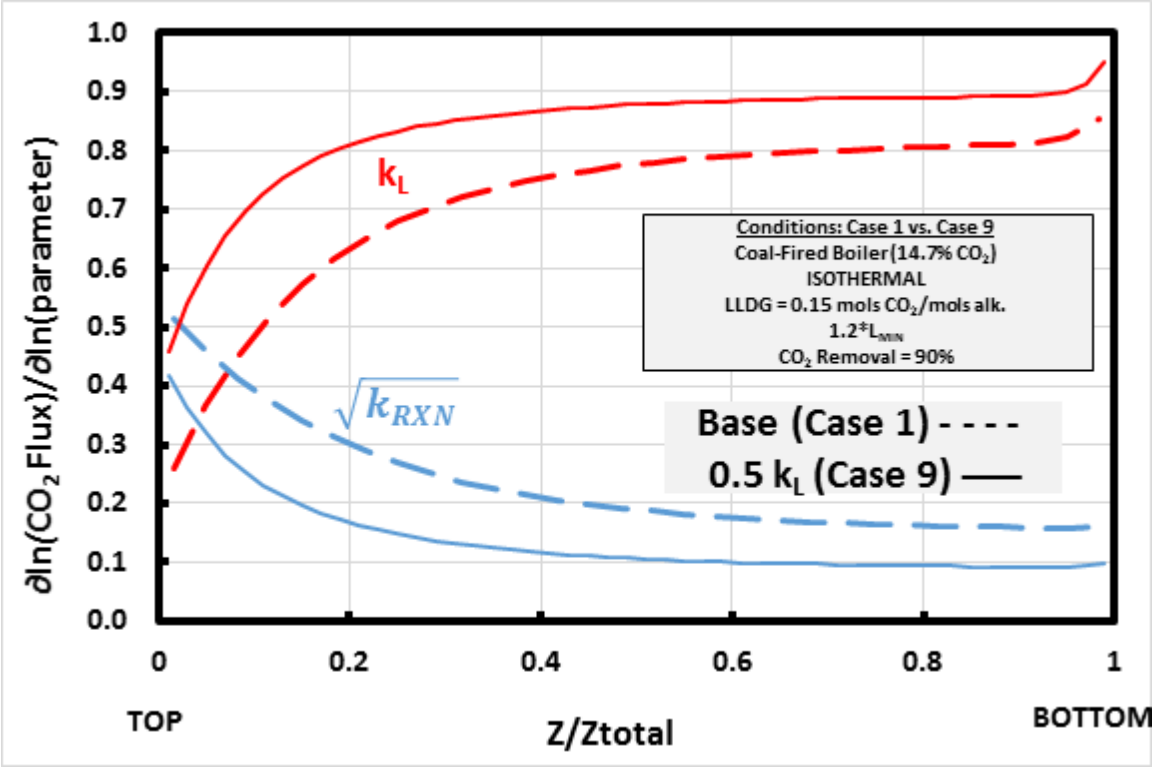

Figure 5-11: Case 1 (Base) and Case 9 (0.5*k_L) isothermal absorber comparison. Sensitivity of CO_2 flux to mass transfer parameters: physical liquid-side (k_L) mass transfer coefficient and reaction rates (k_{rxn}) via kinetic constants in rate expressions. Parameters were independently perturbed +/- 1% from base value at each stage in the absorber. Analysis conducted with 90% CO_2 capture from a coal-fired boiler (14.7% CO_2) using 8 m PZ.

5.4.2.5 Solvent Circulation Rate

Case 3 utilizes a higher solvent rate (1.8 x minimum solvent rate) than the base case (1.2 x minimum solvent rate) to isolate the effect of solvent rate on mass transfer resistance in the absorber. The higher solvent rate was expected to have two major effects:

1) enhance the liquid film mass transfer coefficient (see Equation 5.8);
2) reduce the rich loading achieved (see Table 5-1) minimizing the limitations on equilibrium capacity of the solvent.

Both effects should serve to move the system towards the PFO limit. As seen in Table 5-2, the average liquid-film diffusion resistance for Case 3 is significantly lower than the Case 1, confirming the shift towards PFO limit. The dimensionless group factor analysis (Equation 5.28) in Figure 5-12 is used to identify the mechanism responsible for the shift in the system.

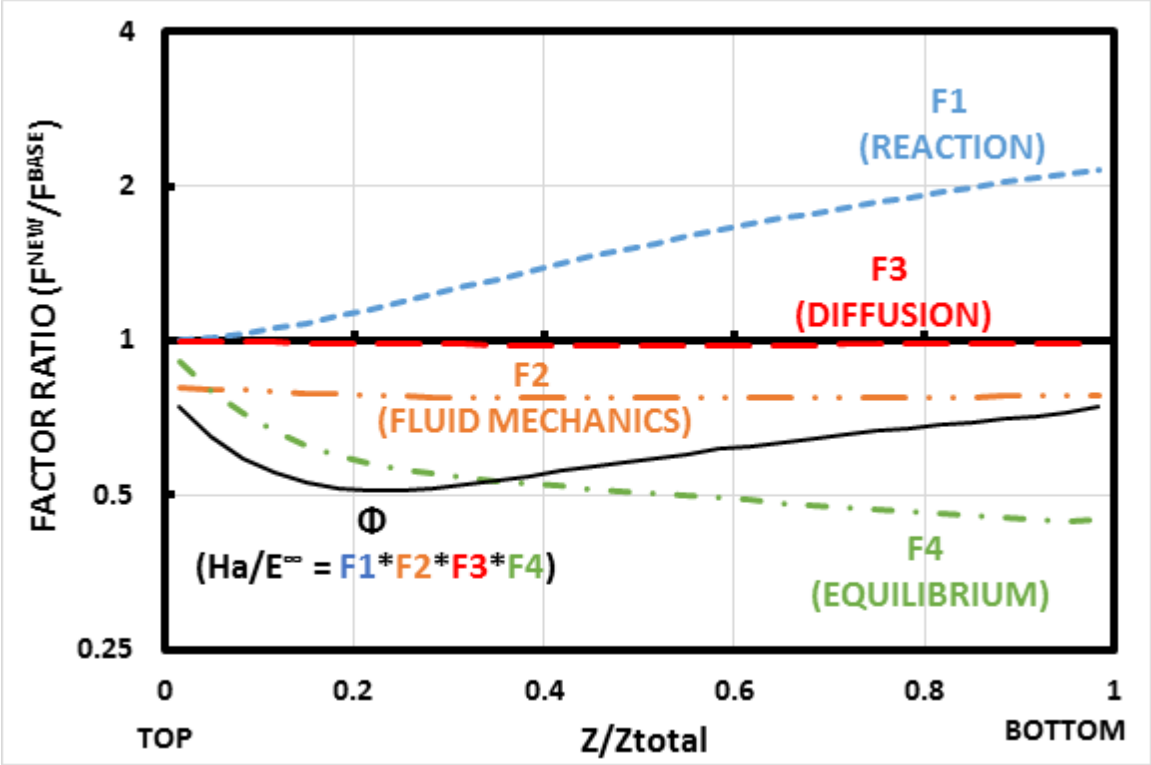

Figure 5-12: Dimensionless group analysis, Case 3 (High solvent rate, 1.8 L_{MIN}) vs. Case 1 (Base, 1.2 L_{MIN}). Each curve in the chart represents a change from the base case as all factors are normalized to Case 1 (c.f., Equation 5.28). Analysis conducted for an isothermal absorber with 90% CO_2 capture from a coal-fired boiler (14.7% CO_2) using 8 m PZ.

Each curve in the chart is represents the change in a factor from the base case (Case 1). The figure confirms that the reaction enhancement ratio (Φ) is consistently lower than the base case ($\Phi^{NEW}/\Phi^{BASE} < 1$) throughout the column for the higher solvent rate (closer to

PFO limit). When comparing the 4 factors that make up Φ, the equilibrium effect is dominant at the lean end of the column. This indicates that the higher solvent rate is limiting the increase in loading and enhancing the equilibrium capacity of the solvent compared to the base case. At the rich end, or bottom of the column, the reaction is enhanced significantly at the higher solvent rate due to the increased availability of free amine and offsets the equilibrium effect. The fluid mechanics effect (higher solvent rate reduces physical mass transfer resistance) becomes important in this rich region as this keeps Case 3 closer to PFO than the base case.

5.4.2.6 Lean Loading

Cases 4 and 5 operate at higher lean loadings than the base case (0.20 and 0.26 mol CO_2/mol alkalinity, respectively). The expected effect of the loading shift was to operate the column in a richer portion of the solvent VLE and move the system towards liquid-film diffusion control compared to the base case. However, the results in Table 5-2 indicate that as the lean loading is increased, the system operates progressively closer to the PFO limit (reduced column average liquid-film diffusion resistance). Case 5 (lean loading = 0.26) was selected for comparison to the base case in utilizing dimensionless group factor analysis (Equation 5.28).

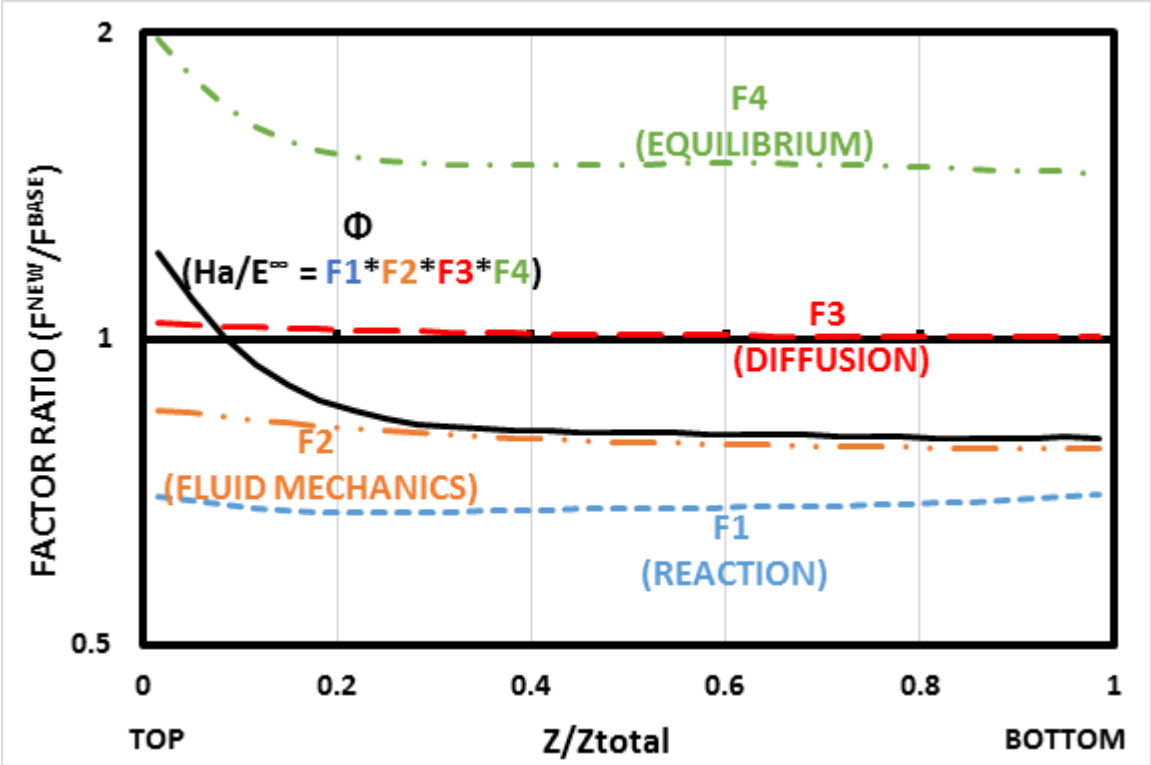

Figure 5-13: Dimensionless group analysis, Case 5 (Lean Loading = 0.26 mol CO_2 / mol alkalinity) vs. Case 1 (Base, Lean Loading = 0.15 mol CO_2 / mol alkalinity). Each curve in the chart represents a change from the base case as all factors in Case 5 were normalized to Case 1 (c.f., Equation 5.28). Analysis conducted for an isothermal absorber with 90% CO_2 capture from a coal-fired boiler (14.7% CO_2) using 8 m PZ.

The reaction enhancement ratio exhibits the expected behavior at the top of the column – Φ is higher and the system is closer to the instantaneous limit for Case 5 (higher loading) primarily due to the equilibrium effect (Case 5 operates in steeper region of VLE curve, see Figure 5-6). However, the rich loading achieved in each case of the column is limited by the equilibrium constraint identified in Figure 5-6, so the loading gap between the two cases shrinks rapidly after the lean end of the column and equilibrium effect is offset by the reaction effects (F1) of operating at richer loadings (depleted free amine in Case 5). The fluid mechanics become important as the higher

solvent rate required for Case 5 reduces liquid-film physical mass transfer resistance and pushes the system closer to the PFO limit than the base case.

5.4.2.7 Flue Gas Concentration

The effect of flue gas concentration is examined in Cases 4 (NGCC, 4.1% CO_2) and 5 (Steel, 27.6% CO_2). Table 5-2 indicates that liquid-film diffusion control increases as the CO_2 concentration in the flue gas increases. The explanation for the trend with CO_2 concentration is consistent with the preceding discussions regarding solvent rate and lean loading.

As depicted in Figure 5-6, lower inlet CO_2 concertation corresponds to operating in a leaner portion of the VLE curve. This reduces equilibrium limitations as CO_2 concentration drops and is the dominant factor (F4) for the reduction in liquid-film diffusion control from steel to coal to NGCC. Increased reaction rates (F1) and reduced solvent rates (F2) push the lower CO_2 concentration system away from the PFO limit, but the equilibrium effect is dominant.

5.4.2.8 Solvent Concentration

The effect of amine solvent concentration was evaluated by testing 5 m PZ in Case 6. Table 5-2 indicates the column average liquid-film diffusion resistance is significantly reduced when operating with lower amine concentration (46% for Case 6 vs. 71% for Case 1). The reduced amine concentration should result in reduced free amine and reaction rates, reduced solvent viscosity (enhanced turbulence/physical mass transfer and diffusion), and increased solvent rate to compensate for reduced amine (enhanced turbulence/physical mass transfer). The difference in VLE effects is expected to be important when comparing 5 m PZ (Case 6) and 8 m PZ (Case 1) since the concentration

of free amine is different at a common loading condition. Figure 5-14 summarizes the effects with a normalized factor analysis using average values over the column.

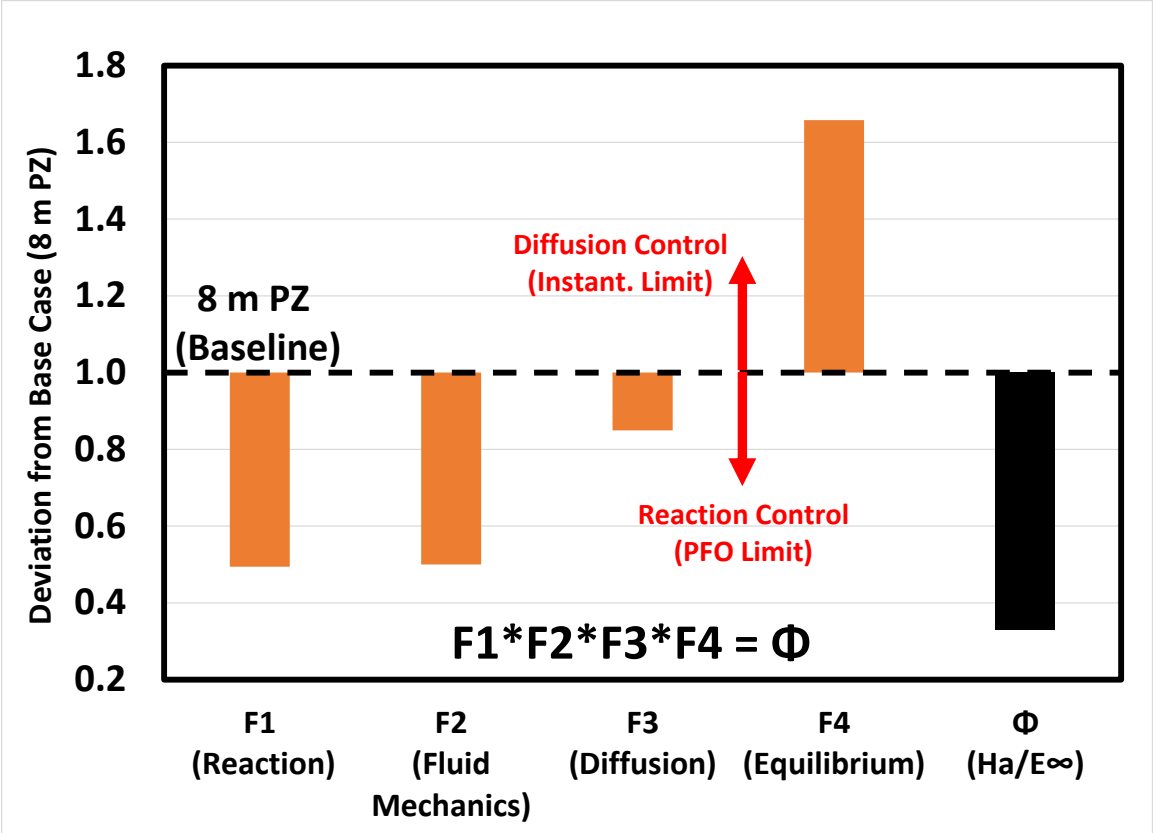

Figure 5-14: Dimensionless group analysis, Case 6 (5 m PZ) vs. Case 1 (Base, 8 m PZ). Each bar in the chart represents a change from the column average value for the parameter at the base case (8 m PZ) as all factors are normalized to Case 1 (c.f., Equation 5.28). Analysis conducted for an isothermal absorber with 90% CO_2 capture from a coal-fired boiler (14.7% CO_2) and LLDG = 0.15 mol CO_2/mol alkalinity.

As expected, the 5 m PZ case results in a significantly lower Φ (reaction enhancement ratio) than the base 8 m PZ case confirming the reduced liquid-film diffusion control identified in the parameter sensitivity analysis. In addition, 5 m PZ does have an equilibrium restriction compared to 8 m PZ that pushes the system towards liquid-film

diffusion control, but all other factors (enhanced diffusion and fluid mechanics and reduced reaction rate) push the system towards PFO when compared to 8 m PZ confirming the important role of viscosity in the PZ system.

5.5 CONCLUSIONS

The goals and corresponding key findings of the current work can be summarized as follows:

- Identify controlling mass transfer resistance in an absorber utilizing concentrated PZ as a function of operating conditions:
    - The model predicts liquid-film control for the PZ system. Gas-film resistance is negligible across conditions tested (column average gas-film resistance does not exceed 10% in any case). Maximum gas-film resistance is localized at the lean end of the column.
    - The liquid-film resistance is dominated by diffusion resistance at the base case parameter values tested in this analysis across all operating conditions and diffusion resistance is greatest at the rich end of the column for all cases.
    - Temperature effects in an adiabatic absorber do not change the overall column trends (diffusion limitation increase from lean to rich) and have a minimal impact on the average contribution of each component to overall mass transfer resistance when compared to an isothermal absorber.
    - At high k_L values (5*Base), the column average reaction resistance indicates significant reaction control of the liquid film (54% of overall

resistance). Operating at high solvent rates (1.8 L_{MIN}) or with 5 m PZ also lead to significant reaction resistance (42% column average in each case).

- Define/identify dimensionless group to predict mass transfer resistance in absorber and validate parameter sensitivity results:
    - The reaction enhancement ratio, Φ, (ratio of pseudo-first-order and instantaneous asymptotic enhancement factors) provides very accurate prediction of liquid-film mass transfer resistance distribution (diffusion vs. reaction) as evaluated by parameter sensitivity analysis.
    - When $\Phi > 10$, the theoretical predictions no longer match sensitivity analysis prediction, indicating the system may have reached instantaneous reaction limit (within calculation ability of parameter sensitivity method)
- Use theoretical model to explain trends in mass transfer resistance in the absorber
    - Liquid-film diffusion resistance increases from the lean to rich end of the column primarily due to the change in the equilibrium capacity of the solvent with loading (slope of vapor-liquid equilibrium curve). The equilibrium contribution to the change in Φ (measure of diffusion vs. reaction resistance) may increase by as much as a factor of 30 from the lean loading to rich loading.

Beyond the conclusions developed directly from results in this analysis, the evaluation of mass transfer resistance should guide absorber design and model development activities:

- The base case predictions of the piperazine rate-based absorber model indicate significant liquid-film diffusion resistance across the full range of operating conditions. Novel absorber design should include features that generate turbulence in the liquid face or enhance physical mass transfer, particularly at the

rich end of the column where the model predicts approach to instantaneous reaction limit.

- Solvent selection should carefully consider the effect of viscosity on absorber performance. As the analysis with 5 m PZ demonstrated, the reduction in viscosity significantly reduces liquid-film physical mass transfer resistance and should enhance overall absorber mass transfer performance.
- The liquid-film mass transfer coefficient model is a critical component of properly modeling absorber mass transfer resistance. The upper limit of k_L evaluated in this work (5*Base k_L) is within the range of commonly used literature models and within the uncertainty in the current model when considering viscosity dependence and uncertainty in experiments. The design approach for absorbers and performance prediction as a function of operating conditions will vary significantly in the range of k_L values considered in the work and may lead to sub-optimal design.
- The reaction enhancement ratio, Φ, can be used to predict the liquid-film control mechanisms for cases not included in this analysis (e.g., different equipment, operating, or solvent specifications) if operating specifications for the absorber are known and a thermodynamic model is available to calculate the asymptotic enhancement factors.

Chapter 6: Novel Absorber Contacting and Intercooling Configurations

The preceding chapters have focused on developing a detailed understanding of modeled absorber performance using concentrated piperazine (PZ), including the underlying mechanisms that explain performance trends with operating and equipment specifications. One goal of developing a fundamental understanding of absorber performance is to guide the development of improved and novel intercooling and contacting concepts for CO_2 capture. The development of these new designs should be supported at a theoretical level by the mechanisms controlling absorber performance. This chapter will introduce and study novel absorber concepts, quantify the potential benefits of the novel designs over the baseline designs considered in previous chapters, and explain the performance enhancement with the mechanistic explanations put forth in the previous chapters. In addition, several conceptual designs will be proposed with a discussion of the data and modeling requirements to further evaluate and develop the concepts.

6.1 Evaluation of Existing Literature

Alternative contacting and intercooling schemes have been developed for a variety of absorption applications. Specifically, there are literature examples of integrating intercooling with the absorption process and enhancing mass transfer with alternative contacting schemes and methods. A few examples have been selected for their relevance to the work in this chapter.

Solvent recycle has been proposed in absorption processes for a variety of reasons. The use of multiple solvent recycle loops was developed for acid gas treating applications (Thirkell, 1971). Recycling solvent was proposed as a method to enhance liquid-film mass transfer via higher liquid velocities and to ensure sufficient wetting of

the column internals. Solvent recycle with cooling has been proposed in the literature for processes utilizing chilled ammonia to capture CO_2 (Mathias, et al., 2010). However, the purpose of the recycle in the chilled ammonia process was to reduce volatile losses of the solvent, not to enhance mass transfer performance.

Integrated intercooling in absorption columns has also been developed for various applications. A novel heat exchanger-absorber combination was proposed for absorption of ethylene vapor into a hydrocarbon liquid (Romano, 1982). The concept would approximate isothermal absorption of the gas, but was specifically developed for small-scale applications where separate external cooling would not be cost effective.

Rotating packed beds (RPB) have also been proposed for CO_2 capture with amine-based solvents (Tan & Chen, 2006). RPBs are designed to significantly reduce the size of gas-liquid contactors by decreasing diffusion resistance and generating additional mass transfer area via the turbulence created by centrifugal acceleration of the contactor.

In this work, several alternative absorber intercooling methods and absorber contacting schemes will be proposed based on the fundamental mechanisms studied in preceding chapters and based on specific process conditions for CO_2 capture from flue gas.

6.2 MODELING OVERVIEW

The absorber model used for the intercooling evaluation was implemented in Aspen Plus® in the RateSep^{TM} module. The key components of the model are rigorous representations of solvent thermodynamics and kinetics, mass transfer and fluid mechanics in packing, and the physical properties of the system over the range of expected operating conditions.

All of the subsequent analysis will utilize 8 m aqueous piperazine (PZ) as the solvent. The thermodynamic model for the PZ-H_2O-CO_2 system was developed from experimental amine pK_a, CO_2 solubility, heat capacity, speciation, and amine volatility data by regression of Gibbs free energy, enthalpy, heat capacity, and activity coefficient parameters within the electrolyte non-random two liquid (e-NRTL) framework (Frailie, 2014).

The kinetics for the PZ model are described by the following reaction set:

$$PZCOO^- + PZH^+ \leftrightarrow H^+PZCOO^- + PZ \quad 6.1$$

$$PZCOO^- + H_2O + CO_2 \rightarrow H^+PZCOO^- + HCO_3^- \quad 6.2$$

$$2PZ + CO_2 \rightarrow PZH^+ + PZCOO^- \quad 6.3$$

$$2PZCOO^- + CO_2 \rightarrow H^+PZCOO^- + PZ(COO)_2^{2-} \quad 6.4$$

The first reaction is an equilibrium (proton transfer) reaction while reactions 2 through 4 are reversible finite rate reactions where the corresponding reverse reactions complete the reaction set for PZ. Arrhenius rate expressions represent the rate constants for the kinetic reactions (including forward and reverse rates) where the pre-exponential and activation energy parameters were regressed from wetted wall column data collected over a range of temperatures, solvent concentrations, and loadings relevant for capture applications considered in this work. Finally, physical property models for binary diffusion coefficients, viscosity, and density were regressed as a function of amine concentration, loading, and temperature. For a detailed description of the "Independence" PZ model, see Frailie (Frailie, 2014).

6.2.1 Packing Mass Transfer Model

The specific effects of fluid mechanics and physical properties of the gas and liquid on mass transfer are determined by incorporating models for mass transfer in packed beds. Two mass transfer models were used through the course of the work in this chapter.

6.2.1.1 Hanley and Chen Mass Transfer Model

The Hanley and Chen mass transfer model was developed internally by Aspen Technology by regressing a large database of distillation and acid gas absorption/stripping experiments (Hanley & Chen, 2012). The effective area of sheet metal structured packing is described by Equation 6.5.

$$\frac{a_e}{a_p} = 0.539 * \mathrm{Re}_V^{0.145} * \mathrm{Re}_L^{-0.153} * We_L^{0.2} * Fr_L^{-0.2} \left(\frac{\rho_V}{\rho_L}\right)^{-0.033} \left(\frac{\mu_V}{\mu_L}\right)^{0.090} \left(\frac{\cos\theta}{\cos\left(\pi/4\right)}\right)^{4.078}$$

$$\mathrm{Re}_V = \frac{\rho_V d_e u_V}{\mu_V} \quad \mathrm{Re}_L = \frac{\rho_L d_e u_L}{\mu_L}$$

$$We_L = \frac{\rho_L d_e {u_L}^2}{\sigma} \quad Fr_L = \frac{{u_L}^2}{g d_e} \qquad 6.5$$

$$d_e = \frac{4\varepsilon}{a_p}$$

where:

a_e= Effective or interfacial area of packing (m^2/ m^3);

a_p = Specific (geometric) area of packing (m^2/ m^3);

ρ = Liquid or vapor mass density (kg/ m^3);

μ = Liquid or vapor dynamic viscosity (Pa-s);

Θ = Packing corrugation angle;

σ = Surface tension (N/m);

u = Superficial velocity of liquid or vapor (m/s);

g = Gravitational acceleration (m^2/s);

d_e = Equivalent diameter (m);

ε = Void fraction of packing.

The mass transfer coefficient models are described by Equations 6.6 and 6.7.

$$k_L = 0.33\,\mathrm{Re}_L\, Sc_L^{1/3}\left(\frac{c_L D_L}{d_e}\right)$$
$$Sc_L = \frac{\mu_L}{\rho_L D_L} \qquad 6.6$$

$$k_G = 0.0084\,\mathrm{Re}_V\, Sc_V^{1/3}\left(\frac{c_V D_V}{d_e}\right)\left(\frac{\cos\theta}{\cos\left(\pi/4\right)}\right)^{-7.15}$$
$$Sc_V = \frac{\mu_V}{\rho_V D_V} \qquad 6.7$$

where:

$k_{\#}$ = Binary physical mass transfer coefficients, # = L(liquid) or G (gas) (m/s);

$D_{\#}$ = Binary diffusion coefficients, # = L(liquid) or G (gas) (m^2/s).

6.2.1.2 Mass Transfer Models Developed at the University of Texas at Austin

Experiments in a pilot scale air-water column operated by the Separations Research Program (SRP) at the University of Texas (UT) Pickle Research Center (PRC) were used to develop semi-empirical models for the effective interfacial area (a_e) and gas-

and liquid-side physical mass transfer coefficients (k_G and k_L). The interfacial area model used in this work was developed by Tsai and is represented in Equation 6.8 (Tsai, 2010):

$$\frac{a_e}{a_p} = 1.34 * \left[\left(\frac{\rho_L}{\sigma} \right) g^{1/3} \left(\frac{Q}{L_p} \right)^{4/3} \right]^{0.116} \tag{6.8}$$

where:

a_e = Effective or interfacial area of packing (m^2/ m^3);

a_p = Specific (geometric) area of packing (m^2/ m^3);

ρ_L = Liquid mass density (kg/ m^3);

σ = Surface tension (N/m);

g = Gravitational acceleration (m^2/s);

Q = Liquid volumetric flow rate (m^3/s);

L_p = Wetted perimeter in cross-sectional slice of packing (m).

The mass transfer coefficient models (Equations 6.9 and 6.10) were developed from data collected by Wang (Wang, 2015). All parameters in the equations were normalized to reference values (not shown) during the regression. Raw data and details of the regression are included in Appendix A.

$$\frac{k_{L,AB}}{D_{AB}^{0.5}} = 1.44 * \left(u_L / a_p \right)^{0.63} * \left(M_i \right)^{0.54} * \left(\mu_L \right)^{-0.5} \tag{6.9}$$

$$\frac{k_{G,AB}}{D_{AB}^{0.67}} = 49 * \left(u_G / a_p \right)^{0.49} * \left(M_i \right)^{0.13} \tag{6.10}$$

where:

$k_{\#, AB}$ = Binary physical mass transfer coefficients, # = L(liquid) or G (gas) (m/s);

$u_{\#}$ = Superficial velocity, # = L(liquid) or G (gas) (m/s);

M_i = Mixing number - dimensionless parameter describing the number of mixing points in a characteristic volume of packing;

μ_L = Liquid viscosity (Pa-s).

The viscosity dependence assigned in Equation 6.9 represents the effect of viscosity on fluid mechanics (not diffusion) and was derived via literature review (Appendix A).

6.2.1.3 Role of Mass Transfer Models in Absorber Development

The effects of physical mass transfer (or diffusion) on absorber performance were highlighted by the analysis in Chapter 5. The CO_2 absorption process can be controlled by physical mass transfer in the gas and liquid films or by chemical reaction – the relative rates of these mechanisms ultimately determine which phenomena are important or controlling in the absorption process. In addition, the mass transfer area is proportional to overall CO_2 transfer rates regardless of the mas transfer mechanism and can be limiting when chemical reaction is the dominant rate mechanism in the liquid film. The analysis in Chapter 5 found that physical mass transfer in the liquid film is an important mechanism in the absorber, particularly at the rich end of the column where it may be controlling. The reaction rate (and, by association, the area) is most important at the lean end of the column where the system can approach the pseudo-first order limit.

The mass transfer models (such as the ones in the preceding discussion) determine the significance of physical mass transfer in the absorption process (magnitude of the transfer coefficients) but also determine the effect of process and equipment changes on overall mass transfer performance. To the extent that the models provide a realistic

representation of the underlying physical phenomena, they can be used to predict or explain process and equipment changes that enhance performance of the absorber. Therefore, the dependence of the aforementioned mass transfer models on operating and equipment specifications that could potentially be used in the development of novel absorber design will be considered explicitly. Two parameters will be considered here – liquid rate and the hydraulic radius or characteristic dimension of the packing (i.e., specific area). For a more rigorous and systematic comparison of the mass transfer models developed at UT to models in the literature, see the work by Wang (Wang, 2015) and Tsai (Tsai, 2010).

The effects of superficial liquid velocity (or liquid load) and the specific area (as a proxy for the inverse of a characteristic dimension or hydraulic radius) primarily represent a measure of turbulence, which enhances surface to bulk mixing and generates additional surface area for mass transfer. In the UT models, the parameters enter as a ratio, indicating the relationship expected in a Reynolds number-type dependence. The dependence of mass transfer parameters on superficial velocity and specific area is defined in Equations 6.11 and 6.12 for the Hanley and Chen and UT models.

$$\frac{a_e}{a_p} \sim u_L^{0.155} \quad \frac{a_e}{a_p} \sim a_p^{-0.155} \quad \text{(Tsai model)}$$
$$\frac{a_e}{a_p} \sim u_L^{-0.153} \quad \frac{a_e}{a_p} \sim a_p^{-0.392} \quad \text{(Hanley and Chen model)} \qquad 6.11$$

$$k_L \sim u_L^{0.63} \quad k_L \sim a_p^{-0.63} \quad \text{(Wang model)}$$
$$k_L \sim u_L^{1} \quad k_L \sim a_p^{0} \quad \text{(Hanley and Chen model)} \qquad 6.12$$

The inverse dependence of fractional area on the specific area of the packing in both models (Equation 6.11) indicates that a coarse packing will generate more mass transfer area per unit of physical surface area than a fine packing. This effect has been observed in other work and it has been hypothesized that it arises from the development of ripples, flow instabilities, and droplets in coarse structured packing (see (Tsai, 2010) or (Henriques de Brito, et al., 1994) for examples and discussion). The implication for absorber design is that the use of coarse structured packing where possible (or necessary to limit pressure drop) will yield better performance than fine structured packing per unit area purchased.

The fractional area dependence on liquid velocity is contradictory between the two models. Tsai predicts a positive relationship between fractional area and liquid velocity while the Hanley and Chen predicts a drop in fractional area with increasing liquid rate. Part of the explanation for this seemingly contradictory prediction of the physical behavior in the packing arises from the difficulty of isolating contributions of a specific physical property or flow condition that appears in multiple dimensionless groups (i.e., is related to multiple mechanisms in the fluid dynamics) in the empirical models developed for packing. In this case, the liquid velocity appears in three of the dimensionless groups (Re, We, and Fr for the liquid) in the generic dimensionless model form used by Hanley and Chen. Their model regression predicts that the Weber and Froude number dependencies on velocity cancel, leaving only a liquid Reynolds number contribution for the velocity. In contrast, Tsai's regression found no significant effect in the liquid Reynolds number contribution, but found contributions from both the We and Fr numbers (Tsai, 2010). Unfortunately, this makes direct physical interpretation of the model dependency difficult; while properties such as surface tension were varied to

develop a We number dependence in the Tsai model, this also connotes dependence on liquid velocity. Ultimately, in the work by Tsai, the dimensionless group separation is discarded and the model is recast in terms of physical properties and a term representing liquid load per perimeter of packing. Tsai concludes this last term (which contains the liquid velocity and packing geometry contribution) is the most significant predictor of mass transfer area. Each of the contributions to Tsai's model can be explained by experimental data supporting his conclusions even if a simple physical mechanism is not necessarily evident. The Hanley and Chen model is regressed on a large database spanning a range of physical systems without clarity about the physical properties and operating conditions varied in the experiments. Therefore, the dependence of the model on underlying independent parameters reflects a statistical fit and care should be taken in arriving at any physical conclusions about the variable dependency.

Finally, the liquid film mass transfer coefficient for the UT model has an overall positive dependence on the ratio of the liquid superficial velocity to specific area (Equation 6.12) indicating enhancement of liquid film mass transfer as the liquid rate is increased or coarse packing is used to create an effectively larger liquid load on the surface of the packing. The Hanley and Chen model predicts a strong dependence on liquid rate but no additional effect of the characteristic dimension of the packing. In either case, the models predict opportunity for enhancement of liquid film mass transfer with high intensity (high liquid rate) contacting.

6.3 Solvent Recycle Intercooling Development

6.3.1 Process Flow Diagram and Design Criteria

The absorber configurations in Figure 6-1 and Figure 6-2 represent an alternate intercooling method which integrates the intercooling function into a solvent recycle loop.

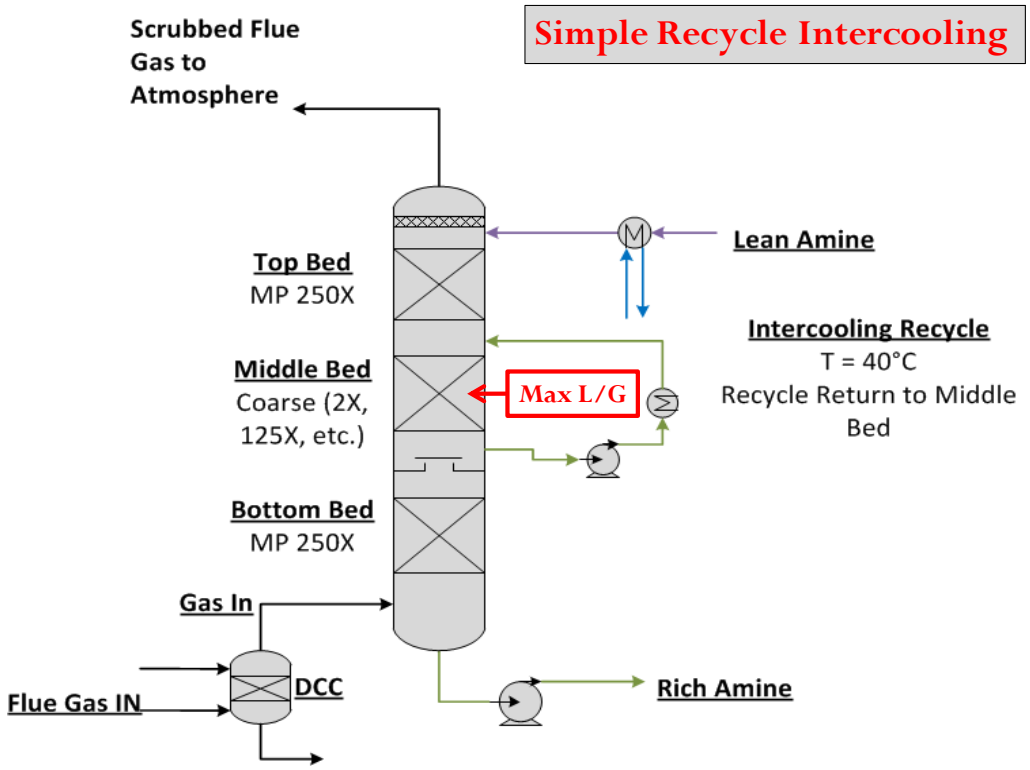

Figure 6-1: Absorber PFD for Simple Recycle Intercooling. Three packing sections are used, with the packing height of each section optimized for each design case to minimize total packing area. MP-250X is used in the top and bottom section and various coarse structured packing is used in the middle (recycle section) to maintain 70% max approach to flood. Solvent is pumped from the bottom of the middle section and cooled to 40 °C.

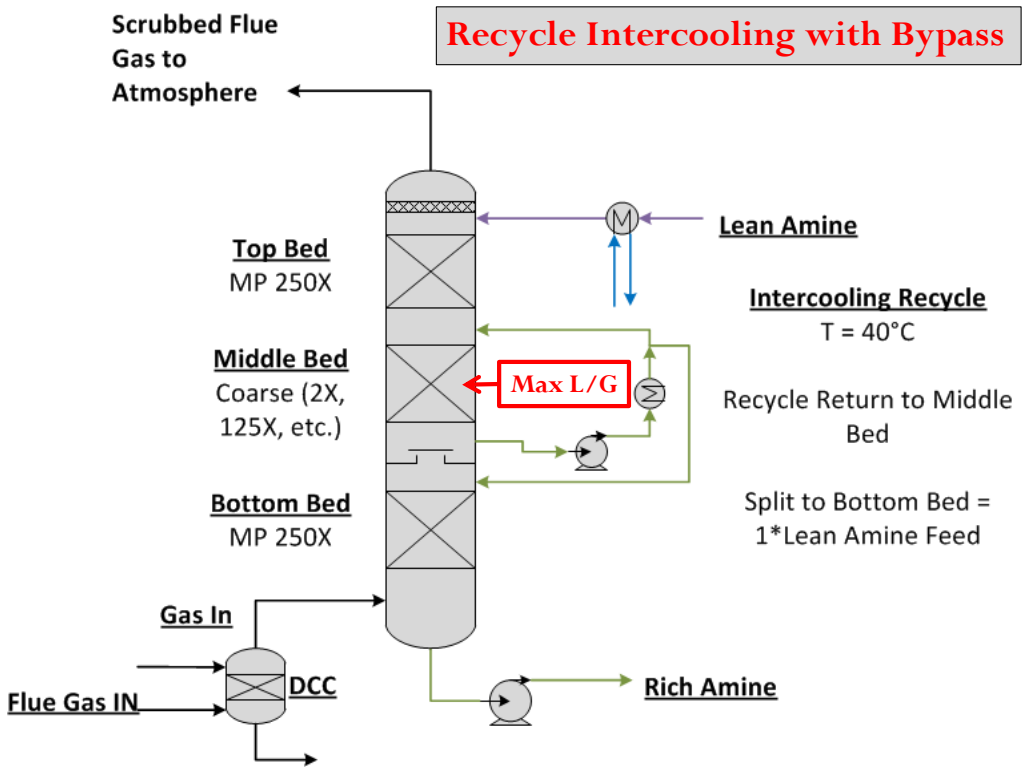

Figure 6-2: Absorber PFD for Recycle Intercooling with Bypass Design. Three packing sections are used, with the packing height of each section optimized for each design case to minimize total packing area. MP-250X is used in the top and bottom section and various coarse structured packing is used in the middle (recycle section) to maintain 70% max approach to flood. Solvent is pumped from the bottom of the middle section and cooled to 40 °C. A portion of the solvent is sent directly to the bottom section of the column (equal to the nominal liquid feed rate of the column) while the remaining liquid is recycled to the top of the middle section.

The solvent recycle design includes a packed bed where the solvent is recirculated. The simple recycle design pumps out a portion of the solvent leaving the recycle bed (defines the recycle rate) and allows the remaining solvent (nominally equivalent to the feed flow rate) to overflow the chimney tray and enter the distributor for the bottom bed without cooling. The recycle with bypass presents an incremental improvement over the simple recycle. All of the solvent leaving the middle packed bed is pumped out of the column and through an intercooling exchanger. Downstream of the

exchanger, a portion of the cooled solvent is sent to the bed below (equal to the nominal feed rate to maintain the steady state material balance) – this feature is referred to as a bypass or split and the benefits will be discussed in subsequent sections.

The design creates new degrees of freedom and design choices as highlighted in Figure 6-3.

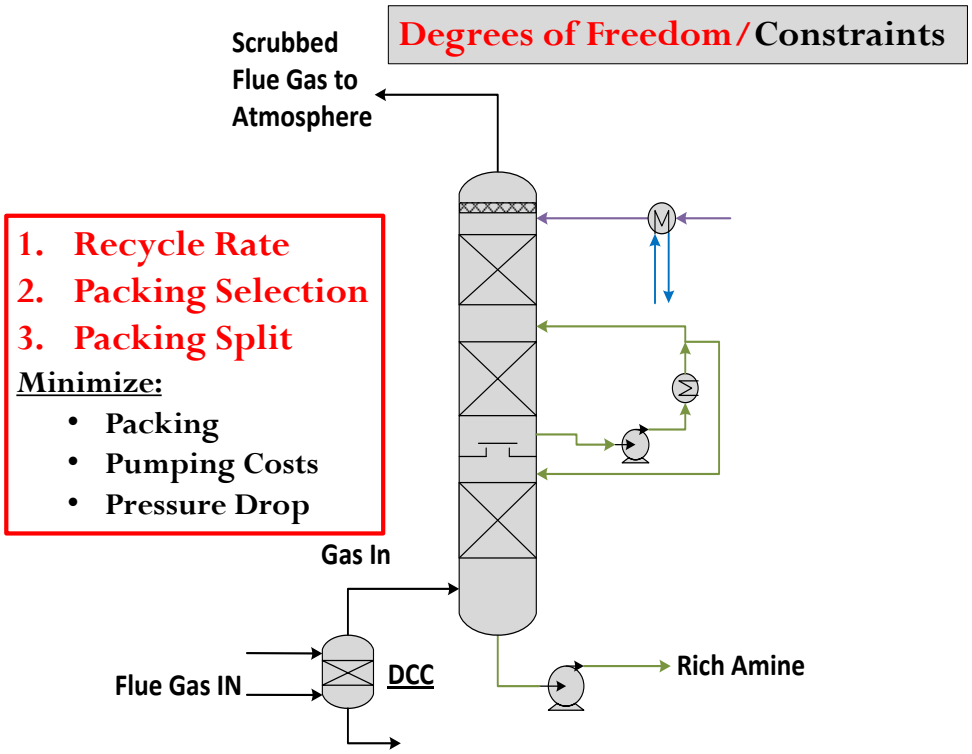

Figure 6-3: Absorber PFD for Recycle Intercooling with Bypass Design. New degrees of freedom and design choices include recycle rate, packing selection for each bed, and the packing split between the 3 beds. The design is constrained by pressure drop and flooding limits in the middle bed and an optimized design will attempt to minimize packing requirements and pumping costs.

The primary degree of freedom introduced with the recycle design is the selection of a recycle rate, which allows an independent value of L/G in the recycle section. In theory,

there is no limit on the solvent recycle rate. In practice, the recycle rate is limited by the pumping costs and pressure drop/flooding constraints (maximum of 70% approach to flood in this study) in the packed section as part of the larger optimization of the absorber and capture system. Recycle rate selection will be discussed in subsequent sections.

The selection of the packing in the middle bed becomes a separate design choice with the implementation of the recycle. This section of the column operates at a much larger L/G than the rest of the column but will likely be in a column with uniform diameter. Therefore, the flooding constraint and associated pressure drop will be limiting in the recycle section. In order to relax this design constraint, different packing can be selected for the recycle. The use of a coarse structured packing in the recycle section can mitigate the pressure drop issues associated with the large L/G and satisfy the flooding constraint without changing the diameter of the entire column.

Finally, as with the simple intercooling method (Chapter 4), the packing distribution can be selected to minimize the overall packing required in the column. The simple intercooling design only had a single degree of freedom (vary a single bed height) while meeting the CO_2 removal constraint. In addition, as discussed in Chapter 4, the packing distribution, or location of intercooling, was primarily a function of the equilibrium constraints or "relative pinch" in each packed section (maximize average driving force in the column). The recycle design will balance similar equilibrium constraints, but the mass transfer efficiency of the 3 sections may vary greatly due to the large L/G and coarse packing used in the recycle. The difference in efficiency of the sections is expected to have an important role in the packing distribution in the column.

6.3.2 Recycle Rate Case Study and Evaluation[4]

Recycle intercooling is implemented as a potential improvement over the simple intercooling (in-and-out intercooling) concepts discussed in detail in Chapter 4. The design was developed to target natural gas combined cycle applications (NGCC) due to the low nominal liquid to gas ratio (L/G) in the absorber for this application. The expected improvement with recycle intercooling is, in part, due to the benefit of cooling the gas with a large L/G in the recycle packed bed. In addition, as discussed in Section 6.2.1, the liquid film mass transfer coefficient and interfacial area for mass transfer are both a function of the liquid rate per wetted perimeter (see Equations 6.5 to 6.9). In addition, the liquid-film mass transfer coefficient is expected to be important for the PZ system, particularly at the rich end of the column (see Chapter 5). The recycle design increases the amount of solvent per unit perimeter of packing. The benefits (and underlying mechanisms of the benefits) of solvent recycle will be discussed in detail in subsequent sections.

The limitations of the recycle design include the mixing of the solvent on the recycle section. The driving forces of the column are reduced by mixing a richer solvent with lean solvent entering the middle section of the column. Furthermore, additional costs are associated with breaking the packed bed in two places for a recycle in the middle of the column (above and below the bed). Finally, for any recycle design, there are additional costs associated with pumping the solvent around the recycle bed (function of the height and solvent rate pumped through the section).

To evaluate the performance of the solvent recycle design, it was compared to in-and-out intercooling and an adiabatic absorber for the NGCC application. The evaluation in Chapter 4 indicated that the NGCC application can benefit from an improved design in

[4] Hanley and Chen model used for this case study.

terms of solvent capacity and mass transfer performance over the simple in-and-out intercooling design. Table 6-1 includes the NGCC flue gas conditions for the evaluation. Table 6-2 summarizes equipment design parameters used in the NGCC intercooling comparison.

Table 6-1: Flue Gas Conditions, Natural Gas Combined Cycle Flue Gas

Gas Conditions		
Gas Feed Rate	114,000	kmol/hr
	3,230,000	kg/hr
Temperature	106	°C
Pressure	1	atm
Composition (Mole %)		
CO_2	4.0%	
H_2O	8.7%	
N_2	74.3%	
O_2	12.1%	
Data from NETL Case 13 (National Energy Technology Laboratory, 2010)		

Table 6-2: Equipment and Process Design Parameters for the Solvent Recycle Evaluation

Equipment and Process Design Parameters		
CO_2 Removal	90%	
Lean Loading (mol CO_2/ mol alkalinity)	0.25	
Flue Gas CO_2 Concentration (post-DCC) (mol%)	4.1%	
Recycle Rate ($L_{Recycle}$/G)	0.5–8	
Maximum Approach to Flooding	70%	
Packing (No Solvent Recycle in Section)**	MP 250X	
Packing (Solvent Recycle in Section)**	0.5 $L_{Recycle}$/G:	MP 250X
	1 $L_{Recycle}$/G:	MP 250X
	2 $L_{Recycle}$/G:	MP 2X
	3 $L_{Recycle}$/G:	MP 170X
	5 $L_{Recycle}$/G:	MP 125X
	8 $L_{Recycle}$/G:	MP 64X
**Coarse Packing required to meet flooding criteria in packing section with solvent recycle. Packing type varied to approximate identical flooding profiles in each case.		

Table 6-2 includes the range of recycle rates evaluated in this study (defined in the table as liquid rate in the recycle relative to the overall gas rate in the column). In addition, the table reflects the design choice regarding packing that is introduced by the recycle configuration. MP 250X is the standard packing used in all cases in packing sections without recycled solvent. However, in the cases *with solvent recycle* (around the middle bed of 3 sections of packing), the maximum approach to flooding is reached in the recycle section due to high liquid rates compared to the rest of the column. Instead of increasing the column diameter with increasing recycle liquid rate, a progressively

coarser packing (reduced specific area) was used to minimize pressure drop and flooding with limited change to column diameter from case to case.

The goal of this case study is to develop an understanding of the effect of solvent recycle on absorber performance to allow better definition of operating conditions ($L_{Recycle}/G$) and equipment specifications (packing distribution, pump head in recycle) for the recycle design.

6.3.2.1 Process Performance: Packing Area and Rich Loading Cross-plots

Two approaches were used to compare the intercooling designs. First, the simple recycle design (no bypass) was compared to the in-and-out intercooling design and an adiabatic absorber (no intercooling) at an operating point of 1.2*minimum liquid flow rate (L_{MIN}) for each case (all achieving 90% CO_2 removal). This approach allows comparison of the designs at a common operating point; the packing requirement and energy performance (as reflected in the rich loading) can be compared for all designs. However, this method requires interpretation or weighting of the capital cost benefits (packing) and the energy benefits (rich loading) on a common basis to provide an absolute comparison of designs.

The second approach involved comparison of intercooling designs at a common rich loading. By fixing the rich loading (and, in conjunction with the 90% removal requirement, fixing the absolute solvent rate), the packing requirements of each design can be compared directly without consideration of energy performance implications.

In both approaches, the packing distribution of the recycle intercooling design was defined to minimize the total packing requirement in the column for every case that was run. This was accomplished by optimizing the packing split between the three sections in the column.

Figure 6-4 and Figure 6-5 provide a comparison of the simple recycle intercooling design to both in and out intercooling and a baseline of no intercooling.

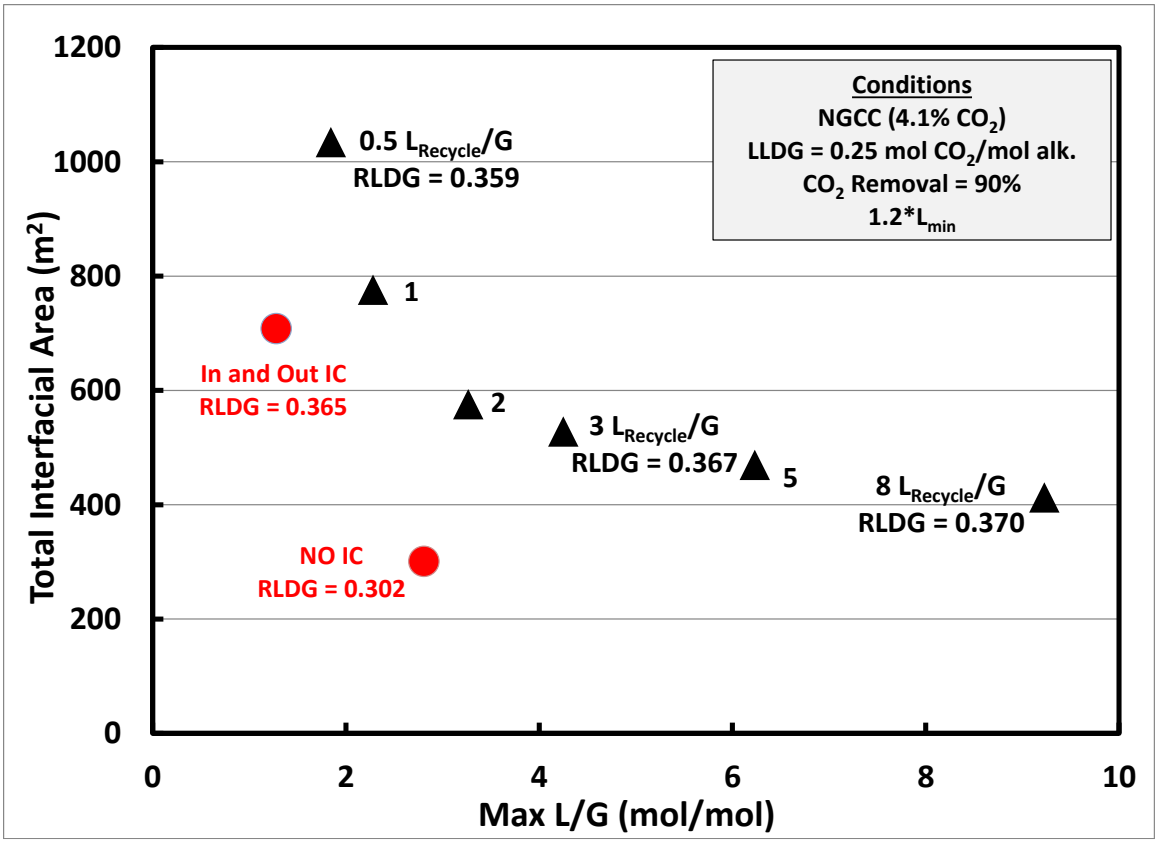

Figure 6-4: Intercooling configuration comparison in terms of total packing requirement: simple recycle intercooling, in-and-out intercooling, and no intercooling. For cases without recycle, the maximum L/G corresponds to the nominal feed L/G. For the recycle cases, this corresponds to the L/G in the recycle section (feed L + recycle L). Recycle intercooling simulated at a series of recycle solvent flow rates (and corresponding max L/G).

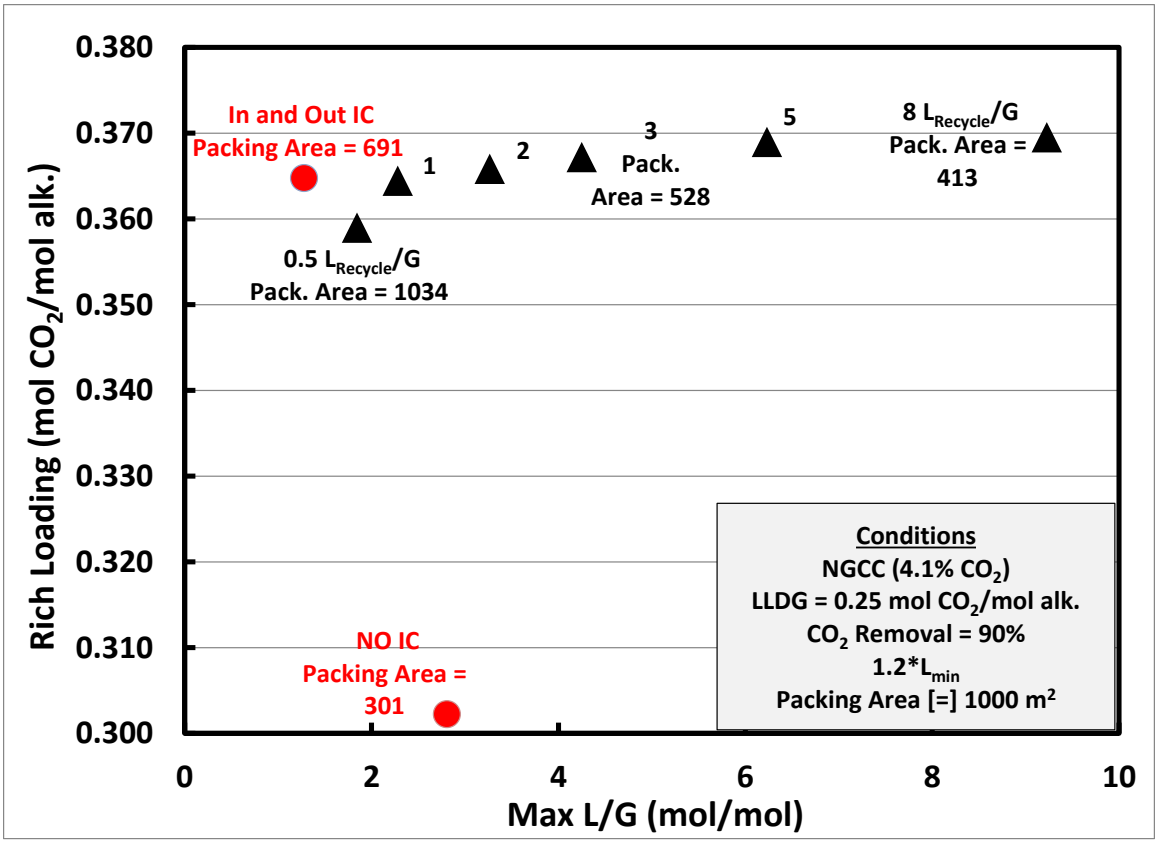

Figure 6-5: Intercooling configuration comparison in terms of rich loading achieved: simple recycle intercooling, in and out intercooling, and no intercooling. For cases without recycle, the maximum L/G corresponds to the nominal feed L/G. For the recycle cases, this corresponds to the L/G in the recycle section (feed L + recycle L). Recycle intercooling simulated at a series of recycle solvent flow rates (and corresponding max L/G).

The preceding figures should be used together when evaluating the designs. For example, Figure 6-4 indicates that a design without intercooling will provide the lowest packing requirement; however, the high liquid rate required leads to a rich loading (Figure 6-5: 0.302 mols CO_2/mols alkalinity) that is impractical from an energy and stripping performance perspective.

More importantly, the chart highlights the minimum recycle rate required for simple recycle to become competitive with in-and-out intercooling. In terms of both

packing requirement and rich loading, a recycle rate of 1 L/G is required (max L/G = 2.28) to make the recycle design comparable to in-and-out intercooling. Given the additional cost associated with the recycle design (pumping liquid around the middle section of packing, potentially larger intercooling equipment, etc.), a higher recycle rate would be needed to justify the recycle design. As both figures show, the higher recycle rates provide both reduced packing and improved rich loading. However, the benefits show diminishing returns with incremental increases in recycle rate, and when considered with costs associated with higher recycle rates, indicate potential for an optimal recycle rate somewhere above 1 L/G but below the 8 L/G value simulated here.

To compare the configurations on a common basis, Figure 6-6 compares all 3 intercooling designs (in-and-out, simple recycle, recycle with bypass) at a constant rich loading of 0.365 mols CO_2/mols alkalinity (constant L/G of 1.28 mol/mol). The fixed rich loading corresponds to that achieved by in-and-out intercooling at $1.2*L_{MIN}$.

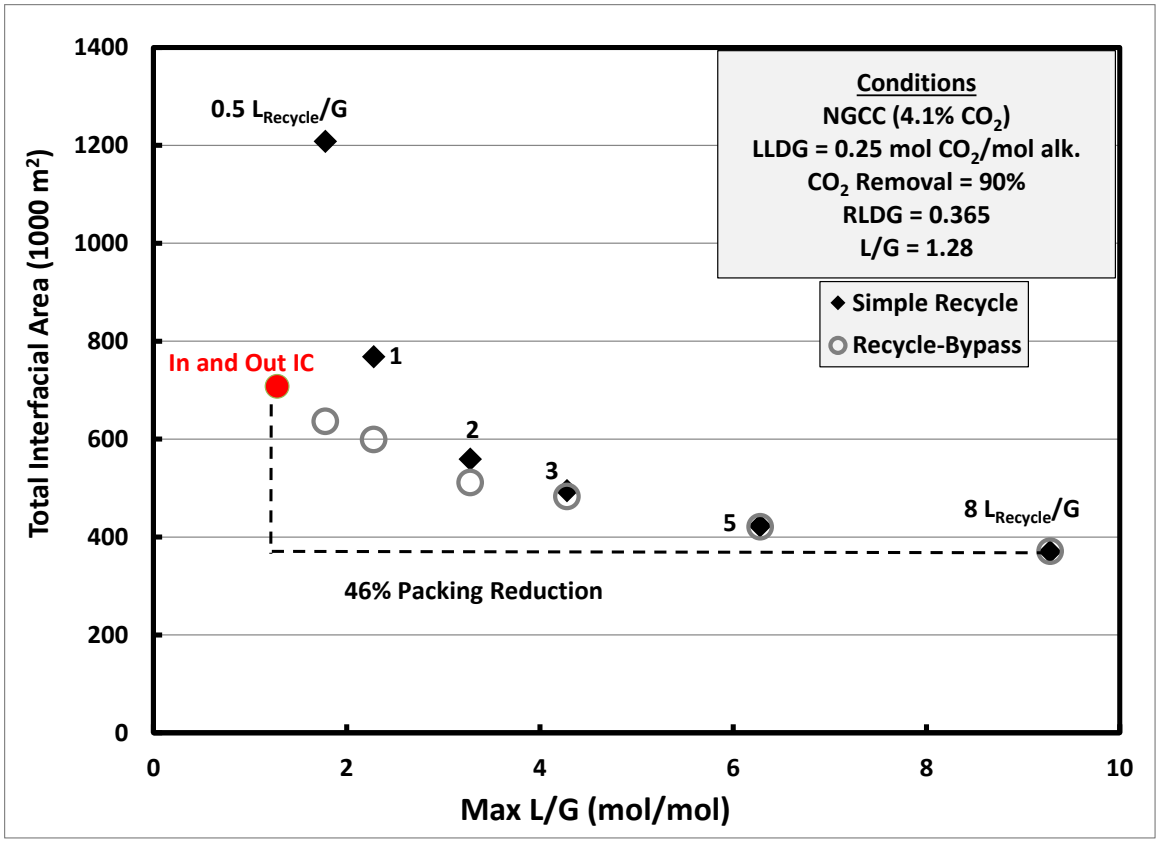

Figure 6-6: Intercooling configuration comparison at constant rich loading (and solvent rate) in terms of total interfacial area: simple recycle intercooling, recycle with bypass, and in-and-out intercooling. For cases without recycle, the maximum L/G corresponds to the nominal feed L/G. For the recycle cases, this corresponds to the L/G in the recycle section (feed L + recycle L). Recycle intercooling simulated at a series of recycle solvent flow rates (and corresponding max L/G).

As in the previous figures, simple recycle intercooling must utilize a recycle rate greater than 1 $L_{Recycle}/G$ to be competitive with in-and-out intercooling. At a recycle rate of 8 $L_{Recycle}/G$, the maximum packing reduction of 46% is achieved compared to in-and-out intercooling. However, the implementation of the recycle with bypass (sending 40 °C solvent to the bottom section of the column and maintaining intercooling benefit) shows drastic improvements at the low recycle rates. At a recycle rate of 0.5 $L_{Recycle}/G$, the implementation of bypass reduces the packing requirement by 47% compared to simple

recycle and by 8% compared to in-and-out intercooling. The benefit of recycling solvent is effectively combined with the intercooling benefit realized with the standard in-and-out design. A similar improvement is seen at a recycle rate of 1 $L_{Recycle}/G$; however, beyond this rate, the benefit of the bypass design is marginal and eventually the bypass and simple recycle designs become indistinguishable. At higher solvent recycle rates, the temperature of the solvent leaving the recycle section approaches 40 °C and the bypass provides limited benefit. This is illustrated in Figure 6-7.

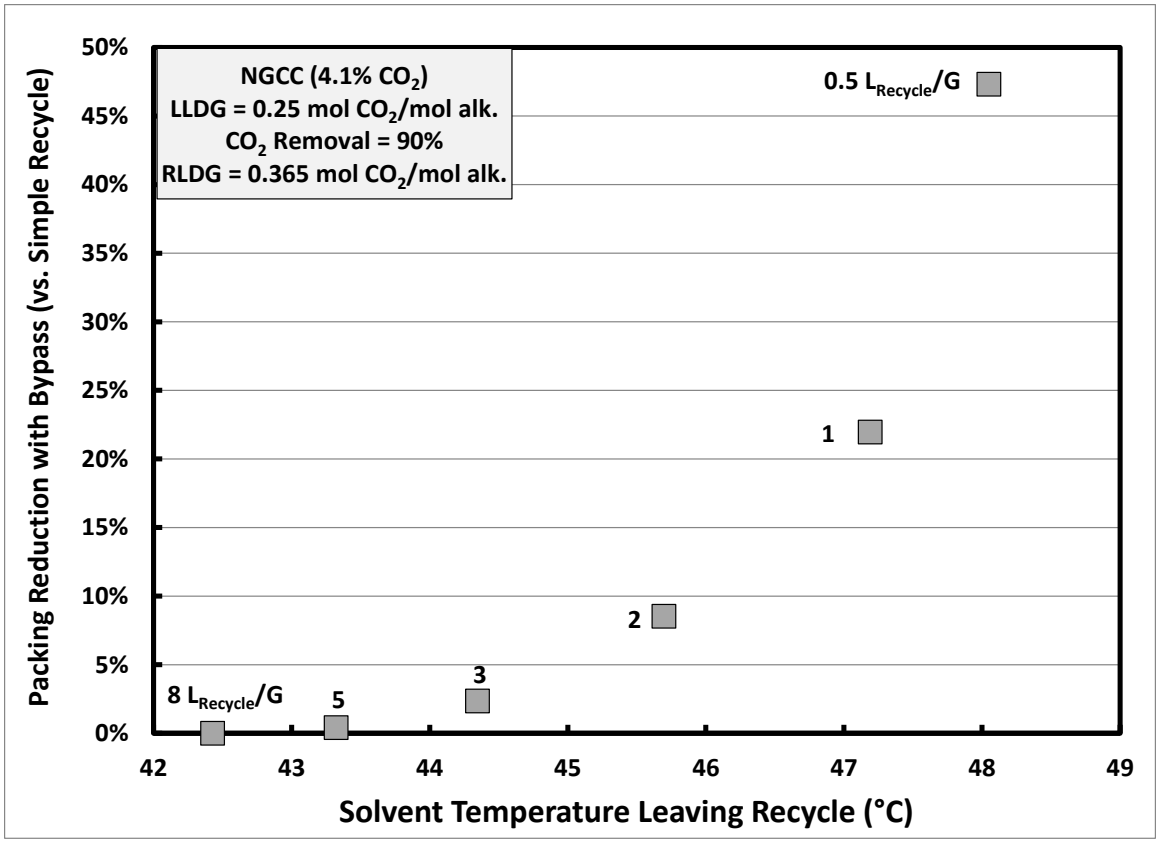

Figure 6-7: The benefit (packing reduction) of recycle intercooling with bypass compared to simple recycle intercooling as a function of the solvent recycle rate and corresponding temperature leaving the recycle section.

As expected, at higher recycle rates the temperature leaving the recycle drops; the temperature is as low as 42.4 °C at the highest recycle rate of 8 $L_{Recycle}/G$. With the drop in temperature leaving the recycle, the benefit of the bypass design compared to the recycle design is diminished. By a recycle rate of 3 $L_{Recycle}/G$ (temperature leaving recycle = 44.3 °C), the benefit is less than 5% reduction in packing.

The preliminary results of the NGCC application intercooling comparison revealed the operating range in which recycle intercooling may be beneficial. A recycle rate above 1 $L_{Recycle}/G$ should be used as this value is close to the nominal solvent feed rate and the benefits of the recycle are limited (mixing with warm solvent from section

above, limited L/G benefits). In addition, at high recycle rates ($\geq$ 5 $L_{Recycle}/G$), the benefits associated with recycle intercooling (reduced packing and higher rich loadings) show diminishing returns.

6.3.2.2 Incremental Economic Analysis: Packing Cost Savings vs. Pumping Costs

An incremental economic analysis will be used to compare the recycle intercooling with bypass design (provides benefits at all recycle rates) to a baseline of in-and-out intercooling. Both designs will be compared at a constant solvent flow rate ($L_{IN\text{-}AND\text{-}OUTIC}/L_{MIN}$ = 1.2) or, equivalently, a constant rich loading of 0.365 mol CO_2/mol alkalinity (cases represented in Figure 6-6). The goal of the analysis is to provide a feasibility or screening assessment of the recycle intercooling design within the range of recycle rates (Table 6-2) evaluated in this study. The incremental analysis will only consider the following factors:

1) Incremental packing cost savings
2) Pumping costs (operating costs only) associated with recycle loop
3) Incremental blower operating costs/cost savings (gas-side pressure drop)

Several other costs may vary between the in-and-out intercooling design and recycle design including incremental cost of column internals (additional liquid distributors, packing supports), differences in size and capital cost of peripheral equipment (intercooling heat exchanger and pump, piping size), differences in process control equipment, differences in cooling water consumption, etc. - see the work by Frailie for an example of detailed absorber economics (Frailie, 2014). However, if the core costs of the recycle intercooling design (pumping and pressure drop associated with the recycle) are not justified by the benefits, the design will not be feasible in general. In addition, the ranking of the recycle intercooling designs (i.e., ranking of recycle rate) are

unlikely to be affected by the costs omitted from the analysis as they should scale with the costs considered in this analysis. Table 6-3 includes key assumptions used in the calculations.

Table 6-3: Assumptions for Incremental Economic Evaluation of Recycle Intercooling

Capital Cost Assumptions		Operating Cost Assumptions	
Interest Rate Of Capital	12.50%	Annual Operating Hours[2]	7446
Amortized Lifetime (years)	15	Cost of Electricity ($/MWh)[3]	56.6
Amortization Factor[1]	15%	Overall Pump Efficiency[4]	64%
		Blower Efficiency	72%

1: Amortization factor calculated from interest rate and loan term. Provides (equal) annual payments when multiplied by principal.

2: Capacity Factor = 85% **(National Energy Technology Laboratory, 2010)**

3: 2012 Texas Industrial Average Cost of Electricity **(U.S. Energy Information Administration, 2013)**

4: Pump efficiency is average value over range of flow rates considered in this analysis **(Peters, et al., 2003)**.

The annualized capital (packing cost) and operating (pumping/blower) costs were calculated by Equations 6.13 through 6.15.

$$Annualized\ Packing\ \text{Cost} = UC_{Packing} * V_{packing} * AF \qquad 6.13$$

$$AF = i + \left(\frac{i}{(1+i)^n - 1} \right)$$

where:

$UC_{Packing}$ = Unit cost of packing ($/m^3) – see Figure 6-8;

$V_{Packing}$ = Volume of packing (m^3).

AF = Amortization factor (or annuity calculation);

i = Annual interest rate (as % or fraction) – See Table 6-3;

n = Term of loan or project (years) – See Table 6-3;

$$Annual\ Pumping\ \mathrm{Cost} = UC_{Electricity} * \left[\frac{\dot{m}_{\mathrm{Recycle}} * g * h_{\mathrm{Recycle}}}{1000 * \eta_{Pump}} \right] \qquad 6.14$$

where:

$UC_{Electricity}$ = Unit cost of electricity ($/kWh) – see Table 6-3;

$\dot{m}_{\mathrm{Recycle}}$ = Mass flow rate through recycle pump (kg/s);

$h_{Recycle}$ = Height of recycle section (m);

η_{Pump} = Pump efficiency – See Table 6-3;

$$Annual\ Blower\ \mathrm{Cost} = UC_{Electricity} * \left[\frac{\Delta P_{Packing} * Q_{Gas}}{1000 * \eta_{Blower}} \right] \qquad 6.15$$

where:

$\Delta P_{Packing}$ = Pressure drop in packed bed (Pa) – from vendor correlation in AspenPlus®;

Q_{Gas} = Volumetric flow rate of gas at blower (m^3/s);

η_{Blower}= Blower efficiency – See Table 6-3;

The incremental economic analysis used the preceding equations to establish baseline annualized costs for in-and-out intercooling and determined the incremental cost (or savings) based on the specific packing and pumping/blower requirements for each recycle case.

The packing costs were calculated using data and a simple linear correlation from previous work by Tsai corrected to 2012 U.S. dollars (Tsai, 2010). The original data and correlation from Tsai are shown in Figure 6-8.

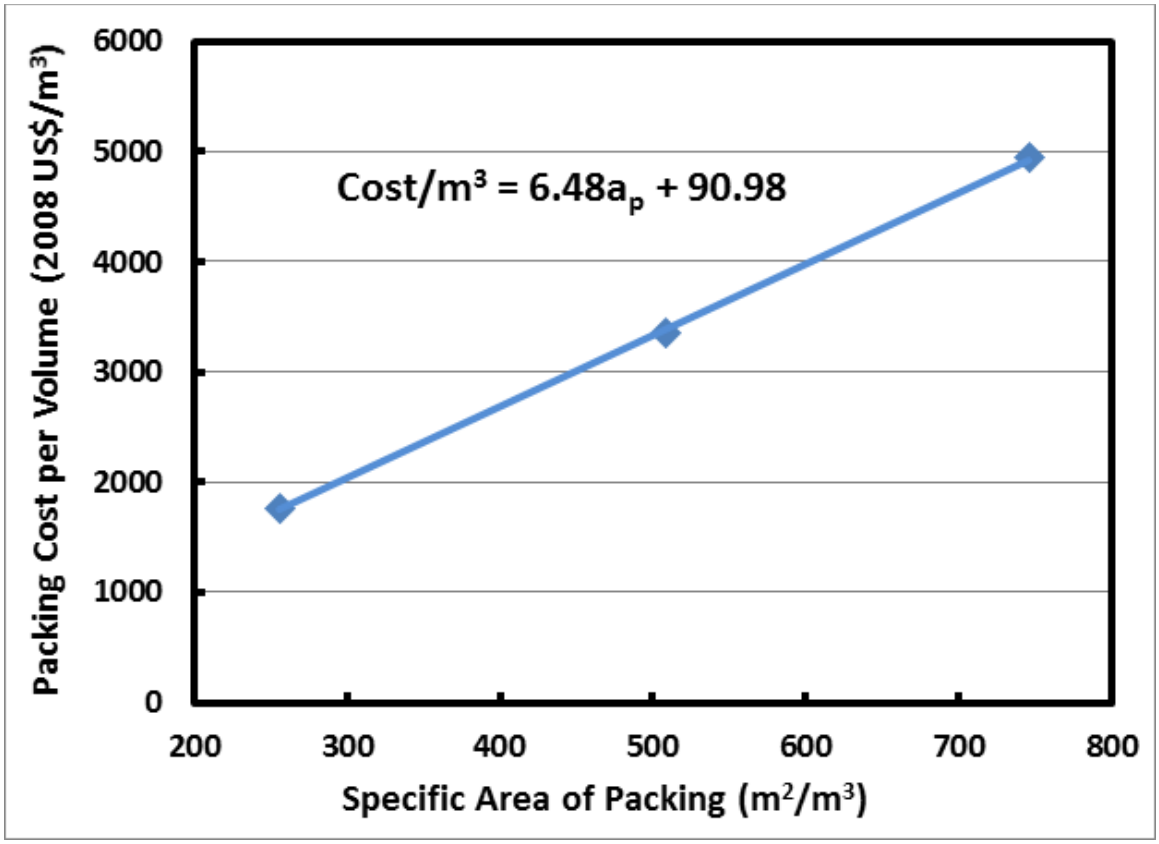

Figure 6-8: Prediction of packing cost per unit volume from the packing specific area based on data collected by Tsai for 3 packing sizes (250, 500, 750 m^2/m^3) (Tsai, 2010)

The packing cost data is limited and restricted to a single set of vendor quotes obtained by Tsai; in addition, the range of packing sizes used in this analysis is beyond the range encompassed by the correlation. However, in the absence of detailed packing cost data, the correlation by Tsai provides relatively recent data on structured packing costs.

The results of the economic evaluation are presented in two parts. The first evaluation only considers the packing and pumping cost components (omitting the pressure drop costs). The second portion of the analysis will include the pressure drop/blower operating costs. The analysis was performed separately to highlight the important effect of gas-side pressure drop on the overall economics. The pressure drop

model used in this work is the proprietary vendor correlation built into AspenPlus® associated with the Mellapak-series packings used in this analysis. Since the vendor pressure drop model is not accessible and the pressure drop data in Mellapak packing has not been independently corroborated for the conditions and packing types tested in this work, the costs associated with pressure drop predictions may be a large source of uncertainty. Therefore, the analysis is presented with and without gas-side pressure drop costs.

Figure 6-9 presents the incremental economic analysis considering pumping and packing costs.

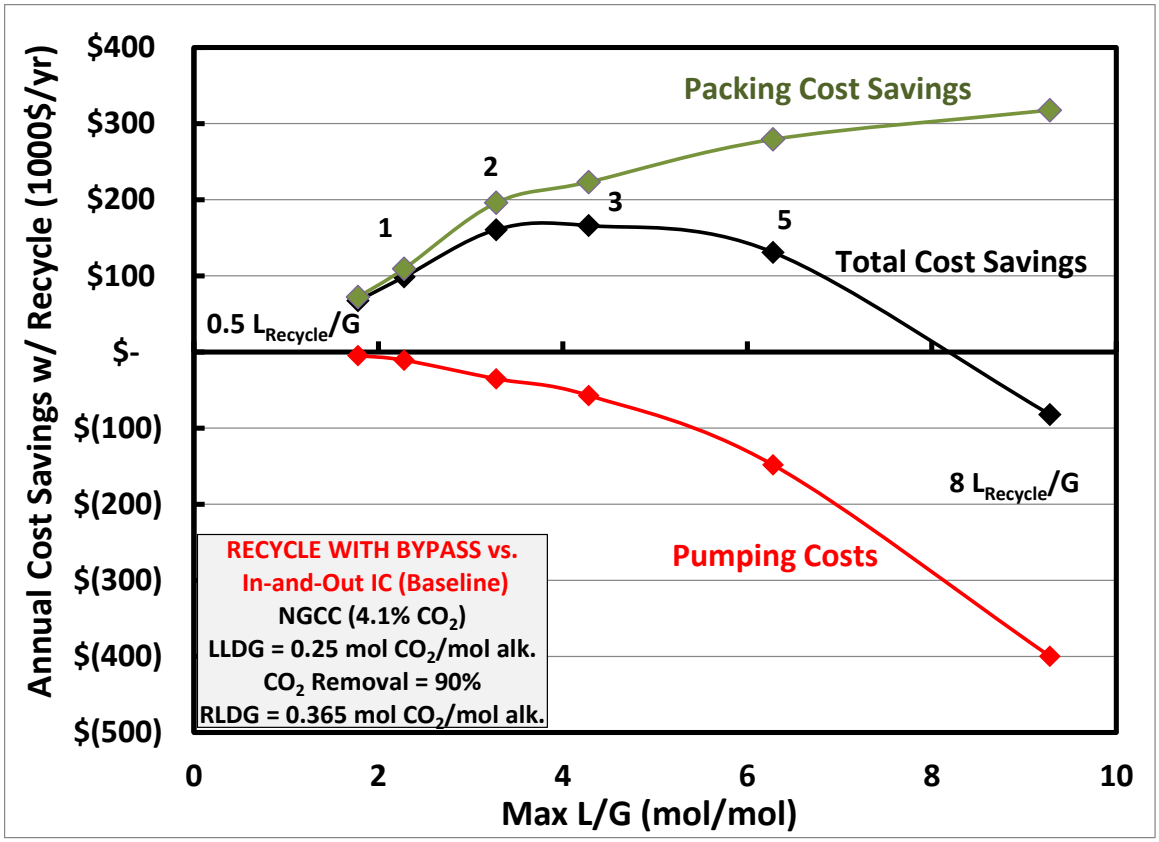

Figure 6-9: Cost savings achieved (compared to in-and-out intercooling at the same rich loading/solvent rate) by recycle intercooling with bypass configuration applied to NGCC flue gas (4.1% CO_2). Each case operated at LLDG = 0.25 mol CO_2/mol alk. to achieve 90% removal. Total cost savings (black curve) calculated by subtracting pumping costs (red curve) from packing cost savings (green curve). All costs on an annualized basis. Max L/G corresponds to the L/G in the recycle section (feed L + recycle L).

The results of the analysis show that the packing cost savings predicted for the recycle intercooling design outweigh the pumping costs for all but the highest recycle rate ($L_{Recycle}/G$ = 8). At the highest solvent recycle rate, the improvement in mass transfer performance (measured as packing reduction) exhibited diminishing returns (Figure 6-6). In addition, the use of progressively coarser packing (less surface are per unit volume) with increasing recycle rate leads to the steep increase in pumping costs seen in Figure

6-9. The figure indicates that the largest incremental savings are achieved with a recycle rate between approximately $L_{Recycle}/G = 2$ and 4.

Figure 6-10 provides the results for the same analysis with the incremental cost savings of pressure drop reduction in the recycle intercooling design.

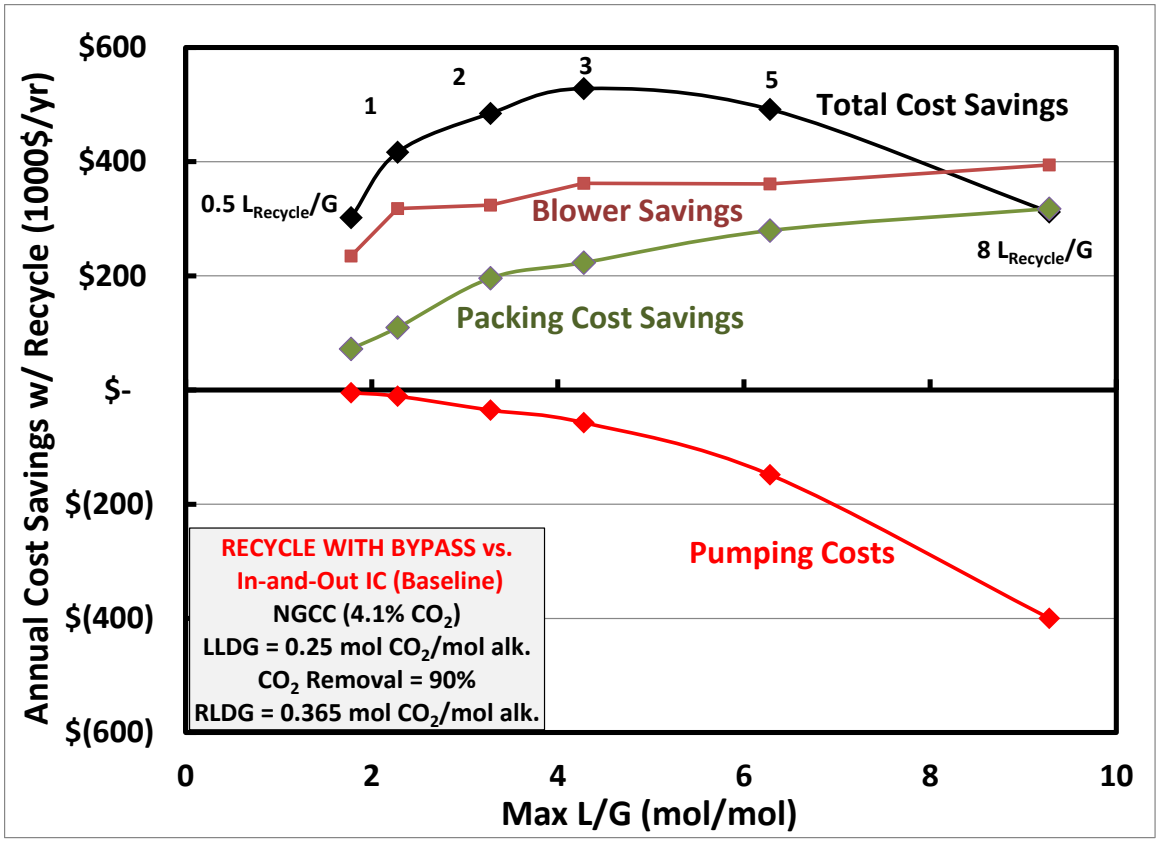

Figure 6-10: Cost savings achieved with blower costs (compared to in-and-out intercooling at the same rich loading/solvent rate) by recycle intercooling with bypass configuration applied to NGCC (4.1% CO_2) and operated at LLDG = 0.25 mol CO_2/mol alk. to achieve 90% removal. Total cost savings (black curve) calculated by subtracting pumping costs (red curve) from packing cost savings (green curve) and blower operating cost savings (maroon curve). All costs on annualized basis. Max L/G corresponds to the L/G in the recycle section (feed L + recycle L).

The figure illustrates the blower operating costs are reduced with the recycle intercooling design across the entire range of recycle rates. The resulting cost savings largely offset the pumping costs, even at the highest recycle rates, and lead to potentially feasible recycle designs across the range of conditions tested. As before, the maximum cost savings are achieved in the range of $L_{Recycle}/G = 2$ to 4. The explanation for the reduced pressure drop with the recycle rate has two components. First, the overall height of packing (i.e., gas path length) is smaller for all but the highest recycle rate ($L_{Recycle}/G = 8$), despite the use of coarse packing in the recycle sections. This indicates that the recycle section has improved the overall efficiency of CO_2 removal via enhanced mass transfer in the recycle section and improved driving forces outside of the recycle (reduced temperatures). Secondly, the improved intercooling and removal of CO_2 in the cooled recycle section mean that the gas temperatures are lower throughout the column than the in-and-out intercooled case (this will be discussed in subsequent sections). The lower gas temperatures lead to lower gas velocities (increased density), reducing the pressure drop compared to the in-and-out intercooling base case.

6.3.2.3 Identifying mechanisms for recycle intercooling benefits

The recycle intercooling design appears to provide significant mass transfer performance enhancement as measured in terms of packing reduction from the baseline in-and-out intercooling case. While improved intercooling performance (cooling the gas) and enhanced turbulence (improved liquid-film mass transfer and effective area) have been proposed as explanations, the preceding analyses do not confirm the source of the benefits. In an effort to de-couple the various mechanisms that may be the source of the recycle design benefits, a series of modeling cases and calculations were developed to isolate the expected mechanisms.

The overall approach of isolating the contribution to the change in packing requirement (compared to the base case in-and-out design) of each of the effects of the recycle intercooling discussed in the preceding section is summarized as follows:

OVERALL PACKING REDUCTION

- CONTRIBUTION FROM EFFECTIVE AREA DEPENDENCE ON LIQUID RATE
- CONTRIBUTION FROM EFFECTIVE AREA DEPENDENCE ON PACKING SELECTION (SPECIFIC AREA)
- CONTRIBUTION FROM MASS TRANSFER COEFFICIENT DEPENDENCE ON LIQUID RATE
- CONTRIBUTION FROM MASS TRANSFER COEFFICIENT DEPENDENCE ON PACKING SELECTION (SPECIFIC AREA)

NET DRIVING FORCE EFFECT (INTERCOOLING BENEFIT – BACK-MIXING PENALTY)

Each of the mass transfer contributions is quantified and removed from the overall packing reduction reported (see Figure 6-6) leaving a remainder which should reflect the net driving force effects. While this does not lead to a direct quantification of the intercooling benefit, the intercooling benefit is coupled with the important deterioration of performance (back-mixing of solvent) expected with the recycle design and therefore reflects the fundamental driving force trade-off central to the recycle concept. The calculation of the individual mass transfer contributions was performed as follows:

1) **MODELING STEP**: The diameter of the column **in the recycle section** in each design case was increased until the superficial liquid velocity matched the values outside of the recycle section and a new packing area requirement is determined. This modeling approach allows the same amount of liquid to be recycled through the intercooling section (same maximum L/G as before) providing the same intercooling benefit as the nominal design, but removes the benefits associated with the high superficial velocity in the recycle section (see preceding discussion of the effect of superficial velocity on wetted area and mass transfer coefficients).

2) **CALCULATION STEP**: Calculate the effect of the liquid superficial velocity on the wetted area directly from the previously presented correlation (Equation 6.5). Using the information from step 1, the changes in the packing requirement due to the effect of superficial liquid velocity on the wetted area and on the mass transfer resistance have now been isolated independently.

3) **CALCULATION STEP**: Calculate the change in total packing requirement due to the use of a coarse packing in the middle section of the recycle design compared to fine packing throughout the in-and-out intercooling design. This can be calculated directly from the preceding correlation (Equation 6.5).

4) The Hanley and Chen model does not predict a dependence of the mass transfer coefficient on packing type (specific area), so no calculation is needed in this analysis.

The mass transfer enhancements (area and mass transfer resistance related) are now independently isolated and the remainder of the reported packing reduction from the in-and-out intercooling base case is the net driving force benefit (intercooling vs. back-mixing). This method has potential shortcomings related to the first (modeling) step. The recycle section is not isolated from the rest of the absorber and changes in this section may yield performance differences outside of the section the section that are secondary benefits of the recycle design. However, to a first approximation, the benefits of the increased liquid rate can be quantified by deduction as in the proposed approach. The results (Figure 6-11) identify the relative contribution of each mechanism to the total packing reduction predicted by the model for the recycle section.

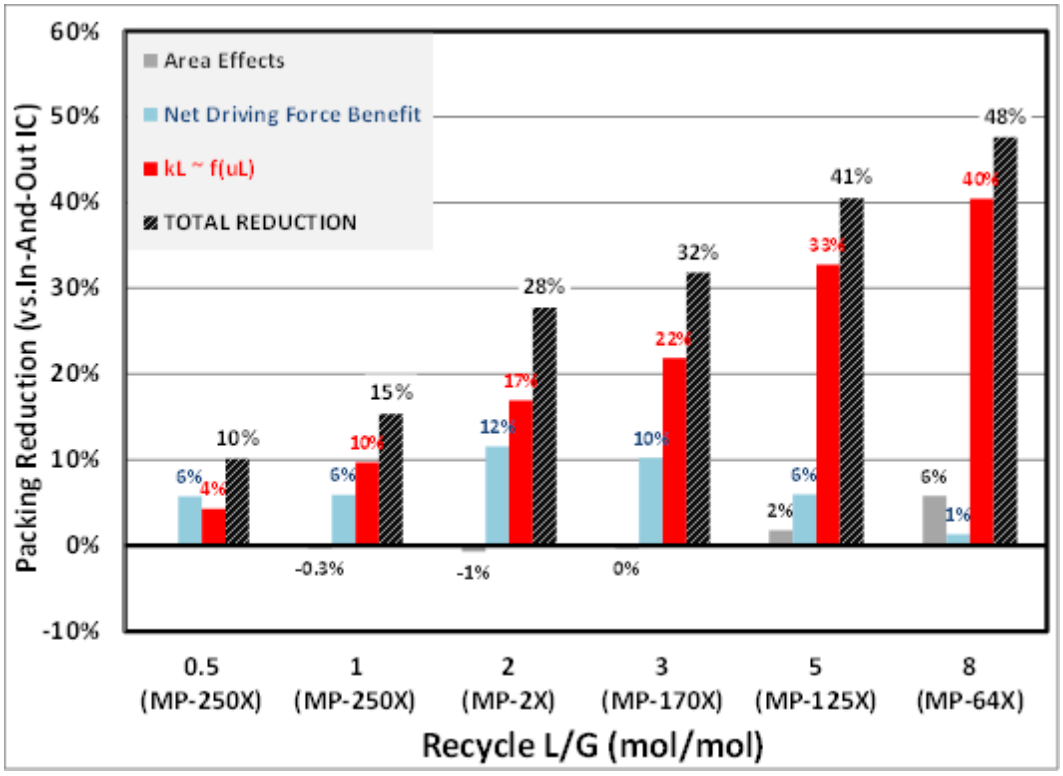

Figure 6-11: Isolated contributions to overall packing reduction for recycle intercooling with bypass design compared to in-and-out intercooling design. Recycle rates from 0.5 to 8 L/G are presented for the NGCC (4.1% CO_2) application. All cases with following specifications: LLDG = 0.25 mols CO_2/mols alkalinity, RLDG = 0.365 mols CO_2/mols alkalinity, CO_2 Removal = 90%. Packing type used in recycle section noted in parentheses under recycle rate.

The area effects (first of four bars in each group, if present, reading from left to right) include the combined effect of liquid rate and packing specific area on the wetted area; the two were combined since the overall contribution to the change in packing requirement is small in all cases. The area effects are negative (or increase the packing requirement compared to in-and-out intercooling) at the lowest recycle rates because the Hanley and Chen model predicts a negative dependence on liquid velocity (as discussed before); as the packing is changed to progressively coarser packing, however, the fractional area dependence on the packing geometry begins to become more important,

and the area effects ultimately contribute to a reduction in the packing requirement. In general, however, it is clear that the Hanley and Chen model predicts minimal effect on wetted area of the packing due to the conditions in the recycle.

The net driving force effect (combined intercooling and back-mixing effect) of the recycle is shown in the second bar (blue) from the left in each case. This trend shows an initially increasing benefit from intercooling at the lowest recycle rates to a maximum of 12% packing reduction at the 2 L/G recycle rate; beyond this recycle rate, the benefit diminishes and appears negligible at the highest recycle rates. There are two explanations for this trend. First, as the recycle rate is increased, the marginal benefit of intercooling diminishes – the temperature in the system is not affected by an incremental increase in liquid rate beyond some point. This would explain a flattening in intercooling benefits with recycle rate. The decline in intercooling benefits (above $L_{Recycle}/G = 2$) is explained by the back-mixing contribution. As illustrated in Table 6-4, more of the packing was allocated to the well-mixed recycle section of the column as the recycle rate increased to minimize the total packing area of the column. Up to ~40% of the mass transfer area is not utilized for counter-current contacting at highest recycle rates. Therefore, the average driving forces in the column are progressively diminished with recycle rates and undercut the driving force benefits from intercooling.

Table 6-4: Packing Distribution by height and metal packing area for NGCC application with recycle intercooling. All cases at lean loading = 0.25, constant rich loading = 0.365, 90% removal. MP-250X in top and bottom sections of column in all cases.

Recycle L/G	Packing in Recycle Section	% of Total Height			% of Total Metal Packing Area		
		Top	Mid	Bottom	Top	Mid	Bottom
0.5	MP-250X	30%	18%	52%	30%	18%	52%
1	MP-250X	31%	23%	46%	31%	23%	46%
2	MP-2X	32%	38%	30%	35%	33%	32%
3	MP-170X	39%	40%	21%	45%	31%	24%
5	MP-125X	31%	56%	13%	45%	37%	18%
8	MP-64X	21%	71%	8%	46%	38%	16%

Finally, the effect of the liquid rate on the mass transfer resistance (as determined indirectly from the modeling step (step 1) in the procedure described before) is quantified in the third bar from the left (red) for each case. Clearly, this is the dominant source of the packing reduction predicted by the model. This result indicates that the physical liquid-side mass transfer coefficient (as predicted by the Hanley and Chen model) is of a magnitude where it is a significant contributor to the overall mass transfer resistance; when coupled with the strong dependence on liquid rate predicted by the model, the mass transfer resistance contribution becomes very important in the recycle configuration. As discussed in Chapter 5, the parameter sensitivity analysis revealed that the overall mass

transfer resistance is controlled by liquid-film physical mass transfer contributions for the absorber model with PZ using the packing models developed at UT (Equations 6.8 to 6.9). Therefore, the general result regarding the importance of the liquid-film mass transfer contribution to the recycle benefits would be expected to be similar with the UT models.

This highlights the importance of isolating these effects. If the intercooling benefit is the primary goal of the design, the current design is less than optimal – the strong dependence on mass transfer resistance contributions led to a large amount of packing in the middle (recycle section) of the column, reducing average driving forces and wiping out the intercooling benefits. If the mass transfer benefits are not realized at the magnitude predicted by the model in a real system, the design will lead to poor performance compared to the cost of the recycle system (in particular, the pumping costs over the large recycle section). This result is not unique to the recycle design. Modeling of any novel contacting scheme (e.g., rotating packed bed, cross-flow), column internals (trays, hybrid packing), operating conditions (e.g., high solvent loads), or solvents with unique physical properties (e.g., high viscosity) will require independent, accurate, and physically representative component mass transfer models to properly design and optimize the system. Therefore, mass transfer model development and experimental characterization of mass transfer phenomena in real contactors are among the most important areas of open research for CO_2 capture systems.

6.3.3 Summary and Recommendations from Recycle Case Study

The evaluation in the preceding sections yielded insight regarding the operating conditions and potential benefits of the recycle intercooling design. Specifically, the following recommendations can be used for further development with the NGCC application:

- A recycle rate of $L_{Recycle}/G = 2 – 4$ is recommended based on the economic analysis and evaluation of the source of recycle benefits. The driving force benefits are maximized in this range even if the mass transfer benefits are ultimately over-predicted by the model.
- The recommended recycle rate is defined for the specific conditions in the case study (LLDG = 0.25 mol CO_2/mol alkalinity, Feed L/G = 1.28). However, the recycle rate can be generalized (as a first approximation) by scaling based on the L/G of alternate conditions evaluated. For example, if a recycle rate of $L_{Recycle}/G = 3$ is selected for the base case study conditions at a nominal L/G = 1.28, a new recycle rate can be defined in terms of the new feed L/G as follows: $(3/1.28)*(L/G)_{FEED}$. This approach ensures that the recycle rate is sufficiently large compared to the feed solvent rate as they mix and enter the recycle section.
- Recycle intercooling benefits were dominated by liquid-film mass transfer enhancement. The case study analysis placed the recycle segment in the middle of 3 beds of packing, but a recycle design at the bottom (rich end) of the absorber would address the portion of the column most-limited by diffusion of reactants and products (see Chapter 5).

6.4 COMPARING RECYCLE INTERCOOLING TO IN-AND-OUT INTERCOOLING[5]

The analysis in Chapter 4 compared simple intercooling (in-and-out intercooling) to limiting cases of an adiabatic and isothermal absorber. Minimum solvent rate analysis identified the region for the NGCC application where simple intercooling could not achieve isothermal solvent capacity and necessitated the use of novel intercooling methods. In addition, the use of design curves to quantify packing and solvent rate relationships at normal solvent operating rates highlighted the need for improved intercooling methods to address mass transfer limitations associated with in-and-out intercooling. The recycle intercooling design will be evaluated in an extension of the analysis in Chapter 4 to determine if the design can address the specific shortcomings of the simple intercooling method for NGCC application. In addition, the use of the mass transfer models developed at UT (Equations 6.8 through 6.9) in this analysis will provide validation for the recycle benefits identified in the case study using the Hanley and Chen model from literature.

6.4.1 Comparison to Simple Intercooling: Minimum Solvent Rate

Figure 6-12 presents the results for the minimum solvent rate analysis for the recycle intercooling with bypass design alongside the previously presented results for adiabatic intercooling and in-and-out-intercooling. All cases for the recycle with bypass design were operated with a recycle rate scaled from the base case ($L_{Recycle}/G = 3$) as described in section 6.3.3. As noted, the recycle rate could be scaled to the nominal L/G, but the effects were found to be small over the limited range of lean loadings where advanced intercooling is applied.

[5] UT mass transfer models used for this analysis. See Equations 6.8 through 6.9.

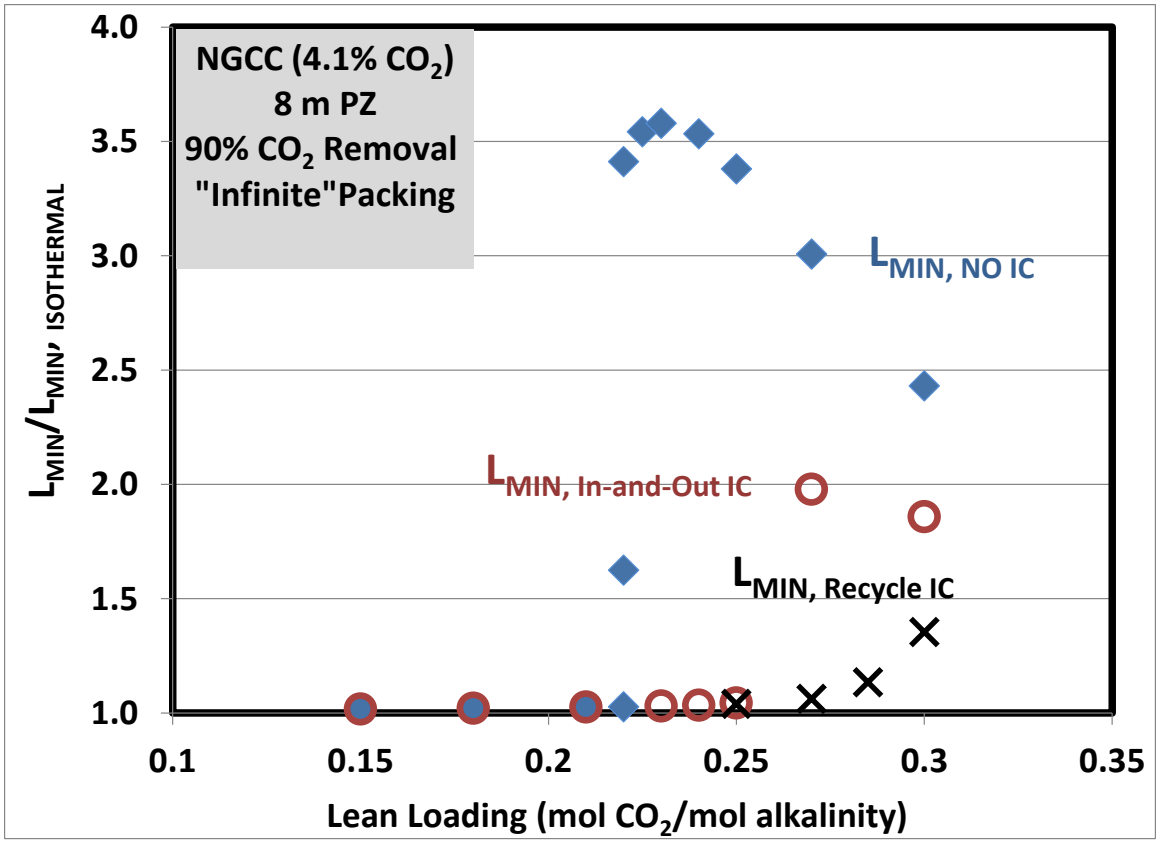

Figure 6-12: Ratio of the minimum solvent rate ("infinite" packing) for an adiabatic absorber (no intercooling), simple intercooled absorber (in-and-out intercooling), and advanced intercooled absorber (recycle with bypass) to an isothermal absorber (T = 40 °C) for 90% CO_2 capture from a NGCC power plant (4.1% CO_2) utilizing 8 m PZ. For the recycle design, the following range of recycle rates were implemented: $L_{Recycle}/G$ = 3 - 4.6 for lean loadings of 0.25 - 0.30 mol CO_2/mol alkalinity.

The recycle configuration improves the approach to the isothermal L_{MIN} across the range of lean loadings where in-and-out intercooling and an adiabatic absorber were significantly limited by temperature-induced mass transfer pinches. The recycle design successfully approximated maximum solvent capacity at all but the highest loading (0.30 mol CO_2/mol alkalinity). This condition operates with near zero driving force at the lean

end of the column (highest lean loading possible to achieve 90% removal for the NGCC case) and thus is not likely a practical operating condition.

As noted in the introduction of the recycle intercooling design, the benefits of the new design were expected to come from cooling of the gas in the low L/G NGCC application and enhanced mass transfer in the recycle section due to high liquid rate per perimeter of packing. Partitioning of benefits in Figure 6-11 indicated that, at operating solvent rates ($1.2*L_{MIN}$), the benefits of solvent recycle were largely related to the enhancement of the liquid film mass transfer coefficient. However, the analysis did not provide details on the source of the driving force benefits quantified and did not consider performance benefits at L_{MIN} (i.e., achieving maximum solvent capacity).

To understand the benefits of solvent recycle at L_{MIN}, the recycle design was compared to an in-and-out intercooled design where the gas is cooled at the same point as the solvent (at the intercooler) to ensure the gas going to the top bed is the same temperature as the intercooled solvent. This modeling scenario is designed to simulate the benefit of gas cooling in the NGCC application and determine if this is an important contribution of the recycle design. In addition, the recycle design was evaluated as a function of the amount of packing in the recycle section when calculating L_{MIN}. The CO_2 that is removed in the recycle section of the column is removed with a large L/G and a cooled solvent, and the heat associated with the CO_2 transfer is removed at the intercooler. Therefore, the benefit of CO_2 transfer in the recycle section is to limit the CO_2 removed in the top and bottom beds where temperature limitations may prevent the absorber from reaching maximum solvent capacity. The results of the comparative analysis are presented in Figure 6-13 and Table 6-5.

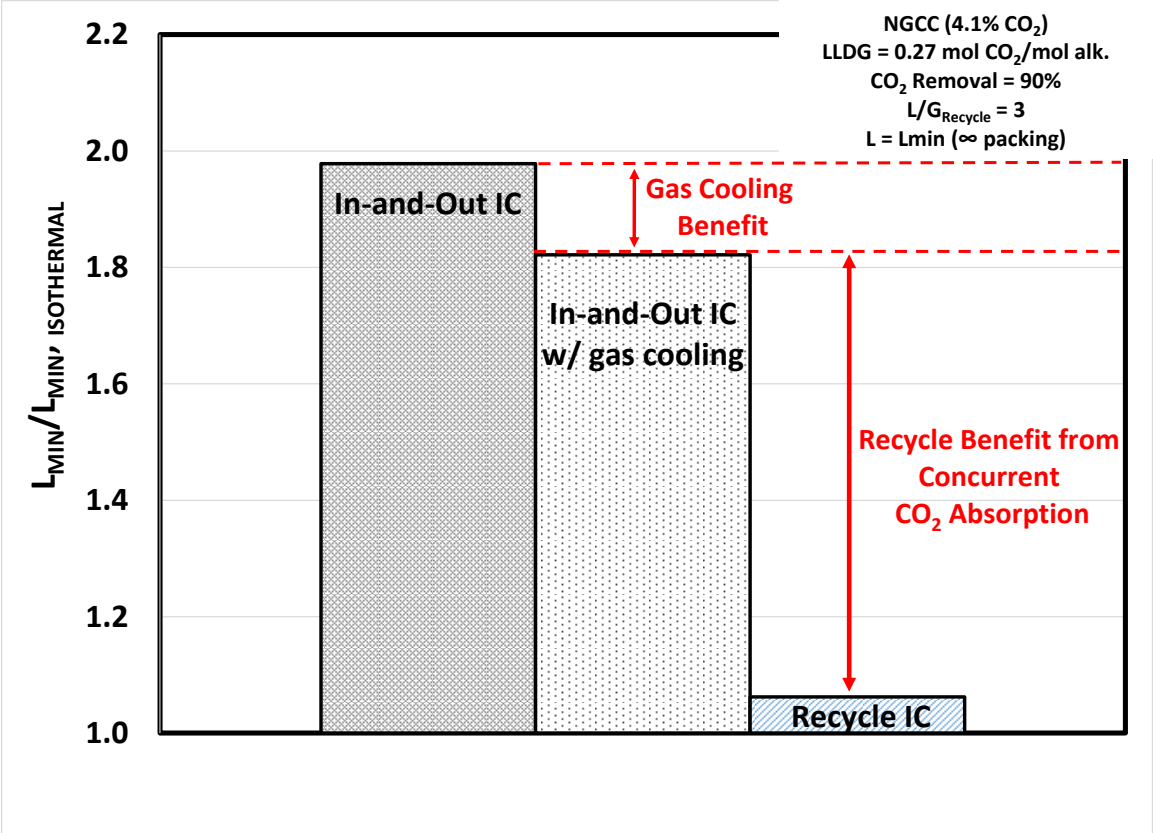

Figure 6-13: Ratio of the minimum solvent rate ("infinite" packing) for specified intercooled absorber configurations to the minimum solvent rate for an isothermal absorber (T = 40 °C) ($L_{MIN,\ INTERCOOLED}/L_{MIN.\ ISOTHERMAL}$). Intercooled absorber designs include in-and-out intercooling, in-and-out intercooling with gas cooling (T = 40 °C) and an advanced intercooled absorber (recycle with bypass) for 90% CO_2 capture from a NGCC power plant (4.1% CO_2) utilizing 8 m PZ. Lean loading = 0.27 mol CO_2/mol alkalinity. For the recycle design, a recycle rate of $L_{Recycle}/G$ = 3 was implemented.

Table 6-5: Minimum Solvent Rate Comparison of Recycle Intercooling, in-and-out intercooling with gas cooling (T=40°C) and in-and-out intercooling (baseline). Amount of packing is varied in the recycle section to evaluate effect of CO_2 removed in recycle on L_{MIN}. "Infinite" packing in the recycle indicates mass transfer pinch in recycle section.

Recycle Section Size	T_{GAS} Out of Intercooling Section	CO_2 removal in recycle	$L_{MIN}/L_{MIN, ISOTHERMAL}$
m	°C		
0.1 m	44.5	0.9%	1.98
0.5 m	43.5	4.4%	1.80
1 m	42.6	7.7%	1.47
2 m	41.7	12.5%	1.11
"Infinite"	41.1	50.5%	1.06
In-and-Out w/ Gas Cool	40	N/A	1.82
In-and-Out IC	45.5	N/A	1.98

Several conclusions can be developed from the table and figure. First, Figure 6-13 clearly illustrates that the benefit of gas cooling is small – the reduction in minimum solvent rate from the standard in-and-out intercooling design to the "gas cooling" design is less than 10%. As seen in Table 6-5, the temperature of the gas leaving the bottom bed (entering the top bed) of the absorber in the standard in-and-out intercooling design is approximately 46°C. Therefore, the hypotheses that the simple intercooling design does not adequately cool the gas is not valid. The benefit of cooling the gas in an intercooling design is primarily to increase the capacity of the gas to pick up water as it rises to the maximum temperature in the top portion of the column. The small change in gas temperature by cooling to 40°C does little to effect the amount of water the gas can carry.

In addition, Table 6-5 highlights the importance of CO_2 removal in the recycle section. While a small amount of packing in the recycle adequately cools the gas (< 2 m) to attain the gas cooling benefits of solvent recycle, as packing is continually added to the recycle section until a pinch forms ("infinite packing" in the recycle), the CO_2 removed in the section is significant – 50% of the CO_2 entering the absorber is removed in the recycle section. This serves to reduce the CO_2 captured outside of the recycle and moderates temperature significantly to limit the development of temperature-related mass transfer pinch (see Chapters 3 and 4 for details on pinch formation at temperature maxima). This is the primary mechanism for the effectiveness of the recycle intercooling method – a section of the column is able to operate with an independent (and large) L/G to capture CO_2 (moderates the temperatures as the CO_2 is captured) and remove the heat associated with CO_2 removal at the intercooler, isolating other sections from the effects of the bulk of the CO_2 removal in the column. This phenomena at the "infinite" packing limit only impacts the maximum solvent capacity of the absorber with recycle; it does not predict the effectiveness of the recycle at a normal solvent operating rate with finite packing and associated mass transfer limitations.

6.4.2 Comparison to Simple Intercooling: Design Curve

The analysis in Chapter 4 highlighted the shortcoming of in-and-out intercooling for the NGCC application in terms of mass transfer limitations at normal operating conditions (i.e., away from L_{MIN}). Specifically, at a loading of 0.25 mol CO_2/mol alkalinity, in-and-out intercooling was able to achieve the isothermal minimum solvent rate (see Figure 6-12), but produced a poor packing-solvent rate trade-off in a normal operating range when compared to an isothermal absorber (see Chapter 4, Figure 4-15). This condition was targeted for evaluation of the mass transfer performance of the

recycle intercooling design via a design curve approach, as used in Chapter 4. Figure 6-14 presents the design curves for the NGCC application at 0.25 mol CO_2/mol alkalinity with the addition of the recycle with bypass design.

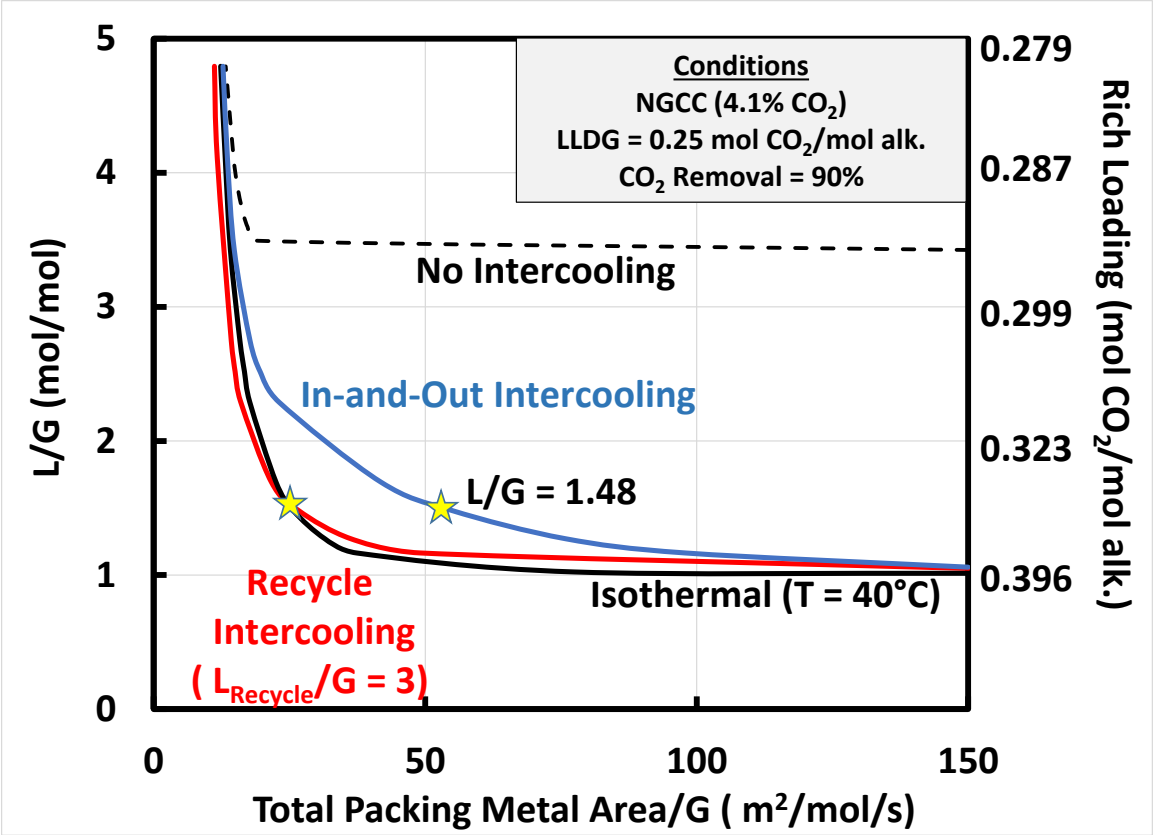

Figure 6-14: Design curves representing the packing-solvent rate trade-off of various absorber configurations for a NGCC power plant flue gas (4.1 mol% CO_2) at LLDG = 0.25 mol CO_2/mol alkalinity. Each curve (dashed = adiabatic, solid = isothermal, blue = intercooled, red = recycle IC) represents the packing requirement (normalized by the gas rate) to achieve 90% CO_2 removal for the fixed lean loading and given liquid to gas ratio (L/G). The recycle configuration was operated at $L_{Recycle}/G = 3$. For each point on the curve, the lean loading, removal, and solvent rates are fixed, so a unique rich loading exists as well (secondary y-axis). The asymptote each curve reaches with increasing packing area is the minimum solvent rate (L_{MIN}).

The benefits of the recycle design are apparent over the entire range of operating conditions as the curve approximately mirrors the isothermal absorber. In some cases, at higher L/G (> 1.5), the recycle design lies outside the isothermal curve indicating that the design is outperforming the isothermal absorber. The isothermal absorber is a limiting design at the "infinite packing limit", but is only a limiting case for the driving forces at

conditions away from L_{MIN}. The recycle intercooling design is outperforming the isothermal design due to the liquid-film mass transfer enhancement discussed in Section 6.3.2.3.

Figure 6-15 compares the packing requirement for the recycle intercooling design with varying recycle rate to in-and-out intercooling and an isothermal absorber at the highlighted constant solvent rate condition from Figure 6-14 (L/G = 1.48).

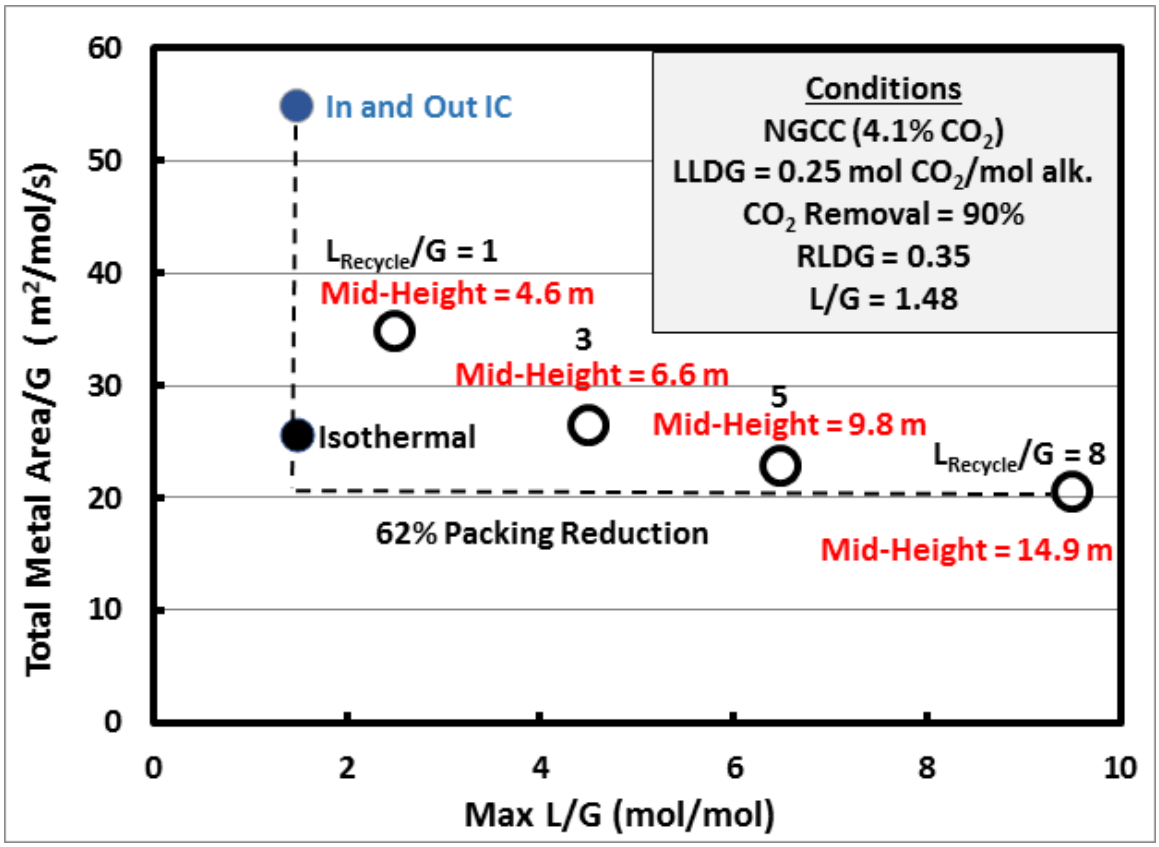

Figure 6-15: Normalized packing requirement for in-and-out intercooling, recycle intercooling, and an isothermal absorber at a constant L/G = 1.48 mol/mol, LLDG = 0.25 mols CO_2/mols alkalinity, and 90% CO_2 removal. A maximum packing reduction of 62% compared to in-and-out intercooling can be achieved with a recycle rate of $L_{Recycle}/G = 8$. The packing height of the recycle section is included as an indication of the pumping cost associated with each recycle rate.

As the figure shows, the recycle intercooling configuration outperforms the in-and-out intercooling design at all recycle rates. At recycle rates above $L_{Recycle}/G = 3$, the recycle design surpasses the isothermal absorber performance as well. However, with increasing recycle rate, the packing height of the recycle section increases, rapidly increasing the energy required for pumping in the recycle design while the packing benefits exhibit diminishing returns. The tall recycle section results from the use of progressively coarser

packing in the recycle section (taller section required to maintain a given mass transfer area) and weighting of packing optimization to the recycle section due to enhanced mass transfer efficiency. These results are consistent with the incremental economic analysis in section 6.3.2.2.

Figure 6-16 compares the temperature profiles for the recycle design and in-and-out intercooled design at the conditions designated in Figure 6-14 (L/G/ = 1.48).

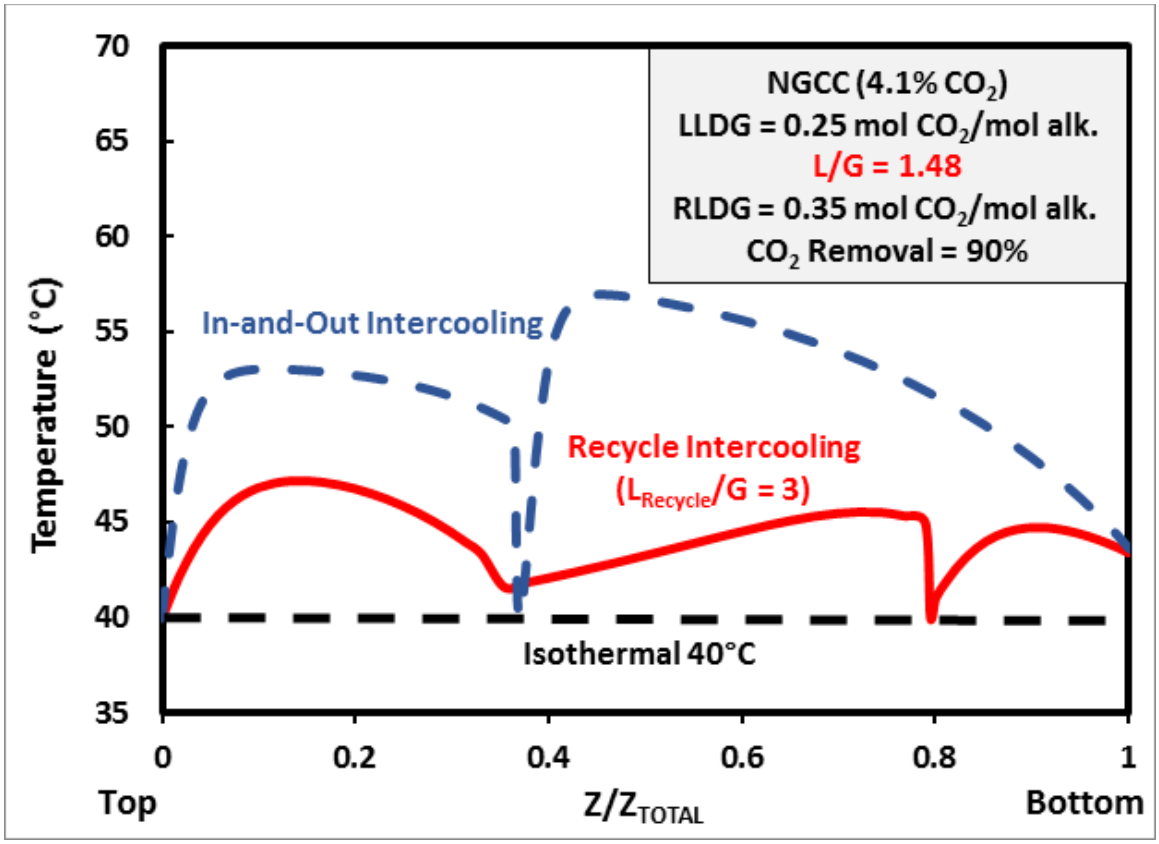

Figure 6-16: Temperature profiles for In-and-Out Intercooling (Blue), Recycle Intercooling at $L_{Recycle}/G = 3$ (Red) and Isothermal operation (Black).Each curve represents the profile 90% CO_2 removal with a lean loading of 0.25 mol CO_2/mol alkalinity and 8 m PZ for the given liquid to gas ratio (L/G = 1.48).

The figure indicates that the temperatures are lower throughout the column with the recycle intercooling design. This is primarily due to the significant CO_2 absorption that occurs in the recycle section (50% of CO_2 into absorber), where the temperatures are moderated and heat is removed at the intercooler to prevent transfer to other sections of the absorber. Therefore, the recycle design benefits from the mass transfer enhancements in the recycle section and reduced temperature-related driving force limitations outside of the recycle section compared to the in-and-out intercooling design.

6.5 NOVEL CONCEPTS: HYBRID CONTACTING

The development of the recycle intercooling design has highlighted the potential performance enhancement of operating a portion of the absorber with a large L/G for NGCC applications. However, as noted in the analysis of the benefits of recycle intercooling (Section 6.3.2.3), a potential downside of the recycle design is the diminished driving forces in the column due to solvent recycle (absorber is no longer a true counter-current contactor). To address this shortcoming of the recycle design while retaining the benefits of high intensity contacting, a new hybrid contacting method was developed.

6.5.1 Description of Hybrid Contacting Concept

The general concept of hybrid contacting is illustrated in Figure 6-17.

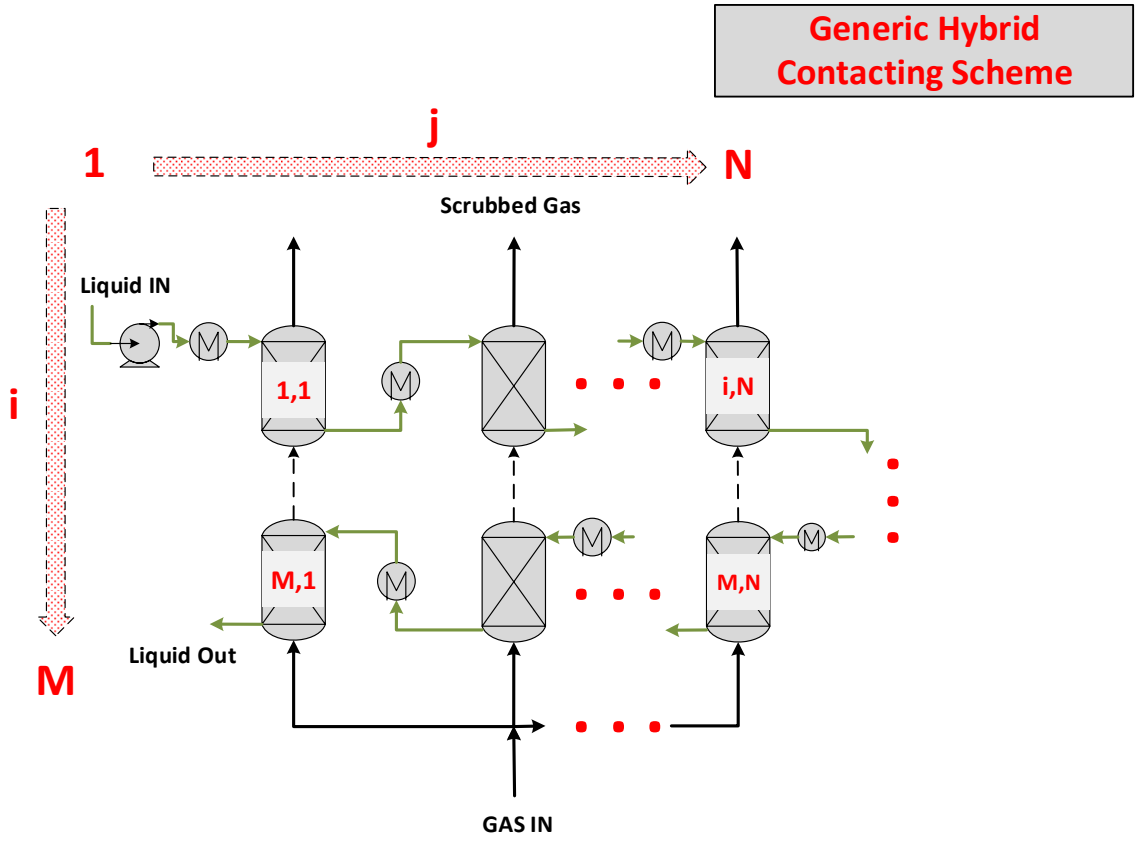

Figure 6-17: General hybrid contacting concept. The contactor, or contacting section, consists of M x N individual absorption beds. The liquid flow pattern moves from bed (1,1) to bed (i, N), then back on the subsequent row from (i+1,N) to (i+1,1). This "serpentine" liquid flow pattern continues until the liquid leaves on row M. The liquid is pumped through an intercooling exchanger between each bed. The gas is split into N identical streams which flow in parallel through each column of beds.

The hybrid contactor design consists of a series of smaller contacting sections (or absorbers) arranged in specific pattern to maximize driving forces for mass transfer, ensure high intensity (high liquid-gas-ratio, L/G) contacting, and to approximate isothermal contacting conditions with repeated intercooling between beds. There are two dimensions for the arrangement of the individual contacting sections: the vertical axis, or rows, from 1 to M, and the horizontal axis, or columns, from 1 to N (M x N contactor "size"). The solvent moves along the rows of the hybrid configuration, alternating flow

direction on each subsequent row (flows from 1 to N on one row, and back from N to 1 on the next row). This forms a serpentine pattern for the liquid flow as it moves down the contactor. In addition, the liquid is cooled between each bed in series to approximate isothermal contacting.

The gas flows along the vertical axis, or columns, of the hybrid design. The inlet gas to the contactor is split into "N" identical streams, each fed to a column, or independent vertical gas flow path, in the contactor. Within each bed in the contactor, the gas counter-currently contacts the liquid flowing down the bed. By splitting the gas and contacting each independent gas stream with the full feed rate of the liquid, the hybrid design has successfully increased the L/G in each contacting section by a factor of "N" over a simple countercurrent contacting scheme with a single contactor. This high intensity contacting generates turbulence to enhance mass transfer and helps moderate temperatures in each bed by damping the effect of heat generated in the absorption process (large amount of liquid compared to the gas treated and solute transferred).

The dimensions (or packing configuration) of the hybrid contactor can be varied (degrees of freedom) to change the performance of the hybrid section as defined by the generic M x N contactor size in Figure 6-17. As additional beds are added to a given row, the L/G in each section increases. Alternately, as additional packed sections are added to each column (increase number of beds vertically), the design becomes more "counter-current" (better average driving forces through the contactor). This effect is a result of the serpentine liquid flow pattern described in Figure 6-17. As each gas stream moves up the contactor, it sees alternating high and low liquid loadings (concentration of solute in the liquid) or, equivalently, alternating high and low driving forces for mass transfer. This has the net effect of balancing the average driving forces for each stream of stream of gas through the contactor. As additional beds are added to as column, the changes in liquid

loading are smaller, and driving forces are more continuous through the contactor, as in a true counter-current or plug flow scheme.

In addition, the diameter (subject to flooding constraints) and height (subject to outlet gas specifications) of each packed section in the hybrid design can be varied independently, subject to practical constraints of constructing the contactor and costs associated with a customized design. It should be noted that any variation in the pressure drop across the independent gas flow paths (or columns) in the hybrid contactor will lead to different gas flows along the independent paths.

6.5.2 Proof of Concept: Hybrid Contacting vs. Recycle Intercooling

To demonstrate and validate the potential benefits of the hybrid concept, the design was compared to a specific recycle intercooling case. The use of hybrid contacting as an intercooling section is depicted in Figure 6-18.

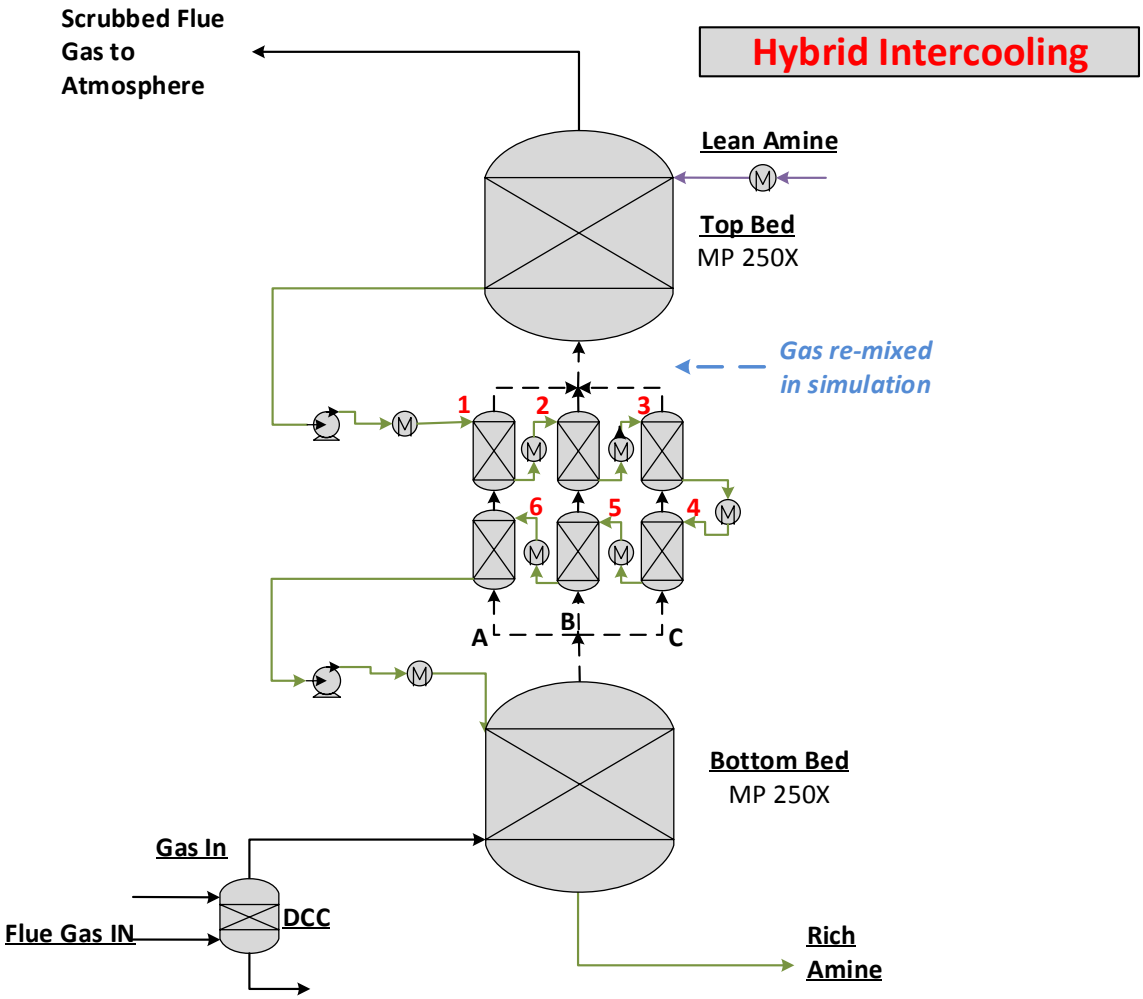

Figure 6-18: Absorber PFD for Hybrid Intercooling Design. The column is divided into three major sections. MP-250X is used in the top and bottom section and various coarse structured packing (MP-170X) is used in the middle (6 packed bed hybrid section) to maintain 70% max approach to flood. The solvent is cooled to 40°C above and below the middle section of the column and between each of the beds in the hybrid section (7 total exchangers). The liquid flow path is indicated by the sequence of numbers in the intercooled section (1-6) and the 3 parallel flow paths are designated A, B, and C.

The recycle section in the middle of the absorber has been replaced by a series of smaller contacting sections. The 2 x 3 hybrid intercooling design replicates the high liquid rate per wetted perimeter of the recycle design by splitting the gas into 3 packed

sections which are counter-currently contacted by the full solvent rate (3 times the L/G in the rest of the column). In addition, the single intercooling function in the recycle design is now discretized as the solvent is cooled between each bed of the hybrid design. Finally, because of the contacting pattern used in the hybrid design (serpentine liquid flow through the two rows), the hybrid contactor is closer to a counter-current design than the fully-back-mixed recycle design and should benefit from better driving forces throughout the section.

A uniform 2 x 3 design (each bed has the same diameter and height) was selected as a baseline for comparison to a recycle intercooling design operated at $L_{Recycle}/G = 3$ to minimize the complexity of a concept still in preliminary development stages. The conditions for the analysis are summarized as follows:

- NGCC (4.1 mol% CO_2) flue gas (See Table 6-1)
- Lean Loading = 0.27 mol CO_2/mol alkalinity
- L/G = 1.5 (L/L_{MIN} = 1.2 based on recycle design)
- 8 m PZ
- 90% CO_2 removal
- MP-250X in top and bottom beds, MP-170X in intercooling bed

The hybrid intercooling design is compared directly to the recycle design by isolating the intercooling section. The solvent and gas entering the recycle intercooling section (from the top and bottom sections) are fed to the hybrid intercooling section and the CO_2 removed in the intercooling section will be matched in the hybrid design by varying the total packing requirement. This approach will highlight the benefit of the hybrid design under identical operating conditions by quantifying the change in packing required in the section. In addition, heat duty and energy requirements for important

peripheral equipment associated with the intercooling loops (pumps, exchangers) are compared in Table 6-6.

Table 6-6: Comparison of Hybrid and Recycle Intercooling Sections

	Recycle Intercooling	Hybrid Intercooling
Total Packing Area MP-170X (1000 m^2)	585	298
Total Packed Height in Intercooling Beds (m)	11.4	17.4 (6 x 2.9)[1]
CO_2 Removal in Intercooling Section[2]	50%	
Total IC Heat Duty (MW)	72.6	79.2
Gas-Side Pressure Drop (Pa)	1297	662
Gas-Side Gross Fan Power[3] (kW)	1037	529
Liquid-Side Gross Pump Power (excl. exchanger ΔP)[3,4] (kW)	476	240
Total Gross Electric Power (kW)	1513	769
Gas Outlet T (K)	314.6	313.5

1: Total packed height of hybrid is sum of all 6 beds. Each bed is 2.9 m. The path length of the gas is only 5.8 m (2 beds).
2: Based on inlet flue gas CO_2
3: Gross power requirement does not account for efficiency
4: Pump power accounts for liquid pumping head in each design for total height of packing.

The hybrid design reduces both the packing requirement and gross electric power requirement of the intercooling section by ~50% for the same CO_2 removal. The packing requirement is a result of the enhanced driving forces in the intercooling section. The gross power requirement reduction is a result of two effects. The overall gas flow path length is reduced - the gas only passes through 5.8 meters of packing (2 sections @ 2.9 m each) to reduce the pressure drop in the intercooling section. In addition, the liquid pumping head is reduced because the solvent rate is cut by 1/3 compared to the recycle design, but the total packing height that the solvent is pumped over (6 x 2.9 m = 17.4 m) did not increase correspondingly from the recycle case. Finally, the overall intercooling heat duty is approximately the same for the two designs despite the addition of several coolers in the hybrid case – the heat of absorption is removed throughout the intercooling section in the hybrid design as opposed to the single exchanger leaving the recycle section.

The driving force and temperature profiles for the two intercooling methods are compared in Figure 6-19 and Figure 6-20.

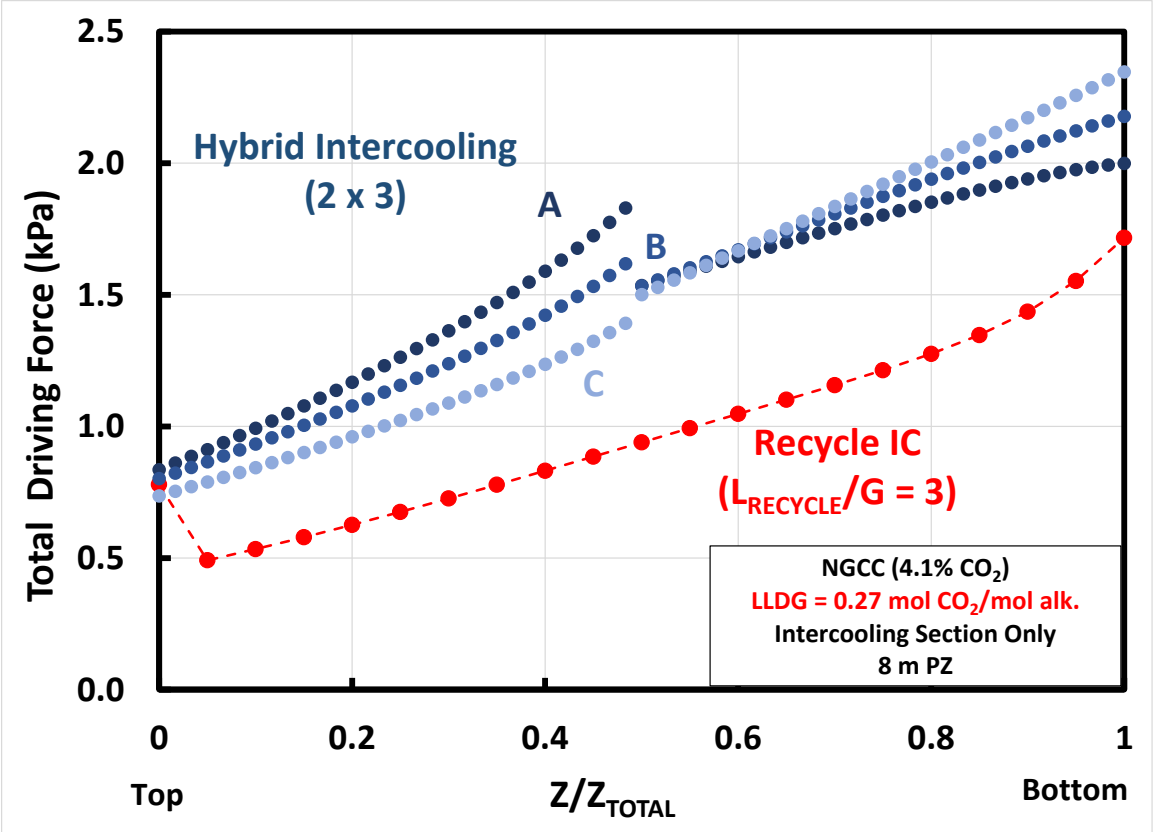

Figure 6-19: Total driving force ($P_{CO2,\ Bulk\ Vapor} - P^*_{CO2,\ Bulk\ Liquid}$) comparison in intercooling section: 2 x 3 hybrid intercooling contactor vs. recycle intercooling with bypass ($L_{Recycle}/G = 3$). Normalized packing height in intercooling sections only from top to bottom of the section. Parallel gas flow paths A, B, and C are labeled in Figure 6-18. LLDG = 0.27 mol CO_2 mol alkalinity, 8 m PZ, MP-170X for both configurations.

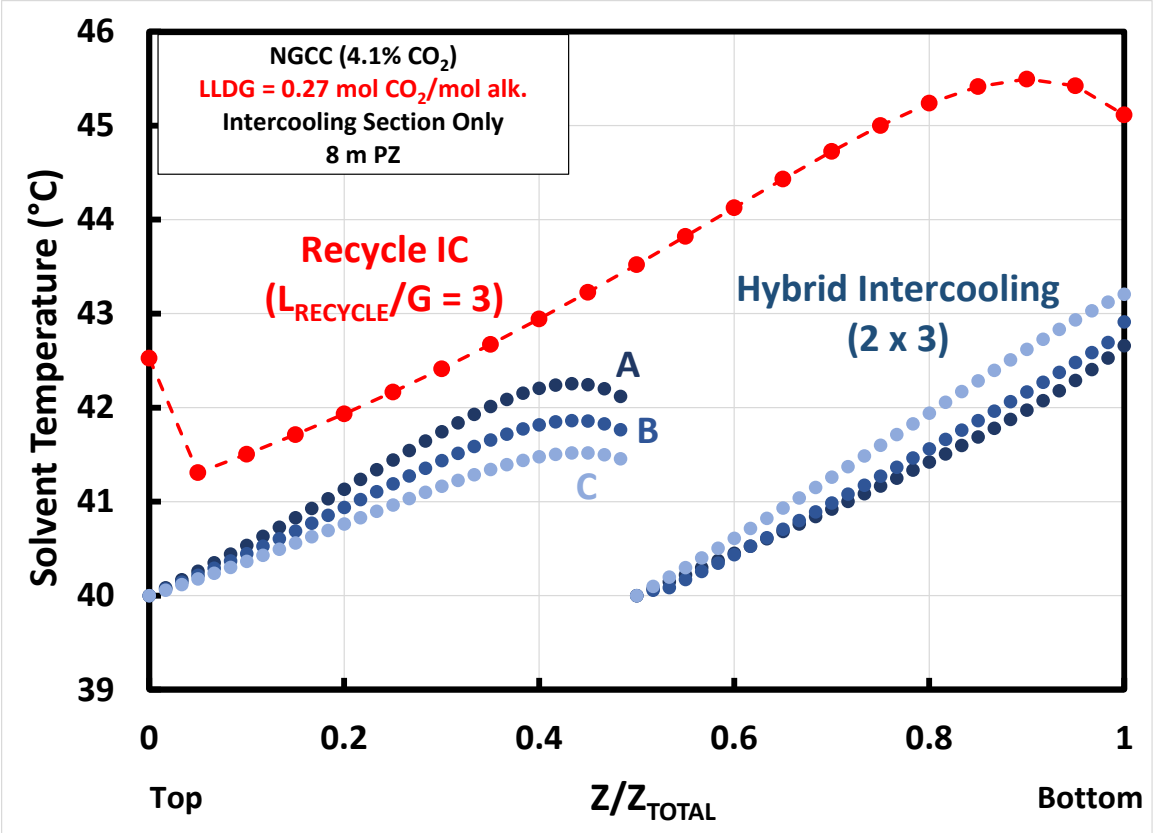

Figure 6-20: Solvent temperature comparison in intercooling section: 2 x 3 hybrid intercooling contactor vs. recycle intercooling with bypass ($L_{Recycle}/G = 3$). Normalized packing height in intercooling sections only from top to bottom of the section. Beds 1 to 6 are numbered along solvent path in Figure 6-18. LLDG = 0.27 mol CO_2 mol alkalinity, 8 m PZ, MP-170X for both configurations.

The figures illustrate the discontinuous nature of the driving forces and temperatures in the hybrid intercooling configuration due to the contact with different gas streams as the solvent moves through the intercooling section and the intercooling of the solvent between every bed. In addition, the driving forces are consistently larger for the hybrid intercooling design compared to the recycle intercooling approach. This is due, in large part, to the closer approach to counter-current contacting in the hybrid design. However, as Figure 6-20 illustrates, the temperatures are also lower throughout the hybrid design contributing to the enhanced driving forces. Because the solvent is intercooled between

each bed, the hybrid design approaches a continuous cooling configuration (isothermal section) while the recycle configuration removes approximately the same amount of heat (Table 6-6) but at one discrete location.

6.5.3 Process Intensification: Integrating the DCC and Intercooling functions

The analysis of the recycle intercooling design highlighted the advantages over in-and-out intercooling for the NGCC application. The discussion in section 6.4.1 concluded that the gas cooling effect of the solvent recycle was not significant compared to the CO_2 removal in the recycle section. However, as Table 6-5 highlighted, the solvent recycle did effectively cool the gas while concurrently absorbing a significant amount of CO_2. In addition, the analysis in Chapter 5 indicated that the rich end of the absorber is expected to be most severely limited by diffusion of reactants and products (most sensitive to the physical liquid-film mass transfer coefficient). Therefore, the rich end (or bottom) of the column should be expected to benefit the most from an absorber design that generates turbulence to enhance the liquid-film mass transfer coefficient. These two points together support the concept of a recycle intercooling section or hybrid intercooling section at the bottom of the column that replaces the direct contact cooler (DCC) that cools the incoming flue gas. The costs associated with a separate unit operation to cool the flue gas are eliminated.

During the initial development of the recycle intercooling concept, a large study to develop absorber and stripper configurations for various natural gas flue gas sources (NGCC, NGCC with exhaust gas recycle (EGR), and natural gas-fired boiler) was completed and the combined recycle intercooling-DCC concept was evaluated[6]. This initial evaluation concluded that the DCC could be replaced by a solvent recycle section,

[6] The work for this study was supported by TOTAL

but a second recycle bed was required in the column to perform the typical intercooling function. The full report for this project is included in Appendix F and demonstrates the feasibility of the DCC replacement concept.

The goal of the current analysis is to develop a DCC replacement that simultaneously performs the function of the DCC and recycle intercooling - primarily to absorb CO_2 to limit absorption required in sections outside of the recycle loop. Therefore, four absorber configurations will be compared to evaluate the performance of DCC integration concepts:

1) Recycle Intercooling with DCC (BASE CASE): 3 bed absorber design with recycle intercooling around middle bed and separate DCC unit operation (Figure 6-2)
2) Recycle Intercooling, NO DCC: 2 packed bed design, bottom bed with recycle IC to replace DCC (Figure 6-21).
3) Hybrid Intercooling (2 x 3), NO DCC: 2 column sections, top section is standard counter-current bed, bottom section is a 2 x 3 hybrid intercooling design (6 beds) (Figure 6-22).
4) Hybrid Intercooling (1 x 3), NO DCC: 2 column sections, top section is standard counter-current bed, bottom section is a 1 x 3 hybrid intercooling design (3 beds) (Figure 6-23).

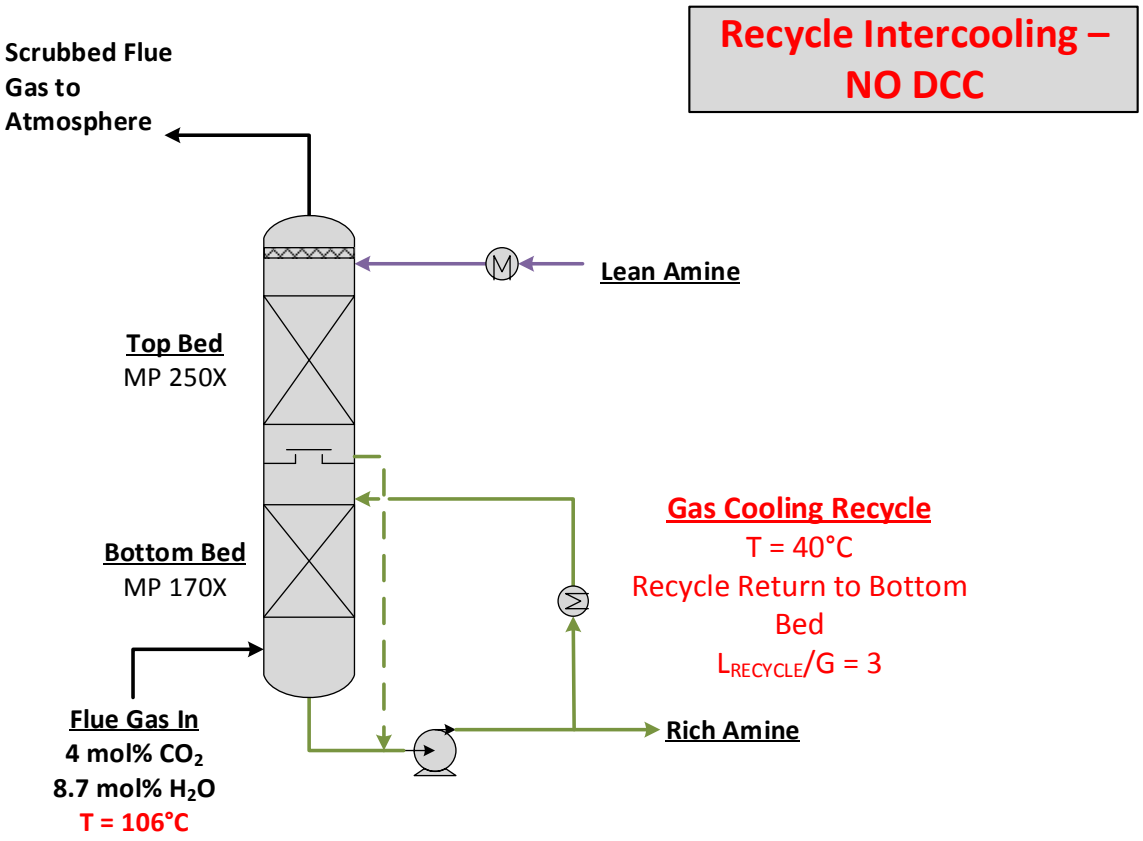

Figure 6-21: Absorber PFD for Recycle Intercooling, NO DCC. The column is divided into two sections. MP-250X is used in the top section and coarse structured packing (MP-170X) is used in the bottom (solvent recycle) bed to maintain 70% max approach to flood. A portion of the rich solvent leaving the absorber (the specified recycle rate) is pumped through an intercooler (T = 40°C) back to the top of the bottom bed of packing. The down-coming solvent from the top bed of packing is mixed with the recycle stream upstream of the exchanger to ensure that all solvent enters the bottom bed at 40°C. The recycle serves the function of the direct contact cooler as it contacts hot flue gas.

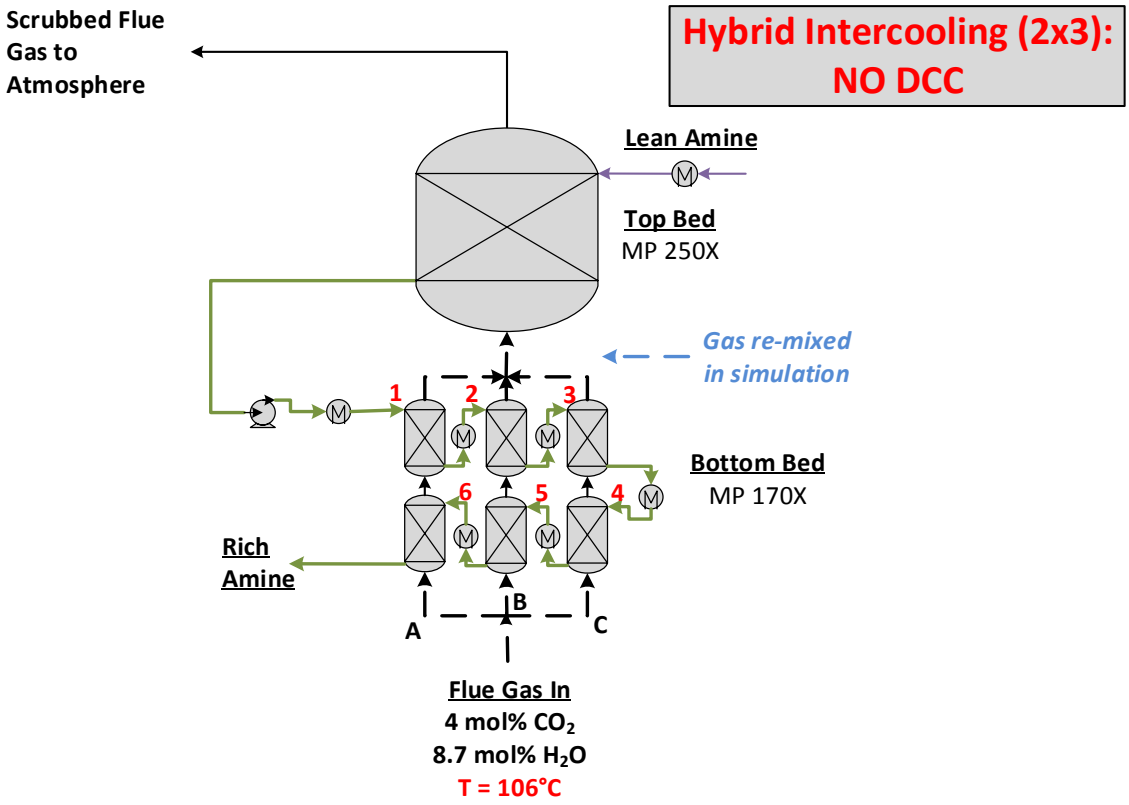

Figure 6-22: Absorber PFD for 2 x 3 Hybrid Intercooling Design, NO DCC. The column is divided into two major sections. MP-250X is used in the top section and coarse structured packing (MP-170X) is used in the bottom section (6 packed-bed hybrid section) to maintain 70% max approach to flood. The solvent is cooled to 40°C above the hybrid section of the column and between each of the beds in the section (6 total exchangers). The liquid flow path is indicated by the sequence of numbers in the intercooled section (1-6) and the 3 parallel gas flow paths are designated A, B, and C. The hybrid section serves the function of the direct contact cooler as it contacts hot flue gas.

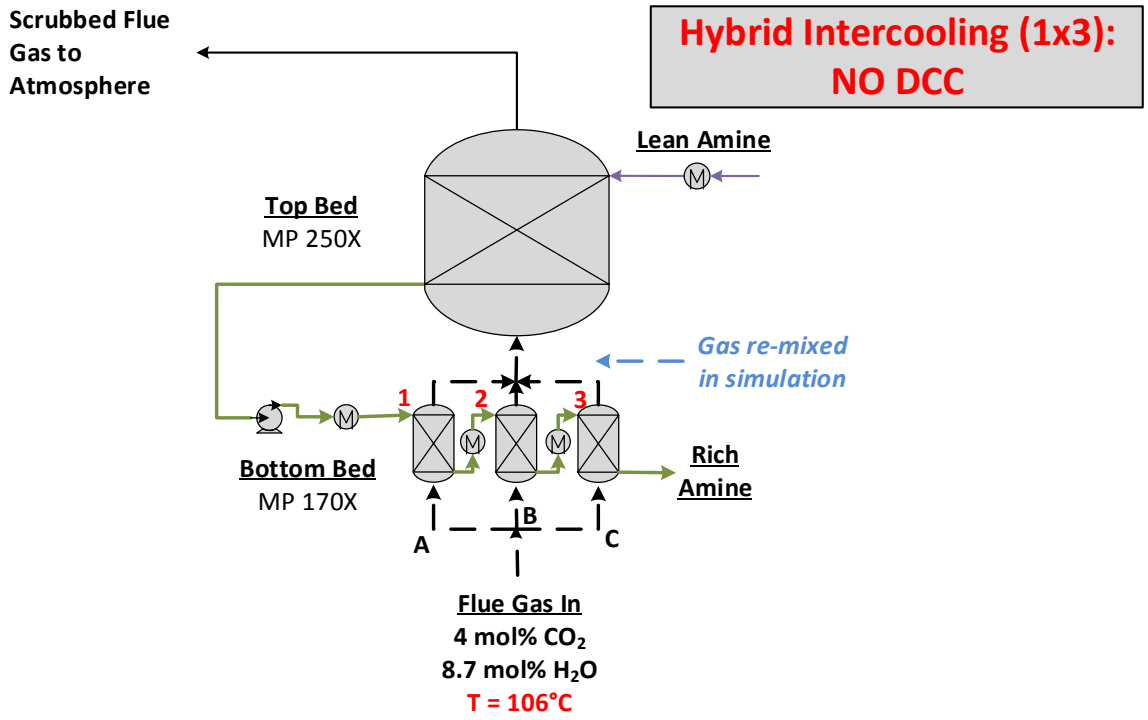

Figure 6-23: Absorber PFD for 1 x 3 Hybrid Intercooling Design, NO DCC. The column is divided into two major sections. MP-250X is used in the top section and coarse structured packing (MP-170X) is used in the bottom section (3 packed-bed hybrid section) to maintain 70% max approach to flood. The solvent is cooled to 40°C above the hybrid section of the column and between each of the beds in the section (3 total exchangers). The liquid flow path is indicated by the sequence of numbers in the intercooled section (1-3) and the 3 parallel gas flow paths are designated A, B, and C. The hybrid section serves the function of the direct contact cooler as it contacts hot flue gas.

The 1x3 hybrid was added to the analysis to test the hybrid intercooling configuration in the simplest format. The design is expected to lose some of the driving force benefits of a design with additional rows (i.e., 2x3) as each fresh gas stream will contact very different solvent loadings and lead to a distribution of CO_2 concentration in the gas outlet (less counter-current design). However, the design will retain benefits of a high L/G and discretized intercooling.

The flue gas conditions (repeated from Table 6-1) and absorber equipment and operating specifications for the study are presented in Table 6-7.

Table 6-7: DCC Integration Study Conditions

Gas Conditions		
Gas Feed Rate	114,000	kmol/hr
	3,230,000	kg/hr
Temperature	106	°C
Pressure	1	atm
Composition (Mole %)		
CO_2	4.0%	
H_2O	8.7%	
N_2	74.3%	
O_2	12.1%	
Data from NETL Case 13 (National Energy Technology Laboratory 2010)		
Absorber Specifications		
Solvent	8 m PZ	
Lean Loading	0.27 mol CO_2/mol alk.	
CO_2 Removal Specification	90%	
L/G	1.5 mol/mol	
Packing Type		
Outside of Intercooling Sections	MP-250X	
Intercooling Sections	MP-170X	
Solvent Recycle Rate	$L_{Recycle}/G = 3$	
Hybrid Bed Configurations	2 rows by 3 columns (6 beds) 1 row by 3 columns (3 beds)	

The important characteristic of the flue gas composition is the water content in the NGCC application. The flue gas contains approximately 9% H_2O at an elevated

temperature of 106°C. The target for flue gas cooling in a direct contact cooler prior to entering the absorber is 40°C, where the saturated flue gas would contain 7.6% H_2O. Therefore, as the flue gas from the NGCC source is cooled, a net transfer of water to the solvent occurs (introduction of water to the capture system). However, in certain natural gas cases, the water content may be lower than the saturation concentration at 40°C (see Appendix F). This allows cooling of the flue gas with the solvent without concern for potentially disrupting the water balance in the capture system.

In addition, the flue gas rapidly cools to the wet-bulb temperature based on the specific vapor composition (driving force for water transfer), so the lower water content in the flue gas for NGCC applications indicates a lower wet-bulb temperature for the vapor. The elimination of the DCC is not possible for flue gas from a coal-fired boiler, for example, which might contain approximately 15% H_2O in the incoming flue gas.

6.5.3.1 Results

The absorber configurations were compared in terms of the minimum solvent rate (L_{MIN}) to assess any temperature restrictions created by the introduction of hot flue gas at the rich end of the absorber and the packing requirement at a common L/G. The results of the L_{MIN} comparison are presented in Figure 6-24.

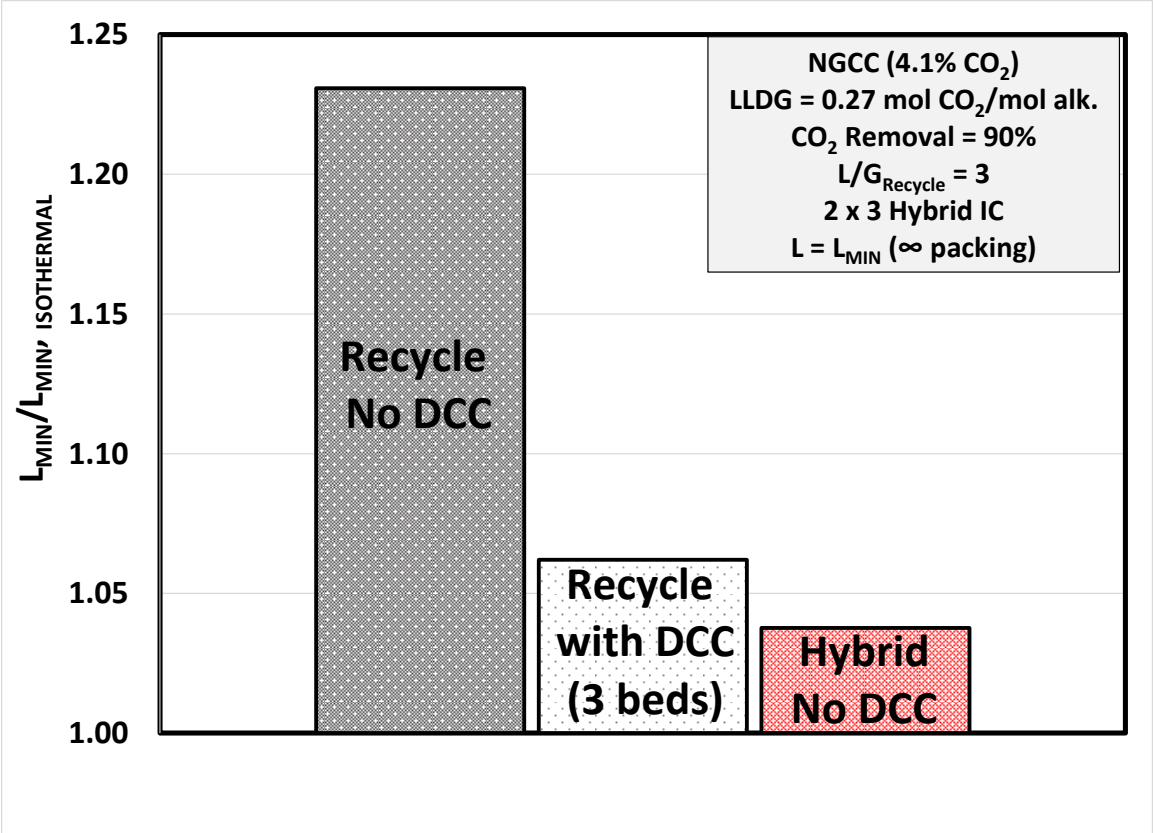

Figure 6-24: Ratio of the minimum solvent rate ("infinite" packing) for specified intercooled absorber configurations to the minimum solvent rate for an isothermal absorber (T = 40 °C) ($L_{MIN,\ INTERCOOLED}/L_{MIN.\ ISOTHERMAL}$). Intercooled absorber designs include recycle intercooling without a DCC (2 beds), recycle intercooling with a DCC (3 beds), and hybrid (2x3) intercooling without a DCC. All designs are for 90% CO_2 capture from a NGCC power plant (4.1% CO_2) utilizing 8 m PZ. Lean loading = 0.27 mol CO_2/mol alkalinity. For the recycle designs, a recycle rate of $L_{Recycle}/G$ = 3 was implemented.

The recycle method to replace the DCC is insufficient to address temperature limitations in the absorber as the minimum solvent rate is ~25% higher than an isothermal absorber. As noted, previous work on the use of solvent recycle to replace the direct contact cooler revealed that a second, separate intercooling loop is needed to separate the gas cooling and intercooling functions in the absorber (Appendix F). While the double recycle design would eliminate the DCC and associated costs, some of the

benefit is offset by the additional complexity in the absorber. The hybrid design, however, outperforms both recycle configurations (with and without a DCC). This indicates that the hybrid design cools the gas and effectively removes CO_2 simultaneously without incurring a significant temperature restriction in the rich end of the column. The large L/G and multiple intercooling loops ensure that the temperatures in the intercooling section are moderated and allow the hybrid design to closely approximate the performance of an isothermal absorber at the limit of "infinite" packing.

The configurations were also evaluated at a common solvent flow rate for all designs (L/G = 1.5) (Table 6-8).

Table 6-8: DCC Replacement Evaluation at L/G = 1.5

	BASE with DCC	**NO DCC**		
	Recycle Intercooling	**Recycle Intercooling**	**Hybrid Intercooling (2 x 3)**	**Hybrid Intercooling (1 x 3)**
L/G (mol/mol)	1.5			
L/L_{MIN}	1.2	1.04	1.23	1.14
Rich Loading (mol CO_2/mol alk.)	0.368			
Total Packing Area (1000 m^2)	1499	2444	816	1138

Table 6-8: Continued

Packing Specifications by Section (m)				
Total Height Outside of IC (MP-250X)	Top: 5.3 Bottom: 7.1	31	1	4.8
Total Height in IC Section (MP-177X)	11.4	10	41 (6.8 x 6 beds)[1]	41 (14.1 x 3 beds)[1]
Column Diameter[2]	19.2	19.75	Top: 19.75 Hybrid: 11.4	Top: 19.75 Hybrid: 11.4
Intercooling Section Performance				
CO_2 Removal in Intercooling Section[3]	50%	66%	87%	74%
Packing/CO_2 Removed: Intercooling section (m^2/mol/s)	915	1980	667	812
Gas Outlet T, Intercooling Section (K)	N/A	313.9	313.3	313.3

1: Total packed height of hybrid is sum of all beds. Each bed is 6.8 m for the 2 x 3 or 14.1 for the 1 x 3. The flow path length of the gas is 13.6 m (2x3) or 14.1 m (1x3).
2: Column diameter for the top counter-current bed and hybrid beds defined to yield the same gas superficial velocity (i.e., cross-sectional area of each hybrid section is 1/3 of top counter-current bed)
3: Based on inlet flue gas CO_2

At a common solvent rate (common rich loading), both hybrid configurations without a DCC significantly outperform the recycle designs. The 2x3 hybrid reduces the total packing requirement by 45% compared to the base design with a DCC and by 67% compared to the recycle configuration without a DCC. The 1x3 hybrid provides a 24%

packing reduction vs. the base design with a DCC and 53% reduction vs. the recycle configuration without a DCC. The subsequent discussion will focus on the 2x3 hybrid design due to the large performance improvements, but the 1x3 design is a promising design with the advantage of reduced complexity, packing sections, and peripheral equipment.

The recycle design without a DCC is severely limited at the selected operating condition as it is operating near the minimum solvent rate for the configuration. However, to operate in a reasonable operating range (e.g., 1.2 L_{MIN}), the rich loading and corresponding energy performance of the system would suffer. The hybrid performance improvement over the recycle design with a DCC indicates that the integrated DCC and intercooling function does not limit the hybrid intercooling performance. This is supported by the normalized packing requirement in the intercooling sections – the 2x3 hybrid reduces the packing required per mole of CO_2 absorbed by nearly a third compared to the base case recycle design.

The top (counter-current) bed in the 2x3 hybrid design contains a limited amount of packing (1 m) and does not remove a significant amount of CO_2 (~ 3% of CO_2 in flue gas). A design was evaluated without the top bed (2 x 3 section only) – the results are summarized in Table 6-9.

Table 6-9: Hybrid Intercooling without a top counter-current section of packing

	Hybrid Intercooling (2 x 3)	
	With CC top Section	**No Top Bed**
L/G (mol/mol)	1.5	
Rich Loading (mol CO_2/mol alk.)	0.368	
Total Packing Area (1000 m^2)	816	842
Packing Specifications by Section (m)		
Total Height Outside of IC (MP-250X)	1	N/A
Total Height in IC Section (MP-177X)	41 (6.8 x 6 beds)[1]	47 (7.8 x 6 beds)[1]
Column Diameter[2]	Top: 19.75 Hybrid: 11.4	Top: N/A Hybrid: 11.4

1: Total packed height of hybrid is sum of all beds. Each bed is 6.8 m for the 2 x 3 with a top section or 7.8 for the 2 x 3, no top section. The flow path length of the gas is only 13.6 m and 15.6m, respectively.
2: Column diameter for the top counter-current bed and hybrid beds defined to yield the same gas superficial velocity (i.e., cross-sectional area of each hybrid section is 1/3 of top counter-current bed)

As the table illustrates, the design without a top section has a slight deterioration in performance (~3% more packing required). However, this small cost in packing is likely offset by the cost and complexity of adding an addition section to the column (packing supports, distributors, column, shell, etc.). The reason that the top section

enhances performance is because the lean end of the column has the lowest gas-side CO_2 concentrations and the beds in the crossflow design are not equally efficient in treating the gas as it approaches the outlet gas concentration – the bed with the most restrictive driving forces drives the packing requirement for the entire hybrid design (under the constraint that each bed must have the same dimensions). The counter-current section ensures that the crossflow beds only operate to their optimal CO_2 removal in each gas section – the top bed then provides the best possible driving forces to complete the required CO_2 removal. This will be more important to achieve high CO_2 removal rates (e.g., 99% removal).

The performance of each bed in the 2x3 hybrid intercooling was also evaluated based on the fraction of inlet CO_2 removed by each bed. The results are presented in Figure 6-25.

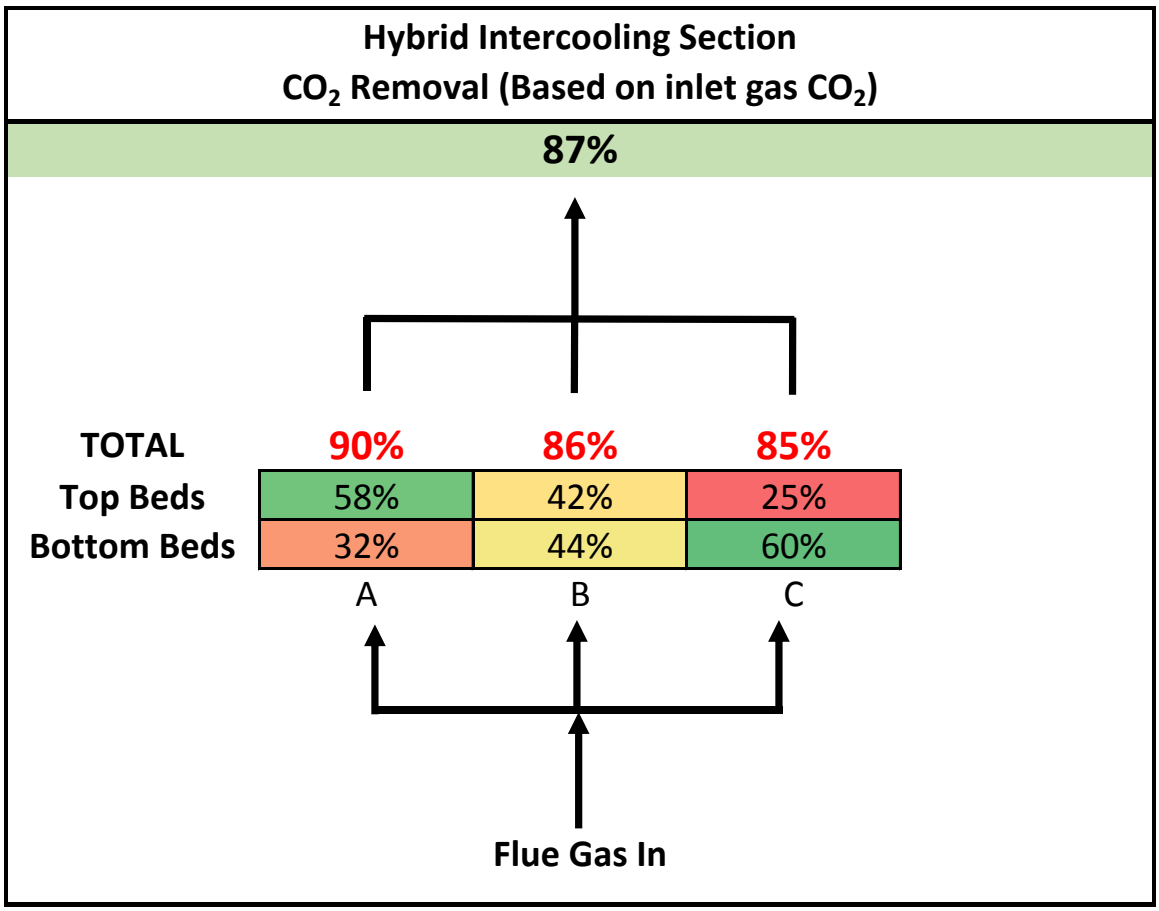

Figure 6-25: Performance (CO_2 removed) of each bed in the intercooling section of the 2x3 hybrid absorber configuration. The 3 gas flow paths (A, B, C) and 6 beds (2 x 3 configuration) are defined in Figure 6-22.

The figure highlights a general pattern associated with the hybrid contacting scheme – the two rows of beds and the liquid flow path (Figure 6-22) ensure the CO_2 removed in any gas flow path is balanced. For example, gas flow path A contacts the richest solvent (bottom left bed) and the leanest solvent (top left bed) in the configuration - the CO_2 removal rate follows this solvent loading pattern. Each of the 3 gas flow paths experiences similar CO_2 removal rates. The balancing of CO_2 removal across rows allows the hybrid design to approach counter-current contacting – additional rows of beds would improve the counter-current nature of the contacting scheme.

The figure also confirms that the introduction of hot flue gas does not have a significant detrimental effect of CO_2 removal performance of the bottom beds – the highest CO_2 removal occurs in a bottom bed (bottom right). This explains the performance of the 1x3 hybrid design as well.

Finally, the temperature profiles for each design were evaluated to determine the effectiveness of each design in cooling the gas and to provide an explanation for the performance improvement seen with the hybrid contactor.

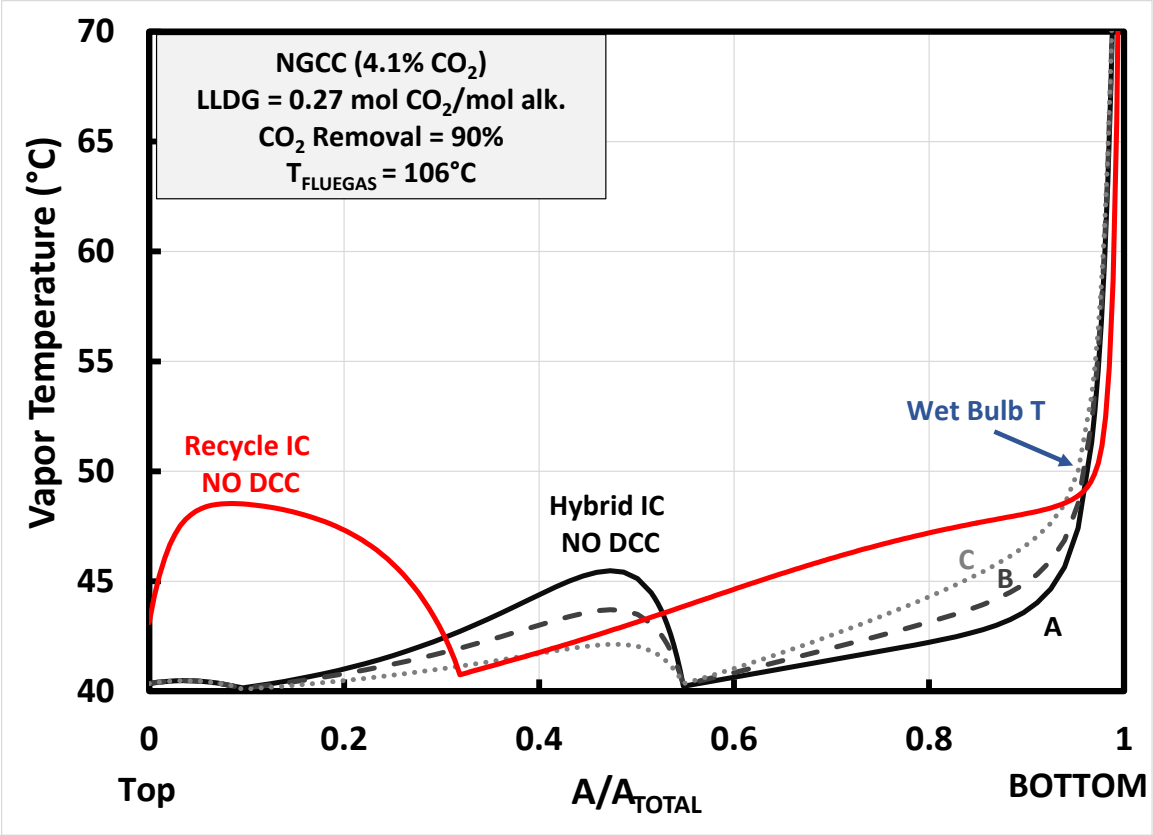

Figure 6-26: Vapor temperature comparison for DCC integration configurations: 2x3 hybrid intercooling contactor vs. recycle intercooling ($L_{Recycle}/G = 3$). Fractional packing area moves from top to bottom of the absorber. For hybrid intercooling, 3 parallel paths exist – A, B, and C in Figure 6-22. Flue gas enters at 106°C with 8.7 mol% H_2O. LLDG = 0.27 mol CO_2 mol alkalinity, 8 m PZ, MP-250X (top bed) and MP-170X (bottom section) for both configurations.

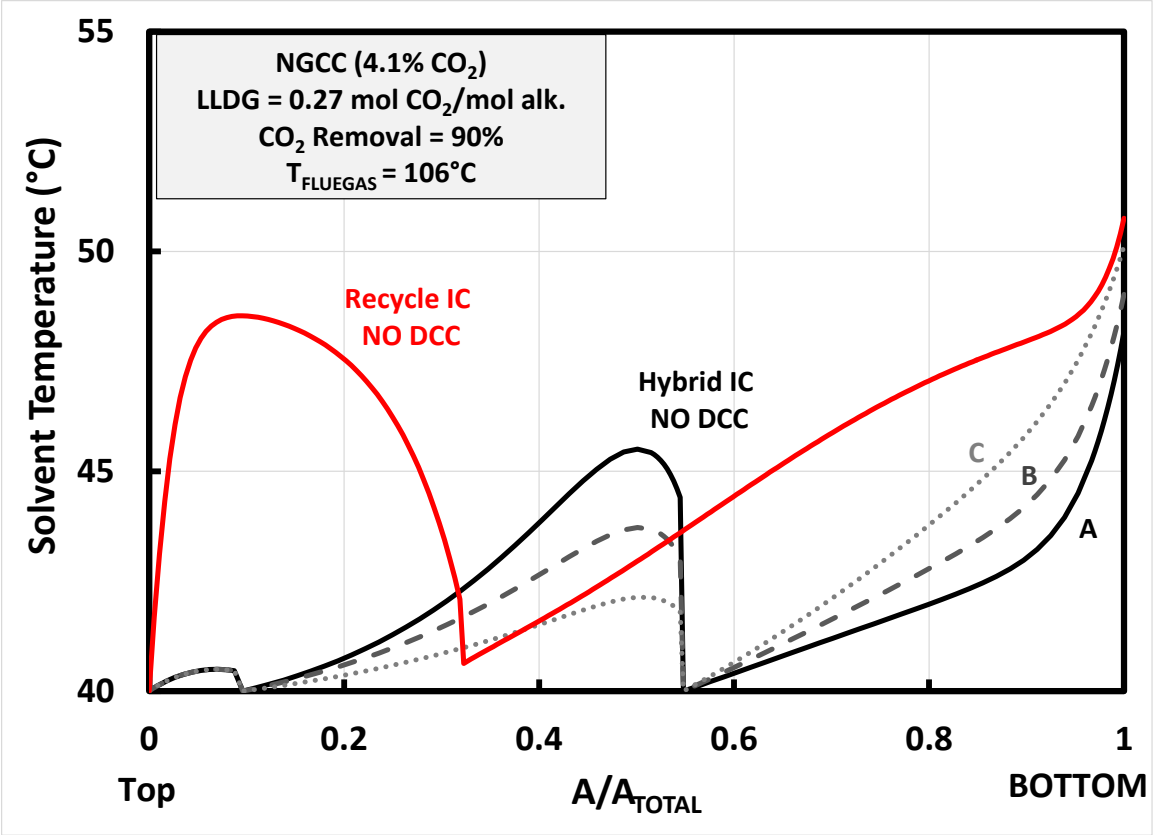

Figure 6-27: Solvent temperature comparison for DCC integration configurations: 2 x 3 hybrid intercooling contactor vs. recycle intercooling ($L_{Recycle}/G = 3$). Fractional packing area moves from top to bottom of the absorber. For hybrid intercooling, 3 parallel paths exist – A, B, and C in Figure 6-22. Flue gas enters at 106°C with 8.7 mol% H_2O. LLDG = 0.27 mol CO_2 mol alkalinity, 8 m PZ, MP-250X (top bed) and MP-170X (bottom section) for both configurations.

The vapor temperature profile compares the ability of the recycle and hybrid intercooling methods to manage the hot flue gas entering the absorber. As the figure shows, both configurations rapidly cool the flue gas to a similar level (presumably the wet bulb temperature, ~50°C) within the first 10% of the packing in the column. Beyond this point, however, the hybrid design continues cooling to near 40°C at the exit of the bottom row of beds – this is a results of intercooling the solvent prior to feeding to every bed in the hybrid design. The recycle design, by contrast, only feeds cold solvent at one

point (top of the recycle section) and the entire recycle bed is required to cool the gas to 40°C while simultaneously capturing CO_2. Therefore, the fine discretization (multiple beds with multiple intercoolers) in the hybrid design provides an advantage in managing the hot flue gas in addition to the expected driving force and solvent cooling benefits.

The solvent temperature profile for the hybrid design follows the CO_2 removal pattern in Figure 6-25 – the beds with highest CO_2 removal exhibit the highest temperatures. Only the top row of beds forms a temperature bulge – this is because the bottom beds contact hot flue gas and therefore the temperature increases monotonically through these beds. In addition, the average temperature of the solvent contacting the 3 identical gas streams is consistently lower than the recycle design. Finally, the solvent temperature in the top (countercurrent) bed of the hybrid design is much lower than the recycle design simply due to the limited CO_2 transferred in this section (~3%). The top bed in the hybrid design is acting as a polishing section, while the counter-current section in the recycle design is essential to maintain adequate driving forces for the overall mass transfer performance of a recycle intercooling configuration with a recycle bed at the bottom (rich end) of the column.

6.5.4 Other contacting concepts for future analysis

An extension of the hybrid intercooling configuration is a true crossflow contacting scheme (Figure 6-28) where the vapor and liquid flow in different planes (perpendicular to one another).

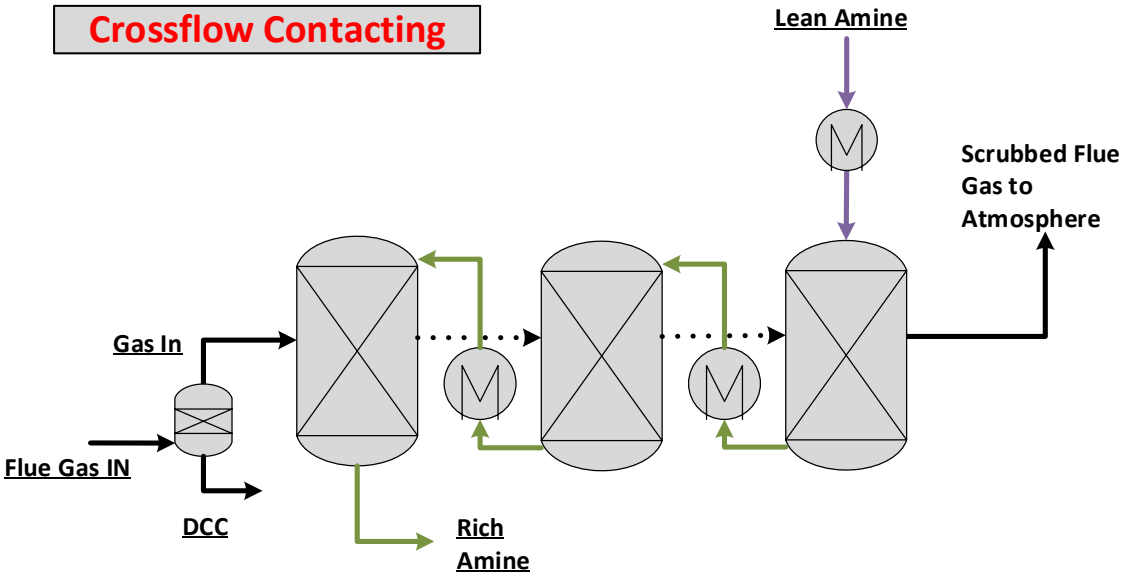

Figure 6-28: Absorber PFD for Crossflow Design. The solvent and gas flow perpendicularly in each bed (crossflow) with an independent column cross-section for each phase. The solvent is cooled between each module of crossflow to serve as intercooling mechanism.

The crossflow approach has created an additional degree of freedom by separating the vapor and liquid flow cross-sections. A high liquid rate per perimeter (high-intensity contacting) is not limited by the vapor cross-section and flooding or pressure drop constraints as in a counter-current contactor. In addition, the solvent cooling can be integrated readily into the modular design proposed in Figure 6-28. The crossflow approach is limited by the sacrifice of driving forces compared to a countercurrent contactor.

The modeling and evaluation of a crossflow contactor requires two major modifications to the methods currently used for countercurrent contactors:

1) Two-dimensional integration of concentration profiles to account for vapor and liquid flow in different axes.

2) Mass transfer models for packing (or other column internals) that account for the flow patterns specific to a crossflow contactor. Vapor "drift" has been observed in crossflow contactors, for example, and requires special attention when modeling mass transfer in crossflow patterns (Thibodeaux, et al., 1977).

Two dimensional integration is not readily available in AspenPlus®. Specifically, the rate-based methods used for absorber modeling in this work will be required in a rigorous two dimensional model as well. A workaround may be to use the rate-based column model in Aspen as individual, small, and well-mixed computational nodes in the crossflow contactor. However, to model a full absorber with this method will be computationally inefficient and may limit the use of design specifications or optimization tools.

Mass transfer models and data for crossflow contacting are very limited in the literature and would necessitate experimental evaluation which might include design and development of column internals specific for the crossflow application (e.g., structured packing that considers the perpendicular flow paths of the solvent and vapor).

6.6 CONCLUSIONS

Novel intercooling concepts were proposed based on the fundamental mechanisms effecting absorber performance, as identified in preceding chapters. The novel concepts were evaluated in comparison to in-and-out intercooling and to one another to identify the best potential configurations for the NGCC application.

6.6.1 Evaluation of Recycle Intercooling Method for NGCC Application

- Recycle intercooling benefits are maximized at recycle rates in the range of $L_{Recycle}/G \approx 2 – 4$ or $L_{Recycle}/ L_{Feed} \approx 2.5 – 5$.

    - Incremental economic analysis indicates pumping costs become prohibitive beyond this range.
    - Evaluation of recycle intercooling benefits reveal that the driving force benefits also fall beyond this range as back-mixing outweighs small incremental intercooling benefits. The mass transfer enhancement of the recycle design also exhibits diminishing returns at high recycle rates.
- Potential pressure drop benefits of recycle intercooling (lower velocities from cool, dense gas and reduced overall column height) can serve to offset pumping costs and make recycle design potentially feasible over the full range of recycle rates tested ($L_{Recycle}/G = 0.5 – 8$)
- Mechanistic evaluation of recycle intercooling benefits revealed that the liquid-film mass transfer enhancement is the dominant source of benefits from the recycle.
- The "intercooling" benefit of the recycle design is the absorption of CO_2 in a section with a large L/G and an integrated intercooling loop. This limits the absorption (and temperature constraints) outside of the recycle section.
- Gas cooling is a relatively minor benefit compared to in-and-out intercooling as the temperature is not reduced significantly and the capacity of the gas to carry water is not increased significantly.
- Recycle intercooling provides significant solvent capacity benefits (improved approach to isothermal L_{MIN}) at lean loadings above 0.25 mol CO_2/mol alkalinity, where adiabatic absorbers and simple intercooling are severely limited by temperature-related equilibrium restrictions.
- Recycle intercooling outperforms simple intercooling in terms of packing-solvent rate (capital-operating cost) trade-off due to significant mass transfer

enhancement realized in the recycle section and the overall reduction of temperatures throughout the absorber compared to in-and-out intercooling. The mass transfer enhancements are also sufficient to equal or outperform a simple isothermal absorber across the entire range of operating L/G.

6.6.2 Novel Absorber Configurations

A hybrid contacting scheme was introduced as a method to enhance mass transfer performance of absorbers by generating turbulence and moderating temperatures (high L/G) and improving driving forces (more "counter-current" than recycle configuration and distributed intercooling throughout absorption process).

- A 2x3 hybrid intercooling design was evaluated as a one-to-one replacement for the recycle intercooling section ($L_{RECYCLE}/G = 3$) in an absorber treating NGCC flue gas (4.1% CO_2):
    - The hybrid intercooling configuration yielded ~50% reduction in packing and ~50% reduction in gross power requirements (solvent pumping and gas-side pressure drop) to achieve identical performance (CO_2 removal, gas and liquid exit temperatures) in the isolated intercooling sections.
    - The hybrid design maintains consistently larger driving forces and lower temperature throughout the intercooling section.
- Hybrid intercooling designs (2x3 and 1x3) were evaluated as a method to replace the direct contact cooler (DCC) and by integrating the gas cooling and intercooling function in one section of the absorber.
    - The hybrid intercooling design was within 5% of the maximum solvent capacity (i.e., isothermal L_{MIN}) for the given conditions (LLDG = 0.27 mol

CO_2/mol alkalinity, 90% CO_2 removal effectively removing any temperature-induced equilibrium constraints.

- At a common operating condition (L/G = 1.5, RLDG = 0.368 mol CO_2/mol alkalinity), the hybrid designs significantly outperformed recycle designs:
    i. The 2x3 hybrid reduced packing requirements by 45 and 67% over the recycle intercooling design with a DCC (base case) and the recycle design without a DCC, respectively.
    ii. The 1x3 hybrid reduced packing requirements by 26 and 55% over the recycle intercooling design with a DCC (base case) and the recycle design without a DCC, respectively.
    iii. A small countercurrent section (~10% of total packing area, 1 m bed) is required at the top of the 2x3 design to account for small imbalances in CO_2 removal in the 3 gas flow paths for the hybrid. This section increases to 4.7 m in the 1x3 design (~33% of total packing area).
    iv. All designs without a DCC (hybrid and recycle) rapidly cool the entering hot flue gas (within the first 10% of the column) to the wet bulb temperature. The hybrid design maintains lower average vapor and solvent temperatures throughout the contactor.

6.6.3 Open Research Issues

- Modeling of any novel contacting scheme (e.g., rotating packed bed, cross-flow), column internals (trays, hybrid packing), operating conditions (e.g., high solvent

loads), or solvents with unique physical properties (e.g., high viscosity) will require independent, accurate, and physically representative component mass transfer models to properly design and optimize the system. As novel absorber concepts move to leveraging detailed mass transfer mechanisms to improve performance, the empirical mass transfer models must provide adequate resolution of the specific mechanisms being used to properly develop and optimize the design. Therefore, mass transfer model development and experimental characterization of mass transfer phenomena in real contactors are among the most important areas of open research for CO_2 capture systems.

- Novel designs, such as hybrid contactor, need to be taken to the next step of conceptual equipment design to understand any potential hidden costs or design challenges prior to further development or evaluation (i.e., economic assessment, pilot testing, etc.).
- Modeling of true cross-flow contacting requires mass transfer data specific to the contacting scheme (limited data) and development of a 2-D integration method for use with rigorous rate-based contactor and solvent models in AspenPlus®.

Chapter 7: Conclusions and Recommendations

7.1 General Absorber Design and Research Recommendations

A primary goal of the work in the preceding chapters was to develop general recommendations regarding absorber design with amine solvents. The following broad recommendations have been developed in the preceding chapters and will be supported by the conclusions for each research objective.

1) Low CO_2 flue gas sources (NGCC, 4% CO_2 in this work) provide the best opportunity for operation without intercooling (large lean loading range) but also require advanced intercooling design once a temperature-limitation is realized (simple intercooling is insufficient).
2) Higher CO_2 flue gas sources (Coal, 15% CO_2 and Steel, 27%, in this work) require intercooling over the entire practical operating range of piperazine, but simple (in-and-out intercooling) is largely effective.
3) Lower capacity solvents (larger inherent solvent circulation rates, 5 m PZ in this work) should be operated with simple intercooling.
4) Operating with reduced CO_2 removal targets (< 90%) expands the lean loading range for operation without intercooling and reduces the penalty of operating with intercooling when a limitation is realized. Higher removal targets (>90%) will require intercooling, including the development of advanced designs.
5) The "optimal" location of the intercooler in an in-and-out intercooling design will be in the middle 50% of the column at normal solvent operating conditions (L/L_{MIN} 1.1 to 1.8) and can be predicted by underlying "pinch" behavior. Extreme locations (high or low) are not expected and movement

from a default location in the middle (Z/Z_{TOTAL} =0.5) of the column provides limited benefit.

6) Liquid-film physical mass transfer is a significant factor in absorber performance with fast amines (especially viscous solvents). The rich-end of the absorber is particularly limited and absorber design or internals should be customized to enhance liquid-film turbulence to maximize absorber performance in these cases.
7) Reducing the viscosity of fast amine solvents (5 m vs. 8 m PZ) has a significant impact on absorber performance and should be considered carefully in solvent development.
8) Measurement (and complete understanding) of the liquid-film mass transfer coefficient (as a function of operating conditions, column internals, and physical properties) is one of the most important research areas for absorber modeling and process development.
9) Novel high intensity (high L/G) contacting schemes (increase L/G without increasing feed solvent rate, i.e. recycle or hybrid scheme in this work) are promising due to coupling of liquid-film mass transfer enhancement and temperature moderation.

7.2 SIGNIFICANT INNOVATIONS

In addition to the general absorber design recommendations, specific innovations and findings in this work are relevant to ongoing research and development of absorbers for CO_2 capture:

1) Solvent Recycle Intercooling: The approach of recycling (and cooling) solvent to create a section of the absorber with a high L/G was demonstrated to

provide significant mass transfer benefits and was an improvement over simple intercooling for the NGCC application.

2) Hybrid Intercooling: This method, which splits the gas into multiple parallel paths sequentially contacting multiple passes of the solvent (e.g., 2 x 3 hybrid intercooling) provides the benefits of a large L/G ratio but with enhanced intercooling (at multiple discrete locations) and more counter-current contacting than the solvent recycle approach and has potential for all solvent absorption applications.
3) Integrating the DCC and solvent cooling functions for NGCC: The recycle and hybrid intercooling methods were both demonstrated to successfully replace the direct contact cooler for NGCC applications while providing additional benefits associated with intercooling.
4) Integrating sprays to create a recycle intercooling section: Tests at the pilot plant and subsequent modeling efforts demonstrated and quantified the benefits of integrating spray nozzles into the intercooling loop to create a solvent recycle section with mass transfer area provided by the spray.

The detailed conclusions supporting these recommendations (and others) follow in the subsequent sections.

7.3 Conclusions and Recommendations by Research Objective

7.3.1 Model Validation with Pilot Plant Data

The rigorous rate-based absorber model using aqueous piperazine as the solvent was validated and adjusted using pilot plant data from the Separations Research Program pilot plant at the University of Texas at Austin. A data reconciliation procedure was implemented to simultaneously account for the measurement uncertainty for the pilot

plant measured inputs and to the model (flows, temperatures, etc.) and the uncertainty in the output metrics of the model (CO_2 removal, outlet temperatures, etc.). In addition, an adjustable parameter was defined to allow fitting of the model to pilot data for any unexplained offset in the reconciliation process. The key findings of this reconciliation process can be summarized as follows:

- A systematic bias between the model and pilot plant data was identified by a consistent model adjustment across two pilot plant campaigns covering a wide range of operating conditions and different types of packing.
    - The model bias could be corrected by an increase in the lean solvent loading of ~7% or by a 25% reduction in packing mass transfer area.
    - The CO_2 correction had independent corroboration from separate stripper model validation and via a modified density-predicted loading.
- The adjusted model was used in a second stage of data reconciliation to isolate the performance of a spray nozzle added to the intercooling loop in the pilot plant.
    - The mass transfer area of the spray nozzle was regressed during the reconciliation process and correlated to the kinetic energy (via mass flow rate) of the solvent.
    - The spray nozzle added between 5 and 20% additional mass transfer area to the column measured as an equivalent packing area.
    - A screening economic analysis to compare the cost of the pressure drop through the spray nozzle to the value of the mass transfer area added (quantified via the cost of an equivalent area of structured packing) revealed that the spray nozzle pumping costs always outweigh the value of area generated. However, the flexibility in design and operation provided by sprays make them a potentially attractive option.

The final approach to model validation consisted of using the adjusted model to predict the performance of a new pilot plant campaign.

- The model predicted NTU with an average error of 22% and over-predicted NTU on average (mean ratio of predicted/measured = 1.08).
- The data showed a correlation with time (i.e., experiment number) exhibiting a distinct shift from consistent under-prediction to over-prediction of CO_2 removal half way through the campaign. The worst fit of individual experiments occurred together in a cluster of runs in the second half of the campaign.
- A pilot plant parametric study of absorber performance as a function of PZ concentration revealed that 5 m PZ significantly outperformed 8 m PZ in terms of mass transfer rates, indicating a strong impact of viscosity on absorber performance and the potential importance of liquid-film physical mass transfer in amine absorbers.

Open Research Issues/Recommendations

- The operation of the absorber at high CO_2 removal conditions provides an opportunity to validate different absorber performance mechanisms related to operating near a pinch (small driving forces). Specifically, equilibrium constraints become controlling at pinched conditions and provide an opportunity to validate model VLE. Further validation of the model is need at these conditions.
- The spray nozzle model developed in this work is largely empirical and is coupled to the packing mass transfer models used in the regression process (spray represented as a packed bed). If the spray nozzle continues to be used as a component of the pilot plant (or other modeling activities), the spray model

should be de-coupled from packing models by regressing a combined k_La to represent the true performance of the spray as a function of operating conditions.

- Mid-loading measurements (or similarly, mid-column gas measurements) create a new degree of freedom for model validation of the absorber via a secondary material balance around half of the absorber. This new degree of freedom can be used to validate rate mechanisms in the absorber by considering the relative rates of CO_2 absorption in each half of the column and identifying the controlling mechanism in the model which can be used to fit the new pilot plant data point. This is particularly relevant for the validation or measurement of physical-liquid film mass transfer coefficients, which are difficult to measure and extrapolate from experimental conditions to conditions in an actual amine absorber. Initial attempts with the approach of varying the overall volumetric mass transfer coefficient (k_La) indicates significant improvement in model prediction of mid-loading compared to the base case, but still exhibits a consistent trend of over-predication.

7.3.2 Adiabatic Absorbers: L_{MIN} and Pinch Phenomena

The key findings of the evaluation of adiabatic absorbers and pinch phenomena associated with minimum solvent rates can be summarized as follows:

- Operation of adiabatic absorbers in specific lean loading ranges can lead to severe penalty in solvent circulation requirements compared to an isothermal baseline. The governing phenomena for these solvent capacity penalties can be summarized as follows:

- Lean end pinch formation at the temperature bulge occurs at all lean loadings. CO_2 removal constraint determines if lean pinch is limiting at given operating conditions.
- Solvent rate increases to overcome lean end pinches initially "trap" heat in the column as the liquid rate is insufficient to moderate temperatures or carry heat away from the bulge. This leads to a drop in removal with increasing solvent rate.
- As the solvent rate is increased further, the total liquid and vapor heat capacities (mC_P) as calculated at the top of the absorber will crossover (The vapor heat capacity includes the enthalpy of vaporization of water for the vapor saturated at outlet conditions). This condition identifies the point where the liquid can effectively moderate bulge temperatures and address the equilibrium constraint.
- The non-monotonic behavior of CO_2 removal as a function of solvent rate through each of the preceding transitions can lead to multiple steady state solvent rates that meet the CO_2 removal specification. Each steady state solvent rate can produce drastically different system design and can present process control challenges (stable operating condition).

- Flue gas CO_2 concentration has two critical effects on pinch formation and the associated solvent capacity penalty:
  - Lower CO_2 flue gas concentrations (and associated lower temperatures) allow operation with a wider range of lean loading without a limiting lean end pinch. This provides flexibility in the design and operation of these systems (operation without intercooling).

- The solvent capacity penalty (measured as the ratio of the adiabatic minimum solvent rate (L_{MIN}) to the isothermal minimum solvent rate ($L_{MIN, ISOTHERMAL}$)) decreases as the flue gas CO_2 concentration increases:
    i. NGCC (4.1% CO_2): Maximum $L_{MIN}/L_{MIN, ISOTHERMAL} = 3.58$
    ii. COAL (14.7% CO_2): Maximum $L_{MIN}/L_{MIN, ISOTHERMAL} = 2.26$
    iii. STEEL (27.1% CO_2): Maximum $L_{MIN}/L_{MIN, ISOTHERMAL} = 1.94$
    iv. The trend is associated with the solvent rate increase required to overcome the difference in total heat capacities (vapor vs. liquid) to allow the solvent to moderate temperatures and address equilibrium constraints. NGCC, with inherently low L/G, has the largest "heat capacity deficit" to overcome.
- Operating 5 and 8 m PZ for the same flue gas (composition and gas rate) and CO_2 removal rate generates an identical maximum temperature and lean end pinch. The same absolute solvent rate is required to overcome this pinch. The inherently lower capacity of 5 m PZ means the increase in solvent rate over the isothermal baseline is relatively smaller for 5 m PZ and limits the benefits of intercooling.
- Operating with lower CO_2 removal targets limits the impact of temperature restrictions in the absorber:
    - Lower removal specifications allow operation over a wider range of lean loading without generating a performance limiting lean end pinch.
    - The solvent capacity penalty increases with CO_2 removal since the leaner operating region yields a lower baseline solvent rate (better solvent capacity) and requires a larger increase to overcome a pinch at higher temperatures.

- Temperature-related pinches are a rate-dependent phenomena, unlike isothermal saturation of the solvent (strictly thermodynamic phenomena):
    - Lean end pinches are affected by relative rates of water and CO_2 transfer and thus are impacted by the mass transfer and kinetic properties in an absorber system. In addition, the minimum solvent rate used in design calculations or for the identification of a pinched condition in a model will be affected by the rate parameters of the specific model.

Open Research Issues/Recommendations

- How do the rates of CO_2 absorption and water transfer effect pinch formation? Is the lean end pinch observed in this work unique to "fast" amine solvents? Development of a dimensionless relationship to predict the effect of CO_2 and water transfer rates on pinch formation would be a useful generalization for absorber design.
- A shortcut method to predict the transition loading for a given solvent and operating condition (CO_2 removal, flue gas concentration) was developed as part of this work but was very sensitive to assumptions about CO_2 removal above the pinch. A better approximation of removal at the mass transfer pinch is needed to improve the prediction of lean loading where adiabatic absorbers become limited by a temperature bulge induced mass transfer pinch.

7.3.3 Evaluating the Limitations of Simple Intercooling

Simple (in-and-out) intercooling was studied as a function of flue gas CO_2 concentration and operating conditions to quantify solvent capacity and mass transfer benefits, identify limitations of simple intercooling, and understand underlying phenomena to explain performance trends. The following major findings were developed:

Solvent Capacity Effects and Pinch Formation in Intercooled Absorbers

- Simple intercooling significantly improves solvent capacity over an adiabatic absorber for all conditions in the analysis:
    - Maximum Deviation from Isothermal (L_{MIN} /$L_{MIN,\ ISOTHERMAL}$):
        i. $NGCC_{INTERCOOLED}$ = 1.98

           $NGCC_{ADIABATIC}$ = 3.58
        ii. $COAL_{INTERCOOLED}$ = 1.31

            $COAL_{ADIABATIC}$ = 2.26
        iii. $STEEL_{INTERCOOLED}$ = 1.18

             $STEEL_{ADIABATIC}$ = 1.94
- Simple intercooling expands loading range where a limiting temperature pinch is avoided and isothermal capacity is approached (L_{MIN} /$L_{MIN,\ ISOTHERMAL}$ ≈ 1):
        i. $NGCC_{INTERCOOLED}$ = ≤ 0.25 mol CO_2/mol alkalinity

           $NGCC_{ADIABATIC}$ = ≤ 0.22 mol CO_2/mol alkalinity
        ii. $COAL_{INTERCOOLED}$ = ≤ 0.20 mol CO_2/mol alkalinity

            $COAL_{ADIABATIC}$ = ≤ 0.18 mol CO_2/mol alkalinity
        iii. $STEEL_{INTERCOOLED}$ = ≤ 0.18 mol CO_2/mol alkalinity

             $STEEL_{ADIABATIC}$ = ≤ 0.17 mol CO_2/mol alkalinity
- Pinch formation and performance limitation is different for an intercooled absorber:
    - True rich end pinch forms (not associated with temperature bulge at lean end).
    - Lean pinch forms at bulge above intercooler, but system is not equilibrium limited if bottom bed still achieves true rich pinch

- "Double pinch" forms associated with bulge in each section (above and below IC). System is equilibrium limited and requires solvent rate increase.

- Intercooling can effectively be viewed as two adiabatic absorbers operated in series:
  - First (top) absorber effectively operates with double the total heat capacity of the nominal inlet solvent – this is because all of the heat generated by CO_2 absorption in this bed is removed at the intercooler instead of returning to the lean end of the column as water condensing from the gas as in a normal adiabatic absorber.
  - Second (bottom) absorber operates as a normal adiabatic absorber.
  - New degree of freedom (CO_2 removed in each section) allows moderation of the effect of temperature bulges in column – bulge is split between two sections and removal in section prevents formation of pinch/minimizes effect of existing pinches.

Design Curves and Packing-Solvent Rate Trade-Offs

- Design curves were developed to evaluate the performance of intercooling in terms of the packing – solvent rate trade-off for each absorber design. The difference between an intercooled (or adiabatic) absorber and an isothermal absorber in normal solvent operating range (1.05 to 1.8 L_{MIN}) was quantified as the area between the design curves. The results for 3 relevant loading regions led to the following conclusions:

i. "Over-stripped" or low lean loading region: Adiabatic absorber provides good performance in terms of solvent capacity and mass transfer and should be the default design for this operating region.

ii. "Simple Intercooling" or mid-loading region: Simple Intercooling is effective for coal and steel (high CO_2 applications) and should be the default design. For NGCC, while in-and-out intercooling approximates isothermal behavior at L_{MIN}, the performance in the operating solvent range is poor due to driving force limitations. Novel intercooling development is warranted.

iii. "Advanced Intercooling" or mid-loading region: Simple intercooling is effective for coal and steel (high CO_2 applications) and should be the default design despite the deviation in solvent capacity at the limiting case of L_{MIN}. NGCC performs poorly compared to an isothermal absorber and novel intercooling design development is needed

- Optimal Intercooling Location: The optimal intercooling location (minimize total packing area) was defined for all flue gas applications and select lean loadings as a function of L/L_{MIN}:
  - Underlying pinch at L_{MIN} determines the trend in optimal intercooling position as a function of solvent rate:
    i. Double pinch or temperature-induced rich pinch @ L_{MIN}: Optimal IC positions starts in bottom half of column (or near the middle) and moves up column as L/L_{MIN} increases
    ii. Only limiting lean pinch: Optimal IC positions starts in top half (above IC) of column and moves down column as L/L_{MIN} increases

iii. ALL CASES: As L/L_{MIN} reaches large values ($L/L_{MIN} > \approx 2$), IC is not needed and optimal location is the nearest "neutral" location in the column (mid-point or top).

iv. ALL CASES: In normal operating range for solvent rates ($L/L_{MIN} < 2$), optimal IC locations falls in the middle 50% of column ($Z_{INTERCOOLER}/Z_{TOTAL}$= 0.25 to 0.75)

- Normalized driving force concept was introduced to explain optimal intercooling location. The driving force through the column is normalized by the partial pressure of CO_2 in the bulk gas to provide a measure of solvent equilibrium constraint. The optimal location of IC occurs when the "relative pinch" (or minimum normalized driving force) is equivalent on both sides of the intercooler. This result is consistent for all flue gas concentrations within the normal solvent operating window (L/L_{MIN} = 1.1 to 1.8).

7.3.4 Mass Transfer Parameter Sensitivity Analysis

The goals and corresponding key findings of mass transfer parameter sensitivity analysis can be summarized as follows:

- Identify controlling mass transfer resistance in an absorber utilizing concentrated PZ as a function of operating conditions:
  - The model predicts liquid-film control for the PZ system. Gas-film resistance is negligible across conditions tested (column average gas-film resistance does not exceed 10% in any case). Maximum gas-film resistance is localized at the lean end of the column.

- The liquid-film resistance is dominated by diffusion resistance at the base case parameter values tested in this analysis across all operating conditions and diffusion resistance is greatest at the rich end of the column for all cases.
- Temperature effects in an adiabatic absorber do not change the overall column trends (diffusion limitation increase from lean to rich) and have a minimal impact on the average contribution of each component to overall mass transfer resistance when compared to an isothermal absorber.
- At high k_L values (5*Base), the column average reaction resistance indicates significant reaction control of the liquid film (54% of overall resistance). Operating at high solvent rates (1.8 L_{MIN}) or with 5 m PZ also lead to significant reaction resistance (42% column average in each case).

- Define/identify dimensionless group to predict mass transfer resistance in absorber and validate parameter sensitivity results:
  - The reaction enhancement ratio, Φ, (ratio of pseudo-first-order and instantaneous asymptotic enhancement factors) provides very accurate prediction of liquid-film mass transfer resistance distribution (diffusion vs. reaction) as evaluated by parameter sensitivity analysis.
  - When $\Phi > 10$, the theoretical predictions no longer match sensitivity analysis prediction, indicating the system may have reached instantaneous reaction limit (within calculation ability of parameter sensitivity method)
- Use theoretical model to explain trends in mass transfer resistance in the absorber
  - Liquid-film diffusion resistance increases from the lean to rich end of the column primarily due to the change in the equilibrium capacity of the solvent with loading (slope of vapor-liquid equilibrium curve). The

equilibrium contribution to the change in Φ (measure of diffusion vs. reaction resistance) may increase by as much as a factor of 30 from the lean loading to rich loading.

Beyond the conclusions developed directly from results in this analysis, the evaluation of mass transfer resistance should guide absorber design and model development activities:

- The base case predictions of the piperazine rate-based absorber model indicate significant liquid-film diffusion resistance across the full range of operating conditions. Novel absorber design should include features that generate turbulence in the liquid face or enhance physical mass transfer, particularly at the rich end of the column where the model predicts approach to instantaneous reaction limit.
- Solvent selection should carefully consider the effect of viscosity on absorber performance. As the analysis with 5 m PZ demonstrated, the reduction in viscosity significantly reduces liquid-film physical mass transfer resistance and should enhance overall absorber mass transfer performance.
- The liquid-film mass transfer coefficient model is a critical component of properly modeling absorber mass transfer resistance. The upper limit of k_L evaluated in this work (5*Base k_L) is within the range of commonly used literature models and within the uncertainty in the current model when considering viscosity dependence and uncertainty in experiments. The design approach for absorbers and performance prediction as a function of operating conditions will vary significantly in the range of k_L values considered in the work and may lead to sub-optimal design.
- The reaction enhancement ratio, Φ, can be used to predict the liquid-film control mechanisms for cases not included in this analysis (e.g., different equipment,

operating, or solvent specifications) if operating specifications for the absorber are known and a thermodynamic model is available to calculate the asymptotic enhancement factors.

7.3.5 Development of Novel Absorber Configurations

Novel intercooling concepts were proposed based on the fundamental mechanisms effecting absorber performance, as identified in preceding chapters. The novel concepts were evaluated in comparison to in-and-out intercooling and to one another to identify the best potential configurations for the NGCC application.

Evaluation of Recycle Intercooling Method for NGCC Application

- Recycle intercooling benefits are maximized at recycle rates in the range of $L_{Recycle}/G \approx 2 - 4$ or $L_{Recycle}/ L_{Feed} \approx 2.5 - 5$.
    - Incremental economic analysis indicates pumping costs become prohibitive beyond this range.
    - Evaluation of recycle intercooling benefits reveal that the driving force benefits also fall beyond this range as back-mixing outweighs small incremental intercooling benefits. The mass transfer enhancement of the recycle design also exhibits diminishing returns at high recycle rates.
- Potential pressure drop benefits of recycle intercooling (lower velocities from cool, dense gas and reduced overall column height) can serve to offset pumping costs and make recycle design potentially feasible over the full range of recycle rates tested ($L_{Recycle}/G = 0.5 - 8$)
- Mechanistic evaluation of recycle intercooling benefits revealed that the liquid-film mass transfer enhancement is the dominant source of benefits from the recycle.

- The "intercooling" benefit of the recycle design is the absorption of CO_2 in a section with a large L/G and an integrated intercooling loop. This limits the absorption (and temperature constraints) outside of the recycle section.
- Gas cooling is a relatively minor benefit compared to in-and-out intercooling as the temperature is not reduced significantly and the capacity of the gas to carry water is not increased significantly.
- Recycle intercooling provides significant solvent capacity benefits (improved approach to isothermal L_{MIN}) at lean loadings above 0.25 mol CO_2/mol alkalinity, where adiabatic absorbers and simple intercooling are severely limited by temperature-related equilibrium restrictions.
- Recycle intercooling outperforms simple intercooling in terms of packing-solvent rate (capital-operating cost) trade-off due to significant mass transfer enhancement realized in the recycle section and the overall reduction of temperatures throughout the absorber compared to in-and-out intercooling. The mass transfer enhancements are also sufficient to equal or outperform a simple isothermal absorber across the entire range of operating L/G.

Novel Absorber Configurations

A hybrid contacting scheme was introduced as a method to enhance mass transfer performance of absorbers by generating turbulence and moderating temperatures (high L/G) and improving driving forces (more "counter-current" than recycle configuration and distributed intercooling throughout absorption process).

- A 2x3 hybrid intercooling design was evaluated as a one-to-one replacement for the recycle intercooling section ($L_{RECYCLE}/G = 3$) in an absorber treating NGCC flue gas (4.1% CO_2):

- The hybrid intercooling configuration yielded ~50% reduction in packing and ~50% reduction in gross power requirements (solvent pumping and gas-side pressure drop) to achieve identical performance (CO_2 removal, gas and liquid exit temperatures) in the isolated intercooling sections.
- The hybrid design maintains consistently larger driving forces and lower temperature throughout the intercooling section.

- Hybrid intercooling designs (2x3 and 1x3) were evaluated as a method to replace the direct contact cooler (DCC) and by integrating the gas cooling and intercooling function in one section of the absorber.
  - The hybrid intercooling design was within 5% of the maximum solvent capacity (i.e., isothermal L_{MIN}) for the given conditions (LLDG = 0.27 mol CO_2/mol alkalinity, 90% CO_2 removal effectively removing any temperature-induced equilibrium constraints.
  - At a common operating condition (L/G = 1.5, RLDG = 0.368 mol CO_2/mol alkalinity), the hybrid designs significantly outperformed recycle designs:
    i. The 2x3 hybrid reduced packing requirements by 45 and 67% over the recycle intercooling design with a DCC (base case) and the recycle design without a DCC, respectively.
    ii. The 1x3 hybrid reduced packing requirements by 26 and 55% over the recycle intercooling design with a DCC (base case) and the recycle design without a DCC, respectively.
    iii. A small countercurrent section (~10% of total packing area, 1 m bed) is required at the top of the 2x3 design to account for small imbalances in CO_2 removal in the 3 gas flow paths for the hybrid.

This section increases to 4.7 m in the 1x3 design (~33% of total packing area).

iv. All designs without a DCC (hybrid and recycle) rapidly cool the entering hot flue gas (within the first 10% of the column) to the wet bulb temperature. The hybrid design maintains lower average vapor and solvent temperatures throughout the contactor.

Open Research Issues

- Modeling of any novel contacting scheme (e.g., rotating packed bed, cross-flow), column internals (trays, hybrid packing), operating conditions (e.g., high solvent loads), or solvents with unique physical properties (e.g., high viscosity) will require independent, accurate, and physically representative component mass transfer models to properly design and optimize the system. As novel absorber concepts move to leveraging detailed mass transfer mechanisms to improve performance, the empirical mass transfer models must provide adequate resolution of the specific mechanisms being used to properly develop and optimize the design. Therefore, mass transfer model development and experimental characterization of mass transfer phenomena in real contactors are among the most important areas of open research for CO_2 capture systems.
- Novel designs, such as hybrid contactor, need to be taken to the next step of conceptual equipment design to understand any potential hidden costs or design challenges prior to further development or evaluation (i.e., economic assessment, pilot testing, etc.).

- Modeling of true cross-flow contacting requires mass transfer data specific to the contacting scheme (limited data) and development of a 2-D integration method for use with rigorous rate-based contactor and solvent models in AspenPlus®.

Appendix A: Mass Transfer Coefficients

BACKGROUND

New empirical mass transfer models were developed to isolate independent variables that impact mass transfer performance and to regress model coefficients from data collected in a pilot scale column operated with structured packing. This approach is expected to provide models that closely represent the packing and hydraulic conditions experienced in the amine-based absorption columns used in CO_2 capture processes. The generalized mass transfer models available in Aspen Plus® (and in literature) represent an average of a wide range of hydraulic conditions, packing types/materials, and fluid properties that may not be representative of capture process conditions.

The new empirical mass transfer models were developed using data collected at the Separation Research Program (SRP) at the University of Texas at Austin (UT). The experimental apparatus at SRP consists of a 16.8" diameter PVC column operated with air and water as the carrier fluids. The apparatus is used to measure interfacial area and gas and liquid mass transfer coefficients. By measuring interfacial area independently, the mass transfer coefficients can be isolated and correlated to relevant physical property and fluid transport parameters. Details regarding the air-water column apparatus and the theory and method of operation can be found in work by Tsai and Wang (Tsai, 2010) (Wang, 2015).

A.1 MASS TRANSFER COEFFICIENTS

A.1.1 Liquid-Side Mass Transfer Coefficient (k_L)

For measurement of liquid-side resistance, toluene is stripped from water by air; the limited solubility of toluene in water (large Henry's law constant or K-value) results in liquid-side controlled mass transfer and allows for direct calculation of the liquid-side

mass transfer coefficient (k_L) from measured mass transfer rates. Data for six types of packing were used to develop the liquid film mass transfer coefficient model (Wang, 2015). The properties of each type of packing are summarized in Table A-1; the packing vendor and proprietary name of each packing are omitted.

Table A-1: Properties of packing used in liquid film mass transfer coefficient model development and regression

	Packing Type	Material of Construction	Specific Area	Corrugation Angle
			m_2/m_3	Degrees
1	Structured	Stainless Steel	205	60
2	Structured	Stainless Steel	350	70
3	Structured	Stainless Steel	250	45
4	Structured	Stainless Steel	250	60
5	Structured	Stainless Steel	350	45
6	Hybrid	Stainless Steel	200	60

The air-water column was operated over a range of conditions for each type of packing (liquid loads of 2.5 to 30 gpm/ft^2 and gas rates of 180 to 450 ACFM); the full set of data for all packing types was used to develop Equation A.1. For details regarding the raw data and experimental conditions, see the work by Wang (Wang, 2015).

$$\frac{\boldsymbol{k_L}}{\boldsymbol{D_{AB}^{0.5}}} = \boldsymbol{A} * \left(\frac{\boldsymbol{u_L/a_P}}{\boldsymbol{u_{L,o}/a_{P,o}}}\right)^{\boldsymbol{x1}} \left(\frac{\boldsymbol{M_i}}{\boldsymbol{M_{i,o}}}\right)^{\boldsymbol{x2}} \left(\frac{\boldsymbol{\mu_L}}{\boldsymbol{\mu_{L,o}}}\right)^{\boldsymbol{-0.5}} \quad \text{(A.1)}$$

where:

k_L = Liquid side physical mass transfer coefficient (m/s);

D_{AB} = Binary diffusion coefficient (m^2/s);

A, x1, x2 = Regression constants;

u_L = Liquid superficial velocity (m/s);

a_p = Packing Specific Area (m^2/m^3);

M_i = Mixing number - dimensionless parameter describing the number of mixing points in a characteristic volume of packing;

μ_L = Liquid viscosity (Pa-s).

Equation A.1 only includes parameters that were explicitly varied during the experiments with the exception of the viscosity and diffusivity. Viscosity dependence is discussed in the subsequent section. The diffusion coefficient dependence is consistent with penetration theory prediction. Each of the parameters is normalized to a reference value in the dataset (represented by the subscript "o" in Equation A.1) to prevent scaling issues of the independent variables and to allow transformation of data for linear regression. The normalized power law form of Equation A.1 was selected over the common dimensionless group form (i.e., Sh = f(Re, Sc)) found in many literature models to avoid assignment of property dependence where it has not been explicitly measured. For example, density does not appear in Equation A.1 since it was not varied explicitly in the experiments. However, if the Reynolds number was used as an independent variable it would imply a dependence on density when density was not actually varied or measured in the experiments. Dimensionless group methods require special care to ensure the dimensionless groups themselves have been varied over the entire relevant range imposed by their constituent variables.

Physical properties were not varied explicitly in the mass transfer coefficient experiments conducted at the SRP facility, but experimental plans are being developed

for viscosity and diffusion dependence. To account for the property dependence in the current model without arbitrary assignment from dimensionless groups, important physical properties were considered individually. In amine systems used for CO_2 capture, the density does not vary much from the experiments using water, and therefore the density dependence term is omitted altogether from the power law model. In contrast, viscosity can vary by more than an order of magnitude relative to water, and is therefore included with a dependence extracted from literature (-0.5).

Finally, the mixing point parameter represents the number of points per unit area of packing where the liquid encounters a junction and changes direction. These junctions represent points where the bulk liquid flow changes directions and the liquid may mix (with the ideal limit of complete mixing at junctions) to renew the surface concentration of the solvent for mass transfer. The mixing point parameter is a function of the packing geometry and size; a detailed derivation for random and structured packing was developed by Wang (Wang, 2015).

The results of the regression are summarized in Figure A-1. All regressed parameters (A, x1, x2) were statistically significant within their 95% confidence intervals.

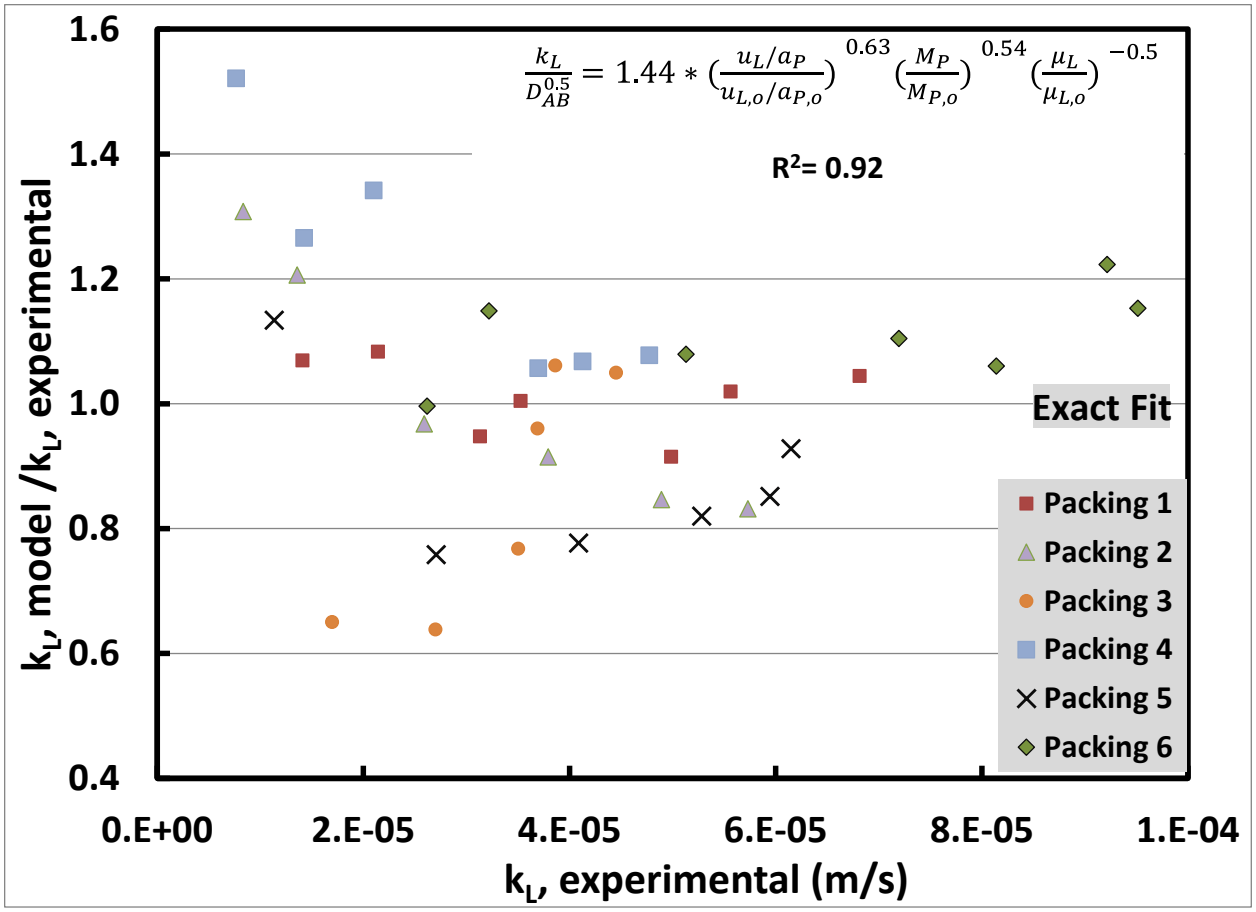

Figure A-1: Model predictions (Equation A.1) of liquid film mass transfer coefficient compared to experimental data measured on pilot scale air-water column. Value of 1 on the ordinate indicates a model prediction consistent with experimental measurements.

The largest errors in Figure A-1 are generally present at the lowest measured mass transfer coefficient values, which might represent the difficulty in separating mass transfer measurements from the underlying error in the experiments at these conditions.

A.1.1.1 Viscosity Dependence of Liquid Film Mass Transfer Coefficients

As noted in the previous section, the viscosity of amine solutions used in CO_2 capture facilities can deviate by more than an order of magnitude from the viscosity of water (the solvent used for mass transfer coefficient measurements in the experimental

apparatus). Therefore, accounting for the dependence of the mass transfer coefficient on viscosity is an important part of model development for amine systems. Viscosity can impact the liquid film mass transfer coefficient in two distinct ways. First, the diffusion coefficient is expected to show an inverse dependence on viscosity due to molecular level drag on particles diffusing in the liquid media. Second, viscosity affects the onset of turbulence in the liquid. Turbulence in the liquid film can enhance mass transfer by increasing the rate surface to bulk mixing. Therefore, an extensive literature review was conducted to find analyses which included explicit variation of the viscosity of solvents in experiments while controlling for the effect of viscosity on the diffusion coefficient. The goal of the review was to isolate the effect of viscosity on the liquid film mass transfer coefficient from the effect of viscosity on the diffusion coefficient. Table A-2 contains selected papers that were used to derive the -0.5 viscosity dependence used in the mass transfer model developed in the previous section.

Table A-2: Review of Liquid-Side Mass Transfer Coefficient Experimental Studies to Evaluate Viscosity Dependence

Reference	Model	Packing/Device	Solvents	Viscosity Range (Pa-s)	Controls for Diffusivity?	Viscosity Dependence (Excluding Diffusion Dependence)
(Delaloye, et al., 1991)	kLa	30 cm I.D. Column 25 mm GLASS Raschig Rings	Alginate, Glycerol, PEG-6000	0.0008 - 0.00963	Yes, Experimental Data	-0.52
(Echarte, et al., 1984)	kLa	40 cm I.D. Column 25 and 50 mm CERAMIC Raschig Rings	Aqueous Glycerol	0.00087 - 0.0061	Yes, Experimental Data	-0.46
(Mangers & Ponter, 1980)	kLa	10 cm I.D. Column 10 mm GLASS Raschig Rings	0–75 wt % Aqueous Glycerol	0.00089 - 0.02611	Yes, Experimental Data	-0.57
(Norman & Sammak, 1963)	kL	String of Discs GRAPHITE	Water, Heptane, Isobutanol, amyl alcohol, eugenol, gas oil	0.000411 - 0.025	Yes, Experimental Data, Laminar Jet	-0.54

The papers selected in Table A-2 reflect the limited availability of data for the systematic variation of viscosity in mass transfer measurements for packed columns. However, the relative consistency in the viscosity dependence reported for independent experiments for a wide range of viscosities and experimental apparatus scales provides some validation of the viscosity dependence selected for the mass transfer model in this work. Three of the models report the viscosity dependence of a combined volumetric mass transfer coefficient (k_La) rather than the isolated mass transfer coefficient (k_L).

However, work by Tsai determined that viscosity does not have a statistically significant effect on the interfacial mass transfer area of packing (Tsai, 2010). If the Tsai model conclusions for structured packing are extended to random packing used in the experimental work in Table A-2, the combined k_La dependence on viscosity can be directly attributed to k_L (as in Equation A.1). However, this conclusion should be verified experimentally.

A.1.2 Gas-Side Mass Transfer Coefficient (k_G)

Gas-side resistance is measured by SO_2 absorption into caustic solution (NaOH solution). The instantaneous, irreversible reaction in the liquid makes the liquid resistance insignificant relative to the gas side diffusion of SO_2 allowing isolation of the gas-side mass transfer coefficient (k_G). Data for six types of packing were used to develop the liquid film mass transfer coefficient model. The properties of each type of packing were summarized previously in Table A-1.

The air-water column was operated over a range of conditions for each type of packing (gas rates of 180 to 750 ACFM); the full set of data for all packing types was used to develop Equation A.2. See Wang for raw data and experimental details (Wang, 2015):

$$\frac{\boldsymbol{k_G}}{\boldsymbol{D_{AB}^{0.67}}} = \boldsymbol{A} * \left(\frac{\boldsymbol{u_G/a_P}}{\boldsymbol{u_{G,o}/a_{P,o}}}\right)^{\boldsymbol{x1}} \left(\frac{\boldsymbol{M_P}}{\boldsymbol{M_{P,o}}}\right)^{\boldsymbol{x2}} \quad \text{(A.2)}$$

where:

k_G = Gas-side physical mass transfer coefficient (m/s);

D_{AB} = Binary diffusion coefficient (m^2/s);

A, x1, x2 = Regression constants;

u_G = Gas superficial velocity (m/s);

a_p = Packing Specific Area (m^2/m^3);

M_p = Mixing point parameter (points/m^2).

As with the liquid-film coefficient, Equation A.2 only reflects parameters explicitly varied in the experiments with the exception of the diffusion coefficient. Each of the parameters is normalized to a reference value in the dataset (represented by the subscript "o" in Equation A.2) to prevent scaling issues of the independent variables and to allow transformation of data for linear regression. The results of the regression are summarized in Figure A-2. All regressed parameters (A, x1, x2) were statistically significant within their 95% confidence intervals and all measurements were predicted within +/- 20% by the model.

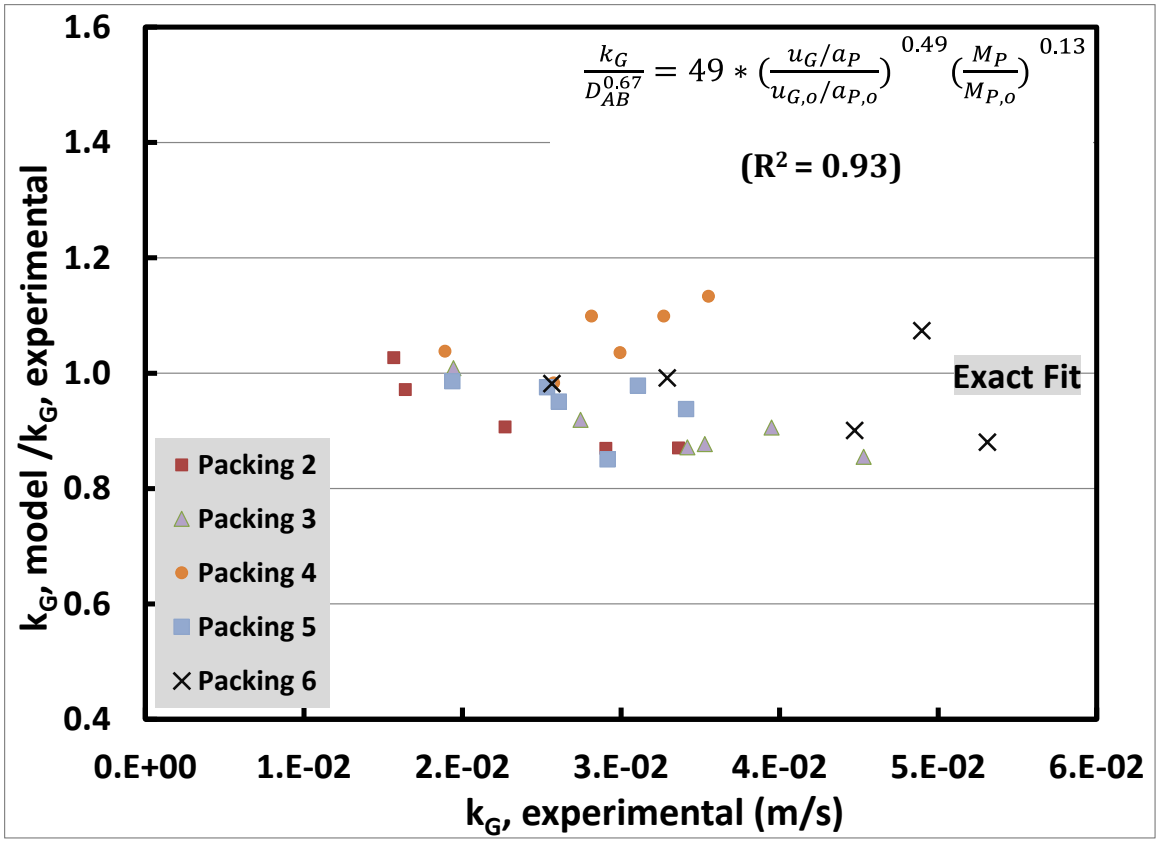

Figure A-2: Model predictions (Equation A.2) of gas film mass transfer coefficient compared to experimental data measured on pilot scale air-water column. Value of 1 on the ordinate indicates a model prediction consistent with experimental measurements.

A.2 Evaluating Uncertainty in Liquid-Film Mass Transfer Coefficient

A.2.1 Comparison to Literature Models

Wang provides an extensive discussion of the liquid film mass transfer coefficient models developed from data collected at SRP (i.e., those used in this work) and commonly used model in the literature. His analysis is mostly confined to a discussion of the combined volumetric mass transfer coefficient (k_La). However, as emphasized in Chapter 5 of this work, the magnitude of the liquid-film coefficient plays a critical role in

determining the controlling mechanism in the liquid-film mass transfer resistance. Therefore, Figure A-3 provides a re-evaluation of Wang's analysis to compare k_L values.

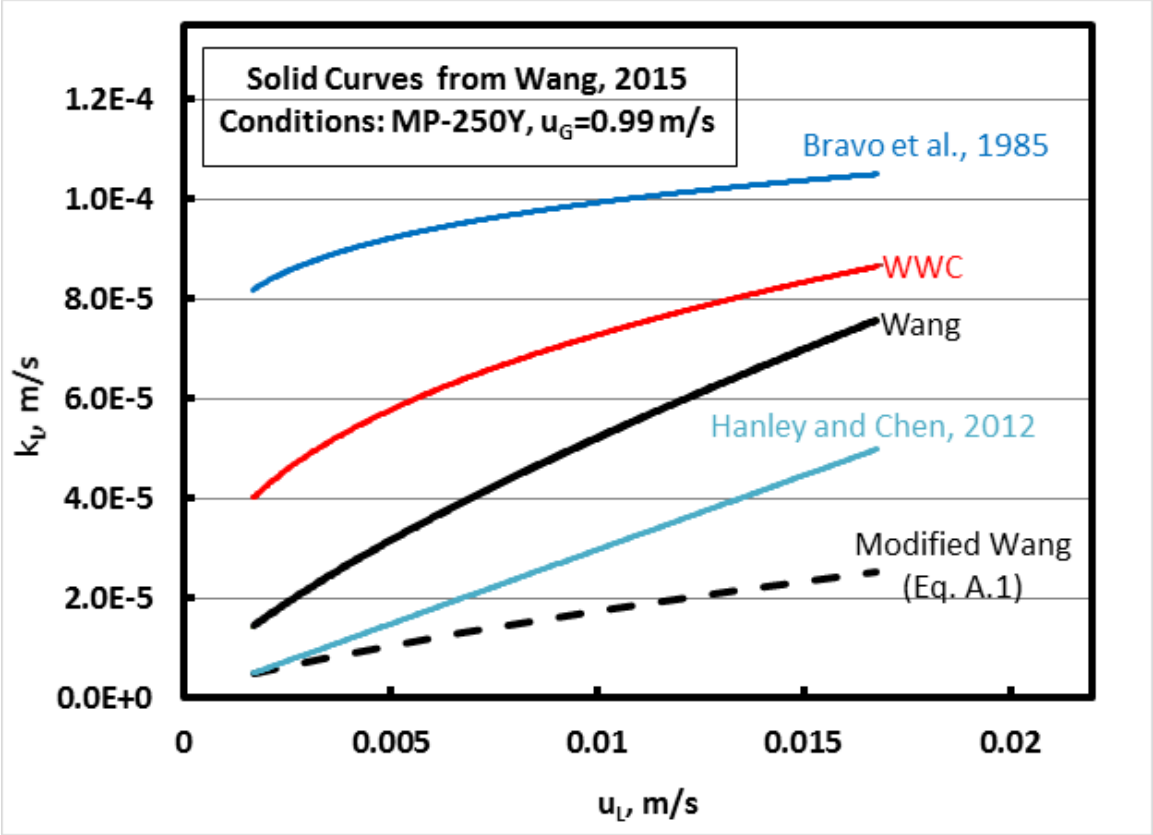

Figure A-3: Liquid-side physical mass transfer coefficient predictions for given liquid and gas rates with MP-250Y. Solid curves were developed from data by (Wang, 2015) and associated literature models (Bravo, et al., 1985) (Hanley & Chen, 2012). Modified Wang model (- - -) with viscosity correction in Equation A.1. WWC = Wetted wall column prediction.

The figure includes two literature models representing high and low values of the liquid film mass transfer coefficient. The Wang model is towards the lower end of the range, and with the strong viscosity correction in Equation A.1, will drop further (other models would fall as well, but do not have same viscosity dependence). Even without the

viscosity correction, the Wang is a factor of ~1.5 – 4 times lower than the upper end of the range (Bravo model) (Bravo, et al., 1985).

A.2.2 Re-Interpretation of Liquid-Film Mass Transfer Coefficients - Channeling

Cussler develops an example that re-evaluates experimental mass transfer data that appears to be inconsistent with penetration theory predictions of velocity dependence. Specifically, penetration theory predicts a half-order dependence of the mass transfer coefficient on liquid rate ($k_L \sim u_L^{0.5}$) while the predictions of the current work predict a dependence of $k_L \sim u_L^{0.63}$. To be clear, penetration theory was not developed to explain the complex flow patterns encountered in packed columns (counter-current liquid-gas flow, junctions for liquid accumulation/change of flow path, surface structures of packing creating turbulence and waves, etc.). The dependence predicted by the experimental work at SRP may well be representative of conditions in a packed bed.

However, an alternative theory, originally posed by Schlunder, is that some portion of the gas in mass transfer experiments is bypassing due to uneven flow in the column (Schlunder, 1977). This bypassing leads to an underestimation of mass transfer coefficients in general and over-estimation of the velocity dependence (Cussler, 2009). For the liquid film, an analogous condition would be channeling. Channeling refers to the phenomena where some portion of the liquid is passing down the walls or other relatively unobstructed path with limited (or no) contact with the gas in the column. Based on the example developed by Cussler for gas bypassing, a method to "correct" the liquid-film mass transfer coefficients was developed. Figures A-4 and A-5 describe the standard liquid-film mass transfer coefficient measurement and calculation method and the effect of liquid channeling on the calculations.

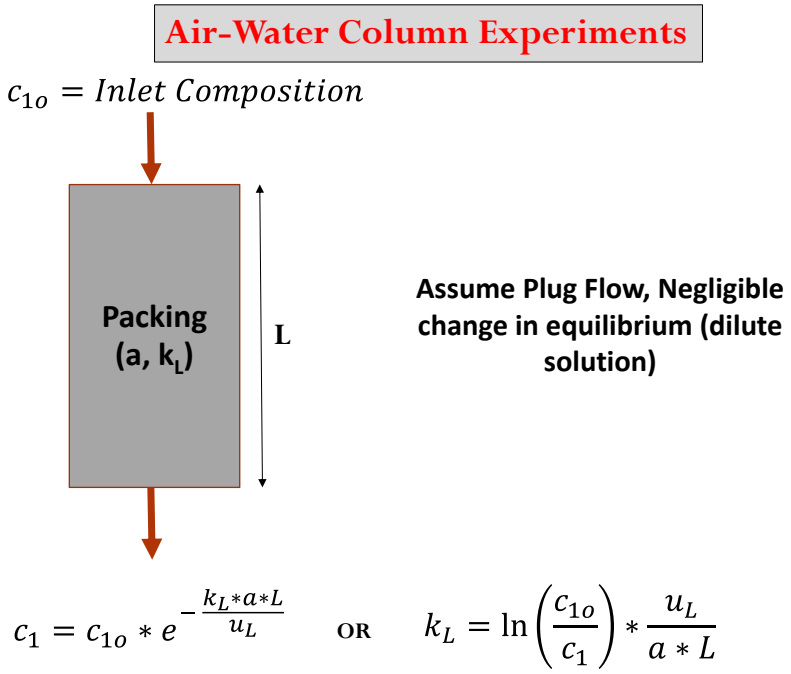

Figure A-4: Standard liquid-film mass transfer experiment and calculation.

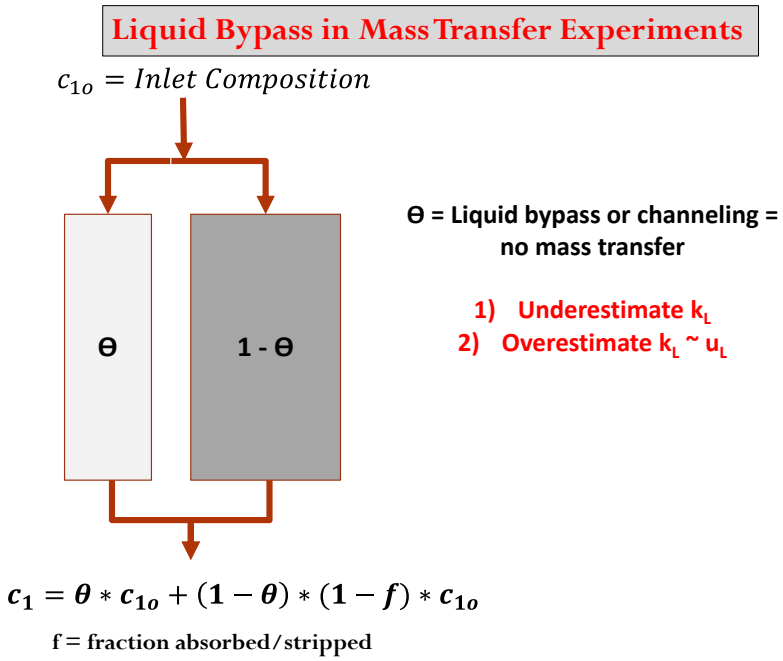

Figure A-5: Effect of channeling on mass transfer experiment and calculations.

The situation described in the figures represents an extreme scenario, or simplification, where the liquid either experiences normal contacting (plug flow) with the gas or no contacting and transfer. In reality, a more complex distribution might describe the contacting efficiency of the liquid based on the true gas-liquid flow patterns in the column. However, the simplification does provide an "average" performance measure and a method to correct the experimental data, as described by the following procedure.

Part 1: Force measured mass transfer coefficients to fit penetration theory predicted velocity dependence.

1) Use functional relationship between mass transfer coefficients and velocity to derive "corrected" mass transfer coefficients:

$$\ln\left(\frac{k_{Measured}}{k_{Measured}^{Center}}\right) = m_1 * \ln\left(\frac{u_{Measured}}{u_{Measured}^{Center}}\right) \quad \text{A.3a}$$

$$\ln\left(\frac{k_{Corrected}}{k_{Corrected}^{Center}}\right) = m_2 * \ln\left(\frac{u_{Measured}}{u_{Measured}^{Center}}\right) \quad \text{A.3b}$$

where:

$k_{Measured}$ = Mass transfer coefficient measured in experiments;

$k_{Corrected}$ = Mass transfer coefficient after correction to match penetration theory velocity dependence;

$u_{Measured}$ = Mass liquid velocity in experiments;

Center = Average values over the range of the parameter (k or u);

m_1 = Measured velocity dependence of k_L;

m_2 = Theoretical velocity dependence of k_L (= 0.5);

2) Subtract Equation A.3b from Equation A.3a. Solve directly for corrected mass transfer coefficient ratio.

$$\ln\left(\frac{k_{Measured}}{k_{Measured}^{Center}}\right)-\ln\left(\frac{k_{Corrected}}{k_{Corrected}^{Center}}\right)=(m_1-m_2)*\ln\left(\frac{u_{Measured}}{u_{Measured}^{Center}}\right) \qquad \text{A.3c}$$

Part 2: Define bypass or channeling variable as part of mass transfer coefficient calculation.

3) Solve differential mass balance on contactor and create fractional distribution (bypass) to correct calculation for portion of liquid that experiences mass transfer:

$$\frac{c_{OUT}}{c_{IN}}=\theta+(1-\theta)*e^{\left(\frac{-k_{Corrected}*a*Z}{u}\right)} \qquad \text{A.4a}$$

where:

c_{OUT} = Concentration of toluene (or solute) exiting contactor;

c_{IN} = Concentration of toluene (or solute) entering contactor;

Θ = Bypass fraction;

a = Specific wetted area of packing (m^2/m^3);

Z = Height of packing (m);

4) Solve Equation A.4a for $k_{corrected}$ in terms of Θ.

$$k_{Corrected} = -\left(\frac{u}{a*Z}\right)*\ln\left(\frac{\frac{c_{OUT}}{c_{IN}}-\theta}{1-\theta}\right) \qquad \text{A.4b}$$

5) Solve system of equations represented A3.C and A.4b simultaneously or iteratively (2 equations, 2 unknowns – $k_{CORRECTED}$, Θ).

The preceding procedure yields a new set of values for measured mass transfer coefficients that have the theoretically predicted dependence on velocity (0.5) and yields a predicted fraction of liquid that is channeling. Figure A-6 and A-7 depict the corrected data for two of the packings. Table A-3. summarizes the data for the 6 packings outlined in Table A.1.

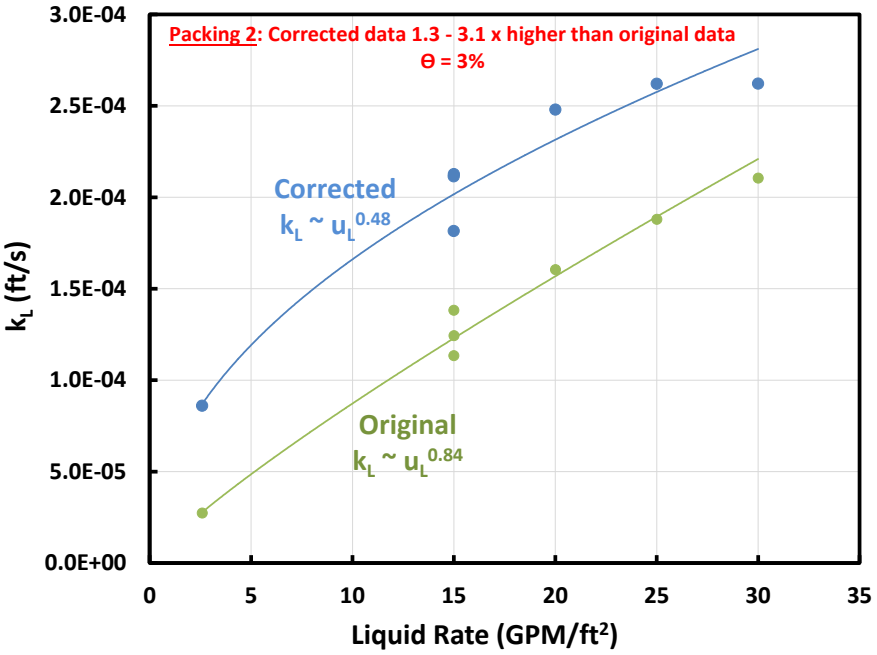

Figure A-6: Liquid-film mass transfer coefficient data for packing 2, corrected to match theoretical velocity dependence (0.5).

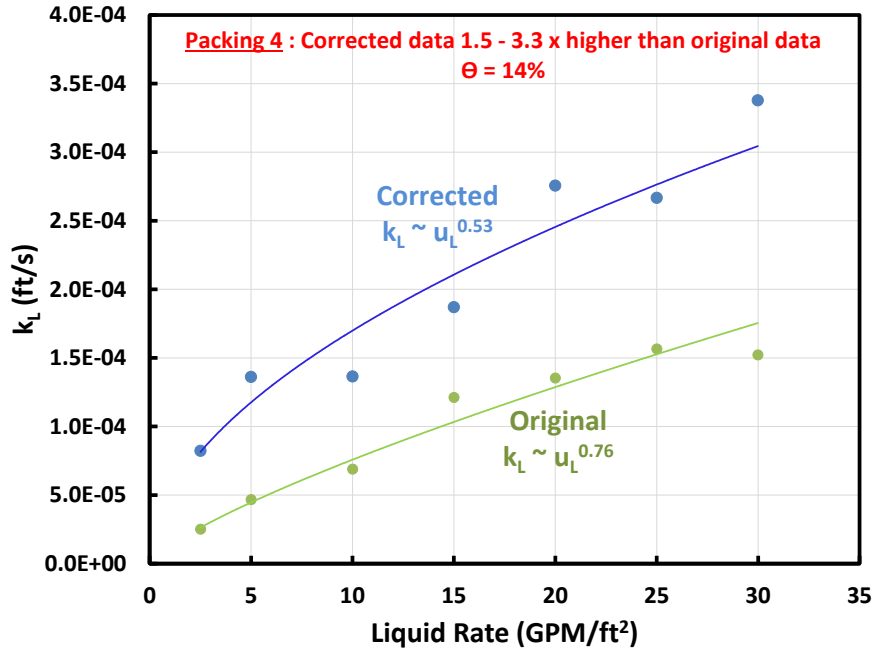

Figure A-7: Liquid-film mass transfer coefficient data for packing 4, corrected to match theoretical velocity dependence (0.5).

Table A-3: Properties of packing used in liquid film mass transfer coefficient model development and regression

	Packing Type	Specific Area	Corrugation Angle	Range of k_L "correction"	Θ
		m_2/m_3	Degrees		
1	Structured	205	60	1.1 – 1.6	2%
2	Structured	350	70	1.3 – 3.1	3%
3	Structured	250	45	1	0%
4	Structured	250	60	1.5 – 3.3	14%
5	Structured	350	45	1 – 1.2	<1%
6	Hybrid	200	60	1 – 1.15	<1%

As the corrected coefficients depict, the new mass transfer coefficients can increase by as a much as a factor of ~3, which is also approximately the deviation of the current model from the top end of the literature range (see Figure A-3). In addition, the 45 degree corrugation angle packing and hybrid packing showed much less sensitivity to the bypass correction method. The method is primarily illustrative, but does provide another approach to define an upper bound for the measured k_L values in this work.

A.2.3 Sensitivity analysis with modified k_L values

One of the cases that was evaluated in Chapter 5 as part of the mass transfer parameter sensitivity analysis was repeated here using the updated k_L values from the preceding section to illustrate the effect of the modified k_L on the absorber mass transfer mechanisms (Figure A-8).

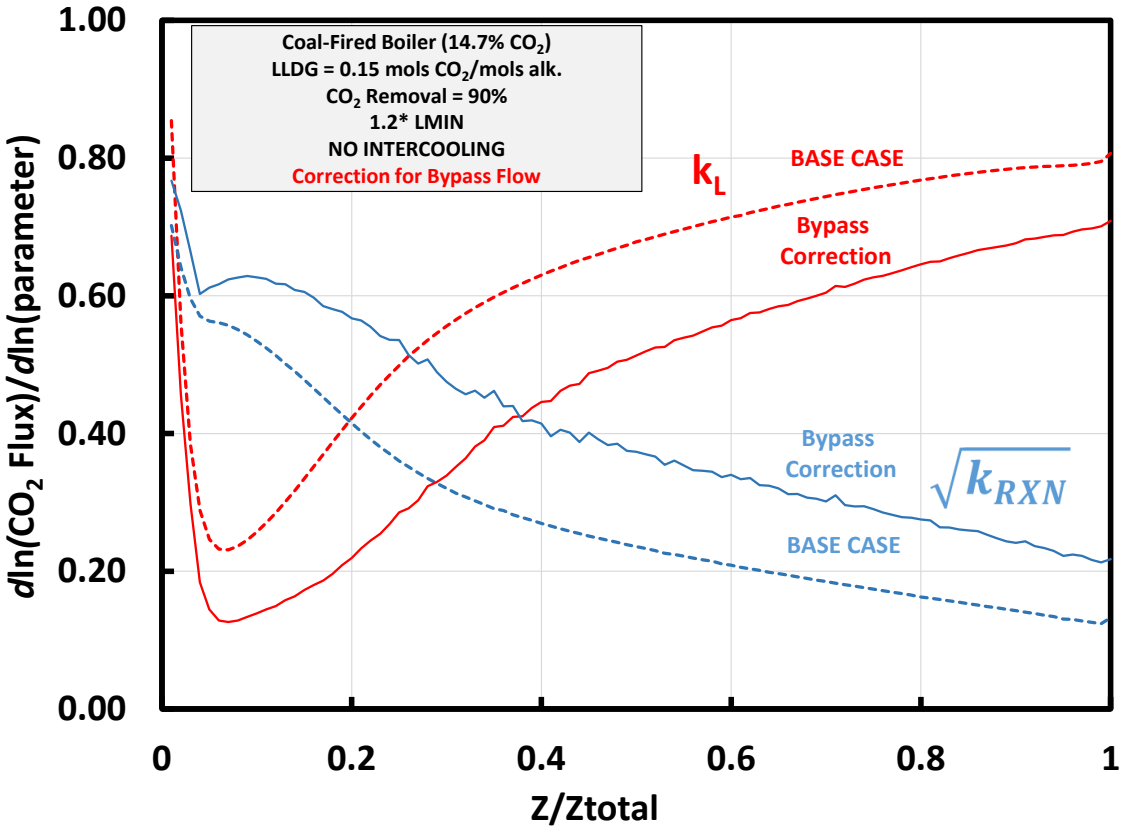

Figure A-8: Mass transfer parameter (k_L and kinetic constants, k_{RXN}) sensitivity analysis updated for "corrected" k_L values. See Chapter 5 for details on sensitivity analysis approach.

As the figure shows, a more significant portion of the column is reaction-controlled (~40% vs. 20% in the base case) after the corrected k_L values are applied. Liquid-film is still dominant at the rich end of the column. The model can be corrected further is the viscosity dependence in Equation A.1 is too strong. Therefore, the uncertainty in the k_L model can play a large role in predicted absorber performance, and justifies the use of a large range of k_L values in Chapter 5 for the sensitivity analysis and Chapter 3 for the pilot plant reconciliation of mid-loading data.

Appendix B: Film Theory Implementation Issue in AspenPlus®

INTRODUCTION

Several researchers in the TxCMP have observed theoretically inconsistent dependence of CO_2 flux on the diffusion coefficient of CO_2 (0.25 predicted vs. 0.5 in theory) and the diffusion coefficient of reactants and products (0.25 predicted vs. 0 in theory) when evaluating absorption of CO_2 at pseudo-first-order conditions in Aspen Plus®. The system of equations in Aspen Plus® can be solved analytically for the flux of CO_2 at pseudo-first-order conditions after a series of simplifications to the multi-component mass transfer framework. The comparison of the differential equations represented by the Aspen Plus® numerical framework and the differential equations used in the theoretical solution of film theory reveals the source of the inconsistency in the pseudo-first-order results. The explicit use of mass transfer coefficients in the constitutive equations in Aspen Plus® (Maxwell-Stefan relations) instead of diffusion coefficients implies that the mass transfer coefficients should be defined by film theory (with corresponding 1st order diffusion dependence). However, the user is allowed to separately define the diffusion dependence of mass transfer coefficients. A value of 0.5 has been applied in the in models developed by the Rochelle research group to maintain consistency with surface renewal and penetration theories. This fundamental inconsistency propagates through the definition of the film thickness used in the integration. The film thickness should reflect only hydrodynamic conditions, but carries a species-specific diffusion dependence via the two definitions of the mass transfer coefficient. The integration of the analytical analogue to the numerical solution in Aspen Plus® isolates the fundamentally inconsistent treatment of mass transfer coefficients as the source of the spurious diffusion dependence observed by previous researchers. The modified film theory method applied in Aspen Plus® is inadequate to represent

appropriate diffusion dependence while simultaneously maintaining consistency with all relevant asymptotic cases (pseudo-first-order and instantaneous limits) and suggests the need for the implementation of an alternate steady state mass transfer theory (i.e., eddy diffusivity theory).

B.1 FILM THEORY SOLUTION FOR PSEUDO-FIRST ORDER REVERSIBLE REACTION

The system of differential equations for reaction and diffusion of CO_2 in amine solutions as defined by Equation B.1 (written at steady state) can be solved analytically by de-coupling the differential equation of CO_2 from other components.

$$0 = -\left(\frac{\partial N_i^L}{\partial x}\right) + R_i, \; for \; i = 1:C \tag{B.1 a}$$

$$\begin{aligned} c_i^L &= c_i^V \; @ \; x = 0 \\ c_i^L &= c_i^{Bulk} \; @ \; x = \delta(Bulk \; Liquid) \end{aligned} \tag{B.1 b}$$

where:

C = Total number of components;

c_i = Molar concentration of species i;

N^L_i = Molar flux of species i in liquid film;

δ = Total film thickness (interface to bulk liquid);

R_i = Rate of production of moles of i per unit volume produced by chemical reaction.

The coupling between CO_2 and other components occurs via the chemical reaction term. The following equations define a generic irreversible chemical reaction and corresponding reaction rate expression for CO_2 with amines:

$$A\mathrm{m} + CO_2 \rightarrow \mathrm{Pr}od \tag{B.2 a}$$

$$R_{CO_2} = -\left(k_2[Am][CO_2]\right) \tag{B.2 b}$$

If the amine concentration is much higher than the CO_2 concentration and the CO_2 flux, the amine concentration can be assumed to be constant throughout the liquid film (pseudo-first order assumption). The reaction term in the differential equation is now only varies with CO_2 concentration, removing any coupling with other components. Finally, if the dilute solution assumption is applied for CO_2 (no diffusion induced convection), Fick's first law can be substituted directly for the flux term in Equation B.1a. Equation B.3 is the final form of the differential equation for CO_2 under these assumptions.

$$0 = D_{CO_2}\frac{d^2[CO_2]}{dx^2} - k_1[CO_2] \tag{B.3}$$

where:

k_1 = Pseudo-first order rate constant = k_2[Am].

The solution of this differential equation follows the approach described by Danckwerts and the resulting expression for CO_2 flux is described by Equation B.4 (Danckwerts, 1970).

$$N_{CO_2} = k_{L,CO_2}\frac{Ha}{\tanh\left(Ha\right)}\left([CO_2]_I - \frac{[CO_2]_B}{\cosh\left(Ha\right)}\right)$$
$$Ha = \sqrt{\frac{k_1 D_{CO_2}}{k_{L,CO_2}{}^2}} \tag{B.4}$$

where:

k_{L,CO_2} = Physical liquid-film mass transfer coefficient = $\frac{D_{CO_2}}{\delta}$ for film theory;

Ha = Hatta number;

$[CO_2]_I$ = CO_2 concentration at gas-liquid interface;

$[CO_2]_B$ = CO_2 concentration in bulk liquid;

When the Hatta number is greater than ~5, the hyperbolic tangent term in Equation B.4 approaches 1 and the hyperbolic cosine term approaches infinity. This range for the Hatta number is consistent with the pseudo-first order assumption (fast, but not instantaneous, reaction). Under this simplification, the flux of CO_2 can be expressed as:

$$\begin{aligned} N_{CO_2} &= k_{L,CO_2} Ha [CO_2]_I \\ N_{CO_2} &= E k_{L,CO_2} [CO_2]_I \\ N_{CO_2} &= \sqrt{k_1 D_{CO_2}} [CO_2]_I \end{aligned} \qquad \text{(B.5)}$$

where:

E = Enhancement factor = $Ha = \sqrt{\frac{k_1 D_{CO_2}}{k_{L,CO_2}^{\ 2}}}$.

The enhancement factor modifies the mass transfer coefficient for physical absorption ($k_{L,CO2}$) for the effect of combined chemical reaction and diffusion. The combined liquid-film mass transfer coefficient ultimately does not depend on physical-liquid film mass transfer coefficient. If the driving force is converted to a partial pressure driving force, Equation B.6 represents the flux with a new definition for the liquid-film mass transfer coefficient.

$$\begin{aligned} N_{CO_2} &= \frac{\sqrt{k_1 D_{CO_2}}}{H_{CO_2}} P_{CO_2}^I \\ N_{CO_2} &= k_g^{'} P_{CO_2}^I \end{aligned} \qquad \text{(B.6)}$$

where:

H_{CO_2} = Henry's constant of CO_2;

$k_g^{'}$ = Liquid-film mass transfer coefficient in terms of gas phase driving force.

The liquid film mass transfer coefficient ($k_g^{'}$) exhibits half-order dependence on the diffusion of CO_2 at pseudo-first order conditions for film theory. An analogous derivation can be developed with reversible reactions (as in the PZ-CO_2 system in this work), but the expression for the liquid film mass transfer coefficient is identical (Bishnoi, 2000). The theoretical prediction is expected to be consistent with the numerical integration in Aspen Plus®, which implements film theory.

B.2 Diffusion Coefficient Dependence Results in Aspen Plus®

Several previous researchers modeling CO_2 absorption with amines in Aspen Plus® have observed diffusion coefficient dependence at pseudo-first order conditions that is inconsistent with theoretical expectations ((Plaza, 2011), (Chen, 2011), (Frailie, 2014)). Sensitivity of the liquid film mass transfer coefficient (k_g') in a wetted wall column to diffusion coefficients (and other mass transfer parameters) revealed the inconsistency; results of a representative analysis utilizing the "Independence" model (PZ and PZ/MDEA blended system) are presented in Figure B.1.

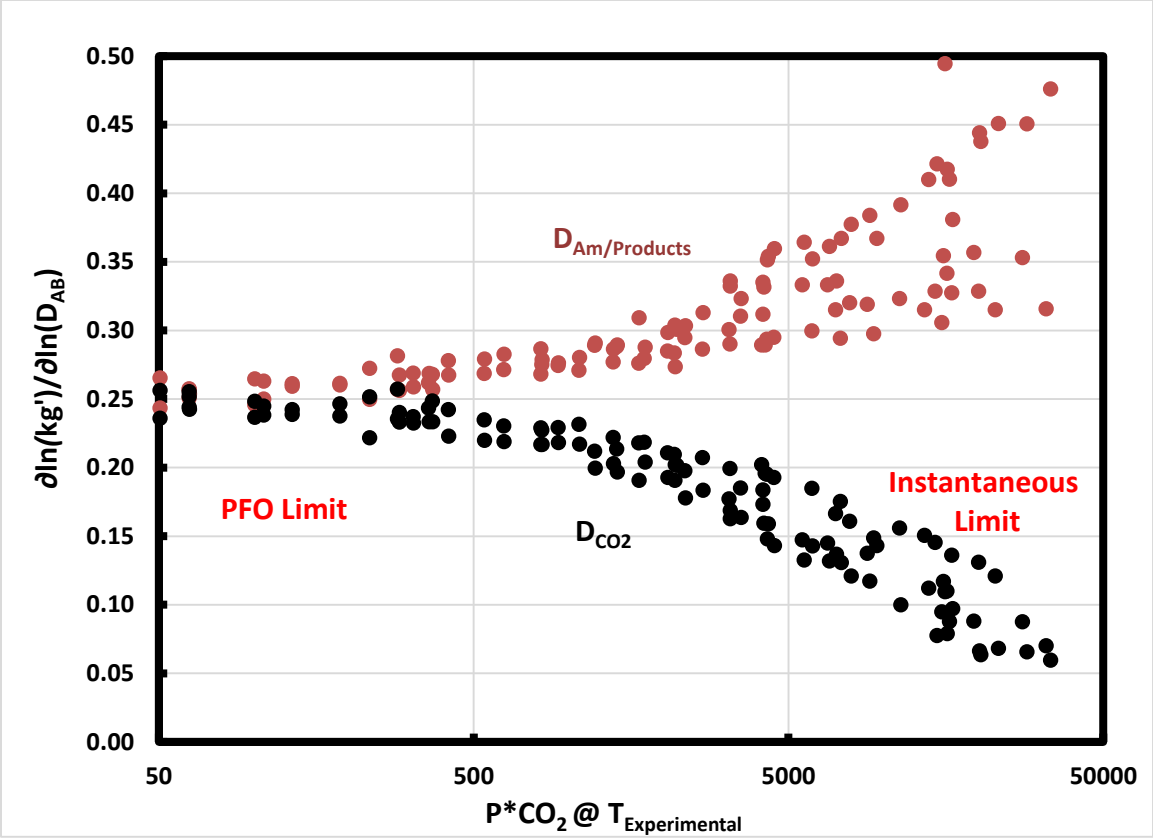

Figure B-1: Sensitivity of liquid film mass transfer coefficient (k_g') to diffusion coefficients for CO_2 absorption into PZ and PZ/MDEA blends in a wetted wall column from 40-100°C. Data from (Frailie, 2014).

As shown in the figure, the liquid-film mass transfer coefficient never exhibits the half-order dependence on the diffusion coefficient of CO_2 as predicted by theory. At low equilibrium partial pressures of CO_2 (lean loading range or lower temperatures) consistent with absorber operation, pseudo-first order behavior is expected. Figure B.1 shows that the combined dependence of the CO_2 diffusion coefficient and amine/products diffusion coefficient is approximately 0.5. The results demonstrate a spurious dependence on $D_{Am/Products}$ in place of the expected dependence on D_{CO2} in the pseudo-first order regime. However, as the equilibrium partial pressure is increased (richer loadings or

higher temperatures), the reaction-diffusion problem should approach the instantaneous reaction limit. In this limit, the mass transfer coefficient should only depend on the diffusion of amine/products (Bishnoi, 2000). Figure B.1 indicates that the model correctly predicts the control by $D_{AM/Products}$ in this limit. To explain the diffusion dependence exhibited in the sensitivity analysis, the integration of a rate-based stage in Aspen Plus will be evaluated with relevant simplifying assumptions for the CO_2/PZ system and the pseudo-first order regime. The numerical method as implemented in Aspen Plus® will be converted to the corresponding differential equation that can be solved analytically at pseudo-first order conditions using the same set of simplifying assumptions to isolate the source of the false dependence in the integration.

B.3 Numerical Method and Assumptions in Aspen Plus® Rate-Based Calculations

The integration of a rate-based stage at steady state includes three sets of differential equations: 1) component bulk material balance, 2) component film material balance, 3) constitutive mass transfer relationships. The following equations (for a total of C components) are presented in difference form (algebraic system) for the liquid phase as implemented in the numerical integration in Aspen Plus®.

$$0 = L_{j-1}x_{ij-1} - L_j x_{ij} + N_{ij}^L + r_{ij}^L \tag{B.7}$$

$$0 = N_{ij}^{INTF} - N_{ij}^L + r_{ij}^{film,L} \tag{B.8}$$

$$0 = \left[\Gamma_j^L\right](\bar{x}_j^{Intf} - \bar{x}_j) + \Delta\phi_j^E(\bar{x}_j \bar{z}_j) + \left[R_j^L\right](\bar{N}_j^L - N_t^L \bar{x}_j) \tag{B.9}$$

where brackets [ ] indicate C-1 x C-1 matrix, overbar indicates C-1 vector, and:

Γ= Thermodynamic non-ideality correction (for chemical potential driving force);

j = Stage number;

$\Delta\Phi^E$ = Electric potential driving force in ionic solutions;

z = Electric charge number of species;

R = Inverse mass transfer coefficient matrix;

N_t = Total molar flux = $\sum_{i=1}^{C} N_i$;

r_{ij}^L = Reaction rate of species i in bulk liquid = $\Re_i \Phi V^T \varepsilon$

$\Re_i$ = Volumetric production rate of species i;

Φ = Fractional volumetric liquid-hold-up for packing;

V^T = Total volume for computational stage (element of packing);

ε = Void fraction of packing;

$r_{ij}^{film,L}$ = Reaction rate of species i in liquid film = $\Re_i^{film} \delta a^I$;

δ = Liquid film thickness;

a^I = Interfacial area available for mass transfer;

Equations B.8 and B.9 are written for each segment in the discretized liquid film (see (Frailie, 2014), (Plaza, 2011), or (Chen, 2011) for discussion of film discretization schemes). Analogous vapor phase equations are implemented without reaction terms or discretization in the vapor film.

B.3.1 Simplification of Maxwell-Stefan Relations

Equation B.9 represents the Maxwell-Stefan constitutive equations for multi-component mass transfer relating the individual flux for each species to the driving force of all other species (Taylor & Krishna, 1993). The first simplification of this system of equations is to neglect the non-ideality effects on driving forces ([Γ] = Identity matrix).

This simplification is applied in all Aspen Plus® absorber modeling throughout this work. Valerio and Vanni found that the non-ideality effects are unimportant for moderately non-ideal systems (infinite dilution activity coefficients in the range of 0.2 to 5), particularly when solutes are dilute (Valerio & Vanni, 1994). In the case of CO_2 absorption in amines, the CO_2 is relatively dilute in the system and the system would not be considered highly non-ideal.

The components of the inverse mass transfer coefficient matrix, which introduces coupling of binary mass transfer coefficients, can be defined as follows:

$$\begin{aligned} R_{ii} &= \frac{x_i}{\rho a^I \kappa_{iC}} + \sum_{\substack{k=1 \\ k \neq i}}^{C} \frac{x_k}{\rho a^I \kappa_{ik}} \quad for\ i = 1:C-1 \\ R_{ik} &= -x_i \left(\frac{1}{\rho a^I \kappa_{ik}} - \frac{1}{\rho a^I \kappa_{iC}} \right) \quad for\ i = 1:C-1, i \neq k \end{aligned} \tag{B.10}$$

The Maxwell-Stefan relationships add coupling of mass transfer of individual components via the mass transfer coefficients in Equation B.10 and interactions of driving forces in Equation B.9. However, these coupling effects are not present for the transfer of CO_2 in the "Independence" model. First, the mass transfer model in "Independence" defines two diffusion coefficients (and two corresponding mass transfer coefficients) for all species in the liquid phase (Frailie, 2014). The binary diffusion coefficients of CO_2, N_2, and O_2 (small molecules with low critical temperatures/limited physical solubility) were treated identically. Equation B.11 specifies the binary diffusion coefficient of CO_2 (and N_2, O_2) in amine solution.

$$D_{CO_2-SOLN} = D_{CO_2,H_2O} \left(\frac{\mu_{H_2O}}{\mu_{Am}} \right)^{0.8} \tag{B.11}$$

where:

D_{AB} = Binary Fickian diffusion coefficients;

μ_{Am} = Viscosity of amine solution.

The relationship between diffusion of CO_2 in amine solutions and in water was determined by the modified Stokes-Einstein relation (Versteeg & van Swaaij, 1988). All remaining binary diffusion coefficients in the system (amine, water, and reaction product binary pairs) are all represented via Equation B.12.

$$D_{Am/Prod-SOLN} = D_O \left(\frac{T}{313.15} \right)^{\beta} \left(\frac{\mu_{Am}}{0.0155} \right)^{-\alpha} \tag{B.12}$$

where:

D_O = Regressed parameter = 2.26 x 10^{-10} m^2/s;

β= Regressed Parameter = -2.58;

α = Regressed Parameter = 1.45.

Equation B.12 is strictly an empirical expression which was regressed via wetted wall column data for PZ and PZ/MDEA blends that included a range of solvent concentration, loading, and temperature (and implicitly, viscosity).

The binary diffusion coefficients are related to the physical liquid-side mass transfer coefficient in the general form of Equation B.13.

$$k_{L,i-k} = k_L^o D_{ik}^{\xi} \tag{B.13}$$

where:

k_L^O = Species independent mass transfer coefficient that represents fluid mechanics dependence of mass transfer specified by the user (regressed from experimental data in this work);

ξ = 0.5 in this work, 1 for film theory.

The diffusion dependence of the binary mass transfer coefficient (ξ = 0.5) was selected in this case to be consistent with penetration theory and the range seen in experimental data for gas-liquid systems (Astarita, 1967) . However, this creates a potential source of inconsistency with film theory (which predicts ξ=1) as will be evident in the next section.

For CO_2 transfer, since $D_{CO2\text{-}k} = D_{CO2\text{-}SOLN}$ (calculated from Equation B.11), $k_{L,CO2\text{-}k} = k_{L,CO2\text{-}SOLN}$ (all binary mass transfer coefficients for CO_2 are identical) for all k. Therefore, Equation B.10 written explicitly for CO_2 transfer simplifies as follows:

$$R_{CO_2CO_2} = \frac{1}{\rho a^I \kappa_{CO_2-SOLN}}$$
$$R_{CO_2k} = 0 \ \ for\ k = 1:C-1, k \neq CO_2 \qquad \text{(B.14)}$$

When combined with Equation B.9, Equation B.14 effectively removes the multi-component diffusion effects of the Maxwell-Stefan equations as CO_2 transfer is only a function of a single mass transfer coefficient (CO_2 in amine solution) and its own driving force.

The simplifications to this point are actively implemented as part of the numerical integration in Aspen Plus® for the "Independence" model. The final two assumptions are only relevant in this discussion (not implemented explicitly in the model). First, the dilute solution assumption will be applied for CO_2 eliminating the effects of diffusion-induced

convection (x_j = 0 in Equation B.9) – free CO_2 is relatively dilute in reactive amine systems. Finally, the electric potential driving force ($\Delta\Phi^E$) effects in Equation B.9 will be neglected in this discussion for simplicity as this term should not affect the diffusion coefficient dependence of the flux. With these additional simplifications, Equation B.9 can be re-written to explicitly represent the flux of CO_2 in Aspen as follows:

$$0 = (x_{CO_2}^{Intf} - x_{CO_2}) + \frac{1}{\rho a^I \kappa_{CO_2-SOLN}} (N_{CO_2}^L) \tag{B.15}$$

Equation B.15 is simply the difference form of Fick's first law written in terms of a mass transfer coefficient. Therefore, the analytical solution (at pseudo-first order conditions) of the component material balance for CO_2 (Equation B.1a) with Fick's first law using mass transfer coefficients should predict a diffusion dependence that is consistent with the results in Figure B.1.

B.3.2 Definition of Film Thickness

The simplified expression in Equation B.15 must be solved with the liquid film component material balance (Equation B.8). The film thickness (δ) term that appears in the source (reaction) term of Equation B.8 is defined by film theory as follows:

$$\delta = \frac{D_i}{k_{L,i}} \tag{B.16}$$

Film theory was developed for physical absorption of a single component in a binary system and defines film thickness in terms of the single binary diffusion and mass transfer coefficient for the system and would be a species independent parameter reflecting fluid mechanics. However, in the case of multicomponent mass transfer, if the individual binary mass transfer coefficients are derived completely empirically or have a

diffusion dependence defined independently of Equation B.10, multiple values may exist for the boundary layer thickness as a function of the binary pair used in the definition. As noted in Equation B.13, the binary mass transfer coefficients in Aspen Plus® have an independent relationship with diffusion coefficients outside of the definition for film thickness. The solution to this issue in Aspen Plus® is to define a film thickness based on mole-fraction weighted average of binary coefficients:

$$\delta = \frac{\overline{D}}{\overline{k_L}}$$

$$\overline{\Psi} = \frac{\sum_{i=1}^{C-1}\sum_{k=i+1}^{C}(x_i x_k \Psi_{ik})}{\sum_{i=1}^{C-1}\sum_{k=i+1}^{C}(x_i x_k)} \tag{B.17}$$

where:

$\overline{D}, \overline{k}$ = Composition-averaged diffusion and mass transfer coefficients,

Ψ = Binary coefficient (D or k_L);

A single film thickness value is defined without assigning a specific binary pair. However, in practice, the amine systems used in CO_2 capture are close to 90 mol % water, meaning the weighted average is dominated by binary coefficients with water. For all species other than CO_2, N_2, and O_2, $D_{H2O\text{-}k} = D_{Am/Prod\text{-}SOLN}$ (calculated from Equation B.11) and $k_{L,H2O\text{-}k} = k_{L,Am/Prod\text{-}SOLN}$. The weighted average for film thickness then reduces to the following approximate expression:

$$\delta = \frac{\overline{D}}{\overline{k_L}} \approx \frac{D_{Am/Prod-SOLN}}{k_{L,Am/Prod-SOLN}} = \frac{D_{Am/Prod-SOLN}}{k_L^o D_{Am/Prod-SOLN}^{0.5}} = \frac{D_{Am/Prod-SOLN}^{0.5}}{k_L^o} \tag{B.18}$$

The film thickness as implemented in Aspen Plus® is not a species-independent fluid mechanics parameter, but also carries the effective diffusion of amine and products in solution.

B.4 Analytical Analog to Aspen Plus® Rate-Based Calculations

B.4.1 Pseudo-First Order Limit

The analysis from section B.1 can be modified for consistency with the numerical approach used in Aspen Plus®. The key modifications to the previous analysis are the following:

1) Change the 2nd order differential equation (Equation B.3) representing the combination of the component material balance and Fick's first law at pseudo-first order conditions to dimensionless form using the film thickness, δ, as follows:

$$0 = D_{CO_2} \frac{d^2[CO_2]}{dx^2} - k_1[CO_2]$$

$$\eta = z / \delta \tag{B.19}$$

$$0 = \frac{D_{CO_2}}{\delta^2} \frac{d^2[CO_2]}{d\eta^2} - k_1[CO_2]$$

2) Use the definition of δ from film theory to convert the diffusion coefficient into a mass transfer coefficient. Aspen Plus® solves the differential equations in terms of mass transfer coefficients (diffusion coefficients are only implicit). This is a critical assumption implicit in the Aspen Plus® formulation. The mass transfer coefficient in Equation B.15 (and by analogy, Equation B.20)

should be consistent with film theory. However, Aspen Plus® allows user-defined diffusion dependence for the mass transfer coefficients via Equation B.13. This is a fundamental inconsistency between the modeling method and the theory from which it was developed.

$$k_{L,CO_2} = \frac{D_{CO_2}}{\delta}$$

$$0 = \frac{k_{L,CO_2}}{\delta}\frac{d^2[CO_2]}{d\eta^2} - k_1[CO_2] \tag{B.20}$$

$$[CO_2] = [CO_2]^I \; @\, \eta = 0$$
$$[CO_2] = [CO_2]^{BULK} \; @\, \eta = 1 (Bulk\ Liquid)$$

3) Solve the differential equation using the same approach as in section B.1. The same simplifications of a large Hatta number (> 5) can be applied. However, the new solution contains a modified version of the Hatta number (λ) that is a function of the film thickness that is defined by Aspen Plus®:

$$N_{CO_2} = k_{L,CO_2}\lambda\left([CO_2]_I\right)$$

$$\lambda = \sqrt{\frac{k_1\delta}{k_{L,CO_2}}} = \sqrt{\frac{k_1\bar{D}}{k_{L,CO_2}\bar{k_L}}} \approx \sqrt{\frac{k_1 D_{Am/\mathrm{Prod}}}{k_{L,CO_2}k_{L,Am/\mathrm{Prod}}}} = \sqrt{\frac{k_1 D_{Am/\mathrm{Prod}}^{0.5}}{\left(k_L^o\right)^2 D_{CO_2}^{0.5}}} \tag{B.21}$$

$$N_{CO_2} = k_L^o D_{CO_2}^{0.5}\sqrt{\frac{k_1 D_{Am/\mathrm{Prod}}^{0.5}}{\left(k_L^o\right)^2 D_{CO_2}^{0.5}}}\left([CO_2]_I\right)$$

$$= \sqrt{k_1 D_{CO_2}^{0.5} D_{Am/\mathrm{Prod}}^{0.5}}\left([CO_2]_I\right)$$

Several conclusions can be developed from Equation B.21:

1) The analytical solution for the flux, developed analogously to the numerical method and implementation in Aspen Plus®, exhibits the 0.25 dependence on each of D_{CO2} and $D_{Am\text{-}Prod}$ (combined 0.5 dependence on diffusion coefficients) evident in the sensitivity analysis of previous authors.

2) The source of the diffusion dependence issue is inconsistent implementation of the mass transfer coefficient. The film theory definition is implicitly applied in the derivation of Equations B.15 and B.20 while an independent mass transfer coefficient is defined via Equation B.13. This is coupled with the definition of the film thickness in Aspen Plus® (Equation B.18) to produce the specific sensitivity results in Figure B.1.

3) Two potential solutions can be implemented:

   a. <u>Define mass transfer coefficients to be consistent with film theory</u>:

$$k_{L,i-k} = k_L^o D_{ik}$$

This will remove the species-dependence of the film thickness and ensure theoretical consistency at all conditions. However, diffusion dependence will be inconsistent with experimental data and more realistic theories (e.g., surface renewal, penetration, etc.).

b. Implement an alternative steady state theory to provide consistency with expected diffusion dependence and independence for the hydraulic parameters of mass transfer. Eddy diffusivity theory has been implemented previously (Bishnoi, 2000). Implementation within the Aspen Plus® integration framework may be possible by redefining the boundary layer in dimensionless coordinates presented by Bishnoi in place of the film theory calculations for film thickness and discretization.

Other solutions within the film theory framework only resolve issues for one limiting case while creating issues at others. For example, defining the film thickness in terms of CO2 instead of amine and products resolves the diffusion dependence issue at pseudo-first-order conditions, but creates inconsistency at the instantaneous reaction limit (false dependence of diffusion of CO2 due to component specific definition of film thickness).

B.4.2 Practical Implications of Diffusion Dependence Issue

The false diffusion dependence impacts the absorber modeling in two ways: regression of the underlying model parameters and propagation of the false diffusion effect into absorber performance. First, the underlying kinetic parameters and diffusion coefficients (Equation B.8) in the "Independence" model are regressed in a wetted wall

column simulation that incorporates the false diffusion effect. As seen in Equation B.5, the wetted wall column data in the pseudo-first order region should only be sensitive to the reaction rate constants and the diffusion coefficient of CO_2. This should allow isolation of the kinetic parameters for regression in the pseudo-first order region. However, the parameters in Equation B.8 representing the diffusion of amine and products are also improperly regressed in this region due the false diffusion dependence. In effect, the reaction kinetics and diffusion coefficients are correlated during the wetted wall column regression. As long as the absorber is operated within the same range of reaction rates and diffusion coefficients as the wetted wall column, the combined reaction-diffusion effects should be properly captured.

In absorber modeling, the effect of the diffusion of amine and products introduces unexpected physical property dependence at absorber conditions. For example, $D_{Am/Products\text{-}SOLN}$ exhibits stronger viscosity dependence than D_{CO2} so the viscosity dependence can be overstated at absorber conditions.

B.5 IMPLEMENTING EDDY DIFFUSIVITY THEORY

The steady state version of the species continuity equations in a reactive system can be represented by the following:

$$0 = -\left(\frac{\partial N_i^L}{\partial x}\right) + R_i, \; for \; i = 1:C \tag{B.22a}$$

$$c_i^L = c_i^V \; @ \; x = 0$$
$$c_i^L = c_i^{Bulk} \; @ \; x = \infty (Bulk \; Liquid) \tag{B.22b}$$

where:

C = Total number of components;

c_i = Molar concentration of species i;

N^L_i = Molar flux of species i in liquid film;

δ = Total film thickness (interface to bulk liquid);

R_i = Rate of production of moles of i per unit volume produced by chemical reaction.

If the dilute solution assumption is applied for the system (no bulk convection effect), Fick's first law can be modified to account for the effect of turbulent eddies on mass transfer as follows (King, 1966):

$$N_i = -(D_i + D_E)\frac{dc_i}{dx} \qquad D_E = \varepsilon x^n + b \tag{B.23}$$

where:

D_i = Molecular diffusion coefficient of component i;

D_E = Eddy diffusivity;

ε = Eddy parameter, proportionality constant;

n = Exponent on distance from gas-liquid interface;

b = Eddy diffusivity at the interface;

The eddy diffusivity at the interface is commonly neglected (b = 0) due to expected eddy damping at the surface, leaving ε and n as the only parameters to be defined for a particular system or problem. In the limit of steady state mass transfer and for values of n > 1, King used dimensional analysis to define a mass transfer coefficient in terms of the remaining eddy parameters (King, 1966):

$$\varepsilon = \left[\left(\frac{\pi}{n \sin\left(\pi / n\right)} \right) \left(\frac{k_L}{D_i^{1-1/n}} \right) \right]^n$$

$$\text{if } n = 2 \qquad \text{(B.24)}$$

$$\varepsilon = \left[\left(\frac{\pi}{2} \right) \left(\frac{k_L}{D_i^{1/2}} \right) \right]^2$$

where:

k_L = Binary liquid-film physical mass transfer coefficient;

The model is sufficiently general to allow the user to define a diffusion dependence; the example of half-order dependence (consistent with penetration theory dependence) is included in Equation B.24. In addition, the user must specify the parenthetical term including the mass transfer and diffusion coefficient – this term represents the species-independent portion of the mass transfer coefficient and can be provided via a user or literature correlation for mass transfer coefficients (already implemented in this form in Aspen Plus®).

B.5.1 Numerical Evaluation Methods

Equations B.22 and B.24 represent the system of equations that need to be solved simultaneously for all components. The differential equations can be evaluated as written (in terms of flux) or can be combined to represent a single second-order differential equation in concentration:

$$0 = \frac{d}{dx}\left[(D_i + \varepsilon x^n) \frac{dc_i}{dx} \right] + R_i$$

or

$$0 = 2\varepsilon x \frac{dc_i}{dx} + D_i \frac{d^2 c_i}{dx^2} + \varepsilon x^2 \frac{d^2 c_i}{dx^2} + R_i \tag{B.25}$$

$$c_i^L = c_i^V \; @ \; x = 0$$

$$c_i^L = c_i^{Bulk} \; @ \; x = \infty (Bulk\ Liquid)$$

The combined second-order differential equation is used here to provide consistency with the method used by previous researchers (Bishnoi, 2000). The infinite domain specified by the boundary conditions is not tractable numerically. Glasscock developed a coordinate transformation for the spatial domain based on the solution to the physical absorption problem (Glasscock, 1990):

$$r = \frac{2}{\pi} \tan^{-1}\left(x \sqrt{\varepsilon / D_{REF}} \right)$$

or (B.26)

$$x = \sqrt{D_{REF} / \varepsilon} \tan\left(\frac{\pi}{2} r \right)$$

where:

r = Dimensionless spatial coordinate that varies from 0 (x=0) to 1 (x = ∞);

D_{REF} = Reference diffusion coefficient for system, typically set to largest value.

Equation B.25 can be re-written after a coordinate transform to the new dimensionless spatial coordinate. The details of the derivation are discussed in detail by Glasscock and Bisnoi ((Glasscock, 1990), (Bishnoi, 2000)). The resulting transformed 2nd-order differential equation is described in Equation B.27:

$$0 = \left[T_1 + T_2 D_i\right]\frac{d^2 c_i}{dr^2} + \left[T_3 + T_4 D_i\right]\frac{dc_i}{dr} + R_i$$

where

$$T_1 = \frac{4\varepsilon}{\pi^2}\sin^2\left(\frac{\pi}{2}r\right)\cos^2\left(\frac{\pi}{2}r\right)$$

$$T_2 = \frac{4}{\pi^2}\frac{\varepsilon}{D_{REF}}\cos^4\left(\frac{\pi}{2}r\right)$$

$$T_3 = -\frac{4\varepsilon}{\pi}\sin^3\left(\frac{\pi}{2}r\right)\cos\left(\frac{\pi}{2}r\right) + \frac{4\varepsilon}{\pi}\tan\left(\frac{\pi}{2}r\right)\cos^2\left(\frac{\pi}{2}r\right) \qquad \text{(B.27)}$$

$$T_4 = -\frac{4}{\pi}\frac{\varepsilon}{D_{REF}}\cos^3\left(\frac{\pi}{2}r\right)\sin\left(\frac{\pi}{2}r\right)$$

$$c_i^L = c_i^V \;@\; r = 0$$

$$c_i^L = c_i^{Bulk} \;@\; r = 1 (\textit{Bulk Liquid})$$

A finite differencing scheme can be applied to develop a system of equations for the interior nodes of the discretized liquid film based on Equation B.27; the boundary conditions define the exterior nodes of the liquid film. An example of a central difference scheme (as employed by Bishnoi) for the derivative terms in Equation B.27 is provided as follows:

$$\frac{dc_i}{dr} = \frac{c_i(j-1) + c_i(j+1)}{2\Delta r}$$

$$\frac{d^2 c_i}{dr^2} = \frac{c_i(j-1) - 2c_i(j) + c_i(j+1)}{(\Delta r)^2} \qquad \text{(B.28)}$$

The terms T_1 through T_4 and the reaction term are evaluated at each interior node (each value of r).

B.5.2 Implementation in Aspen Plus®

The critical components of eddy diffusivity method implementation are the definition of the eddy diffusivity parameters (ε and n) and the coordinate transformation and finite difference formulation of the appropriate differential equations. The eddy diffusivity parameters should be readily accommodated within the existing mass transfer coefficient framework in Aspen. The implementation of the differential equations will require additional discussion and collaboration.

B.5.2.1 Steps and Outstanding Issues Required for Implementation:

1) Define transformed differential equations for Aspen implementation: Method proposed in this document discretizes second-order differential equation in concentration after transformation to dimensionless spatial coordinates. Current approach in Aspen appears to discretize the species continuity (change in flux across a film segment) equation and separately applies the constitutive equation (Maxwell-Stefan) after conversion to dimensionless form that directly incorporates a mass transfer coefficient based on the film theory. Determine if 2^{nd}-order differential equation in concentration can be implemented directly as by Bishnoi (Equation B.27) or if the differential in flux (Equation B.22) and the constitutive equations (Maxwell-Stefan multicomponent form of Equation B.23) need to be transformed to r-coordinates and discretized. Also need to define resistance matrix for eddy diffusivity theory (i.e., replace mass transfer coefficients with diffusion coefficient and eddy diffusivity and possibly coordinate transform parameters). The Maxwell-Stefan definitions for film theory are as follows (Taylor & Krishna, 1993):

$$\frac{dx_i}{dz} = \sum_{\substack{j=1 \\ j\neq i}}^{C} \frac{x_j N_i + x_i N_j}{\overline{\rho} D_{ij}} \quad for\ i = 1:C-1$$

$$or$$

$$\frac{dx_i}{d\eta} = \sum_{\substack{j=1 \\ j\neq i}}^{C} \frac{x_j N_i + x_i N_j}{\overline{\rho} \kappa_{ij}} \quad for\ i = 1:C-1$$

$$\eta = z / \delta \tag{B.29}$$

$$R_{ii} = \frac{x_i}{\overline{\rho a^I \kappa_{iC}}} + \sum_{\substack{k=1 \\ k\neq i}}^{C} \frac{x_k}{\overline{\rho a^I \kappa_{ik}}} \quad for\ i = 1:C-1$$

$$R_{ik} = -x_i \left(\frac{1}{\overline{\rho a^I \kappa_{ik}}} - \frac{1}{\overline{\rho a^I \kappa_{iC}}} \right) \quad for\ i = 1:C-1, i \neq k$$

Modification for eddy diffusivity likely entails replacing the binary diffusion coefficient in the first expression above with the sum of the eddy and binary diffusivity and transforming to r-coordinates:

$$\frac{dx_i}{dr} = \left[\frac{1}{2/\pi \cos^2\left(\frac{\pi}{2} r\right) \sqrt{\varepsilon / D_{REF}}} \right] \sum_{\substack{j=1 \\ j\neq i}}^{C} \frac{x_j N_i + x_i N_j}{\overline{\rho}(D_{ij} + D_E)} \quad for\ i = 1:C-1 \tag{B.30}$$

This modified equation is only a suggested or preliminary approach and requires further consideration.

2) Designation of a reference diffusion coefficient: Can be user-defined or automatic designation of largest diffusion coefficient in the system.
3) Evaluation of reaction rates/reaction volume: Implementation of finite difference method in dimensionless coordinates should not require reaction volume

calculation at any node – spatial step-size appears in finite difference formulation to account for relative size of each segment. Boundary conditions define concentrations at r = 0 (x=0) and r = 1 (x = ∞), and solution of finite difference at interior nodes yields a concentration profile. If total reaction rate for a stage or segment is required for reporting, this can be calculated after the integration. May need further discussion/consideration.

4) Finite Volume Method?: Aspen appears to be using something similar to a finite volume method (not finite difference) which evaluates differential equations over a control volume and ensures conservation of mass in each element. This method includes a reaction volume when the elements are discretized. Need to verify exact implementation method in Aspen as the discretized equations will change depending on the approach.

Appendix C: Pilot Plant Manuscript

Modeling Pilot Plant Performance of an Absorber with Aqueous Piperazine

Darshan Sachde[a], Eric Chen[b], Gary T. Rochelle[a]

[a]*The University of Texas at Austin, Department of Chemical Engineering. Luminant Carbon Management Program, 200 E Dean Keeton St. Stop C0400, Austin, TX 78712-1589* USA.

[b]*The University of Texas at Austin, CO_2 Capture Pilot Plant Project, 10100 Burnet Rd., Bldg 133, CEER, Austin, TX 78758, USA.*

Abstract

Pilot plant data for CO_2 capture with 8 m piperazine (PZ) were reconciled with an absorber model in Aspen Plus® using quantified error in pilot plant input data and a global correction to absorber performance parameters. Four global corrections were applied independently to adjust: interfacial area, liquid side mass transfer coefficient, solvent CO_2 content, or solvent piperazine (PZ) content. Each of the four cases resulted in a reconciled model with pilot plant data and provides a potential route to quantifying and correcting measurement and experimental error as well as enhancing understanding of real absorber performance. The modified absorber model was then used to quantify the performance improvement due to implementation of a spray nozzle in the absorber intercooling loop. The spray nozzle added the equivalent of 7% to 20% more packing to the column as a function of the flow rate through the nozzle.

Selection and/or peer-review under responsibility of GHGT

*Keywords:*absorber; pilot plant; piperazine; data reconciliation; mass transfer; interfacial area; spray nozzle

1. Introduction

Pilot plant operations for CO_2 capture using amine solvents provide mass and energy balance data to validate thermodynamic, kinetic, and mass transfer models built using experimental data. In October 2011, the pilot plant at the University of Texas at Austin Separations Research Program (SRP) was operated with 8 molal (m) piperazine (PZ) in an intercooled absorber with solvent return via a spray nozzle. This paper will present validation results of an absorber model built using Aspen Plus® RateSep™, a thermodynamic and kinetic framework developed by Frailie (Frailie, et al., 2013), and mass transfer and area models developed by Wang (Wang, et al., 2013). The reconciled model was used to quantify the performance benefit of spray nozzle implementation in the intercooling loop.

2. Pilot Plant Overview: October 2011 Campaign

The pilot plant at SRP includes an absorber, stripper, and 2-stage flash skid used in CO_2 capture trials. The October 2011 campaign used the 2-stage flash skid for stripping; see Madan et al. (Madan, et al., 2013)

and Walters et al. (Walters, et al., 2013) for details regarding the stripping section and Chen et al. (Chen, et al., 2013) for an overview of the SRP pilot plant equipment, operations, and overall performance results. The absorber configuration for the October 2011 campaign is depicted in Figure 1.

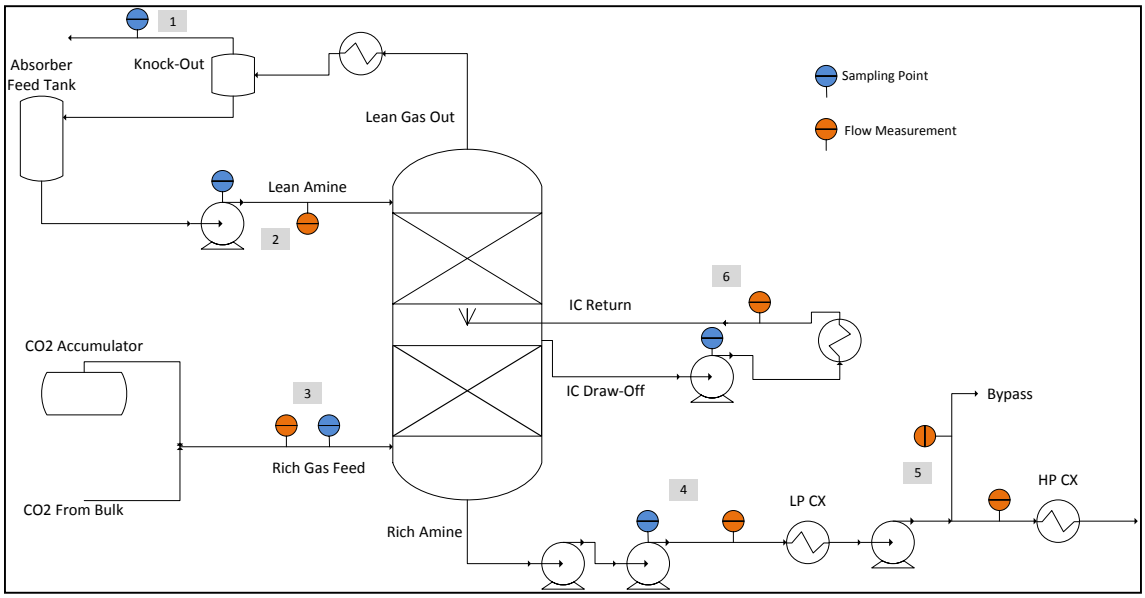

Figure 1 Absorber PFD with flow and sampling points, SRP October 2011 Campaign

The campaign included two absorber-specific equipment modifications from previous campaigns. First, the campaign was the first trial of a 350 series packing (specific area of 350 m^2/m^3) with a 70° corrugation angle used in CO_2 capture applications with 8 m PZ. Second, the intercooling loop included a spray nozzle configured to feed the intercooled solvent into the bottom of the upper section of packing (see Figure 1).

Table 1 provides an overview of equipment and operating specifications relevant to absorber performance and modeling for the 11 runs of the October 2011 campaign.

Table 1. Overview of Equipment and Operating Specifications, October 2011 Pilot Plant Campaign

Equipment Specifications		Operating Specifications	
Column		**Solvent (PZ)**	
Inner Diameter (m)	0.43	*Concentration(m)*	8
Packing (Structured)		*Liquid Rate (GPM)*	11 - 22
Height (m)	6.1 (2 beds x 3.05)	*Lean Loading* *(mols CO_2/mols alkalinity)*	0.24-0.26
Specific Area (m^2/m^3)	350	**Feed Gas**	
Corrugation Angle (°)	70	*CO_2 (mol %)*	12%
Material	Stainless	*Gas Rate (ACFM)*	350 - 675

3. Modeling Framework

The model for the PZ solvent and absorber equipment configurations was developed in Aspen Plus® RateSep™. The thermodynamic model for the PZ-H_2O-CO_2 system was developed from experimental CO_2 solubility, heat capacity, speciation, and amine volatility data by regression of Gibbs free energy, enthalpy, heat capacity and activity coefficient parameters within the electrolyte non-random two liquid (e-NRTL) framework in Aspen Plus®. For a detailed description of the sequential regression methodology used in the development of the PZ thermodynamic model, see Frailie et al. (Frailie, et al., 2011); for details regarding the most recent version of the PZ model, as implemented in the current work, see Frailie (Frailie, et al., 2013).

Mass transfer and area models were developed by Wang (Wang, et al., 2013) via regression of experimental data from a pilot scale column with a variety of random and structured packings. The area model developed by Wang is a modification of a model developed by Tsai (Tsai, 2010) (see Tsai for full theoretical and experimental details of the area model). The mass transfer model is discussed in additional detail in subsequent sections.

4. Data Reconciliation Methodology

The data reconciliation process consists of four broad steps:

- Quantification of error in pilot plant measurements;
- Identification of global adjustable parameters for data reconciliation;
- Reconciliation of pilot plant mass and energy balances for runs *without spray nozzle* implementation;
- Isolation of spray nozzle performance by application of global adjustments from step 3 with independent variation of spray nozzle mass transfer area for each run *with spray nozzle implementation*.

Each of the steps is discussed in further detail in the subsequent sections. The data reconciliation tool in Aspen Plus® used to implement the process described in the steps minimizes the objective function described by Equation 1 to perform a maximum likelihood (errors in variables) regression on the pilot plant data.

$$\underset{v}{Min} \sum_{i=1}^{N} \left(\frac{(Measured_i - Model_i)}{\sigma_{measured,i}} \right)^2 \tag{1}$$

Where:

$\boldsymbol{Measured_i}$ are the pilot plant measured input or result parameters,
$\boldsymbol{Model_i}$ are the process model predicted input or result parameters,
$\boldsymbol{\sigma_{measured,i}}$ are the pilot plant calculated standard deviations for input and result parameters, and
$\boldsymbol{v}$ are the globally varied parameters.

4.1. Error Quantification

Measureable error in the pilot plant data was limited to random error quantified via repeated trials of analytical measurements and continuous data collection of inline measurements at steady state (flows, temperatures, etc.). Table 2 summarizes measurement techniques used for the sampling points around the absorber identified in Figure 1.

Table 2. Measurement Techniques used in October 2011 campaign

Measurement Location and	Inline	Analytical

ID		CO_2 concentration	PZ concentration
Lean Amine/Mid-Column Amine (Point 2 and 6)	Micro Motion® Coriolis Flow Meters	Auto Titration Manual Titration Total Inorganic Carbon	Auto Titration Manual Titration
Rich Amine (Points 4 and 5)	Micro Motion® Coriolis Flow Meter	Auto Titration Manual Titration Total Inorganic Carbon	Auto Titration
Lean Gas (Point 1)	Rosemount® Annubar (Differential Pressure) Meter	Vaisala® GMT220 CO_2 Sensor (NDIR Sensor)	N/A
Rich Gas (Point 3)	Inferred from Inlet	Vaisala® GMT220 CO_2 Sensor (NDIR Sensor)	N/A
Column Temperatures (Throughout Column)	Rosemount® 68-Series RTD	N/A	N/A

Standard deviations were calculated for each measurement from the pilot plant and were propagated through calculations of derived values (e.g., component flow rates) with assumption of uncorrelated random error (covariance terms are omitted). The results of the error analysis allowed verification of mass balance closure within random error in the process (discussed in results section) and provided a range for input variables used in data reconciliation.

4.2. Global Adjustment Parameters

Global adjustment parameters are user-defined model parameters which are adjusted uniformly for all of the experiments in a dataset (i.e., all of the runs in a pilot plant campaign) as part of the error minimization process described by Equation 1. For pilot plant campaigns, parameters were selected to reflect sources of potential systematic bias in data measurements and/or physical parameters linked to column performance. The choice of parameters will guide future pilot plant operations and experimental research. The four parameters selected for evaluation in the October 2011 campaign were mass transfer area, liquid-side mass transfer coefficient, lean solvent CO_2 content, and lean solvent PZ content.

4.2.1. Correction for Mass Transfer Area

The mass transfer area model originally developed by Tsai (Tsai, 2010) from data for 9 different types of structured packing matched experimental data within 13%. The correction to the model-predicted area in the data reconciliation process indirectly accounts for, in part, the model error. In addition, liquid distribution issues (specifically, liquid flows along walls) can result in under-utilization of packing; Yin et al. demonstrated significant wall flow in a column of similar diameter to the SRP pilot plant column (0.5 m vs. 0.43 m) when utilizing random packing (Yin, et al., 2000). Thus the area factor can be used to represent model error and physical performance issues.

4.2.2. Correction for Liquid Side Mass Transfer Coefficient

The liquid side mass transfer model implemented in the reconciliation process is a simple empirical equation (Equation 2) designed to fit data collected by Wang on the 350 series packing with a viscosity

correction to account for the use of a viscous solvent (PZ) instead of the water used in experimental mass transfer studies (Wang, et al., 2013).

$$\frac{k_L}{D^{0.5}} = A * \left(\frac{U_{SL}}{a_p} \right)^B * \mu_L^{-0.5} \quad (2)$$

Where:

k_L is the liquid side mass transfer coefficient (m/s),
D is the binary diffusivity coefficient (m^2/s),
A and B are the regression parameters (A = 281 $kg/s^{0.637}/m^{0.726}$, B = 0.863 for the 350 series packing in this work),
U_{SL} is the superficial liquid velocity (m/s),
a_p is the specific area of the packing (m^2/m^3), and
μ_L is the liquid viscosity (Pa-s).

The model is presented as a diffusion independent mass transfer coefficient (consistent with implementation in Aspen Plus®) with the assumption that the mass transfer coefficient has a square root dependence on diffusivity as predicted by penetration and surface renewal theories. The prediction of diffusion coefficient is not considered in this work, but is developed as part of the thermodynamic framework of Frailie (Frailie, et al., 2013). Equation 2 is not a generally applicable mass transfer model, but rather an empirical expression to represent the experimental data collected for the packing of interest (350 series packing in this work). The exponent on the viscosity term was derived from literature review since viscosity was not varied in the experimental data.

Physical mass transfer resistance in reactive absorption systems with fast (not instantaneous) reaction is not significant under certain conditions (pseudo-first order approximation with high Hatta number (Bishnoi, 2000)). For the liquid side mass transfer model to be a meaningful parameter in the data reconciliation process, the predicted mass transfer coefficient must be low enough to limit diffusion of reactant and products to and from the interface (violating the pseudo-first order approximation), reducing the rate of CO_2 absorption. A sensitivity analysis of the mass transfer coefficient for representative pilot plant conditions (lean loading = 0.28, L/G = 4.3 mol/mol, spray intercooling) is summarized in Figure 2. The results depict two distinct regions of CO_2 mass transfer sensitivity to k_L; the prediction of Equation 2 (red, dashed line) falls in the region of high sensitivity (represented by the slope of the line or exponent on the trend line equation in Figure 2). Thus, current experimental data for the 350 series, 70° packing indicate that the physical mass transfer coefficient is important to overall mass transfer performance in the pilot plant system with 8 m PZ.

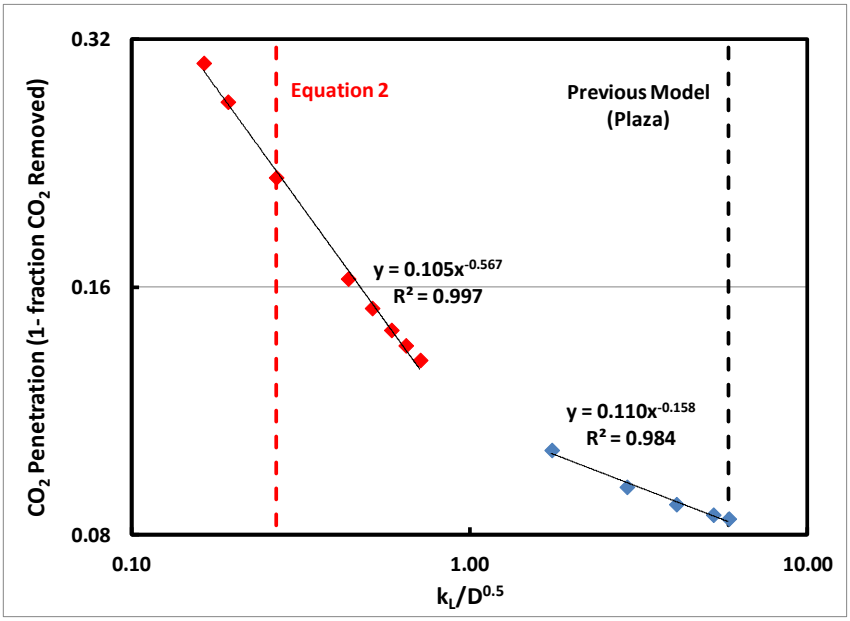

*Figure 2 Sensitivity of CO_2 Absorption (Penetration) to changes in Diffusion-Independent Liquid Mass Transfer Coefficient. Dashed lines represent predictions by the mass transfer model presented in this work **(- -red)** in Equation 2 and the model used by Plaza (Plaza, 2011) **(- - black)** in previous pilot plant analysis. All data in the plot reflect the following modeled case: lean loading = 0.27 mol CO_2/mol alkalinity, L/G = 4.3 mol/mol, and spray intercooling. Mass transfer coefficients are average values over the column.*

Since the model parameters were regressed to fit the data for the packing used in this pilot plant campaign, the average deviation of the model from the experimental data was small (< 1%), but individual experimental points could vary from model predictions by as much as 20%. Therefore, this model error may be represented in the reconciliation process by allowing a correction to the model predicted mass transfer coefficient. In addition, as with the interfacial area, local mass transfer coefficients can be adversely affected by liquid distribution in the column. If large portions of the packing do not receive sufficient liquid flow, the apparent mass transfer coefficient will drop correspondingly; local mass transfer behavior is not easily modeled in packed columns, and thus the correction to the model-predicted mass transfer is needed.

4.2.3. Corrections for CO_2 and PZ

Corrections for CO_2 and PZ component mass flows in the feed stream to the absorber were also implemented (each an independent parameter). The corrections were primarily introduced to represent potential measurement bias in titrations or flow measurements around the absorber. Mass balance reconciliation after random error quantification (section 4.1) showed that the CO_2 and PZ mass balances could not be simultaneously closed within the random error using the same titration and flow meter data sources. This inconsistency pointed to potential bias in either flow or titration data. In addition, work by Walters showed that CO_2 concentration predictions from inline density measurements were inconsistent with CO_2 titration data (Walters, et al., 2013). This evidence supports the need for a bias correction in the reconciliation process. Finally, work by Nielsen indicated evidence of degradation products in the pilot plant solvent (Nielsen, et al., 2013); if the PZ degraded over time, and this corresponds to a loss of alkalinity of the solvent, the modeled PZ concentration should be reduced to reflect reduced alkalinity.

4.3. Data Reconciliation and Spray Nozzle Performance

The pilot plant data and global adjustment parameters were used to reconcile model predicted performance with pilot plant measurements (Equation 1) for the three runs in the October 2011 campaign (runs 1, 8, and 10) that did not implement spray nozzle intercooling; this process identified values for the global adjustment parameters to be applied uniformly to the full campaign. With global parameters fixed, the spray nozzle was modeled as a packed section between the two primary beds of the column. The mass transfer area of the spray nozzle section was treated as an independent variable for each run with the spray nozzle activated and provided a measure of interfacial area generated by the spray without rigorous modeling for the spray. This two-step process identified global adjustments for the entire campaign and isolated the impact for the spray nozzle by run. Table 3 summarizes input, adjustment, and result parameters used in the data reconciliation.

Table 3. Data Reconciliation Parameter Summary

Input Parameters	Global Adjustment Parameters	Results
Lean Solvent - CO_2	Liquid Side Mass Transfer Coefficient (kL)	Rich Solvent Flow
Lean Solvent - PZ	Interfacial Area	Mid Column Loading[1]
Lean Solvent – H_2O	CO_2 Correction	Rich Loading[1]
Lean Solvent –Temperature/Pressure	PZ Correction	Rich Solvent Temperature
Rich Gas Composition[2]		Lean Gas Composition[2]
Rich Gas Temperature/Pressure		Lean Gas Temperature
Rich Gas Flow		Lean Gas Flow
Intercooling Temperature		
Column Pressure Drop		
Column Heat Loss[3]		

1. Mid-Column and Rich Loadings were represented by changes from lean loading
2. Rich and Lean gas compositions were used to calculate CO_2 Removal
3. Steady state heat loss calculated from column RTD measurements.

5. Previous PZ Campaigns and Data Reconciliation

Three previous campaigns were implemented using 8 m PZ at SRP. Plaza performed data reconciliation work on the 3 previous campaigns, using both an interfacial area modification and CO_2 modification to reconcile the pilot plant data with a previous version of the 8 m PZ model (Plaza, 2011). Table 4 provides a summary of absorber conditions and the results of Plaza. The significance of the CO_2 corrections cannot be isolated from the mass transfer area corrections since they were varied concurrently and are likely not independent; this is also reflected in the standard deviations around the corrections which indicate the corrections are not statistically different from 1(no correction) at a 95% confidence level (only the December 2010 area correction is significant). Nonetheless, the corrections provide a reference for comparison and range of expected corrections for the October 2011 campaign.

Table 4. Previous PZ Pilot Plant Campaign Operating Conditions and Reconciliation Results

Pilot Plant Campaigns		November 2009	September 2010	December 2010	October 2011*
Operating Conditions	**Solvent**	5 – 9 m PZ	8 m PZ	8 m PZ	8 m PZ
	Packing Type/Sp. Area(m^2/m^3)/Angle	Structured 205 X	Hybrid 250	Hybrid 250	Structured 350 Z
	Gas Rate (ACFM)	350	250-750	350-650	350-675
	Liquid Rate (GPM)	12-18	8-26	8-26	11-22
	Intercooling	No	Yes/No	Yes	Yes (with Spray)
Modified Model Parameters	**Interfacial Area Factor**	1.17 ± 0.15	1.02 ± 0.16	0.72 ± 0.13	See Results
	CO_2 Multiplier	1.05 ± 0.03	1.05 ± 0.03	1.06 ± 0.04	See Results
	# of Runs Evaluated	14	12	9	11

6. Results

Table 5 summarizes the global parameter sensitivity results of the first step of the reconciliation process (runs without the spray nozzle).

Table 5. Results of Independent Global Parameter Sensitivity Analysis with 95% confidence intervals

Parameter	Correction Factor	Upper 95%	Lower 95%
Interfacial Area	0.74	0.79	0.68
Liquid Side Mass Transfer Coefficient (k_L)	0.65	0.71	0.59
CO_2 Correction	**1.075**	**1.1**	**1.05**
PZ Correction	0.93	0.95	0.91

Each of the individual parameter corrections in Table 5 is statistically significant and reconciled the overall mass and energy balance for the 3 runs without the spray nozzle. The area and CO_2 corrections are similar to previous corrections by Plaza (Plaza, 2011), though a combination of area and loading corrections was not needed to reconcile the data in this work (less severe correction than previous work). The CO_2 correction has corroborating data from the work of Madan in stripper reconciliation and Walters in dynamic pilot plant performance analysis (Madan, et al., 2013; Walters, et al., 2013). Madan was able to reconcile the stripper section (two-stage flash) of the October 2011 campaign with a correction of 4.6% reported in this work (Madan, et al., 2013). Walters work showed that an average increase of 4.5% was required in CO_2 mole fractions to reconcile dynamic simulation around the stripping section (Walters, et al., 2013). The correction in this work is higher than those on the stripper side, and may in reality be coupled with one of the other effects in represented in Table 5. Nonetheless, the CO_2 correction was selected as the global parameter to be applied to all spray nozzle runs.

Figures 3 through 6 show several important result parameters from the data reconciliation process using the CO_2 correction and spray nozzle mass transfer area variation. The reconciliation process matched all input and result variables within 95% confidence intervals (error bars in figures) with the exception of mid column loading (not shown). The single parameter approach used in this analysis is likely insufficient (underspecified) to fit the mid loading measurement, and a secondary parameter would be needed to account for relative mass transfer rates through the column.

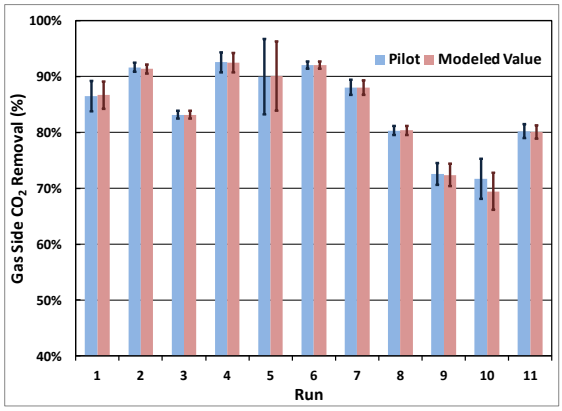

*Figure 3 Gas Side CO_2 Removal by Pilot Plant Run, Measured **(blue)** vs. Model Predicted **(red)** (Error bars = 95% Confidence Intervals)*

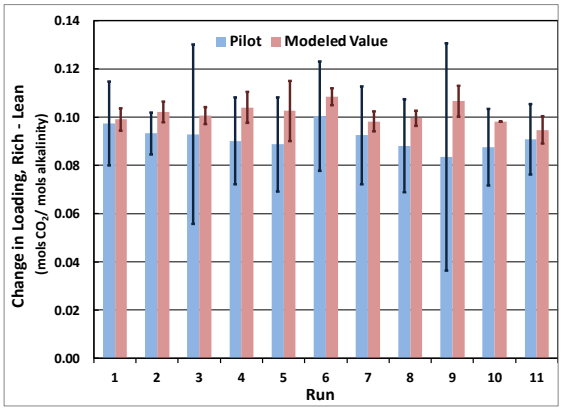

*Figure 4 Loading Difference (Rich – Lean) by Pilot Plant Run, Measured **(blue)** vs. Model Predicted **(red)** (Error bars = 95% Confidence Intervals)*

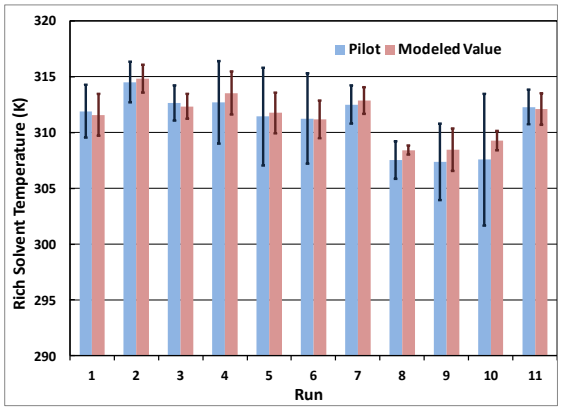

*Figure 5 Rich Solvent Temperature by Pilot Plant Run, Measured **(blue)** vs. Model Predicted **(red)** (Error bars = 95% Confidence Intervals)*

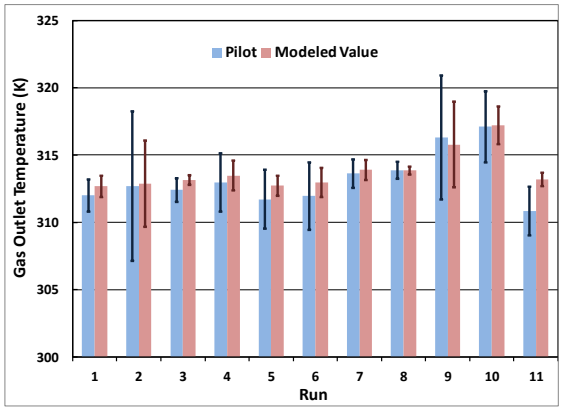

*Figure 6 Gas Outlet Temperature by Pilot Plant Run, Measured **(blue)** vs. Model Predicted **(red)** (Error bars = 95% Confidence Intervals)*

In addition to verification of the reconciliation process, the result parameters provide insight into the pilot plant operations. The rich to lean loading difference (Figure 4) shows a trend of over-prediction by the model (all 11 runs). Random process variations and measurement errors should yield pilot plant results on both sides of the model prediction; it is highly unlikely to find trends such as that in Figure 4 strictly via random variation. Reconciliation results for the rich solvent flow rate revealed an analogous trend; the rich solvent flow rate was shifted towards its lower bound in all but one run. The drop in solvent flow for a

given CO_2 transfer leads to higher rich loading as observed in Figure 4. During the error quantification process of the pilot plant data (section 4.1), the choice of rich flow meter (point 4 vs. point 5 in Figure 1) altered the mass balance closure. An average of flow meter values was used in the reconciliation since this minimized the error in the mass balance; however, as the reconciliation results indicate, the rich solvent flow still shows an apparent bias that should be addressed in future runs.

Figure 7 and 8 provide representative temperature profiles for the column for runs with comparable operating conditions with and without the spray nozzle.

.

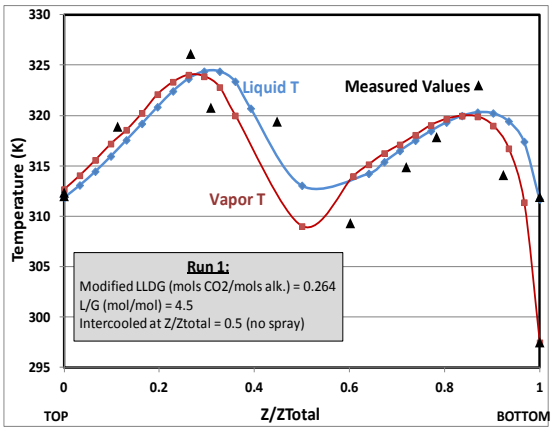

Figure 7 Absorber Column Temperature Profile, Run 1 (Intercooling with No Spray Return). Profile moves down the column from left to right.

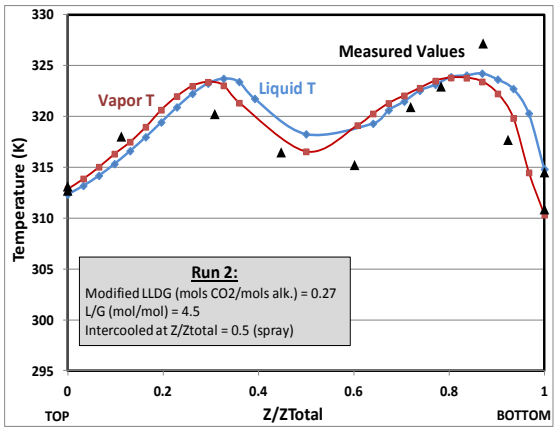

Figure 8 Absorber Column Temperature Profile, Run 2 (Spray Return for Intercooling). Profile moves down the column from left to right.

Despite the fact that the reconciliation process only matched inlet and outlet gas and solvent temperatures, the temperature profile behavior is largely captured by the model. For example, in run 2, the spray nozzle leads to recycle of solvent in the middle of the column (approaches a well-mixed section) and the temperature leaving the middle section of the column is higher than in run 1 where the intercooled solvent goes directly to the lower section of the column; this behavior is replicated well by the model. The model struggled to match the peak temperatures observed at the pilot plant; this may be a function of poor estimates of heat loss at these points or may provide insight into real temperature behavior in operation. These points may be candidates for multiple radial temperature measurements in future campaigns.

Finally, the predicted mass transfer area generated by the spray nozzle was quantified as an equivalent height of packing (Table 6). The predicted height was then correlated to the mass flow rate through the spray nozzle with the purpose of relating the kinetic energy in the flow stream to the mass transfer area generated from the nozzle (Figure 9).

Table 6. Predicted Spray Nozzle Mass Transfer Area (Equivalent Height of Packing) by Pilot Plant Run

Run	Spray Equivalent Height of Packing (m)	% Addition to Total Packing
2	0.44	7%
3	0.58	10%
4	0.96	16%
5	0.57	9%
6	1.03	17%
7	1.09	18%
9	1.26	21%
11	0.88	14%

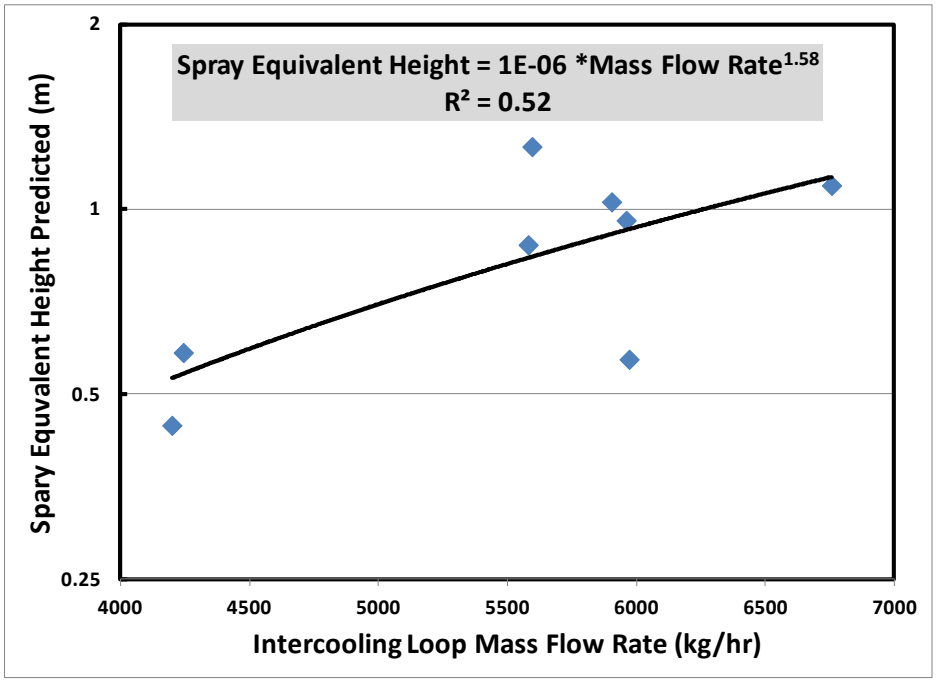

Figure 9 Prediction of mass transfer area produced by the spray nozzle on intercooled solvent return as a function of the solvent mass flow rate through the nozzle. Mass transfer area is reported as an equivalent height of packing (of 350 series packing used in the October 2011 campaign).

The data regarding spray nozzle performance can be used to perform an economic analysis of spray nozzle implementation (trade-off vs. packing) or as a measure of performance improvement in a retrofit application in an absorber column. In the case of the pilot plant, additional mass transfer area was generated where packing could not be added at the cost of a spray nozzle and pressure drop associated with the flow rates enumerated in Figure 9.

7. Conclusions

Pilot plant data reconciliation of mass and energy balances for an absorber column utilizing 8 m PZ were successfully completed with the independent implementation of 4 global adjustment parameters representing potential deviations in pilot absorber performance from model predictions.

- Interfacial Area Correction: A 26% decrease of the model predicted mass transfer area was required to reconcile the October 2011 campaign data with model predictions. The reduced performance compared to the model (and experimentally collected data) in the pilot column may indicate error in the model at pilot plant conditions or issues with column operation such as liquid distribution. The result suggests the need for proper incorporation of experimental error into modeling efforts as well as reduction of model error by packing specific area measurements at pilot plant conditions to reduce error in the model. This objective should be balanced with the need for generalized area models that are applicable to a variety of packing and will inherently have more error than a packing-specific model. In addition, experiments quantifying the performance impact of varying liquid distribution would provide a valuable upgrade to the area models in use currently.

- Liquid Side Mass Transfer Coefficient: Sensitivity analysis of the mass transfer coefficient revealed that column performance is sensitive to the physical mass transfer coefficient. A 35% reduction of the nominal or model predicted mass transfer coefficient was required to reconcile pilot plant data. As with the mass transfer area, repeated experiments at pilot plant conditions could isolate the relevant experimental error in the mass transfer model and liquid distribution experiments could provide an additional important correction parameter. Finally, the viscosity dependence assumed in this work (-0.5 power) should be experimentally verified or updated for systems analogous to the 8 m PZ solvent as this is another source of potential uncertainty currently unaccounted for in the model.

- CO_2 Correction: An increase of 7.5% to CO_2 content (mole fraction) in the lean amine stream was required to achieve reconciliation between model and plant data. As noted, the correction to CO_2 is in part validated by stripper reconciliation work by Madan (Madan, et al., 2013) and Walters (Walters, et al., 2013) who found increases in CO_2 concentration of 4.6 and 4.7%, respectively. The correction in CO_2 concentration implies a bias in pilot plant measurement data (titrations and/or flow measurements); this potential for bias was supported by component mass balance closure problems during error quantification of pilot plant data. However, future campaigns will require re-calibration of flow meters and analysis of standards for analytical methods to quantify or eliminate the bias.

- PZ Correction: A 7% reduction to PZ content (mole fraction) in the lean amine stream was required to achieve reconciliation between model and plant data. As with CO_2, the correction may be explained by un-quantified measurement bias. However, work by Nielsen (Nielsen, et al., 2013) points to the possibility of degradation of the PZ solvent over several campaigns which may ultimately lead to loss of alkalinity in the solvent. However, this effect has not been quantified in a way that can be modeled. The establishment of a baseline for the solvent condition based on Nielsen or the use of fresh solvent in future campaigns will allow the evaluation of modeled compared to actual solvent performance over

time. Alongside analytical data collected with each campaign, changes in expected performance can be correlated to changes in the solvent.

Using the CO_2 model correction, the effect of spray nozzles was quantified in terms of the equivalent height of packing required to replicate spray nozzle performance improvement. The spray nozzle impact was equivalent to the addition of 7 to 20% additional packing to the column as configured in the October 2011 campaign. Further, the spray nozzle mass transfer area generated was correlated to the 1.5 power of the mass flow rate through the nozzle (and intercooling loop). This correlation provides the basis for economic evaluation of the spray nozzle configuration and identification of feasible conditions for operation.

Acknowledgements

This work was supported by the Luminant Carbon Management Program.

References

[1] Frailie PT, Madan T, Sherman B, Rochelle GT. Energy performance of advanced stripper configurations. Presented at GHGT-11, Kyoto, Japan, November 18-22, 2012. *Energy Procedia*, 2013.

[2] Wang C, Perry M, Seibert F, Rochelle GT. Characterization of Novel Packings for Post Combustion Capture. Presented at GHGT-11, Kyoto, Japan, November 18-22, 2012. *Energy Procedia*, 2013.

[3] Madan T, Van Wagener DH, Chen E, Rochelle GT. Modeling pilot plant results for CO_2 stripping using piperazine in a two stage flash. Presented at GHGT-11, Kyoto, Japan, November 18-22, 2012. *Energy Procedia*, 2013.

[4] Chen E, Madan T, Sachde D, Walters M, Nielsen P, Rochelle GT. Pilot Plant Results with Piperazine. Presented at GHGT-11, Kyoto, Japan, November 18-22, 2012. *Energy Procedia*, 2013.

[5] Frailie PT, Plaza JM, Van Wagener DH, Rochelle GT. Modeling Piperazine Thermodynamics. Presented at GHGT-10, Amsterdam. *Energy Procedia*, 2011.

[6] Tsai RE. *Mass Transfer Area of Structured Packing.* PhD Dissertation, The Univeristy of Texas at Austin: Austin, 2010.

[7] Yin F, Wang Z, Afacan A, Krishnaswamy N, Chuand KT. Experimental Studies of Liquid Flow Maldistribution in a Random Packed Column. *The Canadian Journal of Chemical Engineering* **2000;** 78, 449-457.

[8] Bishnoi S. *Carbon Dioxide Absorption and Solution Equilibrium on Piperazine Activated Methyldiethanolamine.* PhD Dissertation, The University of Texas at Austin: Austin, 2000.

[9] Walters MS, Dunia RH, Edgar TF, Rochelle GT. Two-Stage Flash for CO_2 Regeneration: Dynamic Modeling and Pilot Plant Validation. Presented at GHGT-11, Kyoto, Japan, November 18-22, 2012. *Energy Procedia*, 2013.

[10] Nielsen PT, Li L, Rochelle GT. Piperazine degradation in pilot plants. Presented at GHGT-11, Kyoto, Japan, November 18-22, 2012. *Energy Procedia*, 2013.

[11] Plaza JM. *Modeling of Carbon Dioxide Absorption using Aqueous Monoethanolamine, Piperazine and Promoted Potassium Carbonate.* PhD Dissertation, The University of Texas at Austin: Austin, 2011.

Appendix D: Notes on Absorber Modeling Methods

D.1 Minimum Solvent Rate Analysis (Chapter 3 and 4)

Chapters 3 and 4 included evaluations at the minimum solvent rate asymptote (L_{MIN}) for isothermal, adiabatic and intercooled absorbers. The chapters provide a detailed discussion of the evaluation of the pinch conditions that define L_{MIN} for each case. The following discussion will outline some important aspects of modeling the L_{MIN} condition using the rate-based absorber model in Aspen Plus®.

D.1.1 Isothermal L_{MIN}

The minimum solvent rate for an isothermal absorber corresponds to a pinch at the rich end of the absorber. Therefore, L_{MIN} can be calculated from the solvent VLE and a material balance on the absorber. First, the rich loading for the isothermal absorber is defined as the loading where the equilibrium partial pressure (P^*_{CO2}) is equal to the inlet flue gas CO_2 partial pressure ($PCO_{2,IN}$). For a given lean loading and CO_2 removal, the material balance around the absorber can be used to calculate L_{MIN} as follows:

$$L_{MIN} = \frac{f_{CO_2} y_{CO_2}^{IN} V_{IN} MW_{CO_2}}{\left(\omega_{PZ}^{IN} / \omega_{PZ}^{OUT} \right) - 1} \qquad \text{D.1}$$

where:

f_{CO2} = Fraction of CO_2 removed;

$y_{CO_2}^{IN}$ = Mole fraction of CO_2 in flue gas inlet;

V_{IN} = Molar flow rate of flue gas into absorber;

MW_{CO2} = Molecular weight of CO_2 (44.01 g/mol);

ω_{PZ} = Apparent mass fraction of piperazine at solvent inlet (IN =lean) and outlet (OUT = rich);

The apparent mass fractions of PZ can be calculated from the lean and rich loadings. Alternatively, a flash block in AspenPlus® can be used to combine both steps (match P*CO_2 and perform material balance) removing the need for apparent mass fractions.

D.1.2 Adiabatic and Intercooled L_{MIN}

For the cases where the column is not operated isothermally (adiabatic and intercooled absorber), pinches may coincide with temperature maxima in the column (and are a function of CO_2 and water transfer rates as discussed in Chapter 3). In these cases, L_{MIN} is a rate-based phenomena and cannot be predicted by VLE and material balance as in the isothermal case. Instead, the full rate-based model must be used to find L_{MIN} and the corresponding pinch. Figure D.1 illustrates the approach used in this work.

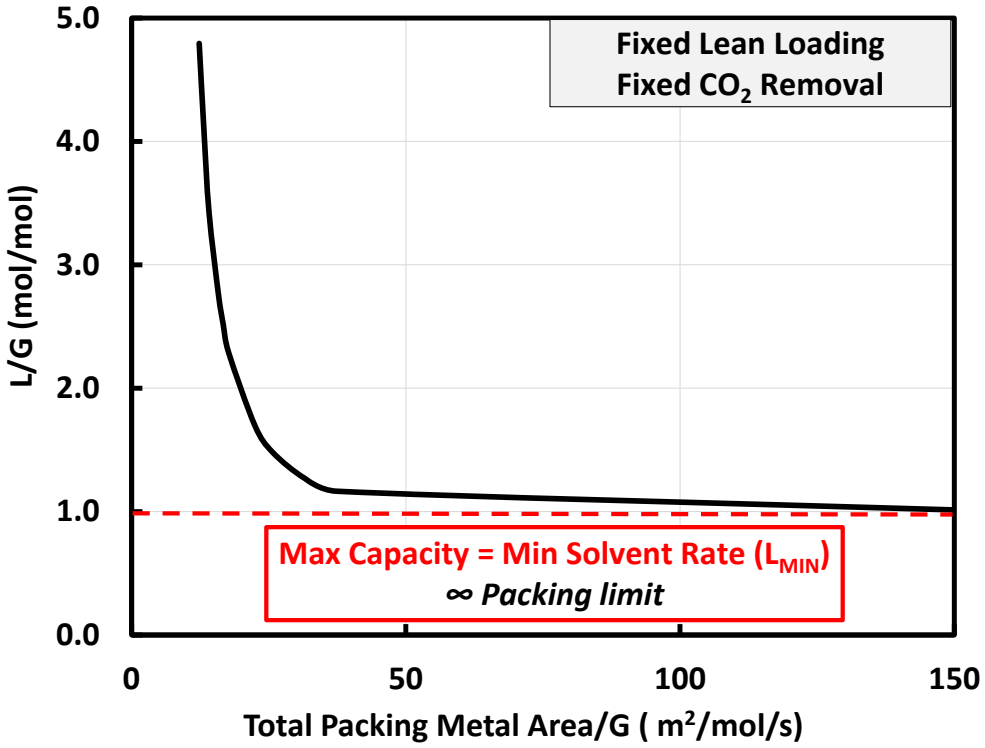

Figure D-1: Minimum Solvent Rate Identification from Absorber Design Curves.

As the figure shows, the horizontal asymptote of an absorber design curve for a given lean loading and CO_2 removal represents L_{MIN} for any absorber configuration. The modeling approach, therefore, is to add packing to a simulated column until the solvent rate required to achieve 90% removal is effectively constant (i.e., changes by less 0.1% from previous step). However, several important factors should be considered in the simulation of this conditions:

1) Stages must be added to the absorber as packing is added to ensure that individual computational stage size is not becoming too large. This is particularly important where large gradients exist (e.g., around a temperature bulge). Therefore, column discretization must be checked after each simulation to ensure all gradients are properly captured (add additional stages around gradients). Once L_{MIN} is

identified, the sensitivity of L_{MIN} to computational stages and column discretization should be checked to ensure the result is not a modeling artifact.

2) The pinch should be verified by an equilibrium-operating line chart (i.e., checking driving forces), checking a CO_2 flux profile, or the CO_2 reaction rate, all of which provide indications of a mass transfer pinch. As with the L_{MIN} specification, a computational limit must be defined to determine a pinch (i.e., finite driving force that defines approximates a pinched condition).
3) For intercooled absorbers, in general, a pinch should occur in each independent packed section of the column and should be verified computationally to ensure simulation of L_{MIN}.

The simulated packing area requirements for the cases in Chapters 3 and 4 are summarized here for reference only (provide an order of magnitude reference for the packing requirement @ L_{MIN} for the specific simulated cases in this work):

- NGCC, 90% Removal; G = 31.2 kmol/s; $y_{CO2,IN}$ = 4.1 mol%:
    - Adiabatic: 4400 – 8200 (1000 m^2)
    - In-and-Out IC: 7600 – 9700 (1000 m^2)
- Coal-fired boiler, 90% Removal; G = 31.2 kmol/s; $y_{CO2,IN}$ = 14.7 mol%:
    - Adiabatic: 3600 – 9800 (1000 m^2)
    - In-and-Out IC: 6300 – 9000 (1000 m^2)
- Steel blast furnace, 90% Removal; G = 10.8 kmol/s; $y_{CO2,IN}$ = 27 mol%:
    - Adiabatic: 1800 – 4000 (1000 m^2)
    - In-and-Out IC: 6400 – 8000 (1000 m^2)

As noted in the preceding discussion, many factors can affect the computational packing requirement for L_{MIN} and once L_{MIN} is reached, packing can be added to the simulation with minimum effect on the results. Therefore, the finite packing requirement has little physical meaning and is only computationally relevant in that it describes the range of values where a pinch might be expected for the given conditions.

D.2 ISOTHERMAL COLUMN (CHAPTER 3, 4, AND 5)

Modeling an isothermal column with a finite packing requirement (i.e., away from L_{MIN}) using the full rate-based model in AspenPlus® requires a method to remove heat generated by absorption and reaction of CO_2 as the mass transfer and thermodynamic models cannot be de-coupled directly. The following approach was used in this work.

1) Specify a "heat loss" section in the Radfrac module corresponding to each stage in the simulation (found under "Blocks>Absorber>Heaters Coolers>Heat Loss").
2) Provide an initial guess for the heat loss for each stage.
3) Column should be fully converged with initial guesses for heat loss profile – may require updating of heat loss specifications. Significant deviations in temperature from target temperature or CO_2 removal from removal specification will create difficulty in converging the column (large steps will be required in heat loss profiles and changes in CO_2 removal will have significant impact on temperature profiles).
4) Define a design specification for each stage to vary the heat loss for each stage (variable name = HTLOSS-SEC) until the solvent temperature is at the target temperature (e.g., 40°C).
5) Design specifications should be defined to converge simultaneously (found under "Convergence>Conv Options>Sequencing>Design Spec Nesting").

6) A design specification to maintain constant CO_2 removal should also be active during heat loss convergence (vary solvent rate for a given packing height or vary packing height for a fixed solvent rate).

D.3 HYBRID CONTACTING SCHEME (CHAPTER 6)

The hybrid contacting scheme (Figure D-3) in Chapter 6 requires that each of the individual packed sections be modeled as an individual rate-based column model in AspenPlus®.

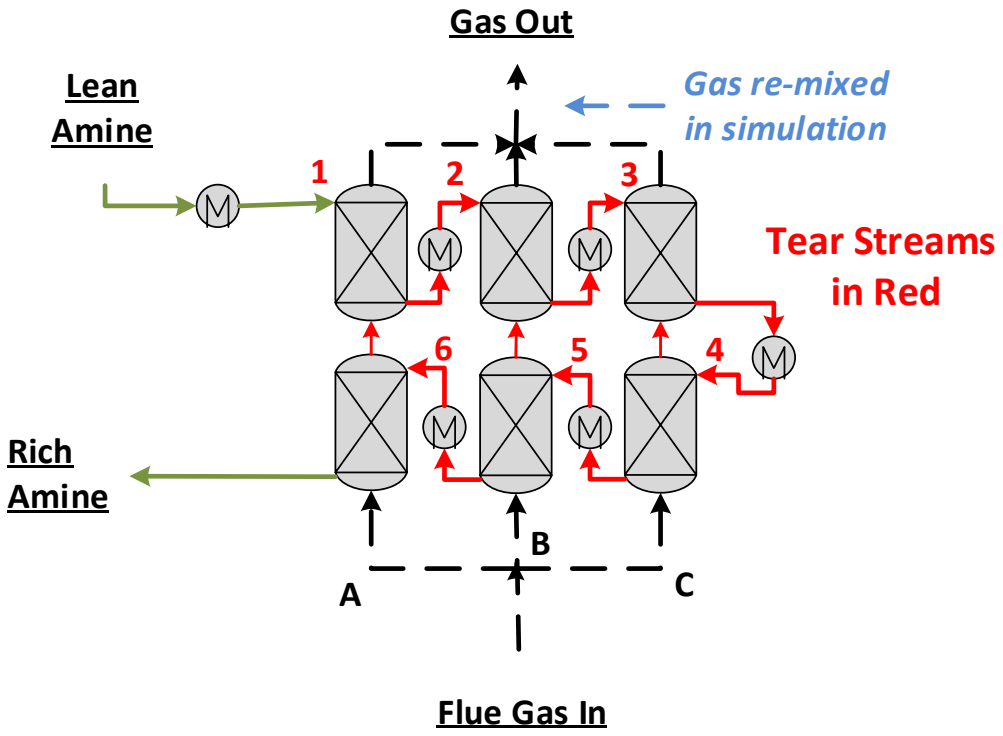

Figure D-2: Hybrid contacting scheme modeling notes. Each section in the hybrid contacting scheme is a separate "absorber" or rate-based Radfrac module in AspenPlus®. The individual gas streams were mixed leaving the hybrid section prior to entering a top bed (if present). The feed streams (gas and liquid for all but the lean feed and entering gas streams represent potential tear streams (red) in the simulation.

The potential tear streams created by the hybrid contacting scheme are highlighted in Figure D-2. These tear streams provide the primary challenge to convergence in the simulation as they define the heat and material balance for all unit operations in the simulations (columns and heat exchangers). Initial guesses for the streams should be provided as part of the initial simulation based on known feed stream (gas and liquid) conditions and can be updated through the convergence process (e.g., as the columns are simulated from physical absorption to full chemical kinetics) by reconciling the stream input with the stream results. The gas streams leaving the hybrid

section were mixed prior to entering a top section of packing, but can be fed separately to three parallel counter-current packed columns to simulate gas distribution in an actual column.

Appendix E: Design Curves for Intercooled Absorbers

The following figures are intended to supplement the discussion in Chapter 3 by completing the set of design curves generated for the analysis in that chapter. The NGCC design curves are repeated here for completeness, and the curves for the coal-fired boiler and steel blast furnace applications appear for the first time. Please reference Chapter 4 for detailed discussion of the results.

"Over-Stripped" Loading Range

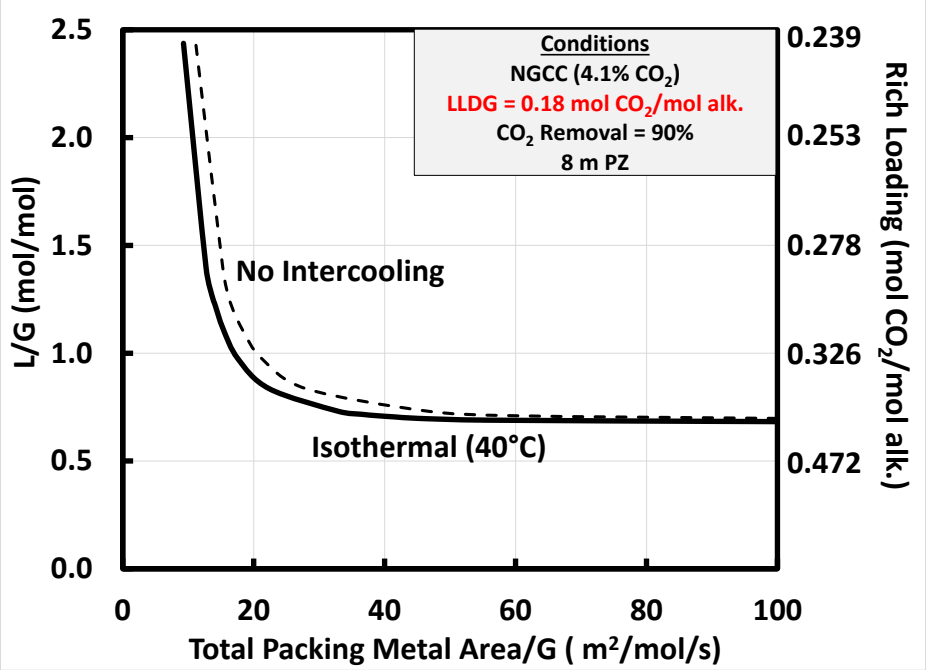

Figure E-1: Packing-solvent rate trade-off, NGCC flue gas (4.1 mol% CO_2), "over-stripped" loading region (LLDG = 0.18 mol CO_2/mol alk.). Each curve (dashed = adiabatic, solid = isothermal) represents constant 90% CO_2 removal. Unique rich loading for each L/G is on secondary y-axis. The horizontal asymptote each curve reaches is L_{MIN}.

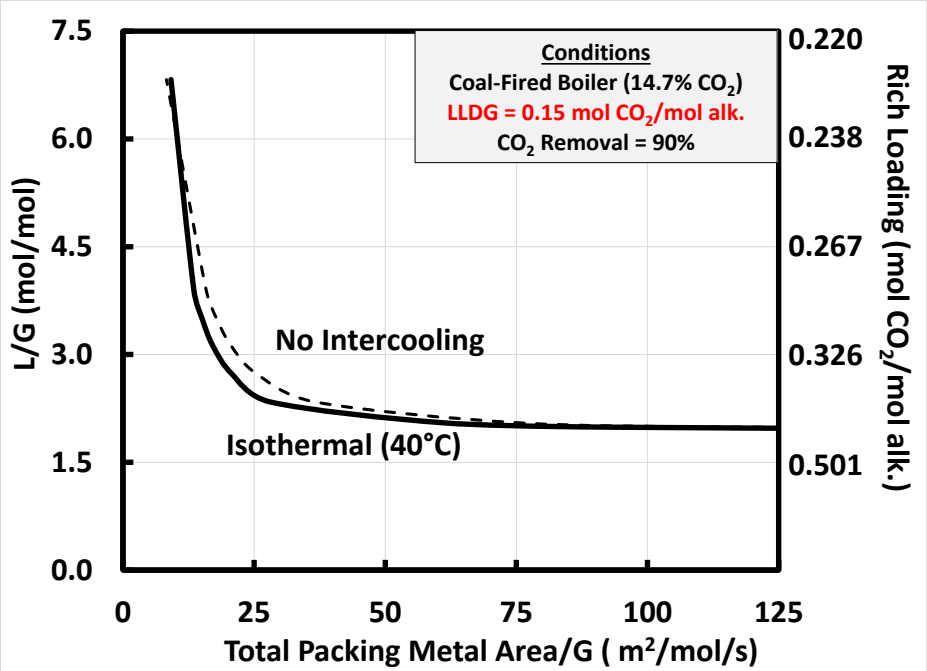

Figure E-2: Packing-solvent rate trade-off, coal-fired boiler flue gas (14.7 mol% CO_2), "over-stripped" loading region (LLDG = 0.15 mol CO_2/mol alk.). Each curve (dashed = adiabatic, solid = isothermal) represents constant 90% CO_2 removal. Unique rich loading for each L/G is on secondary y-axis. The horizontal asymptote each curve reaches is L_{MIN}.

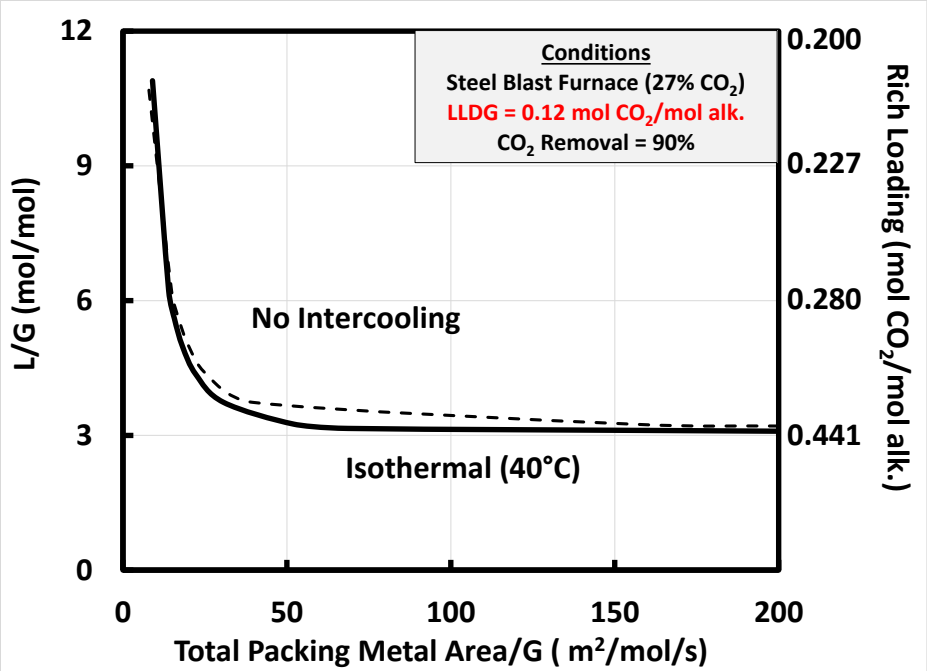

Figure E-3: Packing-solvent rate trade-off, steel blast furnace flue gas (27 mol% CO_2), "over-stripped" loading region (LLDG = 0.12 mol CO_2/mol alk.). Each curve (dashed = adiabatic, solid = isothermal) represents constant 90% CO_2 removal. Unique rich loading for each L/G is on secondary y-axis. The horizontal asymptote each curve reaches is L_{MIN}.

SIMPLE INTERCOOLING LOADING RANGE

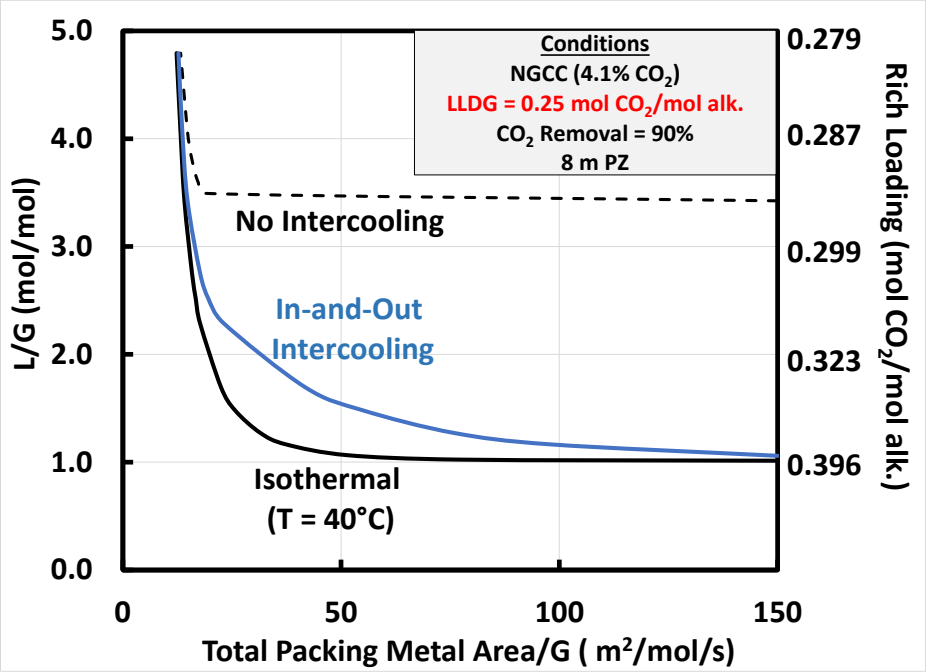

Figure E-4: Packing-solvent rate trade-off, NGCC flue gas (4.1 mol% CO_2), simple intercooling loading region (LLDG = 0.25 mol CO_2/mol alk.). Each curve (dashed = adiabatic, solid = isothermal, blue = intercooled) represents constant 90% CO_2 removal. Unique rich loading for each L/G is on secondary y-axis. The horizontal asymptote each curve reaches is L_{MIN}.

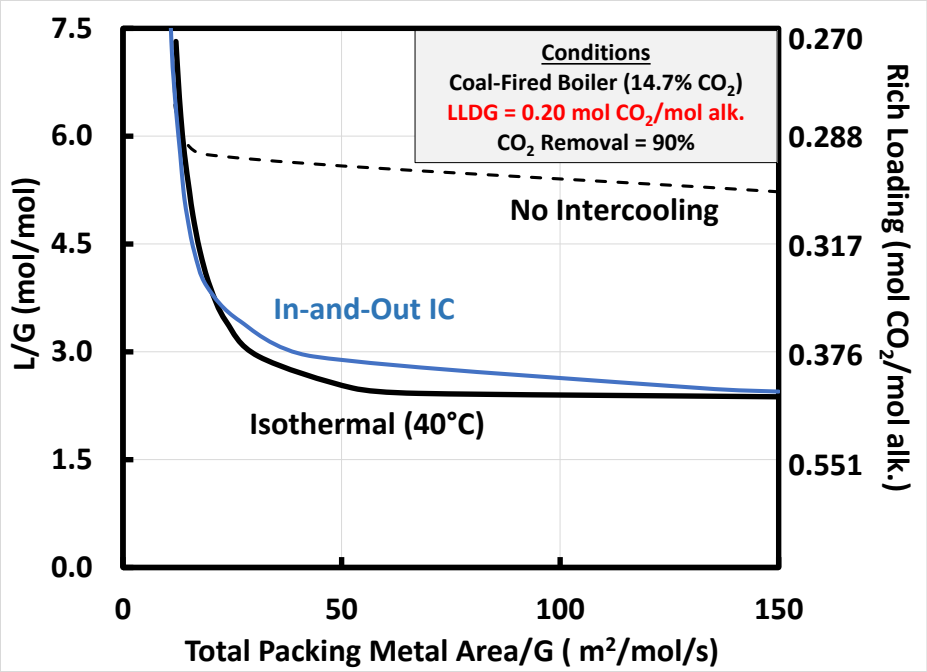

Figure E-5: Packing-solvent rate trade-off, coal-fired boiler flue gas (14.7 mol% CO_2), simple intercooling loading region (LLDG = 0.20 mol CO_2/mol alk.). Each curve (dashed = adiabatic, solid = isothermal, blue = intercooled) represents constant 90% CO_2 removal. Unique rich loading for each L/G is on secondary y-axis. The horizontal asymptote each curve reaches is L_{MIN}.

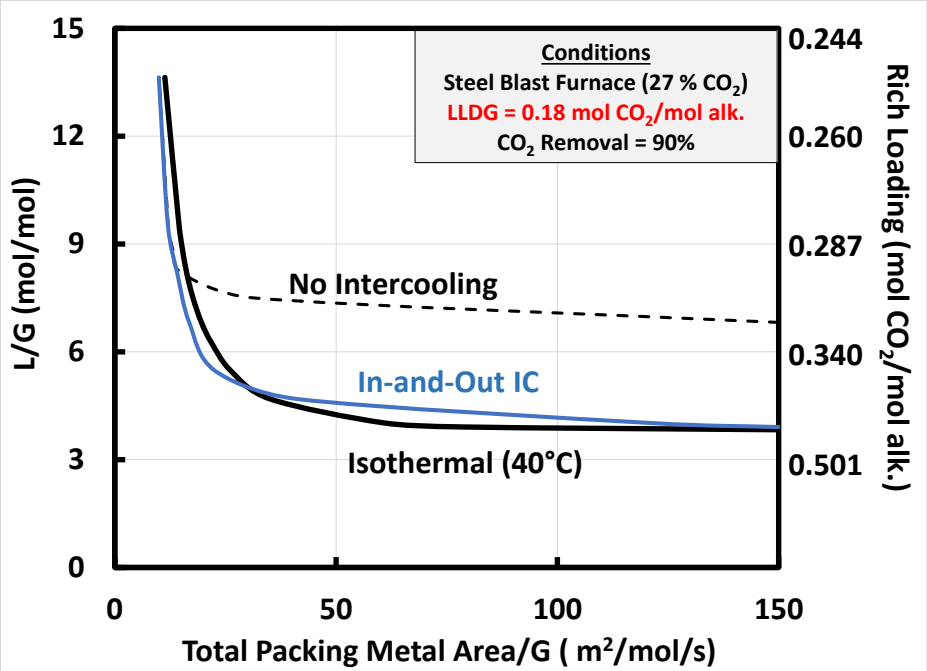

Figure E-6: Packing-solvent rate trade-off, steel blast furnace flue gas (27 mol% CO_2), simple intercooling loading region (LLDG = 0.18 mol CO_2/mol alk.). Each curve (dashed = adiabatic, solid = isothermal, blue = intercooled) represents constant 90% CO_2 removal. Unique rich loading for each L/G is on secondary y-axis. The horizontal asymptote each curve reaches is L_{MIN}.

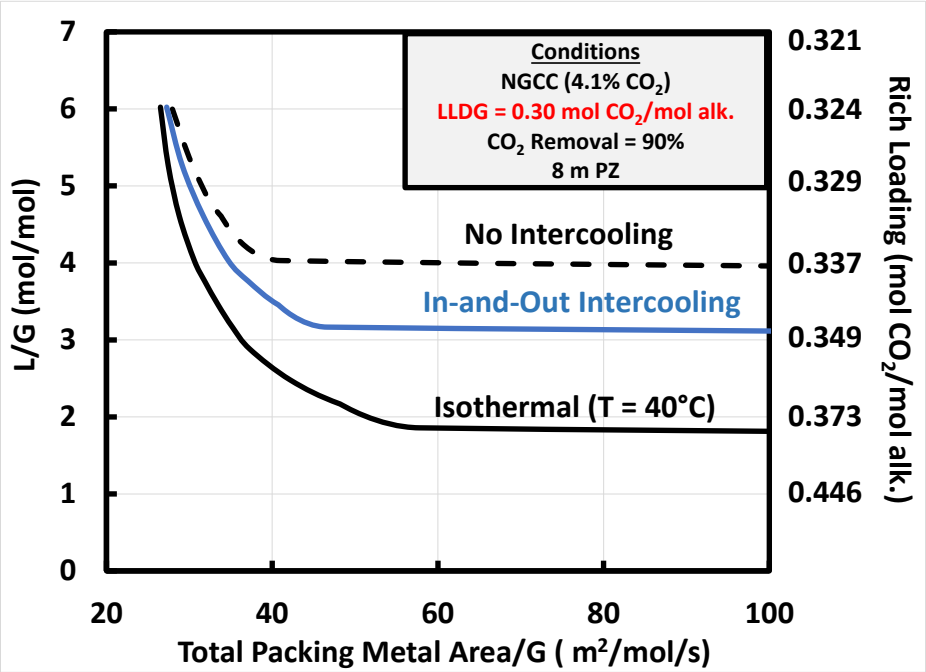

Figure E-7: Packing-solvent rate trade-off, NGCC flue gas (4.1 mol% CO_2), advanced intercooling loading region (LLDG = 0.30 mol CO_2/mol alk.). Each curve (dashed = adiabatic, solid = isothermal, blue = intercooled) represents constant 90% CO_2 removal. Unique rich loading for each L/G is on secondary y-axis. The horizontal asymptote each curve reaches is L_{MIN}.

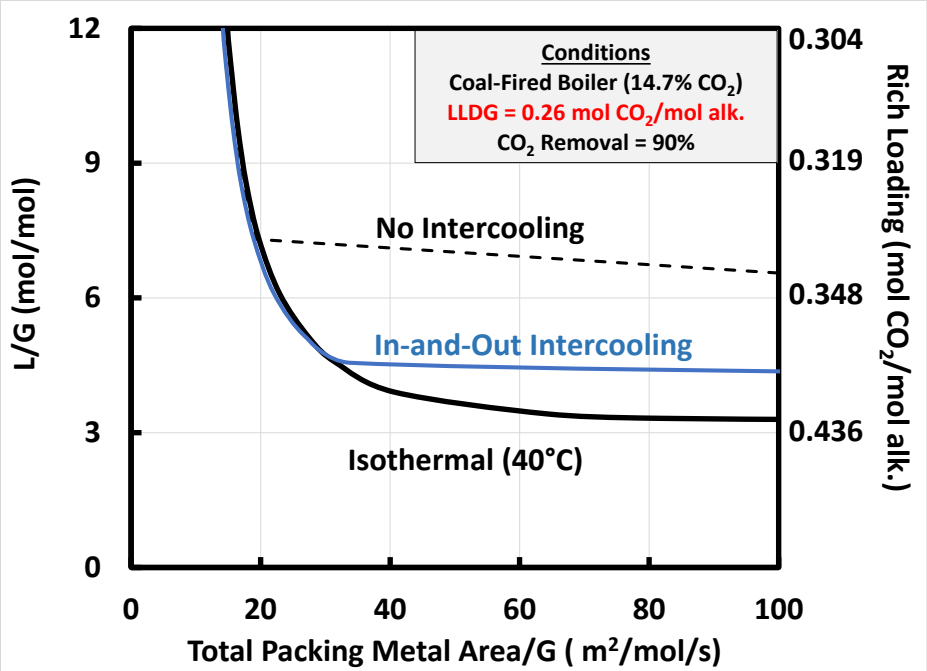

Figure E-8: Packing-solvent rate trade-off, coal-fired boiler flue gas (14.7 mol% CO_2), advanced intercooling loading region (LLDG = 0.26 mol CO_2/mol alk.). Each curve (dashed = adiabatic, solid = isothermal, blue = intercooled) represents constant 90% CO_2 removal. Unique rich loading for each L/G is on secondary y-axis. The horizontal asymptote each curve reaches is L_{MIN}.

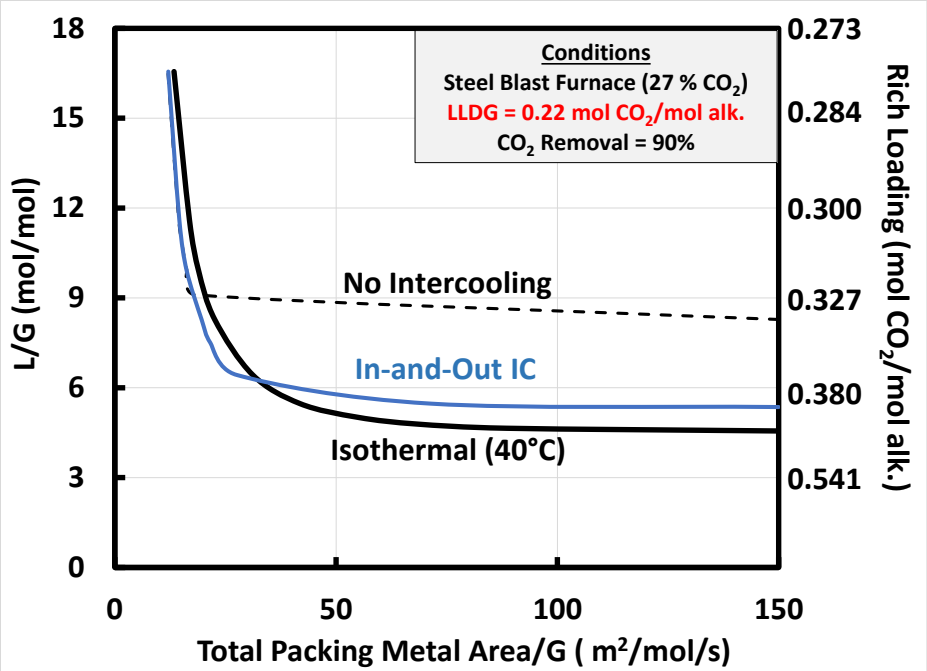

Figure E-9: Packing-solvent rate trade-off, steel blast furnace flue gas (27 mol% CO_2), advanced intercooling loading region (LLDG = 0.22 mol CO_2/mol alk.). Each curve (dashed = adiabatic, solid = isothermal, blue = intercooled) represents constant 90% CO_2 removal. Unique rich loading for each L/G is on secondary y-axis. The horizontal asymptote each curve reaches is L_{MIN}.

LARGE SOLVENT RATE LOADING RANGE

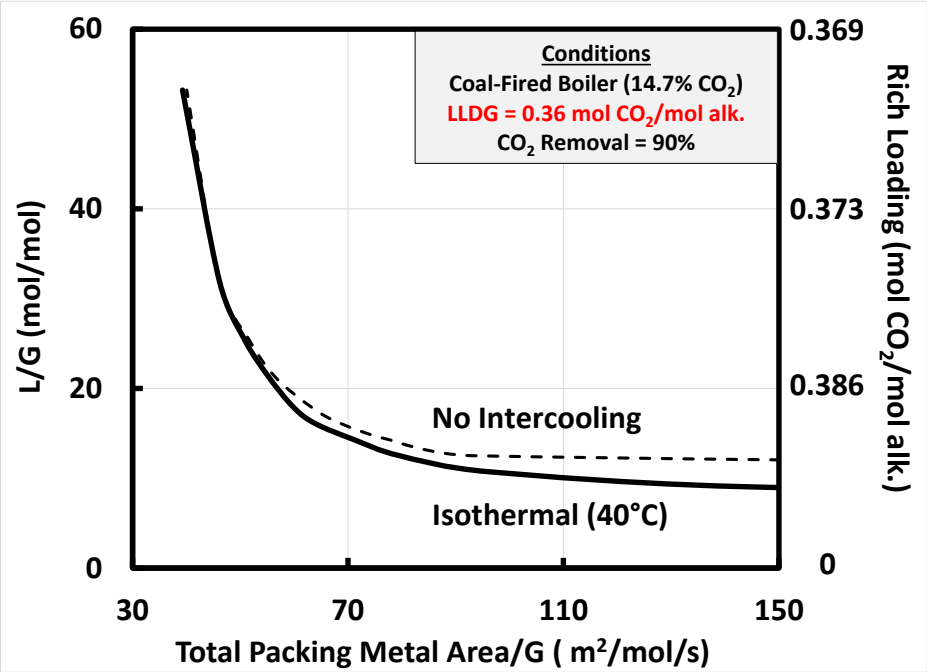

Figure E-10: Packing-solvent rate trade-off, coal-fired boiler flue gas (14.7 mol% CO_2), large solvent rate loading region (LLDG = 0.36 mol CO_2/mol alk.). Each curve (dashed = adiabatic, solid = isothermal) represents constant 90% CO_2 removal. Unique rich loading for each L/G is on secondary y-axis. The horizontal asymptote each curve reaches is L_{MIN}.

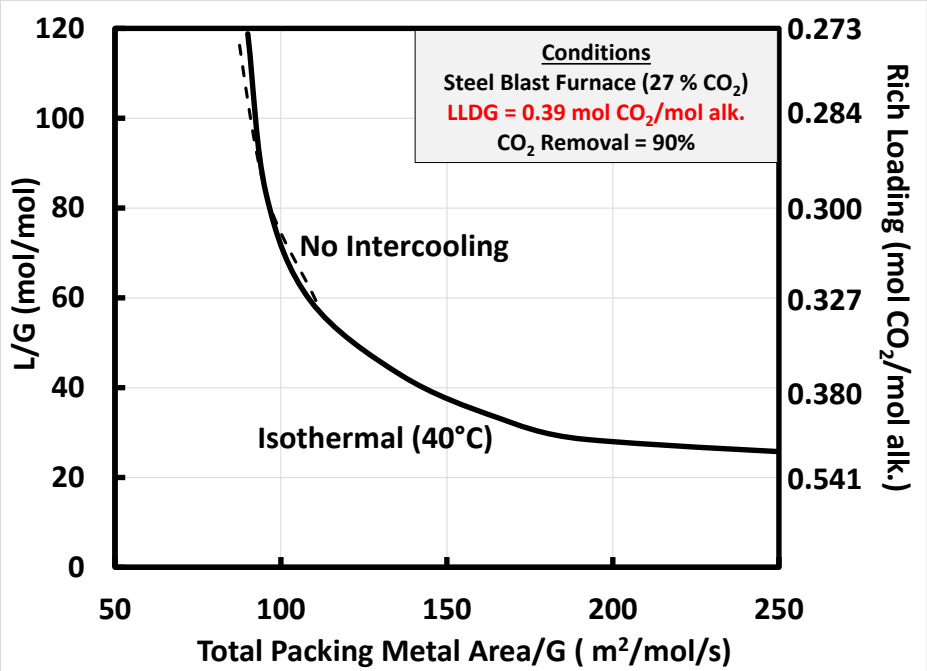

Figure E-11: Packing-solvent rate trade-off, steel blast furnace flue gas (27 mol% CO_2), large solvent rate loading region (LLDG = 0.39 mol CO_2/mol alk.). Each curve (dashed = adiabatic, solid = isothermal) represents constant 90% CO_2 removal. Unique rich loading for each L/G is on secondary y-axis. The horizontal asymptote each curve reaches is L_{MIN}.

Appendix F: TOTAL sponsored Natural Gas Power Plant Case Studies[7]

SUMMARY

During the past year, TOTAL sponsored a project through the Process Science and Technology Center (PSTC) to initiate a techno-economic analysis of amine scrubbing using 8 m piperazine (PZ) for CO_2 removal from flue gas from three natural gas-based applications. The applications and corresponding flue gas CO_2 concentrations are as follows: combined cycle (3% CO_2), combined cycle with exhaust gas recycle (6% CO_2), and natural gas-fired boiler (9% CO_2).

For each application, two bounding economic scenarios were evaluated: high capital and low operating cost (high cap-ex, low op-ex) or low capital and high operating cost (low cap-ex, high op-ex). Within the two major process areas (absorption and stripping), further equipment level design modifications were introduced into each economic scenario; in total, 10 designs were developed for detailed economic evaluation.

Key developments in absorber design included implementation of solvent recycle intercooling around multiple packed sections of the column. The solvent recycle design allows cooling of the gas in an intercooled section in addition to the expected solvent cooling. The high solvent rate per wetted perimeter also provides enhancement of mass transfer to counteract diminished driving forces in the column due to solvent recycle. Sensitivity analyses identified solvent recycle rates to minimize total packing requirements (capital costs) and maximize rich loadings (minimize energy requirement in the stripping section). In addition, the ability to cool gas with solvent allowed the implementation of designs without a direct contact cooler (DCC); a recycle section in the bottom of the column was shown to effectively cool the gas and replace the DCC unit.

[7] The report in this chart served as a deliverable to TOTAL as part of research sponsored through the Process Science and Technology Center at the University of Texas at Austin (Level B project). PI: Gary Rochelle, Authors: Darshan Sachde and Tarun Madan

In the stripping section, an inter-heated stripper was implemented with 5° LMTD for the main cross exchanger to represent a high cap-ex, low op-ex designs. In addition, a simple stripper with cold rich bypass and 5° LMTD for the main cross exchanger were implemented for the low cap-ex, high op-ex designs. For both equipment configurations analysis of the equivalent work requirements was conducted, including sensitivity analysis identifying a range of operable lean and rich loadings for the natural gas applications.

The following report includes analysis of the 10 design cases including detailed heat and material balance results, equipment specifications, and discussion of results.

INTRODUCTION AND PROCESS DESCRIPTION

Absorber and stripper models were developed for CO_2 capture from three natural gas applications with flue gas feed conditions summarized in Table F-1.

Table F-1: Natural Gas Capture Applications, Flue Gas Information

Case 2010-1A: Combined Gas Cycle Turbine		**Case 2010-1B: Combined Gas Cycle Turbine with EGR**		**Case 2010-2: Gas Boiler**	
Flow rate (kmol/h)	40,473	**Flow rate (kmol/h)**	24,172	**Flow rate (kmol/h)**	10,292
Flow rate (t/h)	1,161	**Flow rate (t/h)**	691	**Flow rate (t/h)**	284
T (°C)	121	**T (°C)**	121	**T (°C)**	136
P (kPag)	0	**P (kPag)**	0	**P (kPag)**	0
Composition (mol %)		**Composition (mol %)**		**Composition (mol %)**	
H_2O	6.51	H_2O	7.06	H_2O	18.78
CO_2	3.31	CO_2	6.18	CO_2	8.69
N_2	75.48	N_2	78.94	N_2	69.92
Ar	0.91	Ar	0.95	Ar	0.89
O_2	13.79	O_2	6.87	O_2	1.72

Within the three cases, designs were developed to represent two economic scenarios:

1) High capital cost, low operating cost design (High CapEx, Low OpEx) ***operating with 1.2 times the minimum solvent rate.***
2) Low capital cost, high operating cost design (Low CapEx, High OpEx) ***operating with 1.4 times the minimum solvent rate.***

The primary process parameter used to differentiate the economic scenarios was solvent circulation rate. The high cap-ex, low op-ex cases utilized a solvent rate of 1.2 times the minimum solvent rate required to achieve 90% CO_2 removal ($1.2*L_{min}$); the low cap-ex, high op-ex utilized a higher solvent rate of $1.4*L_{min}$.

In addition, for the first two cases, the water content in the flue gas stream (Table F-1) was low enough (no condensation of water during cooling to 40°C) to permit cooling of the gas in the absorber itself without a direct contact cooler (DCC) upstream of the absorber. Thus, designs were developed with and without a direct contact cooler for the first two flue gas sources.

All designs were developed for 90% CO_2 removal from the corresponding flue gas stream. A total of 10 process configurations were evaluated for the three cases; the list is summarized in Table F-2.

Table F-2: Summary of Design Scenarios Evaluated

Case 2010-1A	**Case 2010-1B**	**Case 2010-2**
High Cap EX, Low Op Ex with DCC	High Cap EX, Low Op Ex with DCC	High Cap EX, Low Op Ex with DCC
Low Cap EX, High Op Ex with DCC	Low Cap EX, High Op Ex with DCC	Low Cap EX, High Op Ex with DCC
High Cap EX, Low Op Ex NO DCC	High Cap EX, Low Op Ex NO DCC	
Low Cap EX, High Op Ex NO DCC	Low Cap EX, High Op Ex NO DCC	

The 10 designs can be represented by 4 flow sheets, presented in the subsequent sections accompanied by a description of the major process steps and design choices.

1. High CapEx, Low OpEx with Direct Contact Cooler

Applied to following cases:

- Case 2010-1A: Gas Turbine (3.3% CO_2)
- Case 2010-1B: Gas Turbine with EGR (6.2% CO_2)
- Case 2010-2: Gas-Fired Boiler (9% CO_2)

Figure F-1 presents the full process flow diagram for absorption and stripping of CO_2 for the high capital cost, low operating cost design utilizing a DCC.

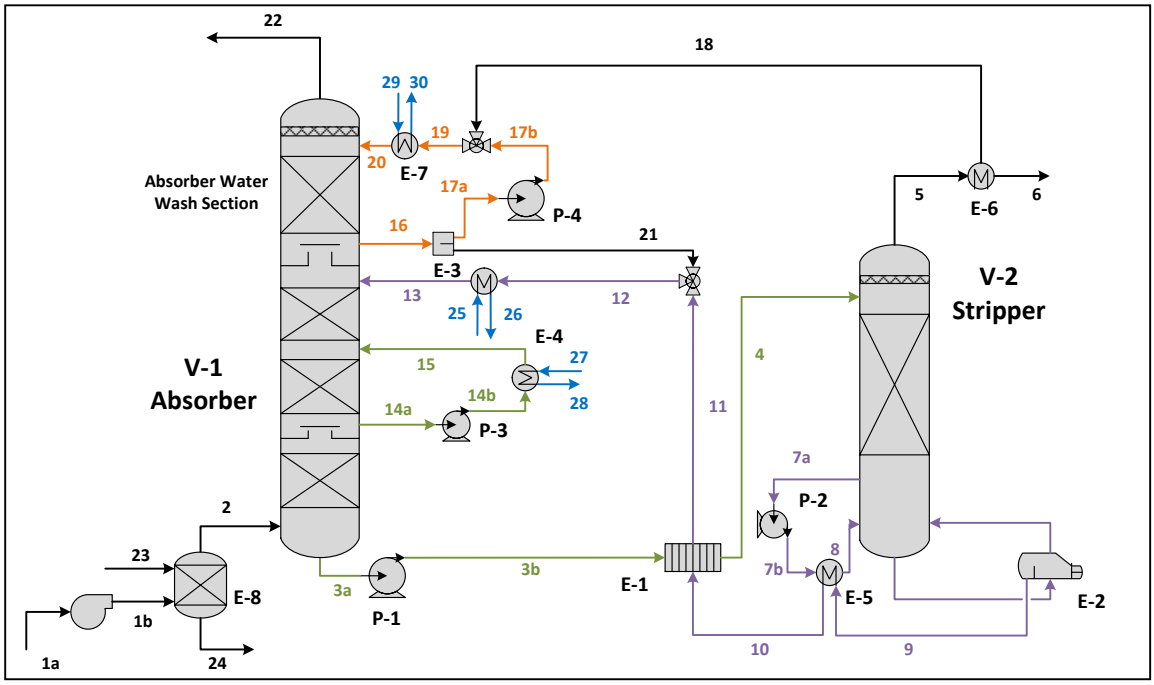

Figure F-1: Process Flow Diagram for the High Capital Cost, Low Operating Cost equipment configuration with a Direct Contact Cooler

Flue gas (1a) at atmospheric pressure is compressed by a blower to overcome pressure drop in the DCC, absorber, and water wash in downstream process steps. The hot, compressed flue gas (1b) is cooled by contact with cooling water in a DCC unit (E-8) to 40°C in all cases. The cooled gas (2) enters the absorber (V-1) and counter-currently contacts amine solvent in three packed sections within the column. The stripped or lean gas leaves the absorber beds and passes through a packed water wash bed (in the same

vessel, V-1) to remove volatile amine products by countercurrent contact with water. The stripped gas (22) is ultimately vented after passing through the wash portion of the column.

Lean amine solvent (13) enters the absorber at 40°C above the top absorber bed. At the bottom of the second (middle) bed of packing in the column, solvent is pumped out of the column and cooled to 40°C in a solvent inter-cooler. The solvent is returned to the top of the middle packed section. This ***solvent recycle with intercooling*** removes heat generated in the solvent by chemical reaction as the solvent is drawn-off and cooled and cools the gas as the solvent is recycled and contacts the gas through the well-mixed middle section of packing. A high rate of solvent is recycled to ensure cooling of the gas and maintain cool solvent through the recycle section. A rate of ***three times the solvent feed*** was withdrawn in the recycle loop in all designs in this analysis. The high solvent rates in the middle packed section lead to the implementation of coarse structured packing in this section to minimize pressure drop and avoid flooding constraints.

The amine solvent leaving the solvent recycle section contacts the gas in the bottom bed of the absorber and leaves the unit as rich solvent (3a). The rich amine is pumped through the main cross exchanger (E-1) where it is heated by hot, lean solvent (10) returning from the stripper. In the ***high capex, low opex designs, a 5°C LMTD was applied around the main cross exchanger (E-1).***

The hot, rich solvent (4) enters the stripper (V-2) where CO_2 is stripped in a single packed bed by heat provided by a steam reboiler (E-2). As the solvent leaves the packed section, it is removed from the column (7a) and passes through an ***interheater*** cross-exchanger (E-5) where it is heated by the rich solvent (9) leaving the reboiler. The "interheated stripper" configuration recovers additional heat from the reboiler via the rich stream leaving the reboiler and results in a cooler rich amine stream (4) reaching the

stripper since less heat is transferred in the main cross-exchanger (E-1) from the hot lean amine (10) to the cool rich amine (4). The cooler rich amine stream entering the stripper reduces the amount of water vapor lost per mole of CO_2 recovered and in turn reduces irreversible heat losses in the condenser.

After the hot lean amine stream passes through the interheater, it is cooled via the main cross exchanger (E-1) and the trim cooler (E-3) to 40°C for the absorption process.

The CO_2 rich gas (5) leaves the stripper and is cooled with water knockout in a condenser (E-6) before proceeding to a compressor (not depicted) to be compressed for end-use/disposal.

2. Low CapEx, High OpEx with Direct Contact Cooler

Applied to following cases:

- Case 2010-1A: Gas Turbine (3.3% CO_2)
- Case 2010-1B: Gas Turbine with EGR (6.2% CO_2)
- Case 2010-2: Gas-Fired Boiler (9% CO_2)

Figure F-2 presents the full process flow diagram for absorption and stripping of CO_2 for the low capital cost, high operating cost design utilizing a DCC.

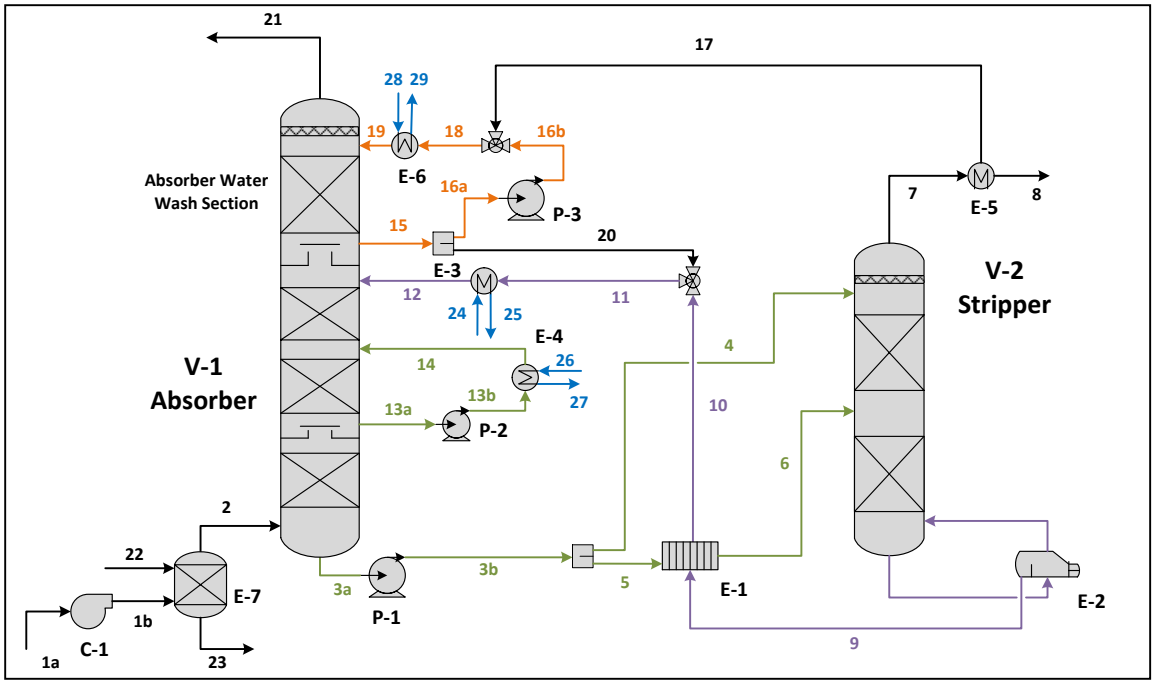

Figure F-2: Process Flow Diagram for the Low Capital Cost, High Operating Cost equipment configuration with a Direct Contact Cooler

The flow sheet for this design is identical to that of the high capex, low opex with DCC design (Figure F-1) with the exception that a **simple stripper (V-2) with cold rich bypass** is used instead of the interheated stripper. In this stripper design, the stripper consists of two packed sections. The cold rich amine stream (3b) leaving the absorber is split upstream of the main-cross exchanger (E-1). A fraction of the flow (4) bypasses the main exchanger and is sent to the top of the stripper. This cold solvent reduces the water lost per mole of CO_2 in the gas leaving the stripper (7). The remaining rich solvent from the absorber (5) passes through the main cross exchanger (E-1) and is heated by the hot, lean amine (9) leaving the stripper reboiler (E-2). In the ***low capex, high opex designs, a 10°C LMTD was applied around the main cross exchanger (E-1)*** to reduce capital costs

associated with the main exchanger. The heated rich amine stream (6) then enters above the second packed bed of the stripper.

All other parts of the flow sheet are identical to those described in section 1.

3. High CapEx, Low OpEx NO DCC

Applied to following cases:

- Case 2010-1A: Gas Turbine (3.3% CO_2)
- Case 2010-1B: Gas Turbine with EGR (6.2% CO_2)

Figure F-3 presents the full process flow diagram for absorption and stripping of CO_2 for the high capital cost, low operating cost design ***without a DCC***.

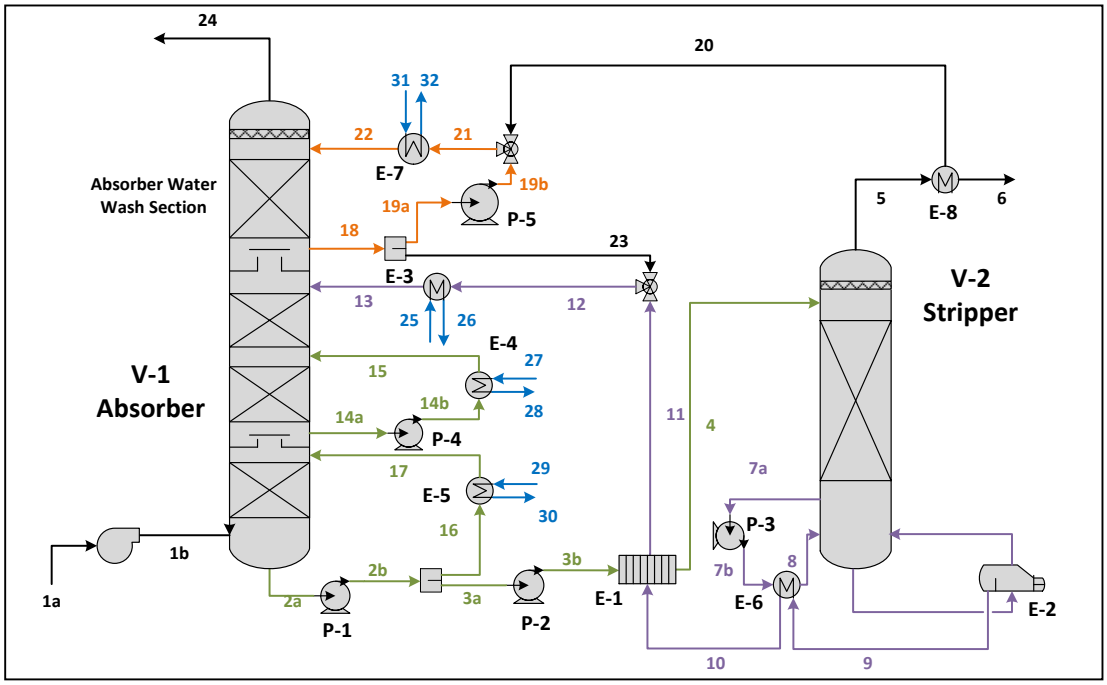

Figure F-3: Process Flow Diagram for the High Capital Cost, Low Operating Cost equipment configuration without a Direct Contact Cooler.

The flow sheet for this design is identical to that of the high capex, low opex design with DCC (Figure F-1) with the exception of the omission of a direct contact cooler and the recycle of solvent around the bottom packed bed of the column to couple the cooling effect of a direct contact cooler with absorption of CO_2 by the solvent. The gas leaving the blower and entering the absorber (1b) ***does not*** pass through a separate unit for gas cooling and instead enters the absorber hot (at approximately the temperature in Table F-1 for the corresponding gas source). In the Case 2010-1A and Case 2010-1B, the water content of the gas is below that of the saturation concentration of water at 40°C, so water condensation from the gas is not expected during cooling of the gas. This allows direct cooling of the flue gas by the solvent in the bottom packed bed of the absorber without adverse effects on solvent water balance. As in the recycle loop described in section 1, the solvent leaving the bottom of the packed bed (2a) is cooled to 40°C and is pumped back to the top of the bed. The solvent recycle rate is three times the feed solvent rate and requires coarse structured packing in the bottom packed bed to minimize pressure drop.

The process beyond the gas entering the absorber and bottom section of the absorber is identical to that described in section 1.

4. Low CapEx, High OpEx NO DCC

Applied to following cases:

- Case 2010-1A: Gas Turbine (3.3% CO_2)
- Case 2010-1B: Gas Turbine with EGR (6.2% CO_2)

Figure F-4 presents the full process flow diagram for absorption and stripping of CO_2 for the low capital cost, high operating cost design ***without a DCC***.

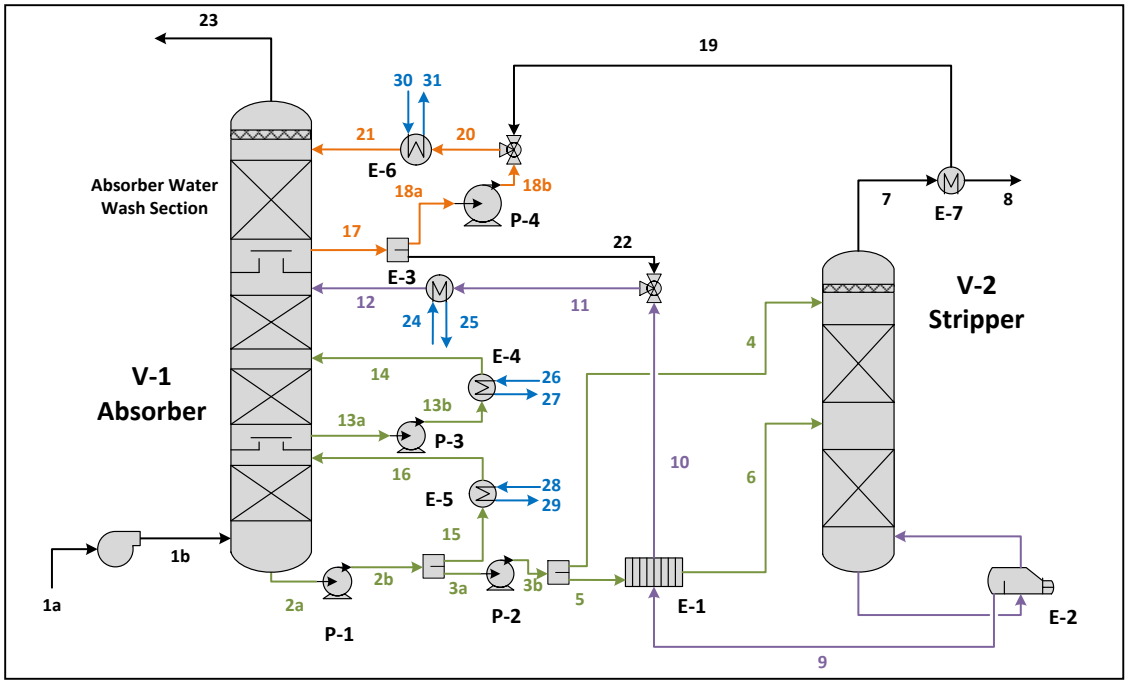

Figure F-4: Process Flow Diagram for the Low Capital Cost, High Operating Cost equipment configuration without a Direct Contact Cooler.

The flow sheet for this design is identical to that of the low capex, high opex design with DCC **(**Figure F-2) described in section 2 with the exception of the omission of a direct contact cooler and the recycle of solvent around the bottom packed bed of the column. The recycle section of in the bottom portion of the absorber (corresponding to the omission of the DCC) is identical to process described in section 3. Thus, no new design features were incorporated for this configuration and the preceding sections provide descriptions of all components of the flow sheet in Figure F-4.

Within the two major process areas (absorption and stripping), further equipment level design modifications were introduced into each economic scenario; the details of these designs are presented in the following sections by process area.

ABSORBER DESIGN

For cases 1 and 2, with hot, under-saturated flue gas streams, two equipment configurations were developed in parallel for the conditions described in Table F-1. The first design (no DCC) is depicted in the process flow diagram (PFD) in Figure F-5.

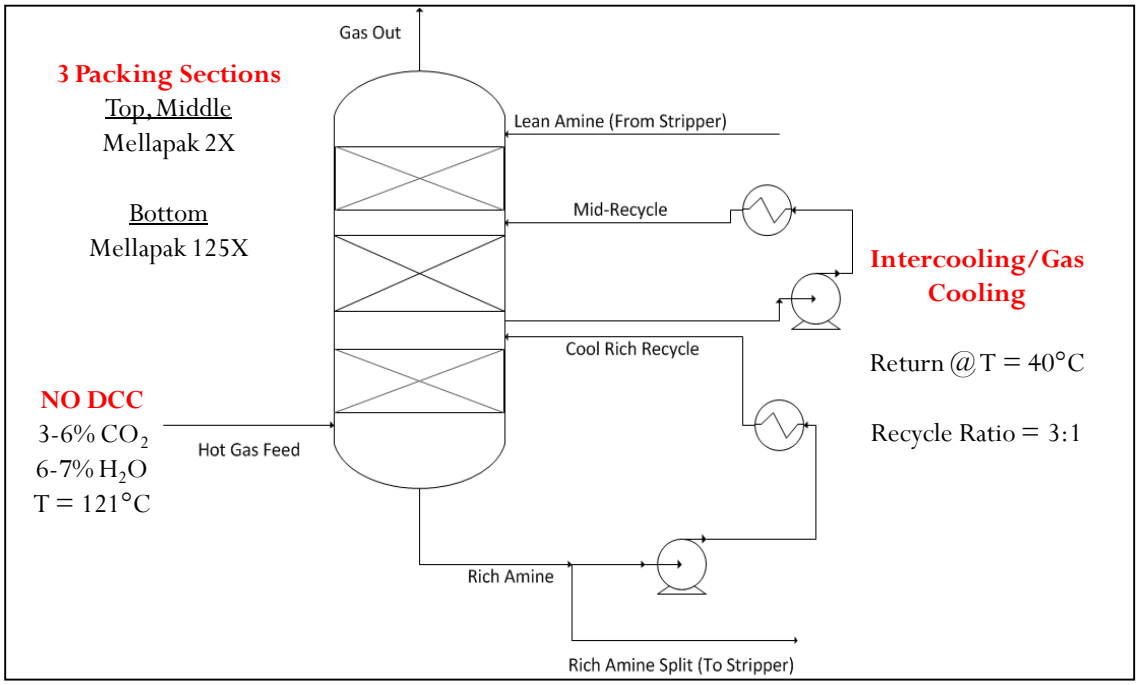

Figure F-5: Case 1 and 2 Absorber PFD, No DCC, Combined Cycle Gas Turbine.

The PFD highlights the novel design features for the combined cycle flue gas stream. The low water content in the gas feed allowed elimination of the DCC since water does not need to be removed from the gas during cooling. Instead, the gas is cooled with a rich amine recycle stream in the lower packed section of the column. This accomplishes the necessary cooling of the gas and allows for absorption of CO_2 during the cooling process. The recycle of solvent in the bottom packed section results in high pressure drop through this section; coarse structured packing was used in the bottom

section to minimize pressure drop. While the bottom intercooling loop serves the primary purpose of cooling the incoming gas, the middle intercooling loop is used to reduce temperature bulges. By using two loops for the two distinct purposes, back-mixing over the length of the column is reduced compared to one large intercooling loop performing both functions.

The second configuration (with a DCC) is shown in Figure F-6.

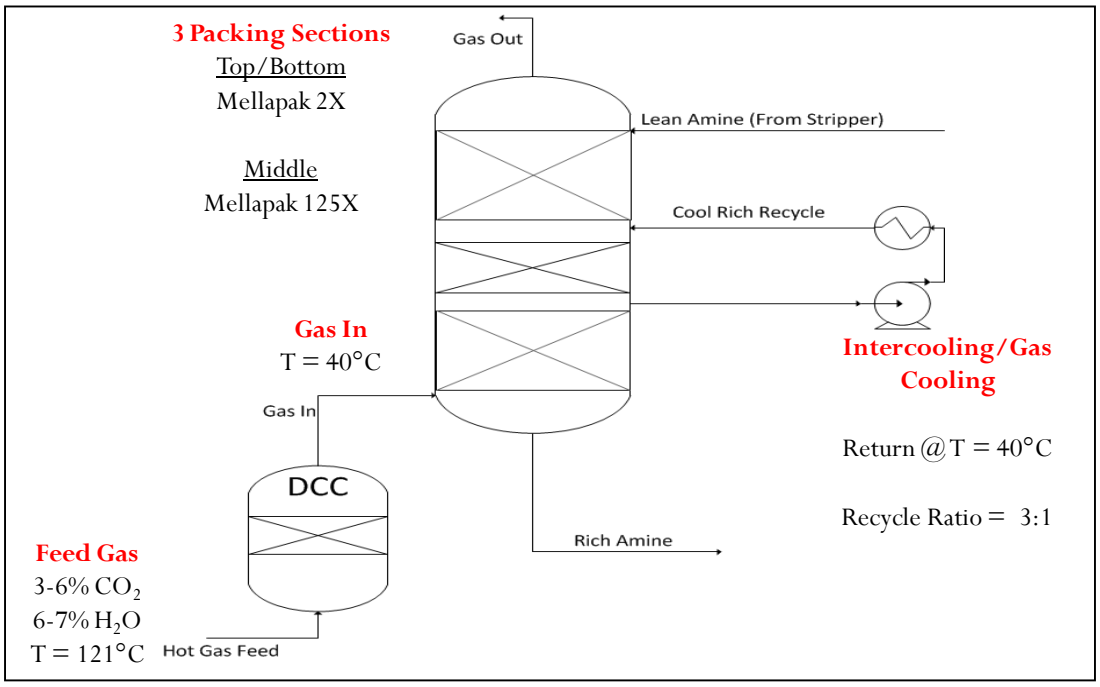

Figure F-6: Case 1, 2 and 3 Absorber PFD with DCC

The absorber configuration is modified to account for the cool gas entering the column; amine recycle is no longer required in the bottom section of the column. Instead, the recycle is placed in the middle of the column to intercool the solvent. Due to the high gas flow rate in the natural gas application (and corresponding low L/G), the

recycle is important to ensure cooling of the gas as well as the liquid in a well-mixed intercooling section.

The third case (gas-fired boiler) cannot omit the DCC due to the high water content in the flue gas stream. Therefore, the PFD for the third case will mirror the combined cycle DCC case (Figure F-6).

Optimization Procedure

The equipment configurations described in the previous section were optimized to minimize total interfacial area of the packing (in lieu of packing height since different packing types were used in different sections of the column) and maximize rich loading (or minimize energy requirements in the stripping section). Variables considered in the optimization process included amine feed flow rate, recycle ratio, and packing height in and out of the recycle section.

Amine Feed Flow Rate

The base case design amine feed flow rate was set at 1.2 times the minimum amine flow rate in an attempt to minimize column height without significant compromise in rich loading; this design flow rate was used in the recycle ratio and packing split optimization. To validate the flow rate assumption, a sensitivity analysis was performed on the amine feed rate with results summarized in Figure F-7.

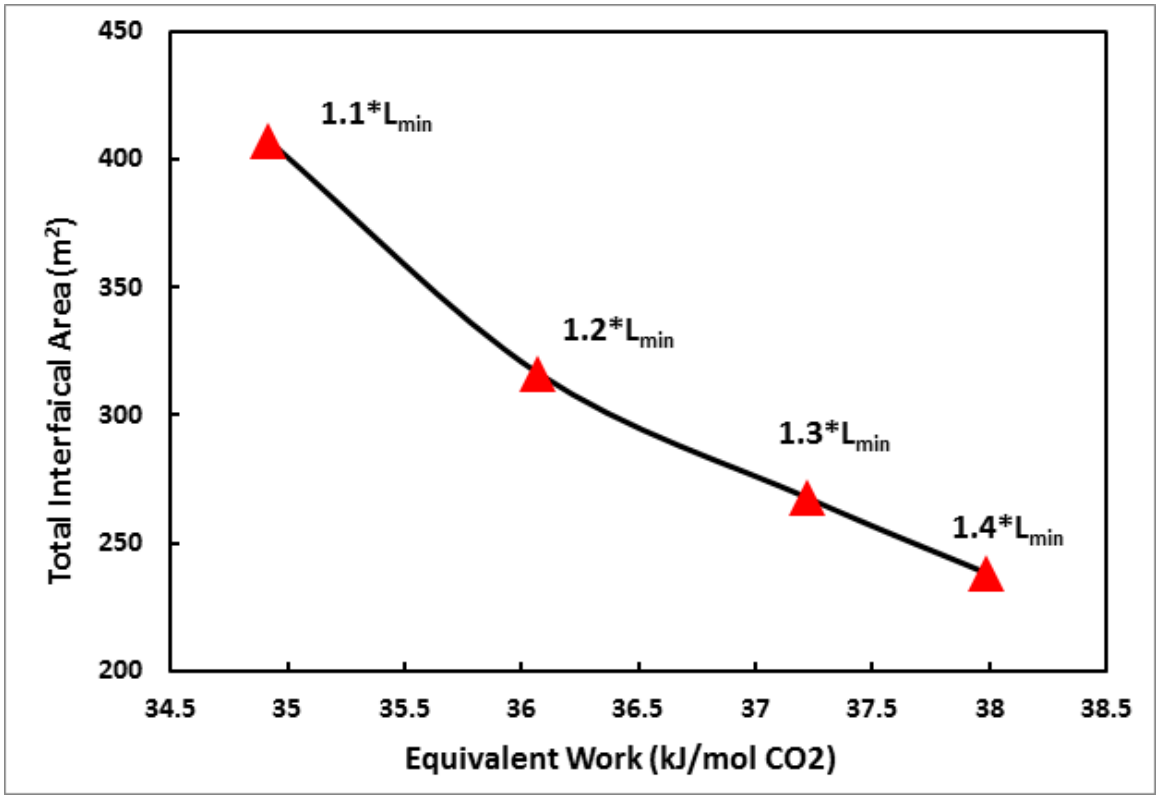

Figure F-7: Total interfacial area and equivalent work as a function of the feed amine flow rate (X*minimum liquid flow rate). Lean Loading = 0.25 mols CO_2/mols alkalinity, 90% CO_2 removal, 3:1 recycle ratio, optimum packing split at each point. Equivalent work extrapolated from stripping analysis by Madan.

As the liquid rate increases, the packing requirement drops monotonically as expected, but the incremental benefit diminishes (22% decrease from 1.1 to 1.2*L_{min}, 24% decrease from 1.2 to 1.4*L_{min}). In contrast, the energy penalty increases nearly linearly with increasing liquid flow rate (3.3% from 1.1 to 1.2*L_{min} and 5.3% from 1.2 to 1.4*L_{min}). Thus, 1.2*L_{min} is near a change in slope (steep to flat) for the range of conditions depicted in Figure F-7 and is a reasonable approximation of a point of diminishing returns on increasing amine flow rate.

Recycle Ratio and Packing Split

The recycle ratio (recycle flow rate/amine feed flow rate) was optimized concurrently with the packing split (packing in the recycle outside the recycle section to packing in the recycle section). Each recycle ratio has a unique optimal packing split since a trade-off exists between cooling of the solvent and diminished driving force due to mixing of solvent through a large section of the column. In addition, for each recycle rate, the process was operated at 1.2 times the minimum amine flow rate required for 90% removal for the given configuration. The result of the optimization for the non-DCC configuration is summarized in Figure F-8.

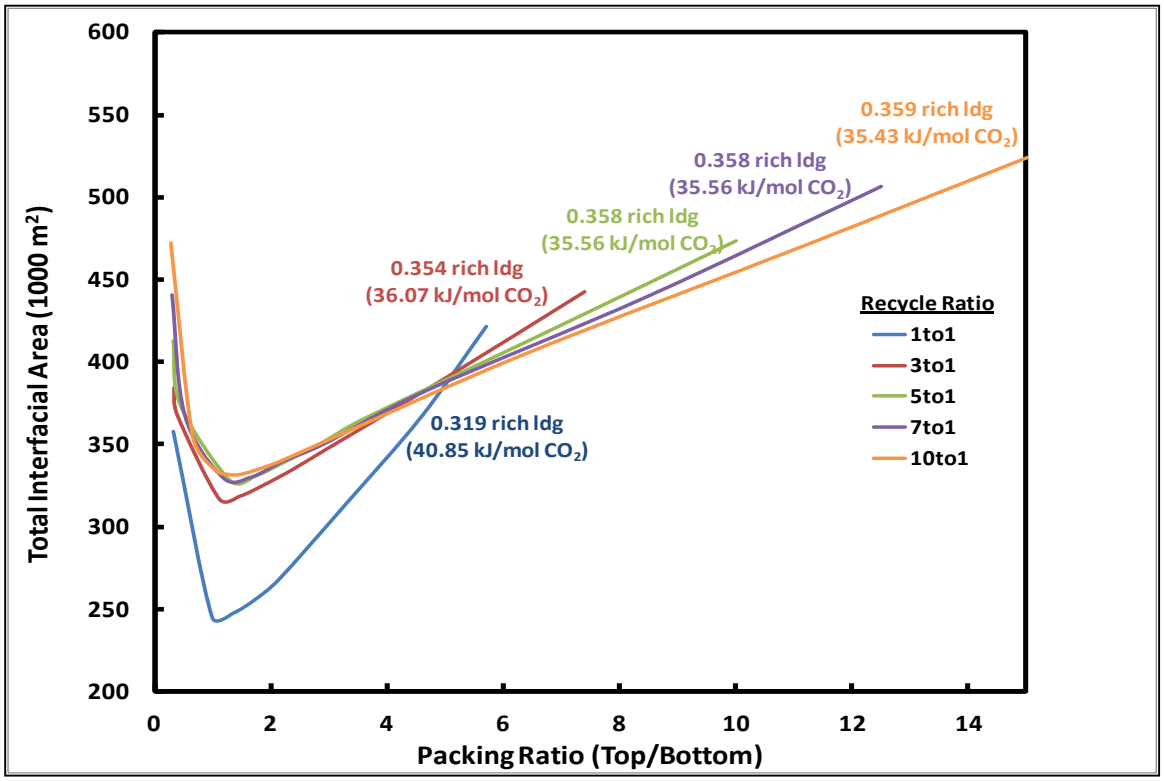

Figure F-8: Recycle Ratio and packing split optimization, no DCC. Lean Loading = 0.25 mols CO_2/mols alkalinity, 90% CO_2 removal, L = 1.2*L_{min}. Equivalent work extrapolated from stripping analysis

As the figure shows, the 1:1 recycle provides the clear minimum in packing interfacial area (29% less than 3:1 recycle), but also imposes the most severe energy penalty (13% higher equivalent work requirement than 3:1 recycle). From a ratio of 3:1 to a ratio of 10:1, very little change occurs in optimum conditions; total interfacial area varies by less than 5% and equivalent work by less than 2%. Therefore, the 3:1 recycle ratio was selected as an operating point that best balanced energy and packing benefits of solvent recycle while limiting the solvent recycle rate (increased pumping and capital costs in the intercooling loop). For the DCC design, a detailed optimization for the recycle rate, as in Figure F-8, was not performed, but sensitivity analysis of recycle ratio showed similar behavior to that of Figure F-8. Therefore, 3:1 recycle was selected as an optimal design condition for the DCC configuration as well.

With a 3:1 recycle rate and a solvent operating point of 1.2 times the minimum solvent rate fixed, the packing distribution (amount of each packing in each section) was optimized to minimize the total packing requirement for each of the 10 design cases. The packing distribution optimization was incorporated into the Aspen Plus® simulation as an objective function of the following form:

$$\boldsymbol{Min}\left[\boldsymbol{A_{Cross-Section}} * \left(\boldsymbol{a_{p,top}} * \boldsymbol{h_{top}} + \boldsymbol{a_{p,middle}} * \boldsymbol{h_{middle}} + \boldsymbol{a_{p,middle}} * \boldsymbol{h_{middle}}\right)\right] \quad \text{(F.1)}$$
$$\boldsymbol{Subject\ to}: \boldsymbol{Max\ Flood} \leq \mathbf{70\%}, \boldsymbol{CO_2 Removal} = \mathbf{90\%}$$

Where:

a_p = Specific area of packing (m^2/m^3);

$h_{section}$ = Specific area of packing (m^2/m^3);

$A_{Cross\text{-}Section}$= Cross-sectional area of column (m^2)

ABSORBER RESULTS

Results for each of the three cases (and corresponding economic scenarios) are summarized in Table F-3 through F-5.

.

Table F-3: Absorber Design Results, Natural Gas Applications Case 1

	Case 1: NGCC, 3% CO_2			
	No DCC		DCC	
	High CapEx Low OpEx	Low CapEx High OpEx	High CapEx Low OpEx	Low CapEx High OpEx
Lean Loading (mols CO_2/mols alkalinity)	**0.25**	**0.25**	**0.25**	**0.25**
L/G (mol/mol)	**1.13**	**1.32**	**1.11**	**1.29**
L*LMIN	**1.2**	**1.4**	**1.2**	**1.4**
Rich Loading (mols CO_2/mols alkalinity)	**0.355**	**0.340**	**0.358**	**0.343**
Total Packing Height (m)	**14.6**	**10.7**	**17.5**	**13.1**
Top	6.4	3.8	6.6	4.3
Middle	3.3	2.8	5.7	5.1
Bottom	5.0	4.1	5.0	3.6
Recycle Ratio/Location	3:1 Bottom	3:1 Bottom	3:1 Middle	3:1 Middle
Column Diameter (m) (@70% of flood)	**11.8**	**12.1**	**10.8**	**11.1**
Total Interfacial Area (m^2)	**285,688**	**212,547**	**289,121**	**217,548**

Table F-4: Absorber Design Results, Natural Gas Applications Case 2

	Case 2: NGCC with EGR, 6% CO_2			
	No DCC		DCC	
	High CapEx Low OpEx	Low CapEx High OpEx	High CapEx Low OpEx	Low CapEx High OpEx
Lean Loading (mols CO_2/mols alkalinity)	**0.25**	**0.25**	**0.25**	**0.25**
L/G (mol/mol)	**1.74**	**2.03**	**1.77**	**2.06**
L*LMIN	**1.2**	**1.4**	**1.2**	**1.4**
Rich Loading (mols CO_2/mols alkalinity)	**0.378**	**0.360**	**0.376**	**0.358**
Total Packing Height (m)	**12.3**	**8.7**	**14.7**	**10.7**
Top	4.4	2.8	5.5	3.5
Middle	3.1	2.4	6.1	4.9
Bottom	4.9	3.6	3.2	2.3
Recycle Ratio/Location	3:1 Bottom	3:1 Bottom	3:1 Middle	3:1 Middle
Column Diameter (m) (70% of flood)	**9.7**	**9.9**	**8.9**	**9.1**
Total Interfacial Area (m^2)	**157,818**	**115,342**	**158,195**	**115,747**

Table F-5: Absorber Design Results, Natural Gas Applications Case 3

	Case 3: Gas Boiler, 10% CO2	
	DCC	
	High CapEx Low OpEx	Low CapEx High OpEx
Lean Loading (mols CO_2/mols alkalinity)	0.27	0.27
L/G (mol/mol)	2.97	3.55
L*LMIN	1.2	1.4
Rich Loading (mols CO_2/mols alkalinity)	0.391	0.371
Total Packing Height (m)	14.9	10.4
Top	4.3	3.3
Middle	8.0	5.2
Bottom	2.6	1.8
Recycle Ratio/Location	3:1 Middle	2:1 Middle
Column Diameter (m) (70% of flood)	5.9	5.8
Total Interfacial Area (m^2)	65,582	44,495

In Cases 1 and 2, the design without the DCC provides comparable energy performance (interpreted via rich loading) and similar packing requirement in the absorber to the cases utilizing the DCC; when considering the additional packing

requirement and cost associated with the DCC itself, omitting the DCC becomes an attractive design option for the NGCC cases. The final case (Table F-5) has notable differences from the NGCC cases. The higher flue gas CO_2 content reduces the packing requirement and allows for a higher lean loading to be utilized in the design (0.27). In addition, the lower gas rate (higher L/G) reduces the need to cool the gas and in the high liquid rate case ($1.4*L_{min}$) allowed for a lower recycle ratio (2:1) than the other cases.

Figures F-9 through F-11 provide representative temperature and mass transfer profiles for the different design cases and equipment configurations.

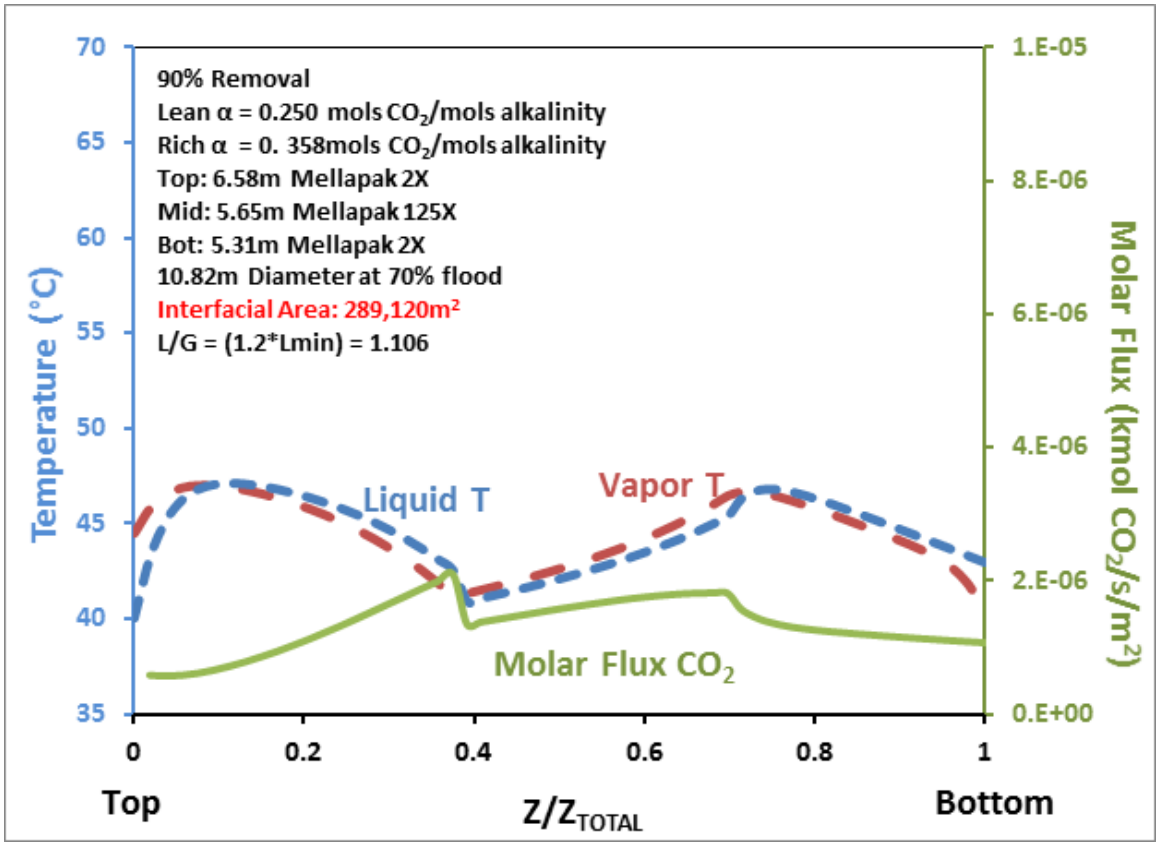

Figure F-9: Molar Flux and temperature profiles, Case 1 (3%CO_2) with DCC. Lean loading = 0.25 mols CO_2/mols alkalinity, lean amine T = 40 °C, rich gas T = 40 °C, 3:1 recycle.

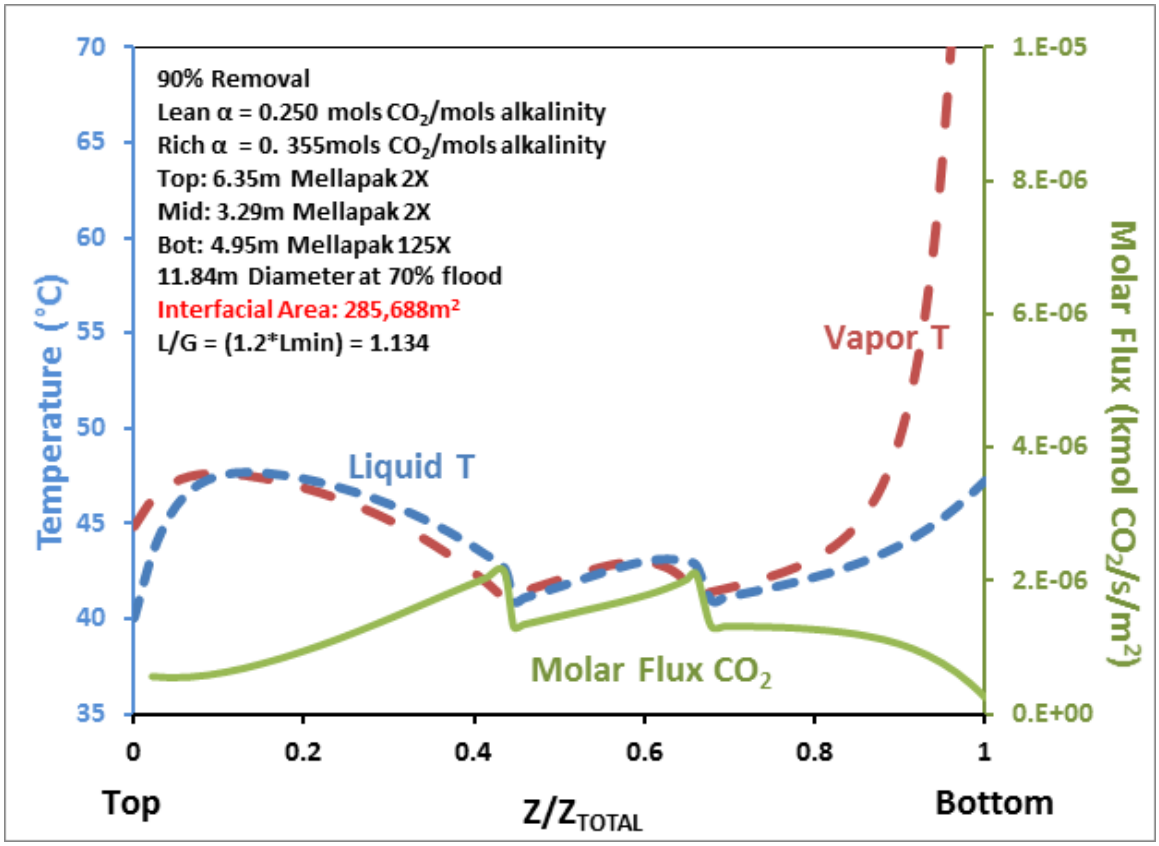

Figure F-10: Molar Flux and temperature profiles, Case 1 (3%CO_2) without DCC. Lean loading = 0.25 mols CO_2/mols alkalinity, lean amine T = 40 °C, rich gas T = 121 °C, 3:1 recycle.

Figures F-9 and F-10 provide a comparison between designs with and without the DCC (3% CO_2 case shown – similar to 6% case). The profiles illustrate the reasons the case without a DCC can closely replicate the performance of a column with the DCC. The recycle in the bottom of the column (Figure F-10) effectively cools the inlet gas (reduces gas temperature to 42°C). Combined with a smaller middle intercooled section, the column without a DCC is able to create a relatively uniform temperature profile throughout the bottom half of the column. Both designs (Figures F-9 and F-10) exhibit similar performance in the top of the column where temperature bulges still exist for the

columns. This area may be a potential area for future performance improvement in the low CO_2 designs.

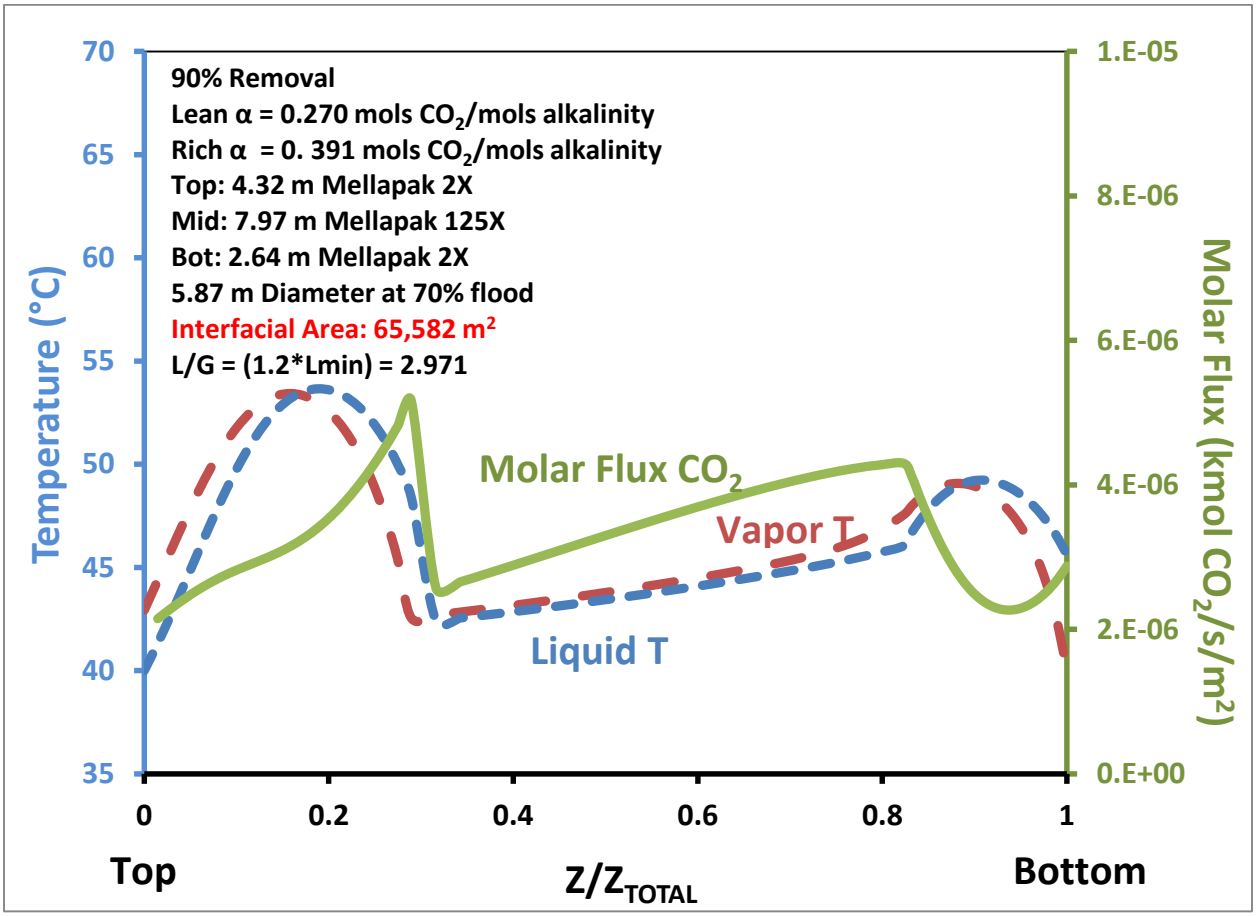

Figure F-11: Molar Flux and temperature profiles, Case 3 (10%CO_2) with DCC. Lean loading = 0.25 mols CO_2/mols alkalinity, lean amine T = 40 °C, rich gas T = 121 °C, 3:1 recycle.

Finally, Figure F-11 provides a representative profile for case 3 (10% CO_2). This case can be compared to Figure F-9 as both cases utilize a DCC and recycle intercooling in the middle of the column. The higher CO_2 concentration in the case 3 leads to an optimal design with a larger middle intercooling section; the large driving forces in the

bottom of the column lead to rapid temperature increases which limit mass transfer performance of the column. The top of the column in Figure F-11 exhibits a temperature bulge as in the lower CO_2 cases, but as with the bottom of the column, the bulge is developed more rapidly and is more severe. This leads to a relatively small top section of the column (and larger intercooled middle section). This final case illustrates that a single-intercooled section may not be versatile enough to address temperature-related performance limitations for high CO_2 cases.

STRIPPER DESIGN

Two stripper configurations corresponding to a high capex case of interheated stripper with 5 °C LMTD cross-exchanger and a low capex case of simple stripper with cold rich bypass and 10 °C LMTD were studied. Other common specifications for modeling these configurations are as follows:

1. Packing – Mellapak Standard 250X
2. Thermodynamic Model – Fawkes Model developed in-house
3. Pump efficiency – 0.72
4. Heater Temperature – 150 °C.

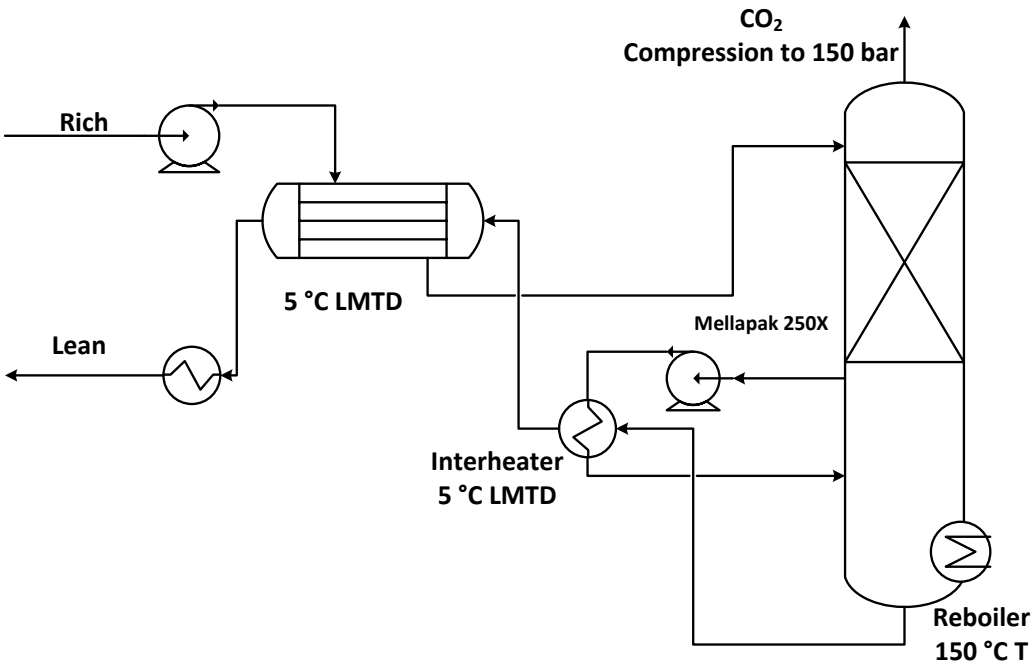

Figure F-12: High capex configuration of interheated stripper and 5 °C LMTD cross-exchanger

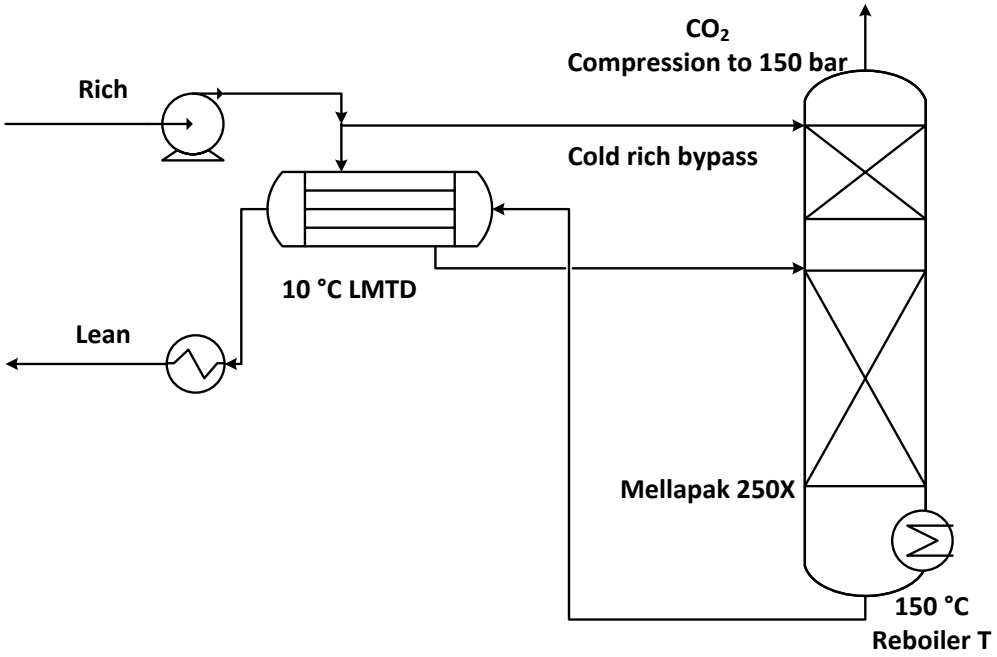

Figure F-13: Low capex configuration of simple stripper with cold rich bypass and 10 °C LMTD cross-exchanger

The configuration was optimized for equivalent work by varying the lean loading (high capex case) and lean loading and cold rich bypass (low capex case).

Tables F-6 through F-8 shows the design value of lean and rich loading achieved in the absorber modeling, along with the corresponding values of equivalent work in the high and low capex cases.

Table F-6: Equivalent work for high and low capex cases for 3% CO_2 (8 m PZ, high capex case of interheated stripper with 5 °C LMTD cross-exchanger, low capex case of simple stripper with cold rich bypass and 10 °C LMTD)

		Without DCC		With DCC	
		High capex Low opex	**Low capex High opex**	**High capex Low opex**	**Low capex High opex**
Rich ldg	mol/mol alk	0.355	0.34	0.358	0.343
Lean ldg	mol/mol alk	0.25	0.25	0.25	0.25
Equivalent Work (compression to 150 bar)	kJ/mol CO_2	35.2	40.9	34.9	40.5*

* optimum cold rich bypass of 6%

Table F-7: Equivalent work for high and low capex cases for 6% CO_2 (8 m PZ, high capex case of interheated stripper with 5 °C LMTD cross-exchanger, low capex case of simple stripper with cold rich bypass and 10 °C LMTD)

		Without DCC		With DCC	
		High capex Low opex	**Low capex High opex**	**High capex Low opex**	**Low capex High opex**
Rich ldg	mol/mol alk	0.378	0.360	0.376	0.358
Lean ldg	mol/mol alk	0.25	0.25	0.25	0.25
Equivalent Work (compression to 150 bar)	kJ/mol CO_2	33.1	38.3*	33.3	38.5*

* optimum cold rich bypass of 8%

Table F-8: Equivalent work for high and low capex cases for 9% CO_2 (8 m PZ, high capex case of interheated stripper with 5 °C LMTD cross-exchanger, low capex case of simple stripper with cold rich bypass and 10 °C LMTD)

		With DCC	
		High capex Low opex	**Low capex High opex**
Rich ldg	mol/mol alk	0.391	0.371
Lean ldg	mol/mol alk	0.27	0.27
Equivalent Work (compression to 150 bar)	kJ/mol CO_2	31.6	37.6*

* optimum cold rich bypass of 6%

COMBINED RESULTS

Packing and energy requirements are summarized in Figures F-14 through F-16 for each of the applications, economic scenarios and designs with and without the DCC where relevant.

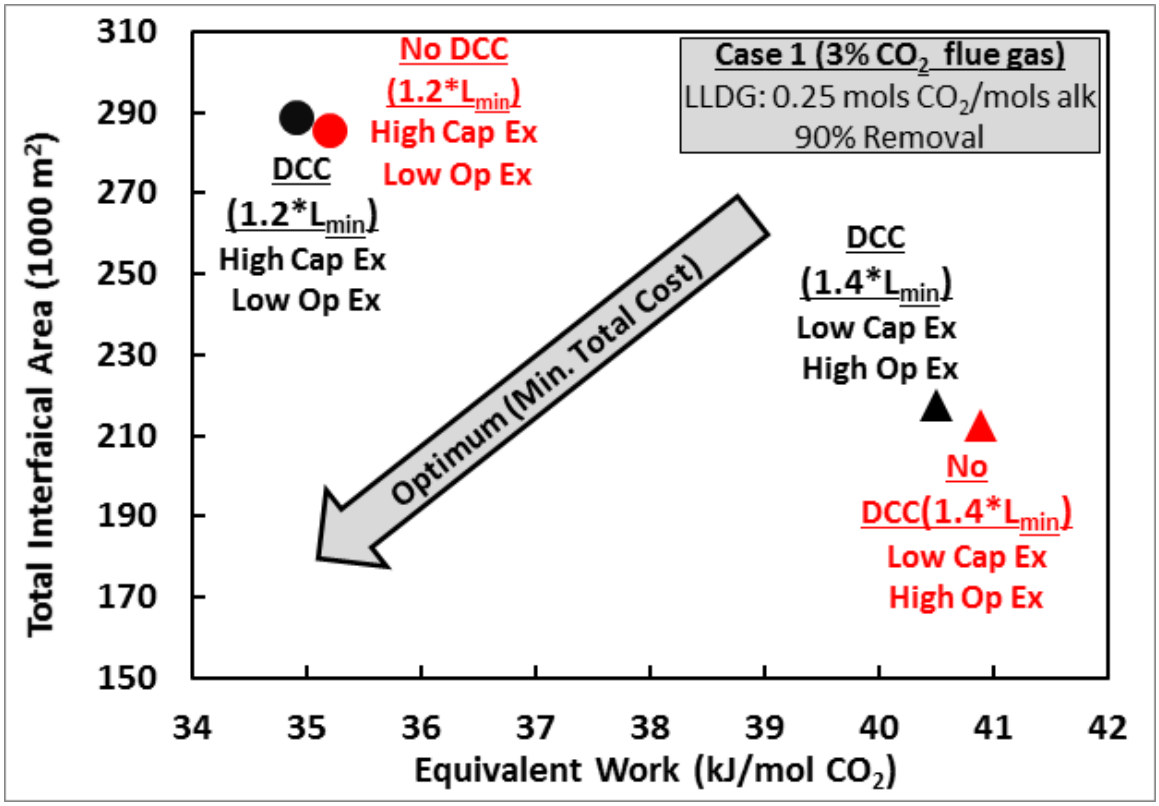

Figure F-14: Capital and operating cost trade-offs in final designs for Case 1 (3% CO_2). Lean loading = 0.25 mols CO_2/mols alkalinity, 90% CO_2 removal, 3:1 recycle ratio, optimum packing split at each point.

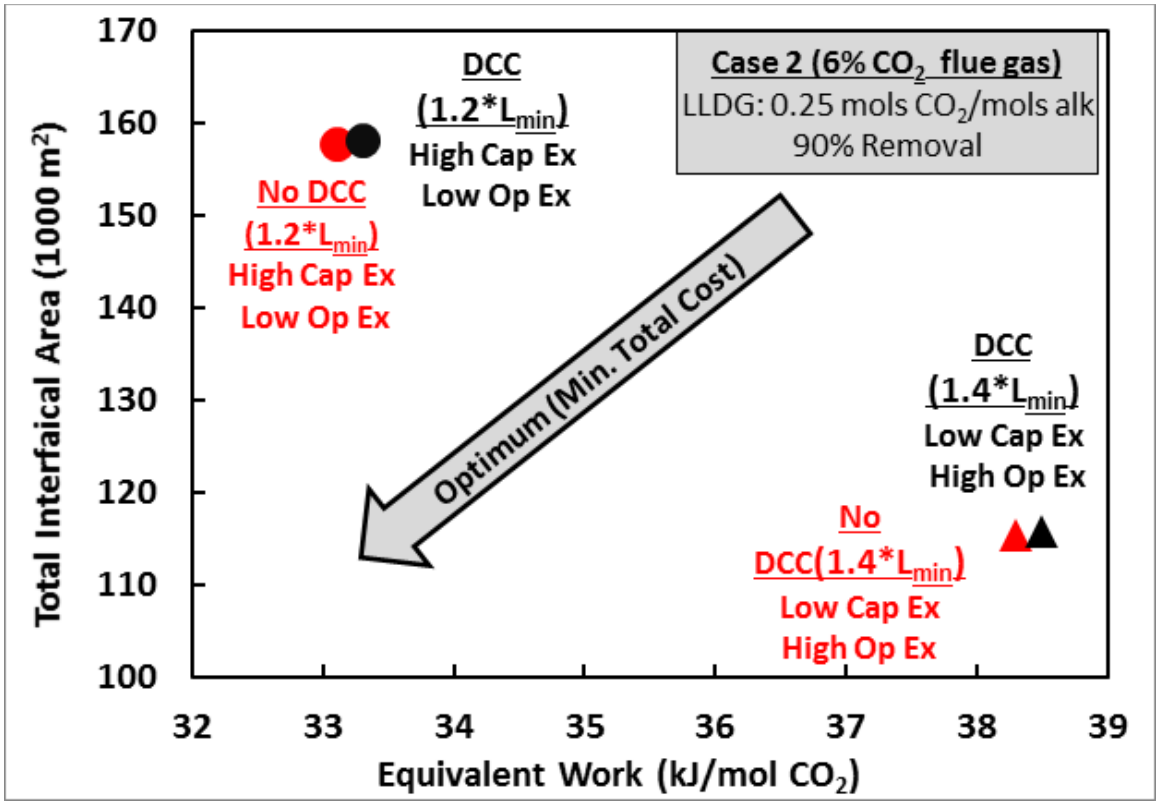

Figure F-15: Capital and operating cost trade-offs in final designs for Case 2 (6% CO_2). . Lean loading = 0.25 mols CO_2/mols alkalinity, 90% CO_2 removal, 3:1 recycle ratio, optimum packing split at each point.

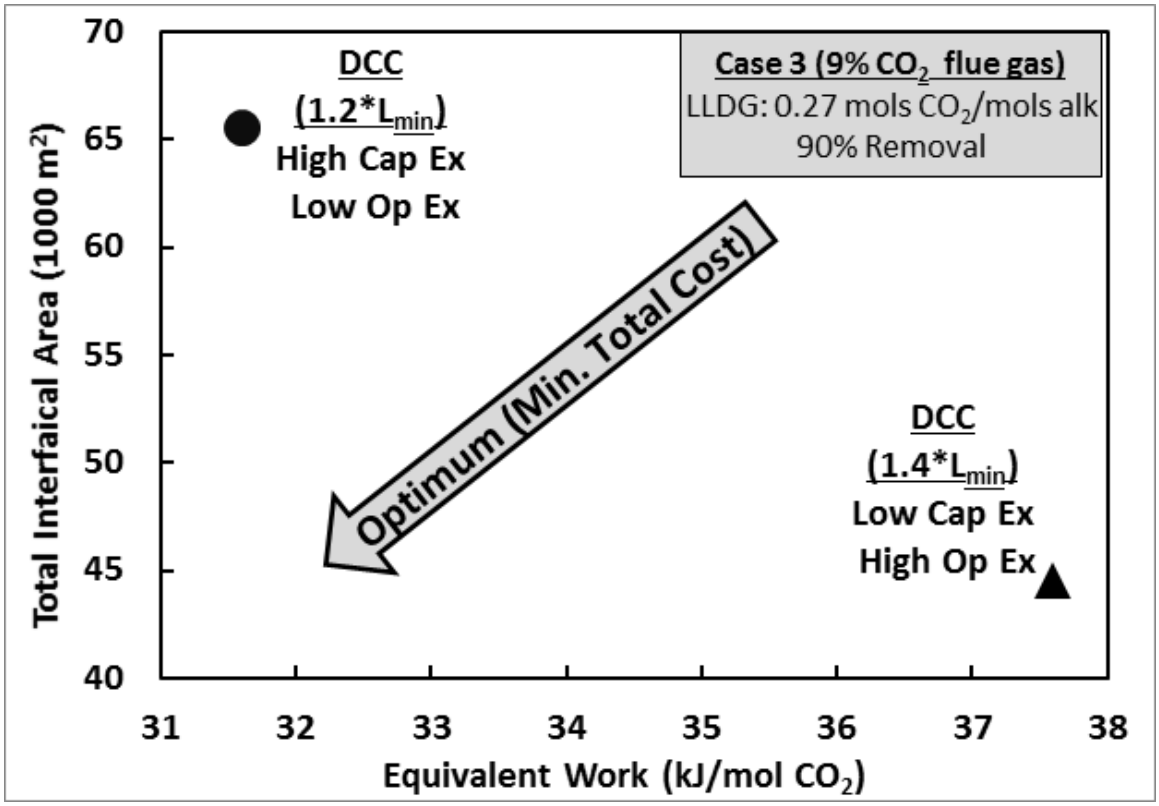

Figure F-16: Capital and operating cost trade-offs in final designs for Case 3 (9% CO_2). Lean loading = 0.27 mols CO_2/mols alkalinity, 90% CO_2 removal, 3:1 recycle ratio for high cap-ex, 2:1 recycle for low-cap-ex, optimum packing split at each point.

References

Astarita, G., 1967. *Mass Transfer with Chemical Reaction.* Amsterdam: Elsevier Publishing Company.

Bhown, A. S. & Freeman, B. C., 2011. Analysis and Status of Post-Combustion Carbon Dioxide Capture Technologies. *Environmental Science and Technology,* pp. 8624-8632.

Bishnoi, S., 2000. *Carbon Dioxide Absorption and Solution Equilibrium on Piperazine Activated Methyldiethanolamine,* Austin: The University of Texas at Austin.

Bourne, J. R. & von Stockar, U., 1974. Gas Absorption with Heat Effects. I. A New Computational Method. *Industrial and Engineering Chemistry,* 13(2), pp. 115-123.

Bravo, J., Rocha, J. & Fair, J., 1985. Mass Transfer in Gauze Packings. *Hydrocarbon Processing,* 64(1), pp. 91-95.

Chen, E. et al., 2013. *Pilot Plant Results with Piperazine.* Kyoto, Japan, November 18-22, 2012., Energy Procedia.

Chen, X., 2011. *Carbon Dioxide Thermodynamics, Kinetics, and Mass Transfer in Aqueous Piperazine Derivatives and Other Amines,* Austin, TX: The University of Texas at Austin.

Cullinane, J. T., 2005. *Thermodynamics and Kinetics of Aqueous Piperazine with Potassium Carbonate for Carbon Dioxide Absorption,* Austin, TX: The University of Texas at Austin.

Cussler, E., 2009. *Diffusion: Mass Transfer in Fluid Systems.* 3rd ed. Cambridge, U.K.: Cambridge University Press.

Danckwerts, P., 1970. *Gas-Liquid Reactions.* New York: McGraw-Hill Book Company.

DeCoursey, W., 1982. Enhancement Factors for Gas Absorption with Reversible Reaction. *Chemical Engineering Science,* 37(10), pp. 1483-1489.

Delaloye, M. M., von Stockar, U. & Xiao-ping, L., 1991. The influence of viscosity on the liquid-phase mass transfer resistance in packed columns. *The Chemical Engineering Journal,* pp. 51-61.

Deutch, J. M. & Moniz, E. J., 2009. *Retrofitting of Coal-Fired Power Plants for CO2 Emissions Reductions: MIT Energy Initiative Symposium,* Boston: Massachusetts Institute of Technology .

Echarte, R., Campana, H. & Brignole, E. A., 1984. Effective Areas and Liquid Film Mass Transfer Coefficients in Packed Columns. *Industrial & Engineering Chemistry Process Design and Development,* pp. 349-354.

Frailie, P., 2014. *Modeling of Carbon Dioxide Absorption/Stripping by Aqueous Methyldiethanolamine/Piperazine,* Austin, TX: The University of Texas at Austin.

Frailie, P. T., Madan, T., Sherman, B. & Rochelle, G. T., 2013. *Energy performance of advanced stripper configurations.* Kyoto, Japan, November 18-22, 2012., Energy Procedia.

Frailie, P. T., Plaza, J. M., Van Wagener, D. H. & Rochelle, G. T., 2011. *Modeling Piperazine Thermodynamics.* Amsterdam., Energy Procedia.

Freeman, S. A., 2011. *Thermal Degradation and Oxidation of Aqueous Piperazine for Carbon Dioxide Capture,* Austin: The University of Texas at Austin.

Glasscock, D. A., 1990. *Modelling and Experimental Study of Carbon Dioxide Absorption into Aqeuous Alkanolamines,* Austin, TX: The University of Texas at Austin .

Hanley, B. & Chen, C.-C., 2012. New Mass-Transfer Correlations for Packed Towers. *AICHE Journal,* pp. 132-152.

Henriques de Brito, M. et al., 1994. Effective Mass-Transfer Area in a Pilot Plant Column Equipped with Structured Packings and with Ceramic Rings. *Industrial and Engineering Chemistry Research,* pp. 647-656.

Hilliard, M. D., 2008. *A Predictive Thermodynamic Model for an Aqueous Blend of Potassium Carbonate, Piperazine, and Monoethanolamine for Carbon Dioxide Capture from Flue Gas,* Austin, TX: The Univeristy of Texas at Austin.

Jackson, R. & Sherwood, T., 1941. Performance of Refinery Gas Absorbers with and without Intercoolers. *American Institute of Chemical Engineers Transactions ,* pp. 959-978.

Karimi, M., Hillestad, M. & Svendsen, H. F., 2011. Investigation of intercooling effect in CO2 capture energy consumption. *Energy Procedia,* Volume 4, pp. 1601-1607.

King, C. J., 1966. Turbulent Liquid Phase Mass Transfer at a Free Gas-Liquid Interface. *Industrial and Engineering Chemistry Fundamentals,* 5(1), pp. 1-8.

Kohl, A. & Nielsen, R., 1997. *Gas Purification.* Houston, TX: Gulf Professional Publishing.

Kvamsdal, H. M., Haugen, G. & Svendsen, H. F., 2011. Flue-gas cooling in post-combustion capture plants. *Chemical Engineering Research and Design,* Volume 89, pp. 1544-1552.

Kvamsdal, H. M. & Rochelle, G. T., 2008. Effects of the Temperature Bulge in CO2 Absorption from Flue Gas by Aqueous Monoethanolamine. *Industrial Engineering and Chemistry Research,* pp. 867-875.

Le Moullec, Y. & Kanniche, M., 2011. Screening of flowsheet modifications for an effcient monoethanolamine (MEA) based post-combustion CO2 capture. *International Journal of Greenhouse Gas Control,* pp. 727-740.

Lin, Y.-J. & Rochelle, G. T., 2014. *Optimization of Advanced Flash Stripper for CO2 Capture using Piperazine.* Austin, TX, Elsevier, pp. 1504-1513.

Madan, T., Van Wagener, D. H., Chen, E. & Rochelle, G. T., 2013. *Modeling pilot plant results for CO2 stripping using piperazine in a two stage flash.* Kyoto, Japan, November 18-22, 2012., Energy Procedia.

Mangers, R. J. & Ponter, A. B., 1980. Effect of Viscosity on Liquid Film Resistance to Mass Transfer in a Packed Column. *Industrial & Engineering Chemistry Process Design and Development,* pp. 530-537.

Massachussetts Institute of Technology, 2015. *Carbon Capture and Sequestration Project Database.* [Online]
Available at: http://sequestration.mit.edu/index.html

Mathias, P. M., Reddy, S. & O'Connell, J. P., 2010. Quantitative evaluation of the chilled-ammonia process for CO2 capture using thermodynamic analysis and process simulation. *International Journal of Greenhouse Gas Control,* pp. 174-179.

National Energy Technology Laboratory, 2010. *Cost and Performance Baseline for Fossil Energy Plants Volume 1: Bituminous Coal and Natural Gas to Electricity,* Washington D.C.: U.S. Department of Energy.

Nielsen, P. T., Li, L. & Rochelle, G. T., 2013. *Piperazine degradation in pilot plants.* Kyoto, Japan, November 18-22, 2012., Energy Procedia.

Norman, W. & Sammak, F., 1963. Gas Absorption in a Packed Column Part 1: The Effect of Liquid Viscosity on the Mass Transfer Coefficient. *Transactions of the Institution of Chemical Engineers,* pp. 109-116.

Olander, D., 1960. Simultaneous Mass Transfer and Equilibrium Chemical Reaction. *A.I.Ch.E Journal,* 6(2), pp. 233-239.

Pacala, S. & Socolow, R., 2004. Stabilization Wedges: Solving the Climate Problem for the Next 50 Years with Current Technologies. *Science,* pp. 928-972.

Peters, M. S., Timmerhaus, K. D. & West, R. E., 2003. *Plant Design and Economics for Chemical Engineers.* Boston: McGraw Hill.

Plaza, J., 2011. *Modeling of Carbon Dioxide Absorption Using Aqueous Monoethanolamine, Piperazine, and Promoted Potassium Carbonate,* Austin, TX: The University of Texas at Austin.

Plaza, J. M., 2011. *Modeling of Carbon Dioxide Absorption using Aqueous Monoethanolamine, Piperazine and Promoted Potassium Carbonate,* Austin: The University of Texas at Austin.

Plaza, J. M., Chen, E. & Rochelle, G. T., 2010. Absorber Intercooling in CO2 Absorption by Piperazine Promoted Potassium Carbonate. *AIChE Journal,* pp. 905-913.

Reddy, S., Johnson, D. & Gilmartin, J., 2008. *Fluor's Econamine FG Plus (SM) Technology for CO2 Capture at Coal-Fired Power Plants,* Baltimore: Fluor.

Rochelle, G. T., 2009. Amine Scrubbing for CO2 Capture. *Science,* pp. 1652-1654.

Romano, G., 1982. *Absorber intercooler.* United States of America, Patent No. US4318872 A.

Sachde, D. J., Chen, E. & Rochelle, G. T., 2013. *Modeling Pilot Plant Performance of and Absorber with Aqueous Piperazine.* Kyoto, Japan, Energy Procedia.

Sachde, D. J. & Rochelle, G. T., 2014. Absorber Intercooling Configurations using Aqeuous Piperazine for Capture from Sources with 4 to 27% CO2. *Energy Procedia,* Volume 63, pp. 1637-1656.

Sachde, D. & Rochelle, G. T., 2014. *CO2 Capture by Aqueous Absorption, First Quarterly Progress Report 2014,* Austin, TX.: Texas Carbon Management Program. The University of Texas at Austin..

Schlunder, E., 1977. On the mechanism of mass transfer in heterogenous systems - in particular in fixed beds, fluidized beds and on bubble trays. *Chemical Engineering Science,* Volume 32, pp. 845-851.

Secor, R. & Butler, J., 1967. Penetration Theory for Diffusion Accompanied by a Reversible Chemical Reaction with Generalized Kinetics. *A.I.Ch.E Journal,* 13(2), pp. 365-373.

Shearer, C., Bistline, J., Inman, M. & Davis, S. J., 2014. The effect of natural gas supply on US renewable energy and CO2 emissions. *Environmental Research Letters,* pp. 1-8.

Song, D. & Rochelle, G. T., 2015. *CO2 Capture by Aqueous Absorption, First Quarterly Progress Report 2015,* Austin, TX: Texas Carbon Management Program. The University of Texas at Austin.

Spraying Systems Co., 2012. *Nozzle Data Sheets.* s.l.:s.n.

Stephenne, K., 2014. *Strat-Up of World's First Commerical Post-Combustion Coal Fired CCS Project: Contribution of Shell Cansolv to SaskPower Boundary Dam ICCS Project.* Austin, TX, Elsevier, pp. 6106-6110.

Tan, C.-S. & Chen, J.-E., 2006. Absorption of carbon dioxide with piperazine and its mixtures in a rotating packed bed. *Separation and Purification Technology,* pp. 174-180.

Taylor, R. & Krishna, R., 1993. *Multicomponent Mass Transfer.* New York: John Wiley and Sons, Inc. .

Thibodeaux, L. J. et al., 1977. Mass Transfer Units in Single and Multiple Stage Packed Bed, Cross-Flow Devices. *Industrial and Engineering Chemistry Research,* 16(3), pp. 325-330.

Thirkell, H., 1971. *Removal of Acidic Gases from Gaseous Mixtures.* Great Britain, Patent No. 3565573.

Tobiesen, F. A., Svendsen, H. F. & Mejdell, T., 2007. Modeling of Blast Furnace CO2 Capture Using Amine Absorbents. *Industrial Enegineering and Chemistry Research,* pp. 7811-7819.

Tsai, R. E., 2010. *Mass Transfer Area of Structured Packing,* Austin: The Univeristy of Texas at Austin.

U.S. Energy Information Administration, 2013. *Electric Power Monthly,* Washington D.C.: U.S. Department of Energy.

U.S. Energy Information Administration, 2014. *Annual Energy Outlook 2014, Early Release,* Washington D.C.: U.S. Department of Energy.

Valerio, S. & Vanni, M., 1994. Interfacial Mass Transfer and Chemical Reaction in Non-Ideal Multicomponent Systems. *Chemical Engineering Science,* 49(19), pp. 3297-3305.

Versteeg, G. F. & van Swaaij, W. P., 1988. Solubility and Diffusivity of Acid Gases (CO2, N2O) in Aqueous Alkanolamine Solutions. *Journal of Chemical Engineering Data,* Issue 33, pp. 29-34.

von Harbou, E., Schmitt, M., Grobmann, C. & Hasse, H., 2013. A Novel Type of Equipment for Reactive Distillation: Model Development, Simulation, Sensitivity, and Error Analysis. *AIChE Journal,* 59(5), pp. 1533-1543.

von Harbou, I., Imle, M. & Hasse, H., 2014. Modeling and simualtion of reactive absorption of CO2 with MEA: Results for four different packings on two different scales. *Chemical Engineering Science,* Issue 105, pp. 179-190.

Walters, M. & Rochelle, G. T., 2012. *CO2 Capture by Aqueous Absorption, Third Quarterly Progress Report 2012,* Austin, Texas: Luminant Carbon Management Program. The University of Texas at Austin Texas.

Walters, M. S., Dunia, R. H., Edgar, T. F. & Rochelle, G. T., 2013. *Two-Stage Flash for CO2 Regeneration: Dynamic Modeling and Pilot Plant Validation.* Kyoto, Japan, November 18-22, 2012., Energy Procedia.

Wang, C., 2015. *Mass Transfer Coefficients and Effective Area of Packing,* Austin, TX: The University of Texas at Austin.

Wang, C., Perry, M., Seibert, F. & Rochelle, G. T., 2013. *Characterization of Novel Packings for Post Combustion Capture.* Kyoto, Japan, November 18-22, 2012., Energy Procedia.

Yin, F. et al., 2000. Experimental Studies of Liquid Flow Maldistribution in a Random Packed Column. *The Canadian Journal of Chemical Engineering,* Volume 78, pp. 449-457.

Ystad Marchioro, P., Bolland, O. & Hillestad, M., 2012. *NGCC and hard-coal power plant with CO2 capture based on absorption.* s.l., Elsevier, pp. 33-44.

Zhang, Y., Sachde, D., Chen, E. & Rochelle, G. T., 2016. *Predicting pilot plant absorber performance for CO2 capture with aqueous piperazine,* Austin, TX: The University of Texas at Austin.

Vita

Darshan Jitendra Sachde was born in El Dorado, Arkansas on October 1, 1982. He graduated from Clear Brook High School in Friendswood, Texas in 2001 before attending the University of Texas at Austin where he earned a B.S. in Chemical Engineering. Following graduation, he worked at Samsung Austin Semiconductor as an equipment engineer before returning to the University of Texas at Austin to complete a dual master's program in Public Policy and Environmental and Water Resources Engineering. Following completion of the dual degree program, he joined Dr. Gary T. Rochelle's research group to pursue his doctoral research in chemical engineering. He has accepted a full-time position with Trimeric Corporation in Buda, TX.

Permanent email: dsach12@gmail.com

This dissertation was typed by the author.